

ASTROPHYSICS AND SPACE SCIENCE LIBRARY 364

Albert Greve
Michael Bremer



Thermal Design and Thermal Behaviour of Radio Telescopes and their Enclosures

AS
SL

 Springer

Thermal Design and Thermal Behaviour of Radio Telescopes and their Enclosures

Astrophysics and Space Science Library

EDITORIAL BOARD

Chairman

W. B. BURTON, *National Radio Astronomy Observatory, Charlottesville, Virginia, U.S.A. (bburton@nrao.edu); University of Leiden, The Netherlands (burton@strw.leidenuniv.nl)*

F. BERTOLA, *University of Padua, Italy*

J. P. CASSINELLI, *University of Wisconsin, Madison, U.S.A.*

C. J. CESARSKY, *E.S.O., Garching bei München, Germany*

P. EHRENFREUND, *Leiden University, The Netherlands*

O. ENGVOLD, *University of Oslo, Norway*

A. HECK, *Strasbourg Astronomical Observatory, France*

E. P. J. VAN DEN HEUVEL, *University of Amsterdam, The Netherlands*

V. M. KASPI, *McGill University, Montreal, Canada*

J. M. E. KUIJPERS, *University of Nijmegen, The Netherlands*

H. VAN DER LAAN, *University of Utrecht, The Netherlands*

P. G. MURDIN, *Institute of Astronomy, Cambridge, UK*

F. PACINI, *Istituto Astronomia Arcetri, Firenze, Italy*

V. RADHAKRISHNAN, *Raman Research Institute, Bangalore, India*

B. V. SOMOV, *Astronomical Institute, Moscow State University, Russia*

R. A. SUNYAEV, *Space Research Institute, Moscow, Russia*

Thermal Design and Thermal Behaviour of Radio Telescopes and their Enclosures

by

Albert Greve

and

Michael Bremer

 Springer

Albert Greve (retired)
Institut de Radio Astronomie
Millimétrique (IRAM)
300 rue de la Piscine
38406 Saint-Martin-d'Hères
Domaine Universitaire de Grenoble
France
greve@iram.fr

Michael Bremer
Institut de Radio Astronomie
Millimétrique (IRAM)
300 rue de la Piscine
38406 Saint-Martin-d'Hères
Domaine Universitaire de Grenoble
France
bremer@iram.fr

Cover Picture: Plateau de Bure 15-m telescopes (France). The telescope in the foreground is partly assembled, the rear cladding and the panels are lacking; the pedestal, fork mount, secondary focus cabin, the CFRP–steel backup structure and the quadripod with subreflector are seen. The telescope in the background has the first generation panels with good specular reflection of visible light. The image in the reflector aperture is the inverted scenery of Plateau de Bure.

ISSN 0067-0057

ISBN 978-3-642-03866-2

e-ISBN 978-3-642-03867-9

DOI 10.1007/978-3-642-03867-9

Springer Heidelberg Dordrecht London New York

Library of Congress Control Number: 2009935700

© Springer-Verlag Berlin Heidelberg 2010

This work is subject to copyright. All rights are reserved, whether the whole or part of the material is concerned, specifically the rights of translation, reprinting, reuse of illustrations, recitation, broadcasting, reproduction on microfilm or in any other way, and storage in data banks. Duplication of this publication or parts thereof is permitted only under the provisions of the German Copyright Law of September 9, 1965, in its current version, and permission for use must always be obtained from Springer. Violations are liable to prosecution under the German Copyright Law.

The use of general descriptive names, registered names, trademarks, etc. in this publication does not imply, even in the absence of a specific statement, that such names are exempt from the relevant protective laws and regulations and therefore free for general use.

Cover design: eStudio Calamar S.L.

Printed on acid-free paper

Springer is part of Springer Science+Business Media (www.springer.com)

Foreword

Every antenna, even those restricted to nighttime operation, is subject to thermal distortion. The greater the degree of surface precision demanded, the greater the relative importance of these distortions. Here again, the usual approximations are likely to be inadequate, and a computer analysis may be necessary. The choice of configuration of the antenna structure should minimize distortions due to temperature differentials in the structure and to changes in the ambient temperature. Consideration should be given to the use of reflective paints, and (for enclosed antennas) to environmental control. Lightweight insulation may be applied in some cases.

H. Simpson (1964)

Four hundred years ago, in 1609, Galileo used an optical telescope to observe the night sky. He saw objects and studied phenomena none had ever seen before. His discoveries mark the beginning of a new era in astronomy that is on the one hand the oldest science, and on the other the one which benefits most from modern technological breakthroughs. Recent examples are the fascinating discoveries made with modern optical telescopes like the Hubble Space Telescope, the ESO Very Large Telescope in Chile and a number of 8 to 10 metre telescopes on Hawaii. Radio astronomy, which exploits the second ‘window’ of the Earth’s atmosphere through which we can observe and study cosmic phenomena, has had since its beginning a similarly revolutionary impact on our picture of the Universe.

The first evidence of cosmic radio signals was found accidentally more than 75 years ago when Karl Jansky detected with his communication antenna unexpected ‘noise signals’ and recognised that they must originate outside the Earth’s atmosphere. Only a few years later, Grote Reber built the first dedicated radio telescope, a parabolic reflector of 10 metre diameter equipped with a receiver for 1.9 metre wavelength. In the short space of time, from this first prototype to today’s radio telescopes, incredible developments have taken place driven by the wish to detect ever

fainter signals, to extend the observations from the longest to the shortest wavelengths observable from the ground, and by the need to increase the angular resolution of radio telescopes by making the single aperture telescopes larger and by constructing multi-element radio interferometers. Today, radio astronomy exploits the entire radio window of the Earth's atmosphere from the microwave region to wavelengths of tens of metres. The ambitious goals of modern radio astronomy pose special challenges to the conceptual design and the construction of the current and future generation of radio telescopes.

Radio astronomy plays a significant role in the study of the Universe. During the early years of radio astronomy one focus was on the non-thermal continuum emission from relativistic electrons that interact with cosmic magnetic fields and emit radiation like the electrons in a synchrotron particle accelerator. Synchrotron radiation is emitted by our own Galaxy and many other galaxies, some of which, the so called radio-galaxies, are particularly bright. Another focus was on the observation (from on 1951) of the hyper-finestructure line of atomic hydrogen at a wavelength of 21 cm. Hydrogen is the most abundant element in the Universe and the observability of this line was predicted in the 1940s. The line carries information about the physical state of hydrogen in our own Galaxy and in different parts of the Universe, and by measuring its radial velocity shift with respect to the rest wavelength it also allows to derive kinematical information and from this, together with a galaxy model, structural information. As a result, the first three-dimensional model of our own Galaxy was constructed.

With the extension of observations to shorter wavelengths, five other emission processes became observable, namely (1) the *free-free emission* from thermal electrons in ionised regions around hot young stars, (2) the *recombination lines* that are emitted when ionised hydrogen atoms capture free electrons and become neutral, (3) the *cosmic microwave background radiation* as a relic from the 'big bang', (4) the *rotational lines* from a multitude of molecules that exist in space, in particular in star forming regions, but more generally in 'cold' parts of the Universe where the temperature is only tens to a few hundred degrees above absolute zero. This is the temperature range in which (5) *cold dust particles emit strongly by re-radiating energy* originally produced at much shorter wavelengths of the optical and ultraviolet domain, but which is strongly absorbed by the dust.

These examples suffice to explain why radio astronomy has made many impressive discoveries since its beginning more than 50 years ago and why much effort has been spent by scientists, engineers and technicians to build ever more powerful telescopes, and more sensitive receivers and spectral backends that allow to analyse cosmic radio signals in great detail. With projects like the Atacama Large Millimeter Array (ALMA) the field will see another giant step forward at the shortest wavelengths accessible from the ground, and with the Square Kilometer Array (SKA) that is currently in its conceptual design phase another step forward will be made at the long wavelength end of the radio window.

The present book is about radio telescopes, and more specifically about their thermal design and behaviour and that of their enclosures where it applies. In addition to gravity that influences the shape and possible deformations of large mechanical

structures, the response to environmental influences determines the quality of a radio telescope. Among these, thermal influences caused by varying solar irradiation, by day-to-night temperature changes and by seasonal variations are the most severe factors, together with strong and time-variable wind loads, that can occur.

The authors belong to the small group of scientific experts who have focused on the theoretical and practical treatment of thermal influences on modern radio telescopes and their enclosures. They have developed and applied techniques that allow to model a telescope structure with all its major components under the influence of realistic environmental conditions. From these computer models they are able to predict the response of a telescope to changing environmental conditions. This helps to check in advance whether a given design concept will meet the specifications within the tolerances that allow to carry out the observations for which a telescope is built.

The authors' approach is unique by combining theoretical and modelling concepts with a large collection of relevant telescope data, in particular a large amount of temperature measurements from existing telescopes. A full chapter is devoted to the measured thermal behaviour of radio telescopes and the authors illustrate in very practical terms how much the modelling helps to predict the actual thermal behaviour both at component and at system level and how far model calculations can help to understand the observed phenomena. The detailed discussion is based on a unique database that the authors have been able to compile because of their involvement in many different projects. Such information is usually very difficult to find because it tends to be hidden in internal technical reports, produced either in institutes or in industry.

The insight that the reader can gain from this comprehensive approach to the thermal design and thermal behaviour of radio telescopes will benefit the scientist and the engineer, both in academia and in industry, who think about the next generation facilities. At the beginning there must always be a set of clearly defined scientific goals that cannot be reached with any of the existing facilities, and that are considered to be of fundamental importance both by the scientific community and by the potential funding agencies. The top priority science goals can be translated into a set of scientific requirements (e.g. wavelength range to be covered, sensitivity limit to be reached, angular resolution to be achieved etc.) which in turn are translated into technical specifications for which the new facility must be designed. These critical performance criteria ultimately determine the design concepts, the choice of materials, the location where the new facility will be operated etc. and, last but not least, the total cost. The better the interdependence between these parameters is understood – and thermal behaviour is among these aspects – the more realistic can a new facility be planned, costed and built.

In addition, the insight that the reader can gain from this study of thermal design and behaviour of radio telescopes will benefit scientists and operators of existing facilities. Many, if not all, of the radio telescopes that are currently in operation underwent significant improvements beyond their original specifications during the years that followed their commissioning. This is due to a long-term monitoring of the mechanical performance and the reactions to the actual environmental conditions,

and a better understanding of the reasons for change. In many places this is a continuous effort that is, of course, not limited to the telescope but includes other components like receivers and backends as well.

The methods described in this book and illustrated with specific examples, and the thermal data that have been collected, are primarily orientated towards radio telescopes. They are, however, also of interest for the design and construction of deep space communication antennas, and even for the design and construction of current generation large and next generation extremely large optical telescopes and their enclosures. Scientists and engineers involved in these projects will, in my view, also benefit from the material that the authors have collected and well documented in this book.

Michael Grewing
St.Martin d'Hères, March 2009

Preface

The success of radio astronomy – especially microwave radio astronomy – and the possibility of communicating with spacecrafts far away in the planetary system is among others due to the construction of radio telescopes and antennas¹ with good beam quality and pointing stability. The design and construction of telescopes has to consider and to suppress, as far as possible, the degrading effect of gravity, temperature and wind. Gravity is a quasi-static force that can be handled exactly in finite element calculations and considered correctly in the construction and operation of a telescope. The influence of gravity does usually not involve a loss in observing time, although perhaps causing some unavoidable degradation of telescope performance as for instance experienced in the gain elevation dependence of a radio telescope. Through contact with the thermal environment a telescope is influenced by temperature changes that may result in thermal deformations of the structural components. Thermal deformations can be calculated with good precision and sometimes compensated in the case the instantaneous temperature distribution throughout the telescope structure is known from measurements or calculations. However, in practice this is usually not the case and direct measures of thermal control are taken through application of white paint, insulation and in some cases ventilation and climatisation. This may help to a large extent although a full thermal control is seldom achieved, especially for open-air telescopes. In several cases this has led to radome or astrodome enclosed radio telescopes. There seems to occur, generally, some loss in observing time due to a telescope's uncontrolled thermal behaviour. An open-air telescope (or even a ventilated telescope in a radome) is in addition exposed to wind forces. While the effect of simulated wind loads can be predicted with good success from finite element calculations, a real time control of wind influences has hardly been tried. Dependent on the characteristics of the observatory site, the loss in observing time due to wind can therefore be high. Finally, the influences of gravity, temperature and wind must be compared to the variability of the atmosphere that is

¹ Astronomy uses the term radio telescope, communication technology the term antenna. The construction of radio telescopes and communication antennas is similar. From our background and the presented examples we speak about radio telescopes, without preference for one or the other term.

today beyond active control in single-dish radio observations. The table summarizes these effects.

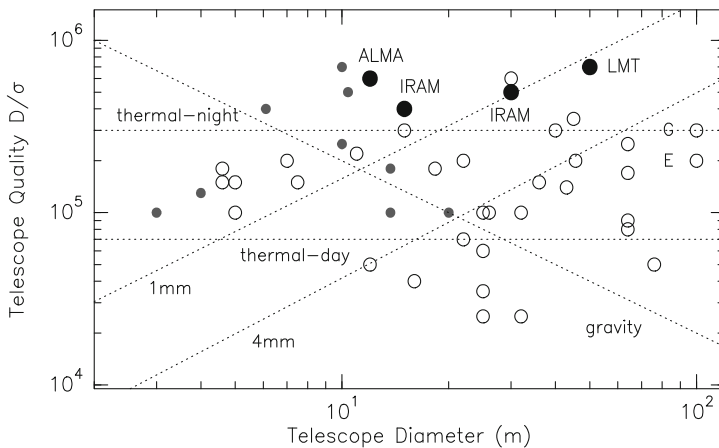
Forces acting on a Telescope (and Enclosure).

Influence/ Force	Time Variability	Components	Loss of Observing Time
Gravity	quasi-static	gravity	negligible
Temperature	slow 1/4 – 3 h	air, wind, sun, sky, ground & internal heat source	some
Wind & Gusts	fast, 1/10 – 10 s	ambient air	important
Atmosphere	fast	temperature, H ₂ O vapour, clouds, precipitation	(dominant)

A large variety of telescope constructions exists, ranging from the earlier long-wavelength dipole and meshwire telescopes to modern high precision reflector telescopes for centimetre, millimetre and sub-millimetre wavelength observations. The desired performance of a radio telescope is calculated from electromagnetic diffraction theory, the actual performance of a radio telescope under gravity, temperature and wind is a matter of design and construction, based on experience and calculations. Central in the study of the thermal behaviour of a telescope, and of the protecting enclosure, is the question of the temperature of telescope components, as a function of time, and of the associated structural deformations. Temperature induced deformations of the telescope may lead to a transient performance degradation with a focus and pointing error and a decrease in sensitivity.

The text deals with full aperture reflector radio telescopes and antennas, of which examples are shown in Chapter 1. Full aperture telescopes for observations at centimetre, millimetre and sub-millimetre wavelengths (λ) require a reflector surface precision of $\sigma \lesssim \lambda/16$ (root mean square value), i.e. of approximately 0.02 to 1 mm, and a focus and pointing stability of $\sim \lambda/10$ and $\sim 1/10$ of the beam width, i.e. between approximately 10 to 1 arcsecond. A connected radio interferometer, which consists of several telescopes observing together, needs in addition a phase stability and hence a mechanical stability of a few $\lambda/10$, at least in between calibrations. By taking proper considerations in the design, these fundamental specifications must be realized in the integrated telescope structure. Von Hoerner [1967 a, 1977 a] estimated the limitations in reflector diameter (D) and reflector quality (D/ σ) when affected by elastic deformations due to gravity, temperature and wind. A summary of centimetre- and mm-wavelength telescopes with respect to structural limitations of stress (mass) and temperature induced deformations is shown in the von Hoerner-diagram. With respect to the behaviour of short wavelength radio telescopes, the situation displayed here illustrates the necessity to reduce the influence of the ambient thermal environment.

Ideally, a radio telescope should maintain a uniform temperature in the variable ambient thermal environment. However, depending on the affordable technical



Von Hoerner–diagram. Telescope quality D/σ (D = reflector diameter, σ = surface precision, rms value) and natural limits of gravity and thermal effects, for mm–wavelength (\bullet) and cm–wavelength telescopes (\circ). The lines labelled 1 mm and 4 mm show the relation $\lambda_{\min} = 16 \sigma$. For the limiting relations see von Hoerner [1967 a, 1977 a] and Baars [2007]. G = GBT telescope, E = Effelsberg telescope.

efforts and costs, this condition can be realized only within certain limits. Tolerable departures from temperature uniformity, expressed for instance as the root–mean–square value (rms) of temperature fluctuations or tolerable thermal gradients across the telescope structure, can be estimated from structural finite element calculations. Such calculations and the known thermal behaviour of existing telescopes define the necessity and the design parameters of a thermal control system. The thermal uniformity and structural stability of a telescope may need to be realized by either *passive* thermal control consisting of a choice of materials, paint and insulation or in addition *active* thermal control employing ventilation and/or climatisation (with heated or cooled ventilating air). Some mm–wavelength radio telescopes, in particular those of the earlier generation built from aluminium, are protected by a radome (or astrodome) with a stable internal thermal environment.

The text contains four main topics, i.e. the Basics of Heat Transfer, Thermal Model Calculations, the Thermal Environment and a Collection of Temperature Measurements of telescope structures. It summarizes the progress in thermal engineering and thermal calculations, including the testing phase of the ALMA prototype telescopes in 2005, and is meant to be a sketch of the established *state of the art* at the time of its publication. The design of other large telescope projects is not yet reported in detail.

Heat Transfer Relations. The thermal state of a telescope is determined by heat transfer between its components, the enclosure and the environment. Heat transfer occurs by conduction, convection and radiation. The relevant physical relations are explained in many textbooks, either on the basis of fundamental physics or engineering purposes. With the exception of relatively simple structures of plates and tubes

that can be treated in analytic form for the fundamental processes, the application of the basic relations to large and complex structures like telescopes and enclosures can become very difficult and not treatable in analytic form because of the many interconnected components, complicated geometrical shapes, natural and forced air flow and complex radiation fields. The text explains the modes of heat transfer as necessary for the understanding and modelling of the thermal behaviour of telescopes and their enclosures. This includes, for instance, heat transfer through plates and honeycomb structures as used for reflector panels and walls of enclosures; relations of convective and radiative heat transfer in tube and plate networks as used in reflector backup structures; ventilation and climatisation systems of backup structures, quadripods, focus cabins and fork supports. These relations include the connection of the telescope and enclosure to the time variable thermal environment with wind induced convection, radiative connection of the telescope and enclosure to the cool sky and the warm ground, and the influence of solar radiation.

Thermal Model Calculations. Thermal model calculations can today be made with good precision, allowing detailed exploratory numerical studies. A significant part of a thermal study occurs during the design of a telescope and enclosure. At that time thermal model calculations are made with the intention of deriving representative temperatures of the telescope and enclosure components. From these calculations a prediction can be made of temperature induced structural deformations and compared with the performance specifications. If necessary, in these model calculations passive/active thermal control is studied and modified until the performance criteria are fulfilled. This may lead to the design of insulation and ventilation systems.

Several thermal models are explained in the text. The models refer to structures of increasing complexity, i.e. of increasing mass and increasing surface area, thus requiring an increasing number of thermal nodes.

The Thermal Environment. A telescope interacts with the local thermal environment, unless the influence of the environment is reduced or nearly eliminated by an enclosure, a radome or an astrodome. Each local environment has its own characteristics that can be taken from meteorological data or must be determined from site tests. The characteristics of the environment are taken into account in the design and operation of a telescope and its enclosure. From the large variety of local conditions a selection is made in the text of a low altitude, grassland and forested site (Effelsberg, Germany), of a mountain site (Plateau de Bure, France, and Pico Veleta, Spain) and of a high altitude desert mountain site (Chajnantor, Chile). From the meteorological data several statistical parameters can be derived that define the thermal specifications for design and operation of a telescope and enclosure, either under normal operation conditions or extreme conditions of survival.

Temperature Measurements and Data Sources. Before starting a thermal design, it is helpful to have some knowledge of the actual thermal behaviour of existing telescopes and enclosures and of the thermal environment in which the telescopes operate. Observatory reports containing a large amount of data are occasionally published, some information is found on the internet. The reports provide valuable guidelines for the design, installation, operation and improvement of thermal

equipment, but also recordings of temperatures of telescopes that can be used as basic test data for model calculations of telescope structures. Another source of information exists with the construction firms. This information is often not available and sometimes classified because of proprietary rights. The text collects representative data, as far as accessible, on thermal conditions at observatory sites and on the thermal behaviour of existing telescopes and their enclosures. The collected data are necessarily incomplete and may provide only a limited view of a telescope's thermal behaviour.

Although the text concentrates on radio telescopes for astronomical research, the design and construction and hence the thermal behaviour of Communication and Deep Space antennas is rather similar. Communication and Deep Space antennas can be open-air antennas or radome enclosed antennas. The main difference is the longer wavelength of operation compared to millimetre and sub-mm telescopes and a comparably lower required structural precision and stability.

Literature

The theory of heat transfer, either from the perspective of fundamental physics or engineering application, is published in many textbooks. There are several publications on the measured thermal behaviour of telescope structures and on corresponding model calculations of their static or time-dependent dynamic thermal behaviour. The publications are scattered throughout many journals and often inaccessible observatory reports; the major accessible publications are mentioned. To our knowledge, the only textbook on *Climatic Influences on Antenna Systems* was published by Bairamov et al. [1988, in Russian]; an English translation is not available. A summary of environmental effects on optical telescopes and enclosures was published by Wilson [1999] in *Reflecting Telescope Optics II*.

Albert Greve and Michael Bremer
July 2009

Acknowledgements

Many persons and several institutes and organizations have contributed directly and indirectly, through discussions, with data and requests of participation in thermal projects of radio telescopes.

Meteorological Data were provided by A. Otarola (SEST, VLA site, Chajnantor; ESO and NRAO), R. Rivera (Chajnantor; Chile), S.J.E. Radford (Chajnantor; NRAO and Caltech), D.A. Graham (Effelsberg; MPIfR), the staff of the IRAM observatories at Plateau de Bure (France) and Pico Veleta (Spain); the ALMA Antenna Evaluation Group (VLA site; NRAO and ESO) provided data of the ALMA VLA (NM, USA) test site.

Temperature Measurements were provided by J. Peñalver (IRAM 30-m telescope; IRAM), M. Dan & P. Chaudet (IRAM 15-m telescopes; IRAM), J. Delannoy & R. Dimper (reflector panels and the ‘chimney’ experiment; IRAM), R. Neri (IRAM, France), G. Delgado and the SEST group (Chile), H. Koch & A. Kraus (Effelsberg, MPIfR), the ALMA Antenna Evaluation Group (VertexRSI and AEC prototype antennas, VLA site, USA). Many aspects of temperature measurements of the ALMA prototype antennas were discussed with J. Mangum (NRAO, USA) and J.W.M. Baars (ESO, Germany). We are grateful for the permission from the National Radio Astronomy Observatory (Charlottesville, USA) to use the ALMA prototype telescope data, which were also published in refereed journals. The temperature data of the Onsala, MIT–Haystack and Metsähovi radome were provided by L.E.B. Johansson & B. Hansen (Onsala Observatory, Sweden), A.E.E. Rogers (MIT Observatory, USA), S. Urpo & P. Könönen (Metsähovi Observatory, Finland). F.P. Schloerb (Amherst, USA) drew our attention on the FCRAO telescope data.

The participation in Thermal Aspects of several Telescope Projects provided an overview of current telescope constructions, thermal specifications and engineering solutions, i.e. of the IRAM telescopes at Pico Veleta (Spain) and Plateau de Bure (France), the Heinrich Hertz Telescope at Mount Graham (USA), the Large Millimeter Telescope at Mount Sierra Negra (Mexico, USA), the Sardinia Telescope (Italy), the ALMA AEC prototype telescope (EIE, Italy, and ESO, Germany), the ESA 35-m antenna at Perth (Vertex Antenna Technik, Germany) and the solar telescope project THEMIS (France).

Several Data are taken from Observatory Reports, mostly available on the observatory web-sites. We especially mention the reports by S. von Hoerner (NRAO archive), J. Lamb (Caltech, USA) on the BIMA and OVRO telescopes, the reports by N. Ukita and N. Satou on the NRO telescopes (Japan) and the web-site data of the JCMT telescope. *Astronomy and Astrophysics*, *Radio Science*, *Journal of Infrared and Millimeter Waves*, *IEEE Transactions on Antennas and Propagation*, *IEEE Antennas and Propagation Magazine*, *Infrared Physics* and *SPIE Conference Publications* gave permission to use some of their published figures and tables. We are pleased with the permission from NRAO, MPIfR, CSO and GMRT to publish pictures of their radio telescopes and the CSO astrodome.

We acknowledge the Discussions with the late B.G. Hooghoudt (The Netherlands), J. Delannoy (IRAM, France), J.W.M. Baars (MPIfR, Germany), H. Kärcher (MAN, Germany), J.L. Casse & J.D. Bregman (Dwingeloo, The Netherlands), N. Ukita (NRO, Japan), S. Busetti (VertexRSI, USA), J.A. Lopez-Perez (OAN, Spain), F. Rampini & S. Stanghellini (EIE, Italy and ESO, Germany), J. Eder & G. Valsecchi (Media-Lario, Italy), D.R. Smith (Merlab, USA) and K. vant Klooster (ESA, The Netherlands).

The Thermal Model Calculations were made with the programme ESACAP (P. Stangerup, Denmark), originally provided by ESA (Noordwijk, The Netherlands), today commercially available.

The interest in the thermal behaviour of radio telescopes started with the participation in the thermal design of the IRAM 30-m telescope, under J.W.M. Baars (MPIfR, Bonn) as project leader. This work was continued at the Institute for Radioastronomy at Millimeter Wavelengths (IRAM, Grenoble, France). IRAM always provided support, time and computer facilities for the mentioned projects.

J. Lamb, J. Mangum and N. Ukita have seen an earlier version of the text, their encouraging remarks stimulated continuation. We are grateful for their help. N. Neininger (formerly at IRAM) and S. Navarro (IRAM) read several chapters and provided clarifying comments.

U. & C. Morton (England) improved the English, we are very grateful for their help.

Especially we mention our long collaboration with J. Peñalver (IRAM, Spain) that advanced significantly the understanding of the thermal behaviour of the IRAM 30-m telescope through installation of temperature sensors and ventilation equipment, temperature monitoring and several dedicated thermal experiments.

Contents

1	Radio Astronomy and Radio Telescopes	1
1.1	Radio Wavelengths and Radio Telescopes	1
1.2	Deep Space Network and Large Communication Antennas	9
1.3	Radio Telescopes in Space	10
1.4	Overview of Telescope Constructions	10
2	Radio Telescope Constructions in View of Thermal Aspects	13
2.1	Optical Configurations	14
2.1.1	The Parabolic Reflector	14
2.1.2	The Cassegrain and Gregory System	15
2.2	Basic Telescope Constructions	19
2.2.1	The Telescope with Alidade Support	20
2.2.2	The Telescope with Pedestal–Yoke Support	22
2.2.3	The Telescope with Pedestal–Fork Support	25
2.3	Telescope Components	29
2.3.1	Reflector Backup Structure (BUS)	29
2.3.2	The Homologous BUS	34
2.3.3	The Open and Closed, Ventilated and Climatised BUS	35
2.3.4	Reflector Panels	38
2.3.5	Active Reflector Surface	42
2.3.6	The Quadripod and Subreflector	43
2.3.7	The Secondary Focus Cabin	43
2.4	The Thermal Design of Radio Telescopes	44
3	Telescope Enclosures	49
4	The Variable Thermal Environment	55
4.1	The Environment and Observatory Sites	55
4.2	The Ambient Air	57
4.3	The Ambient Air Temperature	59
4.3.1	Measured Ambient Air Temperatures	59

4.3.2	Approximation of the Daily Ambient Air Temperature . . .	62
4.3.3	Rate of Ambient Air Temperature Change	64
4.4	Wind Speed and Wind Direction	65
4.4.1	Measured Wind Speeds	65
4.4.2	Wind Speed and Convective Heat Transfer	68
4.5	Ground Temperature	69
4.5.1	Measured Ground Temperatures	69
4.5.2	Approximation of the Ground Temperature	70
4.6	Humidity, Condensation, Icing	71
4.6.1	Humidity and Sky Radiation	73
4.7	Sky Temperature	74
4.7.1	Measured Sky Temperature	75
4.7.2	Calculation of the Sky Temperature	75
4.8	Cloud Coverage	79
4.9	Solar Radiation	79
4.9.1	Measurements of Solar Radiation	81
4.10	Meteorological Design Specifications	82
4.11	Space Environment	83
5	Calculation of Solar Illumination	85
5.1	The Apparent Motion of the Sun	85
5.2	The Plane Surface	88
5.3	The Tube Surface	91
5.4	The Parabolic Reflector Surface	92
5.4.1	Borderline between Shadow and Sunshine	92
5.4.2	Solar Illumination of the Reflector Surface	94
5.5	The Open and Closed BUS	96
5.6	The Box-type Enclosure (Astrodome)	97
5.7	The Cylindrical Enclosure (Astrodome)	98
5.8	The Over-Hemispherical Radome	99
5.9	Manipulation of Insolation through Surface Finish	102
5.10	Sun on Subreflector and Quadripod	104
6	Temperature Measurements and FEM Thermal Deformation	
	Calculations	107
6.1	Electric Resistance Temperature Sensors	108
6.2	Temperature Measurements by Infrared Radiation	110
6.3	Temperature Sampling Rate	110
6.4	Location of Temperature Sensors (Interpolation Matrix and Influence Matrix)	111
6.5	Precision of Temperature Measurements	118
6.6	Prediction of Temperature induced Deformations	118
6.7	Empirical Relations	120
6.8	Temperature related Measurements	120

7	Heat Transfer	123
7.1	Laws of Thermodynamics and Modes of Heat Transfer	123
7.2	Amount of Heat transferred	124
7.3	Heat Content	126
7.4	Heat Transfer by Conduction	127
7.5	Heat Transfer by Convection	130
7.6	Heat Transfer by Conduction and Convection	132
7.7	The Convective Heat Transfer Coefficient (h)	133
	7.7.1 Forced Convection	134
	7.7.2 Natural Convection	138
	7.7.3 Forced Convection and Ventilation	139
	7.7.4 Natural Convection and Ventilation	140
7.8	Radiative Heat Transfer	141
7.9	Heat Transfer by Conduction, Convection and Radiation	145
7.10	Radiative Nodes and View Factors	146
	7.10.1 Radiative Nodes	146
	7.10.2 View Factor Relations	148
	7.10.3 Internal View Factors	149
7.11	Energy/Heat Conservation	152
7.12	The Steady and Non–Steady Thermal State	155
	7.12.1 External Thermal Time Constant τ_{ext}	155
	7.12.2 Internal Thermal Time Constant τ_{int} (Conduction)	159
8	Radiative Coupling towards Sky and Ground (External View Factor)	161
8.1	Vertical and Horizontal Walls	163
8.2	The Radome and Astrodome	165
8.3	The Parabolic Reflector	166
8.4	The Open and Closed BUS	170
9	Measured Thermal Behaviour of Radio Telescopes	173
9.1	Telescope Supports	174
	9.1.1 The Pedestal	174
	9.1.2 The Alidade	178
	9.1.3 The Fork Support	186
	9.1.4 Path Length Variations of Telescope Supports (for radio interferometer and VLBI arrays)	192
9.2	BUS Supports	196
	9.2.1 The (climatised) Yoke	197
	9.2.2 The Central Hub	199
9.3	Backup Structures (BUS)	203
	9.3.1 The Open BUS	206
	9.3.2 The Closed BUS	209
	9.3.3 The Ventilated BUS	216
	9.3.4 Radial and Circular Ventilation	220

9.3.5	The Climatised BUS (IRAM 30–m Telescope)	222
9.3.6	Thermal Deformations and Active Reflector Surfaces	225
9.3.7	The Radome/Astrodome enclosed BUS	226
9.3.8	Temperature Changes of the BUS and Focus Changes	231
9.4	Panels	232
9.4.1	Experimental Data of Panel Temperatures	233
9.4.2	Panel Temperatures measured on Telescopes	234
9.4.3	Thermal Panel Buckling	234
9.4.4	Heated Panels, De–icing of Panels	239
9.5	Quadripod, Subreflector, Focus Cabins	242
9.5.1	Quadripod	242
9.5.2	Subreflector	246
9.5.3	Focus Cabins	247
9.6	Observations in the Direction of the Sun	248
9.7	De–icing of a Telescope	250
9.8	Measured Temperature Uniformity of Radio Telescopes	251
9.9	The measured Thermal Behaviour of Telescopes	255
9.10	Temperature Monitoring and Trouble–Shooting	258
9.11	Other Thermal Effects	261
10	Measured Thermal Behaviour of Enclosures	263
11	Thermal Model Calculations	267
11.1	Mechanical Models of Structural Components	268
11.2	Static Thermal Calculations (The Use of Known Temperature Distributions)	271
11.3	Dynamic Thermal Model Calculations (The Derivation of Temperature Distributions)	271
11.4	Node Structure of Thermal Models	273
11.5	The Thermal Environment as Input Data	274
11.6	Models of Panels	275
11.7	Model of Telescope Supports	279
11.7.1	Model of an Alidade	279
11.7.2	Model of a Yoke	281
11.7.3	Model of a Fork Support	282
11.8	Model of a Backup Structure	288
11.8.1	Model of an Open BUS	289
11.8.2	Model of a Closed BUS with Natural Ventilation	290
11.8.3	Model of a Closed BUS with Forced Ventilation	291
11.9	Model of a Radome and Closed Astrodome	297
11.10	Servo–loop Controlled Ventilation/Heating/Cooling	299
11.11	Model Calculations and Energy Balance	300
11.12	Model Calculations for Operational Purposes	302
11.13	Precision of Model Calculations	303
11.14	Programmes for Model Calculations	304

- 12 Beam Formation and Beam Degradation** 305
 - 12.1 Wave Propagation and Beam Formation 305
 - 12.2 The *Perfect* Radio Telescope 308
 - 12.3 The Beam Pattern of the *Perfect* Radio Telescope 311
 - 12.4 The *Real* Radio Telescope 313
 - 12.4.1 Systematic Wavefront Deformations 313
 - 12.4.2 Repetitive Wavefront Deformations
(Thermal Panel Buckling) 316
 - 12.4.3 Random Wavefront Deformations 318
 - 12.5 Superposition of Random and Systematic (Thermal) Deformations 321
 - 12.6 Beam Deformations and Thermal Tolerances 322

- 13 Thermal Tolerances** 325
 - 13.1 Global Estimates of Temperature Influences 326
 - 13.1.1 Reflector Diameter Estimates 327
 - 13.1.2 Estimated Thermal Behaviour of a BUS 328
 - 13.1.3 Estimated Thermal Behaviour of an Alidade/Fork Support 330
 - 13.1.4 Estimated Thermal Behaviour of Panels 331
 - 13.2 System Alignment Tolerances 331
 - 13.2.1 Displacements and Tilts of Main Reflector and
Subreflector 331
 - 13.2.2 Temperature induced Pointing Errors 335
 - 13.2.3 Alignment Errors: Temperature Tolerance Estimates 336
 - 13.3 Random Reflector Errors 337
 - 13.4 Design Specifications and Error Budget 340

- 14 Optical Telescopes and Enclosures** 343

- 15 A Summary and Further Studies** 347
 - 15.1 A Summary of the Present State 347
 - 15.2 Temperature Measurements and Dynamic Thermal Models 348
 - 15.3 Further Studies 349
 - 15.4 A Dynamic Thermal Error Budget for Design 352
 - 15.5 A Fundamental Investigation of Radio Telescope/Antenna
Constructions 353
 - 15.6 Future Design 355

- A Units and Fundamental Constants** 357

- B Average Value, Root–Mean–Square Value (rms)** 361

- C Pointing Model** 363

- D Zernike Polynomials** 367

- Picture and Graphic Credits** 369

References 373

Indices 383

 Historical Names Index 384

 Author Index 385

 Book Index 388

 Subject Index 389

Acronyms

AZ	Azimuth
BB	Black Body (radiation)
BUS	Backup Structure
CFRP	Carbon Fiber Reinforced Plastic
CTE	Coefficient of Thermal Expansion
DOF	Degrees Of Freedom
EL	Elevation
FBA	Flexible Body Analysis
FEA	Finite Element Analysis
FEM	Finite Element Model
FWHP	Full Width Half Power
HC	Honeycomb (panel)
TM	Trademark
VLBI	Very Long Baseline Interferometry

Telescopes, Observatories, Organizations.

Abbreviation		Country
Radio Telescope		
ALMA	Atacama Large Millimeter Array	Chile
APEX	Atacama Pathfinder Experiment	Chile
ASTE	Atacama Submillimeter Telescope Experiment	Chile
BIMA	Berkeley–Illinois–Maryland Association Millimeter Array	USA
CARMA	Combined Array for Research in Millimeter–Wave Astronomy	USA
CCAT	Cornell Caltech Atacama Telescope	Chile
CSO	Caltech Sub–Millimeter Observatory	Hawaii
Effelsberg	Max Planck Institute for Radioastronomy	Germany
FCRAO	Five College Radio Astronomy Observatory	USA
GBT	Green Bank Telescope	USA
GMRT	Giant Metre–Wave Telescope	India
HHT (SMT)	Heinrich Hertz Telescope	USA
JCMT	James Clerk Maxwell Telescope	Hawaii
Kitt Peak	National Radio Astronomy Observatory	USA
LMT/GTM	Large Millimeter Telescope/ Gran Telescopio Millimetrico	Mexico
LOFAR	Low Frequency Array	The Nether– lands, Germany
MERLIN	Multi–Element Radio Linked Interferometer Network	England
NMA	Nobeyama Millimeter Array	Japan
NOTO	NOTO Radio–Astronomy Observatory	Italy (Sicily)
OVRO	Owens Valley Radio Observatory	USA
PV	Pico Veleta IRAM 30-m Radio Telescope	Spain
PdB	Plateau de Bure IRAM Interferometer	France
RT-70	Russian 70-m Radio Telescope	Russia
SEST	Swedish ESO Sub–Millimeter Telescope	Chile
SKA	Square Kilometre Array	
SMA	Sub–Millimeter Array	Hawaii
SRT	Sardinia Radio Telescope	Italy
VLBA	Very Long Baseline Array	USA
VLA	Very Large Array	USA
Optical Telescope		
CFHT	Canada France Hawaii Telescope	Hawaii
ELT	Extremely Large Telescope	ESO–Germany
MMT	Multi–Mirror Telescope	USA
NTT	New Technology Telescope	Chile
VLT	Very Large Telescope	Chile
Organisations		
ESO	European Southern Observatory	Germany/Chile
IRAM	Institut de Radioastronomie Millimétrique	France/Spain
JPL	Jet Propulsion Laboratory	USA
MIT	Massachusetts Institute of Technology	USA
MPIfR	Max Planck Institute for Radioastronomy	Germany
NRO	National Radio Observatory	Japan
NRAO	National Radio Astronomy Observatory	USA

Chapter 1

Radio Astronomy and Radio Telescopes

1.1 Radio Wavelengths and Radio Telescopes

An astronomical object somewhere in the Planetary System, the Galaxy, a Cluster of Galaxies or far out in the Universe may generate radio waves by one or the other physical process (a topic of *Astrophysics*). If the radio emission is generated inside the object, some of the radio waves propagate through the object until they may leave the radio source at its surface (*Radiative Transfer*). The emitted radio waves then propagate through the intergalactic, interstellar and interplanetary space (*Radiation Propagation*) and finally through the Earth's atmosphere (*Atmospheric Physics*). On the way through space and the Earth's atmosphere the radio waves are more or less severely absorbed and deflected from a straight path (*Atmospheric Physics, Refraction*). In addition, the orientation of polarization of the radio waves may be rotated (Faraday rotation) in a medium with free electric particles anywhere located along the path of propagation. Finally, the radio waves are collected by the radio telescope (*Radio Optics*), detected by the receiver (*Radio Electronics*) and analysed and recorded in the spectrometer and computer (*Data Acquisition*).

Radio Astronomy is interested in the detection, localization and analysis of radiation emitted from celestial objects. A radio telescope used for this purpose is an instrument that collects and detects electromagnetic radiation from a certain area and direction in the sky, allowing to make a calibrated measurement (either of total power or amplitude and phase) or a calibrated image of the object. The electromagnetic radiation observed in ground-based radio astronomy covers the radio window with wavelengths from several metres, say 10 m (= 30 MHz), to a fraction of a millimetre, say 0.3 mm (= 1000 GHz). The Earth's ionosphere reflects the incident electromagnetic radiation at the long wavelength end of the radio spectrum (say below 30 MHz); clouds, water vapour, O₂ and other molecules of the Earth's atmosphere absorb significantly the incident electromagnetic radiation at the short wavelength end (say above ~ 50 GHz). Since a radio telescope must be many wavelengths in diameter in order to collect a useful amount of energy and to provide a good directivity (angular resolution), it is evident that telescopes for metre wavelengths have dimensions of many 10 metres to several 100 metres, or even kilometres, while telescopes for millimetre/sub-millimetre wavelengths have dimensions of several metres to several 10 metres. Evidently, the mechanical

construction of telescopes for metre and millimetre wavelengths is different. Telescopes for m-wavelengths can be constructed as dipole and mesh-wire networks and plate arrays, cm-wavelength and mm/submm-wavelength telescopes are mostly full-aperture solid surface parabolic reflector telescopes. Typical examples of metre, centimetre and short cm-wavelength telescopes are the 45-m telescopes of the GMRT – Array¹ (India) and the Effelsberg and GBT 100-m telescopes (Germany, USA), typical examples of mm/submm telescopes are the IRAM 30-m and 15-m telescopes (Spain, France), the 10-m CSO and 12-m APEX telescopes (Hawaii, Chile) and the 12-m telescopes of the ALMA array (Chile). Despite the diversity of mechanical construction, the telescopes can be understood from basic principles of electromagnetic radiation, optics, diffraction, reception and detection. However, in context of thermal considerations a mesh-wire panelled long wavelength telescope behaves very differently from a compact and solid surface panelled high precision telescope for mm/submm wavelengths.

Table 1.1 gives a subdivision of the radio spectrum, the corresponding principal radiation processes occurring in astronomical sources, and the type of telescope used in the respective wavelength region. A few operational telescopes are mentioned, telescopes under construction are in brackets.

A few radio telescopes are shown to illustrate their construction.

Picture 1.1 shows one of the GMRT 45-m telescopes (Pune, India, altitude 650 m) used for m-wavelength interferometer observations. The telescopes have an open structure. The construction consists of a pedestal with fork, which carries the reflector and the quadripod. Because of the long wavelength of observation and the location at a site without snow and ice, the reflector surface is made of mesh wire.

Picture 1.2 shows the Effelsberg 100-m telescope (Germany, 320 m altitude) used for observations at short cm-wavelengths (and VLBI observations at 3 mm); it is an open structure. However, the shorter wavelength of observation requires a surface precision of ~ 0.5 mm that is achieved by using aluminium honeycomb panels (inner part, today replaced by aluminium plate panels reinforced with ribs) and perforated plate and mesh wire panels (outer part) on a homologous reflector backup structure. The perforated panels provide a relatively smooth aerodynamic transition from a solid surface to the ambient air. The reflector and the backup structure are supported on an alidade. In order to reduce thermal influences, and in particular insolation, the complete telescope is painted white with TiO₂ paint. (The blue painted base frame of the alidade was used during the early years of operation.)

Picture 1.3 shows the GBT 100-m telescope at Green Bank (USA, WVA, 840 m altitude) for short cm-wavelength observations (and 3 mm). This telescope is an off-axis Gregory telescope with a single subreflector support arm. Otherwise it is an open structure with solid surface panels and painted white as most cm-wavelength telescopes. The backup structure and the reflector are supported on an alidade.

¹ Abbreviations of observatory and telescope names are used. See the list of Acronyms for explanations.

Table 1.1 Radio Spectrum – Radiation Processes – Radio Telescopes.

Spectral Range ^{a)} Wavelength (λ)/ Frequency (ν)	Radiation Processes (Astronomical Source)	Telescope Type	Radio Telescope ^{b)}
m-waves 1 m $\lesssim \lambda$ $\nu \lesssim 300$ MHz	Synchrotron Radiation Free-free Radiation	Non-filled (Non-steerable) Dipole/Wire Arrays	[SKA, LOFAR]
cm-waves 1 m – 1 cm 300 MHz – 30 GHz	Synchrotron Radiation Free-free Radiation Lines (H, OH, NH ₃ , H ₂ O ...)	Transit Telescopes, Full Aperture Reflector Telescopes (Cassegrain/ Gregory Systems) Interferometer Arrays	Effelsberg, GBT VLA, MERLIN VLBA
mm-waves 7 mm – 1 mm 40 GHz – 300 GHz	Free-free Radiation Radiation from Dust Molecular Lines (CO, CS, SiO, HCN, HCO ⁺ , C ₂ H ₄ ...) Cosmic Background Radiation	Full Aperture Reflector Telescopes (Cassegrain) Interferometer Arrays	IRAM, [LMT/GMT] CARMA
Submm-waves $\lambda \lesssim 1$ mm 300 GHz $\lesssim \nu$	Free-free Radiation Radiation from Dust Molecular Lines Atomic Lines Cosmic Background Radiation	Full Aperture Cassegrain Telescopes Interferometer Arrays	JCMT, CSO SMA, [ALMA]

^{a)} approximate limits.

^{b)} see list of Acronyms of observatory sites.

Picture 1.4 shows the IRAM 30-m telescope (Spain) for mm-wavelength observations. Because of the higher surface precision (0.1 mm) and pointing precision at mm-wavelengths, because of its location at an exposed site at 2 900 m altitude, and because being built of steel, the telescope is fully insulated and equipped with a climatisation system which provides thermal stability. The telescope is therefore fully closed. The telescope has a pedestal and yoke mount. Because of occasionally severe winter conditions at this site, the telescope surfaces (panels, backup structure rear side, yoke, quadripod, subreflector) can be heated to prevent icing.

Picture 1.5 shows the fork-supported VLA 25-m telescopes (USA, NM, 2125 m altitude) for short cm-wavelength observations. The telescopes have a relatively high pedestal, a wide fork support (for a broad counterweight) and an open backup structure. The telescopes can be displaced on a transporter.

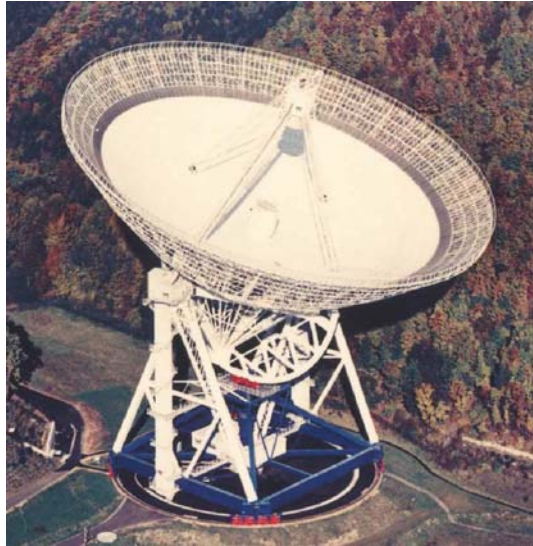
Picture 1.6 shows the SEST 15-m telescope for 3 to 1 mm-wavelength observations, located at 2 300 m altitude on La Silla (Chile)². The telescope structure is closed and heating prevents icing of the panels, the quadripod and the subreflector. The covered backup structure is made of CFRP and steel tubes. The telescope is shown as an example of a construction in which the reflector is attached to the

² The telescope has been taken out of operation.

secondary focus cabin, which is supported on a fork mount. Identical telescopes, though mounted on a movable transporter, are used in the IRAM interferometer array, located at 2500 m altitude in the French Alps (*Picture 1.7*). The mass of the telescopes is relatively small (125 ton) to allow displacement on the tracks to other interferometer stations.



Picture 1.1 GMRT 45-m telescope (Pune, India) [Courtesy National Centre for Radio Astrophysics, Tata Institute of Fundamental Research, India].



Picture 1.2 Effelsberg 100-m telescope (Germany) [Courtesy R. Schwartz, MPIfR Bonn, Germany].



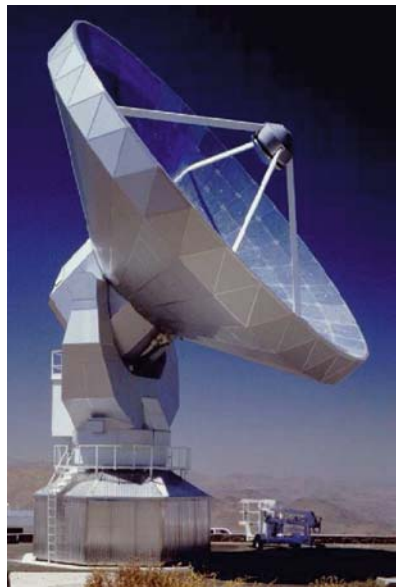
Picture 1.3 Green Bank (GBT) 100–m telescope (WVA, USA) [Image Courtesy of NRAO/AUI/NSF].



Picture 1.4 IRAM 30–m telescope (Pico Veleta, Spain) [Image Courtesy of IRAM, Spain].



Picture 1.5 VLA 25-m telescope (NM, USA) [Image Courtesy of NRAO/AUI/NSF].



Picture 1.6 SEST 15-m telescope (La Silla, Chile) [Courtesy Onsala Observatory, Sweden].

The material of this text concentrates on full aperture parabolic reflector radio telescopes. These radio telescopes are similar to the earlier developed optical reflector telescopes [King 1955, Schroeder 1987, Wilson 1999] and use in particular the Cassegrain (or Gregory) configuration of a parabolic main reflector and a hyperbolic (or elliptical) subreflector [Love 1978, Christiansen & Högbom 1985, Kraus 1986,



Picture 1.7 Plateau de Bure Interferometer (French Alps, 2 500 m altitude). The telescopes can be displaced on the tracks (partially covered by snow) to form various interferometer configurations. At the centre of the observatory is a hangar that can house up to three telescopes for maintenance purposes [Courtesy IRAM, France].

Baars 2007]. In these telescopes is the image of a point-like or extended astronomical object formed at the secondary focus near the vertex of the main reflector where the receiver, or receiver-array, is installed. Most full aperture radio telescopes are steerable in azimuth (AZ) and elevation (EL) direction and able to observe in any direction of the visible hemisphere, with the facility of tracking, scanning and mapping of an object.

Dependent on the electromagnetic diameter of a telescope $\mathcal{D} = D/\lambda$ (D = diameter of the reflector, λ = wavelength of observation), there are several theories for calculation of the imaging properties of a radio telescope or an optical telescope. For the IRAM 30-m radio telescope, as an example, with reflector diameter $D = 30$ m and observation at the wavelength $\lambda = 1.3$ mm, the value is $\mathcal{D} = 30 \text{ m}/1.3 \text{ mm} = 2.3 \times 10^4$. For the ESO VLT optical telescopes, as an example, with mirror diameter $D = 8$ m and observation at the wavelength $\lambda = 0.5 \mu\text{m}$, the value is $\mathcal{D} = 8 \text{ m}/0.5 \mu\text{m} = 1.6 \times 10^7$. As summarized in Table 1.2, generally there is a difference of a factor ~ 1000 in the electromagnetic diameter \mathcal{D} of optical telescopes and centimetre and mm-wavelength single-dish radio telescopes. While the properties of optical telescopes can be understood, to a large extent, from Geometrical Optics with ray tracing and spot diagrams [Born & Wolf 1980, Schroeder 1987, Wilson 1999], this is not at all the case for radio telescopes of which the properties can only be understood from Physical Optics, Antenna Diffraction Theory and Gaussian Optics [Silver 1984, Rush & Potter 1970, Love 1978, Goldsmith 1982, Lo & Lee 1988]. As

a consequence of diffraction, the most prominent characteristic of a single-dish radio telescope, and to some extent also of a connected radio interferometer, is the considerable beam size (point spread function) that significantly blurs an image, even of a point-like radio source.

Table 1.2 Electromagnetic Reflector Diameter and Surface Precision.

Telescope (Country) ^{a)}	Reflector Diameter [m]	Wavelength (λ)/ Frequency (ν) ^{b)} [mm]/[GHz]	Electromagnetic Diameter $\mathcal{D} = D/\lambda$ [$\mathcal{D}/1000$]	Reflector Quality $Q = D/\sigma$ ^{b)} [$Q/1000$]
Radio Telescope				
Arecibo (USA)	300	60/5	5	200
Effelsberg (Germany)	100	10/30	10	150
Nobeyama (Japan)	45	3/100	15	400
IRAM (Spain)	30	1.3/230	23	460
IRAM (France)	15	1.3/230	11	300
JCMT (Hawaii)	15	0.65/460	23	750
CSO (Hawaii)	10	0.37/800	27	500
Optical Telescope				
Palomar (USA)	5	$5 \times 10^{-4}/5 \times 10^{15}$	10 000	100 000
KECK (USA)	10	$5 \times 10^{-4}/5 \times 10^{15}$	20 000	200 000
ELT ^{c)}	~ 50	$5 \times 10^{-4}/5 \times 10^{15}$	100 000	1 000 000

^{a)} see list of Acronyms of observatory sites;

^{b)} approximately shortest wavelength of observation, estimated precision σ ;

^{c)} next generation extremely large optical telescope (see <http://www.eso.org>).

In principle, the electromagnetic performance of a radio telescope can be derived from *Maxwell's* equations or the *Huygens-Fresnel-Silver* formulation of wave propagation [Silver 1984]. However, for many applications in radio astronomy where the object is at a far distance (d) so that the far-field condition

$$D/\lambda^2 = \mathcal{D}/\lambda \ll d \quad (1.1)$$

is fulfilled, it is possible to derive the electromagnetic properties of a radio telescope from the concept of aperture plane and image plane electromagnetic fields in which the *Fourier* transform (**FT**) relates the amplitude-phase distribution $E_{\mathcal{A}}(\mathbf{r})$ in the aperture plane $\mathcal{A}[\mathbf{r}]$ to the amplitude-phase distribution $E_{\mathcal{I}}(\mathbf{u})$ in the focal plane $\mathcal{I}[\mathbf{u}]$, and vice versa. With this concept the calculation of the imaging properties of a radio telescope that observes a far away object is relatively easy

$$E_{\mathcal{I}} = \mathbf{FT}(E_{\mathcal{A}}) \quad (1.2)$$

The *Fourier* transform gives the relation between the telescope diameter and the beam width θ (FWHP)

$$\theta \approx 1.15 \lambda/D = 1.15/\mathcal{D} \text{ [rad]} \quad (1.3)$$

Thus, the larger the diameter of the reflector and the shorter the wavelength of observation, the smaller is the beam width and the higher the spatial resolution, which is proportional to θ . The aim in radio astronomy is the construction of large diameter telescopes that have a small beam width and a large collecting area, i.e. a high sensitivity. For instance a 100-m diameter telescope observing at 2 cm wavelength (15 GHz) has a beam width of ~ 1 arcmin, a 50-m diameter telescope observing at 2 mm (150 GHz) wavelength has a beam width of 10 arcsec.

As illustrated in the von Hoerner diagram (see Preface), there are natural limits in the construction of ever larger single-dish radio telescopes [von Hoerner 1967 a, 1977 a] with higher sensitivities and smaller beam widths. A possibility to overcome the construction limits in order to obtain a high angular resolution of, say, ~ 1 to ~ 0.0001 arcsec is the use of telescope arrays of many smaller telescopes which operate in interferometer mode. There are connected interferometer arrays [which share a common Local Oscillator System] with baselines of several 100 metres to several 10 kilometres, which reach angular resolutions of ~ 1 to 0.1 arcsec, and the Very Long Base Line Interferometer (VLBI) [in which the Local Oscillator Systems are not connected and time and frequency synchronization is obtained from a hydrogen maser and GPS standard (Global Positioning System)] with continental and inter-continental baselines, which reach angular resolutions of ~ 0.0001 arcsec. However, although different in operation and signal processing, the basic elements of interferometer/VLBI arrays are the Cassegrain/Gregory reflector telescopes mentioned above.

A description of the earlier radio telescopes was published by Findlay [1964], Cogdell et al. [1967], Rush [1984] and Kraus [1986]. The construction of the Effelsberg (100-m), IRAM (30-m), HHT (10-m), LMT(50-m) and the ALMA (prototype 12-m) radio telescopes is explained by Baars [2007]. For the ALMA telescopes, see also Mangum et al. [2006] and Wootten & Thompson [2009].

The technique of radio observations with single dish telescopes and interferometer systems, the calibration of measurements and the construction of images is explained in the textbooks *Tools of Radio Astronomy* by Rohlfs & Wilson [1996] and *Interferometry and Synthesis in Radio Astronomy* by Thompson, Moran & Svenson [2001].

1.2 Deep Space Network and Large Communication Antennas

In many technical details is the construction of Deep Space Network Antennas and large Communication Antennas similar to radio telescopes. Typical constructions are the NASA-JPL 34-m and 70-m antennas, pictures are found on the NASA/JPL-websites or in the textbook by Levy [1996]. The antennas are used for signal transmission and signal reception, up to approximately Ka-band at 36 GHz (approximately 8 mm wavelength). The low frequency/wavelength of operation relaxes the mechanical accuracy and hence the thermal specification. Most antennas are painted

white to provide some protection against insolation. Several communication antennas are protected by a radome.

1.3 Radio Telescopes in Space

There are sub-mm wavelength radio telescopes that orbit the Earth, for instance the Odin 1.1-m telescope (120-600 GHz, launched in 2001), the Planck 1.5m telescope (30-860 GHz) and the Herschel 3.5-m telescope (450-5300 GHz), both launched in 2009 (Doyle et al. [2009]). Compared to ground-based telescopes, the diameter of these telescopes is small, however, since the observing wavelength is short their electromagnetic diameter \mathcal{D} is relatively large. The thermal behaviour of a telescope in space is different from those used on the ground, i.e. a telescope in space is subject only to a radiative environment with no convective heat transfer at the outer surfaces. The radiative background is the planetary space (instead of the atmosphere for ground-based telescopes) with an effective radiation temperature of approximately 7 K [Bely 2002]. The insolation is not attenuated as for a ground-based telescope; in a low orbit the telescope in space may experience a frequent change between solar illumination and night.

1.4 Overview of Telescope Constructions

The various telescope constructions illustrated in the Pictures 1.1 to 1.6 can be summarized in three basic sketches, shown in Fig. 1.1.a to Fig. 1.1.c. The designation of the telescope components is inserted for easier orientation in the following discussions.

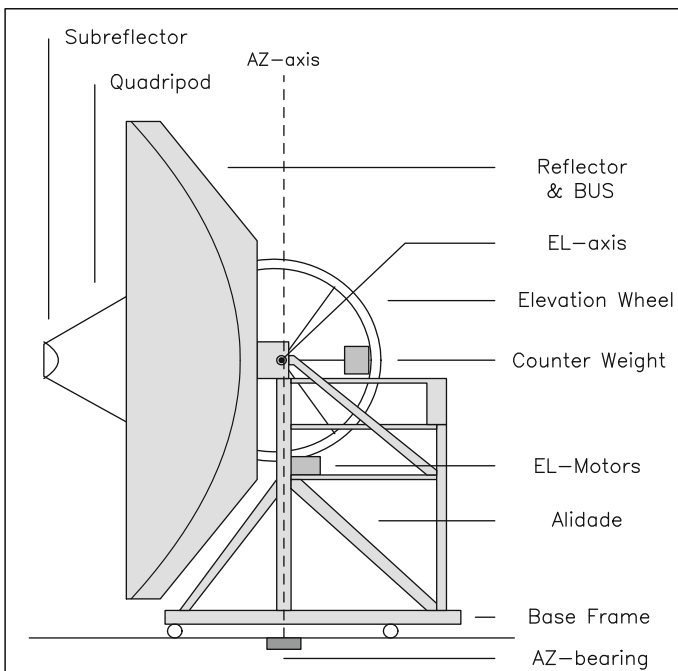


Fig. 1.1.a Alidade supported radio telescope.

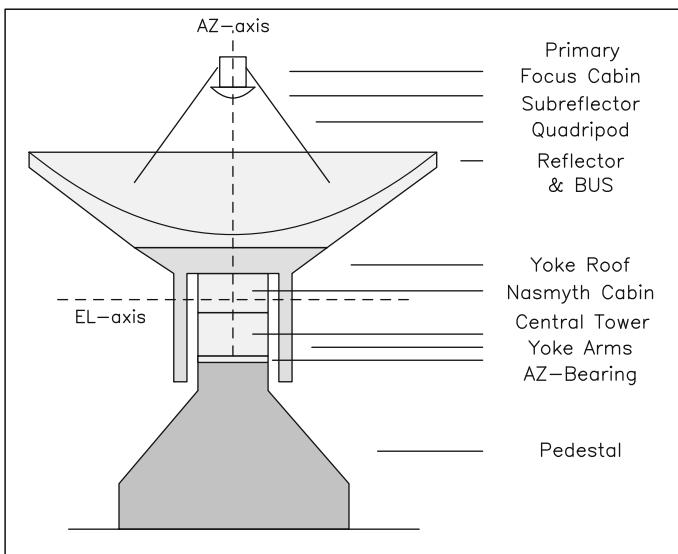


Fig. 1.1.b Pedestal-Yoke supported radio telescope.

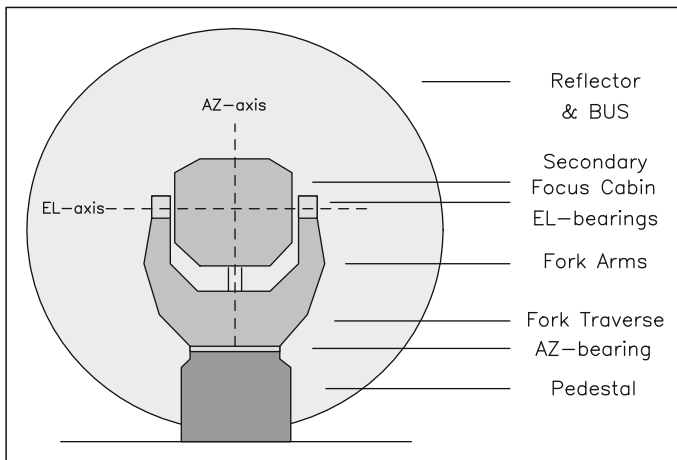


Fig. 1.1.c Pedestal-Fork supported radio telescope.

Chapter 2

Radio Telescope Constructions in View of Thermal Aspects

A radio telescope operates with good performance if all relevant structural components remain stable for a considerable period of time. Adverse influences may arise from gravity, temperature and wind. They affect the focus, the pointing, the reflector surface and the path length. Corrections can be made from pointing and focus measurements that may however consume a substantial part of the observing time. Telescopes with active main reflector or subreflector surface can, in addition, upgrade the performance from temperature monitoring and/or metrology measurements and subsequent real time actuator control¹.

With f the focal length of a telescope, $\theta = 1.2 \lambda/D$ the beam width (D = reflector diameter, λ = wavelength of observation), σ (rms value)² the reflector surface accuracy and H a characteristic height of the telescope (for instance the distance from the ground to the elevation axis, or the focus), the criteria of good performance demand

a focus stability of

$$\Delta f \lesssim \lambda/10 \quad (2.1)$$

a pointing stability

$$\Delta \theta \lesssim \theta/10 \propto (\lambda/10)/D \quad (2.2)$$

a surface stability

$$\sigma \lesssim \lambda/16 \quad (2.3)$$

and for interferometer/VLBI telescopes a path length stability

$$\Delta H \lesssim \lambda/10 \quad (2.4)$$

Since these specifications scale with wavelength, it is evident that mm-wavelength telescopes have tighter tolerances than cm-wavelength telescopes. This Chapter deals with the design and construction of radio telescopes and the efforts to cope

¹ For units and fundamental constants see Appendix A

² see Appendix B

with temperature influences by passive means of paint and insulation and by active thermal control of ventilation, if necessary, so that a good performance is obtained.

2.1 Optical Configurations

Full aperture radio telescopes use as optics configuration the parabolic reflector, the Cassegrain system with parabolic main reflector and hyperbolic subreflector, the Gregory system with parabolic main reflector and elliptical subreflector, and modifications of these systems. Very low-noise radio telescopes use an off-axis Gregory system or off-axis Cassegrain system. The parabolic main reflector in radio telescopes has a small focal ratio (~ 0.3) and thus is very deep and steep. The geometric optics properties of radio telescopes are similar to those of the much earlier developed optical telescopes. The optical configurations are explained by Schroeder [1987], Wilson [1999], Love [1978], Kraus [1986], Baars [2007] and others. The mechanical concept of radio telescopes is explained in the textbooks by Mar & Liebowitz [1969], Goldsmith (ed.) [1988], Polyak & Bervalds [1990], Levy [1996], Baars [2007], Cheng [2009] and many articles.

2.1.1 The Parabolic Reflector

Figure 2.1 illustrates the optics of the parabolic reflector. The on-axis incident plane wavefront (W) emitted by a point source at far distance is (coherently) concentrated at the focus (f) of the parabolic reflector (R). The receiver (RE) is located at this focus. The path lengths $\overline{AA'f}$ and $\overline{BB'f}$ of individual rays are identical for an on-axis incident plane wavefront so that the individual rays arrive in phase at the focus f. For orthogonal coordinates (x,y,z) with the reflector vertex as origin, the (x,y) plane tangential at the vertex and the z axis pointing in the direction of the reflector axis, the parabolic contour is defined by

$$r^2 = x^2 + y^2 = 2pz = 4fz \quad (2.5)$$

with f the focal length of the reflector. The focal ratio n is

$$n = f/D \quad (2.6)$$

with D the diameter of the reflector. Typical values for radio telescopes are $n \approx 0.3$, with exceptions like $n = 0.45$ of the Onsala 20-m reflector and $n = 0.8$ of the Kitt Peak 11-m reflector.

The perfect parabolic reflector concentrates the on-axis incident plane wavefront (W) in phase at the focal point f . The proof of this property follows the derivation by

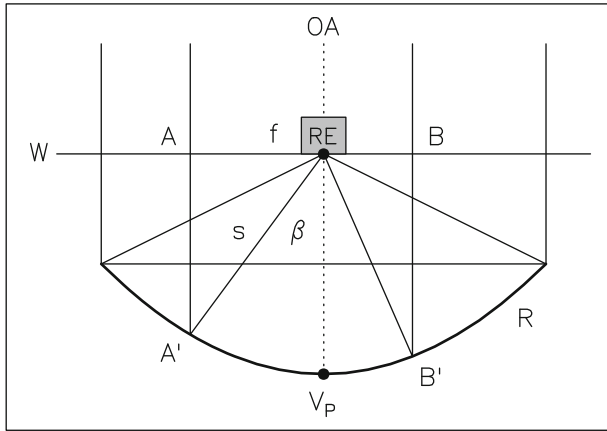


Fig. 2.1 Geometry of the parabolic reflector (R). The on-axis incident plane wavefront (W) is reflected to the focus (f) and detected by the receiver (RE). V_P is the vertex of the parabola; OA is the optical/radio axis.

Rush & Potter [1970] in which the reflector is considered as a transmitting element by reversing the direction of wave propagation. As shown in Fig. 2.1, a ray $\overline{fA'}$ emanating from the receiver under the angle β is reflected at the position A' of the surface. The condition of collimation, i.e. parallel rays, requires that the propagation of the ray $A'A$ is parallel to the reflector axis. This condition is fulfilled for any ray, i.e. any direction β , if

$$\overline{fA'} + \overline{A'A} = \text{constant} = 2f \quad (2.7)$$

With $\overline{fA'} = s$, $\overline{A'A} = s \cos \beta$, $p = 2f$, Eq.(2.7) becomes

$$s = p/(1 + \cos \beta) \quad (2.8)$$

which is the expression of a parabola in polar co-ordinates. Radio telescopes can operate in primary focus mode with the receiver installed at f.

The geometric optic properties of multi-mirror telescopes are derived in a similar way by tracing principal rays through the systems. Details of the wavefront and principle rays in a Cassegrain system are found in Rush & Potter [1970].

2.1.2 The Cassegrain and Gregory System

The combination of con-focal surfaces leads to the Cassegrain and Gregory system, with the Cassegrain system more often used because of the shorter construction length. The Cassegrain system uses a convex hyperbolic subreflector, the Gregory

system uses a concave elliptical subreflector. The receiver is placed at the secondary focus at a convenient position near the vertex of the parabolic main reflector.

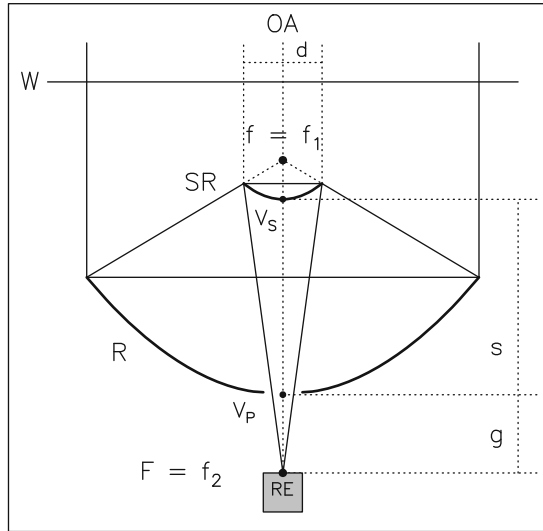


Fig. 2.2 Geometry of the Cassegrain system. The on-axis incident plane wavefront (W) is collected by the parabolic main reflector (R, with focus f) and imaged by the hyperbolic subreflector (SR) to the secondary focus (F). The foci f_1 and f_2 are those of a hyperboloid of which the subreflector is a section. The receiver (RE) is placed at the secondary focus (F). V_p is the vertex of the main reflector, V_s the vertex of the subreflector; OA is the optical/radio axis.

Figure 2.2 illustrates the optics of the Cassegrain system. One virtual focus (f_1) of the hyperbolic subreflector (SR) coincides with the focus (f) of the parabolic main reflector (R), the other virtual focus of the hyperbola (f_2) is the secondary focus of the combined system (F, also called Cassegrain focus) located near the vertex of the main reflector. Here the receiver (RE) is installed. The optical path of an on-axis incident plane wavefront (W), emitted by a point source at far distance, is shown in Fig. 2.2. The geometrical parameters that define the Cassegrain system are

- D = diameter of the parabolic main reflector,
- f = focal length of the parabolic main reflector,
- $n = f/D$ the focal ratio of the main reflector,
- d = diameter of the hyperbolic subreflector,
- $F = Mf$ equivalent focal length of the Cassegrain system,
- $M = F/f$ magnification of the Cassegrain system,
- $N = F/D = Mn$ focal ratio of the Cassegrain system,
- $s = \overline{V_p V_s}$ = distance between the main reflector vertex (V_p) and the subreflector vertex (V_s),

$g = \overline{FV_p}$ = distance of the secondary focus from the vertex of the primary reflector (+ : behind the vertex, - : in front of the vertex).

With the hyperbolic surface of the subreflector given by

$$b^2x'^2 - a^2y'^2 = a^2b^2, \quad e^2 = a^2 + b^2 \tag{2.9}$$

the construction parameters of the Cassegrain system are

$$N = F/D = Mf/D = Mn \tag{2.10}$$

$$2e = f + g \tag{2.11}$$

$$a = s + g - e = s + (g - f)/2 \tag{2.12}$$

$$b^2 = (g + s)(f - s) \tag{2.13}$$

$$d = D(f - s)/f \tag{2.14}$$

$$s = (Mf - g)/(M + 1) \tag{2.15}$$

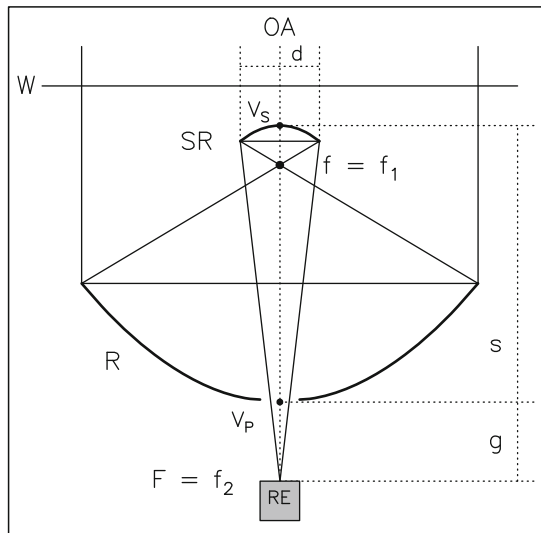


Fig. 2.3 Geometry of the Gregory system. The on-axis incident plane wavefront (W) is collected by the parabolic main reflector (R, with focus f) and imaged by the elliptical subreflector (SR) to the secondary focus (F). The foci f_1 and f_2 are the those of an ellipsoid of which the subreflector is a section. The receiver (RE) is placed at the secondary focus (F). V_p is the vertex of the main reflector, V_s the vertex of the subreflector; OA is the optical/radio axis.

Figure 2.3 illustrates the optics of the Gregory system. One focus (f_1) of the elliptical subreflector (SR) coincides with the focus (f) of the parabolic main reflector

(R), the other focus of the ellipsoid (f_2) is the secondary focus of the combined system (F, also called Gregory focus) located near the vertex of the main reflector. The optical path of an on-axis incident plane wavefront (W), emitted by a point source at far distance, is shown in Fig. 2.3. With the elliptical surface of the subreflector given by

$$b^2x'^2 + a^2y'^2 = a^2b^2, \quad e^2 = a^2 - b^2 \quad (2.16)$$

the construction parameters defined by Eqs.(2.10–2.14) also hold for the Gregory system; Eq.(2.15) becomes

$$s = (Mf - g)/(M - 1) \quad (2.17)$$

As examples, Table 2.1 gives the design parameters of the IRAM 15–m and 30–m Cassegrain systems and of the Effelsberg 100–m Gregory system. An advantage of the Cassegrain system is the shorter construction length, an advantage of the Gregory system is the accessibility of the primary focus.

Table 2.1 Radio Telescope Design Parameters [in metre].

Parameter		IRAM ^{a)} 15–m Cassegrain	IRAM ^{b)} 30–m Cassegrain	Effelsberg ^{c)} 100–m Gregory
Reflector Diameter	D	15	30	100
Focal ratio	n	0.325	0.35	0.30
Focal Length	f	4.875	10.5	30.0
Subreflector Diameter	d	1.55	2.0	6.5
Magnification	M	15.7	27.8	12.1
System Focal Length	F = M f	76.5	291.9	364.0
System Focal Ratio	N = M n	5.10	9.73	3.64

^{a)} Guilloreau et al. [1992], ^{b)} Baars et al. [1987], ^{c)} Hachenberg [1970].

The principle modification of the Cassegrain/Gregory system is the off-axis Cassegrain/Gregory system as for instance realized in the construction of the 7–m Crawford Hill telescope (USA, [Chu et al. 1978]), the 10–m South Pole telescope [Ruhl et al. 2004] and the 100–m GBT telescope (USA, [Jewell & Prestage 2004, Prestage et al. 2009]). The particularity of these constructions is a ‘single’ support arm of the subreflector (see Picture 1.3).

Under the influence of temperature and associated mechanical deformations, the main reflector and subreflector must keep the correct geometrical contour and must stay correctly aligned (distance, centring, tilt). This is the task of the telescope structure. The temperature induced structural deformations may change the design parameters Eqs.(2.5)–Eq.(2.17) and the alignment by small amounts and introduce

- a focus error, because of distance changes;

- pointing errors in azimuth and elevation direction, because of decentring and tilt;
- path length errors in interferometer and VLBI systems, because of distance changes.

The tolerable changes of the design parameters are derived from the performance specifications Eq.(2.1) to Eq.(2.4), the tolerable thermal changes of the design parameters are explained in Chapter 13. The focus and pointing errors can be measured on scans across a radio source, the errors are easily corrected in real time. This is not the case for surface errors and path length changes.

2.2 Basic Telescope Constructions

The mechanical structure of a telescope supports the optical system, shown in Figs. 2.1–2.3, and often allows the pointing of the radio axis (OA) to all directions of the visible sky. When tracking a source, the radio axis follows the sidereal motion of the source or the motion of a spacecraft or satellite.

A radio telescope consists of four principal mechanical components, indicated in Fig. 1.1 :

- (1) the Telescope Mount, consisting of a pedestal, or alidade and rail track or fork support,
- (2) the Reflector Backup Structure (**BUS**) with panels and the BUS support,
- (3) the Subreflector Support (Quadripod) and the Subreflector,
- (4) the Focus Cabin(s) and Counterweight(s).

Disregarding many modifications, especially those of stationary telescopes (for instance, transit telescopes, the Arecibo telescope, the RATAN telescope etc.), and concentrating on modern reflector telescopes with azimuth–elevation axis mount (alt–azimuth mount)³, there are three basic structures which combine the four basic components into a telescope. The three structures are distinguished by the realization of the azimuth (AZ) and elevation (EL) axis, i.e. their supporting mount. The three basic mount structures are

- (1) the Alidade supported reflector (Picture 1.2, 1.3),
- (2) the Pedestal–Yoke supported reflector (Picture 1.4),
- (3) the Fork supported reflector (Picture 1.5, 1.6).

In order to allow observation at low elevation (horizon), the mounts are higher than approximately 1/2 of the reflector diameter.

³ leaving out the equatorial mount, used for instance on the obsolete Green Bank 43–m telescope (<http://www.nrao.edu>, Baars [2007]) and the Westerbork 25–m telescopes [Baars & Hooghoudt 1974].

2.2.1 The Telescope with Alidade Support

The alidade supported reflector is schematically shown in Fig. 1.1.a; an example is the Effelsberg 100-m telescope of Picture 1.2 and Fig. 2.4.

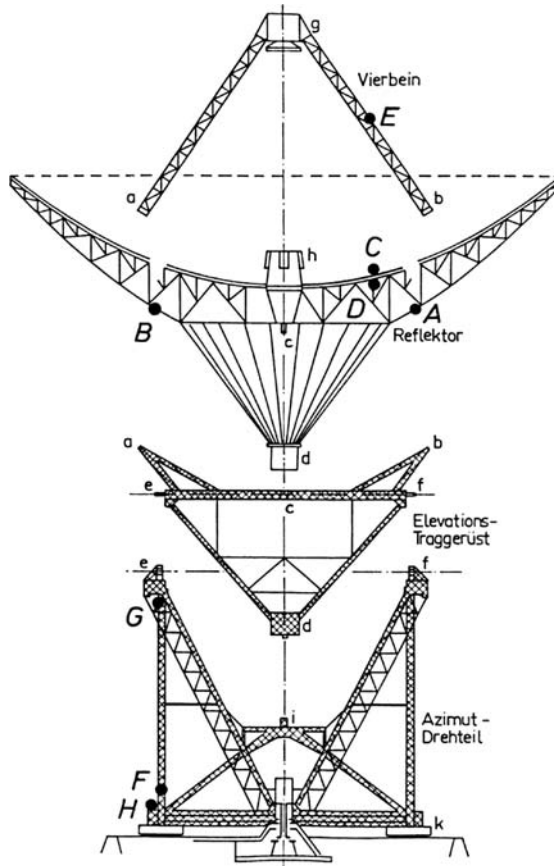


Fig. 2.4 Effelsberg 100-m telescope as example of an Alidade supported telescope; with alidade (Azimut-Drehteil), elevation structure (Elevations-Traggerüst), reflector, and quadripod (Vierbein). k: wheels on track, e-f: EL-axis, i: elevation drive, d: counterweight and elevation gear, h: secondary focus cabin and central hub (c, h), a, b: quadripod supports, g: primary focus cabin and subreflector. A-H: location of temperature sensors [Courtesy B.H. Grahl, MPIfR, Germany].

For larger diameter telescopes, though not exclusively, is the alidade mount chosen. The alidade consists of two A-towers, or ‘broken’ and inclined A-towers (for instance the Cambridge MERLIN 32-m telescope, see Fig. 9.9.a), or a box structure

and upper triangular frame structure (for instance the SRT 64-m telescope⁴) supported on a rectangular base frame. The base frame moves with four wheel systems on a rail (track) allowing rotation of the telescope in azimuth direction. At the upper part of the alidade are the elevation bearings, the EL-axis connects the upper part of the alidade towers. There are several beam inter-connections in the alidade main frames. Often a platform is built at approximately half the height of the alidade where the elevation motors are installed to drive the semi-circular elevation wheel. In the alidade supported Effelsberg telescope shown in Fig. 2.4 [Hachenberg 1970, Geldmacher 1970, Hachenberg et al. 1973] the lower part of the BUS support is a cone of 24 beams, with the counterweight at the point of the cone. At the height of the EL-axis (or already at a lower level) the 24 beams are connected to the base of the BUS and a square frame of which one diagonal arm forms the EL-axis. The cone (Fig. 2.4: d-f, d-e), the EL-axis frame (Fig. 2.4: e-c-f) and the quadripod (Fig. 2.4: a-g, b-g), as also visible in Fig. 2.8, form an octahedron as discussed by von Hoerner [1967 a, 1977 a, see also Baars 2007] in several investigations of fundamental telescope structures. The cone and many tangential and radial inter-connections flare out to form the BUS network. The panels are attached to the BUS, they form the reflector surface. The stability of the BUS determines the stability of the reflector contour. The quadripod is connected to the elevation structure, the quadripod holds the primary focus cabin and the subreflector.

In the alidade supported telescope the thermal state of the alidade is decoupled (no conductive heat transfer) by the small diameter elevation bearings from the thermal state of the elevation structure (cone and EL-axis frame), the BUS and the quadripod. A thermal deformation of the alidade results in a tilt of the alidade, a displacement of the elevation bearings and an integral displacement of the elevation structure and the BUS. This introduces primarily a pointing error. A thermal deformation of the elevation structure introduces a displacement and deformation of the BUS and may appear as a focus and pointing error and a deformation of the reflector surface. A temperature induced deformation of the BUS may introduce a focus, pointing and reflector surface error and a loss in gain. A temperature induced deformation of the quadripod may introduce a focus and pointing error. It is evident that the resulting errors are a complicated superposition of the thermal deformations of the individual structural components, conveniently treated in a thermal finite element analysis. A temperature change of the alidade and the quadripod produces thermal expansions and a path length (phase) error in interferometer/VLBI observations.

The GBT 100-m telescope (Picture 1.3), the JPL-NASA 34-m and 70-m antennas, the SRT 64-m telescope, the LMT/GMT 50-m telescope, the Cambridge MERLIN 32-m telescope and the JCMT 15-m telescope are other examples of alidade supported telescopes.

⁴ <http://www.ca.astro.it/srt>, and Grueff et al. [2004] and Tofani et al. [2008].

2.2.2 The Telescope with Pedestal–Yoke Support

The pedestal–yoke supported reflector is schematically shown in Fig. 1.1.b; an example is the IRAM 30–m telescope of Picture 1.4 and Fig. 2.5.

At the upper part of a cylindrical or pyramidal pedestal is a horizontally aligned rather large diameter bearing that allows rotation of the telescope in azimuth direction. The pedestal is usually built of concrete. On top of the azimuth bearing is a central tower, built of steel, which on the IRAM 30–m telescope has space for the AZ–motors and the Nasmyth focus cabin with receivers. The elevation bearings are on opposite sides of the focus cabin. The yoke, which in essence is an inverted fork, is connected to these bearings. The BUS network is connected to the roof of the yoke (see Fig. 2.9), the quadripod is connected to the BUS; the primary focus cabin and the subreflector are connected to the quadripod. The yoke tilts around the EL–axis and with it the reflector and the quadripod.

In the pedestal–yoke supported telescope is the thermal state of the pedestal, the azimuth bearing and the central tower decoupled by the small diameter elevation bearings from the thermal state of the yoke, the BUS and the quadripod (no conductive heat transfer). A thermal deformation of the pedestal, the azimuth bearing and the central tower appears primarily as a pointing error. Since the BUS is connected to the roof of the yoke, a thermal deformation of the yoke itself may introduce a deformation of the BUS and may appear as a pointing error, but also as a deformation of the reflector surface shape and associated focus error. The installation of ventilation and heating in the yoke of the IRAM 30–m telescope has largely eliminated the thermal deformation of the yoke and the associated print–through astigmatic deformation of the BUS [Peñalver et al. 2002, Greve et al. 2005].

A temperature induced deformation of the BUS may introduce a focus, pointing and reflector surface error and a loss in gain. A temperature induced deformation of the quadripod may introduce a focus and pointing error. A temperature change of the central tower and the quadripod produces thermal expansions and a path length (phase) error in interferometer/VLBI observations.

The Yebes 40–m telescope and the ESSCO 14–m and 20–m telescopes are other examples of pedestal–yoke supported telescopes. On the LMT/GMT 50–m telescope the yoke has the form of two heavy elevation wheels [see Baars 2007]. A special type of pedestal supported telescope is the Parkes 64–m telescope [Jeffery 1964] and the Algonquin 46–m telescope [Jeffery 1969]. Here the azimuth rail is placed on a 3 (or 2)–storey high circular building (the pedestal), the BUS is connected to a compact turret with elevation drives.

Since the thermal behaviour of the IRAM 30–m telescope is in this text often used as an example, a more detailed description of its construction is given here.

The Design of the IRAM 30–m Telescope as an Example

A description of the IRAM 30–m telescope and of its thermal design and thermal behaviour is published by Baars et al. [1987, 1988, 1994, 2007] and Greve et al. [1992, 2005]. As shown in Fig. 2.5, the telescope can be divided into the thermal

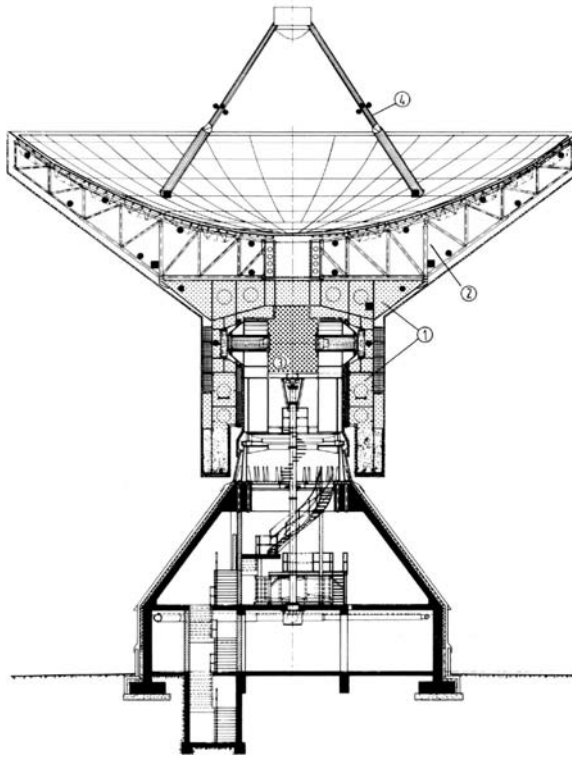


Fig. 2.5 IRAM 30-m telescope as an example of a Pedestal-Yoke supported telescope; with 1: yoke, 2: BUS, 3: central tower on azimuth bearing, 4: quadripod. Solid dots: initial set of temperature sensors (in the BUS, only in tilt direction), solid square (in yoke): reference temperature of the yoke to which the temperature of the BUS and quadripod is actively controlled [From Baars et al. (1988), Courtesy Astron. Astrophys.].

sub-structures of the pedestal, the yoke, the central tower, the secondary focus cabin (Nasmyth cabin), the BUS, the panels, the quadripod and the primary focus cabin.

The concrete pedestal is covered with insulation plates painted white (ordinary paint) in order to reduce the influence of insolation. The pedestal is ventilated with inside air. The thermal coupling (conduction) between the pedestal and the azimuth bearing and central tower is small and can be neglected. Also, the circulation of air between the pedestal and the AZ-motor room and the higher-up secondary focus cabin (Nasmyth cabin) is relatively small. The conductive coupling of the Nasmyth cabin to the yoke via the elevation bearings is negligible. The vertex tunnel is insulated against the BUS and closed at the top with a membrane transparent at radio wavelengths. The heat from the receivers and electrical equipment in the Nasmyth cabin produces a fairly constant temperature of $\sim 20^\circ\text{C}$ inside the cabin.

The yoke consists of two box-type arms and the roof structure (see Fig. 2.9 and Figs. 9.22, 9.23). The lower sections of the yoke arms contain the counterweights of the BUS and quadripod. The yoke is a closed unit and thermally protected by insulation (4 cm polyurethane) cased in thin metal plates, which are painted white with TiO_2 paint. At the roof of the yoke is a circular steel membrane to which the BUS is connected, as indicated in Fig. 2.5.

The BUS is the network of steel tubes supporting the reflector surface panels. The BUS is completely covered by insulation forming a closed air volume. The ventilation/climatisation system acts on this air volume. The front closure of the BUS are the panels separated from the BUS by insulation (4 cm polyurethane and aluminium foil). The rear closure of the BUS, called cladding, is insulation (4 cm polyurethane) cased in thin metal plates, which are painted white with TiO_2 paint. The quadripod is anchored in the BUS. The quadripod legs are steel tubes protected by insulation and painted with TiO_2 paint.

The panels are 4 cm thick Al-honeycomb cores covered on the front and rear side with an aluminium skin (1 to 2 mm thickness), painted white on the front with TiO_2 paint. Heating mats are installed between the panels and their back insulation. The panels are supported on panel frames, with 2 panels per frame (Fig. 2.14). Because of their short thermal time constant of $\sim 1/2$ h, the panels quickly follow the variation of the ambient environment without significant loss of their surface precision, however, thermal gradients in the panel frames can produce panel buckling.

The main structure of the telescope is made of steel. The temperature of the yoke, the BUS network and the quadripod is regulated by a combined passive-active thermal control system. The passive control consists of complete insulation with polyurethane foam and white TiO_2 paint on the outer surfaces. The active control consists of forced ventilation of the BUS, i.e. a circular air flow in the BUS of several m/s speed (Table 2.7, Fig. 9.43.b), with the air either being heated or cooled (climatised) in order to establish a temperature uniformity of $\sim \pm 1^\circ\text{C}$ between the yoke and the BUS, and a temperature uniformity of the BUS of $\text{rms}(T_{\text{BUS}}) \approx 0.5^\circ\text{C}$. The heating of the air inside the BUS counterbalances the radiative cooling of the BUS towards the sky during night, the cooling counterbalances insolation and heat from the fans. A liquid (glycol) is pumped around the quadripod legs, either heating or cooling them to follow the yoke to within $\sim \pm 1^\circ\text{C}$. The temperature of a representative part of the massive and thermally slow yoke (Fig. 2.5) is taken as reference to which the temperature of the BUS and quadripod is actively controlled to guarantee negligible thermal degradation of the radio performance [Baars et al. 1988, 1994]. Since 2000, the upper part of the yoke is also ventilated ($4 \times 4500 \text{ m}^3/\text{h}$) and occasionally heated (6 kW total) to eliminate temperature gradients in the yoke arms. Such gradients cause a bending of the yoke and the print-through to the BUS produced an astigmatic surface deformation [Peñalver et al. 2002, Greve et al. 2005]. During adverse weather conditions the panels, the rear of the BUS and the quadripod can be heated using approximately $100\text{--}200 \text{ W/m}^2$. The power from the de-icing brings the telescope out of thermal balance (Fig. 9.72) but under these climatic

conditions observations are not possible anyway. The yoke, the BUS and the quadripod contain today 156 sensors to monitor the thermal state of the telescope.

Table 2.2 summarizes some parameters of the thermal sub-structures of the IRAM 30-m telescope.

Table 2.2.a Thermal Sub-Structures of the IRAM 30-m Telescope.

Component	Material	Mass M [ton]	Surface S [m ²]	M/S [t/m ²]
Pedestal	concrete			
Yoke	steel	180	220	0.85
Secondary Focus Cabin	steel	~ 20		
BUS network	steel	100	820 ^{a)}	90/820
BUS rear side			1050 ^{b)}	= 0.11
Panels	Al-HC ^{c)}	15	820	0.02
Quadripod	steel	10	45	0.22

^{a)} reflector surface, ^{b)} rear cladding of BUS

^{c)} Al-HC: aluminium honeycomb.

Table 2.2.b Thermal Protection of the IRAM 30-m Telescope.

Component	Thermal Protection
Pedestal	p: insulation, paint
Yoke	p: insulation, TiO ₂ paint, a: ventilation/heating, de-icing
Secondary Focus Cabin	p: insulation, TiO ₂ paint
BUS network	a: ventilation + climatisation
BUS rear side	p: insulation, TiO ₂ paint, a: de-icing
Panels	p: TiO ₂ paint, rear side insulation, a: de-icing
Quadripod	p: insulation, TiO ₂ paint, a: glycol circulation, de-icing

p: passive thermal control, a: active thermal control.

2.2.3 The Telescope with Pedestal-Fork Support

The pedestal-fork supported reflector is schematically shown in Fig. 1.1.c; an example is the IRAM/SEST 15-m telescope of Picture 1.6 and Fig. 2.6.

The pedestal-fork support is mostly used for smaller diameter telescopes, and mostly mm-wavelength telescopes. At the upper part of the pedestal is a horizontally aligned bearing that allows rotation of the telescope in azimuth direction. The pedestal may be anchored in the ground (as for the SEST telescope, Booth et al. [1989]), or may be built as a movable transporter for telescopes of an interferometer array (as for the IRAM Plateau de Bure telescopes, Guilloteau et al. [1992]).

The fork traverse is connected to the azimuth bearing, the elevation bearings are placed at the upper part of the fork arms. The secondary focus cabin, or any similar structure, is located between the fork arms and connected to the elevation bearings. The BUS is connected to the roof of the secondary focus cabin, or a central hub (Fig. 2.6, Fig. 2.10) that is connected to the roof of the secondary focus cabin. The quadripod is connected to the BUS, the subreflector is connected to the quadripod. The secondary focus cabin can tilt around the EL-axis and with it the reflector and the quadripod.

In a pedestal–fork supported telescope the thermal behaviour of the secondary focus cabin, the BUS and the quadripod is decoupled by the small diameter elevation bearings (no conductive heat transfer) from the thermal behaviour of the fork and pedestal. A thermal deformation of the pedestal and fork appears as a pointing error. A temperature change of the pedestal, fork and quadripod produces thermal expansions and a path length (phase) error in interferometer/VLBI observations. A thermal deformation of the secondary focus cabin can result in a deformation of the BUS with associated pointing, focus and reflector surface error. On the IRAM 15–m telescope the thermal behaviour of the BUS (radial and tangential CFRP bars and axial steel bars) matches the thermal behaviour of the steel central hub. On the Japanese ALMA 12–m prototype telescope the central hub is made of invar, matching the thermal behaviour of the CFRP BUS (tubes) [Ukita et al. 2004]. The BUS of this telescope is ventilated. On the ALMA/APEX VertexRSI 12–m telescope the secondary focus cabin is thermally controlled by glycol of constant temperature passing through a pipe system attached to the walls of the cabin. The roof of the secondary focus cabin is replaced by an invar ring, which is ventilated with air from the cabin. The BUS (made of Al–honeycomb CFRP–plate covered plates) is connected to the invar ring [Mangum et al. 2006, Güsten et al. 2006]. Finally, on the 12–m ALMA AEC telescope the secondary focus cabin and the BUS are made of CFRP plates [Mangum et al. 2006].

The GMRT 45–m telescopes (Picture 1.1), the MIT–Haystack 37–m radome enclosed telescope, the VLA 25–m telescopes (Picture 1.5) and the ALMA 12–m telescopes are examples of other pedestal–fork supported telescopes.

Since the thermal behaviour of the IRAM/SEST 15–m telescopes is in this text often used as an example, a more detailed description of the construction is given here.

The Design of the IRAM/SEST 15–m Telescope as an Example

A description of the IRAM/SEST 15–m telescopes is published by Delannoy [1985], Guilloteau et al. [1992] and Booth et al. [1989]. As shown in Fig. 2.6, the telescope can be divided into the thermal sub–structures of the pedestal (or transporter), the fork structure, the secondary focus cabin, the central hub, the BUS, the panels, the quadripod and the subreflector. The steel pedestal (transporter) of the movable IRAM 15–m telescopes is painted white to reduce the influence of insolation. The concrete pedestal of the stationary SEST 15–m telescope is covered with insulation, which itself is covered with shiny aluminium plates (radiation shield), leaving an air gap between the insulation and the plates. The pedestal of the IRAM and the SEST

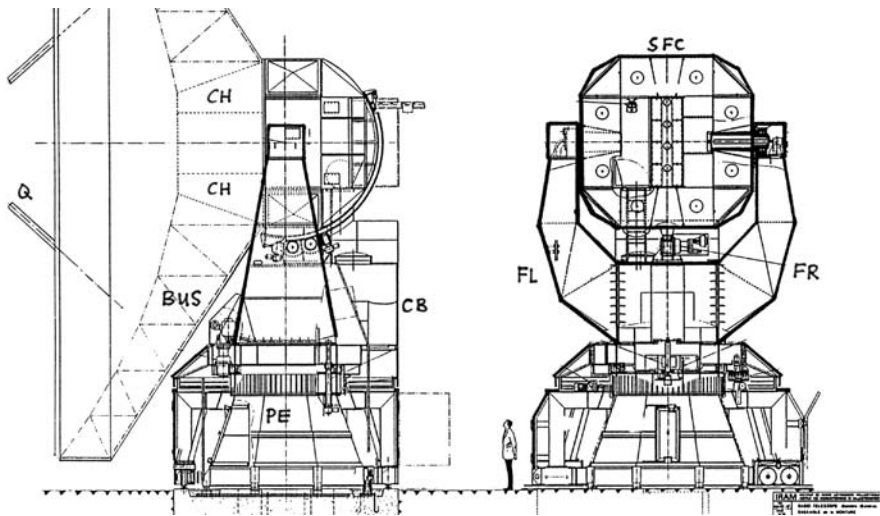


Fig. 2.6 IRAM 15-m telescope (and similar SEST) as example of a Pedestal-Fork supported telescope. PE: pedestal, F: fork (FL: left arm, FR: right arm), SFC: secondary focus cabin, CB: compressor cabin, CH: central hub, BUS: backup structure and panels, Q: quadripod [Courtesy J.-L. Pollet, IRAM, France].

telescope contains a substantial amount of electrical equipment. The heat generated by this equipment can diffuse by natural convection into the air volume of the fork arms (see Fig. 11.16).

The fork structure consists of the traverse and the arms, the traverse contains the azimuth bearing. The steel plates of the fork arms are covered with passive thermal protection consisting of insulation (5 cm polyurethane attached to the steel walls), an air gap (2 cm) and the MetawellTM radiation shield. The MetawellTM radiation shield consists of two aluminium plates (~ 1 mm thickness) of 5 mm separation and connected by corrugated aluminium. The surface of the insulation and the inner surface of the MetawellTM is covered with aluminium foil, the outer surface finish of the radiation shield is anodised aluminium (see Section 11.1). Some MetawellTM plates were later replaced by single aluminium plates (see Fig. 11.15). The air in the gap can be ventilated with ambient air, this ventilation is applied on the SEST telescope but is not applied on the IRAM telescopes because of occasional blockage by snow and ice. Thermal protection is applied to the fork structure to avoid asymmetric expansion of the fork arms and thus to reduce unpredictable time-dependent pointing errors. Estimates indicate that the pointing errors do not exceed ~ 2 arc-sec if the temperature difference between the fork arms does not exceed $\sim 2^\circ\text{C}$, and if the temperature uniformity of the individual fork arms is $\lesssim 0.5^\circ\text{C}$. On one side of the fork structure is a cabin that contains the compressors of the receivers. The cabin is not insulated against the outside (environment) but is insulated against the steel plates of the fork. The walls of the cabin are painted white (ordinary paint).

The compressors in the cabin produce heat (of the order of 5 kW) that may diffuse into the fork structure. The cabin has louvres.

The BUS is attached to the central hub which itself is bolted to the roof of the secondary focus cabin (Fig. 9.26). This cabin is a plate steel frame partially covered with the same passive thermal protection as used on the fork structure. The rear of the secondary focus cabin is unprotected (doors) but painted white. A radio wavelength transparent membrane covers the vertex opening of the secondary focus cabin. The receivers, electrical equipment and heating in the secondary focus cabin produce a rather constant temperature of the internal air.

The quadripod consists of CFRP tubes painted white with TiO_2 paint. Close to the subreflector the legs are covered with shiny aluminium foil. The original subreflector is made of CFRP and a shiny radio wave reflective aluminium front surface layer protected by a HostafionTM film, similar to the panels. Today several subreflectors are machined from aluminium.

The BUS is a network of CFRP tubes (radial and tangential direction) and steel tubes (axial direction) as explained in Fig. 2.7. The BUS network is attached to the central hub made of steel. The CFRP–steel network structure was chosen so that the BUS follows the thermal expansion of the central hub. The initial design of a complete CFRP network indicated buckling of the reflector surface introduced by differential thermal expansion between the steel hub and the CFRP BUS (P. Raffin, IRAM, priv. comm.). The rear of the BUS is covered with MetawellTM plates, or Al-plates, the front of the BUS is closed by the panels and their insulation. The BUS is thus contained in a closed air volume. The panels are attached to the BUS (3–point and 5–point support) by motor controlled screws to ease adjustment. The original panels consist of an Al–honeycomb core (4 cm thickness) covered on both sides with a CFRP skin (1–2 mm thickness). The front skin has a thin radio wave reflective aluminium layer (shiny) protected by a 0.03 mm thick HostafionTM (plastic) film. The original panels will gradually be replaced by machined aluminium panels with a hexagonal support structure similar to those used on optical telescope mirrors (see Fig. 2.13.b). All panels can be heated ($\sim 100 \text{ W/m}^2$) to prevent the formation of ice. A few panels have been replaced by Media–LarioTM Al–honeycomb panels, with front and rear side electroformed Ni–skins (0.6 mm thickness) and rhodium front surface coating, in order to test front and back heating [Bremer et al. 2005].

The IRAM/SEST 15–m telescope uses passive thermal control, either consisting of an elaborate thermal façade of the fork structure and secondary focus cabin or of low thermal expansion CFRP material for the BUS, the panels, the quadripod and the subreflector. Table 2.3 summarizes some characteristic parameters of the thermal sub–structures of IRAM/SEST 15–m telescope.

Table 2.3.a Thermal Sub-Structures of the IRAM/SEST 15-m Telescopes.

Component	Material	Mass M [ton]	Surface S [m ²]	M/S [t/m ²]
Pedestal (SEST) ^{a)}	concrete			
Transporter (PdB) ^{a)}	steel	20	130	0.15
Fork + Traverse	steel	25	70	0.36
Secondary Focus Cabin	steel	45 ^{b)}	110	0.41
Central Hub	steel	5		
BUS	CFRP + steel	15	180	0.08
Panels	Al-HC ^{c)}	13	200	0.015
Quadripod	CFRP			

^{a)} PdB: IRAM Plateau de Bure (France),

SEST: Swedish-ESO Sub-mm telescope (Chile);

^{b)} including the counterweight

^{c)} Al-HC: aluminium honeycomb, partially replaced by machined aluminium panels (Fig. 2.13 b).

Table 2.3.b Thermal Protection of the IRAM/SEST 15-m Telescopes.

Component	Thermal Protection
Pedestal (SEST)	p: insulation, air gap, Al-plates RS ^{a)}
Transporter (PdB)	p: white paint
Fork + Traverse	p: insulation, air gap, Al-foil, RS ^{a)} a: SEST: ventilation of air gap
Secondary Focus Cabin	as for fork
BUS	p: CFRP bars + steel bars p: rear side cladding
Panels ^{b)}	p: CFRP skin, Hostafflon TM cover
Quadripod	p: CFRP tubes, TiO ₂ paint, Al foil

p: passive thermal control, a: active thermal control;

^{a)} RS: radiation shield;

^{b)} aluminium honeycomb panels, partially replaced by machined aluminium panels (Fig. 2.13 b).

2.3 Telescope Components

2.3.1 Reflector Backup Structure (BUS)

A schematic view of a BUS supported by a central hub is shown in Fig. 2.7. The BUS supports the panels, which form the reflector surface. The BUS consists of a network of tubes, beams and plates that guarantees the reflector contour and surface precision (σ) under the influence of gravity, temperature and wind. The reflector surface stability can be obtained by using a rigid BUS with small deflections of the individual members. However, for large steerable telescopes the rigid design becomes prohibitively heavy. As illustrated in the von Hoerner-diagram (see Preface),

gravity imposes a natural limit on the diameter D , thus the mass and the quality D/σ of a reflector. To overcome the mass limitation of the rigid design,

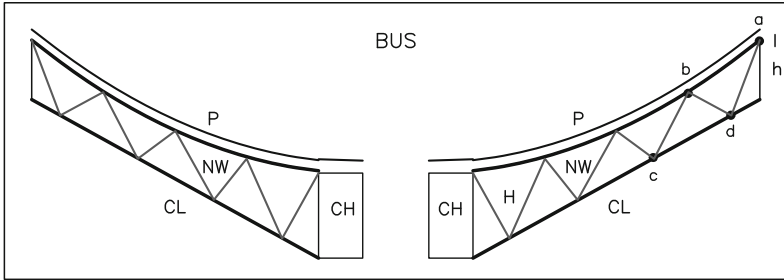


Fig. 2.7 Schematic view of a closed BUS. CH: central hub, P: panels, I: insulation behind panels, CL: rear cladding, NW: tube network. A particular radial and axial network tube extends between a–b, c–d ... and a–d, b–c, b–d etc. (with a,b,c,d,... finite element nodes). For values of the heights H and h of existing telescopes see Table 2.5. (On the IRAM/SEST 15–m telescopes the radial connections a–b, c–d etc. and tangential connections are made of CFRP tubes, the axial connections a–d, b–d, b–c etc. are made of steel tubes. The nodal joints a,b,c,d,... are made of cast steel) [From Greve et al. (2006), Courtesy SPIE].

von Hoerner [1967 a, b] introduced the concept of a homologous BUS by which a favourable mass to stiffness ratio is obtained, allowing the construction of large diameter steerable telescopes. The homologous BUS network guarantees that the reflector surface deviations from a parabolic contour do not exceed the tolerance of $\sigma \lesssim \lambda/16$, while allowing the focal length and the position of the parabola to change by small amounts with elevation. The homology principle is explained in Section 2.3.2

The BUS is made of steel, aluminium and/or CFRP. Steel is used for large diameter (up to 100–m diameter, Effelsberg and GBT) but also small diameter BUS constructions (10 to 15 m diameter, CSO and JCMT). In order to save mass, the BUS of the earlier mm–wavelength telescopes is made of aluminium (Onsala, FCRAO etc., see Fig. 3.5). However, in order to cope with the higher thermal expansion of aluminium, these telescopes are placed in a radome. The modern BUS constructions of mm/submm–wavelength telescopes are made of CFRP, either using CFRP and steel tubes with cast steel joints (IRAM/SEST 15–m) or invar joints (ASTE), or CFRP covered Al–honeycomb plates (VertexRSI ALMA/APEX telescope) or pure CFRP plates (AEC ALMA telescope).

There are three basic support structures of a BUS, i.e. the pyramidal support and modifications of it, the yoke support and the central hub support. The BUS construction and its connection to a pyramidal support, as used on the Effelsberg 100–m telescope and the JCMT 15–m telescope, is shown in Fig. 2.8 and Fig. 9.50. The BUS construction and its connection to a yoke, as used on the IRAM 30–m telescope, is shown in Fig. 2.9; the BUS construction and its connection to a central hub, as used on the IRAM/SEST 15–m telescope, is shown in Fig. 2.10.



Fig. 2.8 Effelsberg 100-m telescope (horizon position) illustrating the connection of the BUS to an octahedron and pyramidal support. The base of the octahedron support of the BUS is visible as the square frame, with one diagonal beam forming the elevation axis. The lower part of the octahedron are the beams of the pyramidal cone, the elevation wheel and the support of the counterweight. The upper pyramid of the octahedron (not visible) forms the quadripod support and the quadripod. The BUS and its support is a homologous design [Courtesy N. Junkes, MPIfR, Germany].

The mechanical deformations of a BUS under the influence of gravity, temperature and wind are studied in a finite element analysis (FEA) and/or flexible body analysis (FBA) [Kärcher 2006] based on a finite element model (FEM) of the telescope (see, for instance, Mar & Liebowitz [1969], Levy [1996], Zienkiewicz & Taylor [1994]). In the FEA the thermal expansions of the individual tube/beam/plate members are interpreted as forces on the finite elements, which result in corresponding mechanical deformations. The panels are supported on the BUS and are considered in the FEA as a load on the BUS nodes that hold the panels. The panels, or panel frames, are assumed to follow the deformations of the BUS. The construction of panels, and panel frames for several panels, may be based on separate FEM calculations (see Eschenauer et al. [1980]).

Table 2.4 gives for several BUS constructions the approximate mass, Fig. 2.11.a shows the diameter (D) to mass (M) relation of the listed values. The data follow the relation $M [\text{ton}] \approx D [\text{m}]^\alpha$ with $\alpha = 1.45 \approx 3/2$, which is inserted in Fig. 2.11.a.

Table 2.5 gives the approximate dimensions of several BUS constructions. It is seen that the average depth $\langle H \rangle = (H + h)/2$ (see Fig. 2.7) to diameter D ratio of these BUS constructions falls into the narrow range of $\langle H \rangle / D \approx 0.1 \pm 0.05$. As a consequence, in thermal discussions the closed BUS can be considered to consist of two



Fig. 2.9 IRAM 30-m telescope illustrating the connection of the BUS network to the roof (membrane) of the yoke. The BUS is a homologous design requiring the membrane connection to the yoke (see also Fig. 6.6) [From Bremer & Peñalver (2002), Courtesy SPIE].

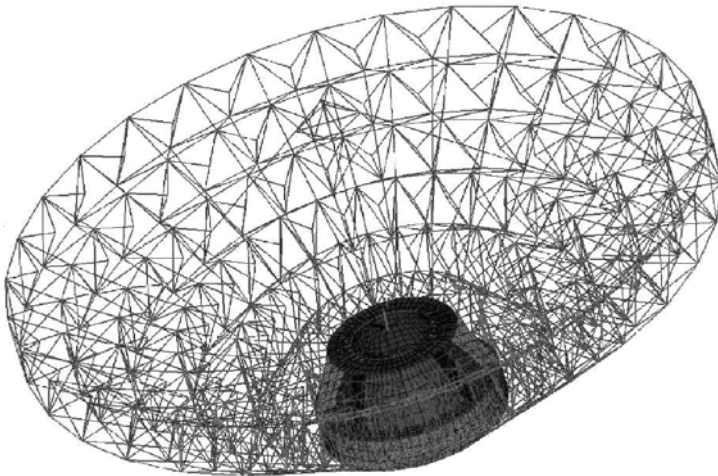


Fig. 2.10 IRAM/SEST 15-m telescope illustrating the connection of the BUS to the central hub, which itself is connected to the roof of the secondary focus cabin.

parallel circular plates at close distance from each other, i.e. at the front the panel surface (without or with insulation) and at the rear the cladding, with the BUS network in between. Therefore, the conductive and radiative heat transfer in a closed BUS is mainly in axial direction from the front to the rear and vice versa, rather than

Table 2.4 Approximate Masses of BUS Constructions.

Telescope ^{a)}	Reflector Diameter [m]	BUS Material	Mass [ton]	Mass/Surface ^{b)} [ton/m ²]	open/closed BUS
SMA ^{c)}	6	CFRP	2.4	0.08	closed
OVRO ^{d)}	10	steel	5	0.06	open
SPT ^{e)}	10	CFRP	18	0.23	closed
IRAM (PdB)	15	CFRP–steel	15	0.07	closed
Onsala ^{f)}	20	aluminium	13	0.04	open/radome
IRAM (PV)	30	steel	115	0.15	closed
Yebes ^{g)}	40	steel	200	0.13	closed
LMT/GMT ^{h)}	50	steel	340	0.15	closed
SRT ⁱ⁾	64	steel	500	0.14	closed
Effelsberg	100	steel	760	0.08	open

Table copied from Greve et al. [2006] (Courtesy SPIE).

^{a)} see list of Acronyms of observatory sites.

^{b)} surface averaged values, for $S = \pi (D/2)^2$.

The BUS tubes/plates have a different mass/surface ratio.

^{c)} SMA: Sub–Millimeter Array [Ho et al. 2004].

^{d)} OVRO: Owens Valley Radio Observatory, now CARMA [Woody et al. 1994].

^{e)} SPT: South Pole Telescope [Ruhl et al. 2004]; mass of BUS, panels, invar cone.

^{f)} P. Raffin [1989]; ^{g)} J.A. Lopez–Perez, priv. comm. [<http://www.oan.es>]

^{h)} LMT/GMT: Large Millimeter Telescope/Gran Telescopio Millimetrico, (Mexico) [Kärcher & Baars 2000].

ⁱ⁾ SRT: Sardinia Radio Telescope [Grueff et al. 2004].

in radial direction. The air in the closed BUS may however have a natural convective flow or a forced ventilated flow.

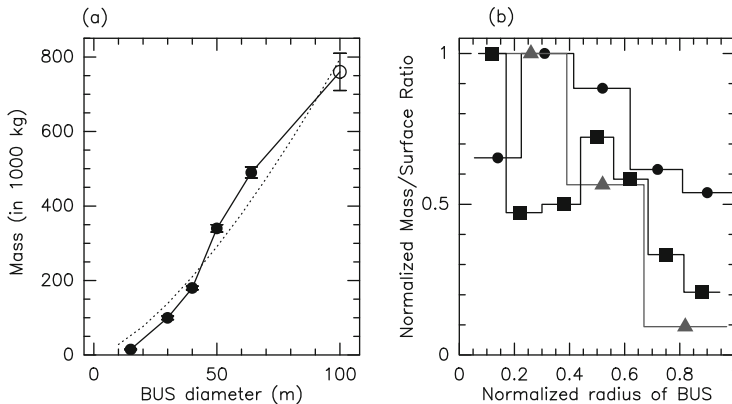


Fig. 2.11 (a) Mass–Diameter relation of BUS constructions (data of Table 2.4). Solid dots: closed BUS, open circle: open BUS. The dashed line is the approximation $M[\text{ton}] = D[\text{m}]^\alpha$ with $\alpha = 1.45$. (b) Mass–Surface ratio, as function of the normalized BUS radius. Dots: LMT/GMT 50–m, triangles: SRT 64–m, square: IRAM 30–m telescopes [From Greve et al. (2006), Courtesy SPIE].

Table 2.5 BUS Dimensions.

Telescope ^{a)}	Reflector Diameter D [m]	λ_{\min} ^{b)} [mm]	h [m]	H [m]	h/H	$\langle H \rangle$ ^{c)} [m]	$\langle H \rangle/D$
CFRP BUS (Closed BUS)							
SMA	6	0.3	0.6	1.0	0.6	0.8	0.133
APEX/ALMA	12	0.3	0.8	1.0	0.8	0.9	0.075
IRAM 15-m	15	1	1.3	2.1	0.6	1.7	0.113
Steel BUS (Closed BUS)							
BIMA	6	1	0.6	1.0	0.6	0.8	0.133
NRO/ASTE	10	0.3	~ 0	1.5	small	~ 0.75	~ 0.075
IRAM 30-m	30	1	2.5	3.7	0.7	3.1	0.10
Yebes	40	3	2.5	4.0	0.6	3.25	0.081
NRO	45	3	1.6	3.5	0.5	2.55	0.056
LMT/GMT	50	1	1.8	5.6	0.3	3.7	0.075
SRT	64	3	3	6.8	0.45	5.8	0.09
Steel BUS (Open BUS)							
CSO/CARMA	10	0.3/3	0.5	1.5	0.3	1.0	0.095
JPL	34	cm	1	2.8	0.35	1.9	0.055
Parkes	64	cm (m)	1.5	6.0	0.25	3.75	0.06
Effelsberg	100	13 (3)	2	10	0.2	6	0.06
average					0.5 ± 0.3		$0.10^{+0.05}_{-0.25}$

Table copied from Greve et al. [2006] (Courtesy SPIE).

^{a)} see list of Acronyms of observatory sites.

^{b)} approximately shortest wavelength of observation;

^{c)} $\langle H \rangle = (h + H)/2$, see Fig. 2.7.

2.3.2 The Homologous BUS

The homologous design of a BUS is not of immediate importance for the thermal behaviour of a telescope. However, the homologous design has an influence on the mass of a BUS, and by this also on the mass of the mount. The homologous design determines the residual gravitational reflector surface deformations, which should not be exceeded by temperature and wind induced deformations.

Von Hoerner [1967 a,b] introduced the concept of homology that allows the construction of lightweight steerable reflectors with acceptable gravitational deformations. In a homologous design the network of the BUS is optimised such that the reflector has a best-fit parabolic contour at all tilt angles with residual rms surface deformations σ within the tolerance of, say, $\sigma \lesssim \lambda/16$. However, the position of the reflector (for instance measured with respect to the stable mount) and the focal length are allowed to change. The change in focal length, position (vertex motion) and tilt of the main reflector, the sag and tilt of the quadripod and the associated change in position and tilt of the subreflector are compensated to a large extent by position correction (shifts and tilt) of the subreflector.

For an alt–azimuth supported homologous BUS tilted at the elevation angle E ($E = 0^\circ$: horizon, H ; $E = 90^\circ$: zenith, Z) the residual elastic deformations $d_i(E)$ of the reflector panel support points $[i]$ are

$$d_i(E) = a_i \cos(E) + b_i \sin(E) \quad (2.18)$$

with a_i and b_i constants depending on the stiffness of the BUS. Evidently, the deformations at horizon position are $[a_i]$, the deformations at zenith position are $[b_i]$. Since the panels are supported by the BUS points $[i]$, the reflector surface usually deforms in an identical way. With $\sigma(Z) = \sigma(E = 90^\circ)$ and $\sigma(H) = \sigma(E = 0^\circ)$ the rms surface deformations with respect to the best–fit parabola at zenith and horizon position of the reflector, respectively, the rms value $\sigma(E)$ at the elevation E is

$$\sigma(E)^2 = \sigma(H)^2 \cos(E)^2 + \sigma(Z)^2 \sin(E)^2 \quad (2.19)$$

The surface of a homologous reflector can be adjusted such that for the elevation angle E_o (rigging angle) the deviations $d_i(E_o)$ are eliminated, i.e. $d_i(E_o) = 0$, so that at this angle the reflector is perfect, i.e. $\sigma(E_o) = 0$. Under the condition of perfect adjustment at E_o , usually selected in the elevation range of most frequent observations, the rms value of the reflector surface is

$$\sigma(E, E_o) = \sqrt{\sigma(H)^2 [\cos(E) - \cos(E_o)]^2 + \sigma(Z)^2 [\sin(E) - \sin(E_o)]^2} \quad (2.20)$$

As an example, Fig. 2.12 shows for the IRAM 30–m telescope the surface deformations at horizon and zenith predicted by the FEM (and verified) for optimal adjustment at $E_o = 45^\circ$. For this telescope $\sigma(H) \approx \sigma(Z) \approx 0.055$ mm. To make full use of the homologous design, the temperature and wind induced surface deformations should not exceed these values at high and low elevation. For comparison, a typical measured temperature induced deformation of the IRAM 30–m reflector is added in Fig. 2.12. The analysis of several years of data shows that the temperature induced surface deformations do not exceed $\sim 1/3$ to $1/2$ of the gravitational deformations $\sigma(H)$ or $\sigma(Z)$. As seen in Fig. 2.12, the thermal surface deformations have a larger spatial scale than the gravitational surface deformations.

2.3.3 The Open and Closed, Ventilated and Climatized BUS

The Pictures 1.2, 1.3, 1.5 and 1.4, 1.6 illustrate the distinctive difference of the open BUS and the closed BUS. Generally, the open BUS is used on large cm–wavelength telescopes, the closed BUS is used on millimetre and sub–mm wavelength telescopes.

The open BUS is directly exposed to the variable thermal environment. When recognizing the large number of tube/beam elements of an open BUS, as for instance

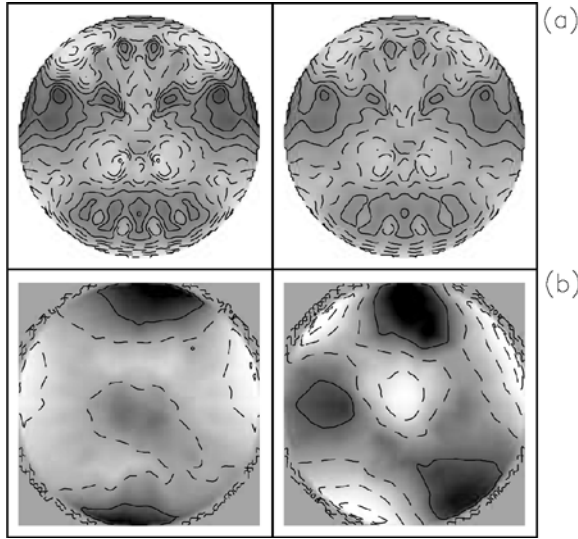


Fig. 2.12 IRAM 30-m telescope. (a) Homology deformations at horizon ($E = 0^\circ$, left) and zenith ($E = 90^\circ$, right), with surface rms values $\sigma(E=0) \approx \sigma(E=90) = 0.055$ mm for adjustment at $E_0 = 45^\circ$ elevation. (b) Thermal reflector deformations derived from measured BUS temperatures, with surface rms values $\sigma = 0.012$ mm (left; midnight) and $\sigma = 0.017$ mm (right, noon). Contours in steps of 0.01 mm.

seen in Picture 1.3 and Fig. 2.8, it is evident that the thermal behaviour of these open structures is, until now, mainly derived from static thermal model calculations. In these a uniform temperature change, a temperature gradient, a temperature step function or a random temperature distribution throughout the BUS is considered. In a more refined way a FEM can implement the influence of convective heat transfer with the ambient air, radiation to the ground and the sky and the influence of sunshine, but this is usually done for a particular condition of the environment rather than its dynamic evolution (see also Sections 11.2, 11.3.). On the other hand, from the FEM of the open BUS the begin and end points of the tube/beam network members are known and from this their orientation with respect to the ground, the sky and the Sun (Figs. 5.6 and 5.12). Applying the conductive, convective and radiative heat transfer relations, the time-dependent temperature of the open BUS network can be calculated for the variable thermal environment. The geometrical symmetry of the BUS and the fact that many BUS members have similar dimensions may greatly reduce the numerical work. Although this seems to be an overwhelmingly large amount of programming, and although such a study has not yet been made, it nevertheless seems to be a way to relate the thermal behaviour of an open BUS to the actual thermal environment instead of using exclusively constructed static thermal conditions. A step in this direction is the thermal calculation of the RT 70-m telescope (Russia) based on the FEM with insolation and convective heat transfer to the ambient air incorporated [Borovkov et al. 2003, Machuyev & Gimmelman

2006]. Thermal FEMs of this telescope based on shell structures and shell and rod structures of different degree of complexity have been investigated.

The closed BUS has a front cover and a rear cover. The front cover are the panels, without or with insulation at the back, the rear cover is formed by the cladding. The rear cladding is made of metal sheets and/or insulation plates. This can add a significant mass to the BUS (~ 30 to 50 kg/m^3 or ~ 1 to 3 kg/m^2) and may become prohibitively high for the larger cm–wavelength telescopes. The closure prevents direct solar illumination of the BUS and radiative cooling towards the cool sky at night. The closure creates a closed air volume that allows ventilation or climatization (ventilation with heated or cooled air). Some characteristics of closed BUS constructions and ventilation systems are summarized in Table 2.6 and Table 2.7. On several telescopes a metrology system, consisting either of a number of temperature sensors (T) and/or a laser metrology system (M), has been installed, or proposed to be installed, for real time measurement of thermal deformations resulting in reflector surface deformations and focus and pointing errors. At present there is no proven metrology system using inclinometers and/or laser rangars for monitoring of structural deformations causing pointing errors and reflector surface errors.

A numerical thermal study of a closed BUS, also with ventilation or climatization included, is easier than a numerical thermal study of an open BUS. For the closed BUS the coupling to the time–dependent thermal environment is via the reflector panels and the flat rear cladding surfaces. In particular, the calculation of solar illumination becomes relatively easy (Fig. 5.13). Under solar illumination and convective heat transfer from the ambient air the exterior surface of the panels and the cladding attain a certain temperature, which via heat conduction through the panels/cladding determines the interior surface temperature of the panels (or of the panel insulation) and the cladding. The inner surfaces radiate at infrared wavelengths diffusely into the closed volume of the BUS. This omnipresent diffuse radiation interacts with the BUS network.

The effect of ventilation/climatization of a closed BUS is a function of the air flow, for instance in radial or circular direction, and of the convective heat transfer of the ventilated tube, beam and plate profiles. The corresponding convective heat transfer coefficients and the formulation of ventilation/climatization are discussed in Sections 7.5 and 7.6 The ventilating air may contain a contribution of outside ambient air. When considering forced ventilation of the air inside a telescope it is important to consider in thermal calculations the heat produced by the fans. In large telescopes the fans are installed in the BUS and the heat from the fans is often released inside the BUS and may have to be taken out by additional cooling. An example is the BUS climatization system of the IRAM 30–m telescope [Baars et al. 1988]. For a calculation it is safe to assume that 10 to 20% of the fan power is released as heat.

The sectors and plates of the BUS of the VertexRSI ALMA 12–m prototype telescope divide the BUS volume into many rather independent compartments (see Fig. 9.29.c). Ventilation is not foreseen and natural convection of the air inside the compartments is small.

Table 2.6 Telescopes with Ventilation/Climatisation and/or Metrology.

Telescope ^{a)}	Reflector Diameter [m]	Thermal Protection of BUS	Ventilation of BUS	Metrology ^{b)}
Operating				
NRO (Japan)	10	cladding	yes	
ASTE (Chile)	10	CFRP, Paint, Insulation	yes	
ALMA/APEX ^{c)} (Chile)	12	CFRP, Paint	(yes) ^{d)}	
ALMA-J (USA)	12	CFRP, Paint, Insulation	yes	(<i>T</i>)
IRAM (Spain)	30	Paint, Insulation	yes	<i>T</i>
NRO (Japan)	45	Paint, Insulation	yes	<i>T</i>
GBT (USA)	100	Paint	no	<i>T(M)</i>
Under Construction				
Yebes (Spain)	40	Paint, Insulation	yes	
LMT/GMT (Mexico)	50	Paint, Insulation	yes	(<i>M,T</i>)
SRT (Italy)	64	Paint, Insulation	no	<i>T</i>

^{a)} see list of Acronyms of observatory sites.

^{b)} *T*: temperature measurements, *M*: metrology (inclinometer, laser ranger).

^{c)} VertexRSI telescope.

^{d)} thermal control of focus cabin and invar ring as support of the BUS.

Further details of BUS configurations can be found in the collection of papers published by Mar and Liebowitz [1969] and the textbook on reflector construction by Polyak & Bernalds [1990].

2.3.4 Reflector Panels

Reflector surfaces smaller than approximately 10 meter diameter can be machine-turned from a single cast element or spin-cast from resin materials. Examples are the machined 2.5-m reflector of the POM-2 telescope [Castets et al. 1988] and the spin-cast Lincoln Laboratory 8-m reflector [Dawson 1962]. Support ribs at the rear usually stiffen such reflectors so that gravitational deformations are negligible. The machining and spin-casting produce high precision surfaces. The original surface of the Kitt Peak 11-m telescope consisted of a single machined aluminium plate [see Baars 1983], however, because of thermal instability this plate was later replaced by panels.

The surfaces of the larger reflectors consist of panels that are segments of the reflector contour. The panels are arranged either as radial sectors or, more often, as rings concentric to the vertex of the reflector, or a combination of both. The panels may have a triangular, trapezoidal or hexagonal shape. The dimension of the panels cover in surface area approximately half a square-metre to several square-metres. Dependent on the wavelength of observation and the required surface precision, the panels may be constructed from mesh wire, perforated plates, metal plates reinforced by ribs or hexagonal structures on the rear and aluminium honeycomb cores

Table 2.7 BUS Ventilation and Climatisation Systems.

Telescope	Ventilation/Climatisation
BIMA 6-m^{a)}	BUS Ventilation (applied)
BUS enclosed Air Volume (V_{BUS})	25 m ³
Number of Ventilators	4
Total moved Air	5 100 m ³ /h = 1.4 m ³ /s
Circulation of Air Volume V_{BUS}	200 times / hour
Ventilation Speed	1 – 15 m/s
Flow Direction	Circular
Heating/Cooling of enclosed Air	none
ASTE 10-m^{b)}	BUS Ventilation (applied)
BUS enclosed Air Volume (V_{BUS})	65 m ³
Number of Ventilators	10
Air moved per Ventilator	780 – 3600 m ³ /h = 0.2 – 1.0 m ³ /s
Total moved Air	32 400 m ³ /h = 9 m ³ /s
Circulation of Air Volume V_{BUS}	500 times / hour
Ventilation Speed	2.2 m/s
Flow Direction	Circular
Heating/Cooling of enclosed Air	none
IRAM 30-m	BUS Climatisation (applied)
BUS enclosed Air Volume (V_{BUS})	1 800 m ³
Number of Ventilators	5
Air moved per Ventilator	12 600 m ³ /h = 3.5 m ³ /s
Total moved Air	63 000 m ³ /h = 17.5 m ³ /s
Circulation of Air Volume V_{BUS}	35 times / hour
Ventilation Speed	~ 3 m/s
Flow Direction	Circular
Heating Capacity of enclosed Air (max)	6 kW/ventilator
Cooling Capacity of enclosed Air (max)	4.5 kW/ventilator
Intake ambient air	~ 10 %
Yebes 40-m^{c)}	BUS Ventilation (prospected)
BUS enclosed Air Volume (V_{BUS})	4154 m ³
Number of Ventilators	20
Air moved per Ventilator	1440 – 5760 m ³ /h = 0.4 – 1.6 m ³ /s
Total moved Air	91 000 m ³ /h = 25 m ³ /s
Circulation of Air Volume V_{BUS}	22 times / hour
Ventilation Speed	~ 3 m/s
Flow Direction	Circular
NRO 45-m^{b)}	BUS Ventilation (applied)
BUS enclosed Air Volume (V_{BUS})	3000 m ³
Number of Ventilators	45 + 10
Total moved Air	359 100 m ³ /h = 100 m ³ /s
Air moved per Ventilator	7140 – 3780 m ³ /h = 2 – 1.1 m ³ /s
Circulation of Air Volume V_{BUS}	120 times / hour
Ventilation Speed	~ 1 – 2 m/s
Flow Direction	Circular
Heating/Cooling of enclosed Air	none
Intake of ambient air	through large panel gaps

Table 2.7 continued.

Telescope	Ventilation/Climatisation
LMT/GMT 50–m ^{d)}	BUS Ventilation (prospected)
BUS enclosed Air Volume (V_{BUS})	7000 m ³
Number of Ventilators	6 × 18
Air moved per Ventilator	12 600 m ³ /h = 8 m ³ /s
Total moved Air	180 000 m ³ /h = 50 m ³ /s
Circulation of Air Volume V_{BUS}	25 times / hour
Ventilation Speed	~ 3 m/s
Flow Direction	to be defined
Heating/Cooling of enclosed Air	none

Private Communication ^{a)} J. Lamb & J. Cheng (USA), ^{b)} N. Ukita (Japan),

^{c)} J.A. Lopez-Perez (Spain), ^{d)} D. Smith (USA).

covered by metal sheets or CFRP sheets. The panel contours are produced by machining, moulding or stretch forming. Occasionally several panels are attached to a panel frame by screws that allow a fine adjustment of the panel contour. The panels must have sufficient rigidity to preserve the surface contour and surface accuracy under gravity, temperature and wind. Thermal stability, especially during sunshine, can be achieved by using white TiO₂ paint, or shiny aluminium surfaces, or anodisation and coatings and/or materials of low thermal expansion (CFRP, invar). The thickness of panels is in the range of several millimetres for solid plate panels (with reinforcing ribs) to several centimetres for honeycomb panels. The typical mass is 10 to 15 kg/m².

Figure 2.13.a shows panels on the VertexRSI ALMA 12–m prototype telescope. The panels are aluminium plates reinforced by ribs that are seen in this picture because of different dew condensation, i.e. thermal background mass. Fig. 2.13.b shows the new generation machined aluminium panels as used on several IRAM 15–m telescopes. Finally, Fig. 2.13.c illustrates the Al–honeycomb core of a panel (with the front skin removed). This core is covered at the front and rear by a metal or CFRP skin, which seals the core.

The panels are attached to the BUS by screws or actuators. 3–point, 4–point and 5–point panel supports are common. On the IRAM 30–m telescope two panels are placed on a panel frame that is supported by the BUS, as shown in Fig. 2.14. The LMT/GMT 50–m telescope uses a similar design of panel frames, though of larger areas and with more panels on a frame [Kärcher & Baars 2000]. The machining of the OVRO 10.4–m reflector surfaces was made in the workshop of the Mount Palomar 5–m optical telescope with a temperature stabilized to 1° C [Woody et al. 1994]. After assembly on the BUS the panel positions are measured and the panels are adjusted to the best–fit contour within the specified tolerance. The temperature influence during telescope assembly and panel adjustments was already discussed by Schönbach [1968].

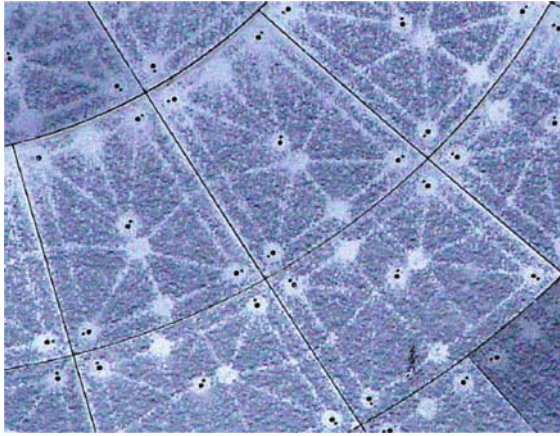


Fig. 2.13.a Aluminium plate panel (VertexRSI ALMA telescope, APEX), The rear side ribs are seen because of different dew condensation [Courtesy R. Snel, ALMA Test Team].



Fig. 2.13.b Machined Aluminium panel (IRAM 15-m telescope); left: rear side with hexagonal support boxes, right: front surface. The panel is machined from a solid aluminium plate [Courtesy IRAM, France].

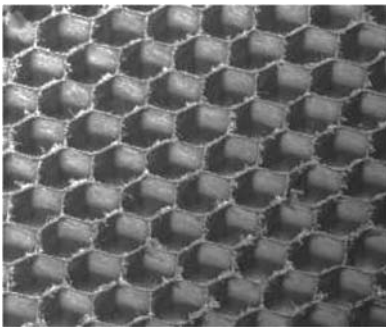


Fig. 2.13.c Honeycomb core; the front skin is removed [Courtesy HEXCEL].



Fig. 2.14 Partial view of the BUS tube network inside the IRAM 30-m telescope. Top of the figure: reflector side of the BUS. Big tubes: BUS network, smaller tubes of panel frames holding each 2 panels. The smaller tubes have a diameter of 2–3 cm [Courtesy J. Peñalver, IRAM, Spain].

The thermal behaviour of panels, especially those used on mm–wavelength telescopes, is studied through measurements of test panels subjected to thermal loads or in thermal model calculations. Special care is taken in the fixation of the panels on the BUS or the panel frames. Fixation hinges have been used to reduce the influence of differential thermal expansion between the BUS and the panels. A particular effect in this context is thermal panel buckling.

The panels face the thermal environment. Their construction aims for good thermal conductivity so that the thermal gradient through the panels is small, and for a short thermal time constant of $\sim 1/2$ hour so that the panels adapt easily to changes of the thermal environment. On several exposed telescopes the panels can be heated to prevent icing.

2.3.5 Active Reflector Surface

On several telescopes (GBT, SRT, LMT/GMT, NOTO, JCMT) the panels are attached to the BUS by actuators that allow a real time adjustment of the reflector surface. This can reduce the temperature induced surface deformations to a large extent. In a similar way a deformable subreflector (Effelsberg), or even a deformable Nasmyth mirror [Greve et al. 1996 a, 1994], may allow the reduction of the large scale thermal deformations of the main reflector surface. However, to do so a real time knowledge of the surface deformations is required that involves a real time

measurement. A method is Out-Of-Focus holography as used for measurements of thermal deformations of the JCMT and GBT reflector surface [Nikolic et al. 2007, Prestage et al. 2009], however this method causes significant interruptions of the astronomical observations. A convenient method is the measurement of the telescope temperature distribution with a large number of sensors (of the order of 100 to 200) and use of the temperatures in the FEM of the telescope for prediction of the surface deformations. This method provides real time data and is precise as demonstrated on the IRAM 30-m telescope [Greve et al. 2005].

2.3.6 The Quadripod and Subreflector

The quadripod (feed legs) supports the primary focus cabin and the subreflector of a Cassegrain or Gregory system and guarantees their correct distance and alignment with respect to the main reflector. The quadripod is either connected to the BUS, a subframe of the BUS or the elevation support system. The quadripod legs of the large cm-wavelength telescopes are usually made of steel beams and some thermal protection through white TiO₂ paint and/or insulation is applied. The quadripod legs of the NAO 45-m telescope and the BIMA (CARMA) 6-m telescopes are ventilated. The determination and compensation of transient thermal expansions of the quadripod legs is through radio measurements of focus and pointing errors and their corrections.

On the IRAM 30-m telescope the quadripod legs are steel tubes. They are insulated, painted white and equipped with a temperature controlled encircling fluid system (glycol) to produce temperature uniformity with the yoke (and BUS) structure. On the smaller mm/submm wavelength telescopes the quadripod legs are made of CFRP, painted white or also covered with shiny sun-reflecting aluminium foil.

The subreflectors are made of steel plates, aluminium plates, machined aluminium, Al-honeycomb and CFRP plates. The subreflectors are usually painted white with TiO₂ paint, while also special coatings (for instance rhodium) or micro-grooving has been applied. For observations of the Sun or close to the Sun, care must be taken that direct sunlight or scattered sunlight does not overheat the subreflector. The subreflectors of the BIMA (CARMA) 6-m telescopes are ventilated.

2.3.7 The Secondary Focus Cabin

The secondary focus cabin of a cm-wavelength telescope is a large structure, the inside of which can be in contact with the ambient air through windows, louvres and ventilators. There can be a substantial heat production by the receivers and the electrical equipment.

The fork-supported Cassegrain telescope, as used for smaller mm-wavelength telescopes, has a secondary focus cabin that is connected to the elevation axis bearings located at the upper part of the fork arms. The BUS is connected to the focus cabin either via a central hub (IRAM 15-m telescope) or via an invar ring that forms the top of the focus cabin (VertexRSI ALMA and APEX 12-m telescope [Mangum et al. 2006, Güsten et al. 2006]). The secondary focus cabin of the IRAM 15-m telescopes and the VertexRSI ALMA 12-m telescopes is made of steel. On the IRAM 15-m telescopes the thermal protection of the secondary focus cabin consists of insulation, an air gap and a radiation shield (aluminium plate). On the VertexRSI telescope the thermal protection of the secondary focus cabin consists of insulation, painted white on the outside and on the inside a liquid thermal stabilization system acting on the steel walls of the cabin, and ventilation of the invar cone with cabin air. The secondary focus cabin of the fork-supported AEC ALMA 12-m antennas is made of CFRP, painted white at the outside.

2.4 The Thermal Design of Radio Telescopes

The materials of which a telescope and enclosure is constructed and their coefficients of thermal expansion (CTE) are summarized in Table 2.8. The CTEs span a range of a factor ~ 20 and it is evident that temperature differences between structural components made of different materials may lead to stress and deformations. However, as summarized in the Table 2.9, large structural subsystems of a telescope are made of the same material with, in addition, often little thermal contact with other subsystems. However, a subsystem itself may have a non-uniform temperature.

Table 2.8 Telescope Materials (coefficients of thermal expansion).

Material	Coefficient of Thermal Expansion (CTE)[$10^{-6}/\text{K}$] ^{a)}	Principal Use
Steel	12	Mount, BUS, Quadripod
Aluminium	22	BUS, Panels
Al-honeycomb	$\sim 10-22$ ^{b)}	Panels
Invar	1	BUS joints, BUS base, Central Hub
CFRP	0-2	BUS, Panels, Quadripod
Insulation	-	BUS, Panels, Quadripod, Yoke, Fork
Concrete	~ 10	Pedestal, Foundation
Glass	~ 0.1 to 2	Optical Telescope Mirror

^{a)} also expressed as $\mu\text{m}/\text{m}/\text{K}$;

^{b)} dependent on the cover skin.

The thermal design of a radio telescope is based on the one hand on a finite element analysis (FEA) with *static* thermal load cases of uniform temperature

variations, temperature gradients and random temperature distributions throughout the structure (Section 11.2). On the other hand, the design can be based on *dynamic* thermal model calculations in which the telescope interacts with the variable thermal environment or the climate inside a radome/astrodome (Section 11.3). Realistic temperature distributions throughout the telescope are obtained from the dynamic thermal calculation that can be used in the FEA.

There are passive and active technical means to manipulate and reduce the influence of the thermal environment. The passive means are

- (1) white paint (for instance TiO_2 paint) with a relatively high absorption of solar radiation and high emission in the infrared; TiO_2 pigmented paint has little specular reflection and good visible light scattering;
- (2) shiny metal surfaces (for instance shiny aluminium) with a low absorption of solar radiation and low emission in the infrared; the shiny surface has a high specular reflection;
- (3) surface coatings (like Al-anodisation or rhodium) with a low absorption of solar radiation and low emission in the infrared; the coatings may have little specular reflection;
- (4) surfaces with micro-grooves or sand blasted finish to reduce specular reflection;
- (5) insulation, air gaps, radiation shields;
- (6) low thermal expansion materials like CFRP and invar.

The active means are

- (1) ventilation and climatisation (heating and cooling), perhaps implemented as a closed-loop system;
- (2) protection by a radome or astrodome, with ventilation;
- (3) temperature monitoring and active focus and pointing control, use of an active main reflector, subreflector or tertiary mirror.

Table 2.9 gives a summary of thermal protection applied on operating telescopes; Tables 2.10 a – 2.10 d summarize the thermal subsystems of existing telescopes, their construction materials and the applied thermal protection, if necessary.

Table 2.9 Applied Passive and Active Thermal Control of Radio Telescopes.

Telescope ^{a)}	Reflector Diameter [m]	Shortest ^{b)} λ [mm]	Thermal Control (p) = passive, (a) = active
cm-Wavelengths			
VLA (USA)	25	7	paint (p), partial fork insulation (p)
Cambridge (UK)	32	~ 60	paint (p), alidade T-measurement (a)
SRT (Italy)	64	10 (3)	insulation (p), active surface
Effelsberg (Germany)	100	10 (3)	paint (p), active subreflector
GBT (USA)	100	10 (3)	paint (p), T-measurement (a), active surface
mm-Wavelengths			
CSO (Hawaii)	10	0.4	astrodome ^{b)} (p)
ASTE (Chile)	10	0.4	CFRP ^{d)} -BUS (p), BUS ventilation (a)
HHT (USA)	10	0.6	astrodome, CFRP-BUS (p)
APEX (Chile)	12	0.3	CFRP-plated BUS (p), focus cabin T-control (a), fork and pedestal insulation (p)
Metsähovi (Finland) ^{e)}	3	3	radome (p) and ventilation (a)
JCMT (Hawaii)	15	0.6	astrodome (p) and ventilation (a), Al-honeycomb panels (p)
IRAM (France)	15	1	CFRP-steel BUS and quadripod (p) focus cabin & fork insulation and radiation shield (p)
Onsala (Sweden)	20	3	radome ^{c)} (p) and ventilation (a)
IRAM (Spain)	30	1	insulation BUS, yoke, quadripod (p) BUS climatisation (a), yoke ventilation (a), glycol circulation on quadripod (a) pedestal insulation (a)
Yebes (Spain)	40	3	BUS insulation (p) and ventilation (a)
Nobeyama (Japan)	45	3	BUS insulation (p) and ventilation (a)
LMT/GMT (Mexico)	50	1	BUS insulation (p) and ventilation (a), active surface

^{a)} see list of Acronyms of observatory sites;

^{b)} approximate value;

^{c)} the radome/astrodome also reduces the wind load;

^{d)} CFRP – carbon fiber reinforced plastic;

^{e)} also FCRAO (USA), Itapetinga (Brazil), Yebes (Spain).

Table 2.10.a Mount Structures.

Mount	Material	Form	Thermal Protection	Telescope ^{a)}
Pedestal	concrete	cone	insulation, paint	IRAM 30-m
Pedestal	concrete	cone	insulation, shiny aluminium radiation shield	SEST 15-m
Pedestal	steel		insulation, paint	ALMA 12-m
Alidade	steel	beams	paint	Effelsberg 100-m
Alidade	steel	beams	paint, some insulation	Medicina 32-m
Alidade	steel	tubes	paint, astrodome	JCMT 15-m
Fork	steel	plates	paint (insulation)	VLA 25-m
Fork	steel	plates	insulation, paint	ALMA 12-m
Fork	steel	plates	insulation, air gap, radiation shield	IRAM 15-m
Yoke	steel	beams	radome + ventilation	Onsala 20-m
Yoke	steel	plates	insulation, paint, ventilation, heating	IRAM 30-m

^{a)} see list of Acronyms of observatory sites.

Table 2.10.b Backup Structures.

BUS	Material	Thermal Protection	Telescope ^{a)}
open	steel	none	GMRT 45-m
open	steel	paint (active subreflector)	Effelsberg 100-m
open	steel	paint, active reflector surface	GBT 100-m
closed	steel	cladding, paint, active reflector surface	SRT 64-m
closed	steel	cladding, paint, ventilation	Yebes 40-m
closed	steel	insulation, paint, climatisation	IRAM 30-m
closed	steel	cladding, paint, ventilation, active reflector surface	LMT/GMT 50-m
closed	CFRP-steel ^{b)}	cladding, paint	IRAM 15-m
closed	CFRP ^{c)}	CFRP cladding, paint	ALMA-AEC 12-m
closed	HC-CFRP ^{d)}	CFRP cladding, paint, T-controlled BUS support (invar)	ALMA-VertexRSI 12-m
open	aluminium	radome + ventilation	Onsala 20-m, MIT 37-m
open	aluminium	radome + ventilation, AL-foil covered	FCRAO 14-m
open	steel	paint, astrodome + ventilation	JCMT 15-m

^{a)} see list of Acronyms of observatory sites.

^{b)} tubes, ^{c)} plates,

^{d)} HC: Al-honeycomb core, CFRP cover plates.

Table 2.10.c Panel Constructions.

Panels	Material	Thermal Protection	Telescope ^{a)}
Mesh-wire		none	GMRT 45-m
Plate-perforated, grid ^{b)}	aluminium	paint	Effelsberg 100-m
Plate	aluminium	anodised	IRAM 15-m ^{c)}
Plate	aluminium	grooves	VertexRSI ALMA 12-m
Plate	aluminium	paint	Effelsberg 100-m
Honeycomb	aluminium	insulation, paint	IRAM 15-m ^{d)} , IRAM 30-m
Honeycomb	aluminium	rhodium coating	ALMA(AEC) 12-m

^{a)} see list of Acronyms of observatory sites.

^{b)} outer panel rings, to reduce wind load;

^{c)} new generation panels, ^{d)} original panels.

Table 2.10.d Quadripod Constructions.

Material	Form	Thermal Protection	Telescope ^{a)}
steel	beams	paint	Effelsberg 100-m
steel	tubes	insulation, internal ventilation	BIMA 6-m, NRO 45-m
steel	tubes	insulation, paint, climatisation	IRAM 30-m
steel	tubes	radome	Onsala 20-m
CFRP	tubes	paint	ALMA/AEC 12-m
CFRP	tubes	paint, part aluminium foil	IRAM 15-m

^{a)} see list of Acronyms of observatory sites.

Chapter 3

Telescope Enclosures

The large cm–wavelength telescopes at Jodrell Bank, Effelsberg, Parkes, Green Bank and others are open–air telescopes. The smaller telescopes, and in particular those for short wavelengths, are either closed or placed in an enclosure. A closed telescope is one in which the BUS is covered by the front panels and the rear cladding in order to prevent direct interaction with the thermal environment, and in some cases to allow ventilation. Several telescopes are placed in an astrodome with a slit that can be opened for observation, or which is more or less permanently covered by a radio transparent membrane. The sides and the rear of an astrodome are usually metal plate walls. The astrodome follows the motion of the telescope. This limits the size to manageable structures, at reasonable costs. The over–hemispherical radome, on the other hand, has a radiowave transparent skin, is fully closed and stationary. The telescope inside the radome can move and observe in all directions through the radome, with blockage by the supporting space frame. The astrodome and radome are part of the telescope’s concept of thermal and wind protection. The earlier mm–wavelength telescopes were built from aluminium in order to reduce mass and placed in a ventilated radome to cope with the larger thermal expansion of aluminium. The HHT, CSO and JCMT telescopes with astrodome protection are listed in Table 3.1 and are shown in Fig. 3.1 to Fig. 3.3, the radome of the Onsala 20–m telescope is shown in Fig. 3.4.

The Kitt Peak 12–m telescope (USA), the HHT 10–m telescope (USA) and the CSO 10–m telescope (Hawaii) use an astrodome with open slit. The JCMT 15–m telescope has an astrodome with the slit covered by a radio transparent membrane. The membrane is partially transparent for solar radiation that causes heating of the inside air and the telescope, ventilation is installed. The Kitt Peak, CSO and JCMT telescopes are made of steel, partially covered with insulation, the HHT telescope has a CFRP BUS.

The thermal behaviour of a telescope in an astrodome with open slit is similar to that of an optical telescope. If the slit is closed during the day, the temperature of the air and the telescope in the astrodome may stay close to the temperature of the previous night. For observations during the day the astrodome can be positioned in a

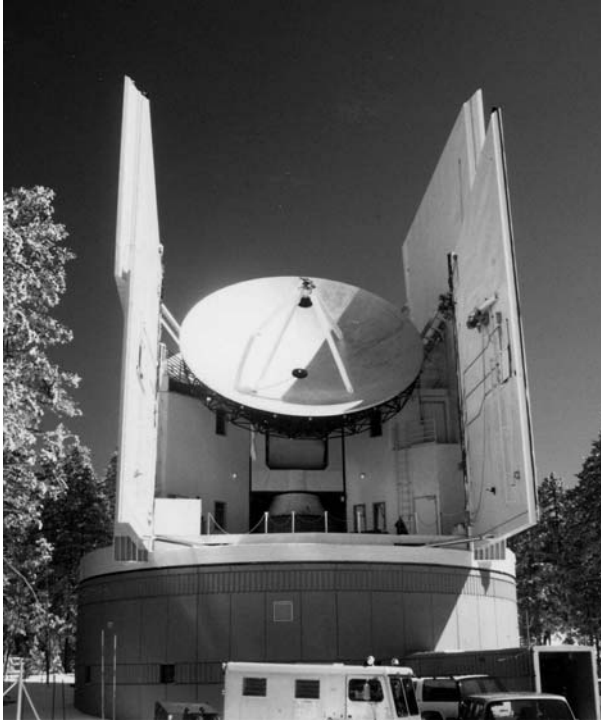


Fig. 3.1 Astrodome of the 10-m Heinrich-Hertz Telescope (HHT, Arizona, USA, 3 200 m altitude). The astro-dome is opened for observations [Courtesy HHT, USA].



Fig. 3.2 Astrodome of the 10-m Caltech Submillimeter Observatory Telescope (CSO, Hawaii, 4 000 m altitude). The astro-dome is opened at night for observations [Image courtesy Sub-mm Observatory, USA. Picture taken by R. Howard, CSO Site Manager].

Table 3.1 Radio Telescope Enclosures.

Telescope ^{a)}	Telescope Diameter [m]	Enclosure Diameter [m]	Volume approximate [m ³]
Astrodome			
HHT ^{b)}	10	~ 15 × 15	open
CSO ^{c)}	10	~ 18 × 14	open
JCMT ^{d)}	15	~ 27 × 22	15 000
Radome			
FCRAO ^{e)}	14	20	3 100
Onsala ^{f)}	20	27	10 500
MIT Haystack ^{g)}	37	46	38 000

^{a)} see list of Acronyms of observatory sites.

^{b)} Baars et al. [1999]; ^{c)} <http://www.caltech.edu/CSO>;

^{d)} <http://www.jach.hawaii.edu/JCMT>;

^{e)} Arny & Valeriani [1977], similar telescopes are at Metsähovi (Finland), Yebes (Spain), Itapetinga (Brazil), see Kaufmann & d'Amato [1973].

^{f)} Menzel [1976]; ^{g)} Weiss et al. [1969], Barvainis et al. [1993].



Fig. 3.3 Astrodome of the 15-m James Clerk Maxwell Telescope (JCMT, Hawaii, USA, 4 000 m altitude). The astrodome consists of a steel housing that can be rotated. The ‘slit’ is covered by a membrane, it can be opened for special observations [Courtesy R.E. Hills, Cambridge, UK].

direction that avoids direct solar illumination of the telescope. During the night, the telescope and especially the reflector surface see the cold sky, a part of the warmer

astrodome walls and the floor and the ground. The JCMT astrodome, which is closed by a membrane, has louvres and ventilation.

The radome is a stationary, closed, over-hemispherical structure. The radome is held by a metal space frame and overpressure of the inside air. The plastic radome skin is often made of GoretexTM material of whitish colour. With respect to solar radiation the GoretexTM material has an absorption coefficient of $a_s \approx 0.05$, a reflectance of $\rho_s \approx 0.70$, and a transmission coefficient of $\tau_s \approx 0.25$.

The thermal behaviour of a telescope in a radome follows the inside climate. The telescope is never exposed to direct solar radiation. However, solar radiation entering through the radome skin and radiation from the warmed-up skin material into the inside produce a diffuse background radiation (at visible and infrared wavelengths) and an increase of the inside air temperature. In order to obtain a uniform temperature distribution, in particular in vertical direction, the inside air is ventilated, often with intake of dried outside ambient air. In many radomes the fans are installed at the periphery, with some upward guidance of the airflow. The ventilation may also partially be directed to the centre of the radome by fans at the centre area [Barvainis et al. 1993]. The air inside the radome is often heated to a few degrees above the ambient air temperature, or the freezing point, in order to prevent condensation at the inside of the skin, and to some extent on the outside of the skin.



Fig. 3.4 Radome of the 20-m Onsala Space Observatory Telescope (OSO, Sweden, sea level). The radome consists of GoretexTM plastic material supported by a space frame and overpressured inside air [Courtesy L.E.B. Johansson, Onsala Observatory, Sweden].

Some telescopes with radome protection are listed in Table 3.1. The BUS constructions of these telescopes are made of aluminium. The FCRAO 14-m telescope BUS is covered with aluminium foil, as shown in Fig. 3.5, to decouple the internal diffuse radiation from the BUS. Other telescopes, like the MIT-Haystack telescope, are painted white. The data of Table 3.1 and Table 3.2.a of the Onsala and the MIT-Haystack radome were used for a thermal study of a possible astrodome for the 50-m LMT/GMT telescope [Greve & MacLeod 2001].

Radomes are no longer used for mm-wavelength radio telescopes. On the one hand, the short wavelength telescopes have become large in diameter (30 to 50 m diameter) and thus would require a large, unmanageable and expensive radome. On the other hand, temperature effects on mm-wavelength telescopes have been reduced by using low thermal expansion CFRP material and ventilated or climatized BUS structures. In addition, the radio transmission of the radome skin can be poor at sub-millimetre wavelengths.



Fig. 3.5 FCRAO telescope (Amherst, USA) inside the radome. The telescope is covered in aluminium foil. Note the ventilator at the periphery of the radome [Courtesy F.P. Schloerb, FCRAO, USA].

Table 3.2.a summarizes the thermal parameters of 3 radomes, Table 3.2.b the thermal parameters of 3 astrodomes. The solar illumination of a radome/astrodome is derived in Chapter 5; temperature measurements inside the Metsähovi and MIT-Haystack radome are presented in Chapter 10; thermal model calculations of the astrodome-enclosed JCMT 15-m telescope were made by Bregman & Casse [1985]; thermal calculations of the Onsala and MIT-Haystack radome are presented in Chapter 11.

Table 3.2.a Radio Telescope Enclosures ^{a)}: Radome (RD).

Parameter		FCRAO ^{b)}	Onsala ^{c)}	MIT–Haystack ^{d)}
Altitude of site	[m]	~ 0	~ 0	~ 0
Latitude of site	[°]	42	60	42
Telescope Diameter	[m]	14	20	37
Telescope Material (BUS)		Al	Al	Steel
Diameter of RD	[m]	20	30	46
Height of RD	[m]		20	45
Surface of RD	[m ²]	950	2 100	5 000
Inside Air Volume	[m ³]	3 100	10 500	38 000
Thermal Control of RD		Ventilation + Heating	Ventilation + Heating	Ventilation + Heating
Louvres	[m ²]	Top Hatch	none	Top Hatch
Forced Ventilation	[m ³ /h]		10 000	25 000
Replenishment of Air			~ 1 h	~ 1.5 h
Thermal Control of Telescope		Al–foil		Water–cooling part of BUS
Heat Input to RD				
Incident Solar Radiation ^{e)} \mathcal{E}	[kW]		~ 800 ^{e)}	~ 2000 ^{f)}
Absorbed Solar Radiation \mathcal{E}_α	[kW]		40	100
Transmitted Solar Radiation \mathcal{E}_α	[kW]		200	500
Capture Coefficient f_c			0.3	0.3
Captured Solar Radiation \mathcal{E}_c	[kW]		60	150

^{a)} further details in Greve & MacLeod [2001].

^{b)} Five College Radio Astronomy Observatory, USA; similar telescopes are at Metsähovi (Finland), Yebes (Spain), Itapetinga (Brazil).

^{c)} Onsala Space Observatory, Sweden; ^{d)} MIT–Haystack Observatory, USA.

^{e)} maximum noon values August 22 (see Section 5.7), ^{f)} May 20.

Table 3.2.b Radio Telescope Enclosures ^{a)}: Astrodome (AD).

Parameter		CSO ^{b)}	HHT ^{c)}	JCMT ^{d)}
Altitude of site	[m]	4 000	3 200	4 000
Latitude of site	[°]	20	33	20
Telescope Diameter	[m]	10	10	15
Telescope Material (BUS)		steel	CFRP	steel
Diameter of AD	[m]	18	15	27
Height of AD	[m]	15	15	22
Surface of AD	[m ²]	1 200	1 200	2 400
Inside Air Volume	[m ³]	open	open	15 000
Thermal Control of AD		open	open	Ventilation
Louvres	[m ²]			~ 20
AD Thermal Protection		shiny Al	paint	outside paint inside shiny
Thermal Control of Telescope			CFRP BUS shiny panel surface	paint shiny panel surface

^{a)} further details in Greve & MacLeod [2001].

^{b)} Caltech Sub-mm Observatory (Hawaii), ^{c)} Heinrich Hertz Telescope (USA);

^{d)} James Clerk Maxwell Telescope (Hawaii).

Chapter 4

The Variable Thermal Environment

4.1 The Environment and Observatory Sites

The local thermal environment interacts with a telescope, or its enclosure, and determines to a large extent the thermal behaviour of a telescope. The thermal environment is therefore investigated with the intention to derive global parameters for the design and operation of a telescope and its enclosure. The global parameters are site dependent and dependent on the season, the month and the day of the year. Each telescope site needs its own investigation, for a considerable length of time to obtain reliable statistical data. A telescope may reach a (quasi-)equilibrium state in the thermal environment, or may follow its variations with a certain time delay and a reduced amplitude. The interaction of structural components with the environment can be reduced by paint, insulation and ventilation, or even be excluded to a large extent by placing the telescope in an enclosure. Important for the design and operation of a telescope are the time constants of the thermal environment and the thermal time constants of the telescope components.

Evidently, a telescope in Space is subject to a different thermal environment than to that experienced on the ground.

The ground-based telescope interacts with

- the *ambient air*, of temperature $T_A(t)$, by convection and conduction,
- the *ground*, of temperature $T_G(t)$, by radiation,
- the *sky*, of effective temperature $T_S(t)$, by radiation,
- the *solar radiation*, as a direct external heat source.

These are ‘infinite’ heat sources, or heat sinks, which affect the thermal state of the telescope and enclosure; the thermal state of the telescope or enclosure, however, does not change the thermal environment. To illustrate the influences of the time variable (t) local thermal environment, an open-air radio telescope is considered as shown schematically in Fig. 4.1.

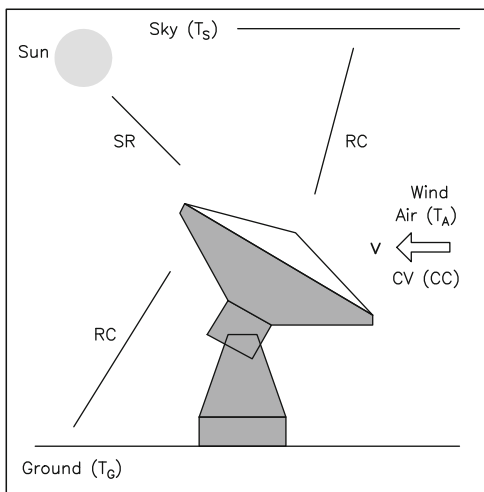


Fig. 4.1 Thermal interaction of an open-air telescope with the variable local thermal environment. CV: convective coupling, CC: conductive coupling, RC: radiative coupling. SR: solar radiation (external energy source).

Although the weather is an immensely variable phenomenon, its global and local characteristics can nevertheless be described by a few parameters, i.e. the ambient air temperature, the air pressure, the wind speed and wind direction, the humidity, the cloud coverage and the solar radiation. Time and season averaged values of these parameters describe the prevailing meteorological conditions of an observatory site. For global thermal considerations of telescope structures it can be sufficient to represent the variable environment by an average condition and extreme conditions, during summer and winter, by the amplitude of meteorological changes, their periodicity and the rate of change. For detailed thermal calculations it is convenient to express the conditions of the environment, as far as possible, by mathematical expressions, as a function of season or day of the year. This, however, is not always possible. The most realistic calculations use *in situ* measured values.

Telescopes are located at many geographic longitudes, latitudes and altitudes. A telescope may operate in a meteorological environment that follows to a large extent the large-scale climate, it may operate in an area with pronounced local effects, like mountain areas, or in a climate artificially created in a radome or astrodome. In populated areas, the climatic parameters of an observatory site are usually known from long-term meteorological records, for remote areas, the climatic parameters are often derived from special site studies (see, for instance, Ardeberg & Woltjer [1983], Vernin et al. [2002], Bely [2002]). For telescope design and operation it is useful to distinguish several climatic zones, for instance (1) the low altitude grassland and forested regions [for instance Jodrell Bank, UK; Effelsberg, Germany; Green Bank, WVA, USA], (2) the moderate altitude ($\sim 1\,500$ – $2\,000$ m) forested and grassland regions [for instance the VLA, NM, USA], (3) the mountain regions ($\sim 2\,000$ – $3\,000$ m) [for instance Plateau de Bure, France, and Pico Veleta, Spain], (4) the high altitude mountain regions ($\sim 3\,000$ – $5\,000$ m) [for instance Hawaii, USA; Atacama Desert, Chile] and (5) the polar regions [for instance Spitzbergen, Norway];

Antarctica]. Information related to the low altitude climate zones is found in the textbook *The Climate near the Ground* by Geiger [1973], for the antarctic sites see *Antarctic Meteorology and Climatology* by King & Turner [1997].

4.2 The Ambient Air

The state of the ambient air is, as for any other gas, characterized by its chemical composition, density (ρ), pressure (p), temperature (T_A) and humidity (H). Since the ambient air is part of the Earth's atmosphere, which is under the influence of gravity, these parameters depend on the altitude (z) of the observatory site. A full description of the ambient air for thermal considerations requires also knowledge of its heat capacity (\mathcal{C}_A), heat conductivity (k_A), viscosity (ν_A) and motion, i.e. the wind at the observatory site. The wind determines the external convective heat transfer. The basic parameters of the ambient air (ρ , p , T , H) are independent of the exact location on the observatory site and the height of the telescope structure. However, this is not necessarily the case for wind. The wind speed and wind direction usually have a profile that depends on the ground topography and the local height on the site. For large telescope structures this profile may need to be taken into account.

The different components of the ambient air (in volume percentage: 78 % N_2 , 21 % O_2 , 1 % Ar, etc.) contribute with their partial pressures to the total pressure of the air. The ideal gas equation can be applied to the air (i.e. the sum of the partial pressures)

$$pV = RT \quad (4.1)$$

with p the air pressure, V the volume, T the absolute temperature and R the gas constant of air, $R = 8.314 \text{ J/mol/K}$. For an isothermal atmosphere with $T(z) = T_0 = \text{constant}$, thus independent of the altitude, it follows that

$$p(z) = p_0 \exp(-gz/RT) \quad (4.2)$$

(with g the gravity constant), for a polytrope atmosphere with $T(z) = T_0 - \gamma z$ and $\partial T/\partial z = -\gamma$ it follows that

$$p(z) = p_0 (T/T_0)^{g/R\gamma} \quad (4.3)$$

As a rule-of-thumb, the ambient air temperature decreases (γ) by approximately 5 to 10° C per 1 000 m increase in altitude.

For thermal considerations of telescope structures it is important to know the properties of the local ambient air (combined dry and wet component, H_2O) in order to select the appropriate value of the heat capacity, conductivity and kinetic viscosity. The highly variable local wet air component is important for estimates of precipitation and radiative properties of the atmosphere (effective sky temperature). The relation of the pressure p with height (z) of the dry air (d) and wet air (w) is often expressed as

$$p(z) = p_0 \exp(-z/\mathcal{H}) \quad (4.4)$$

with the scale height \mathcal{H} of the dry air $\mathcal{H}_d \approx 6-8$ km and of the wet air $\mathcal{H}_w \approx 2$ km. These are approximate values; the actual values depend on the instantaneous state of the atmosphere. While the state of the dry air (p, T, ρ) changes only on relatively long time scales (hours to days), this is often not the case for the wet air component. The state of the wet air component is derived from the instantaneous relative humidity (H) and the air pressure and air temperature.

Table 4.1 gives for observatory sites between sea level and 5 000 m altitude typical average values of the basic parameters of the dry and wet ambient air. The heat conductivity of air is $k = 0.024$ W/m/K and independent of the altitude. Further details of relations describing the ambient air (atmosphere) are found in textbooks on meteorology.

Table 4.1 Variation of Atmospheric Parameters with Height (average values).

Height [m]	Pressure ^{a)} p [mbar]	Density ^{a,b)} ρ [kg/m ³]	Heat Capacity \mathcal{C} [J/kg/K]	Kinetic Viscosity ν [m ² /s]	Water Vapour ^{c)} Pressure [mbar]
sea level	975	1.25	1.01	$13.9 \cdot 10^{-6}$	4.0
1 000	860	1.15	0.92	$15.1 \cdot 10^{-6}$	2.4
2 000	760	1.01	0.82	$17.2 \cdot 10^{-6}$	1.5
3 000	670	0.89	0.72	$19.5 \cdot 10^{-6}$	0.9
4 000	590	0.79	0.64	$22.0 \cdot 10^{-6}$	0.5
5 000	520	0.69	0.56	$25.2 \cdot 10^{-6}$	0.3

^{a)} for $\mathcal{H}_d = 8$ km, $p(0) = 975$ mbar, ^{b,c)} for $T = 273$ K, ^{c)} for $\mathcal{H}_w = 2$ km, $p_w(0) = 4$ mbar, and Eqs.(4.9,4.10).

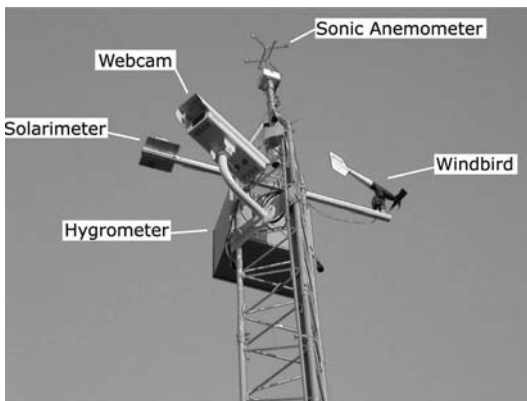


Fig. 4.2 Weather station on a 10 m high tower; VLA site (NM, USA) [Courtesy J.G. Mangum, NRAO, USA].

The meteorological textbooks give advice on how to measure the air pressure, air temperature, relative humidity, dew point temperature, wind speed and wind direction, etc. The meteorological parameters are usually measured at 2 m height above

the ground, in a wind sheltered weather station avoiding direct sunshine. Occasionally, the meteorological instruments are placed on a 10 m to 30 m high tower to probe the meteorological conditions at the height of a telescope or enclosure. A typical weather station at the VLA site (ALMA Test Project; NM, USA) is shown in Fig. 4.2. The temperature is measured with a thermometer to 0.1° Celsius or better, the air pressure with a barometer to 0.5 to 1 mbar, the relative humidity with a hair hygrometer (or a dew point thermometer) to 1 to 2 % and the wind speed with a cup anemometer or ultra-sound anemometer to approximately 0.5 to 0.25 m/s at a sampling rate of 1 to 10 Hz. Often the weather station also contains a solarimeter that measures the instantaneous insolation [W/m^2] and the daily duration of sunshine.

The ambient air is in contact with a telescope and its enclosure. The convective heat transfer between the ambient air and the telescope and enclosure components depends on the speed with which the air moves along the structure, as explained in Section 7.7. The speed and direction of this air flow may be different from the measured global wind characteristics, in particular if the local ground profile has significant structure, as for instance found in mountain areas or even on built-up observatory sites. The investigation of the ambient air temperature should be combined with data of the prevailing wind speed and wind direction.

4.3 The Ambient Air Temperature

4.3.1 Measured Ambient Air Temperatures

For the design and operation of a radio telescope, and enclosure, a sampling rate of the ambient air temperature between 1 to 10 minutes is usually appropriate.

The examples presented in this Chapter illustrate the low altitude forested area at the Effelsberg 100-m telescope (320 m altitude, Germany; zone 1), the mountain area at the Pico Veleta IRAM 30-m telescope (2900 m, Spain; zone 3) and the high altitude desert area at the Chajnantor ALMA site (5000 m, Chile; zone 4). A view of these sites is shown in Fig. 4.3.a-c, the ambient air temperatures measured at these sites throughout a year are shown in Fig. 4.4. Yearly and monthly averages can be derived from these data. For the selected sites the seasonal variations can be approximated by a cosine-variation with amplitude of the order of ~ 10 to 20°C . The daily variation of the air temperature is of similar amplitude. The distribution of the ambient air temperature throughout summer and winter is summarized in Fig. 4.5 and Table 4.2. The summer months cover July and August (northern hemisphere)/January and February (southern hemisphere), the winter months cover January and February/July and August. Figs. 4.4 and 4.5 and Table 4.2 define the global temperature range to which the telescope or enclosure is exposed. These data in combination with humidity data determine whether a site is warm and dry with little precipitation, of a moderate climate or a cold and wet climate with snow and ice.



Fig. 4.3a View of the low altitude forested site Effelsberg, Germany (320 m altitude). The location in a valley provides wind protection [Courtesy N. Junkes, MPIfR, Germany].



Fig. 4.3b View of the mountain site Pico Veleta, Spain. The IRAM 30-m telescope (at 2 900 m altitude) can be seen in the upper right corner. In the foreground is the ski resort Pradollano.



Fig. 4.3c View of the high altitude site Chajnantor, Chile (5 000 m) [Courtesy S. Radford, NRAO, USA].

this figure will be printed in b/w

this figure will be printed in b/w

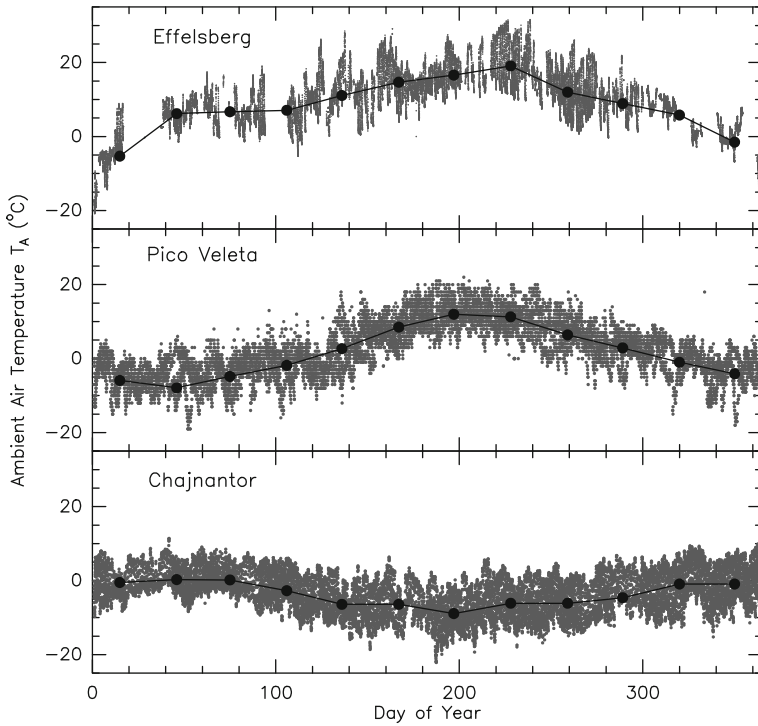


Fig. 4.4 Seasonal variation of the ambient air temperature at Effelsberg (1996, 1997), Pico Veleta (1996, 1998, 1999) and Chajnantor (2001, 2002). The dots are monthly average values.

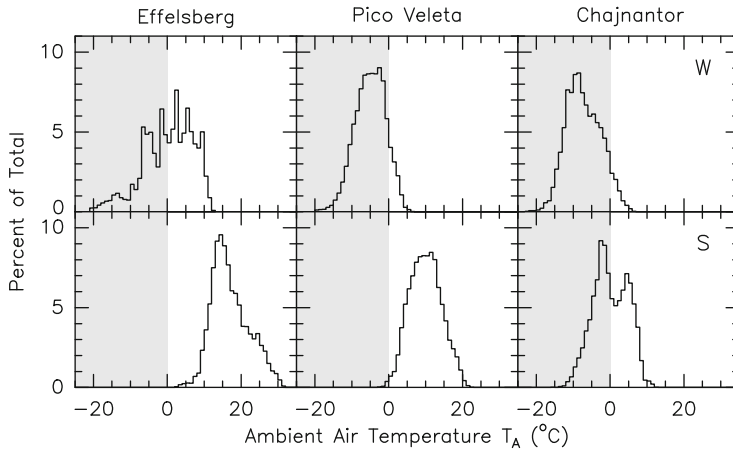


Fig. 4.5 Seasonal distribution of the ambient air temperature at Effelsberg (320 m), Pico Veleta (2900 m) and Chajnantor (5000 m). The shaded areas indicate temperatures below freezing point. W: winter, S: summer.

Table 4.2 Ambient Air Temperature: Seasonal Averages.

Location	Altitude [m]	Winter	Summer
		$\langle T_A \rangle$ [° C]	$\langle T_A \rangle$ [° C]
Effelsberg	320	2.5	15
Pico Veleta	2 900	-5	10
Chajnantor	5 000	-10	0

4.3.2 Approximation of the Daily Ambient Air Temperature

For many considerations of telescope and enclosure design it is sufficient to use a representative daily temperature distribution of the ambient air, perhaps specific for summer and winter. A regular daily variation of the ambient air temperature is illustrated in Fig. 4.6, this variation can be approximated by a cosine-function. As the other extreme, Fig. 4.7 illustrates an irregular variation with no periodicity at all and an extreme temperature decrease during a bad weather front.

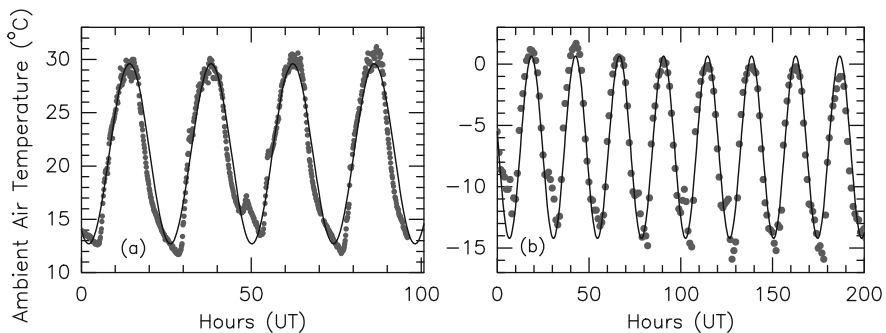


Fig. 4.6 Example of measured regular variations of the ambient air temperature at (a) Effelsberg (summer) and (b) Chajnantor (winter). These variations are approximated by a cosine-form periodicity (black lines).

The nearly perfect 24-hour cosine-form variation of the ambient air temperature $T_A(t)$ as observed in Fig. 4.6 can be expressed as

$$T_A(t) = T_{A0} - \Delta T_A \cos \omega(t - t_a) \quad (4.5)$$

with $\omega = 2\pi/24$ h, $T_{A0} = \langle T_A(t) \rangle$ the daily average temperature, ΔT_A the amplitude of the temperature variation, t in hours and t_a the time delay of the variation with respect to 12 h noon. The value of t_a is of the order of 2–3 hours. A statistical estimate of the amplitude ΔT_A can be obtained from the difference between the daily maximum temperature $T_A(\max)$ and daily minimum temperature $T_A(\min)$, shown in Fig. 4.8. If the ambient air follows a more or less regular temperature variation,

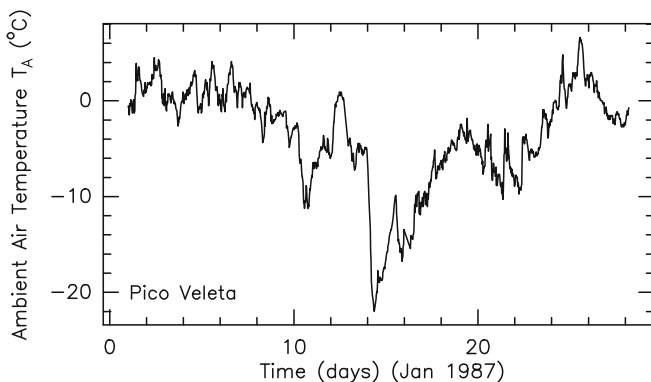


Fig. 4.7 Example of irregular variations and of an extreme and fast decrease of the ambient air temperature at Pico Veleta. On 14 Jan: $\Delta T_A = 17^\circ\text{C}$ within less than 12 hours.

then in this figure $\Delta T_A \approx 1/2 [T_A(\text{max}) - T_A(\text{min})]$. These values ΔT_A can be used in Eq.(4.5).

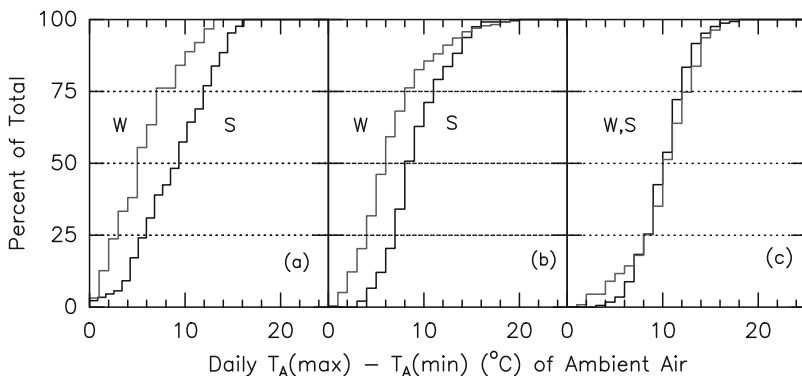


Fig. 4.8 Daily ambient air temperature variation at (a) Effelsberg, (b) Pico Veleta and (c) Chajnantor. W: winter, S: summer.

Cosine-form variations of the ambient air temperature provide some ease in thermal model calculations. These temperature variations describe oscillations around a quasi-stationary state with constant time average $\langle T_A(t) \rangle = T_{A0}$. Disregarding sunshine, a telescope interacting with such temperature oscillations will itself show temperature oscillations of its structural components, though usually of smaller amplitude and a time delay with respect to the air temperature variations. Occasionally, rapid temperature changes of non-periodic character may occur. The reaction of the telescope, and enclosure, on rapid non-periodic air temperature changes provides information on the thermal inertia and the thermal time constants of the telescope components (see Fig. 7.16).

4.3.3 Rate of Ambient Air Temperature Change

Important for the thermal design and operation of a telescope and enclosure is the change δT_A of the ambient air temperature within a given interval δt of time, at a specific hour of the day. This change is easily calculated for a cosine-form variation

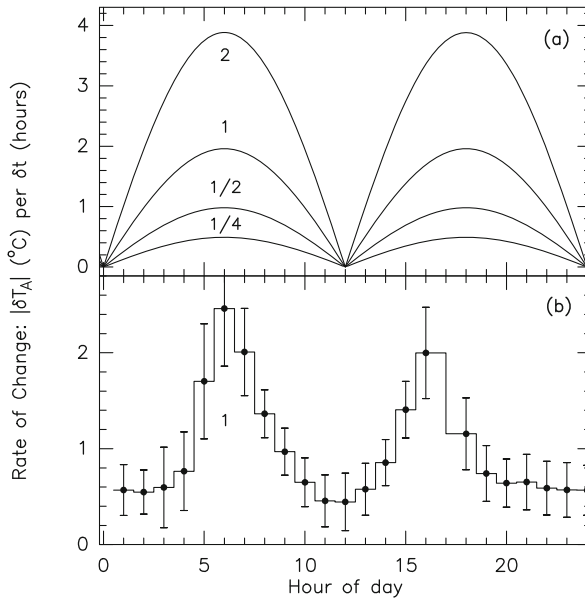


Fig. 4.9 Calculated (a) and measured (b) change of the ambient air temperature within the indicated time interval δt of 1/4, 1/2, 1 and 2 hours. The change shown in (a) is calculated for a cosine-form temperature variation, Eq.(4.5), of amplitude $\Delta T_A = 7.5^\circ\text{C}$, $t_a = 0$ h. (b) The measured values are for Chajnantor (2001), for $\delta t = 1$ h. The error bars are the rms values for 365 days of the measured year.

of the ambient air temperature, Eq.(4.5), namely

$$\delta T_A = \Delta T_A |\cos\omega(t - t_a) - \cos\omega(t + \delta t - t_a)| \quad (4.6)$$

The result of this calculation for a cosine-form with $\Delta T_A = 7.5^\circ\text{C}$ (as for instance seen in Fig.4.6) is summarized in Fig.4.9.a for several intervals δt . For other amplitudes $\Delta T_A'$ the values δT_A can be scaled by their ratios $\Delta T_A'/\Delta T_A$. The rate of temperature change δT_A derived from actual measurements at Chajnantor, for the interval $\delta t = 1$ hour, is shown in Fig.4.9.b.

Evidently, for a cosine-form variation the largest temperature change $\delta T_A/\delta t$ occurs near 6 (+ t_a) hours and 18 (+ t_a) hours while the smallest change occurs near noon and midnight. This agrees with the common experience that (high precision)

radio telescopes need special care in focusing and pointing during morning and evening hours, although the influence of sunrise and sunset plays a significant role in this statement. In general, a telescope component [i] where the temperature $T_i(t)$ depends on the ambient air temperature $T_A(t)$ by $T_i(t) = \gamma T_A(t + \Delta t)$, $\gamma \leq 1$, will show a similar behaviour as displayed in Fig. 4.9, though with a time delay Δt dependent on the thermal time constant. A good example of such a correlation is the measured path length variation of a fork arm, shown in Fig. 9.21.

4.4 Wind Speed and Wind Direction

The wind speed and wind direction are very variable with time and location. Observatory sites are usually characterized by global data that may, in the case of wind, not describe the specific condition at the telescope and enclosure. The wind speed and wind direction is influenced by the local terrain and local buildings and is a function of the height above the ground. It is therefore useful to measure the wind speed and wind direction at several locations of an observatory site. The wind speed, its direction and the air density at the site are important parameters in the calculation of convective heat transfer of the ambient air.

4.4.1 Measured Wind Speeds

The wind contains a steady flow component, characterized by the value of the wind speed and wind direction averaged over several minutes of time, and a gusty and turbulent flow component changing on time scales of sub-seconds to several seconds. However, for thermal considerations only the steady wind is of importance because of the generally long thermal time constant of telescope and enclosure components, of the order of 1/4 hour to several hours. An example of the structure of the wind speed is shown in Fig. 4.10 recorded at the sampling rate of 1 Hz (Plateau de Bure) and shown in Fig. 4.11 for a sampling rate of 10 Hz (VLA site). Such wind spectra can be used to derive the wind power spectrum. Figure 4.12 shows the wind speed measured throughout a year at Effelsberg, Pico Veleta and Chajnantor. The corresponding cumulative distribution of the wind speed is shown in Fig. 4.13.

The wind speed throughout a day is important for the design and operation of a telescope and enclosure. As indicated in Fig. 4.14 there are places with a more or less uniform distribution of the wind speed throughout the day, as for instance at Effelsberg and Pico Veleta, but also places with a significant asymmetry throughout the day, as for instance at Chajnantor [see Beaupuits et al. 2004]. Depending on the asymmetry of the wind speed distribution, an asymmetry of the average convective heat transfer occurs as well.

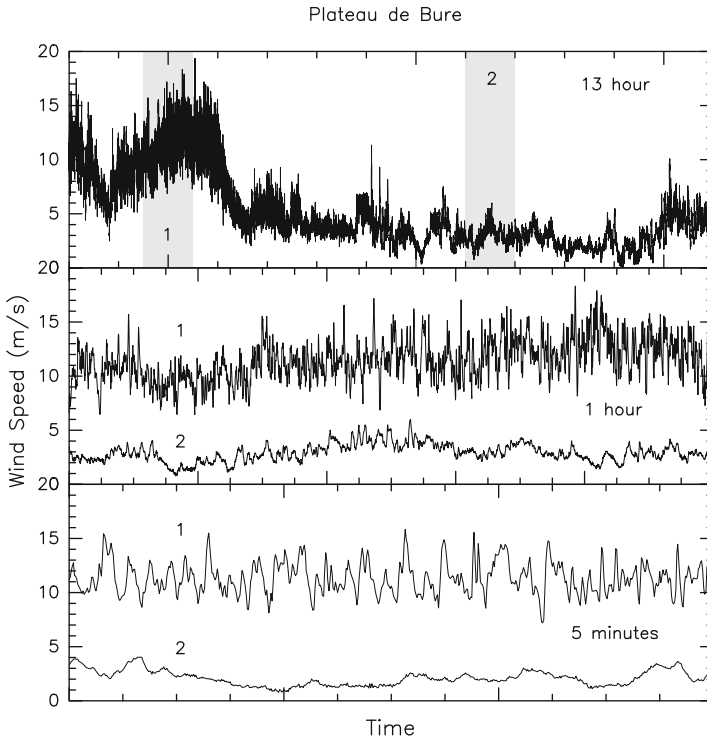


Fig. 4.10 Wind speed measured at Plateau de Bure (French Alps, 2500 m), at 1 Hz sampling rate. The wind measured in the windows 1 and 2 of the upper panel is shown with higher resolution for a 1-hour interval and a 5-minute interval.

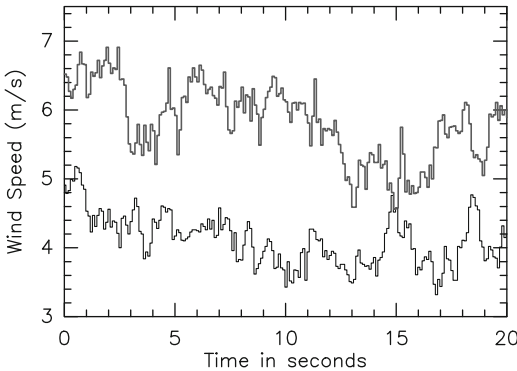


Fig. 4.11 Wind speed measured at the VLA site (NM, USA, 1500 m) at 10 Hz sampling rate; two recordings [Data from R. Snel, ALMA Test Team].

The prevailing wind direction has some influence on the thermal behaviour of a telescope and enclosure. The wind direction and the orientation of the telescope and enclosure define whether convective heat transfer is mainly from the front, i.e. the reflector side or the slit of the dome, or from the rear. However, as illustrated in Fig. 4.15 for Pico Veleta as an example, the wind direction is a highly variable parameter.

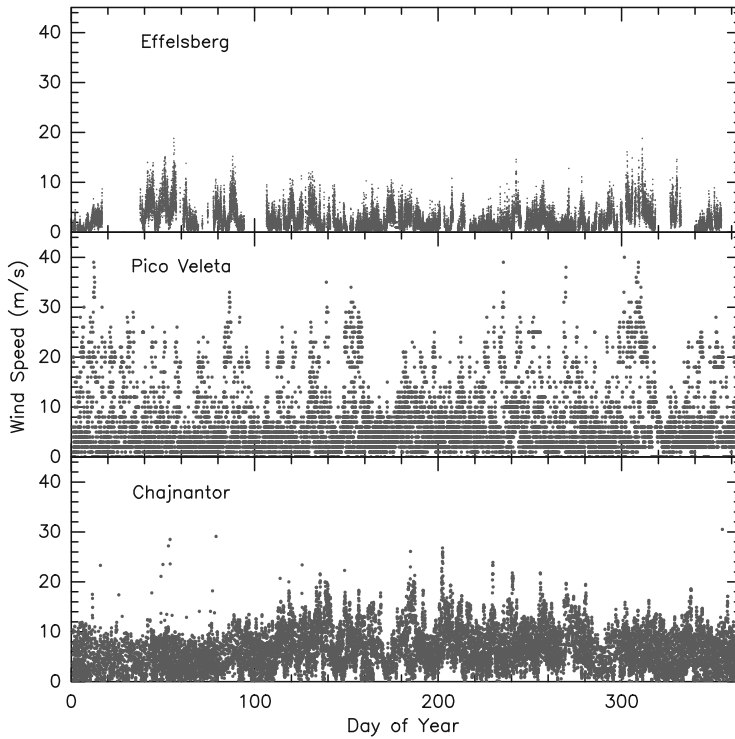


Fig. 4.12 Seasonal change of the wind speed at Effelsberg (1996, 1997), Pico Veleta (1996, 1998, 1999) and Chajnantor (2001, 2002).

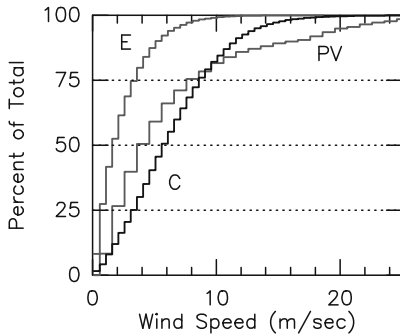


Fig. 4.13 Yearly cumulative distribution of the wind speed at Effelsberg (E), Pico Veleta (PV) and Chajnantor (C).

There are studies of wind and air flows and their prediction on the scale of large land masses, as for instance for the San Pedro Martir Sierra site on Baja California [Vogiatzis & Hiriart 2004], on the scale of an observatory site as shown in the figures above [see also Bely 2002], on the scale of air flow around and in and through an enclosure [Ando et al. 1991, De Young 1996] or in the vicinity of an optical mirror [Bridgeland & Jenkins 1997]. A similar study of wind flow around the ALMA AEC 12-m telescope and the associated heat exchange with influence on path length and pointing changes is mentioned by Stanghellini [2007]. The change of wind speed

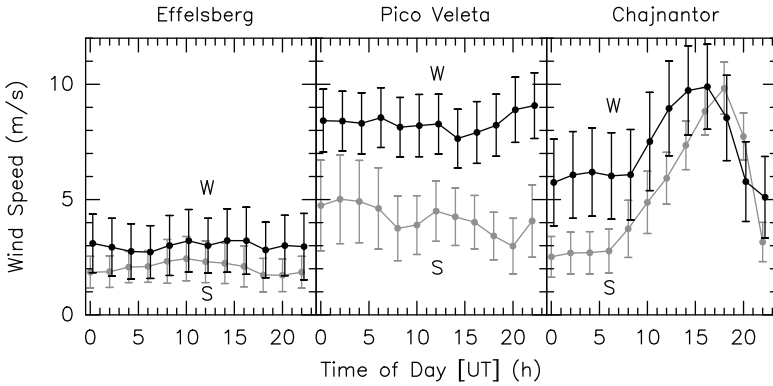


Fig. 4.14 Average wind speed throughout a day at Effelsberg, Pico Veleta and Chajnantor; during winter: W, and summer: S. The bars indicate the yearly dispersion of the average values.

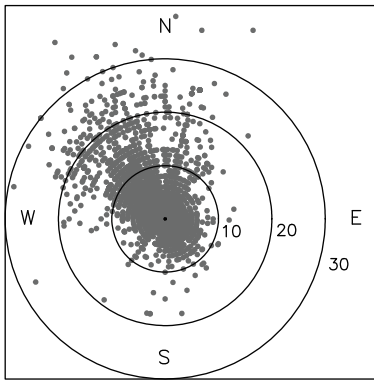


Fig. 4.15 Yearly wind direction at Pico Veleta. The circles give wind speeds of 10, 20 and 30 m/s. There is a preference of stronger wind from the North.

with height above the ground, i.e. the wind profile, is for instance reported by Blackadar [1964], Sherlock [1955], Deacon [1964] and others¹.

4.4.2 Wind Speed and Convective Heat Transfer

As explained in Section 7.7, the convective heat transfer (coefficient h) through wind of speed v and density ρ is proportional to the m -th power of the *Reynolds* number $h \propto \text{RE}^m \propto (v \rho)^m$, with $m = 0.5$ for laminar flow (Eq.(7.30)) and $m = 0.8$ for turbulent flow (Eq.(7.31)). In order to obtain the thermal effect of wind the aerodynamic wind speed is scaled by the exponent m . For a wind speed of $v = 10$ m/s the effective wind

¹ A special edition of the Annals of the New York Academy of Sciences [Cohen, ed., Volume 116, 1964] was dedicated to wind and temperature effects on large radio telescopes. Although 40 years old, the fundamental discussion of these effects is not out of date.

speed of convective heat transfer is $v_{\text{lam}} = (10)^{0.5} = 3$ m/s for laminar flow and $v_{\text{tur}} = (10)^{0.8} = 6$ m/s for turbulent flow. The wind around a telescope and enclosure has usually a turbulent flow. Through the density ρ is the thermal effect of wind also a function of altitude.

4.5 Ground Temperature

The surfaces of a telescope and enclosure are radiatively coupled to the ground surface layer. This radiative coupling is proportional to the radiative constants of the ground, i.e. the emission (e_1) and absorption (a_1) coefficient at infrared wavelengths and to the 4th power of the ground surface temperature $T_G(t)$.

With the large variety of ground surface layers there is also a large variety of surface temperatures and ground layer radiative properties. The radiative properties may not be constant for a given ground, but may change significantly with the wetness of the ground or the coverage with snow and ice. Table 4.3 gives representative values of the thermal properties for several ground surfaces.

Table 4.3 Thermal Properties of Grounds and Soils.

Type of Soil	$e_1 \approx a_1$	Density ρ [kg/m ³]	Heat Capacity \mathcal{C} [J/kg/K]	Heat Conductivity k [W/m/K]
Granite	0.45	2 750	850	3
Concrete	0.9	2 200	880	1.3
Brick (masonry)	0.5–0.7	1 700	850	0.65
Asphalt	0.85–0.95	2 100	920	0.70
Gravel Pavement	0.3	1 000	650	0.4–0.5
Soil (earth)	0.4–0.7	1 500	1 800	0.6–1.5
Snow Layer	0.8–0.98	~ 400	~ 2 000	~ 0.45

4.5.1 Measured Ground Temperatures

Figure 4.16 shows the temperature $T_G(t)$ measured on Plateau de Bure of an asphalt covered ground and a ground covered with snow, Fig. 4.17 shows the temperature of the dry sandy ground at Chajnantor. The measurements of the tarmac and snow covered ground were made with an infrared thermometer (see Chapter 6), the measurements at Chajnantor with an electric resistance thermometer. An illustrative example of different ground temperatures, due to different absorption/emission coefficients, is shown in a comparative measurement of an asphalt surface, a white surface and a cinder surface around the Subaru optical telescope [Usuda et al. 2004]. The measurements were made in the context of local seeing.

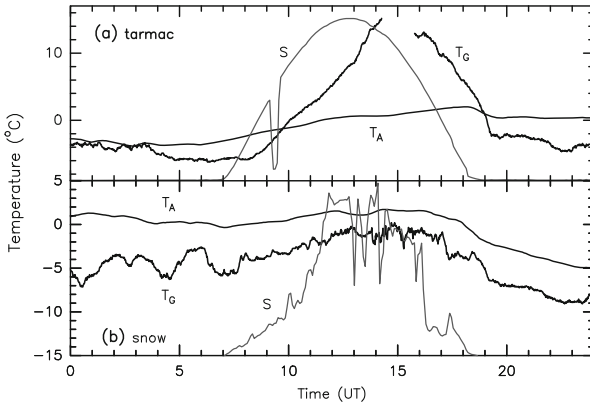


Fig. 4.16 Ground temperature of (a) a grey asphalted surface (rail bedding at Plateau de Bure) and (b) of the same surface covered with a thick layer of snow. T_G : temperature of the ground, T_A : ambient air temperature, S: measured solar irradiation (normalized scale).

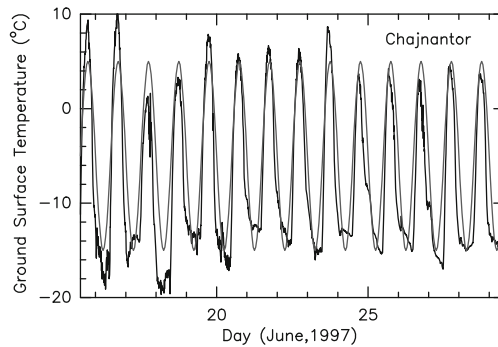


Fig. 4.17 Surface layer temperature of the sandy ground at Chajnantor. The grey line is a cosine-form approximation Eq.(4.7) [Data from S. Radford, NRAO, USA].

4.5.2 Approximation of the Ground Temperature

As illustrated in Fig. 4.17 for the sandy ground at Chajnantor [Snyder et al. 2000], in many cases the time variable ground temperature can be approximated by

$$T_G(t) = T_{G0} - \Delta T_G \cos \omega(t - t_g) \quad (4.7)$$

with $\omega = 2\pi/24\text{h}$, $T_{G0} = \langle T_G(t) \rangle$ the daily average ground temperature, ΔT_G the amplitude of the temperature variation and t_g the time delay of the variation with

respect to 12 h noon. The time delay t_g is of the order of 1–3 hours. However, for many thermal considerations and calculations $T_G(t)$ is often related to the recorded air temperature $T_A(t)$ by applying a (constant) offset ΔT_G

$$T_G(t) = T_A(t) + \Delta T_G(t) \quad (4.8)$$

where ΔT_G may be +5 to +10° C during afternoon and evening and –5 to –10° C during night and early morning. These values ΔT_G take into account the warming of the ground by solar radiation during the day and radiative cooling of the ground towards the sky during the night.

The radiative coupling of the reflector surface of the IRAM 30–m telescope to the ground (and the sky) is illustrated in the infrared picture 8.1. The radiative coupling of structural components to the ground and the sky is explained in Chapter 8.

4.6 Humidity, Condensation, Icing

At most observatories the relative humidity (H) is measured. The value of H, between 0 and 100 %, gives an indication whether the weather is dry (low values H) or wet (high values H) with possible precipitation of rain or snow. The humidity, and by this the amount of precipitable water vapour, determines the effective temperature of the sky T_s to which the telescope and enclosure is radiatively coupled.

Dew, rain, frost, snow and ice are transient phenomena and usually associated with meteorological conditions when observations are not possible. Representative values of the thermal properties of water, ice, snow and frost (estimate) are given in Table 4.4.

Table 4.4 Thermal Properties of Water, Frost, Snow and Ice.

Precipitation	Density ρ [kg/m ³]	Heat Capacity \mathcal{C} [J/kg/K]	Volume Heat Capacity $\rho\mathcal{C}$ [MJ/m ³ /K]	Heat Conductivity k [W/m/K]
Water	1 000	4 200	4.20	0.6
Ice	920	2 000	1.84	2.25
Snow	400	2 000	0.80	0.5
Frost	~ 100–200	~ 600	~ 0.1	~ 0.05–0.2

Besides the degradation of the atmospheric transmission at high humidity, especially at optical, infrared and (sub)mm wavelengths, and the general impossibility to observe at short wavelengths during rain and snow, for thermal aspects of a telescope and enclosure it is mainly the accumulation of snow and the formation of frost and ice which are important. A telescope, and enclosure, may need a de-icing system to keep them dry and free of snow and ice. The objective is the prevention of ice and the accumulation of snow since it is more difficult to eliminate ice and snow after

they have formed and settled on the telescope, or enclosure. The IRAM telescopes are examples of structures with de-icing of the panels and quadripod (PdB) and de-icing of the panels, the cladding of the BUS, the yoke and the quadripod (PV). At climatic conditions of Plateau de Bure and Pico Veleta, which may be classified during certain winter conditions as Nordic sites, it is found that a de-icing capacity of 100 to 200 W/m² is sufficient under moderate snowfall and wind conditions.

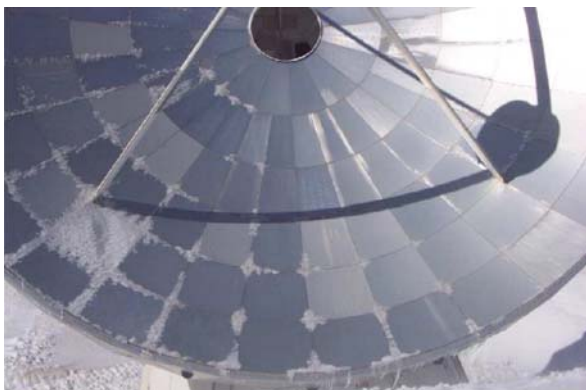


Fig. 4.18 IRAM 15-m telescope showing frost and ice at cold edges (near panel gaps) of rear side heated panels. The heating of the panel below the left quadripod leg is not working, the panel is fully covered with ice [Courtesy R. Neri, IRAM, France].

There are effects of ‘cold edges’, which are either not reached by a heating system or which have a high convective heat loss because of a low heat capacity of the material of the ‘edge’. An example of cold edges on an IRAM 15-m telescope is seen in Fig. 4.18. The high heat (energy) input into a telescope during de-icing may introduce structural deformations that degrade the reflector surface accuracy, the focus and the pointing. Although during de-icing the climatic conditions do not allow observations, of importance is the time during which the telescope returns to normal conditions after the de-icing has been switched off. This is illustrated in Fig. 4.19 that shows for the IRAM 30-m telescope the measured change of focus and the change of focus predicted from simultaneous temperature measurements and FEM calculations, during and after a de-icing period. It is seen that during de-icing the structure is deformed and the focus has changed significantly ($\Delta F \approx 2$ mm). For the shown case useful astronomical observations resumed approximately 3 to 4 hours after the de-icing was switched off. The thermal state of the IRAM 30-m telescope during a de-icing period is also shown in Fig. 9.72, the calculated beam degradation during de-icing is shown in Fig. 12.13.

For thermal aspects of a telescope and enclosure it must be noted that the transition from ice to water requires the energy (heat) of 335 kJ/kg. When fully de-icing the surfaces of a telescope or enclosure this may add up to a large amount of energy. During de-icing either by heating or sunshine, usually only a thin film of water develops between the ice (snow) and the surface on which the ice (snow) may slide causing occasionally significant damage.

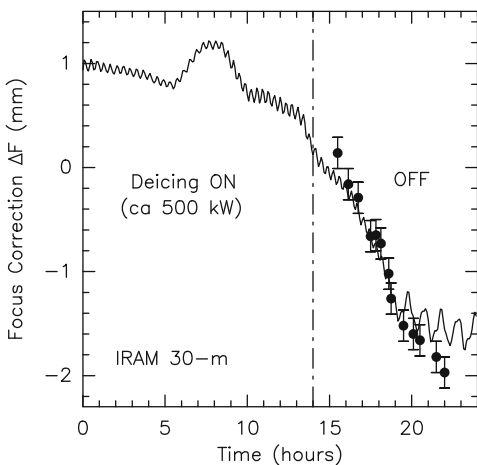


Fig. 4.19 IRAM 30-m reflector during heating for de-icing and after the heating has been switched off at 14 hour. Solid line: FEM calculated reflector surface deformation and associated focus variation due to heat load from de-icing; dots: focus correction measured on a radio source while trying to resume the observations. The telescope reached a stable thermal state around 20 h [From Greve (2002), Courtesy SPIE].

4.6.1 Humidity and Sky Radiation

Usually, at observatories the ambient air temperature (T_A) and the relative humidity (H) is measured, a typical example is shown in Fig. 4.20. As will be explained below, the equivalent black body temperature of the sky (T_S), i.e. of the atmosphere above the site, depends on the amount of the line-of-sight integrated precipitable water vapour. Relations are therefore derived between the dew point temperature (T_D) at the ground, measured with a wet-bulb thermometer, and the sky emissivity. In the case the dew point temperature is not measured one may proceed as follows to obtain T_D from T_A and H . From the measured relative humidity H (in %) the partial pressure of the atmospheric water vapour p_w is obtained from

$$p_w = e_{\text{sat}} H / 100 \quad [\text{mbar}] \quad (4.9)$$

with e_{sat} the surface saturated water vapour pressure given by Crane [1976] as

$$e_{\text{sat}} = 6.105 \exp[25.22((T_A - 273)/T_A) - 5.31 \ln(T_A/273)] \quad [\text{mbar}] \quad (4.10)$$

with T_A the ambient air temperature [in K]. The partial pressure p_w can be used in Eq.(4.1) (with $R_w = 1.086 R$) to calculate the surface water vapour density ρ_w . Evidently, condensation of the water vapour as liquid water (drops), snow or ice occurs when the atmosphere reaches $H = 100\%$.

There is no easy relation between the ambient air temperature, the relative humidity and the dew point temperature to be used in the calculation of the sky emissivity (see below). Following Buck [1981], these quantities are related by

$$H = 100 \exp[F(T_D) - F(T_A)] \quad (4.11)$$

with

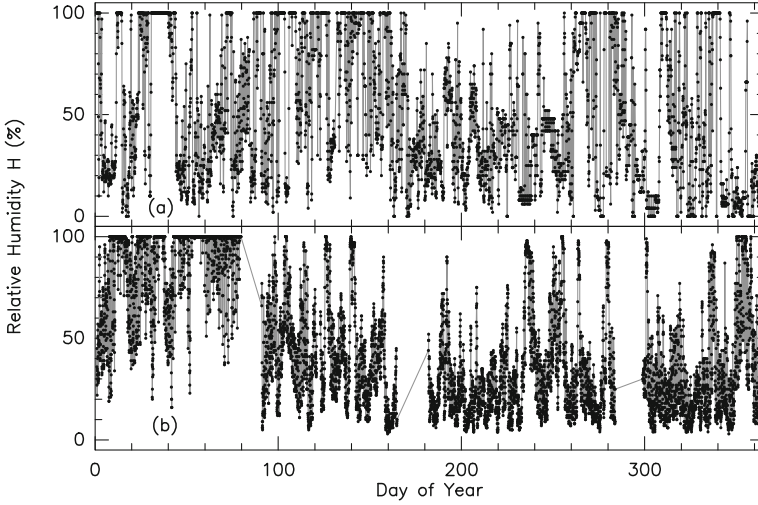


Fig. 4.20 Relative humidity H at (a) Pico Veleta, 1998, and (b) Chajnantor, 2001. A high relative humidity not necessarily involves a high amount of precipitable water vapour (ρ_w).

$$F(T) = [18.678 - (T/234.5)] \times [T/(T_D + 257.14)] \quad (4.12)$$

Denoting by $H(H, T_A) = \ln(H/100) + F(T_A)$, a value which can be calculated from the measured values H and T_A , from Eq.(4.12) can be derived the quadratic relation

$$T_D^2 + 234.5(H - 18.678)T_D + 6.03 \times 10^4 H = 0 \quad (4.13)$$

and solved for T_D . This value T_D is used in Eq.(4.18) to calculate the sky emissivity.

4.7 Sky Temperature

A telescope and enclosure sees the sky and interacts with it by radiation. Because of the temperature of the atmosphere and the telescope and enclosure, the radiative interaction is at infrared wavelengths. In essence, the sky is the atmosphere above the observatory with emission and absorption due to some of its gaseous components. The emitting and absorbing gases are water vapour (H_2O), to a smaller extent carbon dioxide (CO_2) and ozone (O_3) to an even smaller extent. While the amount of CO_2 is relatively constant in time and location, the amount of radiation from the sky to the ground, or leaving the ground through the atmosphere, depends mainly on the variable amount of water vapour in the line-of-sight through the atmosphere. Since the line-of-sight water vapour increases with increasing zenith distance, the emission of the atmosphere increases towards the horizon. Because of the exponential decrease of the water vapour and CO_2 density with height, the layers closer to

the ground contribute most to the emission and absorption. The emission/absorption of the atmosphere is therefore correlated, in first approximation, to the local amount of precipitable water vapour and to the local ambient air temperature.

Important for thermal considerations is the atmospheric transmission since radiation may escape through windows at infrared wavelengths. The transmission through the atmospheric windows changes with the amount of precipitable water vapour. The important window, called N, is at $\lambda = 10.4 \mu\text{m}$, the width of the window is $\Delta\lambda \approx 5 \mu\text{m}$ [see Bely 2002, his figure 1.4]. Surfaces at the temperature of $\sim -50^\circ\text{C}$ to 100°C have their radiation maximum in this window.

4.7.1 Measured Sky Temperature

The effective sky temperature can be measured, for instance, with an infrared thermometer with response in the wavelength region ~ 3 to $20 \mu\text{m}$. A recording of the sky temperature made on Plateau de Bure is shown in Fig. 4.21. The elevation dependence of the effective sky temperature is shown in Fig. 4.22, taken from Zürcher [1982, 1985]. The overcast condition in Fig. 4.22 shows in essence at all elevation angles the temperature of the base of the cloud layer.

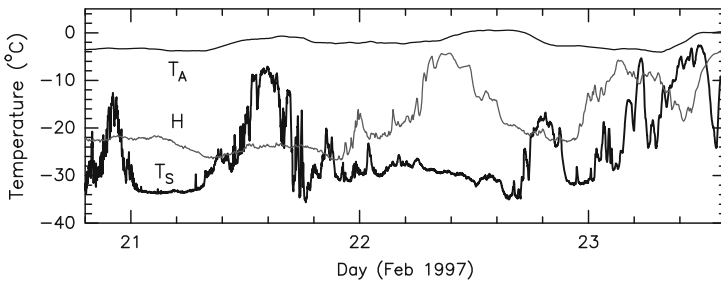


Fig. 4.21 Effective sky temperature T_S measured on Plateau de Bure. T_A is the ambient air temperature, H is the local relative humidity (scale 0 – 100 %).

4.7.2 Calculation of the Sky Temperature

The telescope and enclosure surfaces are radiatively coupled to the sky, primarily by radiation at infrared wavelengths. The emission of water vapour occurs between 3 to $40 \mu\text{m}$, the emission of CO_2 between 13 to $17 \mu\text{m}$. For low altitudes the sky emission (and absorption) has been calculated by Bliss [1961], Granqvist [1981], Eriksson & Granqvist [1982], and others, from molecular emission coefficients and an atmospheric model of density, temperature and composition as a function of

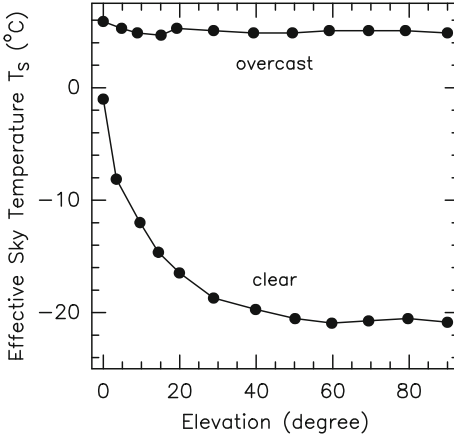


Fig. 4.22 Effective sky temperature for a clear sky and overcast sky. Zenith is at 90° elevation [From Zürcher (1985), Courtesy Infrared Physics].

altitude. The heat loss/gain Δq from a surface of the telescope or enclosure with temperature T_i towards the sky with effective temperature T_s is

$$\Delta q \propto ea \sigma (T_s^4 - T_i^4) \quad (4.14)$$

For clear sky conditions the long wavelength radiation W_s from the sky onto a horizontal surface is represented by Swinbank's [1963] relation

$$W_s(t) = 4.31 \times 10^{-21} T_A(t)^6 [\text{Wm}^{-2}\text{K}^{-6}] \quad (4.15)$$

or, as given by Nowak [1989], by

$$T_s(t) = 0.0553 T_A(t)^{1.5} [\text{K}] \quad (4.16)$$

with the ambient air temperature T_A in [K]. For populated areas this relation gives a sky temperature that is too low by $\sim 10^\circ \text{C}$ [Nowak 1984, 1989] because of pollution, however, this case is probably of little importance for climatic conditions at telescope sites.

A convenient calculation, which considers also the dependence of the effective sky temperature with altitude z of the telescope site, is based on the publications by Berdahl & Fromberg [1982], Berger et al. [1984] and Martin & Behrdal [1984 a, b]. The sky emissivity $e_s(z)$ can be written [Tournaire 1986] as

$$e_s(z) = e_o + e_h + e_z \quad (4.17)$$

with

$$e_o = 0.71 + 0.56 (T_D/100) + 0.73 (T_D/100)^2 \quad (4.18)$$

$$e_h = 0.013 \cos(2\pi t/24) \quad (4.19)$$

$$e_z = 0.00012 (p_A(z) - 1000) \quad (4.20)$$

In Eq.(4.18) is the dew point temperature T_D in [K], the time t in Eq.(4.19) is in [hours], the pressure p_A in Eq.(4.20) is in [mbar]. The term e_h takes into account a daily periodic variation of the emissivity, the term e_z takes into account the altitude (z) of the site through the local air pressure p_A . With T_A [K] the dry air temperature, the effective black body sky temperature T_S is

$$T_S = e_S^{1/4} T_A \quad [\text{K}] \quad (4.21)$$

This also gives

$$\Delta T_S = T_S - T_A = (e_S^{1/4} - 1) T_A < 0 \quad (4.22)$$

since $0 < e_S < 1$. The effective sky temperature calculated from Eq.(4.17)–Eq.(4.22) for Effelsberg, Pico Veleta and Chajnantor is shown in Fig. 4.23.

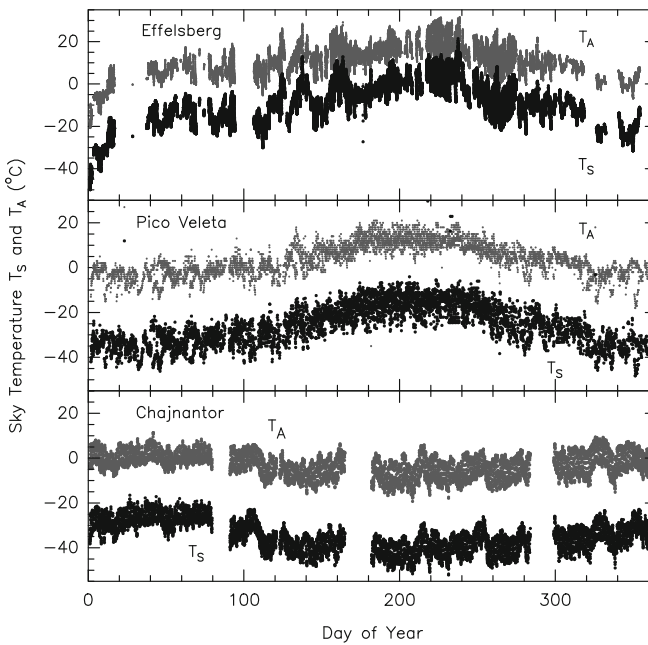


Fig. 4.23 Effective sky temperature T_S calculated from Eq.(4.17)–Eq.(4.21) for Effelsberg, Pico Veleta and Chajnantor. For comparison the ambient air temperature T_A near the ground is also shown.

From Fig. 4.23 it is seen that the clear sky is always significantly cooler than the ambient air and therefore acts as a heat sink. It is also seen that the clear sky is cooler than the ambient air by the approximately constant amount ΔT_S . Therefore, in thermal model calculations the effective sky temperature can be expressed approximately by

$$T_S(t) = T_A(t) - |\Delta T_S| < T_A \quad (4.23)$$

with $\Delta T_S \approx 20-30^\circ\text{C}$. For an arbitrarily selected period of 10 days, Fig. 4.24 demonstrates the validity of Eq.(4.23). The figure shows the measured ambient air temperature $T_A(t)$ and the sky temperature $T_S(t)$ calculated from Eqs.(4.17-4.22). An empirical constant shift ΔT_S is applied that brings $T_A(t)$ and $T_S(t)$ to close agreement. The seasonal differences ΔT_S derived for the sites of Fig. 4.23 are summarized in Table 4.5. Using the average air temperatures during winter and summer listed in Table 4.2, from Eqs.(4.21,4.22) follows the average sky emission coefficient e_S listed in Table 4.5. Because of the decrease of atmospheric water vapour with altitude, the effect of increasing altitude is a decrease in atmospheric emission e_S . The increase of e_S during summer is due to a general increase of the amount of atmospheric water vapour during this time of year.

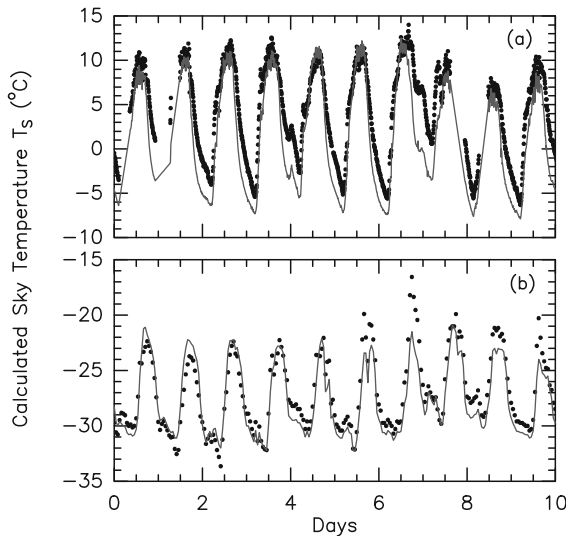


Fig. 4.24 Illustration of Eq.(4.23) for Effelsberg (a) and Chajnantor (b). Dots: calculated sky temperature T_S , solid line: measured ambient air temperature $T_A - \Delta T_S$ with $\Delta T_S = -19^\circ\text{C}$ for Effelsberg and $\Delta T_S = -28^\circ\text{C}$ for Chajnantor, for the time of these data.

Table 4.5 Difference ΔT_S of Sky Temperature and Ambient Air Temperature (Fig. 4.23).

		Winter		Summer	
Location	Altitude [m]	ΔT_S [$^\circ\text{C}$]	e_S	ΔT_S [$^\circ\text{C}$]	e_S
Effelsberg	320	-25 ± 3	0.70	-15 ± 3	0.80
Pico Veleta	2900	-30 ± 3	0.60	-28 ± 6	0.65
Chajnantor	5000	-35 ± 4	0.55	-27 ± 3	0.65

The efficiency of radiative coupling to the sky depends on the absorption and emission coefficient of the telescope and enclosure surfaces, for instance white TiO_2 painted or (shiny) aluminium surfaces. The radiative properties of the surfaces can be manipulated, if necessary, as shown for instance in the publications of Granqvist [1981] and Hamberg et al. [1987]. The radiative coupling (cooling) to the clear sky is evident from the observation that at high humidity a radio reflector surface (in particular when pointing at zenith) may be covered by a thin layer of ice at ambient air temperatures well above 0°C degree.

4.8 Cloud Coverage

Evidently, observations at (sub)millimetre wavelengths are not made when the sky is covered more or less heavily by clouds. The interaction of a cloud cover with the thermal state of a telescope and enclosure is by radiative coupling to the warm clouds rather than to a clear cold sky. Clouds are nearly black body radiators and have a radiation temperature of the ambient air close to the base of the clouds (see Fig. 4.22). A transient cloud cover or permanent cloud cover changes significantly the amount of solar radiation. The transient effect of a cloud can be considered in thermal model calculations by ‘switching-off’ the Sun and using the higher ‘sky’ temperature of the clouds. A typical example of cloud coverage (eye estimates) is

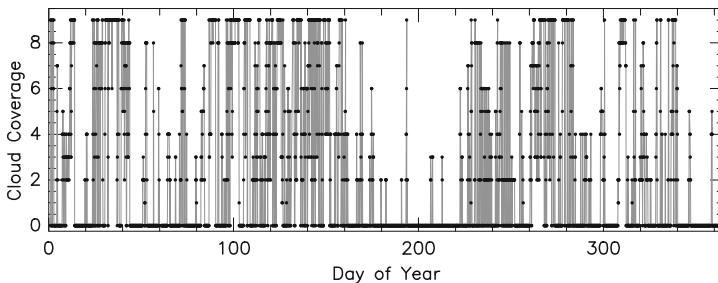


Fig. 4.25 Cloud coverage at Pico Veleta, 1998. Scale: 0 = no clouds, 9 = fully covered.

shown in Fig. 4.25 for Pico Veleta, for 1998. The cloud coverage is designated by values between 0 and 9, i.e. the value 0 defines clear sky, the value 9 defines a fully covered sky.

4.9 Solar Radiation

The major external source providing heat to a telescope, and enclosure, is solar radiation. The amount of solar radiation at the ground is variable in time. Obviously

there is the day–night effect, a seasonal effect and absorption and scattering by fog and clouds. Furthermore there are different illumination aspects according to the orientation of the telescope and enclosure surfaces with respect to the Sun. These are explained in Chapter 5.

The radiation emitted by the Sun is constant in time within 0.1 to 0.2% [Unsöld & Baschek 2001]. The radiation from the Sun passing through the Earth's atmosphere is confined to wavelengths longer than $0.3\ \mu\text{m}$, the radiation shorter than $0.3\ \mu\text{m}$ is absorbed by high altitude ozone. The peak of the solar radiation occurs around $0.5\ \mu\text{m}$, at wavelengths longer than $\sim 3\ \mu\text{m}$ the intensity is low and can be neglected. The average total solar energy received at the top of the atmosphere, though not at the ground, is $S_0 = 1.37\ \text{kW/m}^2$. This value is the solar constant. Dependent on the position of the Earth in its elliptical orbit the value S_0 may change by $\pm 3\%$ between perihelion and aphelion, with 3% less in June–July and 3% more in December–January that amounts to the relatively small change of the incident energy by $\pm 40\ \text{W/m}^2$ (at maximum). Despite strong absorption lines (H, Ca, Na and other Fraunhofer lines), the solar spectrum $I_{\odot}(\lambda)$ shown in Fig. 4.26 [Allen 2000] can be approximated by a black body spectrum of temperature $T_{\text{eff}} = 5780\ \text{K}$ ($F = \sigma T_{\text{eff}}^4$). For comparison, a telescope and enclosure radiates at approximately the temperature of the environment of $T \approx T_A \approx 300\ \text{K}$, the corresponding black body spectrum of this temperature is shown in Fig. 4.26. At this temperature the peak emission occurs around $10\ \mu\text{m}$, i.e. in the atmospheric window N.

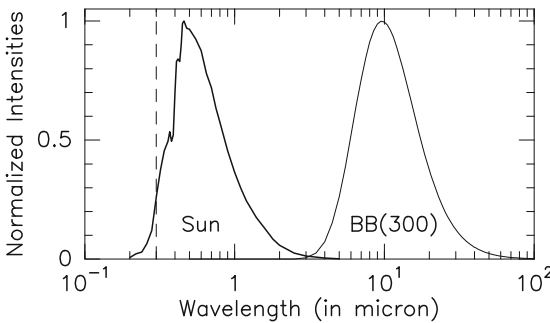


Fig. 4.26 Normalized solar radiation at the top of the atmosphere; radiation below $0.3\ \mu\text{m}$ is absorbed in the Earth's atmosphere. For comparison the black body radiation of a surface at the temperature of the environment $T = 300\ \text{K}$ is shown.

The solar radiation $S(t)$ incident on $1\ \text{m}^2$ surface at the ground (normal incidence) is calculated from

$$S(t) = \alpha_A(t) S_0 \exp[-B/\sin\beta(t)] \quad (4.24)$$

with $S_0 = 1.37\ \text{kW/m}^2$, $\alpha_A(t)$ the variable absorption of the Earth's atmosphere and B the turbidity of approximately 0.1 [Heat Transfer Data Book 1970, Velds 1992, Mecherikunnel et al. 1983]. The angle $\beta(t)$ is the elevation of the Sun at time t (see Eq.(5.2)). The factor α_A depends on the location on Earth (city, open country), the altitude, the cloud cover etc. The radiation $a_S(\lambda)S(\lambda, t)$ modulated by the absorption coefficient $a_S(\lambda) \approx a_S(\sim 0.5\ \mu\text{m})$ of the surface is absorbed by the telescope or enclosure. Some absorption coefficients α_S are given in Table 4.6.

Table 4.6 Solar Radiation Absorption Coefficient a_S ($\sim 0.5 \mu\text{m}$).

Material	Absorption Coefficient a_S
Black Paint	0.8–0.95
White Paint	0.4–0.5
TiO ₂ Paint	0.3–0.4
Anodised / Shiny Aluminium	0.2–0.1

4.9.1 Measurements of Solar Radiation

The solar radiation $S(t)$ incident on 1 m^2 on the ground is measured with a solarimeter (pyranometer). As illustrated in Fig. 4.27, for a site with a dominantly clear sky (like Chajnantor) the daily solar radiation follows a sine-curve (see Eq.(5.2)). At a

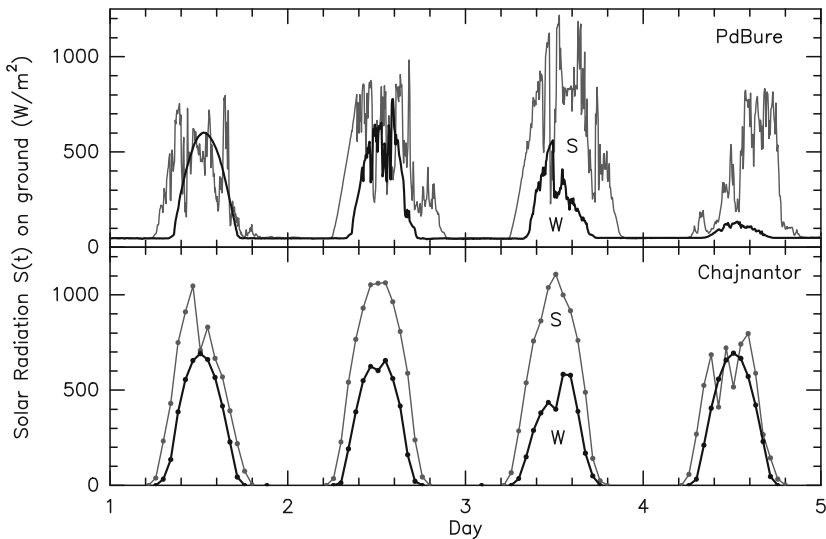


Fig. 4.27 Solar radiation measured at Plateau de Bure and at Chajnantor during 4 summer days (S) and 4 winter days (W). The irregular diminution of the radiation at Plateau de Bure is due to frequent clouds and fog. The seasonal difference of the radiation is due to the difference in the declination of the Sun.

site that is frequently cloudy (like Plateau de Bure) the effective incident solar radiation can be highly variable and on average significantly reduced. This effect should be considered in thermal model calculations.

4.10 Meteorological Design Specifications

For the design of a telescope and enclosure the meteorological data, either available from meteorological services or dedicated site tests, are inspected in order to establish a list of meteorological and thermal conditions under which a telescope should operate with unimpaired performance. In addition, conditions are specified under which a telescope and enclosure should survive. Such a list may have the entries as mentioned in Table 4.7. The table may include the main thermal specification of the telescope under consideration.

Table 4.7 Specification of Meteorological and Thermal Conditions.

Specification	IRAM 30-m Telescope ^{a)}	IRAM 15-m Panels ^{b)}
Location		
Country	Spain	France
Geographic Latitude	37°	45°
Altitude	2 900 m	2 500 m
Weather Conditions ^{c)}		
Average Air Temperature	10° C	10° C
Extreme Air Temperatures	- 30, 20° C	- 30, 30° C
Air Temperature Gradient	1 - 5° C/h	2° C/h
Average Wind Speed	8 m/s	5 m/s
Extreme Wind Speed ^{d)}	18 m/s	15 m/s
Humidity	0 - 100 %	0 - 100 %
Rain	yes	yes
Hail	yes	yes
Snow	Nov - May	yes
Ice ^{e)}	10 cm, 4 cm/h	yes
UV radiation	yes	yes
Survival Condition		
Air Temperature	~ 80° C	~ 80° C
Wind Speed	200 km/h	200 km/h
Rain	some	heavy
Snow, Ice	0.5 m, 10 cm	1 m, 10 cm
Temperature Specification	Telescope $ \Delta T_{BY} \lesssim 1^\circ \text{C} \text{ } ^f)$ $\text{rms}(T_{BUS}) \lesssim 0.5^\circ \text{C}$	Panel $\Delta T_{f,b} \lesssim 0.5^\circ \text{C} \text{ } ^g)$

^{a)} *The 30-m Millimeter Telescope, Design No 6*, MPIfR, 1971.

^{b)} *IRAM-Media-LarioTM Panel Design Study*, 2000.

^{c)} a stricter separation can be made for summer and winter conditions.

^{d)} for telescope operation and observations.

^{e)} leading to the investigation and installation of de-icing.

^{f)} $\Delta T_{BY} = T_{BUS} - T_{Yoke}$, ^{g)} $\Delta T_{f,b} = T_{front} - T_{back}$.

4.11 Space Environment

A telescope in Space interacts with the environment only by radiation, since conduction and convection do not occur in the space environment. The major heat source is solar radiation. Cooling occurs towards the background of the interplanetary space, which has the effective radiation temperature of interplanetary dust of 7 to 10 K [Bely 2002].

Chapter 5

Calculation of Solar Illumination

5.1 The Apparent Motion of the Sun

Solar radiation is the most disturbing external heat source. With solar radiation incident on the ground between approximately 300 to 1000 W/m², a white painted telescope or enclosure surface will absorb approximately 50 to 300 W/m². This power will heat up the surface, but part of the absorbed power is radiated back into the environment at infrared wavelengths. The actual amount of incident and absorbed radiation depends on the shape of the telescope and enclosure surface, its orientation towards the Sun and its surface finish. This Chapter explains the calculation of the solar illumination for several telescope components and enclosures.

The Sun's apparent motion across the sky is calculated from a relation containing the geographic latitude (φ) of the observatory, the declination of the Sun (δ) for the epoch \mathcal{E} (year and fraction of year) and the hour of the day. From the position and elevation of the Sun the solar illumination of vertical, horizontal, inclined and shaped surfaces can easily be derived, as a function of time of the day. The surfaces themselves may rotate, for instance those of a telescope or astrodome, or may be stationary in the case of a radome.

The determination of the Sun's position is made with respect to the local horizon system at the geographic latitude φ , as shown in Fig. 5.1. The +x-axis of this coordinate system points in the direction East, the +y-axis points in the direction North, the +z-axis points towards zenith. The azimuth angle A ($0 \leq A \leq 360^\circ$) in the xy-plane counts from North ($A = 0$), to East ($A = 90^\circ$), to South ($A = 180^\circ$) and West ($A = 270^\circ$), the elevation angle E ($0 \leq E \leq 90^\circ$) counts from the horizontal plane ($E = 0^\circ$) towards zenith ($E = 90^\circ$). As for any other astronomical object, the position of the Sun at the epoch of observation \mathcal{E} is given by its right ascension $\alpha(\mathcal{E})$ (in hours, minutes, seconds) and its declination $\delta(\mathcal{E})$ (in degrees). The time at the observatory is the Local Time (LT), or the Universal Time (UT) and the Local Sidereal Time (LST). The hour angle H of an astronomical source is its azimuthal angular distance in the horizontal plane, counted from the direction South where the source culminates. The hour angle is negative in the direction East and positive in

the direction West. The hour angle of an astronomical object with right ascension α and declination δ is

$$H(t) = LST - \alpha \tag{5.1}$$

The conversion of the angle $H(t)$ is made by noting that 1 hour = 15° , 1 minute = $15'$ and 1 second = $15''$ [arcsec]. For further details see for instance Smart [1977].

The elevation $\beta(t)$ of the Sun above (or below) the horizontal plane is

$$\sin\beta(t) = \cos H(t) \cos\varphi \cos\delta(\mathcal{E}) + \sin\varphi \sin\delta(\mathcal{E}) \tag{5.2}$$

with the declination of the Sun $\delta(\mathcal{E})$ taken from an Astronomical Almanac. For the northern hemisphere during winter solstice $\delta(W) = -23.4^\circ$, during summer solstice $\delta(S) = 23.4^\circ$, during spring and autumn equinox $\delta(SA) = 0^\circ$. In many thermal considerations it is sufficient to consider the extreme cases of winter and summer, thus using $\delta(W)$ and $\delta(S)$. The declination of the Sun for every 21st day of a month is given in Table 5.1.

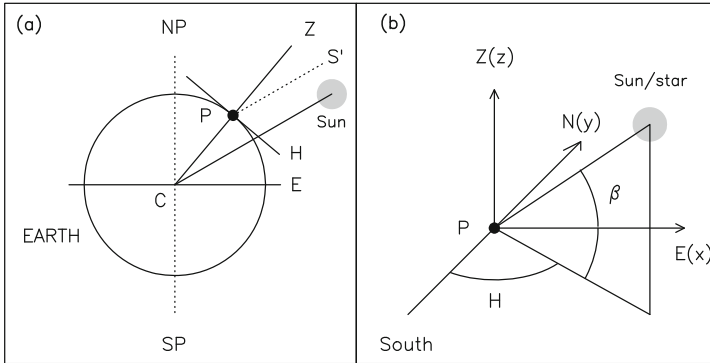


Fig. 5.1 (a) Definition of the horizon H at the location P on Earth. NP and SP is the direction to the northern and southern pole, E is the equator, C is the Earth's centre. The direction Z is towards zenith. Since the Sun is 150 000 000 km away it appears from the centre of the Earth and the location P at nearly the same angle. The angle $(PCE) = \varphi$ is the geographic latitude, the angle $(Sun-CE) = \delta$ is the declination of the Sun (or star). (b) Orientation of the Horizon System $[x,y,z]$ at the location P . Z is the direction towards zenith, N is the north, E the east. H is the hour angle of the Sun (or star), β is the elevation of the Sun (or star). The azimuth angle A of the Sun (star) is $A = H + 180^\circ$, measured from the North, via East, South, West, towards North.

The hour angle H_S of sunrise and sunset is obtained from Eq.(5.2) for the condition $\beta(H_S) = 0$, i.e.

$$\cos H_S = -\tan\varphi \tan\delta(\mathcal{E}) \tag{5.3}$$

The culmination of the Sun at the elevation β_c occurs when the Sun is at the South where the hour angle is $H = 0$ so that

Table 5.1 Declination of the Sun throughout a Year.

21 st of Month	Day of Year	Decl. δ [$^{\circ}$] ^{a)}	21 st of Month	Day of Year	Decl. δ [$^{\circ}$] ^{b)}
March	80	0	September	264	0
April	111	+11.9	October	294	-10.7
May	141	+20.3	November	325	-19.9
June	172	+23.4	December	355	-23.4
July	202	+20.5	January	21	-19.9
August	233	+12.1	February	52	-10.6
September	264	0	March	80	0

^{a)} northern summer, ^{b)} northern winter.

$$\sin(\beta_c) = \cos\varphi \cos\delta(\mathcal{E}) + \sin\varphi \sin\delta(\mathcal{E}) = \cos(\varphi - \delta(\mathcal{E})) \tag{5.4}$$

The culmination of the Sun at the geographic latitude φ occurs in summer, winter and spring–autumn at the elevation $\beta_c(S) = 90^{\circ} - \varphi + 23^{\circ}$, $\beta_c(W) = 90^{\circ} - \varphi - 23^{\circ}$ and $\beta_c(SA) = 90^{\circ} - \varphi$. In particular, the Sun can reach zenith $\sin(\beta) = 1$ at the geographic latitude $\varphi = \delta(\mathcal{E})$. Since $|\delta(\mathcal{E})| \leq 23.4^{\circ}$, this condition is restricted to geographic latitudes $|\varphi| \leq 23.4^{\circ}$.

The maximum elevation $\bar{\beta}$ of the Sun, the maximum insolation $S(\max)$ at the top of the atmosphere and the duration of sunshine T (for $10^{\circ} \leq \beta$) for winter, summer and spring–autumn is given in Table 5.2. Values measured at Chajnantor are shown in Fig. 5.2.

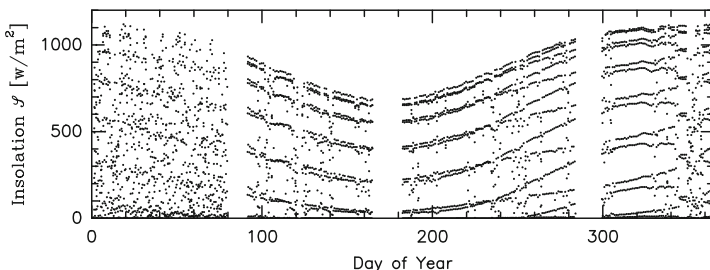


Fig. 5.2 Insolation at Chajnantor ($\varphi = -23^{\circ}$) during one year. The individual lines are for measurements separated by two hours (for $90 \leq d$). The maximum insolation occurs at the daily maximum elevation of the Sun.

In the horizon system of the telescope (Fig. 5.1.b) the azimuth angle of the Sun A_S is

$$A_S(t) = H_{\text{sun}}(t) + 180^{\circ} \tag{5.5}$$

With the elevation of the Sun $\beta(t)$ (Fig. 5.1.b) a unit vector $\mathbf{S}(t)$ in the direction of the Sun is

Table 5.2 Maximum Solar Illumination.

Geographic Latitude [°]	Winter ^{a)}			Spring ^{a)} / Autumn ^{a)}			Summer ^{a)}		
	$\bar{\beta}$ [°]	S(max) [kW/m ²]	$T^{b)}$ [h]	$\bar{\beta}$ [°]	S(max) [kW/m ²]	$T^{b)}$ [h]	$\bar{\beta}$ [°]	S(max) [kW/m ²]	$T^{b)}$ [h]
-60	53	1.1	15	30	0.7	9	7	0.2	-
-45	68	1.3	13	45	1.0	10	22	0.5	6
-30	83	1.4	12	60	1.2	10.5	37	0.8	8.5
-15	82	1.4	11	75	1.3	10.5	52	1.1	9.5
0	67	1.3	10.5	90	1.4	10.6	67	1.3	10.5
15	52	1.1	9.5	75	1.3	10.5	82	1.4	11
30	37	0.8	8.5	60	1.2	10.5	83	1.4	12
45	22	0.5	6	45	1.0	10	68	1.3	13
60	7	0.2	-	30	0.7	9	53	1.1	15

^{a)} seasons of the Northern hemisphere, W = winter: $\delta(W) = -23.4^\circ$,
SA = spring and autumn: $\delta(SA) = 0$, S = summer: $\delta(S) = 23.4^\circ$.

^{b)} for elevations of the Sun $10^\circ \leq \beta$.

$$\mathbf{S}(t) = [\cos\beta(t)\sin A_S(t), \cos\beta(t)\cos A_S(t), \sin\beta(t)], \quad |\mathbf{S}(t)| = 1 \quad (5.6)$$

with components along the (x,y,z) coordinates¹

$$S_x = \cos\beta \sin A_S, \quad S_y = \cos\beta \cos A_S, \quad S_z = \sin\beta \quad (5.7)$$

Using the vector $\mathbf{S}(t)$ and the normal vector $\mathbf{n}(t)$ of a surface element it is possible to calculate any time-dependent solar illumination aspect.

5.2 The Plane Surface

In the Cartesian horizon coordinate system [x,y,z], shown in Fig. 5.1.b, the points $\mathbf{x} = (x,y,z)$ of a plane surface fulfil the equation (scalar product)

$$(\mathbf{n}, \mathbf{x}) = \text{constant} \quad (5.8)$$

with $\mathbf{n} = (n_x, n_y, n_z)$ a unit vector normal to the surface. In a similar way as Eq.(5.6), for the azimuth angle A and elevation angle E of the vector \mathbf{n} its analytic expression is

$$\mathbf{n} = (\cos E \sin A, \cos E \cos A, \sin E) \quad (5.9)$$

For a stationary plane is A = constant and E = constant, for a moving plane is A = A(t) and E = E(t). For a plane co-moving in sidereal time, A(t) = H(t) + A₀ with H(t) the hour angle of the object (Sun, star) and A₀ = constant.

¹ Vectors are written in boldface.

The solar radiation $\Delta \mathcal{S}(t)$ incident on a surface element ΔF with normal vector \mathbf{n} is

$$\Delta \mathcal{S}(t) = S(t) \cdot (\mathbf{S}(t), \mathbf{n}) \Delta F \tag{5.10}$$

with $S(t)$ the solar radiation incident on the ground given by Eq.(4.24). Evidently, only those values of Eq.(5.10) are meaningful for which $0 \leq (\mathbf{S}, \mathbf{n})$.

Of particular interest are the vertical and the horizontal planes. For the *vertical* plane ($E = 0$, Fig. 5.3.b) perpendicular to the azimuth direction A the normal vector is

$$\mathbf{n}_v = (\sin A, \cos A, 0) \tag{5.11}$$

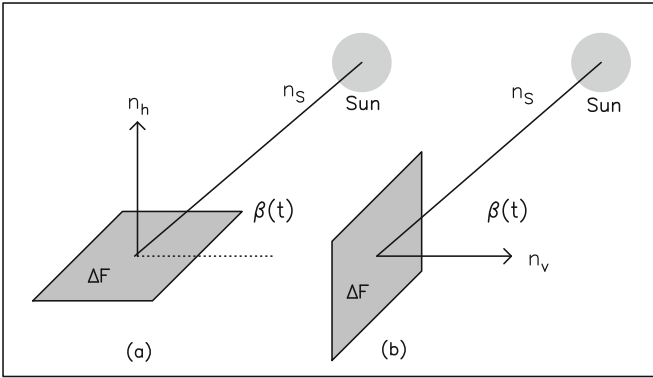


Fig. 5.3 Solar illumination of a horizontal plane (a) and vertical plane (b) with normal vector \mathbf{n} .

For the vertical plane facing North : $A = 0^\circ$ and $\mathbf{n}_v(N) = (0, 1, 0)$, facing East : $A = 90^\circ$ and $\mathbf{n}_v(E) = (1, 0, 0)$, facing South : $A = 180^\circ$ and $\mathbf{n}_v(S) = (0, -1, 0)$, facing West : $A = 270^\circ$ and $\mathbf{n}_v(W) = (-1, 0, 0)$. For the *horizontal* plane ($E = 90^\circ$, Fig. 5.3.a) the normal vector is

$$\mathbf{n}_h = (0, 0, 1) \tag{5.12}$$

The solar illumination of the vertical plane is

$$\begin{aligned} 0 \leq \Delta \mathcal{S}_v(t) &= S(t) \cdot (\mathbf{S}(t), \mathbf{n}_v) \Delta F \\ &= S(t) [\cos \beta(t) \sin A_S(t) \sin A + \cos \beta(t) \cos A_S(t) \cos A] \Delta y \Delta z \\ &= S(t) [\cos \beta(t) \cos(A_S(t) - A)] \Delta y \Delta z \end{aligned} \tag{5.13}$$

Evidently, for the sun-tracking vertical surface skewed by the angle A_0 to the direction of the Sun the solar illumination is

$$\Delta \mathcal{S}_v(t) = S(t) \cos \beta(t) \cos A_0 \Delta F \tag{5.14}$$

The solar illumination of the horizontal plane is

$$0 \leq \Delta \mathcal{S}_h(t) = \mathbf{S}(t) \cdot (\mathbf{S}(t), \mathbf{n}_h) = S(t) \sin\beta(t) \Delta x \Delta y \quad (5.15)$$

For Plateau de Bure as an example ($\varphi = 45^\circ$) the functions $\mathcal{S}_v(t)$ and $\mathcal{S}_h(t)$ are shown in Fig. 5.4. For the horizontal plane the maximum solar illumination occurs during culmination of the Sun at noon, for the vertical plane the maximum solar illumination may occur at a time that is significantly displaced from noon. In Fig. 5.4 it is assumed that the turbidity factor B in the relation S(t) (Eq.(4.24)) is in one case B = 0, in the other case B = 0.1.

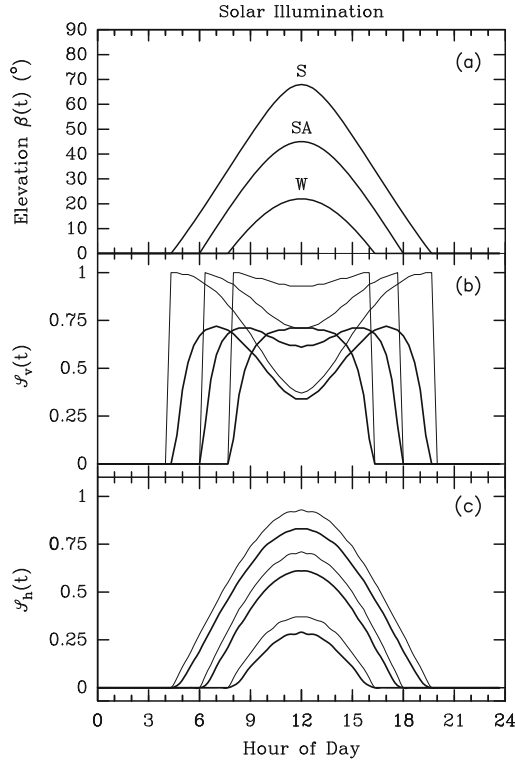


Fig. 5.4 (a) Elevation $\beta(t)$ of the Sun at Plateau de Bure ($\varphi = 45^\circ$) as function of the time of the day; for summer: S, spring and autumn: SA, and winter: W. (b) illumination \mathcal{S}_v of a vertical surface, (c) illumination \mathcal{S}_h of a horizontal surface. The thin lines are for the normalized illumination $\exp[-B/\sin\beta(t)]/\alpha_A S_0$ with turbidity B = 0, the heavy lines are for B = 0.1 (Eq.(4.24)).

As a final illustration the measured temperature of a thick horizontal concrete plate is shown in Fig. 5.5. The temperature of the plate follows the solar illumination, though with a considerable delay because of a high thermal inertia.

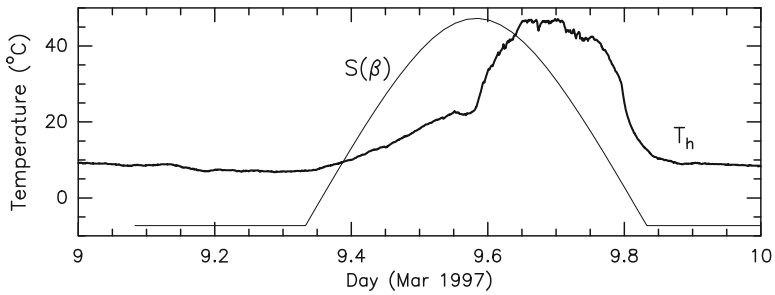


Fig. 5.5 Temperature T_h of a horizontal surface. $S(\beta)$ is the elevation of the Sun (normalized).

5.3 The Tube Surface

As shown in Fig. 5.6, the long axis of a tube of diameter D and length L is defined by the vector

$$\mathbf{n}_T = (n_{Tx}, n_{Ty}, n_{Tz}), \quad |\mathbf{n}_T| = 1 \tag{5.16}$$

Using the solar vector $\mathbf{S}(t)$ of Eq. (5.6), the solar illumination of the tube surface is

$$\Delta \mathcal{S}_T(t) = \mathbf{S}(t) \cdot \sqrt{1 - (\mathbf{S}(t), \mathbf{n}_T)^2} \times DL \tag{5.17}$$

This description is convenient for tubes/beams of an alidade and the tube/beam network of an open BUS.

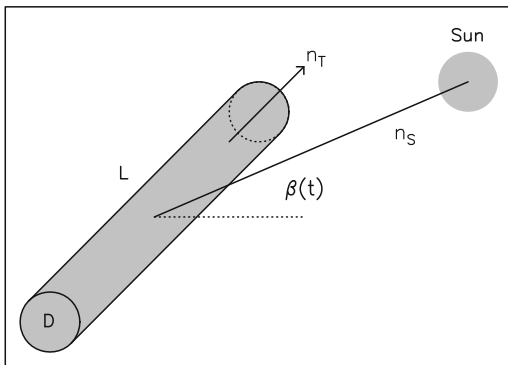


Fig. 5.6 Solar illumination of a tube of length L and diameter D .

5.4 The Parabolic Reflector Surface

Figure 5.7 is an illustration of asymmetric solar illumination of the parabolic reflectors of the VLA telescopes. The telescopes point approximately in the direction South while the Sun is at low elevation in the West. Evidently, the reflector front sections in shadow are cooler than the sections in sunshine. With respect to solar illumination of a parabolic reflector the questions arise of the borderline separating the reflector area in shadow and in sunshine and of the solar energy received per reflector surface area. In particular, for an open BUS these questions also hold for solar illumination of the reflector rear side.



Fig. 5.7 Asymmetric solar illumination of parabolic reflectors of the VLA array (NM, USA) [Image Courtesy of NRAO/AUI/NSF].

5.4.1 Borderline between Shadow and Sunshine

As seen in Fig. 5.7, there exists a curved borderline between the reflector surface area in shadow and the surface area in sunshine. The derivation of the borderline is illustrated in Fig. 5.8. Without loss of generality, the coordinate system in this figure is aligned with the $+x$ -axis pointing in the azimuth direction of the Sun, the elevation of the Sun with respect of the $+x$ -axis is α . The solar rays reaching the reflector rim at $P_R = (x_R, z_R)$ (with $R = D/2$, $D =$ diameter of the reflector) under the angle α produce a shadow area to the borderline at $P_B = (x_B, z_B)$. The borderline is thus the projection of the reflector rim under the angle α in the direction $-x$ into the reflector. In order to calculate the borderline, cuts through the reflector parallel to the x -axis are considered. The equation of a cut parallel to the x -axis at the distance a ($-D/2 \leq a \leq D/2$) is obtained from the equation of the parabola for $y = a$, i.e.

$$x^2 + a^2 = 2pz = 4fz \quad (5.18)$$

For this cut the reflector rim is at the height

$$z_R = (x_R^2 + a^2)/2p = (D/2)^2/2p \tag{5.19}$$

The point P_B of the borderline is obtained from the relation

$$\begin{aligned} \tan \alpha &= \overline{P_R A} / \overline{A P_B} = (z_R - z_B) / (x_R - x_B) \\ &= [(x_R^2 + a^2)/2p - (x_B^2 + a^2)/2p] / (x_R - x_B) = (x_R + x_B) / 2p \end{aligned} \tag{5.20}$$

or with Eq.(5.19)

$$x_B = 2p \tan \alpha - x_R = 2p \tan \alpha - \sqrt{(D/2)^2 - a^2} \tag{5.21}$$

From Eq.(5.21) follows that there is no shadow if $x_B = D/2$, the angle of the Sun then is $1/(4n) \leq \tan \alpha$, with $n = f/D$. The reflector surface is completely in shadow if $x_B = -D/2$ or $\tan \alpha = 0$.

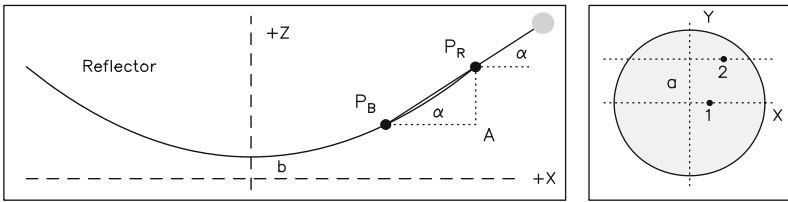


Fig. 5.8 Geometry of shadow in a parabolic reflector. P_R : reflector rim, P_B : borderline of the shadow for the Sun at the angle α . The left panel shows a cut through the reflector surface at the distance $y = a$ where $b = a^2/2p$. The borderline points are 1 for the x -axis and 2 for a parallel cut.

Figure 5.9 illustrates the shadow in a parabolic reflector for different angles α of the Sun. The situation of the VLA telescopes shown in Fig. 5.7 corresponds to $\alpha \approx 10$ to 15° .

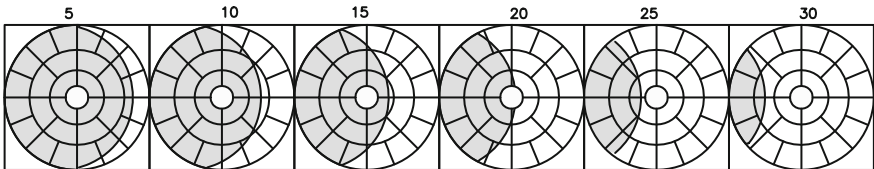


Fig. 5.9 Shadow in a parabolic reflector for the Sun shining from the left side, at the elevation α indicated above the figure.

5.4.2 Solar Illumination of the Reflector Surface

The solar illumination is derived for a parabolic reflector facing South at horizon position, shown in Fig. 5.10. The solar illumination at any other position of the reflector is obtained from coordinate rotation in azimuth and elevation direction. In the Cartesian coordinate system $[x,y,z]$ indicated in Fig. 5.10, with centre at the vertex

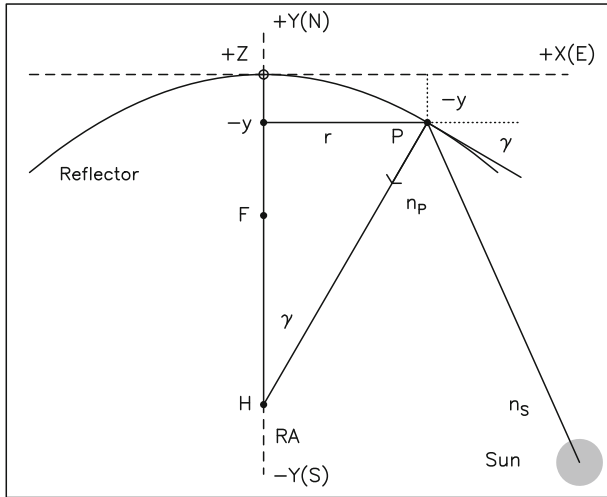


Fig. 5.10 Solar illumination of a parabolic reflector, shown as a two-dimensional cut. The reflector is facing the southern horizon (S). The orientation of the coordinate system is that of the horizon system, Fig. 5.1; N = north, E = east, +Z in direction zenith. RA = reflector axis. The symbols are explained in the text.

of the parabola and the same orientation as the horizon system of Fig. 5.1, a point **P** on the reflector surface has the coordinates $\mathbf{P} = (r, -y) = (x, -y, z)$. The intersection of the prolonged surface normal \mathbf{n}_p at **P** with the reflector axis (RA) has the coordinates $\mathbf{H} = (0, -h, 0)$. The equation of the parabola with focal length f and slope γ of the surface at the position r is

$$r^2 = x^2 + z^2 = -2py = -4fy, \quad \tan \gamma = r/p \tag{5.22}$$

The distance $A = \overline{H(-Y)}$ between the depth of the reflector and the intersection of the prolonged surface normal is

$$\overline{H(-Y)} = A = r/\tan \gamma = r/(r/p) = p = 2f = \text{constant} \tag{5.23}$$

The height h of point **H** is

$$-h = A - y = -p - y \rightarrow \mathbf{H} = (0, -p - y, 0) \tag{5.24}$$

hence

$$\mathbf{N}_p = \mathbf{H} - \mathbf{P} = (0, -p - y, 0) - (x, -y, z) \rightarrow \mathbf{n}_p = (-x, -p, -z) / \sqrt{x^2 + p^2 + z^2} \quad (5.25)$$

Using the solar vector $\mathbf{S}(t)$ of Eq.(5.6), the solar illumination of the parabolic surface element ΔF at \mathbf{P} is

$$\begin{aligned} \Delta \mathcal{S}_p(t) &= \mathbf{S}(t) \cdot (\mathbf{S}(t), \mathbf{n}_p) \Delta F \\ &= \mathbf{S}(t) [(-x \cos \beta(t) \sin A_S(t) - p \cos \beta(t) \cos A_S(t) - z \sin \beta(t)) / \sqrt{x^2 + p^2 + z^2}] \times \Delta F \end{aligned} \quad (5.26)$$

If the reflector moves in elevation by rotation of the angle E around the EL-axis ($\equiv x$), the coordinates $\mathbf{x} = (x, -y, z)$ of point P change to

$$\mathbf{x}' = \mathbf{R}(E) \mathbf{x} \quad (5.27)$$

with

$$\mathbf{R}(E) = \begin{pmatrix} 1 & 0 & 0 \\ 0 & \cos E & \sin E \\ 0 & -\sin E & \cos E \end{pmatrix} \quad (5.28)$$

In horizon position ($E = 0$) the reflector axis is along the $-y$ -axis, i.e. $(0, -1, 0)$. In zenith position ($E = 90^\circ$) the reflector axis (RA) is along the $+z$ -axis, i.e. $(0, 0, 1)$ since

$$\mathbf{R}(90) \times \begin{pmatrix} 0 \\ -1 \\ 0 \end{pmatrix} = \begin{pmatrix} 1 & 0 & 0 \\ 0 & 0 & 1 \\ 0 & -1 & 0 \end{pmatrix} \times \begin{pmatrix} 0 \\ -1 \\ 0 \end{pmatrix} = (0, 0, 1) \quad (5.29)$$

A rotation of the reflector in azimuth direction, i.e. around the z -axis, by the angle A is considered by the matrix $\mathbf{R}(A)$ so that the rotation of the reflector in elevation and azimuth direction becomes

$$\mathbf{R}(A, E) = \mathbf{R}(A) \mathbf{R}(E) = \begin{pmatrix} \cos A & \sin A & 0 \\ -\sin A & \cos A & 0 \\ 0 & 0 & 1 \end{pmatrix} \times \begin{pmatrix} 1 & 0 & 0 \\ 0 & \cos E & \sin E \\ 0 & -\sin E & \cos E \end{pmatrix} \quad (5.30)$$

The solar illumination of a reflector rotated in elevation and azimuth direction is obtained from the transformed reflector normal \mathbf{n}_p' and the solar vector $\mathbf{S}(t)$ with

$$\mathbf{n}_p' = \mathbf{R}(A) \mathbf{R}(E) \mathbf{n}_p \quad (5.31)$$

On an open BUS, the solar illumination of the reflector rear side is obtained by using in the equations the normal vector $-\mathbf{n}_p$ of the rear side surface elements. However, there may occur significant shadowing of the solar illumination by the BUS network.

The illumination of a reflector is illustrated in Fig. 5.11 for a telescope which is stationary all day and facing South at horizon position; the Sun is at the declination $\delta = 0^\circ$ (spring/autumn), the geographic latitude is $\varphi = 37^\circ$. The 17 h situation

is similar to the situation shown in Fig. 5.7. If the telescope trails the Sun, for instance at a distance of 45° in azimuth, an asymmetric solar illumination as shown in Fig. 5.11 for ~ 7 h or ~ 17 h will occur during some time in the morning and the evening. This may result in an asymmetric heating of the reflector and the BUS. Such a model of asymmetric solar illumination was used, in particular, to study the efficiency of BUS ventilation [Greve & Bremer 2005].

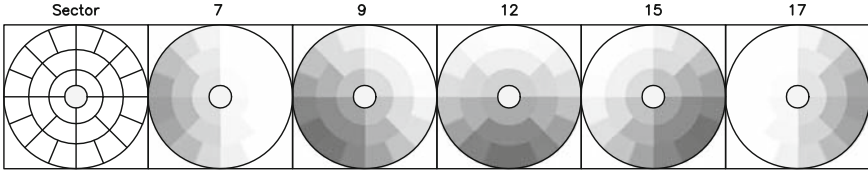


Fig. 5.11 Illumination (power) of a stationary reflector (at horizon position, facing South, $\delta = 0^\circ$, $\varphi = 37^\circ$), consisting of 28 sectors (left). The numbers indicate the hour of the day. White: no sunshine.

5.5 The Open and Closed BUS

Of importance for the thermal behaviour of a radio telescope is the solar illumination of the BUS. The beam network of the BUS may be open as shown in Fig. 5.12, or may be closed by the rear cladding as shown in Fig. 5.13. The front of the BUS consists of panels of which the solar illumination is treated in Section 5.4.

The network of the open BUS is conveniently described by the ensemble of coordinates of the begin points $\mathbf{n}_b(i)$ and end points $\mathbf{n}_e(i)$ of the BUS members, i.e. $[\mathbf{n}_b(i), \mathbf{n}_e(i); i=1, 2, 3, \dots, N]$, where N can be a large number. From the set of coordinates, which are readily available from a FEM, the vectors along the beam/tube axes are calculated

$$\mathbf{n}_T(i, t) = \mathbf{n}_e(i) - \mathbf{n}_b(i), \quad |\mathbf{n}_T(i, t)| = 1 \quad (5.32)$$

as shown in Fig. 5.6 and Fig. 5.12. From these vectors the solar illumination of the complete BUS network (N) can be derived

$$\Delta \mathcal{S}_T(i, t) = \mathbf{S}(t) \cdot \sqrt{1 - (\mathbf{S}(t), \mathbf{n}_T(i, t))^2} \times (DL)_i, \quad i = 1, 2, \dots, N \quad (5.33)$$

The time dependence of the beam/tube vectors $\mathbf{n}_T(i, t)$ and the solar vector $\mathbf{S}(t)$, Eq.(5.6), takes into account the motion of the telescope in azimuth and elevation direction and the apparent motion of the Sun with respect to the BUS. This formalism can include the shadowing of certain BUS members.

The closed BUS is easier to handle. Again, the front of the BUS is the reflector surface treated in Section 5.4. The rear of the BUS consists of the flat surface F_1

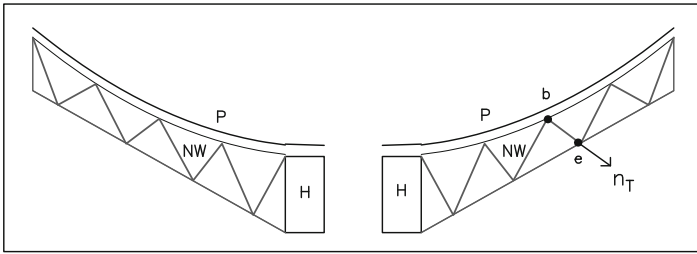


Fig. 5.12 Open BUS. P: panels, NW: BUS network, H: central hub. For one particular BUS member the begin point (b) and end point (e) of the member and its vector \mathbf{n}_T along the axis is shown.

and the rim surface F_2 . Compared to the reflector surface and the rear surface F_1 , the rim surface F_2 is small. The surface elements of both surfaces have the normal vectors $\mathbf{n}(F_{1,t})$ and $\mathbf{n}(F_{2,t})$. The solar illumination of a rear cladding element and rim cladding element as shown in Fig. 5.13 is

$$\Delta \mathcal{S}_i(t) = S(t) \cdot (\mathbf{S}(t), \mathbf{n}(F_{i,t})) \Delta F_i \text{ for } i = 1, 2 \tag{5.34}$$

The solar radiation heats the cladding elements and the elements radiate diffusely at infrared wavelengths into the interior of the BUS.

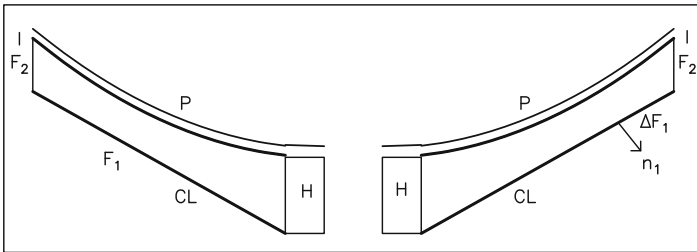


Fig. 5.13 Closed BUS. P: panels, I: a possible insulation layer, H: central hub, CL: rear side cladding. The surfaces F_1 and F_2 may be illuminated by sunshine. The normal vector \mathbf{n}_1 of a surface element ΔF_1 is shown.

5.6 The Box-type Enclosure (Astrodome)

The box-type enclosure of, for instance, the HHT radio telescope (see Fig. 3.1) and the ESO-VLT optical telescope (see Fig. 14.2) consists mainly of vertical and horizontal steel walls and several inclined walls. The enclosures have a slit with a width of at least the reflector diameter. For a radio telescope enclosure the slit may be

covered by a radio wave transparent membrane, which is partially transparent to solar radiation, or may be open for observation. The walls of the enclosure are easily expressed by normal vectors in a Cartesian coordinate system $[x,y,z]$ that rotates with the enclosure, as shown in Fig. 5.14. The solar illumination of such an enclosure is calculated from the vertical and horizontal illumination functions $\Delta \mathcal{S}_v(t)$ and $\Delta \mathcal{S}_h(t)$, Eq.(5.13) and Eq.(5.15). The solar illumination of inclined flat walls is calculated from Eq.(5.10). The astrodome follows the sidereal motion of the observed radio source, a change of radio source will change the solar illumination aspect.

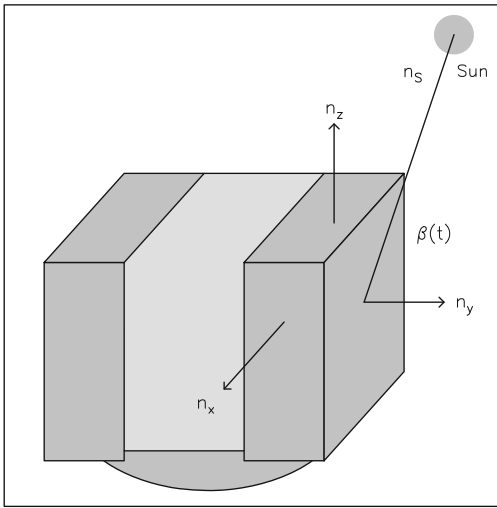


Fig. 5.14 Normal vector description of flat surfaces of a box-type enclosure. A particular position of the Sun is indicated.

5.7 The Cylindrical Enclosure (Astrodome)

The cylindrical astrodome and the quasi-cylindrical astrodome of for instance the JCMT telescope (see Fig. 3.3), schematically shown in Fig. 5.15, is a sequence of vertical surfaces with different position angles $A_o(t) = \theta(t)$ towards the Sun. The walls of the astrodome are easily expressed by normal vectors in a cylindrical coordinate system $[R,\theta,z]$, with R the radius of the astrodome, θ the wall angle ($0 \leq \theta \leq 360^\circ$) and H the height ($0 \leq z \leq H$). The illumination of this enclosure is calculated from the relation $\Delta \mathcal{S}_v(t)$, Eq.(5.13), taking into account the angles $\theta(t)$ and using for the surface elements $\Delta F = R \Delta \theta \Delta z$. The housing of the astrodome consists of steel plates. The slit may be open during observation or covered with a radio wave transparent membrane. The membrane is partially transparent for solar radiation. The astrodome follows the sidereal motion of the observed radio source, a change of radio source will change the solar illumination aspect.

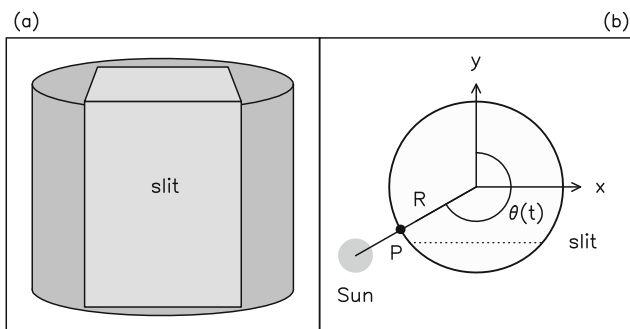


Fig. 5.15 (a) Side view of a cylindrical enclosure of radius R and height H . (b) View from the top. A particular position of the Sun is indicated.

5.8 The Over-Hemispherical Radome

A radio telescope may be protected by a stationary radome. The Sun moves across the stationary radome, some solar radiation enters the radome through its plastic skin.

In the Cartesian coordinate system $[x, y, z]$ of the radome (Fig. 5.16), of radius R , the origin is at the centre of the radome, the $+x$ -axis points towards the East, the $+y$ -axis towards the North, the $+z$ -axis towards zenith. The surface normal of the radome \mathbf{n}_R for a point at azimuth angle A ($0 \leq A \leq 360^\circ$; counting from North to East, South and West) and elevation angle E ($-E_0 \leq E \leq 90^\circ$) is

$$\mathbf{n}_R = (\sin A \cos E, \cos A \cos E, \sin E) \tag{5.35}$$

Using the solar vector $\mathbf{S}(t)$ of Eq.(5.6), the solar illumination of the surface element ΔF is

$$\begin{aligned} \Delta \mathcal{I}_R(A, E, t) &= \mathbf{S}(t) \cdot (\mathbf{S}(t), \mathbf{n}_R) \Delta F \\ &= S(t) [\cos \beta(t) \cos E \cos(A_S(t) - A) + \sin \beta(t) \sin E] \Delta F \end{aligned} \tag{5.36}$$

$$\Delta F = R \Delta E \times R \cos E \Delta A \tag{5.37}$$

The solar illumination during summer ($\delta(S) = 23^\circ$) of a radome at the geographic latitude $\varphi = 20^\circ$ (the latitude of the LMT/GMT observatory²) is shown in Fig. 5.17. Since the geographic latitude of the site is smaller than the declination of the Sun at summer solstice, the position of the Sun at noon is 3° at the northern side of the radome as the figure shows.

For the climate inside a radome it is important to know the amount of solar radiation that is absorbed by the radome material and that is transmitted into the interior. For the frequently used GoretexTM material the reflectance of solar radiation is $\rho_S \approx 0.7$, the absorption is $\alpha_S \approx 0.05$, the transmission is $\tau_S \approx 0.25$. The total amount of solar radiation incident on the radome is

² Investigated during the thermal design study of the LMT/GMT, see Greve & MacLeod [2001].

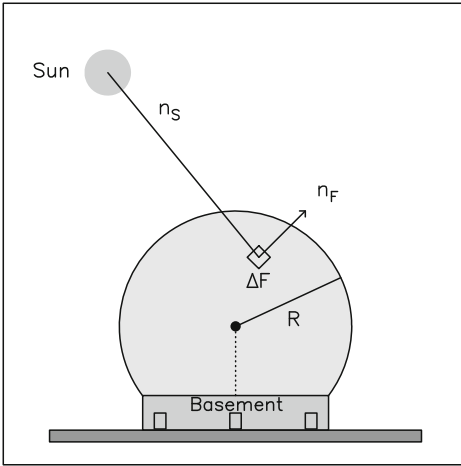


Fig. 5.16 Illustration of an over-hemispherical radome of radius R .

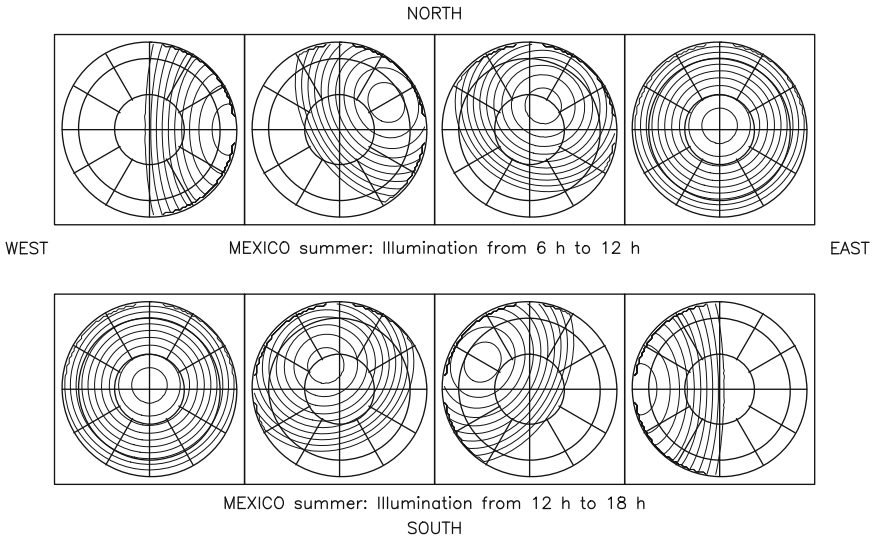


Fig. 5.17 Contour lines of solar illumination of a radome at geographic latitude $\varphi = 20^\circ$ (LMT/GMT site), during summer $\delta(S) = 23^\circ$; viewed from the top. The time in this figure is from left to right. The sectors of the radome surface as used in thermal model calculations (Chapter 11) are drawn.

$$\mathcal{E}(t) = \int_0^{360^\circ} \int_{-E_0}^{90^\circ} \Delta \mathcal{S}_R(A, E, t) R \cos E dA \times R dE \quad (5.38)$$

Figure 5.18 shows for the radome of the Onsala 20-m telescope (at the geographic latitude $\varphi = 60^\circ$) the incident solar radiation $\mathcal{E}(t)$, the solar radiation absorbed by the radome skin $\mathcal{E}_\alpha(t) = \alpha_S \mathcal{E}(t)$ and the solar radiation transmitted into the interior $\mathcal{E}_\tau(t) = \tau_S \mathcal{E}(t)$. These data were used in thermal model calculations of the Onsala radome explained in Section 11.9.

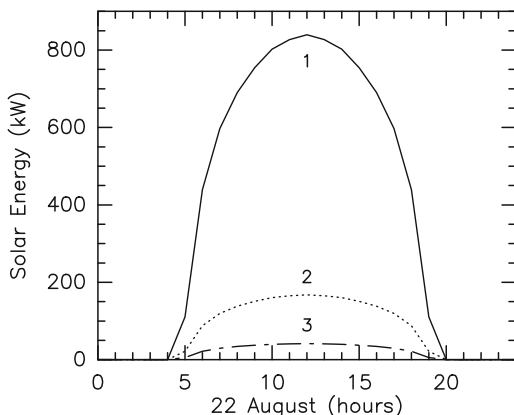


Fig. 5.18 Solar energy incident (1), absorbed (3) and transmitted (2) into the Onsala radome during summer (Aug 22). For the dimension of the Onsala radome see Tables 3.1 and 3.2.a.

The absorbed solar radiation heats the radome skin, which in turn emits at infrared wavelengths partially to the outside and partially to the inside. The transmitted radiation $\mathcal{E}_\tau(t)$ enters the radome in a diffuse way and is partially absorbed by the telescope, the floor and the walls. Part of the diffuse radiation is multiple-scattered and partially transmitted through the radome skin and thus escapes to the outside. With \mathbf{a} the fraction of the diffuse radiation absorbed inside the radome and with ρ ($\approx \rho_S$) the fraction of the radiation reflected back into the interior by the radome skin or the astrodome walls and the slit membrane, the amount of diffuse radiation $e(t)$ captured inside the radome is [Greve & MacLeod 2001]

$$\begin{aligned} e(t) &\approx \mathcal{E}_\tau(t)[\mathbf{a} + \mathbf{a}(1 - \mathbf{a})\rho + \mathbf{a}(1 - \mathbf{a})^2\rho^2 + \dots] \\ &= \mathbf{a}\mathcal{E}_\tau(t)/[1 - (1 - \mathbf{a})\rho] = \mathbf{f}_R \mathcal{E}_\tau(t) \end{aligned} \quad (5.39)$$

Table 5.3 gives representative values $\mathbf{f}_R = e(t)/\mathcal{E}_\tau(t)$, i.e. the fraction of transmitted radiation captured inside the radome. The table distinguishes between a radome and an astrodome, though with the radome skin and the slit membrane made of the same material (for instance GoretexTM). The internal absorption \mathbf{a} is smaller for a radome than for an astrodome. The absorbing surfaces in a radome are those of the telescope and the floor (Fig. 11.27), in an astrodome the absorbing surfaces are the telescope, the floor and, in addition, the large steel wall areas of the housing (Fig. 11.28). Table 5.3 shows that the captured energy is small ($\mathbf{f}_R \approx 0.3$ to 0.4) if the telescope, the floor and the walls are covered by a highly reflective low-absorption finish ($\mathbf{a} \approx 0.1$), for instance aluminium foil. This fact was noticed during the thermal design of the JCMT enclosure [Bregman & Casse 1985]. The FCRAO radome

enclosed 14-m telescope is covered with aluminium foil (see Fig.3.5, Schloerb [1978]).

Table 5.3 Solar Radiation captured inside a Radome or Astrodome.

	Reflection of Radome Skin, ρ_S	Absorption inside Enclosure, a	Captured Radiation $f_R = e/\epsilon_\tau$
Radome	0.70	0.1	0.3
	0.70	0.3	0.6
	0.70	0.4	0.7
Astrodome (covered slit)	0.70	0.6	0.8
	0.70	0.7	0.9

5.9 Manipulation of Insolation through Surface Finish

The geometrical shape of a telescope and enclosure, their surface finish and their orientation with respect to the Sun determine the amount of incident and absorbed solar radiation. With respect to manipulation of insolation a distinction is made between the reflector surface (panel surfaces) and the other surfaces of the telescope and enclosure. A manipulation of insolation on the reflector surface can only be made through the surface finish, on the other telescope and enclosure surfaces through insulation, thermal façades and surface finish. The manipulation of insolation is a subject of building physics, solar energy physics, infrared radiation physics and space technology, and many of the results in these fields are relevant to telescope and enclosure structures. This Section deals with the reflector surface finish.

An easy way to reduce the amount of insolation is by turning the reflector away from the Sun, i.e. by respecting a Sun avoidance zone. This avoidance zone can be small or even not exist at all, as for instance for the ALMA telescopes and other telescopes that allow observations of the Sun. The IRAM 30-m telescope has a Sun avoidance zone of 5°. The fear on this telescope is that solar radiation diffusely scattered from the main reflector surface, painted white with TiO₂ paint, may in a long observation of the Sun heat the CFRP covered Al-honeycomb subreflector to an uncomfortably high temperature. The Sun avoidance zone of the IRAM 15-m telescopes is 35° (45°). This large avoidance zone is dictated by the first generation reflector panels with high specular reflection (see cover picture) that can cause overheating of the CFRP covered subreflector. The caustic from skew solar illumination of the highly reflective surface can overheat the quadripod legs, made of CFRP. To avoid accidental overheating, the upper parts of the quadripod legs are covered with shiny aluminium foil.

There are three types of surface finish for manipulation of solar radiation, i.e. paint, coatings and chemical treatment like etching and mechanical treatment like

micro-grooves and sand blasted roughness. Important for the three types of surface finish is the absorption and reflection of solar radiation, where reflected rays may concentrate energy on the subreflector or the quadripod legs. Reflection may occur with a dominant contribution of specular reflection, or diffuse reflection, or Lambert reflection. Evidently, a paint or coating must have a negligible absorption of radio waves.

An often used thermal protection of reflector, telescope and enclosure surfaces is white TiO_2 -pigmented paint (on pigmentation see Berdahl [1995]) which absorbs 30 to 40 % of the incident solar radiation. At infrared wavelengths the paint emits 70 to 80 % of the black body radiation corresponding to the temperature of the surfaces. The light reflected on TiO_2 paint is diffusely scattered. A test of the light scattering of TiO_2 paint is reported by Norrod [1995], here a 45 cm parabolic reflector was sprayed with different paints and the temperature in the focal point was measured when pointing the reflector towards the Sun. The temperature in the focal point is a measure of the reflectance and scattering of the paint. Another surface finish is anodised or shiny aluminium with a low absorption coefficient of solar radiation, of the order of 10 to 20 %, but also a low emission coefficient at infrared wavelengths, of the order of 10 to 20 %. A shiny aluminium surface can have significant specular reflection. A surface coated with rhodium³ has a low absorption coefficient of solar radiation of $a_S \approx 0.2$ and a low emission coefficient at infrared wavelengths of $e_I \approx 0.08$ [Baars et al 2006]. Paints may show an aging effect of increased absorption and increased emission, i.e. paint darkens, especially under increased UV radiation at the high altitude observatory sites.

For the ALMA telescopes, which are designed to observe also the Sun, the aluminium sheet reflector panels of the VertexRSI telescopes have a micro-roughness from random and regular grooves, which scatter the incident solar radiation. The scattering effect of surface grooves was investigated by Lamb [2000]. Measurements of solar light scattering of panels with steel-wool scratched surfaces, sandpaper scratched surfaces and sand blasted surfaces are reported by Ezawa et al. [2000] and Baars et al. [2006], for rough metal surfaces see Birkebak & Eckert [1965]; the scattering of a rough Ni surface is reproduced in Chapman [1974]. Ezawa et al. find that the scattering angle (FWHM) of the steel-wool scratched panel surface is 24° , the sandpaper scratched panel surface 57° and the sand blasted surface 86° . They estimate that in solar observations the temperature of the subreflector of the ASTE 10-m telescope will be 300° , 100° and 45° C in the case of a steel-wool scratched, sandpaper scratched and sand blasted main reflector surface. For aluminium and nickel surfaces with machined surface finish or fine grooves, Baars et al. [2006] find absorption coefficients of solar radiation between ~ 0.1 to 0.5 and infrared emission coefficients between ~ 0.05 and 0.2. They mention that surfaces with rather regular machined grooves may show grating effects and intense first order sidelobes, in their case at $\sim 15^\circ$ off-axis. The component of specular reflection of the machined,

³ for instance Media-LarioTM panels used on the ALMA AEC prototype telescope, the LMT/GMT telescope and test panels of the IRAM 15-m telescopes.

micro-grooved and sand blasted surfaces is below $\sim 1\%$, with the exception of fine-machined surfaces with $\sim 10\%$ specular reflection [Baars et al. 2006].

5.10 Sun on Subreflector and Quadripod

A radio telescope that is not designed to observe the Sun and that has a main reflector surface with appreciable specular reflection may by accident experience overheating of a quadripod leg or of a section of the main reflector surface from the caustic formed under skew solar illumination. This situation is dangerous if the quadripod and the main reflector panels are made of CFRP or CFRP surface layers. The caustic and the corresponding Sun avoidance zones can be derived from optic ray tracing.

The subreflector experiences an extreme heat load during solar observations. The power incident on the subreflector depends on the reflection coefficient ρ ($0 \leq \rho \leq 1$) and the scatter function $f(\Theta)$ of the main reflector surface finish of paint, coatings, micro-grooves etc.

In the case of specular reflection the scatter function is $f(\Theta) = \delta(\Theta - \Theta_i) = \delta(\Theta - \Theta_e)$ [delta-function] with Θ_i the angle of the incident solar ray with respect to the surface normal and Θ_e the angle of the reflected ray. For a parabolic reflector of diameter D and specular reflection the solar power reflected to the subreflector is

$$P_s(spec) = \rho \pi (D/2)^2 S(t) \quad (5.40)$$

with $S(t)$ given by Eq.(4.24). The power density [W/m^2] on the subreflector of diameter d ($\approx 0.1 D$) is

$$\mathcal{P}_s(spec) = P_s/(\pi d^2/4) = \rho (D/d)^2 S(t) \approx 100 \rho S(t) \quad (5.41)$$

Equation(5.41) states that the power density on the subreflector is the same for telescopes with equal subreflector to main reflector diameter and equal main reflector surface reflectivity ρ .

For the case of scattered reflection the power reflected to the subreflector depends on the scatter function $f(\Theta)$. A normalized Gaussian scatter function is

$$f(\Theta) = C \exp[-(\Theta/\Theta_0)^2] \quad (5.42)$$

with Θ the angle between the surface normal and an arbitrary direction within $0 \leq \Theta \leq 90^\circ$. The FWHM-angle of the scattered radiation is $\Theta(1/2) = 1.66 \Theta_0$. The normalization (C) is made such that the total reflected power is contained within the hemisphere above the surface element, i.e.

$$C \int_0^{2\pi} \int_0^{90^\circ} f(\Theta) \sin(\Theta) d\Theta d\varphi = 1 \quad (5.43)$$

In Eq.(5.43) it is assumed that the scattering is independent of the azimuth angle φ . Other scattering functions can be selected, for instance Gaussian scattering with different scattering in perpendicular directions, scattering by scratches and grooves with preference of reflection in particular directions, Lambert scattering ($f(\Theta) \propto \cos\Theta$) of paints etc. (see, for instance, Drolen [1992], Synnefa et al. [2006], Schwab & Cheng [2008]). However, the mathematical treatment is similar for all these cases of scattering.

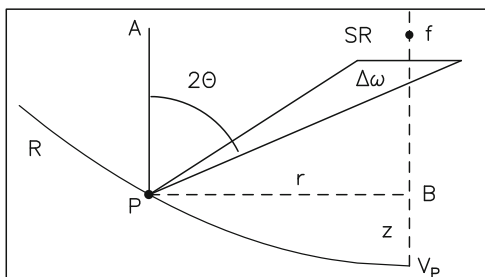


Fig. 5.19 Scattering of on-axis incident solar radiation on a parabolic reflector surface (R). SR = subreflector.

In Fig. 5.19 is AP a ray from the Sun on-axis incident on the main reflector surface at point P. The surface normal at P is the bisectrice of the angle $\angle APf = 2\Theta$. From the geometry of the parabola follows $\tan(2\Theta) \approx r/(f - z)$ with $f = nD$ the focal length of the main reflector. The solid angle of the subreflector, seen from P, is $\Delta\omega = (\pi d^2/4) \cos(\Theta)/s^2$ with $s^2 \approx r^2 + (f - z)^2$. The power incident on the subreflector is

$$P_s = \rho S(t) \int_0^{D/2} 2\pi r \Delta\omega(r) f(\Theta(r)) dr \tag{5.44}$$

With R the reduction of the power density due to scattering, the power density on the subreflector is

$$\mathcal{P}_s = R \mathcal{P}_s(spec) \tag{5.45}$$

Several values R are listed in Table 5.4. Again, these values are independent of the size of the reflector when using the same ratio d/D . The table illustrates the favourable property of a Lambert scatterer, as it is to some extent realized by TiO_2 paint.

Table 5.4 Reduction of Solar Radiation on Subreflector ^{a)}.

Θ_0 [$^\circ$]	Reduction R Eq.(5.45)	\mathcal{P}_s ^{b)} [kW/m ²]
5	0.25	15
15	0.20	12
25	0.14	8.4
35	0.095	5.7
45	0.07	4.2
specular		60
Lambert	0.04	2.4

^{a)} for a Gaussian scatter function, Eq.(5.42),
and reflection coefficient $\rho = 0.6$.

^{b)} for $S(t) = 1 \text{ kW/m}^2$.

Chapter 6

Temperature Measurements and FEM Thermal Deformation Calculations

The temperature (T) and the temperature change with time ($\partial T/\partial t$) are the basic parameters in the discussion of the thermal behaviour of a structural component. The temperature of a component defines, on the one hand, the heat transfer to other components of the telescope, the enclosure and the environment, and on the other hand the thermal expansion of a component and by this a possible force introduced in the structure.

The temperature is measured in degree Kelvin [K], in degree Celsius or centigrade [C] and degree Fahrenheit [F], the latter unit being used in English speaking countries. The linear relations between these temperature scales are

$$T [C] = T [K] - 273.15, \quad T [C] = (5/9) (T [F] - 32) \quad (6.1)$$

The unit of degree Celsius is used throughout the text, the unit of degree Kelvin is appropriate for radiative heat transfer.

The temperature range to be measured on a telescope or enclosure can be large, of the order of 50°C . Extreme environmental temperatures occur in tropical desert areas with temperatures of 50 to 60°C and polar regions with temperatures of -50 to -80°C . Under extreme conditions some thermal properties of materials (like heat conduction) may differ from their behaviour at room temperature.

There are two methods to record the thermal state of a telescope or enclosure. The first method consists of measurements with (many) electric resistance temperature sensors, often permanently installed at various locations of the telescope and enclosure. The second method consists of non-contacting infrared recording and infrared imaging, usually providing an immediate but only one-time thermal picture of a structural component.

6.1 Electric Resistance Temperature Sensors

Electric resistance temperature sensors are available in various classes of relative and absolute precision and various sizes of contact area. Widely used are PT100TM sensors of 0.1°C precision and a good linearity (deviations less than a percent) over a large range of temperature, say –50° to 100° C. At sea level the sensors can be calibrated in freezing water (0° C) and in boiling water (100° C). The sensors are easily installed, the digital recording of the data is simple and they are suited for long-term temperature monitoring. During installation care must be taken that a sensor measures the temperature of the structural component rather than the ambient air, or being heated by direct solar radiation. Fig. 6.1 shows a PT100TM sensor installed inside the VertexRSI ALMA 12-m diameter prototype telescope. As shown in Fig. 6.2, a sensor exposed to the environment may be enclosed in an insulated box covered on the outside by the surface finish of the component to be measured, for instance white paint or shiny aluminium foil (see also Bayley et al. [1994]¹). Most telescopes have at least a few temperature sensors, the telescopes mentioned in Table 6.1 have a rather large number. BUS constructions with 30 to 50 sensors and telescopes with 100 to 150 sensors, or more, allow detailed temperature monitoring and detailed thermal modelling for prediction of focus, pointing and reflector surface changes.



Fig. 6.1 PT 100TM electric resistance temperature sensor installed inside the VertexRSI ALMA 12-m prototype antenna. Although the sensor is located at one spot, due to good thermal conduction of the metal wall the measured temperature is representative for a large area [Courtesy N. Emerson, NRAO, USA].

¹ The shown ambient air ventilation holes in their sensor cover may influence the measurement of the structural component; see Chapman [1974] for the installation of sensors and measurement errors.

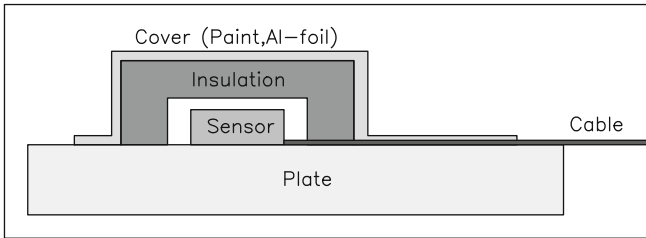


Fig. 6.2 Temperature monitoring of a plate. The sensor is glued to the plate (thermal conductive paste), surrounded by insulation and covered as the plate by paint or aluminium foil, etc.

Table 6.1 Temperature Sensors on Telescope Structures.

Telescope ^{a)} (reference)	Reflector Diameter [m]	Measured Component	Number of Sensors
BIMA (1)	6	BUS	32
NMA (2)	10	BUS	16/34
ASTE (3)	10	BUS, Pedestal, Fork ^{c)}	170
OVRO (4)	10.4	BUS	48
CSO (5)	10.4	BUS	8
VertexRSI-ALMA ^{b)} (6)	12	Pedestal, Fork, BUS ^{d)}	89
AEC-ALMA ^{b)} (7)	12	Pedestal, Fork	101
APEX (8)	12	Fork	20
ALMA-J ^{b)} (9)	12	BUS ^{e)}	227
Metsähovi (10)	14	Reflector, Radome	5 + 3
FCRAO (11)	14	BUS, Quadripod, Subreflector	20 + 10
JCMT (12)	15	BUS, Alidade	220 (240)
IRAM (13)	15	Fork, BUS, Quadripod	12 + 6 + 4
SEST (14)	15	BUS, Central Hub	8 + 8
IRAM (15)	30	Yoke, BUS, Quadripod	44 + 104 + 8
NRO (16)	45	BUS	140 (orig.)
Parkes (17)	64	BUS, Turret, Central Hub	24 + 14
RT-70 (18)	70	BUS	200
Effelsberg (19)	100	Alidade, BUS, Quadripod	19
GBT (20)	100	Alidade, BUS, Arm	25
LMT/GMT and SRT (21)	50 / 64	BUS, Alidade	

^{a)} see the list of Acronyms of observatory sites.

^{b)} ALMA prototype telescopes.

^{c)} 14 sensors on pedestal and fork.

^{d)} Pedestal: 7, fork: 42, invar cone: 12, BUS: 24.

^{e)} 55 on BUS, 25 on central hub, 32 on BUS CRFP plates.

References for Tab. 6.1: (1) Lamb & Forster [1993]; (2) Satou [1998]; (3) Ukita et al. [2007]; (4) Lamb & Woody [1998]; (5) Chamberlin [2003]; (6) Greve & Mangum [2008]; (7) ALMA-AEG, priv. comm.; (8) Güsten (MPIfR), priv. comm.; (9) Ukita et al. [2004]; (10) priv. comm.; (11) Schloerb [1978]; (12) Baas [1995], Wouterloot

[2005]; (13) Greve [1992]; (14) G. Delgado (SEST), priv. comm; (15) Greve et al. [2005]; (16) Akabane [1983], Ukita [1999]; (17) Jeffery [1964]; (18) Machuyev & Gimmelman [2006], Bairamov et al. [1988]; (19) A. Kraus (MPIfR), priv. comm.; (20) Ray [2003]; (21) temperature sensors to be defined.

6.2 Temperature Measurements by Infrared Radiation

One-dimensional thermal infrared radiation detection uses a (hand-held) radiation meter sensitive to wavelengths from ~ 5 to $12\ \mu\text{m}$ in the infrared window N with good atmospheric transmission and small atmospheric emission. In addition, maximum emission of surfaces at room temperature occurs at these wavelengths (see Section 7.8 and Fig. 4.26). The radiation meter measures within a certain solid angle (for instance a cone of $\sim 2-5^\circ$ opening) the power (P) of the infrared radiation emitted by the object under investigation. Through comparison with an internal black body source is the received power expressed as an equivalent black body temperature T_m . This temperature is not necessarily the physical temperature T of the object. If e is the infrared emissivity of the object at the wavelength to which the radiation meter responds, the relation $P = \sigma(T_m)^4 = e \sigma T^4$ holds so that $T = T_m/e^{1/4}$ with $T_m \leq T$ since $e \leq 1$. The instrument can usually be set to the actual value e . Infrared measurements of this kind can be in error if the surface of the object, especially when glossy [Inagaki & Okamoto 1996], reflects a significant fraction of the cold sky or warm ground radiation. The measurements of the ground and snow shown in Fig. 4.16 were obtained in this way.

Two-dimensional infrared imaging uses a camera with response at, for instance, $\sim 5-8\ \mu\text{m}$. Usually global thermal pictures of an object are taken to investigate temperature distributions with heat sinks and heat sources. A classic example is the investigation of heat sources that affect the local seeing inside the MMT optical telescope enclosure [Williams et al. 1986] and the dome of the CFHT optical telescope [Cowley et al. 1988]. Fig. 6.3 is the infrared picture of the reflector of one IRAM 15-m telescope.

6.3 Temperature Sampling Rate

The thermal time constants of telescope and enclosure components determine the rate of temperature sampling. For example, the thermal time constant of reflector panels and cladding walls of a BUS is of the order of 15 to 30 minutes, the thermal time constant of a BUS, a yoke, of fork arms and heavy enclosure walls is of the order of one hour to several hours. Meaningful temperature monitoring is made on time scales of, say, 1/10 to 1/30 of the thermal time constant of the object, or time scales of minutes, 10 minutes, or even 1/2 to one hour. A decision of the sampling

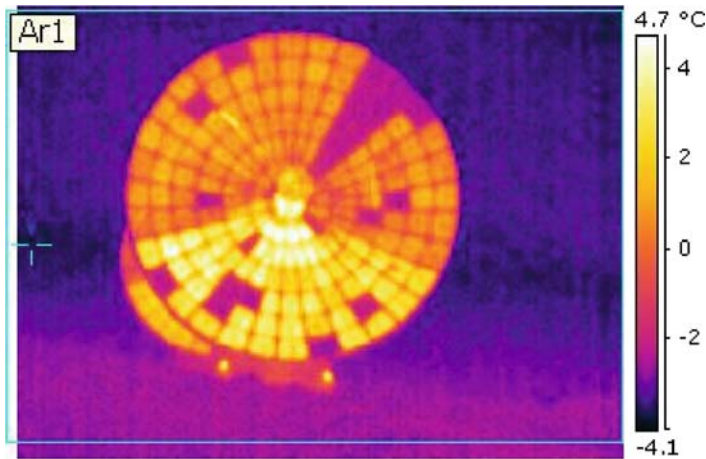


Fig. 6.3 Infrared image (at $\sim 5-8 \mu\text{m}$ wavelength, camera FLIR E65TM) of one Plateau de Bure telescope. The individual panels of the reflector are seen. The picture was taken to check the panel heating system, heating defects show up as dark areas [Courtesy R. Neri, IRAM, France].

time is easily made, corresponding thermal model calculations should be made with the same resolution in time.

6.4 Location of Temperature Sensors (Interpolation Matrix and Influence Matrix)

Temperature monitoring of relatively small telescope components like a panel, a subreflector or a quadripod leg can be made with a few sensors, say 5 to 10. Here the choice of the location, often made on intuition, and the installation of the sensors are easy. The installation of a few hundred sensors on a telescope however needs a strategy to decide on their locations. For a large structural component the decision of sensor locations depends on the purpose of the temperature monitoring and on the availability of its FEM.

In the case the FEM is not available, even for a large structure, the only, though somewhat unsatisfactory way to decide on the location of sensors is based on intuition, experience and the general idea that the sensors should at least monitor the temperature of sections of approximately equal mass, equal volume or equal surface areas. In this way the location of 89 sensors was selected on the VertexRSI ALMA 12-m prototype telescope², as shown in Fig. 6.4 and Fig. 6.5.a-b, using on the fork support approximately equal surface areas and on the BUS approximately

² of which the FEM could not be used in time.

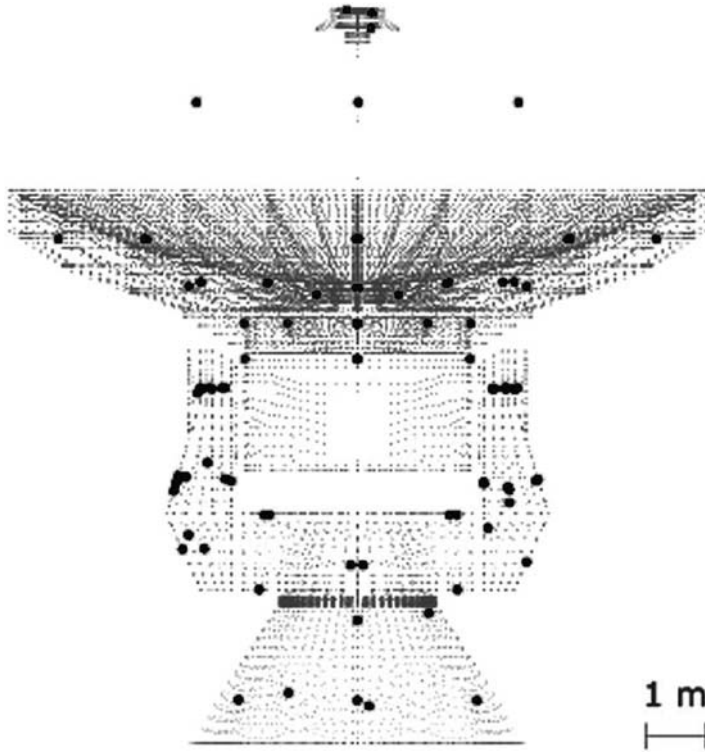


Fig. 6.4 Temperature sensors on the VertexRSI ALMA 12-m prototype telescope; elements of the FEM: small dots, temperature sensors: big dots [Courtesy N. Emerson and NRAO/AUI/NSF].

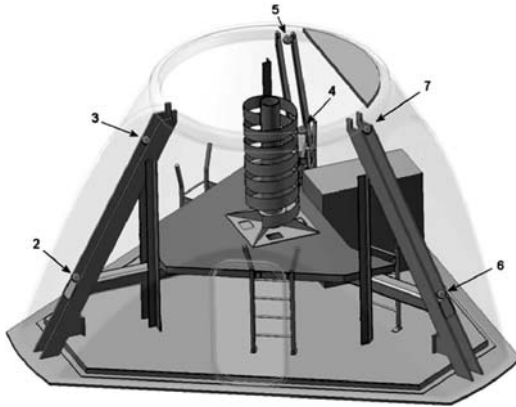


Fig. 6.5.a Temperature sensors on the pedestal of the VertexRSI ALMA 12-m prototype telescope [Image Courtesy of NRAO/AUI/NSF].

equal volume elements. A measurement of the temperature of the VertexRSI ALMA prototype telescope made with this arrangement of sensors is shown in Fig. 9.76.

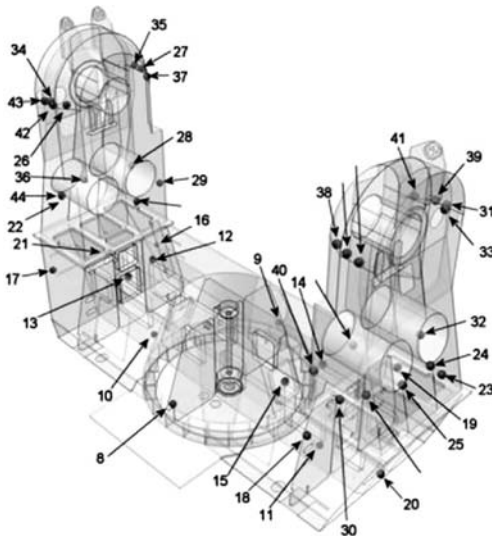


Fig. 6.5.b Temperature sensors on the fork support of the VertexRSI ALMA 12-m prototype telescope [Image Courtesy of NRAO/AUI/NSF].

It can today be assumed that when a few hundred temperature sensors are to be installed on a telescope also the FEM of the structure is available. Such a FEM may contain several 10 000 structural elements (N). The question arises at which elements, or groups of elements, the much smaller number of temperature sensors ($K \ll N$) is to be installed so that a reliable temperature distribution of all N elements can be derived for use in the FEM in order to predict in the most accurate way a specific temperature sensitive parameter, like the focus, the pointing, the reflector surface shape etc. This question is answered in context of a required interpolation procedure and the selection of thermally important elements.

A FEM can predict thermal deformations only in the case a temperature is assigned to each element. The temperatures of the FEM elements $N - K$ without sensor are obtained from interpolation of the K actually measured temperatures $[T_K]$. The selection of an interpolation procedure starts from an intuitive initial distribution of the K sensors throughout the FEM structure. The quality of the interpolation procedure is checked in a numerical simulation by adopting a certain temperature distribution $[T_N]$ throughout the FEM elements, selection of the location of the sensors (elements K) and their temperatures $[T_K]$, subsequent application of the interpolation procedure to the selected temperatures $[T_K]$ to obtain all temperatures $[T_N]'$, and thereafter comparison of the reconstructed temperature distribution $[T_N]'$ with the initially adopted temperature distribution $[T_N]$. The interpolation procedure is accepted when the differences $[T_N]' - [T_N]$, or the rms value of the differences, are small. This method was applied on the IRAM 30-m telescope [Bremer & Peñalver 2002] and a reliable interpolation procedure for the temperatures $T(i)(i=1, \dots, N-K)$ of the elements $[i]$ without sensor was found to be (on this telescope)

$$T(i) = \sum_{j, j \neq i} T(j)W(i, j) / \sum_{j, j \neq i} W(i, j) \quad (6.2)$$

with $T(j=1,\dots,K)$ the measured temperatures and the weighting function $W(i,j) = s(i,j)^{-2}$ with $\varepsilon < s(i,j) = |\mathbf{x}_i - \mathbf{x}_j|$ the distance between element \mathbf{x}_i and \mathbf{x}_j . In this relation the limiting value ε (for instance = 0.1 m) avoids a singularity. In essence, Eq.(6.2) gives the interpolation matrix \mathbf{I}

$$\begin{aligned} (T_1, T_2, \dots, T_{N-K}) &= \mathbf{I} \times \begin{pmatrix} T_1 \\ T_2 \\ \dots \\ T_K \end{pmatrix} \\ &= \begin{pmatrix} w_{1,1} & w_{1,2} & \dots & w_{1,K} \\ w_{2,1} & w_{2,2} & \dots & w_{2,K} \\ \dots & \dots & \dots & \dots \\ w_{N-K,1} & w_{N-K,2} & \dots & w_{N-K,K} \end{pmatrix} \times \begin{pmatrix} T_1 \\ T_2 \\ \dots \\ T_K \end{pmatrix} \end{aligned} \quad (6.3)$$

with $w_{ij} = W_{ij}/\sum W(i,j)$. Using the matrix \mathbf{I} , for any set of measured temperatures $[T_K]$ the temperature distribution $[T_N] = [T_{N-K}] + [T_K]$ of the entire structure can be calculated.

The search of the interpolation algorithm is linked to the search of sensor locations that answer in an optimal way the thermal question under consideration. The location of the sensors should, for instance, be optimal for prediction from the FEM of temperature induced reflector surface deformations, of pointing errors, of interferometric path length variations etc., or of a combination of such questions. If, for instance, searching for optimal location of sensors with respect to temperature induced reflector surface deformations it is convenient to calculate for each element (\mathbf{N}) of the FEM the influence that a temperature change of, say, $\Delta T = 1^\circ\text{C}$ has on the set of FEM elements ($\mathbf{n} < \mathbf{N}$) that defines the reflector surface. This gives the influence matrix $\mathbf{M}(\mathbf{n} \times \mathbf{N})$. The elements that appear to have the largest influence on the surface shape, i.e. the thermally important elements, should evidently be equipped with temperature sensors. However, the thermally important elements for temperature induced reflector surface deformations may be different from, for instance, those for prediction of temperature induced pointing errors and hence may require a different or compromise sensor installation.

The investigation of the interpolation procedure and the selection of sensor locations thus leads to the construction of the temperature influence matrix \mathbf{M} . If $\delta = (\delta_i, i=1,\dots,n)$ is the temperature sensitive parameter, for instance the reflector surface shape defined by the individual deformations δ_i of the panel support points, to be predicted from the FEM with \mathbf{N} elements and measured temperatures $[T_j, j = 1,\dots,K]$, then the influence matrix \mathbf{M} is

$$\delta = (\delta_1, \delta_2, \dots, \delta_n) = \mathbf{M} \times \begin{pmatrix} T_1 \\ T_2 \\ \dots \\ T_N \end{pmatrix} = \begin{pmatrix} A_{1,1} & A_{1,2} & \dots & A_{1,N} \\ A_{2,1} & A_{2,2} & \dots & A_{2,N} \\ \dots & \dots & \dots & \dots \\ A_{n,1} & A_{n,2} & \dots & A_{n,N} \end{pmatrix} \times \begin{pmatrix} T_1 \\ T_2 \\ \dots \\ T_N \end{pmatrix} \quad (6.4)$$

The values $A_{i,j}$ are derived from the FEM by subjecting each element $[\mathbf{N}] \ni i$ of the FEM to a temperature change of $\Delta T_i = 1^\circ \text{C}$ while keeping the other elements $[\mathbf{N}] \ni j \neq i$ at a constant temperature.

On the IRAM 30–m telescope there are $\mathbf{n} = 260$ FEM elements that determine the positions $(x,y,z)_i$ ($i = 1,2,\dots,n$) of the panel frame support points and thus the shape of the reflector surface. There are $\mathbf{K} = 148$ temperature sensors with $\mathbf{K}_{\text{BUS}} = 104$ sensors installed on the BUS and $\mathbf{K}_Y = 44$ sensors installed on the yoke, thus $\mathbf{K} = \mathbf{K}_{\text{BUS}} + \mathbf{K}_Y$. In total there are $\mathbf{N} = 2376$ FEM elements³. When starting from the measured temperatures $[T_{\mathbf{K}}]$ the temperature induced surface deformations δ are obtained from

$$\delta = (\delta_1, \delta_2, \dots, \delta_n) = \mathbf{M} \times \mathbf{I} \times \begin{pmatrix} T_1 \\ T_2 \\ \dots \\ T_{\mathbf{K}} \end{pmatrix} \quad (6.5)$$

The first matrix application (\mathbf{I}) interpolates the measured temperatures to all elements of the FEM (i.e. $\mathbf{K} = 148 \rightarrow \mathbf{N} = 2376$), the second matrix application (\mathbf{M}) calculates the temperature influence on the reflector surface support points (i.e. $\mathbf{N} = 2376 \rightarrow \mathbf{n} = 260$). Once derived, the surface deformations are calculated from application of the matrix $\mathbf{P} = \mathbf{M} \times \mathbf{I}$ without running the FEM for each individual case. During the construction of the influence matrix \mathbf{M} it may appear that certain structural components have no influence on the question under investigation. Their elements can be left out in further discussions, thus perhaps reducing significantly the size of the matrix \mathbf{M} .

The distribution of temperature sensors on the IRAM 30–m telescope selected in this way for optimal prediction of temperature induced reflector surface deformations is shown in Fig. 6.6 [Bremer & Peñalver 2002]. Radio holography measurements have shown that with these temperature measurements, interpolated and used in the FEM, the thermal reflector surface deformations are predicted with the precision of $\sim 0.005 \text{ mm}$ [Greve et al. 2005, and Fig. 6.9].

The location of temperature sensors on the pedestal and fork of the AEC ALMA 12–m prototype telescope selected in this way for optimal prediction of temperature induced pointing errors is shown in Fig. 6.7. Here the search for optimal sensor location for the prediction of pointing errors was supported by FEM calculations of the temperature induced tilt (α, β) of the roof of the secondary focus cabin, which supports the BUS.

A convenient aid in the search of temperature sensor locations used by Bremer & Peñalver [2002] is to assign the FEM elements a brightness code according to their thermal importance with respect to the thermal question under investigation. For the

³ This is a small number of FEM elements. The original FEM was not available and a new FEM for the thermal investigation reported here was built (P. Raffin, IRAM) from the construction drawings. This FEM contains the BUS, the yoke and the quadripod. It is, however, encouraging that a FEM with this small number of elements gives very accurate predictions of the reflector surface shape (see Fig. 6.9).

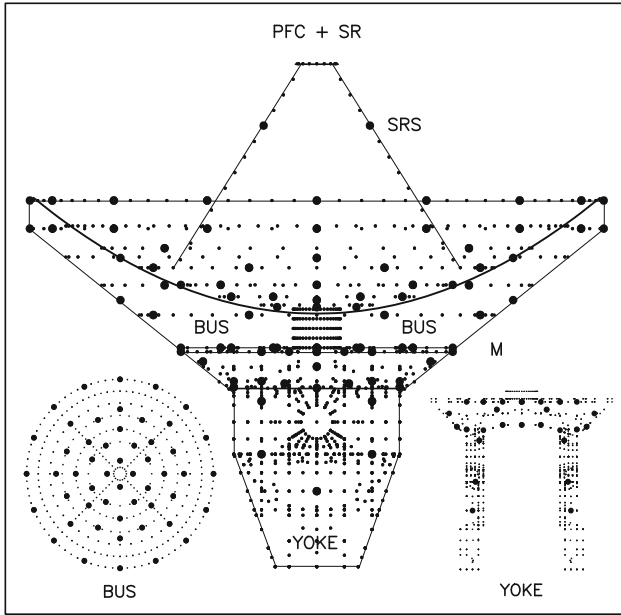


Fig. 6.6 IRAM 30-m telescope, BUS and yoke. Small dots: elements of the FEM, big dots: location of temperature sensors for optimal prediction of temperature induced reflector surface deformations. M: membrane, SRS: subreflector supports, SR: subreflector, PFC: primary focus cabin [From Greve et al. (2005), Courtesy IEEE Trans. Ant. Propag.].

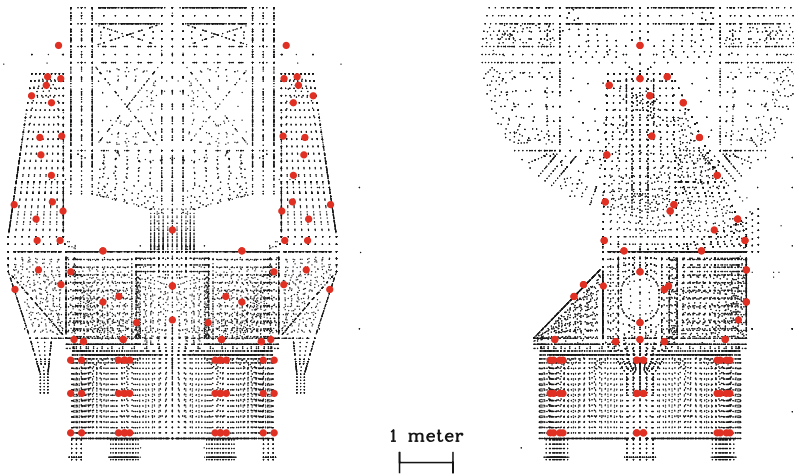


Fig. 6.7 AEC ALMA 12-m prototype telescope, pedestal and fork. Small dots: elements of the FEM; big dots: location of temperature sensors for optimal prediction of temperature induced pointing errors [From Greve & Mangum (2008), Courtesy IEEE Ant. & Propag. Magazine].

IRAM 30-m telescope this is shown in Fig. 6.8. Panel (a) of the figure shows the FEM elements (nodes), panel (b) shows the elements that are important for temperature induced reflector surface deformations, panel (c) shows the elements that are important for temperature induced pointing errors. The comparison of panel (b) and (c) shows the elements (and sensors) that are important for both thermal questions. The choice of sensor locations was made from panel (b) of Fig. 6.8.

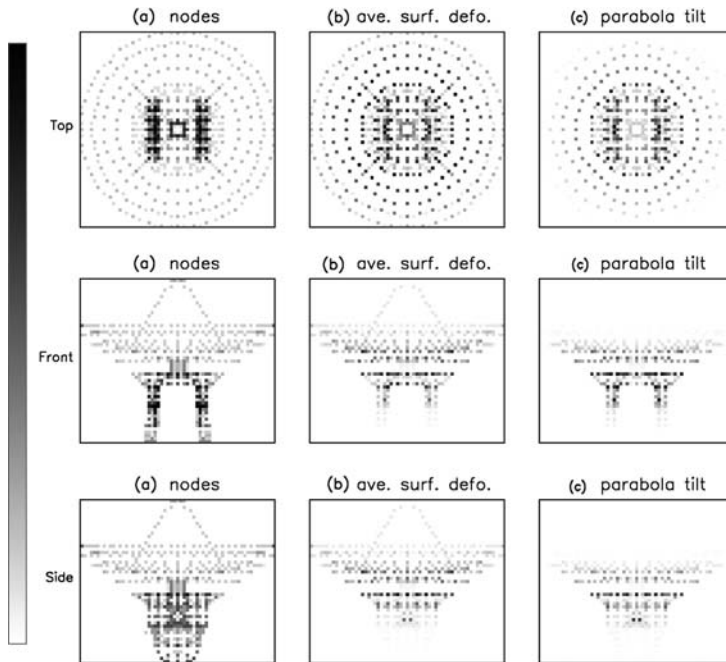


Fig. 6.8 IRAM 30-m telescope. Illustration of thermally important elements (black = highest importance). Panels (a): FEM elements, panels (b): importance with respect to reflector surface precision, panels (c): importance with respect to pointing [From Bremer & Peñalver (2002), Courtesy SPIE].

Similar investigations of the JCMT 15-m telescope are reported by Baas [1995], Smith [1998] and Baas & Wouterloot [2002]; the arrangement of 220 temperature sensors on the BUS is explained by Wouterloot [2005, see Fig. 9.50]. The measurements of these sensors were used in the FEM of the JCMT telescope to predict temperature induced surface deformations, to be corrected with motor controlled panel adjusters.

6.5 Precision of Temperature Measurements

The comparison of structural deformations calculated from the FEM for a temperature distribution $[T_N]$ and a slightly different temperature distribution $[T_N + \Delta T_N]$ can be used to determine the precision with which temperature measurements must be made in order to obtain a useful result. Test calculations of the IRAM 30-m telescope indicate that a temperature sensor precision of $\Delta T \approx 0.1^\circ \text{C}$ is sufficient to obtain surface deformations with the accuracy of $\sim 0.005 \text{ mm}$, using the FEM with 2376 elements.

6.6 Prediction of Temperature induced Deformations

It is important to determine the accuracy of thermal deformation calculations when applying the choice of temperature sensor locations and the temperature interpolation algorithm explained in the previous section. For this a comparison of the predicted and measured reflector surface shape, focus variation and pointing correction was made for the IRAM 30-m telescope. Fig. 6.9 compares the reflector surface deformations derived from a holography measurement with those obtained from the FEM calculation using the temperature data of the telescope recorded at the time of the holography. In order to enhance the temperature induced surface deformations the telescope was taken out of thermal control and a heat load was inserted into the BUS. The agreement between the measurement and the calculation is excellent and indicates that for this telescope and FEM (consisting of the yoke, BUS and quadri-pod, $N = 2376$ FEM elements) the temperature induced surface deformations are predicted with the accuracy of $\sim 0.005 \text{ mm}$.

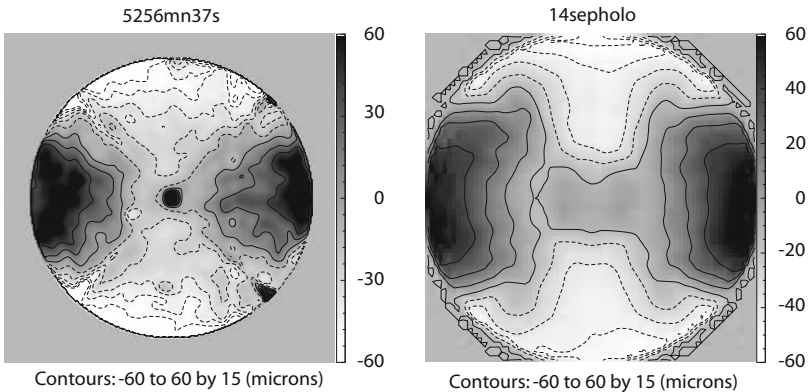


Fig. 6.9 IRAM 30-m telescope. Reflector surface deformations derived from a holography measurement (left panel) and calculated from the FEM using the temperatures of the BUS recorded during the holography (right panel). Contours between -0.060 and 0.060 mm in steps of 0.015 mm .

Figure 6.10 shows the comparison of measured and predicted focus variations Δz using the corresponding temperature recordings of the yoke, BUS and quadripod in the FEM. In order to enhance the temperature effect the telescope was again taken out of thermal control and a heat load was introduced. There is agreement within ~ 0.1 mm between the measured and calculated focus variation, for primary focus and Cassegrain focus observation. Finally, Fig. 6.11 shows the comparison between pointing measurements and predictions using the temperature measurements in the FEM. For this measurement the telescope was also taken out of thermal control and a heat load was introduced. The agreement between the measurements and predictions is not fully satisfactory, especially for the pointing correction in azimuth direction. The discrepancy is perhaps explained by the fact that the FEM is not complete since it contains only the yoke, the BUS and the quadripod. A better agreement may be obtained from a complete FEM containing also the azimuth bearing and the central tower with Nasmyth cabin, i.e. of the entire steel structure of the telescope (Fig. 2.5). Nevertheless, the examples demonstrate that a good and complete FEM can predict from temperature measurements with good accuracy temperature induced deformations of the reflector surface (BUS) and focus and pointing variations.

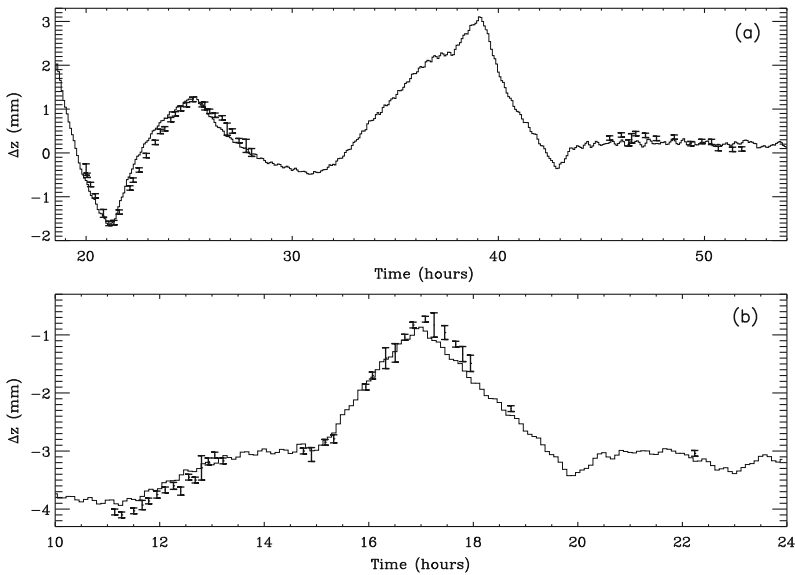


Fig. 6.10 IRAM 30-m telescope. Measurement (bars) of focus variations using a radio source and predictions using temperature measurements of the telescope structure and the FEM (continuous lines). (a) for measurements in prime focus, (b) for measurements in Cassegrain focus. [From Greve et al. (2005), Courtesy IEEE Trans. Ant. Propag.].

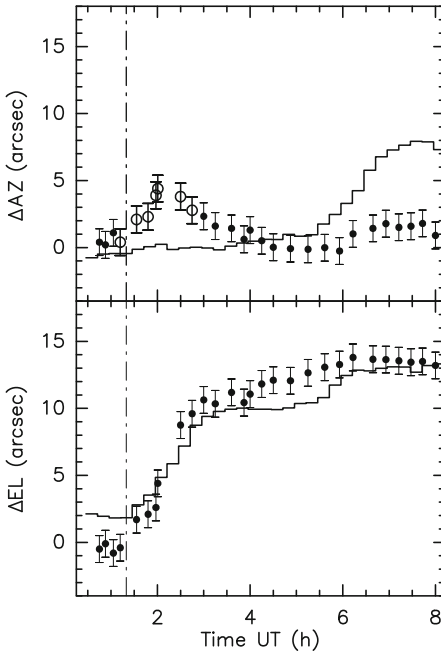


Fig. 6.11 IRAM 30-m telescope. Measurement (dots and error bars) of pointing corrections ΔAZ (azimuth) and ΔEL (elevation) using a radio source, and predictions (continuous lines) using temperature measurements of the telescope and the FEM (containing the yoke, BUS and quadripod). A heat load is introduced in the telescope at the time marked by the dash-dotted line [From Greve et al (2005), Courtesy IEEE Trans. Ant. Propag.].

6.7 Empirical Relations

On several telescopes a small number of temperature sensors is installed with the intention to find, sometimes by trial and error, significant correlations that allow the prediction and ultimate correction of, for instance, temperature induced focus and pointing errors. This approach has been successful for focus corrections, for instance on the Kitt Peak 11-m telescope [von Hoerner & Herrero 1971] as shown in Fig. 6.12, on the IRAM 30-m telescope [Baars et al. 1988] and on the GBT 100-m telescope [Prestage et al. 2004]. An empirical correlation, supported by FEM calculations, between the cross elevation pointing error and the temperature difference of the front and rear legs of the alidade support has been reported for the Cambridge MERLIN 32-m telescope [Bayley et al. 1994] and for the JCMT 15-m telescope [<http://www.jach.hawaii.edu/JCMT/telescope>].

6.8 Temperature related Measurements

A telescope is a flexible structure and deforms continuously under the influence of gravity, temperature and wind. Sometimes it is possible to derive, for instance, the associated pointing and focus changes in a direct way from a strain gauge measurement, a laser distance measurement, an inclinometer measurement, a beam pattern measurement or other means. While on the basis of such control measurements

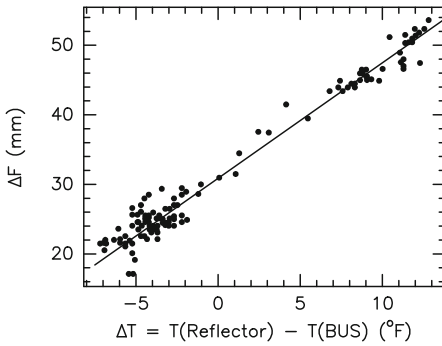


Fig. 6.12 Kitt Peak 11-m telescope (NRAO, USA). Empirical correlation between the focus position and the temperature difference between the reflector surface and the BUS. The straight line is the best-fit [after von Hoerner & Herrero, 1971].

[Greve & Kärcher 2009] a correction may be made, and thus the ultimate purpose is reached, it is usually difficult to decide how much of the monitored effect is due to temperature instead of gravity or wind. Since temperature measurements are easy, even a small number of temperature sensors at well-chosen locations can provide direct information on the thermal behaviour of a telescope component. Prestage et al. [2004] report a method, applied on the GBT 100-m telescope, to separate thermal influences and gravity and wind influences by observing on calm days (no wind influence) the quasar 0117+8928 that lies within 1° of the celestial north pole (no change of gravity force).

Chapter 7

Heat Transfer

7.1 Laws of Thermodynamics and Modes of Heat Transfer

Heat Transfer is a topic of theoretical physics and engineering physics, covered in many articles, journals, textbooks and tables. This Chapter explains the fundamentals of heat transfer as required for a general understanding of the thermal behaviour of large and complex structures, like telescopes and enclosures, and as required for the construction of thermal models of such structures, either for design or operational purposes. While it is possible to summarize heat transfer in a general way, any specific heat transfer problem of mechanical structures may need the consultation of a specific thermal engineering textbook.

The *First Law of Thermodynamics* says that ‘The energy content of a closed system is constant, although a transition between different forms of energy may occur, for instance between potential energy, kinetic energy (heat) and electromagnetic energy’. In the context of heat transfer considerations this means that the involved energies must be accounted for, there is no magic global loss or gain. The *Second Law of Thermodynamics* says that ‘Heat ‘flows’ from a hot to a cold body, increasing the entropy of a closed system’.

Heat transfer is discussed in terms of the temperature of bodies, here of telescope and enclosure components and of the thermal environment. The temperature of a body is a unique and measurable quantity. The unit of the absolute temperature T_K is degree Kelvin [K]; a unit adapted to common life and used here is degree Celsius [C] with $T [C] = T [K] - 273.15^\circ$. Heat is a form of measurable energy. It may be related to atomic or molecular motion of a gas, a liquid or a solid body and to electromagnetic radiation. Heat can flow in a telescope and enclosure if there are temperature differences in the telescope and enclosure itself, or between the telescope and the enclosure and the ambient thermal environment. Heat transfer occurs through conduction, natural and forced convection and radiation.

Heat transfer by conduction occurs if two bodies (1,2) of different temperatures ($T_1 \neq T_2$) are in direct contact. In this form of heat transfer, the kinetic energy of the atoms/molecules of the hotter body is partially transferred to the atoms/molecules of

the cooler body, however without mass exchange between the bodies. Heat transfer by conduction applies in particular to solid bodies that do not exchange matter when being in contact.

Heat transfer by convection between two bodies (1,2) occurs if one of the bodies is a moving gas or a moving fluid. The gaseous/fluid body moves along the solid body and is temporarily in contact with it. Heat is transferred if there is a temperature difference between the solid body and the gas/fluid ($T_1 \neq T_2$). Forced convection occurs when the gas/fluid moves along the body in an artificially controlled way, usually with a higher flow speed than under normal conditions. Natural or free convection occurs when the motion of the gas/fluid is caused by gravity acting on a temperature induced difference in density of the gas/fluid. Again, heat is transferred if there exists a temperature difference between the solid body and the gas/fluid. The flow can be external if the body (for instance a plate) is immersed in the gas/fluid, the flow can be internal if the gas/fluid is contained by the body (for instance a pipe).

Heat transfer by radiation occurs through electromagnetic waves that do not need a medium for propagation. A body at a temperature $T_K \neq 0$ always emits electromagnetic radiation and by this loses energy continuously. This energy loss is often balanced by energy/heat reaching the body in another way so that a thermal equilibrium may exist.

A telescope in the local thermal environment, or in an enclosure, can be in thermal equilibrium, or not. It is unlikely that a telescope that is exposed to the changing local thermal environment will be in thermal equilibrium for a long time, while for a telescope in an enclosure this may be the case. A strong external thermal disturbance is solar radiation, a strong internal thermal disturbance is, for instance, heating applied for de-icing. The thermal state of a telescope is therefore in most cases variable with time.

It is the intention that thermal studies predict the temperature of telescope and enclosure components. From these temperatures the thermal deformation of the telescope can be calculated and from this the degradation of the telescope performance, unless thermal protection is applied.

The principles of heat transfer¹ are illustrated by examples to understand the magnitude and the dimension of thermal relations. Chapter 8 explains the special situation of radiative heat transfer between the telescope, enclosure components, the sky and the ground.

7.2 Amount of Heat transferred

In order to have a feeling of the amount of heat transferred by conduction, convection and radiation, three situations close to reality are presented in Fig. 7.1. The

¹ This Chapter contains several citations from the textbooks *Heat Transfer* by Chapman [1974, BTU units; 1984, SI units] and *Heat Transfer* by Bejan [1993].

effect of heat transferred by conduction is illustrated in Fig. 7.1.a for an aluminium plate of 1 m^2 surface area (A) and $0.005 \text{ m} = 5 \text{ mm}$ thickness (Δx). The temperature difference from one side of the plate with temperature T_1 to the other side with temperature T_2 is $\Delta T = T_1 - T_2 = 10^\circ \text{ C}$. The heat is flowing from side **1** to side **2**. The heat conductivity², explained below, of aluminium is $k = 140 \text{ W/m/K}$. The effect of heat transferred by convection is illustrated in Fig. 7.1.b for a plate of 1 m^2 surface area (A) with temperature T_1 in a flow of air with temperature T_a and temperature difference $\Delta T = T_a - T_1 = 10^\circ \text{ C}$. The heat is flowing from the warmer air to the cooler plate. The convective heat transfer coefficient, explained below, is assumed to be $h = 10 \text{ W/m}^2/\text{K}$. The effect of heat transferred by radiation is illustrated in Fig. 7.1.c for two plates of 1 m^2 surface area (A) facing each other at 1 m distance. The absolute temperature of side **1** is $T_1 = 280 \text{ K}$, the absolute temperature of side **2** is $T_2 = 270 \text{ K}$, i.e. $\Delta T = T_1 - T_2 = 10^\circ \text{ K} = 10^\circ \text{ C}$. The net radiative heat transfer is from the warmer to the cooler surface. The surfaces are greyish with emission/absorption coefficient $e = a = 0.5$. The geometry of this heat transfer is expressed by the view factor φ , explained below, with $\varphi = 0.2$. The factor that defines the amount of radiative heat transferred is the *Stefan–Boltzmann* constant $\sigma = 5.67 \times 10^{-8} \text{ W/m}^2/\text{K}^4$.

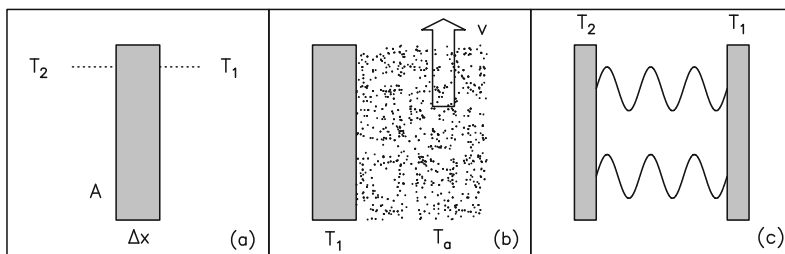


Fig. 7.1 Illustration of heat transferred by conduction through a plate (a), by convection to a plate immersed in a flow of air (b) and by radiation between two plates facing each other (c).

The heat (Δq) transferred by conduction through the aluminium plate is

$$\Delta q_{Al} = k A \Delta T / \Delta x = 140 [\text{W/m/K}] \times 1 [\text{m}^2] \times 10 [\text{K}] / 0.005 [\text{m}] = 280\,000 \text{ W} \quad (7.1)$$

If, however, the plate is $3 \text{ cm} (= 0.03 \text{ m})$ thick insulating material with heat conductivity $k_{ins} = 0.04 \text{ W/m/K}$ so that $k_{Al}/k_{ins} = 140/0.04 = 3\,500$, then the amount of heat conducted through the insulation is

$$\Delta q_{ins} = 0.04 \times 1 \times 10 / 0.03 = 13 \text{ W}$$

² The dimension of heat conductivity as an example is $\text{Wm}^{-1}\text{K}^{-1}$ that here is written W/m/K . Bejan [1993] uses the notation $\text{W/m}\cdot\text{K}$.

The heat transferred by convection between the ambient air and the plate is

$$\Delta q = hA\Delta T = 10 [\text{W}/\text{m}^2/\text{K}] \times 1 [\text{m}^2] \times 10 [\text{K}] = 100 \text{ W} \quad (7.2)$$

The heat transferred by radiation between the walls facing each other is

$$\begin{aligned} \Delta q &= \varphi e_1 a_2 \sigma A [(T_1)^4 - (T_2)^4] \\ &= 0.2 \times 0.5 \times 0.5 \times 5.67 \times 10^{-8} [\text{W}/\text{m}^2/\text{K}^4] \times (280^4 - 270^4) [\text{K}^4] \times 1 [\text{m}^2] = 2.3 \text{ W} \end{aligned} \quad (7.3)$$

7.3 Heat Content

Heat is not an absolute quantity, heat is related to a change in energy content ΔQ due to one or the other physical or chemical process. If the temperature of a body of mass M [kg] is changed by ΔT [K, C], for instance by putting the body in a fire, then its heat content is changed by

$$\Delta Q = \mathcal{C} M \Delta T [\text{J}] \quad (7.4)$$

Since in this expression only the temperature difference occurs, the Celsius temperature can be used instead of the absolute temperature ($1^\circ [\text{K}] = 1^\circ [\text{C}]$). The heat capacity \mathcal{C} in this relation depends on the material under consideration and the mode of heat supply or extraction, i.e. whether the temperature is changed by keeping the volume (\mathcal{C}_v) or the pressure of the body (\mathcal{C}_p) constant. This distinction of heat supply or extraction is of particular importance for gases. For solid bodies and incompressible fluids it is found that $\mathcal{C}_v = \mathcal{C}_p = \mathcal{C}$. The heat capacity is determined experimentally and is usually given for one kilogramme of the particular substance, its dimension is $[\mathcal{C}] = [\text{J}/\text{kg}/\text{K}]$. Defining \mathcal{C} in this way it is evident that the mass M [kg] of the material under consideration appears in Eq.(7.4). For the range of temperatures of telescope and enclosure components, say from -30°C to 60°C , the heat capacity of the materials can be taken as independent of the temperature (with the exception of gases). The heat capacity of common materials are listed in textbooks, for instance Chapman [1974, 1984] and Bejan [1993], and engineering tables, those of important materials used in telescope and enclosure constructions are given in Table 7.1.

In the following is ΔQ an amount of energy/heat, of dimension Joule \equiv [J]. Furthermore, $\Delta q = \Delta Q/\Delta t$ is an amount of energy/heat per time interval Δt , i.e. a power, of dimension Joule/s = Watt \equiv [W].

As an example, from Eq.(7.4) and Table 7.1 it can be calculated that a temperature change of $\Delta T = 1^\circ \text{C}$ of a 10 kg panel made of aluminium involves a change in heat content of $\Delta Q_{\text{panel}} = 10 [\text{kg}] 860 [\text{J}/\text{kg}/\text{K}] 1 [\text{K}] = 8600 \text{ J}$. A temperature

Table 7.1 Heat Capacities and Thermal Conductivities.

Material	Density ρ [kg/m ³]	Heat Capacity c [J/kg/K]	Volume Heat Capacity ρc [MJ/m ³ /K]	Thermal Conductivity k [W/m/K]
Steel	7 800	450	3.51	45
Invar	8 000	500	4.00	15
Aluminium (solid)	2 600	860	2.24	140
Al-Honeycomb	200	860	0.17	15
CFRP	1 600	700 – 1 300	~ 1.6	0.5 – 4 ^{a)}
Glass	600	840	0.50	0.75
Insulation	35 – 50	1 500 – 2 000	~ 0.07	0.04
Glassfiber	1 900	1 000	1.90	0.27
Adhesive	1 100	~ 1300	~ 1.43	0.2
Air	1.0	1 000	0.001	0.024
Concrete	3 000	750	2.25	0.3
Ground (hard rock)	2 500	850	2.12	1.7
Ground (sand, gravel)	1 500	1 000	1.50	1

^{a)} dependent on the direction of the fibers.

change of $\Delta T = 1^\circ \text{C}$ of a 100 ton BUS made of steel is $\Delta Q_{\text{BUS}} = 100 \times 1000 [\text{kg}] 450 [\text{J/kg/K}] 1 [\text{K}] = 45\,000\,000 \text{ J} = 45 \text{ MJ}$.

7.4 Heat Transfer by Conduction

Heat transfer by conduction is governed by *Fourier's* law that – without loss of generality – is here explained for a linear geometry. The material is a long and thermally insulated rod of material and in this rod an infinitesimal volume element is considered as shown in Fig. 7.2. The surface area A [m²] of this element is $A = A_1 = A_2 = \Delta y \Delta z$. The right side of the rod is cooler so that the heat flows in the direction of the arrow in Fig. 7.2. The temperature at the surface A_1 is $T_1 = T(x_1)$, at the surface A_2 it is $T_2 = T(x_2) = T(x_1 + \Delta x)$ with $T_2 < T_1$. According to *Fourier's* law the conductive heat transfer through this element, without displacement of material, is

$$\Delta q = -kA(T_2 - T_1)/(x_2 - x_1) = -kA\Delta T/\Delta x = -kA \frac{\partial T}{\partial x} [\text{W}] \quad (7.5)$$

Since in this expression only the temperature difference occurs, the Celsius temperature can be used instead of the absolute temperature. Relation (7.5) is defined as a heat flow rate, i.e. Δq is in Watt, the minus sign ensures that $0 \leq \Delta q$. In this relation is k [W/m/K] the thermal conductivity of the material, the value of which must be determined experimentally or taken from a table. For several materials the value k is given in Table 7.1. The heat conductivity of many solid bodies follows the relation $k = k_0(1 + bT)$, however, for the temperatures of telescope and enclosure components under discussion it is safe to use $k = k(0^\circ \text{C})$. The thermal

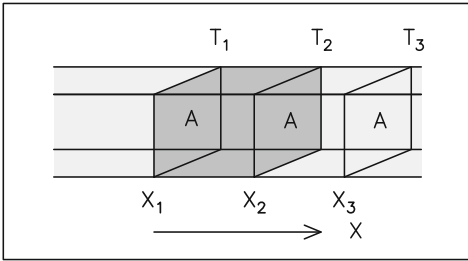


Fig. 7.2 Illustration of heat transfer by conduction in a rod of cross section A . The rod is cooler at the right side ($T_2 < T_1$) so that heat is flowing in the direction of the arrow.

properties of telescope and enclosure materials (metals, foams etc.) are homogeneous and isotropic. An exception can be Al-honeycomb panels and woven CFRP material with anisotropic properties.

A practical parameter of heat conduction is the specific thermal resistance \mathcal{R} and the thermal resistance R defined as

$$\Delta q = -kA\Delta T/\Delta x = -A\Delta T/\mathcal{R} = -\Delta T/R \quad (7.6)$$

so that

$$\mathcal{R} = \Delta x/k, \quad R = \Delta x/(kA) = \mathcal{R}/A \quad (7.7)$$

The dimensions are $[k] = [\text{W/m/K}]$, $[\mathcal{R}] = [\text{m}^2\text{K/W}]$ and $[R] = [\text{K/W}]$.

If in Fig. 7.2 the volume element $V_{12} = (\Delta x\Delta y\Delta z)_{12}$, between x_1 and x_2 , is in contact with the adjacent volume element $V_{23} = (\Delta x\Delta y\Delta z)_{23}$, between x_2 and x_3 , at the temperature T_3 ($< T_2 < T_1$), then

$$T_2 - T_1 = -\Delta q_{12}R_{12}, \quad T_3 - T_2 = -\Delta q_{23}R_{23} \quad (7.8)$$

Since energy/heat is conserved, $\Delta q_{12} = \Delta q_{23} = \Delta q$ so that

$$\begin{aligned} T_3 - T_1 &= (T_2 - T_1) + (T_3 - T_2) = -\Delta q_{12}R_{12} - \Delta q_{23}R_{23} \\ &= -\Delta q(R_{12} + R_{23}) = -\Delta qR_{\Sigma} \end{aligned} \quad (7.9)$$

It is found that the total thermal resistance R_{Σ} of two consecutive materials in contact is

$$R_{\Sigma} = R_{12} + R_{23} \quad (7.10)$$

with evident further generalizations, in particular different heat conductivities of the materials.

As an example, a composite plate of $A = 2 \text{ m}^2$ surface area consisting of 5 mm aluminium (Δx_{Al}) and 3 cm insulation (Δx_{ins}), in contact with each other, gives

$$\begin{aligned} R_{\Sigma} &= R_{\text{Al}} + R_{\text{ins}} = (\Delta x/kA)_{\text{Al}} + (\Delta x/kA)_{\text{ins}} = 0.005/(140 \times 2) + 0.03/(0.04 \times 2) \\ &= 0.000018 + 0.375 \approx 0.375 \text{ K/W}. \end{aligned}$$

It is seen that the insulation dominates the thermal resistance and thus the heat transfer of the combined plates.

The parameter $G = 1/R$, or $\mathcal{G} = 1/\mathcal{R}$, is the thermal conductance or specific thermal conductance with

$$\Delta q = G \Delta T = A \mathcal{G} \Delta T \quad (7.11)$$

The notation of thermal conductance allows an easy derivation of the thermal resistance of several modes of heat transfer acting in parallel. Typical examples of multi-mode heat transfer are two types of conductive heat transfer between opposite walls, for instance conduction through spacers (mode 1) holding a layer of insulation and conduction through the air (mode 2) in the gap itself, or convective heat transfer and radiative heat transfer through an air gap etc. If T_1 and T_2 are the temperatures of the walls and the conductance of mode 1 and mode 2 is G_1 and G_2 , then, as shown in Fig. 7.3, the heat transfer is

$$T_2 - T_1 = -\Delta q (G_1 + G_2) = -\Delta q G_\Sigma \quad (7.12)$$

This gives

$$G_\Sigma = G_1 + G_2 \quad (7.13a)$$

which is

$$\frac{1}{R_\Sigma} = \frac{1}{R_1} + \frac{1}{R_2} \quad (7.13b)$$

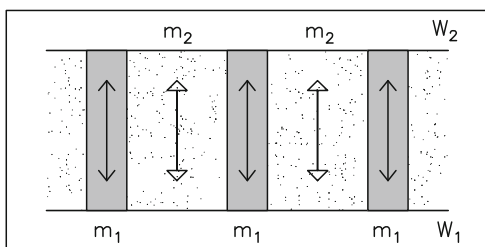


Fig. 7.3 Double-mode heat transfer between the walls W_1 and W_2 , with for instance m_1 : conduction in steel spacers, m_2 : convection/conduction in air.

Consider as an example a steel plate of $A = 1 \text{ m}^2$ surface area, protected by insulation, with an air gap of $\Delta x = 2 \text{ cm}$ width between the steel plate and the insulation. The insulation is fixed to the steel plate by 4 steel spacers. The heat transfer of mode 1 is by conduction through the 4 steel spacers of $3 \text{ cm}^2 = 3 \times 10^{-4} \text{ m}^2 = A'$ cross section each, length $2 \text{ cm} = 0.02 \text{ m} = \Delta x$ and conductivity $k_{steel} = 45 \text{ W/m/K}$. The heat transfer of mode 2 is by conduction through the air in the gap (assuming that the air is not in motion) with conductivity $k_{air} = 0.024 \text{ W/m/K}$. Hence

$$R_{spacers} = \Delta x / (4k_{steel} A') = 0.02 / (4 \times 45 \times 3 \times 10^{-4}) = 0.37 \text{ K/W}$$

$$R_{air} = \Delta x / (k_{air}A) = 0.02 / (0.024 \times 1) = 0.80 \text{ K/W}$$

and

$$1/R_{\Sigma} = 1/R_{spacers} + 1/R_{air} = 1/0.37 + 1/0.8 = 1/0.25 \text{ W/K}, R_{\Sigma} = 0.25 \text{ K/W}$$

The heat conduction in radial direction through a pipe of inner diameter r_i , outer diameter r_o and length L , as shown Fig. 7.4.a, is

$$\Delta q = \frac{2 \pi k L}{\ln(r_o/r_i)} (T_i - T_o) \tag{7.14}$$

The thermal resistance in radial direction through the pipe is

$$R = \frac{\ln(r_o/r_i)}{2 \pi k L} \tag{7.15}$$

The derivation of this relation is given in Section 7.10. As an example, the thermal resistance in radial direction through a steel pipe of $r_o = 5 \text{ cm}$ diameter, $\Delta r = 5 \text{ mm}$ wall thickness and $L = 1 \text{ m}$ length is $R = \ln(0.05/0.045) / (2 \pi \times 1 \text{ [m]} \times 45 \text{ [W/m/K]}) = 0.00037 \text{ K/W}$.

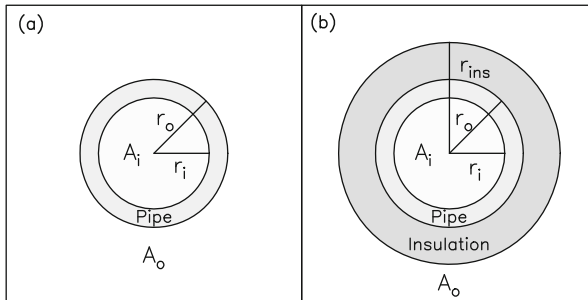


Fig. 7.4 Conductive heat transfer in radial direction through a pipe without insulation (a), with insulation (b). A_i is the inside air, A_o the outer air.

7.5 Heat Transfer by Convection

Convective heat transfer occurs between a solid body and a gas or a fluid. For thermal considerations of telescopes and enclosures the gas or fluid does not change the phase, i.e. it remains a gas or a fluid. The flow can be external with the body immersed in the gas or fluid, like ambient air moving around a telescope or enclosure,

or internal with the gas or fluid contained by the body, like a cooling liquid moving in a pipe.

On first view, the mathematical description of convective heat transfer seems to be easy. Following *Newton's* law as illustrated in Fig. 7.5 the relation is

$$\Delta q = -h_f A (T_s - T_f) = -h A (T_s - T_o) \quad (7.16)$$

where T_s is the temperature of the body (surface), $T_f = T_o$ the temperature of the gas/fluid far away from the contact area, A the contact area and $h_f = h$ [$\text{W}/\text{m}^2/\text{K}$] the convective heat transfer coefficient, also called film coefficient. In a similar way as explained for conduction, the thermal resistance for convection is

$$\Delta q = -A (T_s - T_o) / \mathcal{R}_f = -(T_s - T_o) / R_f \quad (7.17)$$

so that

$$\mathcal{R}_f = 1/h_f, \quad R_f = 1/(h_f A) = \mathcal{R}_f/A \quad (7.18)$$

The dimensions are $[h] = [\text{W}/\text{m}^2/\text{K}]$, $[\mathcal{R}_f] = [\text{m}^2\text{K}/\text{W}]$ and $[R_f] = [\text{K}/\text{W}]$. With this definition the convective heat transfer resistance (conductance) can be combined with the conductive heat transfer resistance (conductance).

The value of the convective heat transfer coefficient h is the hard work in this relation since it depends on the fluid material (viscosity), the flow velocity, the type of flow, i.e. whether being laminar or turbulent, on the geometry of the body, and for ambient air through the air density also on the altitude of the telescope site. The derivation of the convective heat transfer coefficient h for a number of realistic conditions is explained in Section 7.7. Three representative values of h are given in Table 7.2.

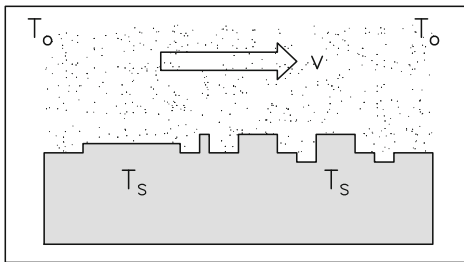


Fig. 7.5 Illustration of convective heat transfer between a fluid/gas of global temperature $T_o = T_f$ and a body of temperature T_s . The fluid/gas moves with the velocity v along the solid body.

Table 7.2 Values of h for Air and Water.

Gas/Liquid	h [$\text{W}/\text{m}^2/\text{K}$]	Application
Air	5	Ambient Air: calm (laminar flow)
Air	10 – 25	Ambient Air: wind, ventilation (turbulent flow)
Water	200 – 500	Cooling Fluid / Rain

7.6 Heat Transfer by Conduction and Convection

Conductive and convective heat transfer can be combined. As an example, Fig. 7.6 shows a plate in contact on both sides with a moving gas/fluid. Using Eqs.(7.6,7.17) and the fact of energy conservation

$$\Delta q_{r,1} = \Delta q_{1,2} = \Delta q_{2,\ell} = \Delta q \tag{7.19a}$$

the individual convective and conductive heat transfer relations are

$$T_1 - T_o(r) = -\Delta q_{r,1} R_f(r,1) = -\Delta q R_f(r,1) \tag{7.19b}$$

$$T_2 - T_1 = -\Delta q_{1,2} R_{1,2} = -\Delta q R(1,2) \tag{7.19c}$$

$$T_o(\ell) - T_2 = -\Delta q_{2,\ell} R(2,\ell) = -\Delta q R_f(2,\ell) \tag{7.19d}$$

These relations have an analytic solution. Summation of Eq.(7.19) gives

$$T_o(\ell) - T_o(r) = -\Delta q [R_f(r,1) + R(1,2) + R_f(2,\ell)] \tag{7.20}$$

or

$$T_o(\ell) - T_o(r) = -\Delta q R_\Sigma \tag{7.21}$$

with

$$R_\Sigma = R_f(r,1) + R(1,2) + R_f(2,\ell) = \frac{1}{h_r A} + \frac{\Delta x_{12}}{kA} + \frac{1}{h_\ell A} \tag{7.22}$$

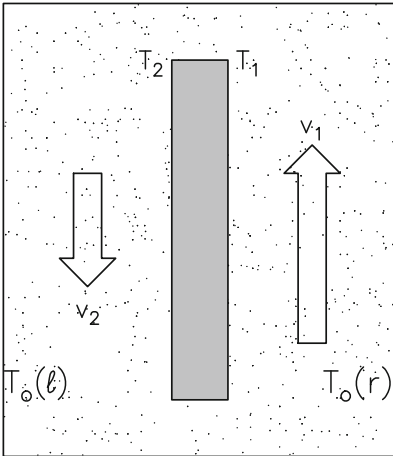


Fig. 7.6 Illustration of heat transfer by convection and conduction through a plate immersed in an inner (v_1) and outer (v_2) fluid/gas stream.

From Eq.(7.21) in which $T_o(r)$, $T_o(\ell)$ and R_Σ are known the value Δq can be derived. With this value Δq the temperatures T_1 and T_2 can be derived from Eq.(7.19b) and Eq.(7.19d) and the system is fully determined.

As an example consider again a 5 mm ($= \Delta x$) thick aluminium panel of $A = 1 \text{ m}^2$ surface area surrounded by two fluids (Fig. 7.6). One fluid is the outside ambient air, the other fluid is the air inside the BUS. The temperatures of the air and their convective heat transfer coefficients are $T_o(r) = 30^\circ \text{C}$, $T_o(\ell) = 10^\circ \text{C}$, $h_r = 5 \text{ W/m}^2/\text{K}$, and $h_\ell = 2 \text{ W/m}^2/\text{K}$. The resistances between the air and the surfaces of the panel are $R_f(r) = 1/(h_r A) = 1/(5 \times 1) = 0.2 \text{ K/W}$, $R_f(\ell) = 1/(h_\ell A) = 1/(2 \times 1) = 0.5 \text{ K/W}$. The thermal resistance through the panel is $R(1,2) = R_{Al} = \Delta x/(k A) = 0.005/(140 \times 1) = 0.000036 \text{ K/W}$. The total thermal resistance is $R_\Sigma = 0.5 + 0.000036 + 0.2 \approx 0.7$. Eq.(7.20) then gives $\Delta q = -(10 - 30)/0.7 = 28.57 \text{ W}$. From Eq.(7.19 c) and Δq follows that $T_2 - T_1 = 28.57 \times 0.000036 = 0.0010^\circ \text{C}$, from Eq.(7.19 d) follows that $T_1 - 30 = -28.57 \times 0.5$ or $T_1 = 15.71^\circ \text{C}$.

In a similar way the heat transfer in radial direction through an insulated pipe, embedded at the inner and outer side in a convective gas/fluid stream (Fig. 7.4.b), is

$$\begin{aligned} R_\Sigma &= R_{conv}(i) + R_{pipe} + R_{ins} + R_{conv}(o) \\ &= \frac{1}{h_i 2\pi r_i L} + \frac{\ln(r_o/r_i)}{2\pi k_p L} + \frac{\ln(r_{ins}/r_o)}{2\pi k_{ins} L} + \frac{1}{h_o 2\pi r_{ins} L} \end{aligned} \quad (7.23)$$

It is seen that thermal resistances (conductances) follow the same rules as electrical resistances (conductances). Thermal models can for this reason be translated into electrical networks and solved with corresponding electrical network programmes. The electrical network programme used in this text to solve heat transfer equations is ESACAP [Stangerup 1982, 1999].

7.7 The Convective Heat Transfer Coefficient (h)

Convective heat transfer involves the heat exchange between a moving fluid/gas, of global temperature T_f , and a solid surface, of temperature T_s , given by Eq.(7.16). It is the convective heat transfer coefficient h that has to be determined for the geometry of the telescope and enclosure components and the fluid flow.

The moving body under discussion is the ambient air, with its motion called wind, and the air inside the telescope and enclosure. On certain telescopes and enclosures the internal air can be ventilated and heated or cooled (climatisation). For the wind speeds and ventilation velocities under discussion the air can be considered to be incompressible and non-dissipative. Occasionally, the moving body is a liquid (glycol) used for thermal control of a specific structural component, like the thermal control of the quadripod of the IRAM 30-m telescope. The solid surface in contact with the ambient or ventilated air can be a flat surface, a corrugated surface, a shaped surface with edges, the surface of a tube, the curved surface of a reflector etc., at all position angles with respect to the flow direction. Depending on the flow speed, the surface geometry and the surface finish, i.e. being smooth, rough or structured, the airflow can be laminar or turbulent. In a laminar flow the air elements are

displaced in the direction of the flow with no exchange of air in the direction perpendicular to the flow. In a turbulent flow air is also exchanged perpendicular to the flow direction.

The airflow may also be natural in a free way, leading to natural or free convection. Natural convection (buoyancy) occurs through density differences between the air elements itself and between the air close to the surface at a temperature different to the global temperature of the air; at greater distances from the surface the air does not move.

7.7.1 Forced Convection

The aerodynamic and energetic behaviour of a forced moving gas/fluid is governed by complicated coupled differential equations (*Navier–Stokes* equation, continuity equation, heat transfer equation) that cannot be put into a form for application on a telescope or enclosure. However, instead of these equations the heat transfer can be expressed by a number of parameters describing the geometry, the gas/fluid properties and the flow velocity³. Since telescopes and enclosures can be located at the altitude z , it is important to specify if and in which way the parameters depend on z .

A basic parameter is the dimensionless *Prandtl* number (PR)

$$\text{PR} = \nu/\alpha = \mu/\rho(z)\alpha, \quad \nu = \mu/\rho(z) \quad (7.24)$$

with ν the kinetic viscosity [m^2/s] of the moving gas/fluid, μ its absolute viscosity [kg/s/m], $\rho = \rho(z)$ its density [kg/m^3] and $\alpha = k/\rho\mathcal{C}_p$ its thermal diffusivity [m^2/s]. For air the *Prandtl* number is $\text{PR} \approx 0.71$, independent of altitude. The flow velocity⁴ v and the shape of the surface are combined in the dimensionless *Reynolds* number (RE)⁵. For a flat surface of total length L over which the air flows, and a tube of diameter D and an air flow perpendicular to the length of the tube, the corresponding *Reynolds* numbers are (RE_L for the flat surface, RE_D for the tube)

$$\text{RE}_L = \nu L/\nu = \nu L\rho/\mu, \quad \text{RE}_D = \nu D/\nu = \nu D\rho/\mu \quad (7.25)$$

For typical dimensions (L) of a flat surface and diameters (D) of a tube, the *Reynolds* numbers RE_L and RE_D are given in Table 7.3 and Table 7.4 for air at sea level with $\rho_o = 1.20 \text{ kg/m}^3$ and air at 5 000 m altitude with $\rho(5000) = 0.75 \text{ kg/m}^3$ (Table 4.1). The absolute viscosity $\mu = 17.3 \times 10^{-6} \text{ kg/s/m}$ is nearly independent of altitude,

³ These parameters allow the description of a large variety of structures and scales of (turbulent) flows, from air flow in a confined volume to air flows in the atmosphere or even the solar atmosphere. See Kadanoff [2001] for a review.

⁴ in order to avoid confusion with the kinetic viscosity ν , in this Chapter the flow velocity (wind speed) is written v [m/s].

⁵ also the Local Reynolds number, RE_l , is used that determines the transition from a laminar to a turbulent flow, see Bejan [1993] and Feynman [1966] for an illustrative explanation.

a change of $\sim 2\%$ occurs between sea level and 5 000 m altitude [Perry & Chilton 1973, Cheng 1998]. Through the kinetic viscosity $\nu = \mu/\rho(z)$ are the *Reynolds* numbers RE_L and RE_D a function of z . The values in Table 7.3 and Table 7.4 are calculated for $\nu(z=0) = 1.45 \times 10^{-5} \text{ m}^2/\text{s}$ and $\nu(z=5000) = 2.31 \times 10^{-5} \text{ m}^2/\text{s}$ (Table 4.1).

Table 7.3 *Reynolds* Number a RE_L for Flat Surfaces of Length L .

L [m]	$\nu = 1$ [m/s]	$\nu = 5$ [m/s]	$\nu = 10$ [m/s]
1	$6.8 (4.4) \times 10^4$	$3.4 (2.2) \times 10^5$	$6.8 (4.4) \times 10^5$
5	$3.4 (2.2) \times 10^5$	$1.7 (1.1) \times 10^6$	$3.4 (2.2) \times 10^6$
10	$6.8 (4.4) \times 10^5$	$3.4 (2.2) \times 10^6$	$6.8 (4.4) \times 10^6$

a) for air at sea level, in brackets at 5 000 m altitude.

Table 7.4 *Reynolds* Number a RE_D for Tubes of Diameter D .

D [cm]	$\nu = 1$ [m/s]	$\nu = 5$ [m/s]	$\nu = 10$ [m/s]
5	$3.4 (2.2) \times 10^3$	$1.7 (1.1) \times 10^4$	$3.4 (2.2) \times 10^4$
10	$6.8 (4.4) \times 10^3$	$3.4 (2.2) \times 10^4$	$6.8 (4.4) \times 10^4$
30	$2.0 (1.3) \times 10^4$	$1.0 (0.6) \times 10^5$	$2.0 (1.3) \times 10^5$
60	$4.1 (2.7) \times 10^4$	$2.0 (1.3) \times 10^5$	$4.1 (2.7) \times 10^5$

a) for air at sea level, in brackets at 5 000 m altitude.

From experiments it is found that the flow is laminar if, in a very approximate way, $RE \lesssim 4 \times 10^5$ and turbulent if $4 \times 10^5 \lesssim RE$. This transition of the flow characteristic depends also on the shape of the body and its surface structure. The parameter that determines the forced convective heat transfer is the dimensionless *Nusselt* number for a flat surface NU_L and for a tube NU_D with

$$NU_L = hL/k, \quad NU_D = hD/k \quad (7.26)$$

The corresponding heat transfer coefficients are

$$h_L = NU_L k/L, \quad h_D = NU_D k/D \quad (7.27)$$

with k the heat conductivity of air $k = 0.024 \text{ W/m/K}$, which is independent of altitude. Following Chapman [1984], for a flat surface and laminar flow the average *Nusselt* number is

$$NU_L = 0.664 (RE_L)^{1/2} PR^{1/3} \quad (7.28)$$

for turbulent flow the average *Nusselt* number is

$$NU_L = 0.036 (RE_L)^{1/1.25} PR^{1/3} \quad (7.29)$$

With these values the forced convective heat transfer coefficient h for a flow over a flat surface is

$$h_L = 0.664 (\text{RE}_L)^{1/2} \text{PR}^{1/3} k/L \quad (\text{laminar flow}) \quad [\text{W}/\text{m}^2/\text{K}] \quad (7.30)$$

$$h_L = 0.036 (\text{RE}_L)^{1/1.25} \text{PR}^{1/3} k/L \quad (\text{turbulent flow}) \quad [\text{W}/\text{m}^2/\text{K}] \quad (7.31)$$

From the *Reynolds* numbers RE_L of Table 7.3, the *Prandtl* number $\text{PR} = 0.71$ and for air at sea level and 5 000 m altitude the corresponding average *Nusselt* numbers NU_L and convective heat transfer coefficients h_L are given in Table 7.5.

Table 7.5 Average *Nusselt* Number ^{a)} NU_L and Heat Transfer Coefficient h_L [$\text{W}/\text{m}^2/\text{K}$] for a Flat Surface of Length L (laminar flow).

L [m]	$v = 1$ [m/s]	$v = 5$ [m/s]	$v = 10$ [m/s]
NU_L	154 (124)	345 (277)	486 (391)
NU_L	345 (277)	769 (618)	1087 (875)
NU_L	486 (391)	1087 (875)	1538 (1237)
h_L	3.7 (2.9)	8.3 (6.6)	11.6 (9.4)
h_L	1.6 (1.3)	3.7 (3.0)	5.2 (4.2)
h_L	1.2 (0.9)	2.6 (2.1)	3.7 (3.0)

^{a)} for air at sea level, in brackets at 5 000 m altitude.

From Table 7.5 it is calculated, for example, that at sea level the heat transfer to ambient air of temperature $T_A = 10^\circ \text{C}$, moving at the speed of $v = 5$ m/s along a flat plate of $L = 5$ m length and 2 m width ($A = 5 \times 2 = 10 \text{ m}^2$) and temperature $T_L = 25^\circ \text{C}$ is

$$\Delta q = h_L A (T_L - T_A) = 3.7 [\text{W}/\text{m}^2/\text{K}] 10 [\text{m}^2] (25 - 10) [\text{K}] = 555 \text{ W}$$

For the same plate at 5 000 m altitude the value is $\Delta q = 3.0 \times 10 \times (25 - 10) = 450 \text{ W}$, hence 20 % lower.

Following Chapman [1984], the average *Nusselt* number NU_D for a single tube is

$$\text{NU}_D = 0.3 (\text{RE}_D)^{1/1.75} \quad (7.32)$$

and for a bundle of tubes (approximately like a BUS network)

$$\text{NU}_{nD} = 0.33 (\text{RE}_D)^{1/1.66} \text{PR}^{1/3} \quad (7.33)$$

The corresponding convective heat transfer coefficients h_D and h_{nD} are

$$h_D = \text{NU}_D k/D, \quad h_{nD} = \text{NU}_{nD} k/D \quad (7.34)$$

From the *Reynolds* numbers RE_D of Table 7.4, the *Prandtl* number $PR = 0.71$ and for air at sea level and 5 000 m altitude the corresponding *Nusselt* numbers NU_D and NU_{nD} and the convective heat transfer coefficients h_D , h_{nD} are calculated and given in Table 7.6 and Table 7.7.

From Table 7.7 it is calculated, for example, that at sea level the heat transfer to ambient air of temperature $T_A = 10^\circ\text{C}$, moving at the speed of $v = 5\text{ m/s}$ perpendicular to a tube of diameter $D = 10\text{ cm}$, length $L = 1\text{ m}$ ($A = 0.1 \times 1 = 0.1\text{ m}^2$) and temperature $T_L = 25^\circ\text{C}$ is

$$\Delta q = h_D A (T_D - T_A) = 28 [\text{W}/\text{m}^2/\text{K}] 0.1 [\text{m}^2] (25 - 10) [\text{K}] = 42\text{ W}$$

For the tube at 5 000 m altitude the value is $\Delta q = 21 \times 0.1 \times (25 - 10) = 31.5\text{ W}$, hence 25 % lower.

Table 7.6 Average *Nusselt* Number ^{a)} NU_D , NU_{nD} for a Tube, and Bundle of Tubes, of Diameter D .

	D [cm]	$v = 1$ [m/s]	$v = 5$ [m/s]	$v = 10$ [m/s]
NU_D	5	31 (24)	77 (60)	115 (89)
NU_D	10	46 (36)	115 (89)	170 (133)
NU_D	30	85 (66)	212 (166)	315 (247)
NU_D	60	127 (100)	315 (247)	475 (374)
NU_{nD}	5	38 (29)	101 (78)	153 (118)
NU_{nD}	10	58 (45)	153 (118)	231 (178)
NU_{nD}	30	111 (86)	292 (223)	442 (342)
NU_{nD}	60	171 (133)	442 (342)	680 (530)

^{a)} for air at sea level, in brackets at 5 000 m altitude.

Table 7.7 Heat Transfer Coefficient ^{a)} h_D , h_{nD} [W/m²/K] for a Tube, and Bundle of Tubes, of Diameter D .

	D [cm]	$v = 1$ [m/s]	$v = 5$ [m/s]	$v = 10$ [m/s]
h_D	5	15 (11)	37 (29)	55 (43)
h_D	10	11 (9)	28 (21)	41 (32)
h_D	30	7 (5)	17 (12)	25 (20)
h_D	60	5 (4)	13 (10)	19 (15)
h_{nD}	5	18 (14)	48 (39)	73 (57)
h_{nD}	10	14 (11)	37 (28)	55 (43)
h_{nD}	30	9 (7)	23 (17)	35 (27)
h_{nD}	60	7 (5)	18 (14)	27 (21)

^{a)} for air at sea level, in brackets at 5 000 m altitude.

The tables and the examples illustrate that at higher altitude the *Nusselt* numbers, and by this the convective heat transfer coefficients h , are lower than at sea level.

Therefore the temperature equalizing effect of wind is lower at high altitude so that the relative importance of solar radiation is increased. In addition, forced ventilation of telescope and enclosure structures becomes less efficient [Cheng 1998].

7.7.2 Natural Convection

Natural convection occurs when a hot or cold plate or tube or other body of temperature T_s is immersed in a fluid of temperature T_f . At some distance from the object is the fluid not in motion. Due to the temperature difference $\Delta T = T_s - T_f$ a density difference develops in the contact layer and under the influence of gravity the fluid starts to move along the surface. If the surface is cooler than the fluid, the motion is downward, if the surface is warmer, the motion is upward. In the contact layer the moving fluid exchanges heat with the object/wall. The fluid under consideration is the ambient air or the internal air of the telescope and enclosure. In the most general way, natural convection occurs if a warm air element is by one or the other process below a cool air element, and vice versa.

Natural convection is governed by the dimensionless *Grashof* number

$$GR = gL^3 \beta \Delta T / \nu^2 = gL^3 \rho^2 \beta \Delta T / \mu^2 \quad (7.35)$$

with L a typical length of the contact area, g the gravity constant, β the thermal expansion coefficient, which for air (taken to be an ideal gas) is $\beta = 1/T_f$, ρ the density of the air and ν and μ the kinetic and absolute viscosity. Through the dependence on $\rho(z)$ is the *Grashof* number a function of altitude. The induced natural flow of the air is laminar if, in a very approximate way, $GR < 10^9$ and turbulent if $10^9 < GR$. The *Nusselt* number for plates and tubes in a stream of natural convection is

$$NU_{nc} = C \times (GR \times PR)^m = h_{nc} L / k \quad (7.36)$$

with $m = 1/4$ for laminar flow and $m = 1/3$ for turbulent flow. Evidently, the natural heat transfer coefficient h_{nc} depends on the type of surface (plate or tube etc.) and on the orientation of the surface with respect to the flow. For laminar natural convection ($10^4 < GR \times PR < 10^9$) along a horizontal cylinder (of diameter D), or vertical plate (of length L), or a horizontal plate with the hot side upwards, Chapman [1984] gives

$$h_{nc} \approx 1.35 (\Delta T / D)^{1/4} [\text{W/m}^2/\text{K}] \quad (7.37)$$

and for turbulent natural flow ($10^9 < GR \times PR$)

$$h_{nc} \approx 1.3 (\Delta T)^{1/3} [\text{W/m}^2/\text{K}] \quad (7.38)$$

As an example, for a vertical plate of $A = 2 \text{ m} \times 2 \text{ m} = 4 \text{ m}^2$ surface and temperature $T_s = 45^\circ \text{C}$, and ambient air of temperature $T_A = 15^\circ \text{C}$, the natural convective heat transfer coefficient is $h_{nc} \approx 1.35 (30/2)^{1/4} = 2 \text{ W/m}^2/\text{K}$. The heat transfer from

the warm plate to the ambient air is

$$\Delta q \approx 4 [\text{m}^2] 2 [\text{W}/\text{m}^2/\text{K}] 30 [\text{K}] = 240 \text{ W}$$

The concept of the *Prandtl* number (PR), *Reynolds* number (RE), *Nusselt* number (NU) and *Grashof* number (GR) has been explained in order to illustrate the technique by which the convective heat transfer coefficient h is derived. Since these numbers depend on the geometry and the type of convective flow, a vast multitude of situations do occur that need a special analysis to obtain or estimate the appropriate convective heat transfer coefficient h . The *Reynolds* number of a particular situation indicates whether the flow of the gas/fluid along/across a body is laminar or turbulent. The corresponding heat transfer coefficient is, in general, obtained from the *Nusselt* number, which for forced convection is $\text{NU} \propto \text{RE}^m \text{PR}^n$ and for natural convection $\text{NU} \propto (\text{GR} \times \text{PR})^m$. The thermal engineering handbooks give *Reynolds*, *Nusselt* and *Grashof* numbers and the exponents m , n of laminar and turbulent flow for many particular situations, which may also be applicable to telescope and enclosure structures. The tables and the numerical examples are presented here to obtain an impression of the magnitude of the convective heat transfer coefficient.

7.7.3 Forced Convection and Ventilation

Forced convection plays an important role in thermal considerations of ventilated telescopes and enclosures. Forced ventilation can be made with internal air, with internal air and a contribution of outside ambient air or a contribution of conditioned air. Forced ventilation acts in two ways. On the one hand, the stream of ventilating air reaches a volume element of air in the telescope or enclosure and replaces part of the present air since the air is incompressible. This is in effect a change of heat content and can be modelled as such. On the other hand, the ventilating air is moving along the tubes, plates and walls etc. of the structural component that is ventilated. This then causes a heat transfer between the structural component and the ventilating air and can be treated by Eq.(7.16) and the appropriate convective heat transfer coefficient h .

The heat (energy) exchange $\Delta E_{\text{fv}}(i,t)$ through forced ventilation by fans etc. is

$$\Delta E_{\text{fv}}(i,t) = -[T_{\text{Ai}}(t) - T_{\text{V}}(t)] f_{\text{fv}} \mathcal{C}_{\text{Ai}} m_{\text{A}} \quad (7.39)$$

In this equation is T_{Ai} the temperature of the air of the ventilated volume element [i], T_{V} the temperature of the ventilating air, f_{fv} the ventilation efficiency ($0 \leq f_{\text{fv}} \leq 1$), \mathcal{C}_{Ai} the heat capacity of the air element and m_{A} its mass. Evidently, if $T_{\text{Ai}}(t) < T_{\text{V}}(t)$ then $0 < \Delta E_{\text{fv}}(i,t)$ and the ventilating air provides energy (heat) to the ventilated air volume, and vice versa. Further details on the application of this relation are found in Greve & MacLeod [2001], Greve & Bremer [2005], Greve et al. [2006] and Chapter 11 on thermal model calculations.

7.7.4 Natural Convection and Ventilation

Ventilation by natural convection occurs if air at a lower level (T_ℓ) is warmer than air at a higher level (T_u), or if a warm (vertical) wall is surrounded by cooler air, and similar cases. The warmer air at the lower level, or the warmer air at the wall, moves upward and transports heat from the warmer lower level/wall to the cooler upper level. Also, in the reverse situation cool air at an upper level can sink into warm air at a lower level. This heat transport occurs in ‘thermals’ or pockets of warm/cool air of which illustrative pictures of the complexity of the process are published by Bejan [1993; fig. 7.8 and fig. 7.12]. In modelling natural convection in telescope and enclosure structures it is convenient to distinguish between (a) natural convection with strong mixing in which the thermals lose their identity when moving from the lower level to the upper level, or vice versa, and (b) natural convection with little mixing so that most of the warm thermals arrive at the higher, or the highest, level with little mixing and little cooling on the way upwards, or vice versa. In the case (a) the air is gradually heated from below, or cooled from above, and eventually reaches a uniform temperature. In the case (b) the gradual heating is small and a temperature gradient develops, which is permanent for some time since warm thermals arrive at the upper level. The modelling of case (a) is relatively easy, however it is complicated for case (b) in which a more detailed handling of the air motion is required.

The effect of case (a) is modeled in thermal calculations by the heat (energy) exchange between the adjacent lower $-\Delta E_{nc}^{(\ell)}$ and upper $+\Delta E_{nc}^{(u)}$ air volumes (with $\Delta E_{nc}^{(u)} = \Delta E_{nc}^{(\ell)}$) using the relation

$$\Delta E_{nc}(t) = -[T_\ell(t) - T_u(t)] f_{nc}(\ell, u) \mathcal{C}_A m_A \times \delta(T_\ell, T_u) \quad (7.40a)$$

with

$$\delta(T_\ell, T_u) = [T_\ell - T_u + \text{abs}(T_\ell - T_u)] / [2 \text{abs}(T_\ell - T_u)] \quad (7.40b)$$

so that $\delta(T_\ell, T_u) = 1$ for $T_u \leq T_\ell$ and $\Delta E_{nc}^{(u)}$ and $\Delta E_{nc}^{(\ell)} \neq 0$ and $\delta(T_\ell, T_u) = 0$ for $T_\ell \leq T_u$ and $\Delta E_{nc}^{(u)} = \Delta E_{nc}^{(\ell)} = 0$. The ventilation efficiency in Eq.(7.40a) is f_{nc} ($0 \leq f_{nc} \leq 1$), the heat capacity of the air element is \mathcal{C}_A and m_A its mass. The upward flow speed of the air is $v_{nc} \approx \gamma(H_{nc}g\Delta T/T)^{1/2}$ with H_{nc} a representative height (for instance 1/4 to 1/3 of a radome/astrodome height) between the air layers with temperature difference $\Delta T = T_\ell - T_u$ in an environment of average temperature T . The gravity acceleration is g . The factor γ takes into account possible turbulence of the air flow, in general $\gamma \approx 0.25 - 0.5$. As an example, for a height $H_{nc} = 10$ m and a temperature difference $\Delta T = 5^\circ\text{C}$ of the air as in the Onsala radome of temperature $T = 273 + 25 = 298$ K (see Fig. 11.29) this gives $v_{nc} \approx 0.6$ m/s. For the programming of natural convection in a thermal model see Stangerup [1985]. Further details are found in Greve & MacLeod [2001], Greve & Bremer [2005], Greve et al. [2006] and Chapter 11 on thermal model calculations.

7.8 Radiative Heat Transfer

If radiation of intensity \mathbf{I} falls onto the surface of a body, part of the radiation is reflected either in specular or diffuse way expressed by the scattering function⁶ $f(\Theta)$, i.e.

$$\mathbf{I}_{\text{ref}} = \rho \mathbf{I} \int_0^{2\pi} f(\Theta) d\Theta = \rho \mathbf{I} \quad (7.41)$$

with ρ ($0 \leq \rho \leq 1$) the reflection coefficient. Part of the radiation is absorbed, i.e.

$$\mathbf{I}_{\text{abs}} = \alpha \mathbf{I} \quad (7.42)$$

with α ($0 \leq \alpha \leq 1$) the absorption coefficient. Part of the radiation is transmitted, i.e.

$$\mathbf{I}_{\text{tr}} = \tau \mathbf{I} \quad (7.43)$$

with τ ($0 \leq \tau \leq 1$) the transmission coefficient. These coefficients can be a function of the wavelength λ . Conservation of energy requires that

$$\rho + \alpha + \tau = 1 \quad (7.44)$$

Most materials of telescope and enclosure components are opaque, hence $\tau = 0$ so that $\rho + \alpha = 1$. The exception are radome skins and astrodome membranes with τ of the order of 25 % at visible and infrared wavelengths. Many telescope and enclosure components are separated by air. The absorption of radiation by these air volumes is very small and can be neglected in thermal considerations.

A body of absolute temperature $T \neq 0$ emits radiation. The Black-Body radiator (BB) is of special importance since it provides a relation between the absolute temperature T [K] of a black body and the emitted continuum radiation $B_\nu(T) = B_\lambda(T)$. *Planck's* radiation law gives the intensity of BB radiation at the frequency ν , or the wavelength $\lambda = c/\nu$, as

$$B_\nu(T) = \frac{2h\nu^3}{c^2} \frac{1}{(e^{h\nu/kT} - 1)} \quad [\text{W}/\text{m}^2/\text{Hz}/\text{sr}] \quad (7.45)$$

with k *Boltzmann's* constant, h *Planck's* constant and c the light velocity (see Table A.3). For temperatures of telescope and enclosure structures of $T = 243 \text{ K} = 273 - 30^\circ \text{ C}$, $T = 273 \text{ K} = 273 - 0^\circ \text{ C}$ and $T = 323 \text{ K} = 273 + 50^\circ \text{ C}$ the corresponding BB radiation is shown in Fig. 7.7.

For a given temperature T the function $B_\lambda(T)$ has its maximum at the wavelength λ_{max} (*Wien's law*)

$$\lambda_{\text{max}} T = 2.89 \times 10^{-3} \quad [\text{m}/\text{K}] \quad (7.46)$$

⁶ The scattering function $f(\Theta)$ is, for instance, important for reflection of solar radiation on a panel surface, see Fig. 5.19.

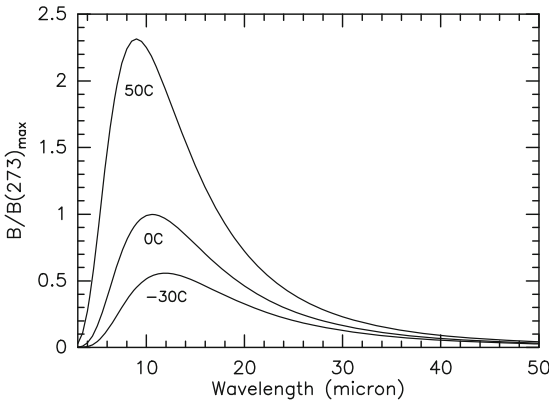


Fig. 7.7 Black Body radiation at $T = 243\text{ K } (-30^\circ\text{ C})$, $T = 273\text{ K } (0^\circ\text{ C})$ and $T = 323\text{ K } (+50^\circ\text{ C})$, normalized to the peak $B(273\text{ K})$.

At $T = 243\text{ K}$, $T = 273\text{ K}$ and $T = 323\text{ K}$ this is $\lambda_{\max}(243) = 11.9\ \mu\text{m}$, $\lambda_{\max}(273) = 10.6\ \mu\text{m}$ and $\lambda_{\max}(323) = 9.0\ \mu\text{m}$. Since telescope and enclosure components are at these temperatures they radiate at infrared wavelengths (mainly in the band N). Evidently, for the Sun of surface temperature $T_{\odot} = 5780\text{ K}$ the corresponding radiation maximum occurs at $\lambda_{\max} \approx 0.5\ \mu\text{m}$ (Fig. 4.26).

For a surface of temperature T the total electromagnetic power emitted into the hemisphere above the surface is given by the *Stefan–Boltzmann* law

$$Q(e) = e \sigma T^4 \quad [\text{W/m}^2] \tag{7.47}$$

with σ the *Stefan–Boltzmann* constant (Table A.3). For a BB radiator the emission coefficient e and the absorption coefficient a is $e(\lambda) = a(\lambda) = 1$. The emitted radiation of the BB radiator is $Q(-30^\circ\text{ C}) = 198\text{ W/m}^2$, $Q(0^\circ\text{ C}) = 315\text{ W/m}^2$ and $Q(50^\circ\text{ C}) = 617\text{ W/m}^2$, i.e. the hot surface radiates 3 times more energy than the cold surface. For a non–BB radiator, as most paints, surface finishes, the sky and the ground are, the surface behaves at least for a significant wavelength region as a grey body with $e(\lambda) < 1$ and $a(\lambda) < 1$.

The diffuse radiative heat transfer $\Delta q_{1 \rightarrow 2}$ between two bodies (**1, 2**) with surfaces A_1, A_2 depends on the temperature T_1, T_2 of the surfaces, their emissivities e_1, e_2 , their absorptivities a_1, a_2 , their distance r and their orientation β_1, β_2

$$\Delta q_{1 \rightarrow 2} = e_1 a_2 \sigma A_1 \varphi_{1,2} (T_1^4 - T_2^4) \tag{7.48}$$

The relative orientation of the surfaces illustrated in Fig. 7.8 is expressed by the view factor

$$\varphi_{1,2} = (1/\pi A_1) \int_{A_1} \int_{A_2} [\cos(\beta_1) \cos(\beta_2)/r^2] dA_1 dA_2 \tag{7.49}$$

which, generally, must be determined by numerical methods. Some view factors are explained below, those of telescope and enclosure components with respect to the sky and the ground are explained in Chapter 8.

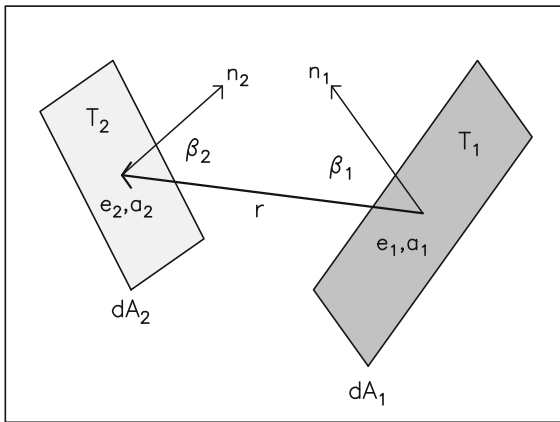


Fig. 7.8 Explanation of the view factor $\phi_{1,2}$ of the surface elements dA_1, dA_2 at the temperature T_1, T_2 and at distance r . The surface normal vectors are $\mathbf{n}_1, \mathbf{n}_2$. The emission/absorption coefficients are e_1, a_1 and e_2, a_2 .

For the special case of very extended plane parallel walls, Eqs.(7.48,7.49) become [Chapman 1984]

$$\Delta q_r = A\sigma [T_1^4 - T_2^4] / [(1/e_1) + (1/e_2) - 1] = A\sigma (T_1^4 - T_2^4) E_{1,2} \quad (7.50)$$

with the ‘paint factor’

$$E_{1,2} = \frac{1}{(1/e_1) + (1/e_2) - 1} \quad (7.51)$$

The values $E_{1,2}$ of combinations of a black body with $e = 1$, white paint with $e_1 = 0.8$ and shiny aluminium with $e_1 = 0.2$ are given in Table 7.8. It is seen that opposite white walls (0.8, 0.8) reduce the radiative heat transfer by $\sim 30\%$ while opposite shiny aluminium walls (0.2, 0.2) reduce the radiative heat transfer by $\sim 90\%$. The radiation shield (and the dewar) is based on this principle.

Table 7.8 Paint Factor $E_{1,2}$ of Facing Walls.

		Black Body $e_1 = 1$	White Paint $= 0.8$	Shiny Aluminium $= 0.2$
Black Body	$e_2 = 1$	$E_{1,2} = 1$	$= 0.8$	$= 0.2$
White Paint	$e_2 = 0.8$	$E_{1,2} = 0.8$	$= 0.67$	$= 0.19$
Shiny Aluminium	$e_2 = 0.2$	$E_{1,2} = 0.2$	$= 0.19$	$= 0.11$

In a similar way as used for conductive and convective heat transfer a resistance R_r or conductance G_r can be introduced for radiative heat transfer. Using the relation

$$T_1^4 - T_2^4 = (T_1 - T_2)(T_1 + T_2)(T_1^2 + T_2^2) = \mathcal{F}(T_1, T_2) \Delta T \quad (7.52)$$

with

$$\mathcal{F}(T_1, T_2) = (T_1 + T_2)(T_1^2 + T_2^2) \quad (7.53)$$

the radiative heat transfer relation is written as

$$\Delta q_r = A_1 (T_1 - T_2) / \mathcal{R}_r = A_1 \mathcal{G}_r (T_1 - T_2) = A_1 \mathcal{G}_r \Delta T \quad (7.54)$$

with

$$\mathcal{G}_r(T_1, T_2) = e_1 a_2 \sigma \varphi_{1,2} \mathcal{F}(T_1, T_2) \quad \text{and} \quad \mathcal{R}_r = 1/\mathcal{G}_r \quad (7.55)$$

The radiative resistance and radiative conductance are non-linear functions of the absolute temperature T_1 and T_2 of the bodies that makes a calculation including radiative effects more cumbersome. However, for many cases it is sufficient to use the value $\mathcal{F}(273 \text{ K}, 273 \text{ K}) = \mathcal{F}_0 = 8.138 \times 10^7 \text{ [K}^3]$. The values $F = \mathcal{F}(273, 273 \pm \Delta T) / \mathcal{F}_0$ listed in Table 7.9 give an impression of the error when using the value \mathcal{F}_0 instead of the actual value $\mathcal{F}(T_1, T_2)$. In particular, the use of the parameter \mathcal{P}_0

$$\mathcal{P} = \sigma \mathcal{F} \approx \mathcal{P}_0 = \sigma \mathcal{F}_0 = 5.67 \times 10^{-8} \times 8.138 \times 10^7 = 4.61 \text{ [W/m}^2/\text{K}] \quad (7.56)$$

leads to an error of $\sim \pm 25 \%$ in the extreme condition of radiative heat transfer between bodies with a temperature difference $\Delta T \approx 40 - 50 \text{ K}$. This is a large temperature difference between telescope and enclosure components, even between telescope and enclosure components and the clear sky (see Table 4.5) so that the error seldom exceeds 25 %.

Table 7.9 Values $F = \mathcal{F}(273, 273 \pm \Delta T) / \mathcal{F}_0$.

ΔT [K]	F	ΔT [K]	F
10	1.06	-10	0.95
20	1.12	-20	0.89
30	1.18	-30	0.85
40	1.24	-40	0.80
50	1.31	-50	0.76

With this notation the radiative heat transfer between parallel walls is

$$\Delta q_r \approx A E_{1,2} \mathcal{P}_0 \Delta T = A G_r \Delta T = 4.61 A E_{1,2} \Delta T \text{ [W]} \quad (7.57)$$

The relations of radiative heat transfer contain the emission coefficient e and the absorption coefficient a of the surfaces in radiative contact. The radiative heat transfer between telescope and enclosure components and the sky and ground occurs at infrared wavelengths so that the coefficients e_1 and a_1 must be known at infrared wavelengths in the region $\sim 3 \mu\text{m} \lesssim \lambda \lesssim 30 \mu\text{m}$. Representative values of $e_1 \approx a_1$ are given in Table 7.10. It must be remembered that old paint often darkens with age. The maximum of the solar radiation is at visible wavelengths so that with respect to solar radiation the absorption coefficient a_S must be known at $\lambda \approx 0.5 \mu\text{m}$ (Table 4.6).

Table 7.10 Approximate Values of e_1 ($3\ \mu\text{m} \sim \lambda \lesssim 30\ \mu\text{m}$).

Surface Finish	e_1	Environment	e_1
Black Paint	0.8–0.9	Sky	0.6–0.9
White Paint	0.8	Clouds	0.8–0.9
Rusty Iron/Stainless Steel	0.75–0.85/0.7	Ground	0.3–0.8
TiO ₂ paint (new)	0.7		
TiO ₂ paint (old)	0.75–0.85		
Shiny/anodised Aluminium	0.05–0.15		
Nickel oxidized	0.3–0.4		
Rhodium	0.18		

The subject of radiative heat transfer is, for instance, treated in the textbook *Thermal Radiation Heat Transfer* by Siegel & Howell [1982].

7.9 Heat Transfer by Conduction, Convection and Radiation

In many realistic situations of telescope and enclosure components the conductive, convective and radiative mode of heat transfer act at the same time. An example is shown in Fig. 7.9 of a panel of a 5 mm (= 0.005 m) thick aluminium plate, of 1 m² surface area, with 3 cm (= 0.03 m) thick insulation glued to the inner side. The front of the panel is exposed to the ambient air of temperature T_A (convection, heat transfer coefficient $h_A = 5\ \text{W/m}^2/\text{K}$) and to the sky of effective temperature T_S (radiation). The insulation faces the air inside the BUS of temperature T_{AB} (convection, heat transfer coefficient $h_{AB} = 2\ \text{W/m}^2/\text{K}$) and the BUS network of temperature T_B (radiation). The thermal resistance through the Al-plate is $R_{12} = 0.000036\ \text{K/W}$, through the insulation $R_{23} = 0.75\ \text{K/W}$. The thermal resistance of the glue is difficult to evaluate and taken to be $R_{\text{glue}} = 1\ \text{K/W}$. The radiative heat transfer conductance between the panel outer surface (1) and the sky (S) is $G_r(1,S) = e_S a_1 \sigma \varphi \mathcal{F}_o \approx e_S a_1 \varphi \mathcal{P}_o \approx 0.6 \times 0.8 \times 0.5 \times \mathcal{P}_o = 1.1\ \text{W/m}^2/\text{K}$, between the insulation inner surface (4) and the BUS (B) is $G_r(4,B) \approx 0.8 \times 0.8 \times 0.5 \times \mathcal{P}_o = 1.5\ \text{W/m}^2/\text{K}$. The heat transfer relations are

$$T_1 - T_A = -(1/h_A) \Delta q_{1A} = -0.2 \Delta q_{1A} \quad (7.58\ \text{a})$$

$$T_1 - T_S = -\Delta q_{1S}/G_r(1,S) = -0.9 \Delta q_{1S} \quad (7.58\ \text{b})$$

$$T_2 - T_1 = -\Delta q_{12}(\Delta x/kA)_{\text{Al}} = -0.000036 \Delta q_{12} \quad (7.58\ \text{c})$$

$$T_3 - T_2 = -\Delta q_{23} R_{\text{glue}} = -\Delta q_{23} \quad (7.58\ \text{d})$$

$$T_4 - T_3 = -\Delta q_{34}(\Delta x/kA)_{\text{ins}} = -0.75 \Delta q_{34} \quad (7.58\ \text{e})$$

$$T_4 - T_{AB} = -(1/h_{AB}) \Delta q_{4AB} = -0.5 \Delta q_{4AB} \quad (7.58\ \text{f})$$

$$T_4 - T_B = -\Delta q_{4B}/G_r(4,B) = -0.67 \Delta q_{4B} \quad (7.58\ \text{g})$$

To solve these equations a knowledge of the energy conservation of the quantities Δq_{1A} , Δq_{1S} , Δq_{12} , Δq_{23} , Δq_{34} , Δq_{4AB} , Δq_{4B} is required. This is difficult since

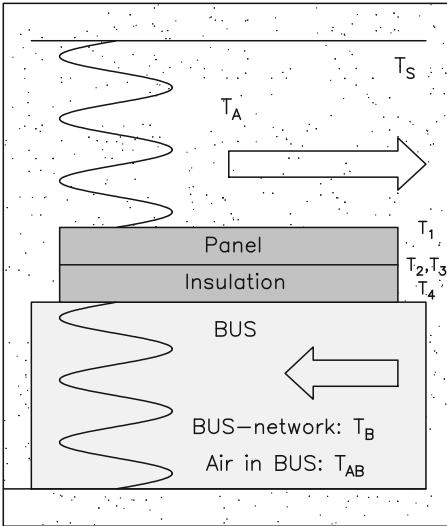


Fig. 7.9 Combination of conductive, convective and radiative heat transfer.

depending on the equilibrium temperature T_1 of the front, the heat transfer by convection from the ambient air can either be into the panel or out of the panel. It is, however, very easy to construct a thermal model of this configuration and obtain the solution from a network programme. Taking as example $T_A = 20^\circ\text{C}$, $T_S = T_A - 25^\circ = -5^\circ\text{C}$ and $T_B = T_{AB} = 30^\circ\text{C}$, the solution is $T_1 = 20.8^\circ\text{C}$, $T_3 = 24.9^\circ\text{C}$, $T_4 = 27.9^\circ\text{C}$. Since the resistance R_{12} of the thin aluminium panel is very small it is evident that $T_2 = T_1$. The gradient through the panel and the insulation is $\Delta T = T_4 - T_1 = 7.1^\circ\text{C}$.

7.10 Radiative Nodes and View Factors

The description of radiative heat transfer needs in addition an explanation of the construction of radiative nodes in enclosures and an explanation of some basic view factors.

7.10.1 Radiative Nodes

The radiative heat transfer and, in particular, the construction of radiative nodes in thermal models requires a formalism that takes into account the emission/absorption of grey surfaces that face each other in an enclosure. Here the radiative heat transfer has to take into account reflected and absorbed radiation. Assume that in an enclosure is also a grey surface that belongs to a solid body with physical temperature T .

If the surface were black, the radiation emitted from the surface into the hemisphere is $Q_{BB} = \sigma T^4$. Following Chapman [1984], and others, there are three quantities which determine the radiation of the facing grey surfaces, i.e.

- W_i : the total emissive power of the surface [i], i.e. the intrinsic radiation energy leaving the surface;
- J_i : the radiosity, i.e. the total radiation energy leaving the surface, including also reflected radiation;
- G_i : the total radiation incident on the surface.

For the grey surface the emission coefficient e and the absorption coefficient a are $e = a < 1$. Since the surface is that of a solid body, the absorption coefficient a , the reflection coefficient ρ and the transmission coefficient τ are related by $a + \rho + \tau = a + \rho = 1$ ($\tau = 0$). Evidently, for this surface

$$J = W + \rho G = W + (1 - a)G = W + (1 - e)G \tag{7.59}$$

The *net* radiative energy Δq leaving the surface is the total radiation leaving the surface (J) minus the total radiation incident on the surface (G), i.e.

$$\Delta q = A(J - G) \tag{7.60}$$

which together with Eq.(7.59) gives

$$\begin{aligned} \Delta q &= A(J - G) = A(W + (1 - a)G - G) = A(W - aG) = A(W - eG) \\ &= A\left(\frac{W}{1 - e} - \frac{eJ}{1 - e}\right) = A\left(\frac{eQ_{BB}}{1 - e} - \frac{eJ}{1 - e}\right) = \frac{e}{1 - e}A(Q_{BB} - J) \end{aligned} \tag{7.61}$$

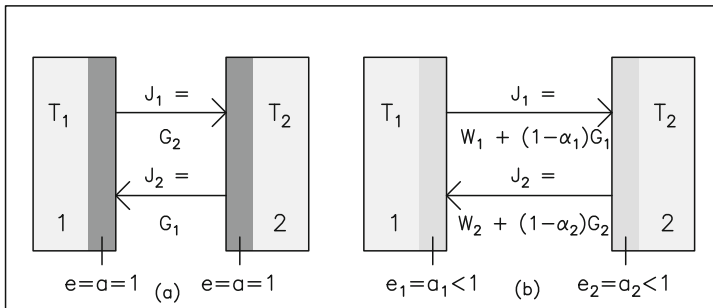


Fig. 7.10 Radiative heat transfer between black body surfaces facing each other (a) and grey surfaces facing each other (b).

As illustrated in Fig. 7.10, from these relations follows that the radiative heat transfer between two black surfaces (**1,2**) with temperature T_1, T_2 facing each other is $J_1 = G_2, J_2 = G_1, J_1 = Q_{BB}(1), J_2 = Q_{BB}(2)$ and

$$\Delta q_1 = -\Delta q_2 = A(J_1 - G_1) = A(J_1 - J_2) = A(Q_{BB}(1) - Q_{BB}(2)) = A\sigma(T_1^4 - T_2^4)$$

As furthermore shown by Chapman [1984], and others, for grey surfaces (1,2) facing each other with $e_1 = a_1 < 1$ and $e_2 = a_2 < 1$ and temperature T_1, T_2 follows that $J_1 = W_1 + (1 - a_1 G_1)$, $J_2 = W_2 + (1 - a_2 G_2)$ and from this follows Eq.(7.61). Important for the construction of grey radiative nodes is the resistance

$$R_{grey} = (1 - e)/(eA) \tag{7.62}$$

which must be introduced between the body with temperature T and its grey surface, as shown in Fig. 7.11. In thermal models a radiating surface of an enclosure needs therefore two nodes (N_1 and N_2 in Fig. 7.11) connected by the resistance Eq.(7.62). If the surface is black, then $e = 1$ and $R_{grey} = 0$.

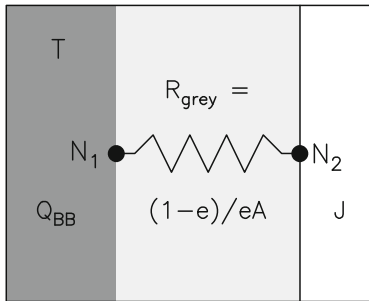


Fig. 7.11 Radiative resistance of a grey surface in an enclosure. The black (metal) surface with node N_1 has the temperature T, the grey surface with emission coefficient e has the node N_2 .

7.10.2 View Factor Relations

The view factor $\varphi_{1,2}$ of radiative heat transfer is defined by Eq.(7.49). It is evident that the large variety of structural configurations and geometrical shapes leads to a large number of view factors. The textbooks on heat transfer contain certain, usually simple examples. Analytic expressions, calculations or graphic representations of view factors are published, for instance, by Chapman [1984], Bejan [1993], the VDI-Wärmeatlas [1984], Emery et al. [1991] and others. Before starting the analysis of complicated telescope and enclosure shapes it is useful to try a reduction to simpler geometries, even if this may introduce an error of 10 to 15 %. In case a view factor has to be derived *ab initio* there are three properties that may be useful for calculations. From the definition of the view factor, Eq.(7.49), follows the reciprocity property

$$A_1 \varphi_{1,2} = A_2 \varphi_{2,1} \tag{7.63}$$

If the surface A_1 is divided into n sub-areas $A_1 = A_{1,1} + A_{1,2} + \dots + A_{1,n}$ then the additive property can be applied

$$A_1 \varphi_{1,2} = \int_{A_1} \int_{A_2} [\] dA_1 dA_2 = \sum_j^n \int_{A_{1,j}} \int_{A_2} [\] dA_1 dA_2 = \sum_{j=1}^n A_{1,j} \varphi_{i,j} \quad (7.64)$$

For an enclosure consisting of n sub-areas the enclosure property holds

$$\sum_{j=1}^n \varphi_{i,j} = 1, \quad i = 1, 2, \dots, n \quad (7.65)$$

In an enclosure a convex sub-surface $[k]$ may see itself so that $\varphi_{k,k} \neq 0$. The enclosure property must be applied, for instance, to the interior of hollow support beams, the interior of radomes and astrodomes and other closed internal surfaces.

With respect to radio telescopes and enclosures it is convenient to distinguish view factors related to the internal geometry of a telescope and enclosure and view factors related to the external geometry. The internal view factors of a telescope and enclosure concern, in particular, plates facing each other and tubes of a BUS network facing each other or facing the front and rear closure of the BUS. The external view factors relate an outer surface of the telescope or the enclosure to the sky and/or the ground, which can be considered to be very extended surfaces. The external view factors are explained in Chapter 8.

7.10.3 Internal View Factors

Many radiative connections in a telescope and enclosure can be treated with the view factors of parallel plates, illustrated in Fig. 7.12.a, and right-angle plates, illustrated in Fig. 7.12.b. Typical examples are parallel and right-angle plates of yoke structures, focus cabins, fork arms, pedestals etc. The corresponding view factors $\varphi_{1,2}$ are found in all textbooks on heat transfer, either in analytical or graphical form. A special situation, as for instance applicable to air gaps between panels and insulation, radiation shields etc., occurs if the separation D of plate **1** and plate **2** (Fig. 7.12.a) is small with respect to the dimension $W \times L$ of the plates. In this case the view factor (paint factor $E(1,2)$) of plane parallel walls, Eqs.(7.50,7.51), can be used. Right-angle plates may have a common corner or are separated by the distance D as shown in Fig. 7.12.b. These cases are also treated in textbooks. For the view factor between inclined rectangles see Krishnaprakas [1997].

As will be explained in Section 9.1.2, the thermal behaviour of beams, for instance of an alidade, requires a knowledge of temperature gradients across the beams. The internal surfaces of the beam must be radiatively coupled by appropriate view factors and conductive and convective heat transfer of the internal air. The geometry of such a beam is shown in Fig. 7.13 (see also Fig. 11.9) with, for instance, the dimension $L = 1.3$ m and $W = H = 0.5$ m. The beam may be closed at the top, or the bottom, or both so that the interior forms an enclosure. Following Figure 7.13 and the treatment of view factors of enclosures (for instance Chapman [1974], his figs. 11.15, fig. 11.16 and the parameters R_1 and R_2), the relevant view factors of the selected geometry are summarized in the following table.

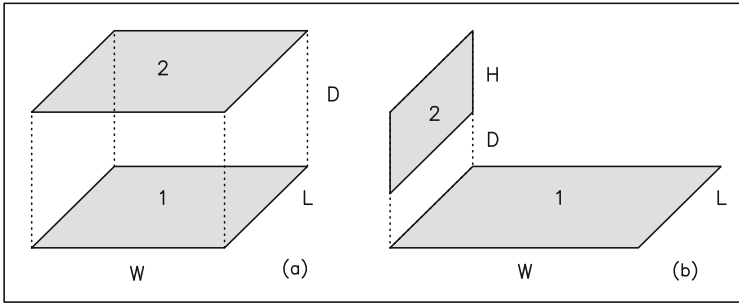


Fig. 7.12 Configuration of parallel plates (a), configuration of right-angle plates (b).

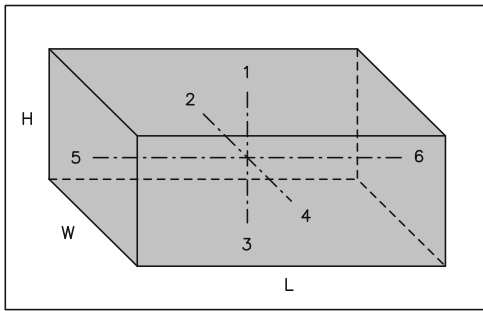


Fig. 7.13 Internal view factors of a beam (enclosure property).

Radiative Connection	R_1	R_2	ϕ
1 → 3	= $H/W = 1$	= $L/W = 2.6$	$\phi_{13} = 0.31$
1 → 2 = 1 → 4	= $H/L = 0.385$	= $W/L = 0.385$	$\phi_{12} = \phi_{14} = 0.27$
1 → 5 = 1 → 6	= $W/H = 1$	= $L/H = 2.6$	$\phi_{15} = \phi_{16} = 0.1$
5 → 6	= $H/L = 0.385$	= $W/L = 0.385$	$\phi_{56} = 0.05$

For illustration, these view factors follow the enclosure property Eq.(7.65)

$$\phi_{1,1} + \phi_{1,2} + \phi_{1,4} + \phi_{1,3} + \phi_{1,5} + \phi_{1,6} = 0 + 0.27 + 0.27 + 0.31 + 0.1 + 0.1 = 1.05 \approx 1$$

(The deviation from 1 is due to the inaccuracy of reading the values $\phi_{i,j}$ from published graphs).

The view factor of BUS constructions is more complicated because of the BUS network. Evidently, there is a difference between an open BUS (see Fig. 5.12) and a closed BUS (see Fig. 5.13). In addition there is also a difference in radiative transfer through the BUS in axial direction, i.e. from front to rear, and in radial direction, i.e. from centre to the rim. For the closed BUS the main radiative heat transfer is in axial direction between the front closure (panels or insulation) and the rear closure (rear side cladding). For the axial direction the view factor of parallel, equal size and concentric disks is useful for a global discussion of radiative heat transfer between the front and rear closures. It is evident from Table 2.5 that for many BUS

constructions the average depth to diameter ratio is $\langle H \rangle/D \approx 0.1$. Following Chapman [1974, his fig. 11.17] or the analytic expression by Bejan [1993], this gives $1/R_1 = 2 \langle H \rangle/D = 0.2$ and $R_2 = 1/R_1 = 5$ and the corresponding parallel disk view factor of $\phi_{1,2} \approx 0.82$. This value does not take into account a possible and often significant shadowing by the BUS network so that the value $\phi_{1,2}$ can be lower, of the order of 15 to 30%. For a detailed analysis of radiative heat transfer in a BUS, and especially for asymmetric solar illumination and cooling towards the cold sky, the BUS needs to be divided into smaller sectors, for instance the 28 sectors shown in Fig. 5.9. The view factor of the front and rear side of the sectors can be calculated from parallel plates and off-set parallel plates as shown in Fig. 7.14, again taking into account the shadowing by the network but also the radiation of the BUS network of the sectors under consideration. The view factors of off-set parallel plates are available in the literature. The view factors of a BUS consisting of plates or box-type compartments (as for instance used on the VertexRSI ALMA/APEX telescopes, see Fig. 9.29.c) can be reduced to parallel and right-angle plates and off-set plates.

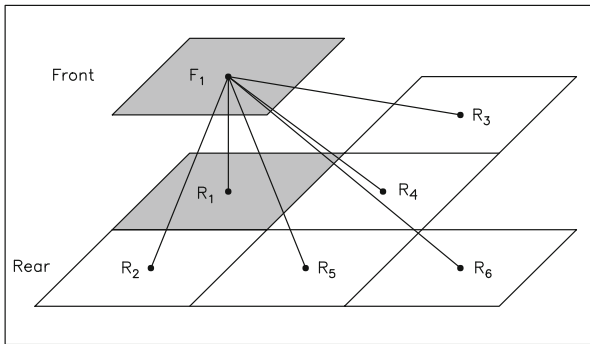


Fig. 7.14 View factors of parallel plates (front $F_1 \rightarrow$ rear R_1) and off-set parallel plates ($F_1 \rightarrow R_2, R_3, \dots R_6$, etc.).

The view factor of a BUS tube/beam network, however, is special and not treated in readily applicable form in the literature. The BUS network can be very 'loose' as on the IRAM 15-m telescopes (seen on the cover picture), or very compact as on the IRAM 30-m telescope (seen in Fig. 2.14). Some network members may be parallel to each other, inclined or even perpendicular to each other. In addition, the network members may be perpendicular, inclined or parallel to the closure of the BUS, i.e. the panel rear surfaces in an open BUS or the panel rear surfaces and the rear cladding in a closed BUS. Many network members connect the front and rear of the BUS and therefore are mainly perpendicular to the panel/cladding surfaces, or only slightly inclined. An estimate of the view factor of parallel and slightly inclined members can be obtained from the view factor of parallel tubes/beams, as treated in the literature, as also the view factor of tubes/beams parallel to a surface. However, these view factors barely resemble the complexity of a BUS network. When starting to derive the view factor of a closed BUS network in axial direction it is useful to evaluate the surface area S_{NW} of the network projected onto the front and rear of the BUS and compare this area with the surface area of the BUS front side

and rear side cladding S_{CL} . The surface area S_{CL} and especially S_{NW} can easily be found from the FEM of the BUS. If $S_{NW} \ll S_{CL}$, the radiative coupling between the network and the BUS front and rear surface is small and can be neglected. If $S_{NW} \approx S_{CL}$ or $S_{CL} \lesssim S_{NW}$, then the radiative coupling should be taken into account. The view factor may then be approximated by $\varphi \approx S_{NW}/2$. This approximation was used in the thermal model calculations of a closed BUS presented in Chapter 11, however, this subject needs further detailed studies and guidelines. In radial direction of a BUS the radiative transfer is through a loose or dense forest of network tubes/beams. An estimate of the view factor is $\varphi \propto \gamma S_{NW}/4$ with $1/2 \lesssim \gamma \approx 1$ for a compact network with significant shadowing and $\gamma \approx 1/2 - 1/4$ for a loose network with little shadowing. These situations, however, also need further detailed study and guidelines.

7.11 Energy/Heat Conservation

Since energy is conserved as stated by the first law of thermodynamics, also power (= energy per time interval) is conserved. Following Bejan [1993], using Fig. 7.2, and explaining for simplicity only the linear (one-dimensional) case, energy conservation states that

$$q_1 - q_2 + w = \frac{\partial E}{\partial t} \quad (7.66)$$

with q_1, q_2 the heat flow through the surfaces A_1 and A_2 , $\partial E/\partial t$ the energy change in the volume element $\Delta x \Delta y \Delta z = A \Delta x$ located between A_1 and A_2 , and w the heat released from or inserted into the volume element per unit of time. The energy change $\partial E/\partial t$ is the change of heat content through a change in temperature, while w is related to the energy release/supply q^* , per volume element and element of time, so that

$$\frac{\partial E}{\partial t} = \rho \mathcal{C} (A \Delta x) \frac{\partial T}{\partial t} \quad \text{and} \quad w = A \Delta x q^* \quad (7.67)$$

Using *Fourier's* law of heat conduction with $q_2 - q_1 = (\partial q/\partial x) \Delta x = -A \partial(k \partial T/\partial x)/\partial x$ and relation Eq.(7.67), Eq.(7.66) becomes

$$\frac{\partial}{\partial x} \left(k \frac{\partial T}{\partial x} \right) + q^* = \rho \mathcal{C} \frac{\partial T}{\partial t} \quad (7.68)$$

Since in the discussion of telescope and enclosure components the respective conduction coefficients are constants in space and time, Eq.(7.68) is for 3 dimensions

$$k \left(\frac{\partial^2 T}{\partial x^2} + \frac{\partial^2 T}{\partial y^2} + \frac{\partial^2 T}{\partial z^2} \right) + q^* = k \nabla^2 T + q^* = \rho \mathcal{C} \partial T / \partial t \quad (7.69)$$

Using the parameter of thermal diffusivity $\alpha = k/\rho \mathcal{C}$ [m^2/s], Eq.(7.69) is

$$\nabla^2 T + q^*/k = \frac{1}{\alpha} \frac{\partial T}{\partial t} \tag{7.70}$$

The energy conservation relation Eq.(7.70) is expressed in Cartesian coordinates (x,y,z). This expression is useful for the discussion of flat plate-like and box-type structures. The relation in cylindrical coordinates (r,θ,z) as illustrated in Fig. 7.15 is convenient for rods, pipes and tubes. The derivation is given by Bejan [1993] and others and is not repeated here. The energy conservation relation in the cylindrical coordinate system is

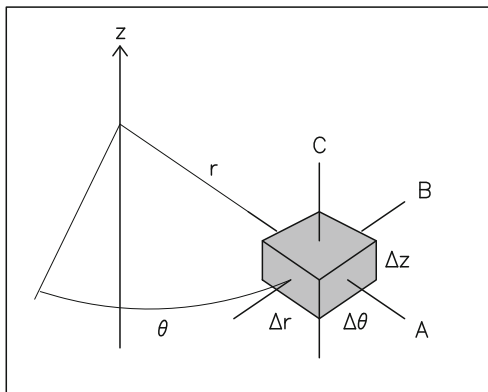


Fig. 7.15 Cylindrical coordinates used in Eq.(7.71). The heat transfer can occur in radial direction: A, azimuth direction: B and vertical direction: C.

$$\frac{\partial^2 T}{\partial r^2} + \frac{1}{r} \frac{\partial T}{\partial r} + \frac{1}{r^2} \left(\frac{\partial^2 T}{\partial \theta^2} \right) + \frac{\partial^2 T}{\partial z^2} + q^*/k = \frac{1}{\alpha} \frac{\partial T}{\partial t} \tag{7.71}$$

A similar relation can be written for spherical coordinates. However, spherical surfaces of telescopes and enclosures have large radii and segments of these surfaces can be considered as being flat in most heat transfer calculations.

A steady thermal state occurs if $\partial T/\partial t = 0$, a transient thermal state occurs if $\partial T/\partial t \neq 0$. The steady state equation with source term $\nabla^2 T + q^*/k = 0$ is the *Poisson* equation, the steady state equation without source term $\nabla^2 T = 0$ is the *Laplace* equation. Since the environment is in a variable thermal state, the telescope and enclosure is usually also in a transient thermal state, though often with long time constants.

For heat transfer in one direction, i.e. the linear case, the steady state energy conservation relation without heat source or heat sink ($q^* = 0$) is

$$\nabla^2 T = \partial^2 T / \partial x^2 = 0 \tag{7.72}$$

with solution

$$T(x) = ax + b \tag{7.73}$$

The constants a, b that determine the actual case under consideration are determined from the boundary conditions. For the steady state with heat sink or heat source ($q^* \neq 0$), the equation for the x -direction is

$$\nabla^2 T + q^* = \partial^2 T / \partial x^2 + q^* = 0 \quad (7.74)$$

with solution

$$T(x) = (-q^*/k)(x^2/2) + ax + b \quad (7.75)$$

The constants a, b are determined from the boundary conditions. Without heat source term $q^* = 0$ the temperature distribution is linear, with heat source term $q^* \neq 0$ the temperature distribution is parabolic in x . For heat transfer in radial direction (r, θ) through a pipe (Fig. 7.4) the steady state energy conservation relation without heat source or heat sink ($q^* = 0$) is

$$\partial^2 T / \partial r^2 + (1/r)(\partial T / \partial r) = \frac{\partial}{\partial r} \left(r \frac{\partial T}{\partial r} \right) = 0 \quad (7.76)$$

with solution

$$T(r) = a \ln r + b \quad (7.77)$$

Again, the coefficients a, b that determine the actual case under consideration are determined from the boundary conditions. For a pipe with inner radius r_i and outer radius r_o and temperatures T_i and T_o , as shown in Fig. 7.4 a, this gives

$$T_i = a \ln r_i + b, \quad T_o = a \ln r_o + b \quad (7.78 a)$$

$$a = (T_i - T_o) / \ln(r_i / r_o) \quad (7.78 b)$$

Combining Eq.(7.78) with the conduction relation $\Delta q = -A_r k (\partial T / \partial r)$ gives for a pipe of length L and surface area $A_r = 2\pi r L$ the relations of Eqs.(7.14, 7.15). The derivation illustrates the origin of the $\ln(r)$ -dependence of radial conductive heat transfer through the walls of a pipe.

So far, the heat transfer relations in one dimension have been explained. Two-dimensional heat transfer for instance in the plane of a plate, either of a steady state or a transient state, and with heat sources or heat sinks is expressed by

$$\frac{\partial^2 T}{\partial x^2} + \frac{\partial^2 T}{\partial y^2} + q^*/k = (1/\alpha) \partial T / \partial t \quad (7.79)$$

This equation can be solved for a number of simple cases as explained by Chapman [1984], Bejan [1993] and others. However, for telescope and enclosure components with an asymmetric distribution of heat sources (sunshine) and asymmetric convective heat transfer (wind), it is easier, and probably unavoidable, to construct a thermal model in which the components are thermally connected in x, y, z -direction. The model is then solved with a network programme. As an example, the

subdivision in x,y,z -direction of a large plate/box-structure of a yoke arm is explained in Fig. 11.11.

These remarks and examples conclude the explanation of the three modes of heat transfer, i.e. conduction governed by Eq.(7.5), convection governed by Eq.(7.16) and radiation governed by Eqs.(7.48,7.49). From these basic relations are developed the complicated analytic relations applied in engineering heat transfer. However, for many thermal problems of heat transfer in telescope and enclosure structures a simple and reliable analytic expression cannot be found, while over-simplification may lead to dubious results. A thermal model is then constructed and solved for appropriate initial and environmental conditions. However, when constructing a thermal model the heat transfer relations appear in the model in nearly the same easy form as stated above.

7.12 The Steady and Non–Steady Thermal State

The energy/heat conservation relation Eqs.(7.70,7.71) defines the steady thermal state $\partial T/\partial t = 0$ and the non-steady thermal state $\partial T/\partial t \neq 0$. Because the thermal environment is in a non-steady thermal state, a telescope is usually also in a non-steady thermal state, unless the telescope is protected by a radome or astrodome with a stable inside climate. The rate of heat exchange in a telescope, or a telescope component, determines the speed of temperature equalization of the telescope/component, i.e. the *internal* thermal time constant τ_{int} . The rate of heat exchange of the telescope/component with the thermal environment determines the speed of temperature equalization with the environment, i.e. the *external* thermal time constant τ_{ext} . If $\tau_{int} < \tau_{ext}$, a temperature inhomogeneity in the telescope/component is equalized by heat transfer inside the telescope/component; if $\tau_{ext} < \tau_{int}$, a temperature difference between the telescope/component and the environment is equalized by heat transfer to/from the environment.

7.12.1 External Thermal Time Constant τ_{ext}

7.12.1.1 $\tau_{ext}(h)$ for Convective Heat Transfer

The non-steady thermal state of the environment influences the thermal state of the telescope. If the temperature T_i of a component of volume V , density ρ and heat capacity \mathcal{C} is determined by the temperature T_A of the surrounding ambient air via convective heat transfer (coefficient h) at the surface A of the component, then the heat balance of the component is

$$hA(T_i - T_A) = \rho \mathcal{C} V \partial(T_i - T_A)/\partial t \quad (7.80)$$

Here it is assumed that the heat conduction inside the component is fast with respect to the convective heat transfer at its surface. Following Chapman [1984] the relation describing this situation is

$$\frac{\partial(T_i - T_A)}{(T_i - T_A)} = -(hA/\rho\mathcal{C}V)\partial t \quad (7.81)$$

If the temperature of the telescope component is T_o at the time $t = 0$ and $T_o - T_A = \Delta T_o$, the integration of Eq.(7.81) gives

$$T_i - T_A = \Delta T_o \exp[-t/\tau_{ext}(h)] \quad (7.82)$$

The thermal time constant with respect to interaction with the thermal environment, i.e. the external thermal time constant $\tau_{ext}(h)$, is

$$\tau_{ext}(h) = \rho\mathcal{C}V/hA = \mathcal{C}M/hA = \mathcal{C}\mathcal{M}/h = \mathcal{C}\mathcal{M}\mathcal{R}_h \text{ [s]} \quad (7.83)$$

with $M = \rho V$ the mass of the object, $\mathcal{M} = M/A$ the mass to surface ratio and $\mathcal{R}_h = 1/h$ the specific convective resistance. If, on the other hand, the component is covered by insulation of thickness Δx with heat conduction coefficient k_{ins} , then the total specific thermal resistance between the ambient air and the component is

$$\mathcal{R}_\Sigma = \mathcal{R}_h + \mathcal{R}_{ins} = \frac{1}{h} + \frac{\Delta x}{k_{ins}} \quad (7.84)$$

For $h = 10 \text{ W/m}^2/\text{K}$, $\Delta x = 0.03 \text{ m}$ and $k_{ins} = 0.04 \text{ W/m/K}$, as an example, this is $\mathcal{R}_\Sigma = \mathcal{R}_h + \mathcal{R}_{ins} = 0.1 + 0.75 = 0.85 \approx 0.75$ so that the thermal resistance through the insulation is the leading term. The external thermal time constant under this condition is

$$\tau_{ext}(h) \approx \mathcal{C}\mathcal{M}\mathcal{R}_{ins} \quad (7.85)$$

As an example, the external thermal time constant of an aluminium honeycomb panel of $A = 1 \text{ m}^2$ surface area, mass $M = \rho V = 10 \text{ kg/m}^2$, heat capacity $\mathcal{C} = 860 \text{ J/kg/K}$, in an air stream with convective heat transfer coefficient $h = 10 \text{ W/m}^2/\text{K}$ gives $\tau_{ext}(h) = 10 \text{ [kg]} 860 \text{ [J/kg/K]}/10 \text{ [W/m}^2/\text{K]} 1 \text{ [m}^2] = 860 \text{ s} \approx 15 \text{ minutes}$. This is close to measured values.

Figure 7.16 illustrates the thermal time constant of the IRAM 15-m telescope fork arm when not covered with insulation. The antenna mount was in the hangar (see Picture 1.7) with a large part of the door open during evening and night. During the night the temperature of the air in the hangar and the temperature of the fork was $\sim 14^\circ \text{C}$. During the day the hangar door was closed and the temperature put on $\sim 20^\circ \text{C}$. The temperature of the fork rose exponentially to this temperature. Late in the afternoon the hangar door was again opened, the temperature of the inside air dropped and exponentially also the temperature of the fork. The steel section of the measured fork arm has a mass of $M \approx 5 \text{ ton}$ and a surface of $A \approx 20 \text{ m}^2$ (Table 11.5). Adopting for the convective heat transfer coefficient $h = 5$ to $10 \text{ W/m}^2/\text{K}$, the

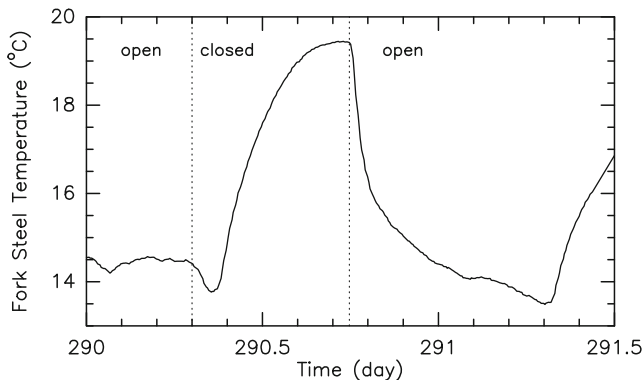


Fig. 7.16 Illustration of the thermal time constant and associated exponential change in temperature of the IRAM 15-m telescope fork, not insulated. The telescope was inside the hangar (Picture 1.7).

thermal time constant is $\tau_{ext}(h) = 5000 \times 450 / (5 - 10) 20 \approx 4 \text{ hours} \approx 0.2 \text{ day}$, which is actually observed in Fig. 7.16.

7.12.1.2 $\tau_{ext}(rad)$ for Radiative Heat Transfer

There occurs also radiative heat transfer between the object and the cold sky with a corresponding radiative thermal time constant $\tau_{ext}(rad)$. For a body of mass M , surface area A , heat capacity \mathcal{C} , emissivity e and temperature T in the thermal environment with black body temperature T_o (for instance the sky temperature T_S) the radiative heat transfer is

$$M\mathcal{C} \partial T / \partial t = e\sigma A [(T_o)^4 - (T)^4] \quad (7.86a)$$

of which, when using $\theta = T - T_o$, the linear approximation gives

$$M\mathcal{C} \partial \theta / \partial t = 4e\sigma A (T_o)^3 \theta \quad (7.86b)$$

Using $\mathcal{M} = M/A$, the external thermal time constant for radiative heat exchange $\tau_{ext}(rad)$ is

$$\tau_{ext}(rad) = \mathcal{C} M / 4e\sigma A (T_o)^3 = (\mathcal{C} \mathcal{M}) / 4e\sigma (T_o)^3 \quad (7.87)$$

Taking for the ambient radiation temperature a sky temperature of $T_o = T_S = 270^\circ - 30^\circ \text{ K}$, from the ratio

$$R = \tau_{ext}(h) / \tau_{ext}(rad) = 4e\sigma (T_o)^3 / h \approx 3e/h \quad (7.88)$$

follows that the equalizing effect of convection (wind) is dominant whenever $\tau_{ext}(h) < \tau_{ext}(rad)$, or $R < 1$, or $3e \approx 3 < h$, and that the equalizing effect of radiation is dominant whenever $\tau_{ext}(rad) < \tau_{ext}(h)$, or $1 < R$, or $h < 3e \approx 3$. These relations express the known situation that on calm days the radiative loss dominates and that on days with strong wind the convective loss dominates. Following Eq.(7.13 b), the simultaneous action of convective and radiative heat transfer gives a combined resistance

$$\frac{1}{\mathcal{R}_\Sigma} = \frac{1}{\mathcal{R}_h} + \frac{1}{\mathcal{R}_{rad}} = \frac{1}{(1/h)} + \frac{1}{(1/4e\sigma T_0^3)} \tag{7.89}$$

so that

$$\tau_{ext}(h + rad) = \mathcal{C} \cdot \mathcal{M} \mathcal{R}_\Sigma = \mathcal{C} \cdot \mathcal{M} \frac{1}{(h + 4e\sigma T_0^3)} \tag{7.90}$$

Using Eq.(7.90), Table 7.11 gives for a number of telescope components the calculated external time constants τ_{ext} . The value R_Σ used in the calculation is indicated.

Table 7.11 External Thermal Time Constants τ_{ext} for \mathcal{R}_Σ as indicated.

Material	Dimension ^{a)}	Mass [kg]	Surface [m ²]	\mathcal{M} [kg/m ²]	\mathcal{R}_Σ [m ² K/W]	τ_{ext}
Plates						
Al-panel	1-1-0.003	7.8	1	7.8	0.1 ^{b)}	11 min
Al-HC	1-1-0.04	10	1	10	0.1	14 min
steel	1-1-0.01	78	1	78	0.1	1 h
steel + insulation	1-1-0.01	78	1	78	0.85 ^{c) d)}	8 h
Beams						
steel	5-0.5-0.02	1.6 ton	10	160	0.1	2 h
steel + insulation	5-0.5-0.02	1.6 ton	10	160	0.85 ^{c) d)}	17 h
CFRP	3-0.25-0.01	48	3	16	0.1	1/2 h
Tubes						
Al	1-0.05-0.005	2	0.16	12.5	0.1	18 min
Al	1-0.1-0.01	8	0.31	26	0.1	37 min
Al + insulation	1-0.05-0.005	2	0.16	12.5	2.5 ^{f) g)}	8 h
Al + insulation	1-0.1-0.01	8	0.31	26	1.3 ^{f) g)}	8 h
steel	1-0.05-0.005	6	0.16	38	0.1	30 min
steel	1-0.1-0.01	24	0.31	79	0.1	1 h
steel + insulation	1-0.05-0.005	6	0.16	38	2.5 ^{f) g)}	12 h
steel + insulation	1-0.1-0.01	24	0.31	78	1.3 ^{f) g)}	13 h
CFRP	1-0.05-0.005	1.2	0.16	8	0.1	15 min
CFRP	1-0.1-0.01	5	0.31	16	0.1	30 min

^{a)} Length – width – thickness; tubes: length – diameter – wall thickness [m,m,m].

^{b)} $\mathcal{R}_\Sigma = 1/[h + 4e\sigma(T_0)^3]$.

^{c)} Plates: 3 cm insulation, ^{d)} calculated from Eqs.(7.84,7.85).

^{e)} hollow rectangular beam.

^{f)} tubes: 2 cm insulation, ^{g)} calculated from Eq.(7.23).

7.12.2 Internal Thermal Time Constant τ_{int} (Conduction)

The internal thermal time constant depends on the components of a telescope, or enclosure, their geometry, their material and their thermal connections. These parameters define the speed with which a temperature disturbance propagates through the component, until thermal uniformity is established. The internal thermal time constant due to conduction in a component of typical size L is [see von Hoerner 1967 c, Lamb 1992]

$$\tau_{int} = \frac{4}{\pi^2 k} \mathcal{C} \rho L^2 \quad (7.91)$$

Using the data of Table 7.1, the internal thermal time constant of a $L = 1$ cm thick plate made of steel or aluminium is $\tau_{int} = 3$ sec (steel) and $\tau_{int} = 0.5$ sec (aluminium). If the typical length is $L = 2$ m, like a fork arm made of steel, the internal thermal time constant is $\tau_{int} \approx 5$ hours.

External and internal thermal time constants can also be determined from a thermal model when subjecting the component under discussion either to a step-like change of the external/internal temperature or to a periodic change as occurring in the environment. Such model calculations are published for the JCMT telescope inside its astrodome [Casse & Bregman 1984].

Chapter 8

Radiative Coupling towards Sky and Ground (External View Factor)

A significant radiative coupling can occur between the outer surfaces of a telescope, its enclosure, the sky and the ground. This radiative coupling is illustrated in Fig. 8.1 for the IRAM 30–m telescope. In the left picture the telescope is at horizon position so that the upper part of the reflector surface sees the warmer ground while the lower part sees the cooler sky. There exists an up–down temperature difference of the reflector panels (panel surfaces) of 4 to 5 °C. In the right picture the telescope points towards 45° elevation and the reflector surface sees more or less uniformly the cool sky so that the panels have a lower and more uniform temperature compared to the situation shown for horizon position. The measured temperatures are summarized in Fig. 8.2. In this interpretation it is assumed that the contribution of reflected radiation from the sky and the ground is small (TiO₂ painted panels with little specular reflection). A consequence of the asymmetric radiative cooling is shown in Fig. 8.3 for the IRAM 15–m telescope that pointed during the night towards horizon. The lower part of the reflector, facing primarily the cool sky, is iced up at the panel gaps, the upper part, facing primarily the warmer ground (even when covered with snow), is free of ice.

This Chapter explains the radiative coupling of the telescope and enclosure outer surfaces to the sky and the ground, expressed by the view factor of the corresponding structural elements. The view factor was introduced in Section 7.8; here it is the radiative coupling between the sky and the ground that are very extended, or even of infinite extent, compared to the relatively small telescope and enclosure surfaces. The view factor of the surfaces A_1 and A_2 (see Fig. 7.8 and Eq.(7.49)) is

$$\varphi_{12} = (1/\pi A_1) \int_{A_1} \int_{A_2} \frac{\cos\theta_1 \cos\theta_2}{r^2} dA_1 dA_2 \quad (8.1)$$

Evidently, in Eq.(8.1) the surface area of the ground and the sky $A_2 \rightarrow \infty$. The ground and the sky have the temperature $T_G(t)$ and $T_S(t)$, which may change with time. It is assumed that the ground everywhere has the temperature $T_G(t)$. Usually this is not the case for the effective sky temperature, which is a function of elevation (Fig. 4.22).

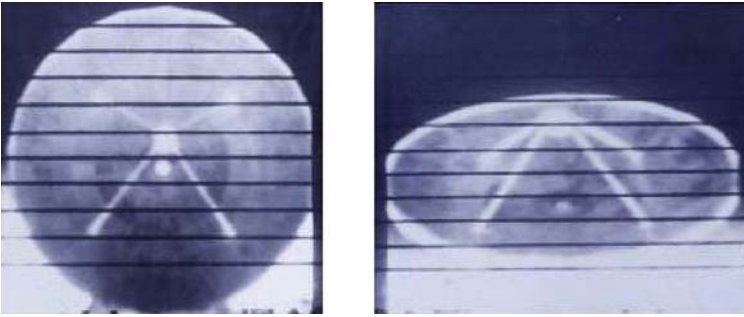


Fig. 8.1 Infrared picture of the IRAM 30-m telescope facing the horizon (left side) and pointing at 45° elevation (right side). Dark areas are cool, white areas are warm. Measurement made with the AGATM 780 Thermograph System, 1987.

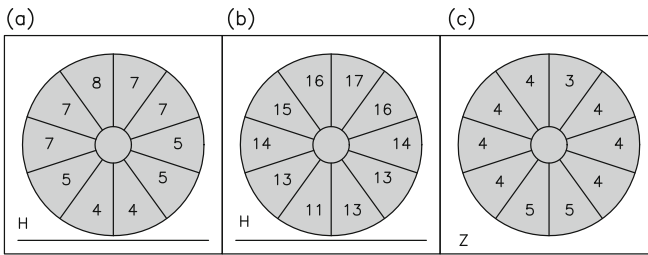


Fig. 8.2 IRAM 30-m telescope. Panel temperatures measured with the reflector at horizon position H (a,b) and zenith position Z (c). At horizon position $\Delta T \approx 4^\circ \text{C}$, at zenith $\Delta T \approx 1^\circ \text{C}$.

From the pictures of telescopes and enclosures shown in Chapter 2 and Chapter 3 (and Chapter 14 for optical telescope enclosures) it is seen that most of the walls are vertical, with a few exceptions of horizontal walls, for instance the roofs of enclosures. However, the surface of a radome is always curved while an astrodome may have mainly vertical walls and a curved membrane. A special case is the parabolic reflector surface and the BUS. In an open BUS the panel front and rear may see the sky and the ground. In this case the front surface is concave while the rear surface is convex. In a closed BUS the front surface is the concave reflector surface while the rear side are the flat cladding surfaces. Depending on the elevation of the telescope, the reflector surface and the cladding surfaces can be inclined to the sky and the ground. From the large variety of surfaces facing the sky and the ground a few examples are selected to explain the view factor calculation.



Fig. 8.3 IRAM 15-m telescope. The reflector pointed during nighttime towards horizon so that the lower part faced the cool sky and is iced up while the upper part faced the relatively warm layer of snow. There are cold edges at the panel gaps and several panels of which the de-icing was not working and that are iced up [Courtesy R. Neri, IRAM, France].

8.1 Vertical and Horizontal Walls

As shown in Fig. 8.4, a vertical wall may have the width W , height H and distance D above the ground. This wall (A_1) sees a very large area of the isothermal ground (A_2), say to a distance $\sim 500 \times H$ in front of the wall and to either side. From simple geometrical arguments, and actual calculations, it is evident that the view factor of the wall with respect to the ground is $\phi_G = 0.5$.

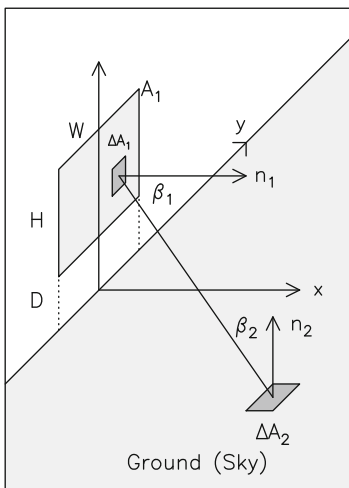


Fig. 8.4 Illustration of a vertical wall facing the very extended ground (or sky).

The same geometry as shown in Fig. 8.4 can be used to find for the vertical wall the view factor φ_S of the sky. The effective sky temperature of the clear sky is a function of elevation with the sky at zenith being cooler than at horizon, while a cloud cover is similar to a sky with elevation independent temperature (Fig. 4.22). A cloud covered sky is a grey body radiator ($e \approx 0.8$) with the temperature that of the base of the clouds. The view factor of the cloud covered sky is $\varphi_S = \varphi_{\text{cloud}} \approx 0.5$.

The radiative heat transfer between a telescope component [i] of temperature T_i and the sky at elevation E and temperature $T_S(E)$ is

$$\Delta q(E) \propto \varphi_{i,S} [(T_i)^4 - T_S(E)^4] \quad (8.2)$$

If $T_S(90)$ is the effective sky temperature at zenith ($E = 90^\circ$), the sky temperature at intermediate elevations can be expressed, in first order, by

$$T_S(E) = T_S(90) [1 + (\Delta T/T_S(90)) \cos E] = T_S(90) [1 + \varepsilon \cos E] \quad (8.3)$$

The effective sky temperature at horizon is $T_S(0) = T_S(90) + \Delta T$ with $0 \leq \Delta T$ and $0 \leq \varepsilon$. Seen from the vertical wall element shown in Fig. 8.4, the elevation-averaged sky temperature T_S^* can be used in the relation

$$\Delta q \propto \varphi_{i,S} [(T_i)^4 - (T_S^*)^4] \quad (8.4)$$

so that the view factor remains $\varphi_{i,S} = 0.5$. The temperature T_S^* is obtained from the weighted integration over the 1/2 hemisphere in front of the surface element $\Delta F = W \times H$, i.e.

$$\begin{aligned} T_S^* &= \int_0^\pi \int_0^{\pi/2} T_S(E) (\Delta F \cos E) \times \cos E dE dA / \int_0^\pi \int_0^{\pi/2} (\Delta F \cos E) \times \cos E dE dA \\ &= T_S(90) [1 + \varepsilon \int_0^{90} \cos^3 E dE / \int_0^{90} \cos^2 E dE] = T_S(90) [1 + 0.85 \varepsilon] \end{aligned} \quad (8.5)$$

In Eq.(8.5) is A the azimuth angle and E the elevation angle of a ray from the vertical wall in the direction of the sky.

If a horizontal wall faces the ground the view factors are $\varphi_G = 1$ and $\varphi_S = 0$, i.e. the wall does not see the sky. If the horizontal wall faces the sky, the view factors are $\varphi_G = 0$ and $\varphi_S = 1$ when using the weighted sky temperature

$$\begin{aligned} T_S^* &= T_S(90) [1 + \varepsilon \int_0^{90} (\Delta F \sin E) \cos E \cos E dE / \int_0^{90} (\Delta F \sin E) \cos E dE] \\ &= T_S(90) [1 + 0.67 \varepsilon] \end{aligned} \quad (8.6)$$

With approximately $\varepsilon = \Delta T/T_S(90) \approx 30/270 = 0.1$ (Fig. 4.22), the effective average sky temperature T_S^* is 5 to 10 % higher than the sky temperature at zenith $T_S(90)$. Evidently, for a cloud covered sky $\varepsilon \approx 0$ and $T_S^* = T_{\text{cloud}}$.

8.2 The Radome and Astrodome

In order to derive the view factor of a radome (Fig. 3.4) or of the curved slit of an astrodome (Fig. 3.3), it is sufficient to consider a vertical cut through the radome as shown in Fig. 8.5.

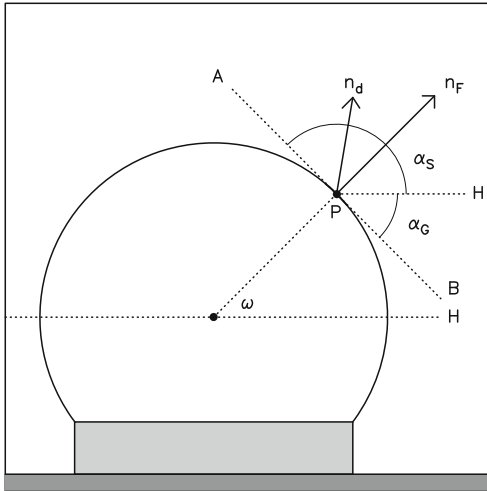


Fig. 8.5 Illustration of the view factor calculation of a radome, or of the curved slit of an astrodome.

In Fig. 8.5 is P the centre of a surface element ΔF on the radome, at the elevation angle ω with respect to the horizontal plane. \overline{AB} is the tangential plane at P; H is the horizontal plane. All directions within the angle <(HPA) = α_S see the sky, all directions within the angle <(HPB) = α_G see the ground. In a Cartesian coordinate system the vector normal to the surface element is

$$\mathbf{n}_F = (\cos\omega, 0, \sin\omega) \tag{8.7}$$

with ω between -ω₀ (over-hemispherical) and 90° (zenith). A vector in the direction d is

$$\mathbf{n}_d = (\cos\alpha, 0, \sin\alpha) \tag{8.8}$$

The connection of the surface element in the direction n_d to the sky, or the ground, is

$$\Delta S = (\mathbf{n}_F, \mathbf{n}_d) \Delta F = \cos(\alpha - \omega) \Delta F \tag{8.9}$$

The view factor φ_S and φ_G in the direction of the sky and the ground is

$$\varphi_S = \int_0^{\alpha_S} \cos(\alpha - \omega) d\alpha, \quad \varphi_G = \int_0^{\alpha_G} \cos(\alpha - \omega) d\alpha \tag{8.10}$$

which gives

$$\varphi_S = [1 + \sin\omega]/2 \tag{8.11}$$

and

$$\varphi_G = 1 - \varphi_S \tag{8.12}$$

In the special case of a surface element at the top of the radome $\omega = 90^\circ$ and $\varphi_S = 1$ and $\varphi_G = 0$, for a vertical surface element at the periphery of the radome $\omega = 0$ and $\varphi_S = \varphi_G = 1/2$. In Eq.(8.9) the elevation dependence of the sky temperature is not taken into account, this can be done by introducing Eq.(8.3) in Eq.(8.10). However, when using a constant sky temperature, for instance that at elevation 45° , the error is between 5 and 10 %.

With T_S the effective sky temperature and T_G the ground temperature, the radiative heat transfer between a radome surface element ΔF at the position ω , with temperature T_R , and the sky and the ground is

$$\Delta q(\omega) = e_S a \sigma \varphi_S(\omega) [(T_R)^4 - (T_S)^4] \Delta F + e_G a \sigma \varphi_G(\omega) [(T_R)^4 - (T_G)^4] \Delta F \tag{8.13}$$

where $a = e$ is the absorption/emission coefficient of the radome material at infrared wavelengths.

8.3 The Parabolic Reflector

Figure 8.6 shows a parabolic reflector tilted at the elevation E . A surface element ΔF at the position P of the reflector sees the sky and the ground and the surface of the reflector at other positions P^* , with view factors $\varphi_S(P)$, $\varphi_G(P)$ and $\varphi_R(P,P^*)$. At zenith position ($E = 90^\circ$) the reflector sees only the sky so that $\varphi_S = 1$ and $\varphi_G = 0$. Below the elevation $E_0 = 90^\circ - \beta^*$, with $\tan \beta^* = 1/(4n)$ ($n = \text{focal ratio}$), all reflector surface elements see the sky and the ground.

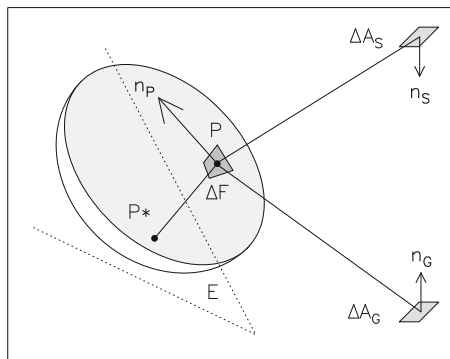


Fig. 8.6 Illustration of a parabolic reflector, tilted at the elevation E , seeing the sky (element ΔA_S) and the ground (element ΔA_G). n_P is normal of the surface element of the reflector at point P ; n_S and n_G is the normal of a sky element and a ground element. P^* is another point of the reflector surface seen from P .

A surface element ΔF , with surface normal \mathbf{n}_p , at the position P_1 of the tilted reflector sees the sky and the ground¹ and some part of the reflector surface, as illustrated in Fig. 8.7.a. The view factors φ_S and φ_G are calculated with respect to the horizontal plane H through P_1 . All directions below the horizon within the angle α_G are radiatively connected to the ground at temperature $T_G(t)$, all directions above the horizon within the angle α_S are radiatively connected to the sky at temperature $T_S(t)$. In order to derive the view factor of the surface element at position P_1 (upper part of the reflector), or position P_2 (lower part of the reflector), Fig. 8.7.b shows a cut through the parabolic surface and the corresponding Cartesian coordinate system $[x,z]$, with $+z$ -axis along the direction of the reflector axis (RA). In this orientation of the coordinate system the horizontal plane H is tilted by the angle E . The surface element at P_1 sees the sky within the angle $\angle(R_1P_1H) = \alpha_S$, the sky is blocked by the upper reflector rim R_1 . The surface element at P_1 sees the ground within the angle $\angle(R_2P_1H) = \alpha_G$, the ground is blocked by the lower reflector rim R_2 . With \overline{AB} the tangential plane at P_1 (i.e. the plane perpendicular to \mathbf{n}_p), within the angle $\angle(AP_1R_1)$ the surface element sees the upper reflector surface, within the angle $\angle(BP_1R_2)$ the lower reflector surface. For a corresponding position P_2 of the opposite reflector surface the relations are similar. The situation explained in this way considers the radiative connection to the sky and the ground in tilt direction (elevation direction); the nearly symmetric secondary effect of the azimuth direction (perpendicular to the plane of Fig. 8.7) is neglected in the radiative coupling to the sky and the ground. This geometry excludes directions (P,P^*) skew to the plane of Fig. 8.7 so that the view factor φ_R derived in the following is only an approximation.

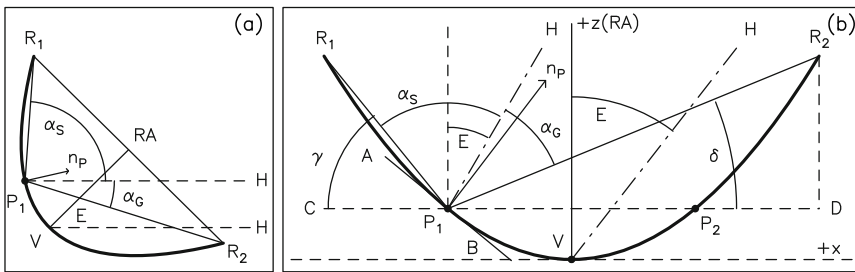


Fig. 8.7 (a) Illustration of a parabolic reflector tilted at the elevation E , seeing the sky within the angle α_S and the ground within the angle α_G . \mathbf{n}_p is the vector normal to the surface element at P_1 . (b) Coordinate system and angles used to calculate the view factors for the position P_1 .

For a reflector of diameter D , focal ratio n , the coordinate system of Fig. 8.7.b and the normalized radius $\rho = x/(D/2)$ ($-D/2 \leq x \leq D/2$), the relation of the parabolic surface is

¹ The derivation excludes reflection on the reflector surface so that a surface element cannot see indirectly the sky and the ground. This condition does not hold for shiny reflector surfaces.

$$x^2 = 2pz = 4fz \text{ or } \rho^2 = 16nz/D \quad (8.14)$$

The angle $\angle (AP_1C) = \beta$ of the tangential plane is

$$\tan\beta = \rho/(4n) \quad (8.15)$$

the angle $\angle (R_1P_1C) = \gamma$ to the upper rim R_1 is

$$\tan\gamma = (1 + \rho)/(8n) \quad (8.16)$$

the angle $\angle (R_2P_1D) = \delta$ to the lower rim R_2 is

$$\tan\delta = (1 - \rho)/(8n) \quad (8.17)$$

For the positions P_1 and P_2 the normal vectors $\mathbf{n}_P(1)$ and $\mathbf{n}_P(2)$ at the surface are

$$\mathbf{n}_P(1) = (\sin\beta, \cos\beta), \quad \mathbf{n}_P(2) = (-\sin\beta, \cos\beta) \quad (8.18)$$

If $\mathbf{n}_d = (\sin\omega, \cos\omega)$ is any direction from the position P_1 , the view factor of the sky $\varphi_S(1)$ is

$$\begin{aligned} \varphi_S(1) &= (1/2) \int_{90-E}^{180-\gamma} (\mathbf{n}_P(1), \mathbf{n}_d) d\omega = (1/2) \int_{90-E}^{180-\gamma} \sin(\beta + \omega) d\omega \\ &= (1/2) [\cos(\beta - \gamma) - \sin(\beta - E)] \end{aligned} \quad (8.19)$$

The view factor $\varphi_G(1)$ of the ground is

$$\begin{aligned} \varphi_G(1) &= (1/2) \int_{\delta}^{90-E} (\mathbf{n}_P(1), \mathbf{n}_d) d\omega = (1/2) \int_{\delta}^{90-E} \sin(\beta + \omega) d\omega \\ &= (1/2) [\cos(\beta + \delta) - \sin(\beta - E)] \end{aligned} \quad (8.20)$$

The view factor $\varphi_R(1)$ of the upper and lower reflector surface seen from P_1 is

$$\begin{aligned} \varphi_R(1) &= (1/2) \int_{180-\gamma}^{180-\beta} (\mathbf{n}_P(1), \mathbf{n}_d) d\omega + (1/2) \int_{-\beta}^{\delta} (\mathbf{n}_P(1), \mathbf{n}_d) d\omega \\ &= (1/2) [2 - \cos(\beta - \gamma) - \cos(\beta + \delta)] \end{aligned} \quad (8.21)$$

From the position P_2 at the lower reflector surface the equivalent relations are

$$\begin{aligned} \varphi_S(2) &= (1/2) \int_{90-E}^{180-\delta} (\mathbf{n}_P(1), \mathbf{n}_d) d\omega = (1/2) \int_{90-E}^{180-\delta} \sin(\omega + \beta) d\omega \\ &= (1/2) [\cos(\beta + \delta) + \sin(\beta + E)] \end{aligned} \quad (8.22)$$

$$\begin{aligned} \varphi_G(2) &= (1/2) \int_{\gamma}^{90-E} (\mathbf{n}_P(1), \mathbf{n}_d) d\omega = (1/2) \int_{\gamma}^{90-E} \sin(\omega + \beta) d\omega \\ &= (1/2) [\cos(\gamma - \beta) - \sin(\beta + E)] \end{aligned} \quad (8.23)$$

$$\begin{aligned} \varphi_R(2) &= (1/2) \int_{\beta}^{\gamma} (\mathbf{n}_P(1), \mathbf{n}_d) d\omega + (1/2) \int_{180-\delta}^{180+\beta} (\mathbf{n}_P(1), \mathbf{n}_d) d\omega \\ &= (1/2) [2 - \cos(\gamma - \beta) - \cos(\beta + \delta)] \end{aligned} \tag{8.24}$$

The factor 1/2 is introduced in Eqs.(8.19–8.24) so that for P_1 and P_2

$$\varphi_S + \varphi_G + \varphi_R = 1 \text{ with } 0 \leq \varphi \leq 1 \tag{8.25}$$

The elevation dependence of the sky temperature can be introduced by using Eq.(8.3).

With T_S the effective sky temperature, T_G the ground temperature and T_R the average temperature of the reflector surface, the radiative heat transfer between a reflector surface element ΔF , with temperature T_P , and the sky, the ground and the reflector itself is

$$\begin{aligned} \Delta q &= e_S a \sigma \varphi_S [(T_P)^4 - (T_S)^4] \Delta F + e_G a \sigma \varphi_G [(T_P)^4 - (T_G)^4] \Delta F \\ &\quad + e_R a \sigma \varphi_R [(T_P)^4 - (T_R)^4] \Delta F \end{aligned} \tag{8.26}$$

where $a = e$ is the absorption/emission coefficient of the reflector surface at infrared wavelengths. The third term of Eq.(8.26) is small and can be neglected since $T_P \approx T_R$.

Applying Eqs.(8.14–8.24), Fig. 8.8 shows for different elevation angles the calculated view factors of a parabolic reflector of focal ratio $n = 0.3$. These view factors can be used in a thermal model of a reflector to calculate the temperature of the surface panels. A calculation of this kind for insulated panels on a closed BUS (see Chapter 11) is shown in Fig. 8.9 for the elevation $E = 0^\circ$ and $E = 60^\circ$. The calculated temperature is similar to the measurements of Fig. 8.2.

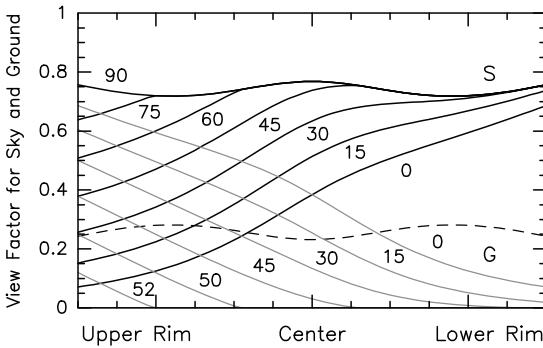


Fig. 8.8 View factor φ_S and φ_G of a parabolic reflector for the sky (lines S) and the ground (lines G). The numbers at the lines is the tilt angle E (in degree). The dashed line is the view factor φ_R by which a surface element sees the surface of the reflector. For the definition of the upper and lower rim see Fig. 8.7.

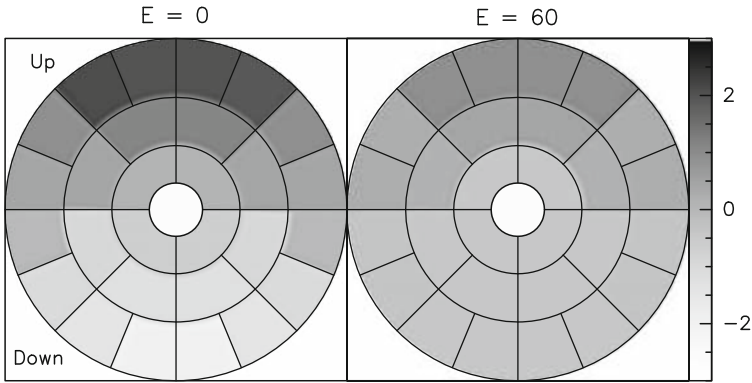


Fig. 8.9 Model calculation of the panel surface temperature (28 sectors) of a parabolic reflector when pointing towards horizon ($E = 0^\circ$) and being tilted at $E = 60^\circ$. The displayed temperatures (in $^\circ\text{C}$) are the deviations from the average temperature. In the calculations the ambient air temperature is $T_A = 30^\circ\text{C}$, the sky temperature is $T_S = T_A - 25^\circ\text{C}$, the ground temperature is $T_G = 22^\circ\text{C}$. The view factors are those of Fig. 8.8. The thermal model of the BUS + panels + insulation is that of Fig. 11.23.

8.4 The Open and Closed BUS

The open BUS network shown in Fig. 5.12 has no rear cladding. The panel front surface and the panel rear surface can see the sky and the ground. The panel rear sides are, however, more or less shadowed by the BUS network. The view factor of the panel front surface is discussed in the previous section. The view factors of the panel rear sides are obtained from similar integral relations (Eqs.(8.14–8.24)) and inversion of the normal vectors of the surface (Eq.(8.18)) from $\mathbf{n}_P(1)$ to $\mathbf{n}_P(1)^* = (-\sin\beta, -\cos\beta)$ and from $\mathbf{n}_P(2)$ to $\mathbf{n}_P(2)^* = (\sin\beta, -\cos\beta)$. A rear surface element does not see other parts of the rear surface.

The closed BUS shown in Fig. 5.13 has rear cladding, usually consisting of flat closure or insulation panels. The rear cladding forms a truncated polygonal cone. A segment of the cone wall is a flat surface element, inclined to the ground and the sky. The view factor of the panel front surface of the reflector is discussed in the previous section. The view factors of the rear cladding are obtained from the view factors of flat surfaces being inclined to the sky and the ground, calculated from Eq.(8.1), taking into account that the sky and the ground are very extended surfaces. Fig. 8.10 is an infrared picture of the IRAM–30m telescope pointing at 45° elevation. The lower rear cladding faces the warm ground, and hence this cladding section is warm (light areas), the upper rear cladding faces the cool sky, and hence this cladding section is cool (dark areas).

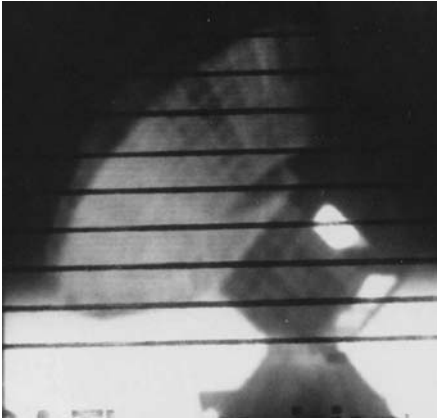


Fig. 8.10 Infrared picture of the IRAM 30-m telescope (pointing at 45° elevation) showing the warm lower rear cladding (light areas) facing the warm ground and the cool upper rear cladding (dark areas) facing the cool sky. Note the warm exhaust air in the yoke area. Measurements made with the AGATM 780 Thermograph System, 1987.

Chapter 9

Measured Thermal Behaviour of Radio Telescopes

A radio telescope consists of a pedestal, or an alidade or fork, of a BUS connected to the elevation structure or connected to the secondary focus cabin, of panels on the BUS that form the reflector surface, and of a quadripod with the primary focus cabin and subreflector (Fig. 1.1). Not all of these components are in direct thermal contact, but they are all exposed to the variable thermal environment or an artificial environment in a radome or astrodome. As the components are mechanically connected, a thermal inhomogeneity in one or several of the telescope components may introduce a mechanical deformation that may affect the performance of the whole telescope.

The measured thermal behaviour of telescope components is summarized in this Chapter. The collected data should be seen in the context of telescope performance, i.e. of a temperature induced focus error, pointing error, path length error and beam degradation, as summarized in Table 9.1. In the table a distinction is made between a uniform temperature change of the structural component, or a temperature difference/gradient, or a random temperature distribution. Globally, it is seen that uniform temperature changes cause focus and path length errors, while temperature differences/gradients cause pointing errors.

Table 9.1 Possible Degradation in Telescope Performance due to a Uniform Temperature Change (U), a Temperature Difference/Gradient (D) or a Random Temperature Change (R) in the specified Telescope Component.

Telescope Component	Focus Error	Pointing Error	Path Length Error	Beam/Sensitivity Degradation
Alidade		D	U	
Pedestal		D	U	
Fork		D	U	
BUS/BUS-support	U	D	U	U,D,R
Panels				U,D,R
Quadripod	U	D	U	U,D
Subreflector	U	D		U,D

The data of this Chapter are inhomogeneous and incomplete and provide only a limited picture of the thermal life of the reported telescopes. Nevertheless, for the design of a radio telescope it is useful, on the one hand, to have information on the thermal behaviour of existing telescopes and of the efficiency of thermal protection if applied. On the other hand, data on the actual thermal behaviour of telescope components may be used as test cases for model calculations of similar components. If a thermal model calculation reproduces the observed thermal behaviour then the model can be applied with confidence on a similar, scaled component. The thermal calculations reported in Chapter 11 of a panel, fork, BUS and radome were first checked in this way.

With respect to data of structural components with thermal protection it must be remembered that generally there are no data for comparison of the same components without thermal protection. Therefore it is often difficult to estimate the efficiency of thermal protection, although thermal model calculations may give an answer.

9.1 Telescope Supports

The telescope supports are

- (1) the pedestal,
- (2) the alidade,
- (3) the fork mount.

As listed in Table 9.1, temperature differences in telescope supports cause pointing errors, uniform temperature changes cause path length errors.

9.1.1 *The Pedestal*

There are several telescopes, both small and large, which have a pedestal and in particular a pedestal built of concrete. Typical examples are the SEST 15-m telescope [Booth et al. 1989], the radome enclosed Onsala 20-m telescope [Menzel 1976], the IRAM 30-m telescope [Baars et al. 1987, 1994], the Parkes 64-m telescope [Jeffery 1964] and others. Evidently, the thermal behaviour of a pedestal is different if the pedestal is exposed to the environment or is protected with the telescope by a radome/astrodome. The pedestal carries at its upper part either the azimuth rail and wheel drive system (for instance the Parkes 64-m telescope) or the azimuth bearing (for instance the IRAM 30-m telescope). While the pedestal of a cm-wavelength telescope can be a large and unprotected building (for instance the Parkes telescope with 3 floors), in order to reduce a possible temperature induced pointing error, the pedestal of a (sub-)mm-wavelength telescope is thermally protected by either insulation plates (IRAM 30-m telescope, ALMA telescopes) or by insulation and an additional radiation shield consisting of aluminium plates (SEST 15-m telescope).

In addition, on the IRAM 30-m telescope the air inside the pedestal is ventilated. A tilt of the pedestal either due to temperature or wind results in an inclination of the AZ-axis and an associated pointing error. Evidently, since the pedestal is anchored in the ground, a movement of the ground causes also a tilt of the pedestal. In measurements of the telescope AZ-axis inclination it is therefore rather difficult to separate temperature, wind and ground effects, although the rate of change may give some indication of the origin of an inclination change.

The tilt of the AZ-axis (Δ) due to a tilt of the azimuth bearing or azimuth rail, which in turn may be due to a tilt of the pedestal as shown in Fig. 9.1, is considered in the pointing model of a telescope. Thus, when analysing the variation of the corresponding pointing model parameters (for the IRAM 30-m telescope P_4 , P_5 with $P_4 = \Delta \cos A$, $P_5 = \Delta \sin A$ and A the tilt direction, see Appendix C and Greve et al. [1996 b]), it is possible to obtain some insight in the thermal stability of the pedestal.

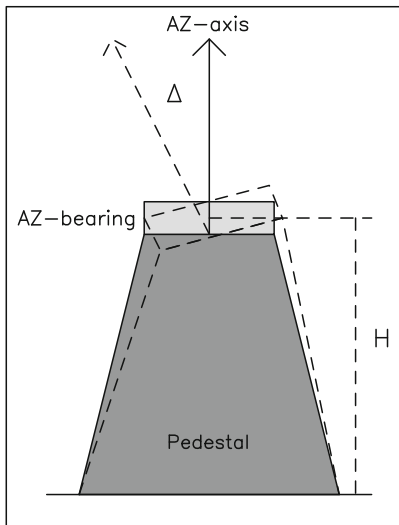


Fig. 9.1 Temperature induced inclination of a pedestal with associated tilt Δ of the Az-bearing and AZ-axis.

Because of a generally large mass, the thermal time constant of a pedestal is long so that systematic temperature effects are measurable only over a long time interval. Fig. 9.2 shows the seasonal change of the AZ-axis tilt Δ of the SEST telescope ($H = 3$ m) and Fig. 9.3 of the IRAM 30-m telescope ($H = 9$ m) as derived from the change of the pointing model parameters ΔP_4 and ΔP_5 with $\Delta = \sqrt{(\Delta P_4)^2 + (\Delta P_5)^2}$. Throughout a year the tilt Δ of the pedestal of the SEST telescope and the IRAM 30-m telescope is stable within ~ 5 to 10 arcsec. During the year(s) shown in Fig. 9.2 and Fig. 9.3.a the AZ-axis tilt direction (A) of the SEST telescope changed by a few degrees, the AZ-axis tilt direction of the IRAM 30-m telescope changed by $\sim 90^\circ$ (Fig. C.1, Appendix C). The influence of the environment on the tilt of the IRAM 30-m telescope pedestal is suggested from the

correlation between the tilt amplitude Δ and the ambient air temperature T_A shown in Fig. 9.3.b. The change of tilt is of the order of $\partial\Delta/\partial T_A \approx 0.5 \text{ arcsec}/^\circ\text{C}$.

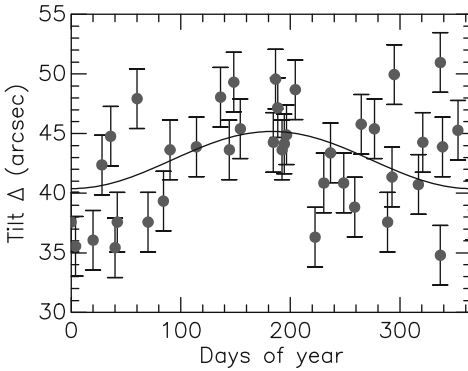


Fig. 9.2 SEST 15-m telescope. Change of the AZ-axis tilt Δ due to a tilt of the concrete pedestal, derived from changes of the pointing model parameters P_4, P_5 . The line is the best-fit sinusoidal approximation with amplitude $\Delta/2 = 2.5 \text{ arcsec}$; the rms value of the fit of 4 arcsec is however large [Data from L.B.G. Knee].

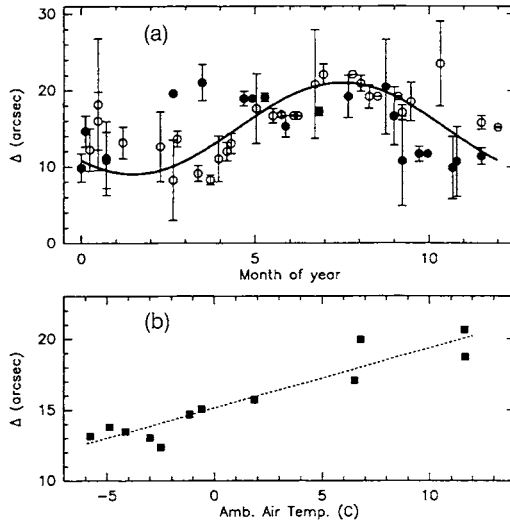


Fig. 9.3.a,b IRAM 30-m telescope. (a) Change of the AZ-axis tilt Δ due to an inclination of the concrete pedestal, derived from changes of the pointing model parameters P_4, P_5 . Dots and open circles are data of two consecutive years, the line is the best-fit sine approximation. (b) Correlation of the tilt amplitude with the ambient air temperature. The dashed line is the linear approximation [Greve et al. (1996), Courtesy Astron. Astrophys.].

Using a x,y-axis inclinometer, Peñalver et al. [2001] have shown that the instantaneous inclination of the AZ-axis (Δ, A) of the IRAM 30-m telescope can be derived whenever the telescope slews over an azimuth distance of a least $\sim 80^\circ$. This slew range and the constant slew speed allows the correction of linear drifts of the

inclinometer. Fig. 9.3.c shows 3 940 measurements of the tilt Δ made throughout the year 2005 and mostly used for an instantaneous upgrade of the pointing model. Again, the measurements show a yearly amplitude of Δ of ~ 5 arcsec and several periodic short-term variations of similar amplitude.

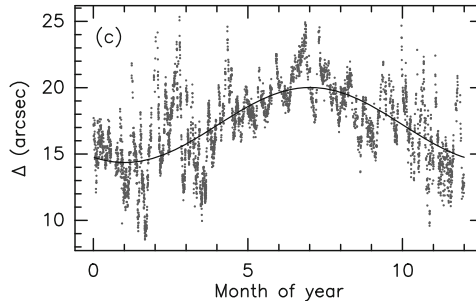


Fig. 9.3.c IRAM 30-m telescope. Inclinometer measurements of the AZ-axis tilt Δ . The line is the best-fit sine approximation [Data from J. Peñalver, IRAM, Spain].

The support structure below the azimuth bearing of a fork mount shown in Fig. 9.11 is similar to a pedestal. This pedestal is a construction anchored in the ground, as used on the APEX 12-m telescope and SEST 15-m telescope, or a movable construction in interferometer arrays on which the entire telescope can be displaced, as used on the IRAM 15-m telescopes and ALMA 12-m telescopes. Temperature measurements are available for the pedestal of the fork-supported ALMA VertexRSI and AEC prototype telescopes [Mangum et al. 2006, and NRAO-ESO ALMA Test Reports]. The pedestal of the ALMA VertexRSI telescope is a three-sided structure with heavy support beams at the three corners holding at the upper part the azimuth bearing (see Fig. 6.5.a). The room inside the pedestal contains a louvre and a fan to extract heat from the electrical equipment. The pedestal is insulated by a few centimetres thick foam covered with a protective metal skin. Of importance is the temperature uniformity of the three support beams (of approximately 2 m length) and by this the stability of the AZ-axis. Fig. 9.4 shows the temperature difference of beam [i] from the average temperature of the three beams, i.e. $\Delta T_i = T_i - \sum_{i=1,3} T_i / 3$. The temperature difference of the beams is within $\sim \pm 1^\circ\text{C}$, while the daily temperature variation of each support beam is of the order of 0.5°C . The daily thermal stability of the AZ-axis is estimated to be of the order of ~ 2 arcsec.

Temperature measurements and simultaneous inclinometer measurements of the pedestal of the fork-supported ASTE 10-m telescope are reported by Ukita et al. [2007]. On the stationary pedestal of 1.8 m height (H) and 2.7 m diameter they measured temperature differences ΔT_{N-S} in North-South direction between -3 and 6°C and temperature differences ΔT_{E-W} in East-West direction between -3 and 2°C . These temperature differences are correlated with a tilt of the pedestal of $\Theta_{N-S} = 1.07 \pm 0.04$ arcsec/ $^\circ\text{C}$ and $\Theta_{E-W} = 1.73 \pm 0.23$ arcsec/ $^\circ\text{C}$. Relations of this kind

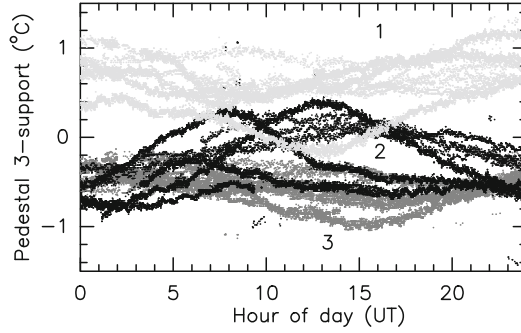


Fig. 9.4 Temperature uniformity of the pedestal of the VertexRSI ALMA 12-m prototype telescope pedestal. Shown are the temperature deviations of the 3 support beams (Fig. 6.a) from the average temperature. Each trace corresponds to a particular day [ALMA Test Data].

can be used for telescope control using as control parameter the temperature differences ΔT_{N-S} and ΔT_{E-W} of the pedestal.

Temperature measurements of pedestals and other telescope supports were made in order to investigate height changes (ΔH), and thus thermal path length variations of telescopes used for interferometry and VLBI. These measurements are explained in Section 9.1.4.

9.1.2 The Alidade

Many cm-wavelength radio telescopes and a few mm-wavelength radio telescopes have a rotating alidade supporting the elevation structure, a central hub or secondary focus cabin, the BUS and the quadripod and subreflector. Many alidades are built from A-towers as seen in Picture 1.2 and Picture 1.3 of the Effelsberg and GBT 100-m telescope. However, rectangular alidades with triangular upper towers (for instance the SRT 64-m telescope) or ‘broken’ alidades (for instance the Cambridge MERLIN 32-m telescope, Fig. 9.9.a) are also used. The alidade is made of steel beams. To reduce thermal effects the alidade is usually painted white (TiO_2 paint), while some alidade beams are also insulated. The thermal behaviour of several alidade (and fork) structures has been reported, in more or less detail (Table 9.2).

The influence of the thermal expansion of an alidade on the position of the EL-axis is illustrated in Fig. 9.5.a for a tilt¹ along the EL-axis ($\Delta \epsilon_1$) and in Fig. 9.5.b for a tilt perpendicular to the EL-axis ($\Delta \epsilon_2$). With $\langle T_{A1} \rangle$ and $\langle T_{A2} \rangle$ the average temperature of the A_1 and A_2 -tower and B the separation of the A-towers, the tilt

¹ The telescopes explained in this Chapter have an alt-azimuth mount with AZ-axis and EL-axis and pointing errors in azimuth and elevation direction, ΔA and ΔE . The misalignments $\Delta \epsilon_1$, $\Delta \epsilon_2$, $\Delta \epsilon_\Sigma$, $\Delta \alpha$, Δ of the telescope axes are called tilt errors since they may not appear directly as pointing error, although $\Delta A = f_A(\Delta \epsilon_1, \Delta \epsilon_2, \Delta \epsilon_\Sigma, \Delta \alpha, \Delta)$ and $\Delta E = f_E(\Delta \epsilon_1, \Delta \epsilon_2, \Delta \epsilon_\Sigma, \Delta \alpha, \Delta)$.

Table 9.2 Reported Thermal Behaviour of Alidade and Fork Support Structures.

Telescope	Reflector Diameter [m]	Reference
Alidade Structures		
JCMT (in astrodome)	15	www.jach.hawaii.edu/JCMT/telescope Coulson & Sandell [1996]
Medicina	32	Ambrosini et al. [1996]
Cambridge	32	Bayley et al. [1994]
Effelsberg	100	priv. comm.
GBT	100	www.nrao.edu/GBT (PTCS reports)
Fork Structures		
ALMA VertexRSI/AEC	12	Mangum et al. [2006], ALMA reports
IRAM	15	Greve [1992], Greve et al. [1992]
VLA	25	Janes [1991]
Green Bank	43	von Hoerner [1975 b] polar axis, declination fork

along the EL-axis is

$$\Delta \varepsilon_1 \approx \Delta L/B \approx \alpha L \Delta T/B \approx \alpha L (< T_{A1} > - < T_{A2} >)/B \quad (9.1)$$

with α the CTE of steel. The tilt $\Delta \varepsilon_1$ along the EL-axis results in a pointing error that is not seen by the encoders (E_1 and E_2 in Fig. 9.5.a).

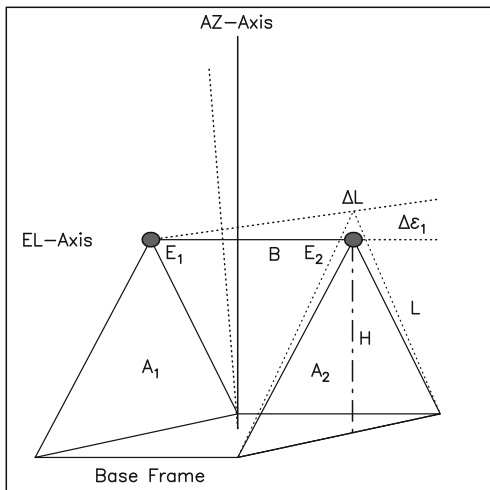


Fig. 9.5.a The alidade consists of the base frame and the A-towers A_1 , A_2 with interconnections, separated by the distance B . The differential thermal expansion ΔL ($\approx \Delta H$) causes a tilt $\Delta \varepsilon_1$ along the EL-axis. E_1 and E_2 are the EL bearings and the encoders.

A temperature difference between the front (A_f) and the rear (A_r) of the A-towers, as shown in Fig. 9.5.b, causes a differential expansion ΔL that results in a tilt $\Delta \varepsilon_2$ perpendicular to the EL-axis (elevation nodding). There occurs in addition

a rotation of the top of the A-towers ($A-B \rightarrow A'-B'$: $\Delta\epsilon_{\text{rot}}$) with an associated rotation of the elevation encoders ($E \rightarrow E'$). The total tilt perpendicular to the EL-axis (cross elevation error) is $\Delta\epsilon_{\Sigma} = \Delta\epsilon_2 + \Delta\epsilon_{\text{rot}}$. This tilt is discussed in detail by Ambrosini et al. [1996] for the Medicina 32-m telescope.

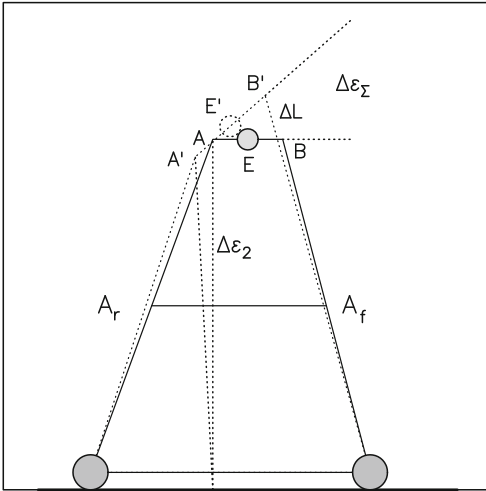


Fig. 9.5.b The differential thermal expansion ΔL between the front (A_f) and the rear (A_r) of the A-tower causes a tilt $\Delta\epsilon_2$ perpendicular to the EL-axis and a rotation of the top of the alidade, with an associated encoder (E) error. The total tilt perpendicular to the EL-axis is $\Delta\epsilon_{\Sigma} = \Delta\epsilon_2 + \Delta\epsilon_{\text{rot}}$.

From the early beginning of operation of large telescopes, like the Effelsberg 100-m telescope and the NRAO Green Bank telescopes, temperature measurements of the alidade structures have been made with the intention of understanding their general thermal behaviour and in particular temperature induced pointing errors. An investigation of the thermal behaviour of the 140-ft (43-m) NRAO telescope was made by von Hoerner and his associates. The now obsolete 43-m telescope has an equatorial mount with polar axis allowing rotation in right ascension and a fork that carries the reflector and allows a tilt in declination². The measurements with temperature sensors and inclinometers resulted in the decision to insulate the polar shaft and the fork arms with 8 cm sprayed-on foam and to cover several parts of the building platform with heat pads. The pointing, at the time 1976–1977, was improved by a factor 2 in hour angle and a factor 3 in declination to ~ 6 arcsec (rms) for both axes [von Hoerner 1975 b].

The early investigation of the Effelsberg 100-m telescope resulted in the permanent installation of temperature sensors throughout the telescope structure as shown in Fig. 2.4, and the installation of inclinometers at the level of the elevation bearings. An early result of the investigation [Schmitz-Görtz 1973] indicated that the base frame (Fig. 9.5.a), which was painted blue (Picture 1.2), had during the day a 5 to 10°C higher temperature than the other members of the alidade, which are painted white. It was decided to paint the base frame white and it was reported that

² For a picture of the telescope see www.nrao.edu/telescopes/43m, or Baars [2007].

the ‘thermal screaming’, occasionally heard during large and fast ambient air temperature variations, had then disappeared. Further work concentrated on the derivation of useful correlations between alidade temperatures, inclinometer readings and pointing errors. However, only some success was achieved.

Figure 9.6 shows a temperature measurement of the A–towers of the Effelsberg 100–m telescope, made during a winter day (Feb) and a summer day (Jun), 1996. The telescope was in stationary position and pointed at zenith, the sky was clear. The figure shows that the temperature of the exposed alidade follows the temperature of the ambient air (see also Fig. 9.32.a) though with an indication of a cooler alidade during the night (winter) because of cooling towards the sky. The temperature uniformity is good during the night with $\text{rms}(T_{A1})$ and $\text{rms}(T_{A2})$ below $\sim 0.5^\circ\text{C}$ while during the day this value may reach 1.5°C . For the alidade height of $H = 50\text{ m}$ (Fig. 9.5.a) the daily temperature change of 10 to 20°C introduces a change of the alidade height of $\Delta H \approx 6$ to 12 mm/day [Nothnagel et al. 1995]. With $T_0 = 20^\circ\text{C}$ as reference temperature and $T_A(t)$ the ambient air temperature, the change in height is $\Delta H = \alpha H (T_A(t) - T_0)$ and the corresponding phase delay is easily calculated for reduction of VLBI observations.

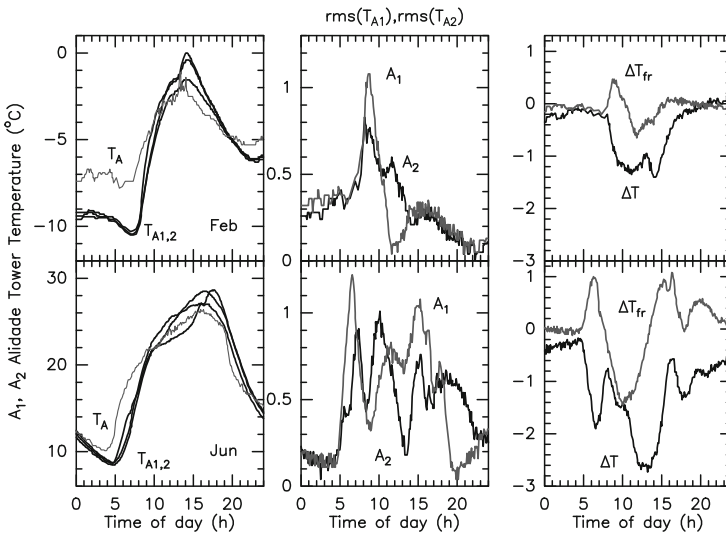


Fig. 9.6 Temperatures of the Effelsberg alidade (A–towers A_1, A_2). Left Panel: $T_{A1,2}$ temperatures of the A–towers and of the ambient air, T_A . Middle Panel: rms value of tower A_1 and tower A_2 . Right Panel: temperature difference of tower A_1 and tower A_2 : $\Delta T = \langle T(A_1) \rangle - \langle T(A_2) \rangle$, and temperature difference of front and rear side: $\Delta T_{fr} = \langle T(A_f) \rangle - \langle T(A_r) \rangle$ [Data MPIfR Effelsberg, Germany].

The temperature differences between the A–towers and between the front and rear of the towers may reach 2 to 3°C , with a tendency of small differences during the night. Significant changes of these temperature differences occur during morning

and afternoon due to larger temperature changes of the ambient air (Fig. 4.9) and the influence of sunrise and sunset. The difference of the average temperature of the A_1 -tower and A_2 -tower, i.e. $\langle T_{A_1} \rangle - \langle T_{A_2} \rangle$, and between the front and rear, i.e. $T_A(\text{front}) - T_A(\text{rear})$, measured during 24 days in winter and summer are shown in Fig. 9.7. For the investigated period there are maximum temperature differences between the A-towers of $\sim \pm 4^\circ \text{C}$, occurring mainly during morning and evening. The temperature difference between the front and rear side of the alidade towers was a factor 2 smaller.

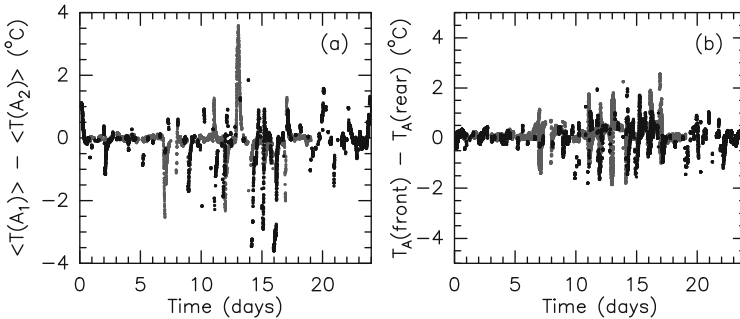


Fig. 9.7 (a) Temperature difference between the Effelsberg alidade towers A_1 and A_2 , this temperature difference may cause a pointing error along the EL-axis. (b) Temperature difference between the front and rear of the alidade towers, this temperature difference may cause a cross elevation pointing error. The temperature measurements were made during the time of radio observations [Data MPIfR Effelsberg, Germany].

A thermal study of the A-towers of the Medicina 32-m telescope (Italy) is reported by Ambrosini et al. [1996]. Some agreement exists between temperature measurements of the A-towers and inclinometer measurements near the elevation axis, as reproduced in Fig. 9.8, however, the use of the temperature data in FEM calculations for prediction of the corresponding pointing errors seems not to be trivial. The shown agreement between inclinometer measurements and predictions from temperature measurements is obtained if the FEM calculations also take into account in a semi-empirical way the temperature gradients across the alidade beams (reported to be of the order or 3°C despite the good thermal conductivity of steel), and the associated rotation of the inclinometer platforms. Ambrosini et al. conclude from their study that:

- the thermal shields of individual beams [thin plates] can actually worsen the situation if the shields lower the natural air convection, which is very efficient in minimizing thermal gradients, in open frame structures like our radio telescope
- a simple FEA model, taking into account only the overall lengthening of the beams, considered at uniform but different temperatures, fails to explain the observed tilts with sufficient accuracy, although qualitatively there is reasonable agreement.

- relatively large thermal gradients are observed across the sections of some beams [of the A-towers], and taking them into consideration (with an empirically determined rotation coefficient) improves the modelling of the tilts [of the A-towers] considerably,
- horizontal beams [of the alidade] can contribute very substantially to the tilt, contrary to some naive expectations.

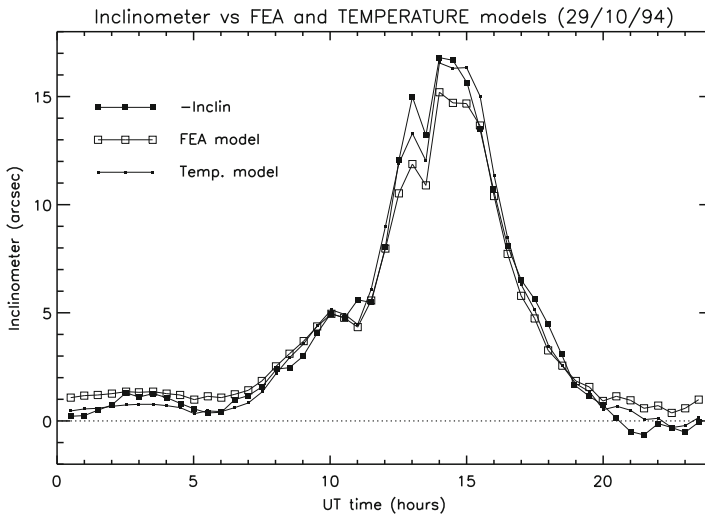


Fig. 9.8 Medicina 32-m telescope. Inclinometer measurements (top curve) compared with predictions from FEM calculations (lower curve) and from a temperature model taking into account temperature gradients across the alidade beams (middle curve). Clear sky after 11 hour UT, with some clouds for 1/2 hour at 13 UT [From Ambrosini et al. (1996), Courtesy Astrophys. Space Science].

Bayley et al. [1994] report a successful application of temperature measurements of the alidade of the Cambridge MERLIN 32-m telescope (UK). The thermal time constant of the alidade beams is 3 to 4 hours while those of the thinner BUS members is of the order of 20 minutes. It was found that temperature differences of $\sim 6^\circ\text{C}$ occur between the front (1, 3) and rear (2, 4) of the inclined alidade beams, shown in Fig. 9.9.a, which have cross sections of $\sim 0.5\text{ m} \times 0.5\text{ m}$. This temperature difference is due to sunshine ($\sim 5^\circ\text{C}$ during sunrise, with the upper side warmer than the back) and virtually disappears at night ($\sim 1.5^\circ\text{C}$, with the upper side cooler than the back). The measurements indicated a pointing error in elevation of $\Delta\epsilon_\Sigma/\Delta T \approx 10\text{ arcsec}/^\circ\text{C}$ with the temperature difference ΔT measured between T_1 and T_2 , T_3 and T_4 (Fig. 9.9.a). The measurements $T_1 - T_2$, $T_3 - T_4$ combined with relations derived from FEM calculations could reduce the pointing error from $\sim 20\text{ arcsec}$ to $\sim 6\text{ arcsec}$, even during sunshine. This study obtained the important result that the vertical beams of the alidade have a significantly smaller influence than the inclined beams (because of larger insolation and a stronger coupling to the cold sky),

which is the reason to use primarily the temperature sensors on the inclined beams for control. Fig. 9.9.b illustrates the improvement of the pointing in elevation (cross elevation error) when using these temperature measurements.

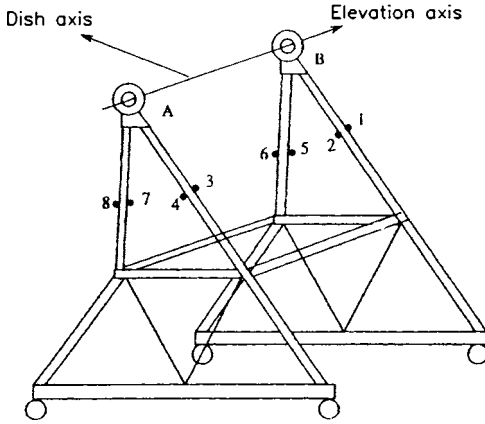


Fig. 9.9.a Cambridge MERLIN 32-m telescope, alidade with temperature sensors 1–8 [From Bayley et al. (1994), Courtesy Astron. Astrophys.].

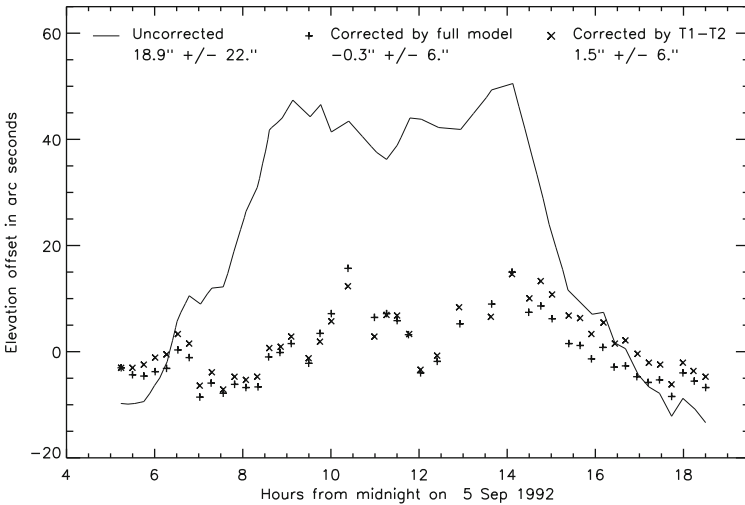


Fig. 9.9.b Cambridge MERLIN 32-m telescope. Measured pointing offset in elevation (solid line) and correction (crosses) using the measured temperature difference $T_1 - T_2$ [From Bayley et al. (1994), Courtesy Astron. Astrophys.].

The JCMT 15-m telescope is protected by an astrodome (Fig. 3.3) with the slit covered by a membrane and ventilation of the inside air. The telescope has an A-type alidade mount. As Coulson & Sandell [1996] report, a differential warming of the front and back legs of the A-towers due to solar radiation transmitted through the membrane causes an elevation pointing error (nodding error). On the web-site³ is shown a figure, reproduced in Fig. 9.10, which illustrates that the temperature difference $T_f - T_b$ between the front and back legs of the alidade is correlated with the time of day and the solar illumination of the membrane. If the front legs are 1°C warmer than the back legs the radio beam moves 6.5 arcsec higher in elevation, as expected from engineering calculations. The readings of 2 temperature sensors on each A-tower leg (8 sensors in total) are used to correct this error via the pointing model. The thermal behaviour of the astrodome enclosed telescope was investigated during the design by Bregman & Casse [1985] in model calculations and a similar behaviour was predicted.

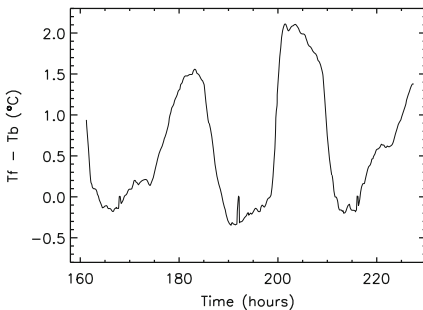


Fig. 9.10 JCMT 15-m telescope. Temperature difference between the alidade front legs (side of the astrodome slit) and back legs $T_f - T_b$ [From J. Wouterloot (2005), Courtesy JCMT].

Finally, an illustrative example of EL-axis nodding of the alidade supported JPL 34-m antenna is published by Gawronski et al. [2000]. On this antenna several inclinometers were installed on the alidade for measurement of the level of the azimuth rail. When having parked the antenna for 2 days, during the night the measured EL-axis nodding was ~ 2 arcsec while during the day and sunshine the EL-axis nodding reached ~ 15 arcsec within approximately 3 hours' time. It is not explained which amount of this nodding appears as a pointing error.

The GBT 100-m telescope, commissioned around 2002, and the SRT 64-m telescope and LMT/GMT 50-m telescope, under construction, have and will have temperature sensors in order to understand and control the focus and pointing variations and to provide information for control of the active reflector surface. Some measurements of the GBT have been published by Constantakis, Balser, Prestage and others [[http://www.nrao.edu/GBT PTCS reports](http://www.nrao.edu/GBT_PTCS_reports)] and mentioned by Nikolic et al. [2007] and Prestage et al. [2009]. However, a full account is not yet given. Details of the plans for the SRT can be found under <http://www.ca.astro.it/srt/project-book>, for the LMT/GMT under <http://www.lmtgtm.org/telescope>.

³ <http://www.jach.edu/JCMT/telescope>

9.1.3 The Fork Support

Several centimetre and mm-wavelength telescopes have a pedestal, a fork support structure and a secondary focus cabin/platform which supports the BUS and the quadripod with subreflector (Fig. 1.1.c).

Figure 9.11 shows the structure of a fork and the tilt errors $\Delta\epsilon_1$, $\Delta\epsilon_2$, $\Delta\alpha$ and path length errors ΔL_1 , ΔL_2 that this mount may introduce. The fork rests on a stationary pedestal or on a transporter that can be moved to displace interferometer telescopes. The pedestal holds at its upper part the azimuth bearing. The fork consists of the traverse and the right and left fork arm. At the upper part of the fork arms are the elevation bearings, which define the EL-axis. A tilt of the pedestal or the ground produces a tilt $\Delta\alpha$ of the AZ-axis. A differential thermal expansion of the fork arms causes a tilt $\Delta\epsilon_1$ along the EL-axis, a temperature difference between the front and rear of the fork arms causes a tilt $\Delta\epsilon_2$ perpendicular to the EL-axis (cross elevation error). Important for interferometer/VLBI operation is a change of the pedestal temperature that causes a variation of the path length L_1 , and a change of the fork arm temperature that causes a variation of the path length L_2 .

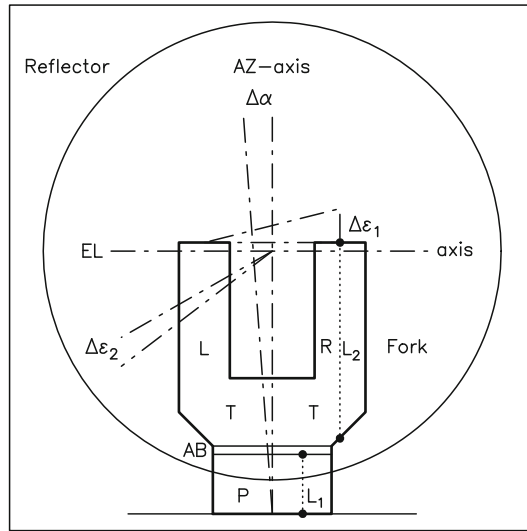


Fig. 9.11 Fork support and associated tilt errors $\Delta\epsilon_1$, $\Delta\epsilon_2$, $\Delta\alpha$. P: pedestal, T: traverse of the fork, R and L: right and left fork arm, AB: azimuth bearing. L_1 is the path length of the pedestal, L_2 the path length of the fork arms.

A fork structure is made of steel. From the geometry of the fork, shown in Fig. 9.11, it is evident that the tilt error $\Delta\epsilon_1$ along the EL-axis is

$$\Delta\epsilon_1 \approx \Delta L_2/B \approx \alpha L_2 \Delta T_{LR}/B \approx \alpha L (< T_L > - < T_R >)/B \quad (9.2)$$

where $\Delta T_{LR} = \langle T_L \rangle - \langle T_R \rangle$ is the temperature difference between the left and the right fork arm, of length L_2 and separation B . For many constructions is $L_2 \approx B$ so that for the CTE of steel follows $\Delta \varepsilon_1 \approx 2.5 \Delta T$ [arcsec]. The tilt error $\Delta \varepsilon_1$ is not seen by the elevation encoders at the upper part of the fork arms. In a similar way as discussed for the alidade, a temperature difference between the front (f) and the rear (r) of the fork causes a cross elevation tilt error $\Delta \varepsilon_2$ proportional to the temperature difference $\Delta T_{fr} = T_f - T_r$. However, here a rotation of the top of the fork arms will also occur so that an empirical relation between ΔT_{fr} and $\Delta \varepsilon_2$ is difficult to establish without support from FEM calculations.

Estimates show that for a temperature difference $\Delta T_{LR} \approx 1^\circ \text{C}$ between the fork arms the tilt error is $\Delta \varepsilon_1 \approx 1$ to 2 arcsec (Eq.(9.2)). Evidently, in order to have temperature differences of this value, or smaller, the fork structure needs insulation of a simple or more refined type. Simple insulation is foam, at the outer surface covered with a thin protective metal (aluminium) plate. A more refined insulation based on tests and thermal model calculations is used on the IRAM/SEST 15–m telescopes (see Figs. 11.15, 11.16). Here the thermal protection consists of hard foam (5 cm) attached with plastic screws to the fork, a reflective layer of aluminium foil, an air gap (2 cm) and a radiation shield consisting of an aluminium plate covered on the inside with aluminium foil. The outer surface of the radiation shield is anodised. On the SEST telescope, the air in the gap is ventilated, however, this ventilation is not used on the Plateau de Bure telescopes since the air gaps fill up with snow and ice.

With the exception of a few temperature measurements of the VLA telescopes (Picture 1.5) and their fork structures reported by Janes [1991] there are no detailed data of thermally unprotected fork structures for comparison. The thermal behaviour of unprotected fork structures should however be similar to vertical beams of alidade structures. Detailed temperature measurements are available of the fork of the VertexRSI (and AEC) ALMA 12–m prototype telescope. Both fork structures have a relatively simple insulation of soft or hard foam and a metal skin cover. Some temperature measurements of the fork of the first IRAM 15–m telescope were made during its commissioning.

The VertexRSI ALMA 12–m prototype telescope was tested at the VLA site, New Mexico (USA), the measurements shown in Fig. 9.12 were made from 1st to 10th May, 2004. During the day, the telescope was parked with the reflector facing south at a low elevation so that the fork was aligned in the direction East–West, during the night, the telescope was used for observations. Fig. 9.12.a shows the average temperature of the eastern (Left) and western (Right) fork arm $T_F = (\langle T_L \rangle + \langle T_R \rangle)/2$ together with the ambient air temperature T_A . The days were clear. The temperature uniformity of the fork was $\text{rms}(T_F) \lesssim 1^\circ \text{C}$. Fig. 9.12.b shows the temperature difference $\Delta T_{LR} = \langle T_L \rangle - \langle T_R \rangle$ between the left and right fork arm, Fig. 9.12.c shows the temperature difference $\Delta T_{fr} = \langle T_f \rangle - \langle T_r \rangle$ between the front (facing South during the day) and the rear (facing North during the day) of the fork. It is seen that $\Delta T_{LR} \lesssim 1.5^\circ \text{C}$ and $\Delta T_{fr} \lesssim 1^\circ \text{C}$. While for the tilt along the EL–axis the proportionality $\Delta \varepsilon_1 \propto \Delta T_{LR}$ exists, only FEM calculations may give a useful relation between ΔT_{fr} and the cross elevation tilt $\Delta \varepsilon_2$. Ukita

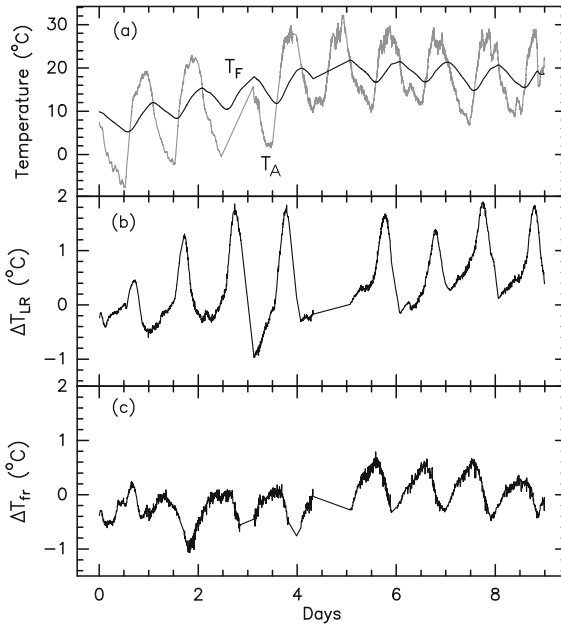


Fig. 9.12 VertexRSI ALMA 12-m telescope. (a) Average temperature of the left and right fork arm T_F and the ambient air temperature T_A . (b) Temperature difference between the left and right fork arm ΔT_{LR} , (c) Temperature difference ΔT_{fr} between the front and rear of the fork arms [ALMA Test Data].

et al. [2004] found on the ALMA-J 12-m prototype telescope a useful correlation between the temperature difference of the front and back of the fork arms and the pointing error in elevation.

Evidently, constant gradients ΔT_{LR} and ΔT_{fr} produce constant tilts while the differentials $\partial(\Delta T_{LR})/\partial t$ and $\partial(\Delta T_{fr})/\partial t$ produce a change of the tilt/pointing $\partial(\Delta \varepsilon_1)/\partial t$ and $\partial(\Delta \varepsilon_2)/\partial t$ that must be determined and corrected through pointing observations. Fig. 9.13 shows the temperature differences ΔT_{LR} and ΔT_{fr} measured on the VertexRSI ALMA 12-m prototype telescope⁴ displayed as function of the hour of the day. The largest change of ΔT_{LR} occurs during sunrise and sunset, of the order of $\partial(\Delta T_{LR})/\partial t \approx \sim 0.3^\circ \text{C/h}$, introducing a similar time-dependent change of the tilt/pointing. During the night, the temperature differences ΔT_{LR} and temperature changes $\partial(\Delta T_{LR})/\partial t$ are very small. The temperature differences ΔT_{fr} and the temperature changes $\partial(\Delta T_{fr})/\partial t$ are very small during the whole day.

Ukita et al. [2007] report for the ASTE 10-m telescope a good correlation between inclination changes (measured with an inclinometer) along (LR) and perpendicular (fr) to the fork arms and changes of corresponding temperature gradients in

⁴ Temperature measurements made during the same time on the ALMA AEC 12-m prototype telescope are similar to those shown in Fig. 9.12 and Fig. 9.13.

the fork. The change of the inclination of the fork with temperature is $\Delta\epsilon_1/\Delta T_{LR} = \Phi_y = 0.4 \pm 0.10 \text{ arcsec}/^\circ\text{C}$ and $\Delta\epsilon_2/\Delta T_{fr} = \Phi_x = 1.54 \pm 0.03 \text{ arcsec}/^\circ\text{C}$. Correlations of this kind can be used for telescope control.

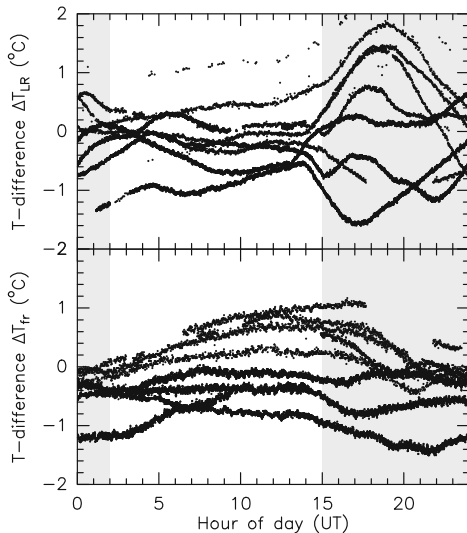


Fig. 9.13 VertexRSI ALMA 12–m telescope. Upper panel: Temperature difference between the left and right fork arm ΔT_{LR} , lower panel: temperature difference between the front and rear of the fork arms ΔT_{fr} . Each trace represents a particular day of measurement. The shaded area is day time [ALMA Test Data].

Figure 9.12 shows quasi–periodic variations of the ambient air temperature of amplitude ΔT_A and quasi–periodic variations of the fork temperature of the VertexRSI ALMA telescope of amplitude ΔT_F . The ratio $\gamma = \Delta T_F/\Delta T_A$ is an indication of the efficiency of the fork insulation. The ratios γ measured on the VertexRSI and AEC ALMA prototype telescopes and the IRAM 15–m telescope are summarized in Table 9.3.

Table 9.3 Insulation Efficiency γ of Fork Structures.

Telescope	γ Fork	γ Fork
	Traverse	Arms (L/R)
VertexRSI ALMA	0.20	0.24/0.26
AEC ALMA	0.22	0.22/0.14
IRAM 15–m	–	0.28 – 0.32

The fork of the IRAM/SEST 15–m telescopes has a sophisticated thermal insulation consisting of foam, an air gap and a radiation shield. The fork arms are open

at the traverse so that warm air of the pedestal or of the transporter machinery can move into the fork arms, perhaps in an asymmetric way (Fig. 11.16).

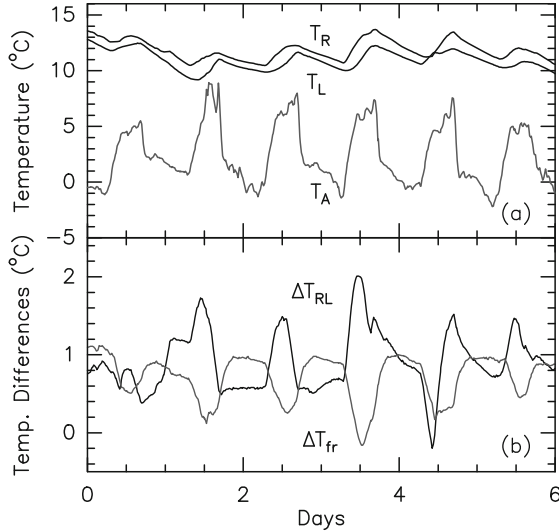


Fig. 9.14 IRAM 15–m telescope. (a) Average temperature of the left T_L and right T_R fork arm, T_A is the temperature of the ambient air. (b) Temperature difference between the Left and Right fork arm $\Delta T_{RL} = T_R - T_L$ and between the front and rear of the fork $\Delta T_{fr} = T_f - T_r$.

Figure 9.14.a shows for one IRAM 15–m telescope the measured temperature of the Right (R) and Left (L) fork arm together with the temperature of the ambient air. The fork arms are significantly warmer than the ambient air as a result of internal heat supply. Fig. 9.14.b shows the temperature difference ΔT_{LR} between the left and the right fork arm and between the front and the rear of the fork ΔT_{fr} . It is seen that the temperature differences are 1 to 2°C as intended and predicted in model calculations during the design study of the thermal protection. The rate of temperature change is $\partial(\Delta T_{LR})/\partial t \approx \partial(\Delta T_{fr})/\partial t \lesssim 0.5$ to 1°C/h so that the tilt error $\Delta\varepsilon_1$ (and $\Delta\varepsilon_2$) changes by less than 1 to 2 arcsec/h. Fig. 9.15 shows that the temperature differences change mainly during the day.

As evident from Fig. 9.14.a, the IRAM 15–m telescope fork has daily temperature oscillations of the steel plates of amplitude $\Delta T_F \approx 1^\circ\text{C}$. The energy ΔQ oscillating within 24 hours in the upper section of one fork arm is of the order of

$$\Delta Q = M_u \mathcal{C} \Delta T_F \approx \pm 2200 \text{ [kJ]} \tag{9.3}$$

with $M_u \approx 5$ ton. This amount of energy is absorbed (+) by the steel plates during the day (≈ 12 hours) and emitted (–) towards the environment during the night (≈ 12 hour). The average energy flow $\langle q \rangle$ through the thermal protection is $\langle q \rangle \approx \Delta Q/(12 \text{ h}) \approx \pm 50 \text{ W}$. The surface area of the upper section of the fork arm is

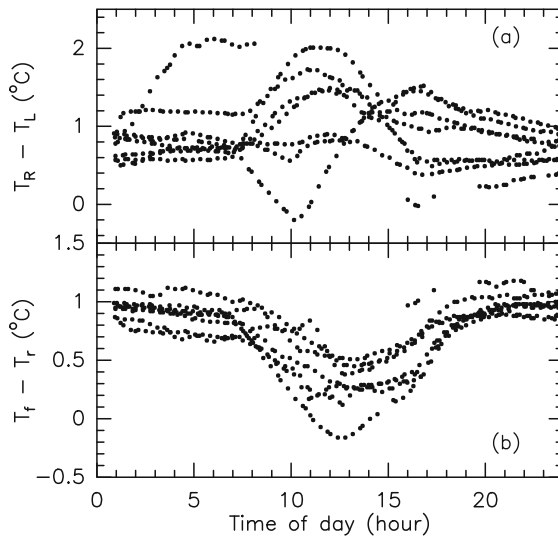


Fig. 9.15 IRAM 15-m telescope. Right-Left (a) and Front-Rear (b) temperature difference measured during six days. These figures determine the rate of change of the temperature differences.

approximately $S \approx 15 \text{ m}^2$ so that the average energy flow through 1 m^2 surface area is $q_s = \langle q \rangle / S \approx \pm 3 \text{ W/m}^2$.

An 8-hour recording, starting in the late evening when the change of ambient air temperature is largest, of the pointing and focus stability of the six IRAM 15-m interferometer telescopes is shown in Fig. 9.16. During the time of observation the pointing in AZ and EL direction did not change by more than 10 arcsec and the focus was stable within 0.2 mm, for all telescopes.

Finally, a measurement comparable to the measurement of the Medicina 32-m telescope alidade [Ambrosini et al. 1996] with inclinometer and temperature sensors (Fig. 9.8) was made on the fork of the VertexRSI ALMA 12-m telescope using an API 5 DOF SystemTM. As illustrated in Fig. 9.17, the laser emitter was installed on the base of the fork traverse while the detector for x, y, α, β -measurements was installed just below the elevation bearing at the upper part of the fork arm. The displacements $\Delta x, \Delta y$ and tilts $\Delta \alpha, \Delta \beta$ (pitch and yaw) are measured with respect to the laser beam, the distance change Δz between the laser emitter and the target is measured with the same laser beam in interferometer mode. The displacements and tilts recorded during two consecutive days are shown in Fig. 9.18 (for more data see Greve & Mangum [2008]). The regular and repeatable nature of the measured displacements and tilts is believed to represent a thermal effect. However, a FEM calculation using the temperature measurements of 14 sensors installed in the fork could not reproduce the $\Delta x, \Delta y, \Delta \alpha$ and $\Delta \beta$ measurements, even when taking the calculated rotations of the fork plates into account. This failure illustrates the complexity of using similar measurements for telescope control.

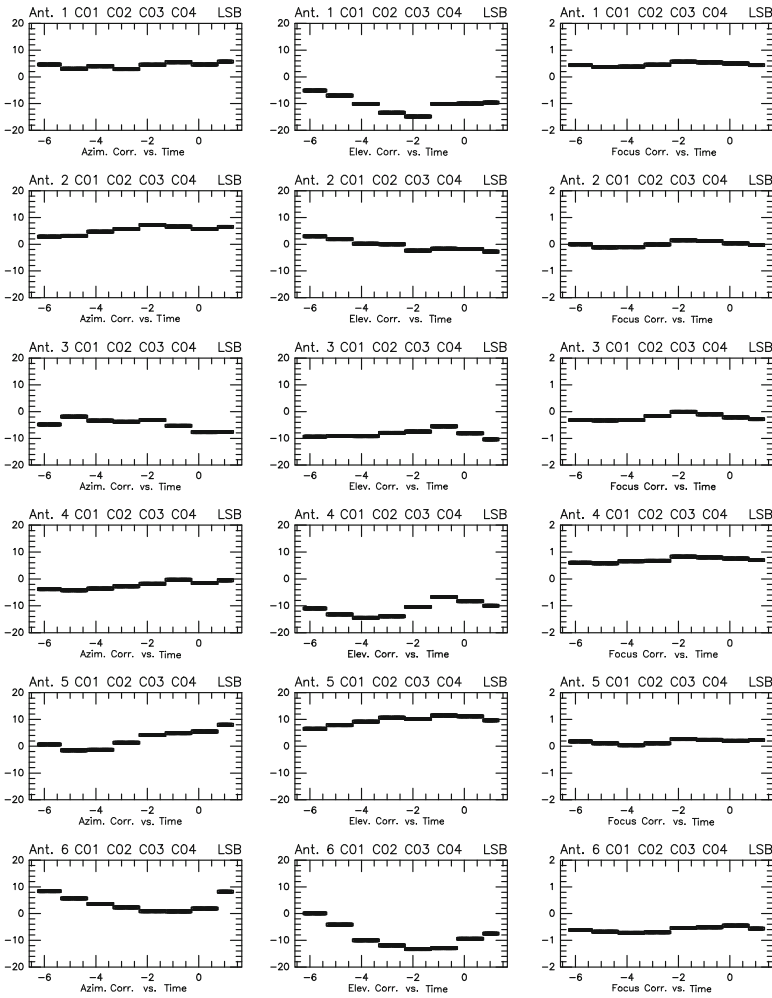


Fig. 9.16 IRAM 15-m interferometer telescopes. Pointing (arcsec) and focus (mm) corrections (from left to right) applied on the six interferometer telescopes (from top to bottom), during an observation lasting ~ 8 hour. The steps in the recordings indicate the time of pointing, focus and phase calibration of the array [Courtesy R. Neri, IRAM, France].

9.1.4 Path Length Variations of Telescope Supports (for radio interferometer and VLBI arrays)

A telescope has with respect to a geodetic coordinate system a reference point and a reference height, as illustrated in Fig. 9.19. The reference height is for instance the position of the EL-axis (EL, H_{EL}) or the receiver (R, H_R). The reference height is unimportant in single telescope observations. However, the reference height and

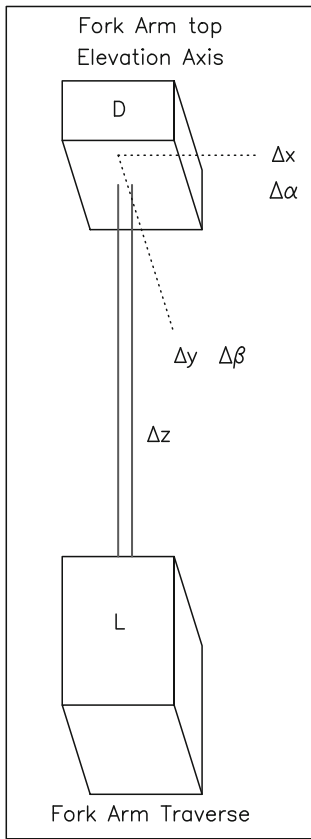


Fig. 9.17 Laser interferometer measurement of the path length variation $\Delta z = \Delta L_2$ of a fork arm (Fig. 9.11) and position measurement of the base of the elevation bearing (displacement: Δx , Δy , tilt: $\Delta \alpha$, $\Delta \beta$) using an API 5 DOF systemTM. L is the laser emitter, D the position detector or target [From Greve & Mangum (2008), Courtesy IEEE. Ant. Propag. Magazine].

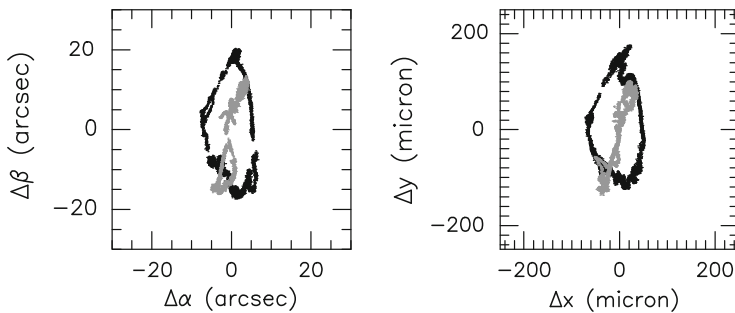


Fig. 9.18 VertexRSI ALMA 12-m prototype telescope. Linear displacement Δx , Δy and tilt measurement $\Delta \alpha$, $\Delta \beta$ of the elevation bearing platform with respect to the base of the fork traverse (Fig. 9.17), for two consecutive days. Grey scale: $\Delta \alpha$, $\Delta \beta$ measurement (scale indicated on the left side panel), black scale: Δx , Δy measurement (scale indicated on the right side panel). X and α : displacement and tilt perpendicular to the EL-axis (nodding); Y and β : along the EL-axis [From Greve & Mangum (2008), Courtesy IEEE Ant. Propag. Magazine].

especially the variation of this height is important in interferometer observations and Very Long Baseline Interferometer (VLBI) observations. Taking the receiver as reference, the path length changes $\Delta H_R[i]$ of the participating telescopes [i] introduce phase changes of the interferometer/VLBI array. In interferometer observations these instrumental phase changes (with phase changes from the atmosphere superimposed) are determined and corrected from regular observations of a phase calibration radio source (Fig. 9.16); in VLBI observations these phase changes are determined in the fringe finding procedure.

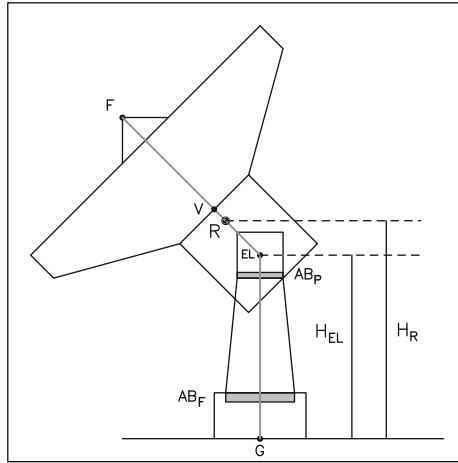


Fig. 9.19 Reference points and path lengths of a telescope used for interferometer or VLBI observations. AB_F : position of the AZ-bearing of a fork support, AB_P : position of the AZ-bearing of a pedestal support, EL: elevation axis of height H_{EL} , R: reference position of the receiver of height H_R , V: vertex of primary reflector, F: focus, G: ground.

The instrumental path length change ΔH_R , which may be a combination of the distance changes G–EL, EL–V, V–F (Fig. 9.19), is mainly due to thermal expansion of the telescope structure. The path length variation ΔL_1 (= G– AB_F) of the pedestal and ΔL_2 (= AB_F –EL) of the fork arm(s) (Fig. 9.11) was measured with a laser interferometer on the VertexRSI and AEC ALMA 12-m prototype telescopes [Mangum et al. 2006, Greve & Mangum 2008]. Fig. 9.20 shows that the measured path length variation ΔL_2 is due to the thermal expansion of the fork arm, i.e. $\Delta L_2 = \alpha L_2 \Delta T_F$. For the fork arm of $L_2 \approx 3$ m length, Fig. 9.20 gives $\Delta L_2/\Delta T_F/L_2 \approx 10 \mu\text{m}/\text{K}/\text{m}$ in agreement with the CTE of steel (Table 2.8). For interferometer telescope control, the path length variation can be calculated from the thermal expansion using the temperature variation of the pedestal (ΔT_P) and the fork (ΔT_F).

The path length variations measured in the same way within time intervals of 3 min, 10 min and 30 min are shown in Fig. 9.21 for the VertexRSI ALMA telescope, the values for the AEC ALMA telescope (ΔL_2) are similar [Mangum et al. 2006]. The 3-min interval is typical for wind induced deformations, the 30-min interval

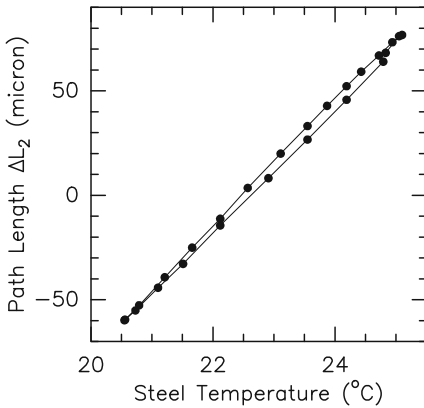


Fig. 9.20 VertexRSI ALMA prototype telescope. Correlation between the path length variation ΔL_2 and the steel temperature of the fork arm, illustrating the applicability of the law of thermal expansion. The measurements cover the time of one day [ALMA Test Data].

is typical for ambient air temperature and solar illumination induced variations. It is also a typical time between calibrations of the ALMA interferometer array. The measured rate of change $\partial(\Delta L_2)/\partial t$ of the fork arm is correlated with the rate of change of the ambient air temperature $\partial T_A/\partial t$, as illustrated by the solid lines in Fig. 9.21. The inserted rate of change $\partial T_A/\partial t$ is calculated for a daily cosine-form variation of T_A as discussed in Section 4.3.3.

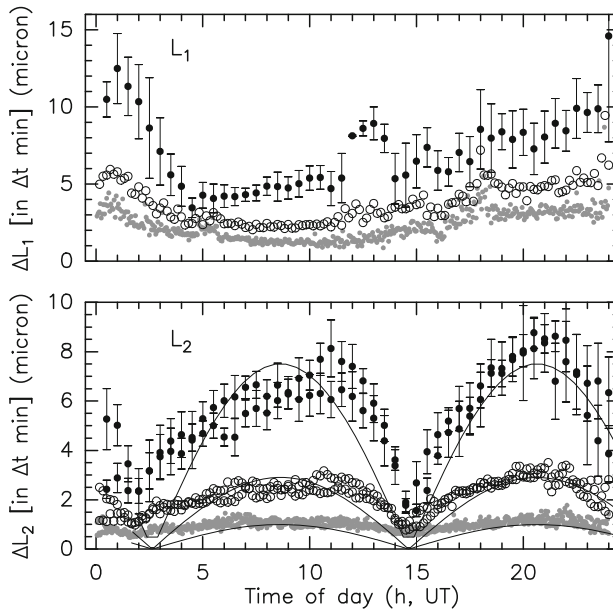


Fig. 9.21 VertexRSI ALMA prototype telescope. Path length variation ΔL_1 of the pedestal and ΔL_2 of the fork arm (see also Fig. 9.11) within time intervals of 3 min (grey dots), 10 min (open circles) and 30 min (solid dots). A similar result (L_2) is obtained for the AEC ALMA telescope [From Greve & Mangum (2008), Courtesy IEEE Ant. Propag. Magazine].

In a VLBI array the telescopes are not connected to a common oscillator and a phase calibration as for a connected interferometer array is not possible. For several VLBI telescopes the temperature sensitivity of the telescope support (pedestal, alidade) is experimentally established and used in the determination of baseline lengths [Nothnagel et al. 1995, Wresnik et al. 2006]. Carlsson [1996] and Wresnik et al. [2006] report temperature and expansion measurements of the 4.4 m diameter, 30 cm thick and 11.3 m high (H) concrete pedestal of the radome enclosed Onsala 20-m telescope equipped with 16 temperature sensors and an invar wire-inductive transducer system that measures the height variation of the pedestal [Johansson et al. 1996]. For 2001 the measured thermal expansion of the pedestal was $\Delta H/\Delta T_P = 2.5 \text{ [mm]}/25[^\circ\text{C}] = 0.1 \text{ mm}/^\circ\text{C}$ or $\Delta H/H/\Delta T_P \approx 0.01 \text{ mm/m/K}$. Similar measurements [Zernecke 1999] for 2001–2003 of the 8 m high (H) concrete pedestal of the open-air Wettzell 20-m telescope give $\Delta H/\Delta T_P = 0.15 \text{ mm}/^\circ\text{C}$ or $\Delta H/\Delta T_P/H \approx 0.02 \text{ mm/m/K}$. These CTE's are typical for concrete. A relation is published by Wresnik et al. [2006], based in essence on the thermal time constant of the pedestal for a fast (12 hours) and a slow (3 days) change of the ambient air temperature, which allows the prediction of the temperature of the pedestal T_P from the ambient air temperature T_A with the accuracy of 0.082°C (rms) for Onsala and 1.42°C (rms) for Wettzell. The corresponding accuracies in the prediction of the height changes are 0.07 mm (Onsala) and 0.13 mm (Wettzell). The precision and repeatability of VLBI baseline determinations has increased when using these corrections. The Effelsberg 100-m telescope is used for VLBI and a correction of the change of the reference height with temperature can be made in a similar way. Fig. 9.32.a below shows that the temperature of the alidade follows roughly the ambient air temperature. However, the deviations from a linear correlation are large so that actual temperature measurements of the alidade with the installed sensors are preferred for correction.

9.2 BUS Supports

A prerequisite of a stable BUS is a mechanically and thermally stable support of the BUS. In an alidade-supported telescope, like the Effelsberg 100-m telescope, the BUS support is the pyramidal elevation structure and the elevation cross beam structure (Figs. 2.4, 2.8). In a yoke-supported telescope, like the IRAM 30-m telescope, the BUS support is the yoke and especially the roof of the yoke (Fig. 2.9). In a fork-supported telescope, like the IRAM 15-m telescope, the BUS support is the central hub that is connected to the roof of the secondary focus cabin (Fig. 2.10). An important aspect of the thermal performance of a telescope is the temperature uniformity of the BUS support and of the BUS network itself. The thermal design aims at a small print-through of thermal deformations of the BUS support to the BUS network.

9.2.1 The (climatised) Yoke

The yoke structure is used on telescopes of 20 to 50 m reflector diameter, like for instance the IRAM 30-m telescope, the ESA Perth 35-m antenna, the Yebes 40-m telescope and in modified form on the LMT/GMT 50-m telescope. The yokes of these telescopes are box-like structures built from steel, painted white and occasionally covered with insulation. The earlier 14-m and 20-m diameter mm-wavelength telescopes built from aluminium are protected by a radome, a special thermal control of their yoke structure is not applied.

The yoke structure is schematically drawn in Fig. 9.22. The arms of the yoke are connected via the elevation bearings to the central tower/turret or the pedestal. The counterweights are at the lower part of the yoke arms. The BUS is attached to the roof of the yoke. A temperature difference ΔT_{LR} between the left and right yoke arm and temperature gradients ΔT_{UD} in the yoke arms in the direction Up-Down may deform the yoke roof $ABCD \rightarrow A'B'C'D'$, which may cause a print-through deformation of the BUS network. On the IRAM 30-m telescope it was found from temperature measurements of the yoke and the BUS and FEM calculations that a temperature gradient in the direction Up-Down ΔT_{UD} bends the yoke arms, which results in a bending of the yoke roof, a subsequent bending of the BUS membrane (Fig. 6.6) and an astigmatic deformation of the BUS network and reflector surface. The astigmatic reflector surface deformation was noticed in focus determinations as an elliptic out-of-focus beam (Fig. 12.8 and Greve et al. [1994]).

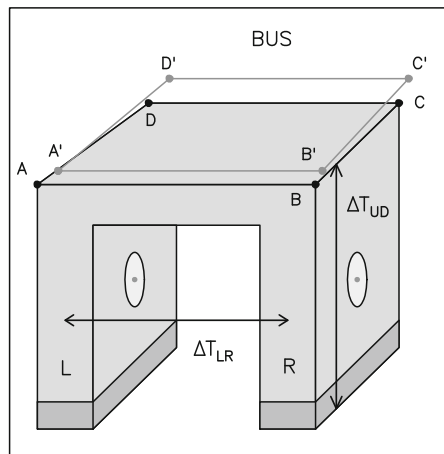


Fig. 9.22 View of a yoke with left (L) and right (R) yoke arm and counterweights at their ends. The BUS is attached to the yoke roof ABCD. A temperature difference ΔT_{LR} between the left and right yoke arm and a temperature gradient $\Delta T_{UD(L,R)}$ in the direction Up-Down in the left and right yoke arm deforms the base ABCD to $A'B'C'D'$.

Detailed temperature measurements are available for the yoke of the IRAM 30–m telescope; the location of temperature sensors is shown in Fig. 9.23.a and Fig. 9.23.b. The yoke of the IRAM 30–m telescope is insulated with a layer of foam with an aluminium sheet cover painted white with TiO_2 paint; the insulation front cover can be heated to prevent icing. The climatization of the BUS is controlled to a reference temperature of the yoke, measured close to the membrane (Fig. 2.5). A ventilation and heating system was installed in the yoke in recent years [Peñalver et al. 2002, Greve et al. 2005] to obtain a better temperature uniformity and smaller temperature gradients in the yoke arms (direction Up–Down). The yoke ventilation system consists of 4 fans installed near the roof of the yoke. The ventilation capacity of a fan is $4\,500\text{ m}^3/\text{h}$. The heating system is installed close to the counterweights, it can supply 6 kW. Heating is applied whenever the temperature measured near the counterweights falls 0.15°C below the reference temperature of the yoke.

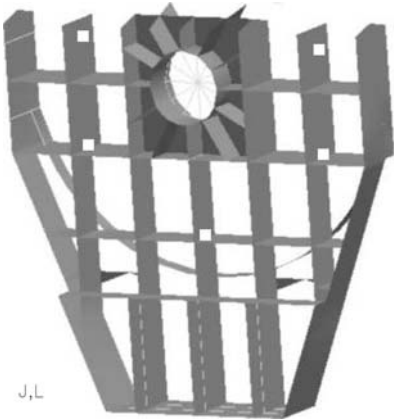


Fig. 9.23.a IRAM 30–m telescope. Location of temperature sensors (squares) in the yoke arms (J,L). The upper part contains the elevation bearing, the lower part the counterweight [From Bremer & Peñalver (2002), Courtesy SPIE].

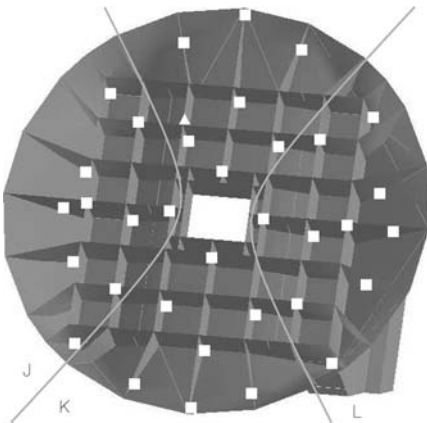


Fig. 9.23.b IRAM 30–m telescope. Location of temperature sensors (squares) in the yoke roof (J,K,L) [From Bremer & Peñalver (2002), Courtesy SPIE].

Figure 9.24.a to 9.24.f illustrate the temperature uniformity of the IRAM 30–m telescope yoke when using the recently installed ventilation/heating system. Important for possible mechanical deformations is the temperature uniformity of the yoke rms(T_Y) shown in Fig. 9.24.a, the temperature difference between the Left and the Right yoke arm ΔT_{LR} shown in Fig. 9.24.b, the temperature gradient in the direction Up–Down of the yoke arms (between the yoke roof and the corresponding counterweights) $\Delta T_{UD}(L,R)$ shown in Fig. 9.24.c–d, the temperature uniformity of the membrane rms(T_M) to which the BUS network is connected shown in Fig. 9.24.e, and the temperature difference between the base of the BUS and the membrane/roof of the yoke $T(BUS) - T(Y)$ shown in Fig. 9.24.f. The displayed measurements were recorded during 14 days in July and October 2004. It is seen that the temperature uniformity and the temperature gradients are around 0.5°C , compared to earlier values of $\sim 2^\circ\text{C}$ when the thermal control of the yoke was not installed.

The improvement of the thermal stability of the yoke by ventilation/heating is evident from Fig. 9.25. The figure shows the amplitude $\alpha_{2,2}$ (see Section 12.4.1) of astigmatism of the reflector surface as function of the hour of the day, calculated from a large number of temperature measurements under the condition of no ventilation/heating of the yoke (I), ventilation only (II) and ventilation and heating in operation (III). The maximum amplitude reduced from $\alpha_{2,2}(I)_{max} \approx 0.12\text{ mm}$ to $\alpha_{2,2}(II)_{max} \approx 0.075\text{ mm}$ and $\alpha_{2,2}(III)_{max} \approx 0.03\text{ mm}$ with a correspondingly cleaner radio beam and increase in gain of the telescope [Greve et al. 2005].

The story of the thermal improvement of the yoke is the story of the reduction of print–through of yoke deformations on an otherwise thermally stable BUS. Such a print–through between the central hub (steel) and the BUS network (then CFRP) was noticed during the initial design of the IRAM/SEST 15–m telescopes when the BUS was intended to be built exclusively from CFRP tubes [P. Raffin, priv. comm.]. A print–through is reduced on the VertexRSI ALMA 12–m telescope by using a thermally stabilized invar ring support of the BUS and on the AEC ALMA 12–m telescope by using a CFRP BUS support. Evidently, the thermal design of a BUS support needs as much attention as the thermal design of the BUS network itself.

9.2.2 The Central Hub

Large cm–wavelength radio telescopes like the Effelsberg 100–m telescope (Fig. 2.4) have a central hub (secondary focus cabin) that is however not a supporting structure of the BUS. The BUS of the Effelsberg telescope is supported by the pyramidal elevation structure and the elevation cross beams (Fig. 9.29.a). The thermal state of the central hub (secondary focus cabin) has little influence on the thermal state of the BUS. The situation is different for fork–supported mm/sub–mm wavelength telescopes.

Several fork–supported telescopes use a central hub to which the BUS network is connected. The central hub itself is connected (bolted) to the secondary focus cabin,

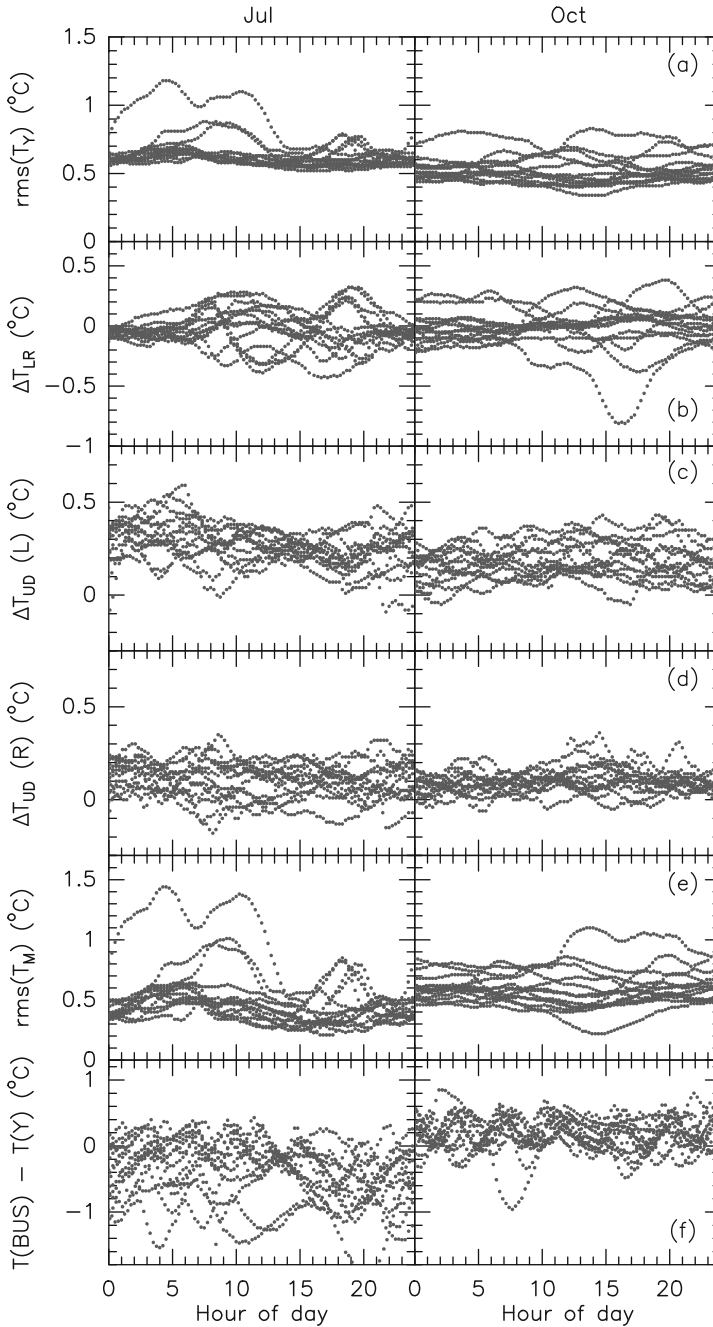


Fig. 9.24 IRAM 30-m telescope. (a) Temperature uniformity of the yoke. (b) Temperature difference between Left and Right yoke arm. (c,d) Temperature difference in the yoke arms in Up-Down (UD) direction, for the Left (L) arm and the Right (R) yoke arm. (e) Temperature uniformity of the yoke roof (membrane). (f) Temperature difference of the BUS base and the yoke roof.

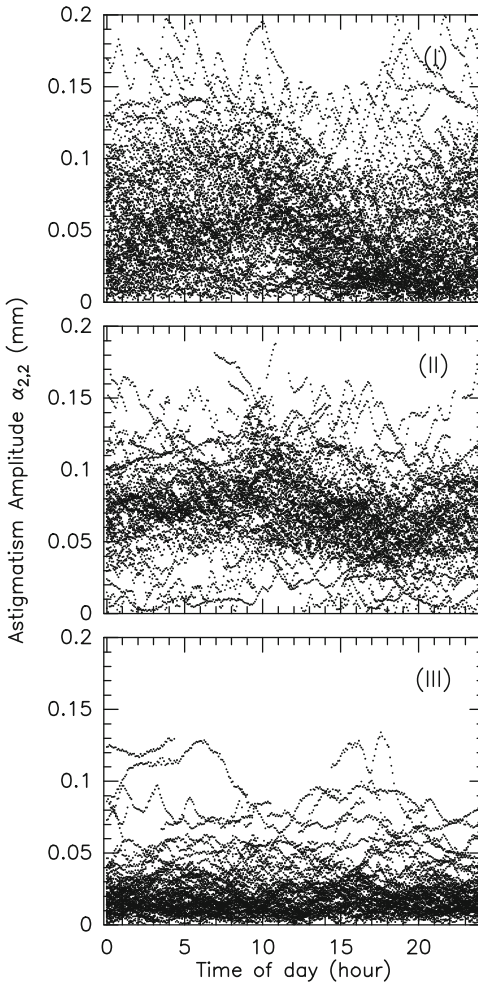


Fig. 9.25 IRAM 30-m telescope. Improvement of the thermal stability of the yoke by ventilation/heating, noticeable as reduction of the astigmatism of the reflector surface, expressed as the astigmatism amplitude $\alpha_{2,2}$. For the cases I, II, III see the text [From Greve et al. (2005), Courtesy IEEE Trans. Ant. Propag.].

which itself is supported by the EL-axis of the fork. The central hub is usually compact and massive and made of steel, as on the IRAM/SEST 15-m telescopes (see Fig. 2.10). The BUS network of the IRAM/SEST telescope is made of steel and CFRP tubes and cast steel joints. The ALMA-J 12-m prototype telescope [Ukita et al., 2004] has an invar central hub and a BUS made of CFRP tubes, invar joints and CFRP plates. The BUS is ventilated by 16 blowers. On the VertexRSI ALMA/APEX 12-m telescope the central hub is modified to an invar ring that is an integral part of the secondary focus cabin [see Güsten et al., 2006, for sketches of the APEX telescope]. The invar ring is thermally stabilized through ventilation with air from the thermally stabilized secondary focus cabin. On these telescopes the BUS is made of Al-honeycomb panels covered with CFRP plates.

The connection of the BUS network or the BUS plates to the central hub or the invar ring is illustrated in Fig. 9.26. Temperature induced deformations of the central hub may cause a deformation of the BUS and by this a reflector surface deformation. Temperature uniformity of the central hub and a synchronous temperature variation of the central hub and the BUS is important for good telescope performance.

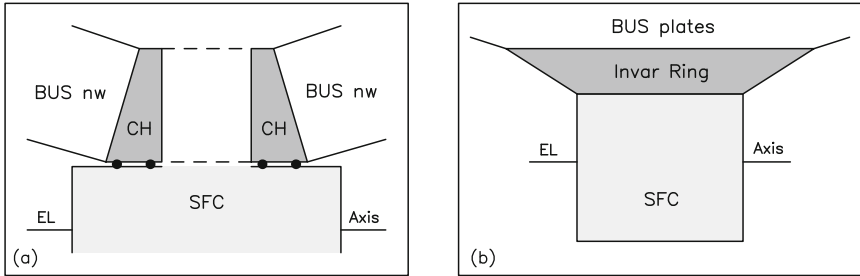


Fig. 9.26 (a) IRAM/SEST 15-m telescope. Connection of the BUS network (nw) to the central hub (CH) and the connection of the central hub to the secondary focus cabin (SFC). (b) VertexRSI ALMA/APEX telescope. Connection of BUS plates to the invar ring and the connection of the invar ring to the secondary focus cabin.

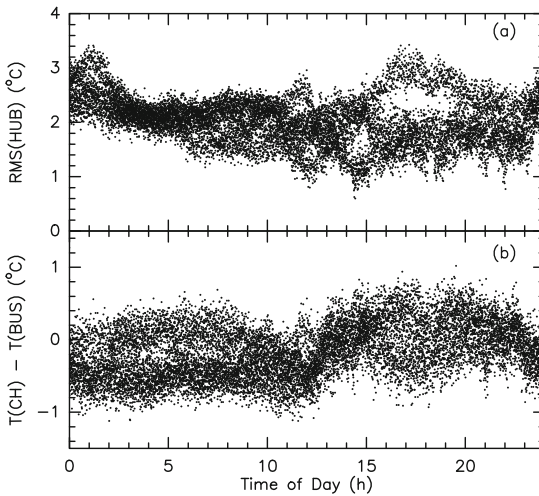


Fig. 9.27 SEST 15-m telescope. (a) Temperature uniformity (rms value) of the central hub. (b) Temperature difference $T(\text{CH}) - T(\text{BUS})$ between the central hub and the BUS. Measurements of 6 consecutive days [Data from SEST-Group, Chile].

Figure 9.27 and Fig. 9.28 illustrate the temperature uniformity of the SEST telescope central hub and the temperature uniformity of the VertexRSI ALMA telescope invar ring, respectively. The corresponding rms value of the central hub and invar ring temperature is $\text{rms}(\text{SEST}) \approx 2$ to 3°C (8 temperature sensors) and $\text{rms}(\text{ALMA}) \approx 0.25^\circ\text{C}$ (12 temperature sensors). On the SEST telescope the temperature of the

central hub and the temperature of the BUS agree within $\sim 1^\circ\text{C}$, on the VertexRSI ALMA telescope the temperature of the invar ring and of the BUS are, however, rather different. The temperature of the invar ring follows the temperature of the thermally stabilized secondary focus cabin, while the BUS follows to a large extent the temperature of the ambient air, as seen in Fig. 9.76 below.

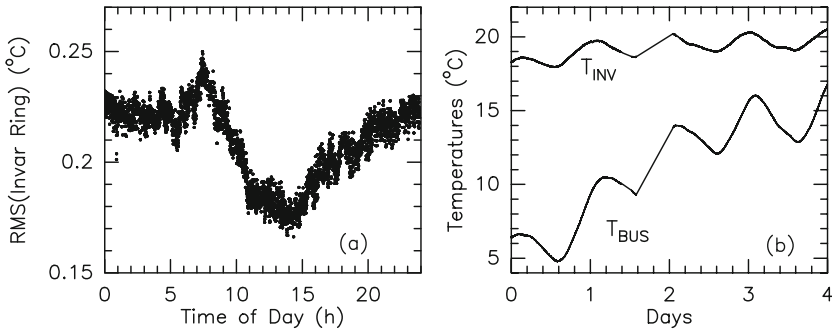


Fig. 9.28 VertexRSI ALMA 12-m prototype telescope. (a) Temperature uniformity (rms value) of the Invar Ring. (b) Temperature of the invar ring T_{INV} and of the backup structure T_{BUS} . Measurements of 4 consecutive days [ALMA Test Data].

9.3 Backup Structures (BUS)

There are four basic backup structures

- (1) the open BUS,
- (2) the closed BUS,
- (3) the closed and ventilated BUS,
- (4) the closed and climatized BUS.

The BUS, which carries the panels, is designed to guarantee the reflector surface contour and surface precision under the influence of gravity, temperature and wind at all tilt angles of the reflector. As listed in Table 9.1, a uniform temperature change of the BUS causes a focus error, a temperature difference/gradient in the BUS causes a pointing error. A random temperature distribution in the BUS causes reflector surface deformations with an associated beam deformation and loss in gain.

Table 9.4 Construction of Backup Structures.

Telescope ^{a)}	Reflector diameter [m]	BUS Material	open/closed	Ventilation
BIMA (1)	6	steel	closed	yes
NMA (2)	10	steel	closed	yes
OVRO (CARMA) (3)	10.4	steel	open	no
CSO (4)	10.4	steel	astrodome	no
ALMA VertexRSI (5)	12	Al–HC+CFRP cover	closed	no
ALMA AEC(5)	12	CFRP plates	closed	no
Metsähovi/FCRAO	14	aluminium	radome	yes
IRAM/SEST (6)	15	CFRP/steel	closed	no
JCMT (7)	15	steel	astrodome	yes
Onsala	20	aluminium	radome	yes
IRAM (8)	30	steel	closed	yes
MIT–Haystack (9)	37	aluminium	radome	yes
NRO (10)	45	steel	closed	yes
Parkes (11)	64	steel	open	no
Effelsberg (12)	100	steel	open	no
GBT (13)	100	steel	open	no
Yebes ^{b)}	40	steel	closed	yes
LMT/GMT ^{b)}	50	steel	closed	yes
SRT ^{b)}	64	steel	closed	no

^{a)} see list of Acronyms for observatory sites.

^{b)} under construction.

References for Tab. 9.4: (1) Lamb & Forster [1993]; (2) Satou [1998]; (3) Woody et al. [1994], Lamb & Woody [1998]; (4) Chamberlin [2003]; (5) Mangum et al. [2006], Greve & Mangum [2008]; (6) Greve [1992], Greve et al. [1992], Booth et al. [1989]; (7) Baas [1995], Wouterloot [2005]; (8) Greve et al. [1992, 2005]; (9) Barvainis et al. [1993]; (10) Akabane [1983]; (11) Jeffery [1964]; (12) Hachenberg [1970], Hachenberg et al. [1973]; (13) <http://www.nrao.edu/GBT>.

The important difference between cm–wavelength telescopes and mm/sub–mm wavelength telescopes is the exposure of the BUS to the environment, i.e. cm–wavelength telescopes have in general an open BUS, while most mm/sub–mm wavelength telescopes have a closed BUS in the case the telescope is not placed inside a radome or astrodome. In addition, the closed BUS may have a ventilation system or even a climatisation system. It is worthwhile to show again the important structural difference with respect to the exposure to the thermal environment of the open BUS illustrated in Fig. 9.29.a by the Effelsberg 100–m telescope, of the closed BUS illustrated in Fig. 9.29.b by the IRAM 15–m telescope, and of the closed BUS with compartments illustrated in Fig. 9.29.c by the ALMA VertexRSI telescope. Table 9.4 gives information on BUS constructions, whether they are open or closed and whether ventilation is applied or not.



Fig. 9.29.a Effelsberg 100-m telescope. The picture shows the rear side of the OPEN BUS fully exposed to the thermal environment [Courtesy N. Junkes, MPIfR, Germany].



Fig. 9.29.b IRAM 15-m telescope of which the BUS is CLOSED by the panels and the rear cladding; the BUS network is protected against solar illumination and, to a large extent, against the thermal environment. An enclosed air volume can be ventilated/climatised.

A thermal deformation of the BUS can introduce

- a pointing error in azimuth (AZ) and elevation (EL) direction due to a rotation of the best-fit parabola in AZ and EL direction; a corresponding AZ and EL pointing error is expected to be related, in first order, to a temperature gradient through the BUS in horizontal direction ($\Delta T_h \equiv \Delta T_{LR}$, Left-Right: AZ pointing error) and vertical direction ($\Delta T_v \equiv \Delta T_{UD}$, Up-Down: EL pointing error).
- a focus error due to a change in shape of the best-fit parabola; a corresponding focus error is expected to be related, in first order, to a temperature gradient through the BUS in axial direction from front to rear (ΔT_{fr}).
- a focus error due to a temperature gradient in radial direction through the BUS from the centre to the rim (ΔT_r).
- a change in reflector surface precision (σ_T), expected to be related, in first order, to a random temperature distribution in the BUS, $rms(T_{BUS})$.



Fig. 9.29.c ALMA VertexRSI 12-m telescope. Illustration of a CLOSED BUS (the rear cladding is taken off) built from plates forming COMPARTMENTS. Natural convection inside the compartments is small [Image Courtesy of NRAO/AUI/NSF].

Evidently, the BUS must be equipped with many temperature sensors to perform an analysis of these temperature distributions. If this is the case, and the FEM of the BUS is available, a real time calculation of the focus, pointing and surface error can be made.

9.3.1 The Open BUS

The network of the open BUS is exposed to the ambient air and associated convective heat transfer, to the sky and the ground by radiative heat transfer and to direct solar illumination. Although the tubes and beams of the BUS network may have a large diameter, up to 1/2 m and more, and a considerable length, nevertheless their thermal time constant is relatively short (see Table 7.11) so that at least individual members of the network are expected to have a uniform temperature. The temperature of a member may be close to that of the ambient air, especially if there is wind and no direct solar illumination. The parts of the BUS exposed to sunshine and shadow may have significant temperature differences that may introduce significant differential thermal deformations. The reflector panel surface may produce a large shielding of the BUS network from direct sunshine.

One of the earliest temperature measurements of an open BUS are reported for the Parkes 64-m telescope. Jeffery [1964] writes that 8 sensors on three ribs at 120° azimuthal distance gave temperature differences of $\sim 2^\circ\text{C}$, with little variation during the day and night.

The thermal behaviour of the open BUS of the OVRO 10.4-m mm-wavelength telescopes (now CARMA, USA) is discussed by Woody et al. [1994] and temperature measurements of 48 sensors on this BUS have been analysed and published by

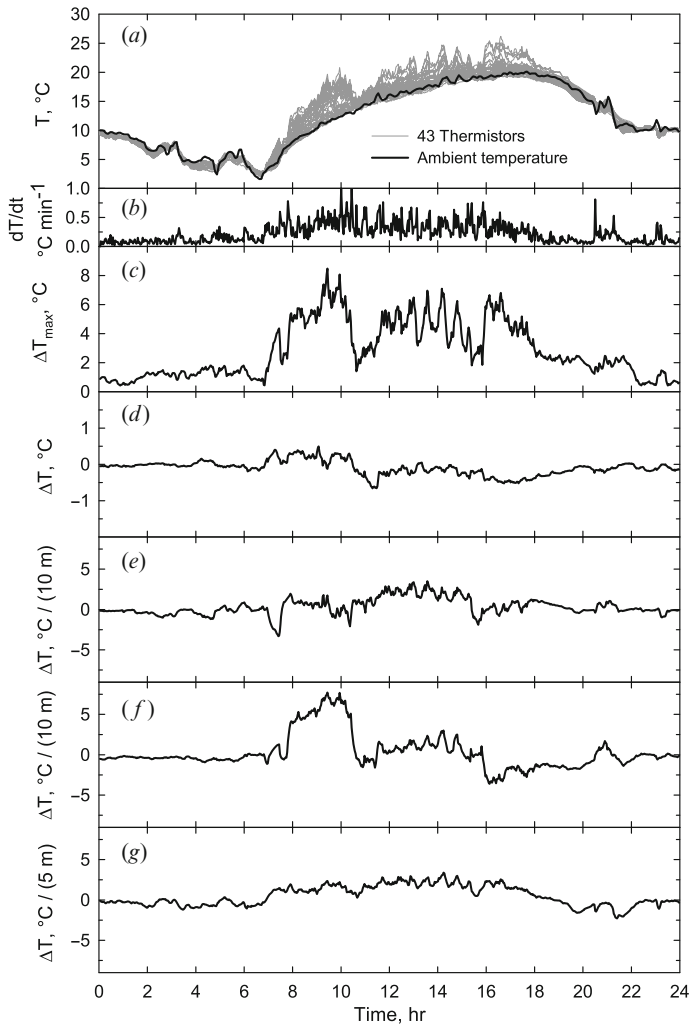


Fig. 9.30 Temperature distribution and gradients measured on the Leighton 10.4-m telescope BUS at OVRO. (a) temperature at multiple points in the BUS compared to the air temperature, (b) maximum rate of temperature change, (c) maximum difference between any two sensors, (d) front to back difference, (e) left to right gradient, (f) top to bottom gradient and (g) radial gradient [Courtesy J. Lamb].

Lamb & Woody [1998]. A representative set of measurements taken under rather variable weather conditions (10 May 1998) is reproduced in Fig. 9.30. The conclusions from this investigation (for the period April to June, 1998), as also representative for other open BUS constructions, are

- the open BUS follows closely the temperature of the ambient air;
- the open BUS responds quickly to environmental temperature changes with rates as high as $1.5^{\circ}\text{C}/\text{min}$; the temperature distribution of the BUS becomes uniform in 10 to 15 min after arrival of a shadowing cloud cover;
- the largest change of the BUS temperature and of temperature differences in the BUS occurs during morning and evening hours;
- during the night the maximum temperature difference in the BUS is approximately 1°C ; during the day the temperature difference may reach approximately 10°C , with large fluctuations due to wind and solar illumination;
- the cumulative distribution shows that for 50 % of the time the maximum temperature difference in the BUS is below 0.8°C at night and 2.4°C at day, 95% of the time the values are below 1.8°C and 5.6°C ;
- there is a clear indication of the temperature equalizing effect of wind from the correlation between the wind speed and the maximum temperature difference in the BUS; the maximum temperature during the day on the OVRO 10.4-m telescope (with solar illumination from the front and the rear) decreased from $\Delta T \approx 10^{\circ}\text{C}$ at wind speeds of ~ 0 to 2 m/s to $\Delta T \approx 3^{\circ}\text{C}$ at wind speeds of 8 to 12 m/s; at night the temperature difference was $\Delta T \approx 2^{\circ}\text{C}$ for all wind speeds, with a small decrease towards higher wind speeds;
- during the night there are negligible temperature gradients in vertical, horizontal and radial direction; the gradients increase during the day by at least a factor of 2 to 3;
- FEM calculations for temperature gradients through the BUS can predict with good accuracy the pointing errors in AZ and EL direction (due to horizontal and vertical temperature gradients) and the focus error (temperature gradient in axial direction);
- a real time FEM calculation, using measured temperatures and a quadratic interpolation procedure, can give a reliable prediction of pointing errors and focus errors.

Figure 9.31 shows the temperature of the open BUS of the Effelsberg 100-m telescope measured at the positions A, B, D (Fig. 2.4). The data were taken while the telescope was parked and the reflector pointed towards zenith; the BUS did not receive direct solar radiation. The figure shows that the temperature of the BUS follows closely the temperature of the ambient air. Since this is an important fact of open BUS constructions, Fig. 9.32 shows in detail the correlation between the average BUS temperature (A, B, D in Fig. 2.4) and the ambient air temperature, for a period of 14 days during summer (Jul) and during autumn (Oct) when the telescope was used for observations. The correlation may illustrate the effect that the BUS at the positions A, B, D is largely shielded from direct sunshine by the panels and that

the heat transfer is dominated by convective heat transfer to the ambient air. The temperature uniformity at the three locations of the BUS is of the order of 5°C .

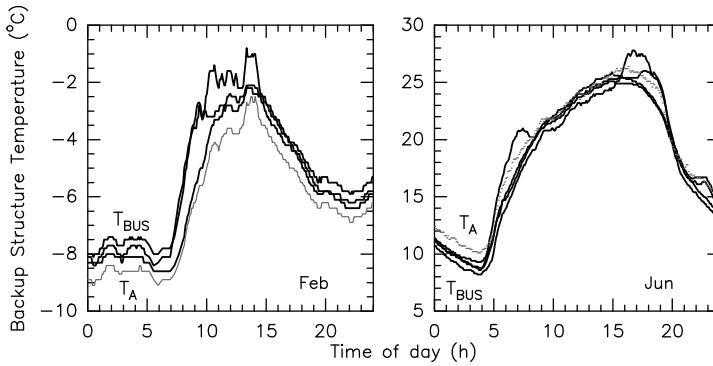


Fig. 9.31 Effelsberg 100-m telescope. Temperature T_{BUS} of the BUS (heavy lines) and of the ambient air T_{A} ; for a winter day and a summer day [From Greve et al. (2006), Courtesy SPIE].

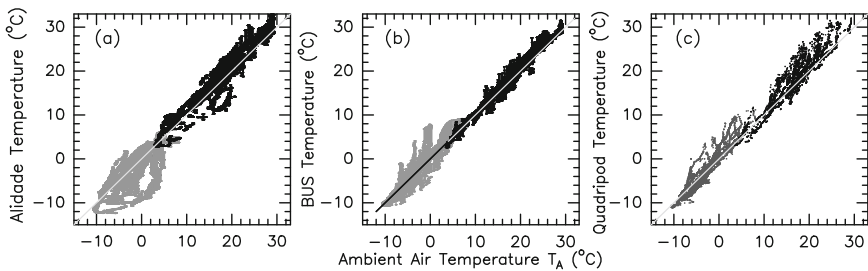


Fig. 9.32 Effelsberg 100-m telescope. (a) Correlation between the average temperature of the alidade (8 sensors) and the ambient air temperature; (b) correlation between the average temperature of the BUS (3 sensors) and the ambient air temperature, (c) correlation between the quadripod temperature (2 sensors) and the ambient air temperature; for summer: black region, for autumn-winter: grey region. The straight line is a one-to-one correspondence [Data MPIfR Effelsberg, Germany].

9.3.2 The Closed BUS

The BUS may be closed, but is not ventilated. Temperature measurements of the IRAM/SEST 15-m telescope are an example of the thermal behaviour of a closed and non-ventilated BUS. On these telescopes is the BUS network attached to the central hub, made of steel. As explained in Fig. 2.7, the BUS is a network of CFRP

tubes (radial and tangential members) and steel tubes (axial members). The tubes are connected by spherical joints made of cast steel. The front of the BUS is closed by the reflector panels with insulation on the rear. Between the panel and the insulation is a heating mat to prevent icing. The rear of the BUS is covered with MetawellTM double walled aluminium plates, some of which have later been replaced by single aluminium plates. There exists some natural ventilation of the air inside the BUS. The temperature recordings shown below were made when the sky was clear and the telescope was used for observations; the solar illumination of the reflector (with the Sun at a large distance from the radio axis) and of the rear cladding changed frequently. The wind speed was low. The temperature of the IRAM/SEST 15-m telescope BUS network was measured on the axial steel members, the location of the sensors is shown in Fig. 9.33. The recorded temperatures relate to the upper section of the BUS (in tilt direction): $T_U = (T_1 + T_2)/2$, the lower section (in tilt direction): $T_D = (T_3 + T_4)/2$, the right (R) side: $T_R = (T_5 + T_6)/2$ and the left side (L): $T_L = (T_7 + T_8)/2$.

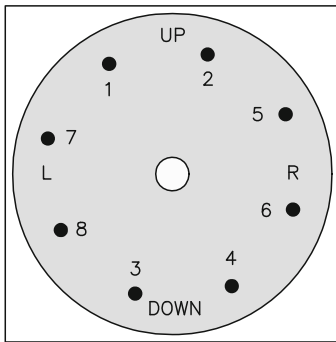


Fig. 9.33 IRAM/SEST 15-m telescope. Location of temperature sensors on the BUS network, horizon position of the reflector.

Figure 9.34.a is a measurement made on the IRAM 15-m telescope of the average temperature of the BUS, T_{BUS} , and of the temperature of the ambient air T_A . Although the BUS is closed, the figure indicates that during the day the temperature of the BUS follows closely the ambient air temperature. During the night the temperature of the BUS falls approximately 5°C below the ambient air temperature, probably by radiative cooling of the outer surfaces towards the cool sky and transfer of this cooling effect to the inside. This effect is also seen on the SEST telescope (Fig. 9.37). The temperature uniformity of the BUS is illustrated by the value $\text{rms}(T_{BUS})$ shown in Fig. 9.34.b. At night $\text{rms}(T_{BUS}) \approx 2^\circ\text{C}$, during the day the value increases by a factor $\sim 2-3$ so that $\text{rms}(T_{BUS}) \approx 4-6^\circ\text{C}$. The larger value $\text{rms}(T_{BUS})$ measured during the day is associated with a significant vertical temperature gradient of the BUS and the inside air.

Figure 9.35 shows the temperature gradient of the IRAM 15-m telescope BUS in vertical direction (Up-Down), i.e. $\Delta T_{UD} = T_U - T_D$, and in horizontal direction (Left-Right), i.e. $\Delta T_{LR} = T_L - T_R$. Both gradients show a characteristic daily behaviour. During the night the Up-Down gradient is $\Delta T_{UD} \approx 2^\circ\text{C}$, during the day

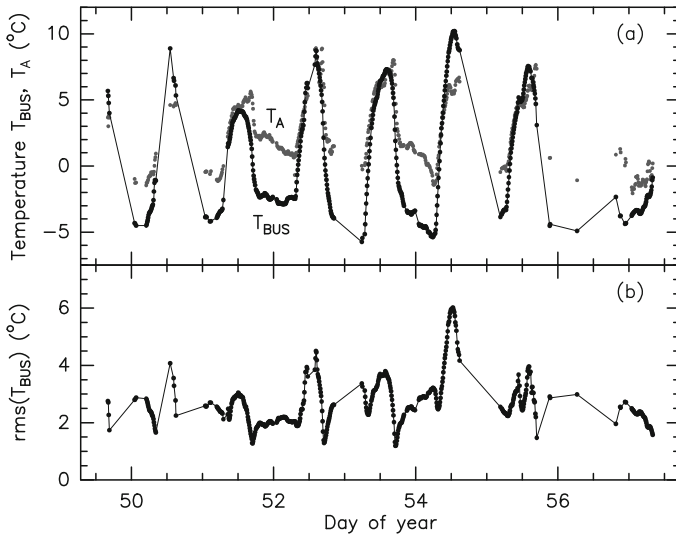


Fig. 9.34 IRAM 15-m telescope. (a) Average temperature T_{BUS} of the BUS (connected by a line) and ambient air temperature T_A , (b) Temperature uniformity of the BUS expressed as $\text{rms}(T_{\text{BUS}})$, derived from 8 sensors.

the gradient can reach $\Delta T_{\text{UD}} \approx 10^\circ \text{C}$ and more. The upper part of the BUS is always warmer. With $L \approx 2 \text{ m}$ the typical length of an axial steel member of the BUS (see Fig. 2.7), the gradient $\Delta T_{\text{UD}} = 10^\circ \text{C}$ can build up to a pointing error in elevation direction of $\Delta \varepsilon \approx \alpha L 10 [\text{K}]/D \approx 3 \text{ arcsec}$, with $D = 15 \text{ m}$ and $\alpha = 12 \mu\text{m}/\text{m}/\text{K}$ (steel). The origin of the vertical temperature difference ΔT_{UD} is not clear, however, the largest values occur around noon. This suggests a correlation with sunshine. Fig. 9.36 illustrates that there is no correlation of ΔT_{UD} with the ambient air temperature T_A and no clear correlation with the wind speed, with the exception that the higher values of ΔT_{UD} occur at low wind speeds when the temperature equalizing effect of wind is small. A temperature gradient ΔT_{LR} exists also in Left-Right direction, though being smaller during the day and disappearing at night.

Temperature measurements of the SEST telescope BUS with an arrangement of sensors as in Fig. 9.33 are shown in Fig. 9.37. The data indicate that during the day/night the average BUS temperature is $\sim 5^\circ \text{C}$ above/below the ambient air temperature. The temperature uniformity of the BUS is shown in Fig. 9.38.a, the Up-Down and Left-Right temperature gradients are shown in Fig. 9.38.b. There is a noticeable degradation of the temperature uniformity during the day (from $\sim 12 \text{ h}$ to 22 h UT) associated with an increase of the temperature gradients in both directions.

For BUS networks, and especially those built from aluminium or steel, it is important to know how a non-uniform temperature of the BUS affects the reflector surface precision (σ_T). This is a difficult question since it requires many temperature sensors on a BUS and at the same time a determination of σ_T . The IRAM 30-m

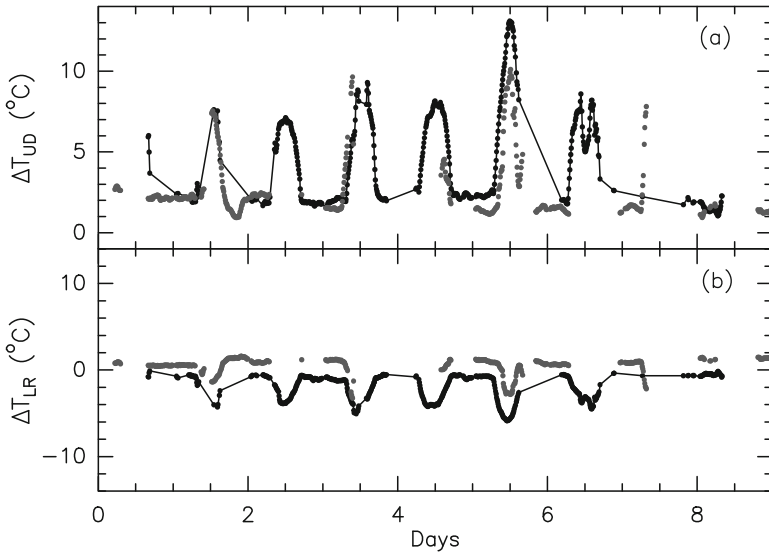


Fig. 9.35 IRAM 15-m telescope. (a) Temperature difference ΔT_{UD} of the BUS in the direction Up–Down, (b) temperature difference ΔT_{LR} of the BUS in the direction Left–Right. The black and grey dots are for a summer and winter period.

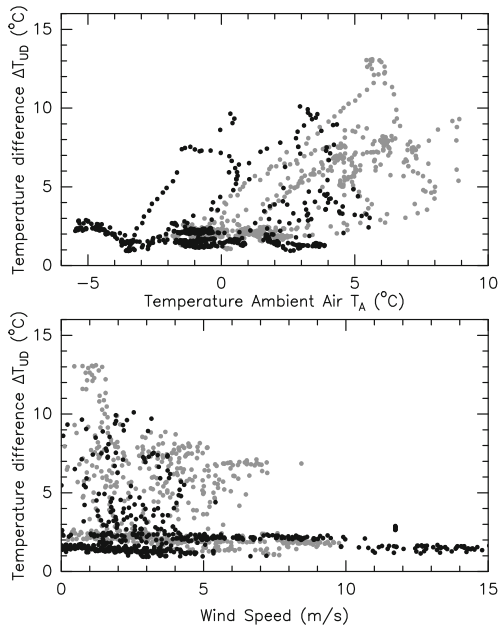


Fig. 9.36 IRAM 15-m telescope. Lack of a correlation between the temperature difference ΔT_{UD} of the BUS in the direction Up–Down and the ambient air temperature T_A , and similar for the wind speed. The black and grey dots are for a summer and winter period.

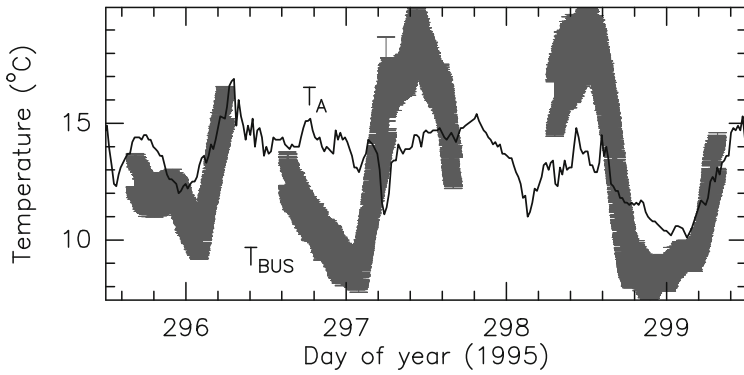


Fig. 9.37 SEST 15-m telescope. Average temperature of the BUS T_{BUS} and temperature of the ambient air T_{A} . The width of the BUS temperature recording represents the temperature uniformity $\text{rms}(T_{\text{BUS}})$ [Data SEST-Group, Chile].

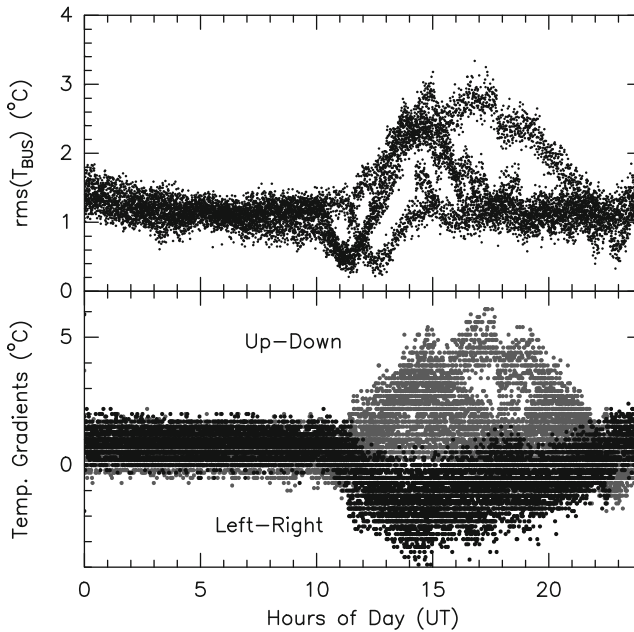


Fig. 9.38 SEST 15-m telescope. Upper panel: Temperature uniformity of the BUS expressed by the value $\text{rms}(T_{\text{BUS}})$, lower panel: Temperature gradients in the direction Up-Down (grey) and Left-Right (black). Nighttime is from ~ 0 h to 10 h UT [Data SEST-Group, Chile].

telescope has 148 temperature sensors on the BUS and the yoke and it is possible to determine σ_T from these measurements and FEM calculations of the associated surface deformations. Unfortunately, for this investigation, the BUS of the IRAM 30-m telescope is climatized so that the value $\text{rms}(T_{\text{BUS}})$ is rather small. The correspondence of $\text{rms}(T_{\text{BUS}}) - \sigma_T$ obtained in this way is shown in Fig. 9.39. A clear conclusion cannot be drawn from this figure. Ukita et al. [2004] used in a similar way the temperature measurements of the ALMA-J 12-m prototype telescope to calculate the surface rms value σ_T . For 170 days of measurements with the ambient air temperature changing between -5 and 30°C the reflector surface supported on the ventilated CFRP BUS did not change in precision by more than $\Delta\sigma_T \approx 3.1\ \mu\text{m}$. As reported by Mangum et al. [2006], holography measurements of the ALMA VertexRSI and AEC prototype telescopes gave $\Delta\sigma_T/\Delta T_A \approx 0.6$ to $0.8\ \mu\text{m}/\text{K}$. Since the BUS of the VertexRSI telescope follows the ambient air temperature (Fig. 9.76) it is perhaps allowed to conclude that $\Delta\sigma_T/\Delta T_A \approx \Delta\sigma_T/\Delta T_{\text{BUS}}$. However, from the holography measurements it is not clear how much of the change in reflector precision is due to the BUS and due to the panels. Since the ambient air at the ALMA site Chajnantor changes the temperature daily by ~ 10 to 20°C (Figs. 4.4, 4.6), the reflector precision of the ALMA telescopes may change daily by $\Delta\sigma_T \approx 5$ to $15\ \mu\text{m}$. Holography revealed that on the ALMA VertexRSI telescope some very local print-through of the BUS support occurred, with no consequence for the radio performance [Mangum et al. 2006].

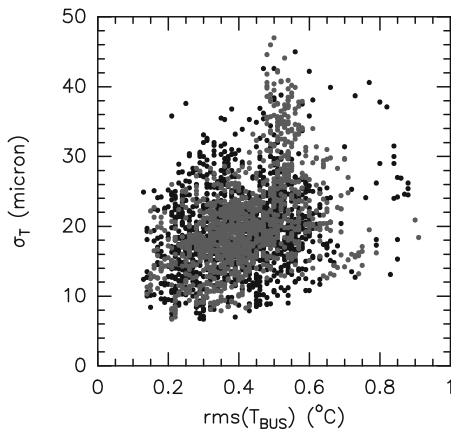


Fig. 9.39 IRAM 30-m telescope. Temperature uniformity of the BUS $\text{rms}(T_{\text{BUS}})$ and associated thermal surface deviation σ_T (rms value). Black and grey dots: summer and winter period.

The VertexRSI ALMA/APEX 12-m telescope has a closed BUS that is divided into 24 azimuthal sectors with each sector containing several compartments (Fig. 9.29.c). There is no air exchange between the sectors and the compartments. The Al-plate surface panels are fixed at 5-points to the BUS, there is an air gap between the panels and the CFRP BUS front cover. Temperature measurements of the BUS plates were made at 24 points of the BUS, representing approximately equal volume elements of the BUS. A typical recording of the measured temperature distribution is shown in Fig. 9.40.a (May, 2003). The figure indicates that during the

day the rim of the BUS is warmer than the BUS centre; the situation is reversed during the night. The investigation of ten days of measurements indicates that the average temperature of the BUS follows approximately the ambient air temperature (see also Fig. 9.76). As illustrated in Fig. 9.40.b, the maximum deviation from the average BUS temperature did not exceed $\sim \pm 5^\circ\text{C}$, the temperature uniformity of the BUS is $\text{rms}(T_{\text{BUS}}) \approx 1 - 2^\circ\text{C}$ during the day (with sunshine) and $\text{rms}(T_{\text{BUS}}) \approx 0.5^\circ\text{C}$ during the night, the temperature gradient in vertical (Up–Down) and horizontal (Left–Right) direction did not exceed 0.5 to 1°C during the night.

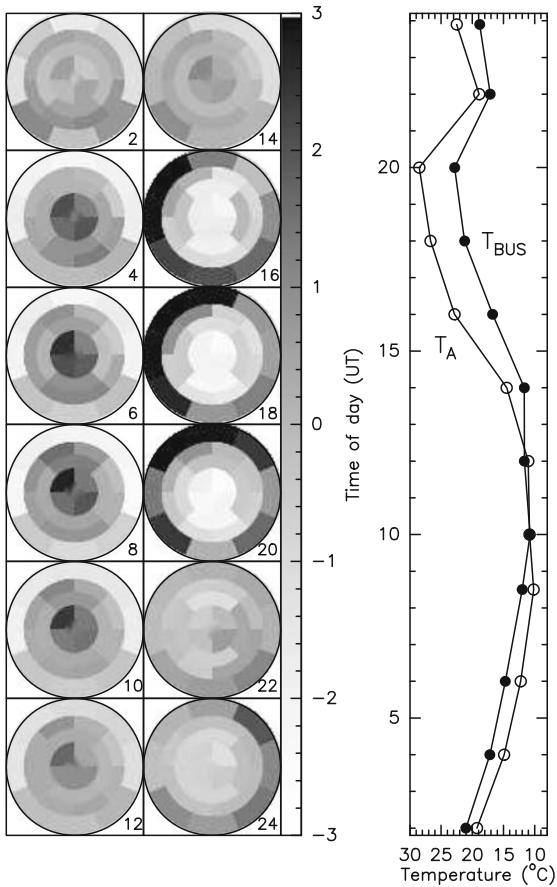


Fig. 9.40.a VertexRSI ALMA 12-m prototype telescope. Left panel: deviation of the 24 BUS elements, with sensors, from the average BUS temperature. The numbers indicate the time of day (UT); daytime is from ~ 15 h to 2 h (UT). Right panel: average temperature T_{BUS} of the BUS and temperature of the ambient air T_{A} . The measurements were made during a clear day [From Greve & Mangum (2008), Courtesy IEEE Ant. Propag. Magazine].

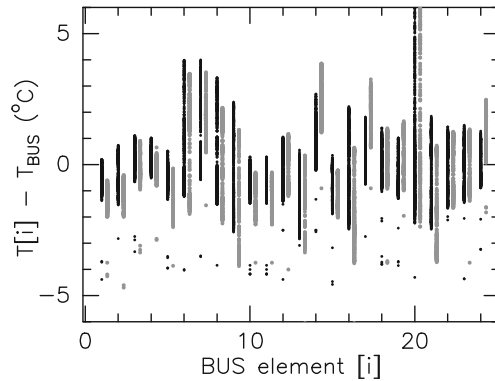


Fig. 9.40.b VertexRSI ALMA 12-m prototype telescope. Temperature difference $T[i] - T_{\text{BUS}}$ between the BUS element $[i]$ and the average temperature of the BUS. Black dots: 4 days of 24-hour measurements, not in the direction of the Sun; grey dots: measurement during a day while tracking the Sun (sensor 20 produced some faulty readings) [ALMA Test Data].

9.3.3 The Ventilated BUS

Some detailed information of a ventilated BUS is available for the BIMA (now CARMA) 6-m telescopes [Lamb & Forster 1993], the NRO 10-m telescopes [Satou 1998], the NRO 45-m telescope [Akabane 1983] and the IRAM 30-m telescope [Greve 1992]. Information on the BUS ventilation of the Yebes 40-m telescope and the LMT/GMT 50-m telescope will become available in the near future.

As summarized in Table 2.7, the closed BUS of the BIMA 6-m telescopes is ventilated in circular direction by 4 fans [Lamb & Forster 1993]. The BUS consists of square cross section steel members and plane trusses for tangential bracing. At the front is the BUS closed by 48 cast and machined Al-panels, the rear of the panels is rough and matte. The BUS is closed at the rear by 5 cm thick insulation plates, covered at the outer side by an Al-sheet. A 6-day temperature measurement was made with 16 sensors near the front and 16 sensors near the rear of the BUS. The weather was hot (June) and clear and the telescope was used for observations, pointing at different positions in the sky. The BUS of the BIMA 6-m telescope shows a typical daily temperature variation with the average temperature changing by $\sim 20^\circ\text{C}$. The temperature uniformity during the day is $\text{rms}(T_{\text{BUS}}) \approx 0.4^\circ\text{C}$, at night $\text{rms}(T_{\text{BUS}}) \approx 0.2^\circ\text{C}$. The temperature gradients in the direction Up-Down, Left-Right and Front-Rear never exceeded 1°C , while most of the time being smaller than 0.5°C .

A summary of the thermal behaviour of the NRO 45-m telescope BUS was published by Akabane [1983]. The BUS, made of steel, is covered at the front and rear with ~ 3 cm thick insulation plates of $\sim 0.5\text{ m} \times 2\text{ m}$ size and with 2 to 3 mm wide gaps between them. The surface panels are made of Al-honeycomb cores with CFRP skins. All outer surfaces are painted white. The air inside the BUS is ventilated in circular direction by 55 fans (400 W each) producing a flow speed of about

1.5 m/s or more (see Table 2.7). The measurements of the NRO 45-m telescope BUS show a radial symmetric temperature gradient of $\sim \pm 3^\circ\text{C}$ and a gradient in axial direction through the BUS of 0.5 to 1°C . As seen in Fig. 9.41, a noticeable reversal of the radial gradient occurs between day and night. During the day, the rim of the BUS is warmer than the ambient air, at night it is cooler. This effect is assumed to be due to solar illumination, radiative cooling towards the sky during the night and a rather good exchange of air inside the BUS with ambient air through the gaps between the panels and between the insulation plates. The radial temperature gradient and the reversal of the gradient between day and night is probably due to the smaller mass-to-surface ratio at the rim of the reflector (see Fig. 2.11) and a shorter thermal time constant of the outer areas of the reflector. Such an effect is discussed for the radome enclosed FCRAO 14-m telescope [Schloerb 1978], explained in Section 9.3.8.

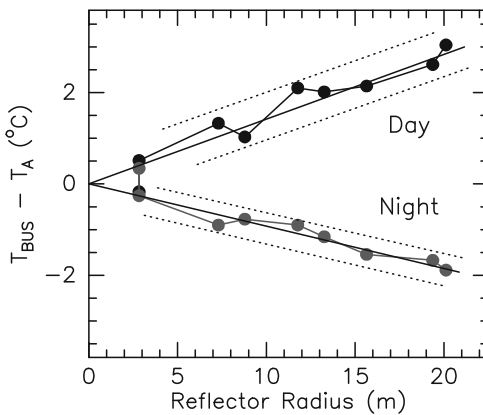


Fig. 9.41 NRO 45-m telescope. Radial temperature difference $T_{\text{BUS}} - T_{\text{A}}$ between the BUS and the ambient air, during daytime and nighttime. The dashed lines show the measured maximum and minimum deviations of $\pm 0.5^\circ\text{C}$ (daytime) and $\pm 0.3^\circ\text{C}$ (nighttime) [After Akabane (1983), Courtesy Springer].

At the IRAM 30-m telescope, a two-week break-down of the climatisation system (no heating to compensate radiative cooling towards the sky, no cooling to compensate heating from insolation and energy dissipation from the fans, no thermal control of the quadripod) provided the exceptional opportunity to record the thermal behaviour of the BUS when only being ventilated. The ventilation has an intake (exchange) of approximately 10% ambient air (Table 2.7). Fig. 9.42.a shows the temperature of the yoke, the BUS and the quadripod recorded during this period with the initial set of temperature sensors shown in Fig. 2.5; Fig. 9.42.b shows the temperature uniformity expressed by the corresponding rms values. If only ventilated and with no thermal control of the quadripod, the telescope is *outside* the thermal specification of $|T_{\text{yoke}} - T_{\text{BUS}}| \approx |T_{\text{yoke}} - T_{\text{quadripod}}| \lesssim 1^\circ\text{C}$ and $\text{rms}(T_{\text{BUS}}) \lesssim 0.5^\circ\text{C}$. As seen in Fig. 9.42.a, during the time of insufficient thermal control the telescope components show a long-term temperature drift and 24-hour periodic temperature oscillations, both correlated with a similar drift and oscillations of the ambient air temperature. The rms values expressing temperature uniformity, Fig. 9.42.b, show periodic variations as well though not of a clear 24-hour period as observed for

the average temperature of the components. The oscillations of the temperatures are caused by periodic variations of the insolation and of the ambient air temperature [Greve 1992]. For 6 consecutive days of this period (day 13 to 18) with the telescope in an oscillatory state the time averaged temperatures and the time averaged rms values of the cosine approximations are listed in Table 9.5. The data indicate $\langle T_{\text{BUS}} \rangle \approx \langle T_{\text{yoke}} \rangle \approx \langle T_{\text{quad}} \rangle \approx \langle T_{\text{A}} \rangle$ so that on average the telescope was in thermal equilibrium with the ambient air. During this period the $\langle \text{rms} \rangle$ value of the BUS temperature is by a factor 2 to 4 outside the specification.

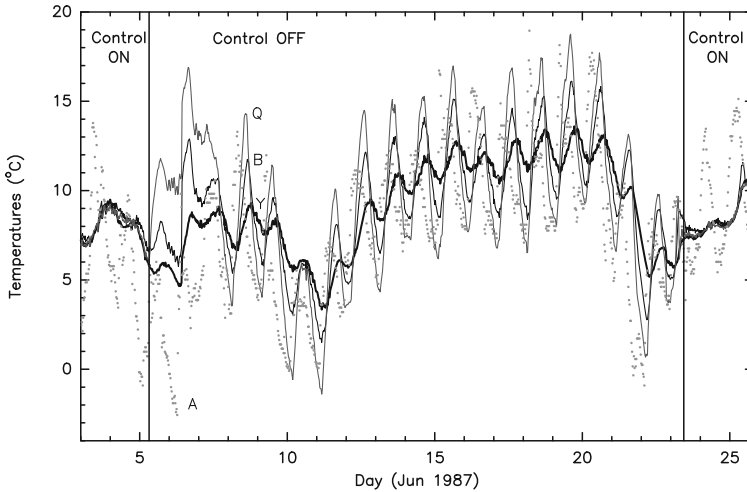


Fig. 9.42.a IRAM 30-m telescope. Temperature recordings of the BUS (B), the yoke (Y), the quadripod (Q) and the ambient air (A, dots) when the BUS was only ventilated (no heating/cooling). Note the temperature uniformity when the thermal control is fully working [From Greve et al. (1992), Courtesy IEEE Trans. Ant. Propag.].

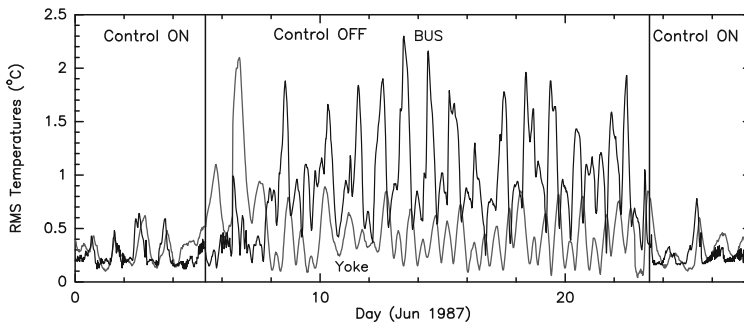


Fig. 9.42.b IRAM 30-m telescope. Temperature uniformity for the time of no heating/cooling (see Fig. 9.42.a) expressed as rms value of the BUS temperature and rms value of the yoke temperature.

Table 9.5 IRAM 30-m telescope. Temperature Averages and RMS Deviations (no heating/cooling; average of 6 days).

Component	$\langle T \rangle$ [$^{\circ}$ C]	$\langle \text{rms} \rangle$ [$^{\circ}$ C]
Ambient Air	11.3	
Yoke	11.9	0.4–1
BUS	11.9	1.0–2
Quadripod	12.1	0.3–0.7

The cosine-form temperature oscillations of 24-hour period and the small long-term temperature drift seen in Fig. 9.42.a are approximated by

$$T_i(t) = T_{oi} + A_i t - \Delta T_i \cos(\omega t + t_{oi}) \quad (9.4)$$

with $\omega = 2\pi/24\text{h}$, i = ambient air, yoke, BUS and quadripod, A_i the gradient of the temperature drift, ΔT_i the amplitude of the oscillation and t_{oi} the time delay with respect to 12 h noon. For the 6 consecutive days, the parameters of the cosine-form approximations are listed in Table 9.6. The ambient air reaches the maximum temperature at ~ 12.5 h UT noon (~ 13.5 hour LT), which is approximately the time of maximum insolation. The yoke, the BUS and the quadripod reach maximum temperatures 9 h, 6.5 h and 5 h later, respectively. The time delays of the BUS and quadripod are similar, hence the BUS and quadripod oscillate approximately synchronous, though with different amplitude. This synchronous behaviour may explain the fact that no exceptional pointing and focus corrections were reported during this time of *no* heating/cooling control.

Table 9.6 IRAM 30-m telescope. Cosine-form Approximations of the Temperature Oscillations, Eq.(9.4) (no heating/cooling).

Component	T_o [$^{\circ}$ C]	A [$^{\circ}$ C/day]	ΔT [$^{\circ}$ C]	t_o [h]
Ambient Air	11.3	0.009	3.4	0.5
Yoke	11.9	0.008	0.8	9.25
BUS	11.9	0.014	2.6	6.5
Quadripod	12.1	0.020	4.3	5.25

For model calculations it is useful to estimate the amount of energy oscillating in the telescope structure. Neglecting the small long-term temperature drifts, the cosine-form oscillations (Tables 9.5 and 9.6) indicate a quasi-steady energy state of the telescope. The energy absorbed by the telescope during the day (time between minimum temperature and maximum temperature) is emitted during the night (time

between maximum temperature and minimum temperature), i.e. the increase in temperature during the day equals its decrease at night. Using the mass M_i of component [i] listed in Table 2.2.a and the amplitude ΔT_i of the oscillation listed in Table 9.6, the energy Q_i oscillating in this component is

$$Q_i = \mathcal{C} M_i (2\Delta T_i) \quad (9.5)$$

with $\mathcal{C} = 450 \text{ J/kg/K}$ the heat capacity of steel. Because of the cosine-form of the oscillations, the time averaged energy flow rate $\langle q_i \rangle$ is approximately

$$\langle q_i \rangle = \pm Q_i / 12 \text{ h} \quad (9.6)$$

with the + sign indicating an energy gain during the day and the – sign indicating an energy loss during the night. The values Q_i and $\langle q_i \rangle$ are listed in Table 9.7. Since the yoke and the quadripod were not ventilated and thermally controlled during these measurements, at least for these components the energy exchange is assumed to have occurred through the outer surfaces. Taking the surface areas S_i from Table 2.2.a, the average energy passing through 1 m^2 surface per 1 s is $\pm \langle q_i \rangle / S_i$. These values are also listed in Table 9.7.

Table 9.7 IRAM 30-m telescope. Energy Balance of the Temperature Oscillations (no heating/cooling).

Component	Mass (t) [ton]	$2\Delta T$ ^{a)} [°C]	Q ^{b)} [kJ]	$\langle q \rangle$ ^{c)} [kW]	Surface S [m ²]	$\langle q \rangle / S$ [W/m ²]
Yoke (total)	180	1.6	$1.3 \cdot 10^5$	3.0	220	14
BUS	100	5.2	$2.3 \cdot 10^5$	5.3	(1870)	(3)
Quadripod (one)	2.5	8.6	$1.0 \cdot 10^4$	0.2	45	4

^{a)} Eq.(9.4) and Table 9.6, ^{b)} Eq.(9.5), ^{c)} Eq.(9.6).

9.3.4 Radial and Circular Ventilation

There are two basic methods of ventilating a closed BUS, i.e. radial ventilation and circular (tangential) ventilation or a combination of both. This is illustrated in Fig. 9.43.a and Fig. 9.43.b. For radial ventilation the air is taken from the volumes near the centre of the BUS and blown into the BUS by a radial stack of successive fans, or by radial ducts that extend to approximately 1/3 to 2/3 of the reflector radius. From the fans, or the mouths of the ducts, the air moves towards the rim of the BUS and either escapes partially to the outside through louvres at the rim or is sucked back to the centre in a complicated flow pattern. For circular ventilation the fans may blow in tangential direction, or the intake of the air is near the centre and the air is brought by radial ducts into the BUS to approximately 1/2 to 3/4 of the reflector

radius. There are openings in the ducts where blades guide the air in tangential direction so that a more or less well established circular flow of the air occurs. In a complicated flow pattern the air is sucked back to the centre. The flow speed of the ventilated air is of the order of 3 to 10 m/s as explained in Table 2.7. Some outside ambient air (of the order of 5 to 10 %) is mixed with the enclosed air. In a climatisation system the ventilated air is heated or cooled at the outflow openings of the fans as illustrated in Fig. 9.43.b. The heat generated by the fans may stay, at least partially, inside the BUS, this effect has to be taken into account in thermal model calculations.

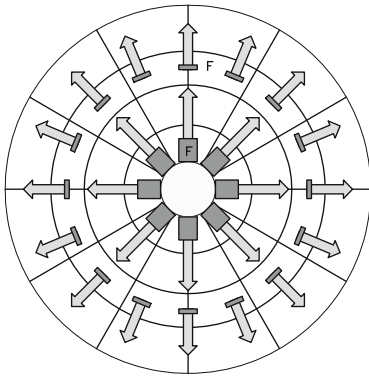


Fig. 9.43.a Illustration of radial ventilation. F = fans.

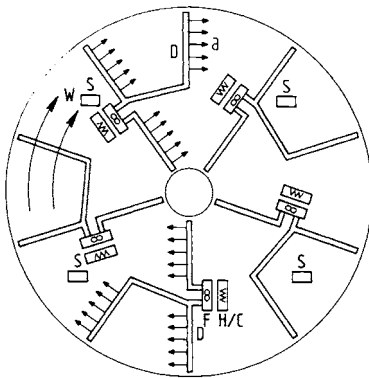


Fig. 9.43.b IRAM 30-m telescope. Illustration of circular ventilation, 5 units. F: fans, H/C: heaters/coolers, D: ducts, S: temperature sensors [From Baars et al. (1988), Courtesy Astron. Astrophys.].

Radial ventilation is applied on the NRO 10-m interferometer telescopes, circular ventilation is applied on one NRO 10-m telescope and on the IRAM 30-m telescope. Satou [1998] published an investigation that compares radial and circular ventilation of the NRO 10-m telescopes. The telescopes with radial ventilation have 12 fans, at 1 m distance from the centre, with inlet windows near the centre and outlets (louvres) at the rim of the reflector. The telescope with circular ventilation also had 12 fans, but no inlet and outlet windows. The published values $rms(T_{BUS})$, which are summarized in Fig. 9.44, indicate on average a higher efficiency of the

circular ventilation. During two months of measurement the temperature uniformity varied between 0.2 and 0.8° C (rms) for radial ventilation and between 0.2 and 0.5° C (rms) for circular ventilation. The ratio of the daily rms values of radial ventilation (two telescopes) and circular ventilation (one telescope) is 0.66 and 0.72, i.e. in these terms and for this period the circular ventilation was on average 30 % more efficient.

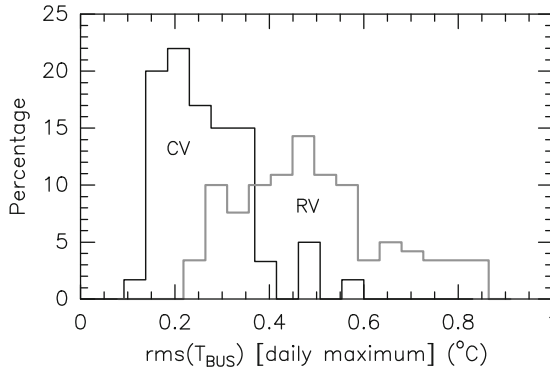


Fig. 9.44 NRO 10–m telescopes. Statistics of temperature uniformity of the BUS expressed as daily maximum value $\text{rms}(T_{\text{BUS}})$, for radial ventilation (RV) and circular ventilation (CV) [after Satou (1998)].

9.3.5 The Climatised BUS (IRAM 30–m Telescope)

Finally, the BUS may be closed, ventilated and climatised. This type of active thermal control is applied on the IRAM 30–m telescope [Baars et al. 1988, 1994, Greve et al. 1992, 2005]. The lay–out of the circular ventilation/climatisation system is shown in Fig. 9.43.b, the capacity of the climatisation is summarized in Table 2.7. The cooling/heating of the climatisation is installed to eliminate solar energy entering the BUS during the day (cooling) and to provide energy (heating) to the BUS to counterbalance radiative cooling towards the cool sky during the night. The specification requires a temperature uniformity between the yoke and the BUS and the quadripod of $\lesssim \pm 1^\circ\text{C}$ and a temperature uniformity of the BUS of $\text{rms}(T_{\text{BUS}}) \lesssim 0.5^\circ\text{C}$. The climatisation system takes the reference temperature at a location in the yoke close to the membrane of the BUS (Fig. 2.5), the temperature of the BUS and quadripod is controlled against this reference temperature. The yoke was selected as reference because of its large mass (Table 2.2.a) and consequently long thermal time constant (Table 9.6). The original control system had 14 temperature sensors on the BUS and 5 sensors on the yoke (Fig. 2.5). The present system (after 2000) has 104 PT100TM sensors on the BUS and 44 PT100TM sensors on the yoke.

The present location of the sensors on the BUS is shown in Fig. 9.45. The temperature of the glycol pumped around the quadripod legs is taken as the temperature of the legs. The temperatures are recorded every 5 minutes.

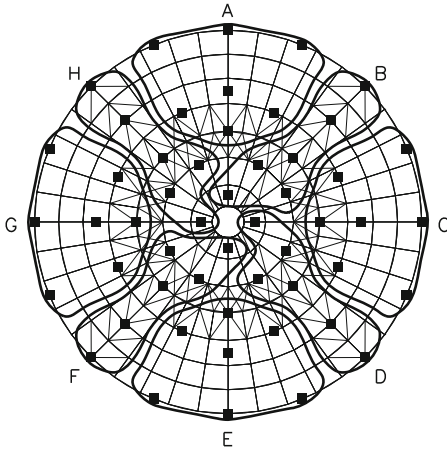


Fig. 9.45.a IRAM 30-m telescope. Location of temperature sensors on the BUS, face on view [From Bremer & Peñalver (2002), Courtesy SPIE].

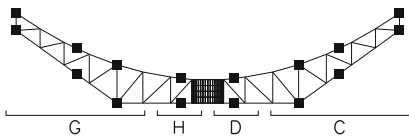


Fig. 9.45.b IRAM 30-m telescope. Location of temperature sensors on the BUS, side view [From Bremer & Peñalver (2002), Courtesy SPIE].

Figure 9.46 shows two 24-hour recordings of the temperature of the BUS sectors A to H (Fig. 9.45) and the yoke sectors J, K, L (Fig. 9.23). The figure on the left is a recording made before installation of ventilation/heating in the yoke, the figure on the right is a recording for the time after installation of ventilation/heating [Greve et al. 2005]. The BUS and the yoke follow the reference temperature within $\sim \pm 1^\circ\text{C}$ for both operations. The close-loop control with approximately 1 hour cycle time is visible. The uniformity of the temperature distribution is better after installation of ventilation/heating in the yoke.

The temperature uniformity of the IRAM 30-m telescope BUS under operation of the climatisation system is evaluated in Fig. 9.47 from the rms value $\text{rms}(T_{\text{BUS}})$, the temperature gradient $\Delta T_{\text{BUS,UD}}$ in the direction Up-Down (derived from the average temperature of sector A and E, Fig. 9.45 a), from the temperature gradient between the left and right side $\Delta T_{\text{BUS,LR}}$ (derived from the average temperature of sector C and G, Fig. 9.45.a) and the temperature gradient through the BUS in axial direction $\Delta T_{\text{BUS,ax}}$ (derived from the average temperature of the front and rear side sensors, Fig. 9.45.b). The value $\text{rms}(T_{\text{BUS}})$ is an indication of the reflector surface

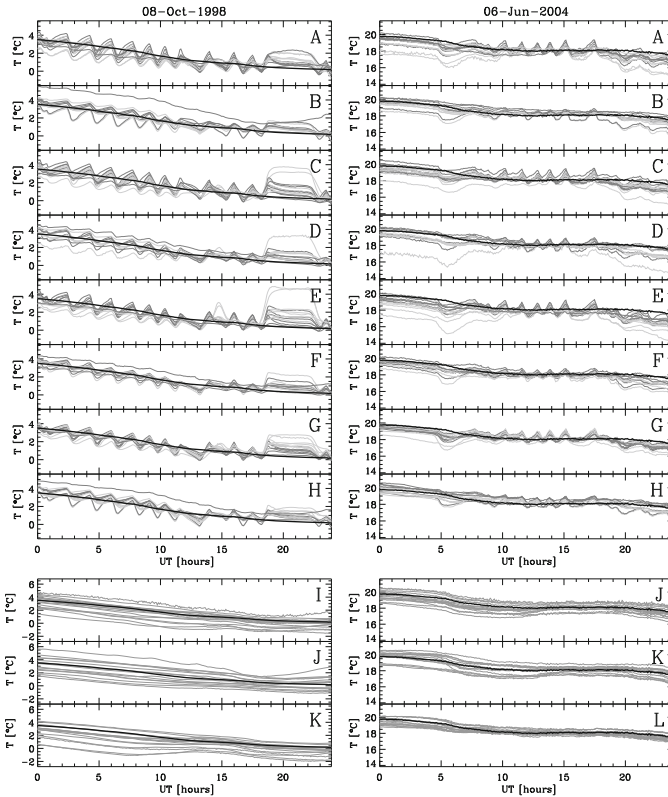


Fig. 9.46 IRAM 30-m telescope. Temperature regulation and temperature of the BUS sectors A, B, ..., H (see Fig. 9.45) and of the yoke sectors J, K, L (see Fig. 9.23). The figure on the left shows the situation before installation of ventilation/heating in the yoke, the figure on the right after installation of ventilation/heating. The heavy line is the reference temperature, measured inside the yoke [From Bremer & Peñalver (2002), Courtesy SPIE, and Greve & Mangum (2008), Courtesy IEEE].

precision, the gradients Up–Down and Left–Right indicate a possible pointing error in El and AZ direction, the axial gradient indicates a possible focus error. Furthermore of importance is the temperature uniformity between the roof of the yoke and the base of the BUS. A temperature gradient in the yoke arms and a temperature difference between the roof of the yoke and the BUS base may introduce reflector surface deformations. The mentioned parameters are shown in Fig. 9.47 for a 14-day period in July and October, 2004, after installation of ventilation/heating in the yoke. With a few exceptions, the measurements indicate that the specified temperature uniformity of $\text{rms}(T_{\text{BUS}}) \lesssim 0.5^\circ\text{C}$ is achieved and that the gradients are smaller than $\sim \pm 1^\circ\text{C}$ with a correspondingly small pointing and focus error. This

uniform thermal state of the BUS–yoke–quadripod is one of the reasons of the good radio performance of the IRAM 30–m telescope.

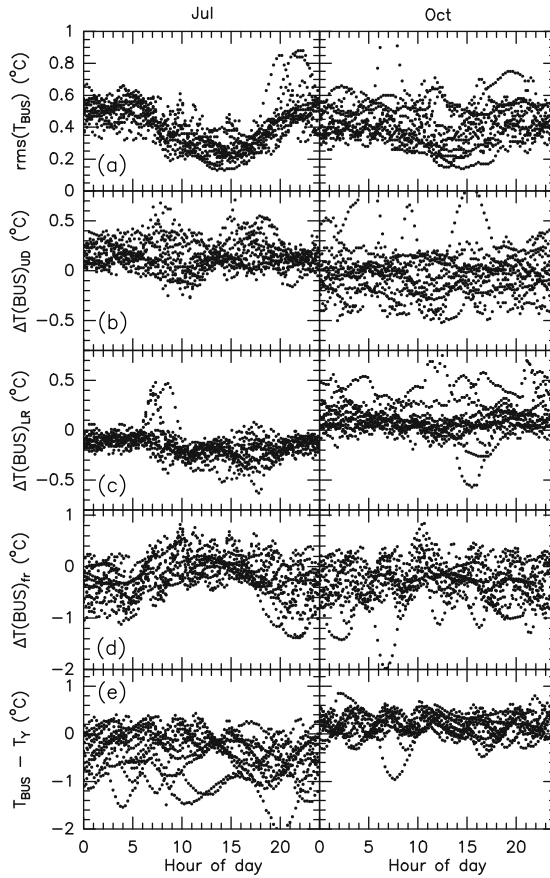


Fig. 9.47 IRAM 30–m telescope. (a) Temperature uniformity of the BUS expressed by the value $\text{rms}(T_{\text{BUS}})$, (b) temperature gradient in the BUS $\Delta T(\text{BUS})_{\text{UD}}$ in the direction Up–Down, (c) in the direction Left–Right $\Delta T(\text{BUS})_{\text{LR}}$, (d) between front (panel) and rear $\Delta T(\text{BUS})_{\text{fr}}$ and (e) between the roof of the yoke and the base of the BUS, $T_{\text{BUS}} - T_{\text{Y}}$. The measurements are shown for a 14–day period in July and October 2004.

9.3.6 Thermal Deformations and Active Reflector Surfaces

The solution of active thermal control as applied on the IRAM 30–m telescope is perhaps already out–of–date for the next generation radio telescopes. On a telescope with an active main reflector surface or a deformable subreflector the temperature

induced reflector surface deformations and with this the associated focus and pointing errors can be corrected in real time. To achieve this, temperature sensors must be installed at thermally significant finite elements as explained in Chapter 6. The temperature readings are used in the FEM or the influence matrix \mathbf{M} (Eq.(6.4)) to calculate the instantaneous surface deformations. The investigation of the IRAM 30–m telescope has demonstrated [Greve et al. 2005] that in this way the temperature induced reflector deformations can be derived with the accuracy of ~ 0.005 mm, and with good accuracy the associated focus and pointing errors in the case a complete FEM is available. Direct temperature measurements of structural nodes have the advantage over, for instance, out-of-focus holography measurements [Nikolic et al. 2007] in that they are instantaneous and for immediate use in the FEM. As discussed by Kärcher [2006] for the LMT/GMT 50–m telescope, such an approach avoids the installation of a climatisation system with heaters and coolers, of considerable energy consumption and considerable operation costs. Nevertheless, a good *passive* thermal design of a telescope is a prerequisite for a good operation.

9.3.7 The Radome/Astrodome enclosed BUS

A telescope is placed in a radome or astrodome in order to decrease the influence of temperature and wind. There are three concepts of a telescope in an enclosure, i.e.

- (1) a telescope in a radome with ventilation (Figs. 3.4, 3.5),
- (2) a telescope in an astrodome where the slit is opened for observation (Figs. 3.1, 3.2),
- (3) a telescope in an astrodome where the slit is covered by a radio transparent membrane (Fig. 3.3).

Information is available of the radome enclosed Metsähovi 14–m telescope [Metsähovi staff, priv. comm.], the FCRAO 14–m telescope [Schloerb 1978] and the MIT–Haystack 37–m telescope [Barvainis et al. 1993, Ingalls et al. 1994, A.E.E. Rogers, priv. comm.], of the astrodome enclosed CSO 9.4–m telescope [Chamberlin 2003], where the astrodome is opened for observations, and of the JCMT 15–m telescope [Baas 1995, Wouterloot 2005], where the astrodome slit is covered with a radio transparent membrane. The JCMT astrodome is usually not opened for observations although the doors and the roof can be opened for ventilation.

9.3.7.1 Radome enclosed Telescopes

The Metsähovi 14–m telescope (Finland) is enclosed in a radome of similar dimension as the radome of the FCRAO 14–m telescope summarized in Table 3.2. The BUS and the central hub structure of the Metsähovi telescope consist of Al–beams and Al–panel plates (Fig. 3.5), the yoke beams are made of steel. The surface finish of the BUS beams and the panels is that of machined aluminium. The receiver

and electronics are located in the vertex tunnel and the secondary focus cabin. The radome is ventilated with a large contribution of outside ambient air. The temperature of the reflector is measured at the top, bottom, left, right and middle section, the temperature of the radome space frame is measured at the bottom, middle and top area. The outside ambient air temperature and the insolation is recorded. Fig. 9.48.a shows the ambient air temperature, the insolation and the average reflector temperature (5 sensors). The figure indicates that the temperature of the reflector follows approximately the temperature of the outside ambient air. This is especially evident for Mar 20, 2002, when the outside ambient air temperature and the reflector temperatures were significantly below zero degree. The temperature uniformity of the reflector is expressed by the value $\text{rms}(T_{\text{ref}})$ (4 sensors only) shown in Fig. 9.48.b. The temperature gradients in the direction Up–Down and Left–Right were $\sim 2^\circ\text{C}$ or smaller.

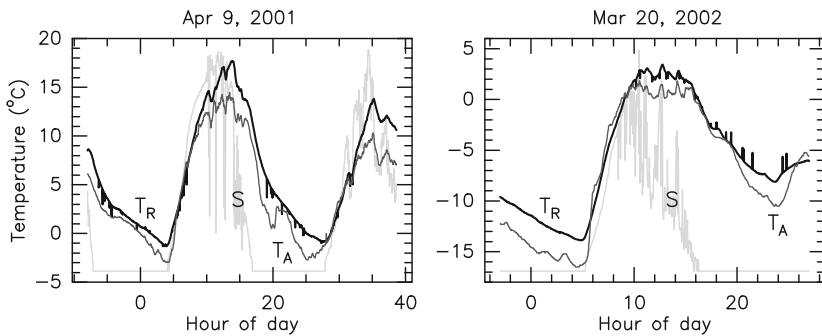


Fig. 9.48.a Metsähovi 14-m telescope. Average reflector (BUS) temperature: T_R , outside ambient air temperature: T_A , insolation: S (9 Apr: max $S = 660\text{ W/m}^2$, 20 Mar: max $S = 500\text{ W/m}^2$) [Data from Metsähovi Observatory, Finland].

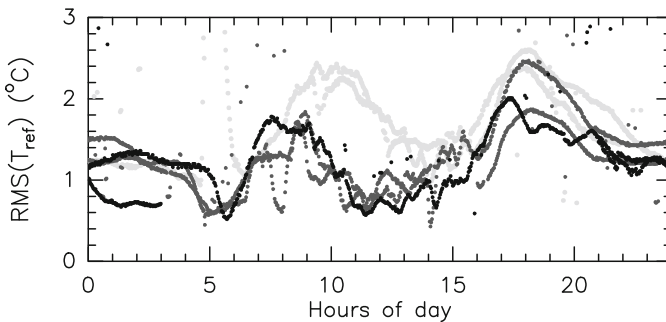


Fig. 9.48.b Metsähovi 14-m telescope. Temperature uniformity of the reflector $\text{RMS}(T_{\text{ref}})$. Each trace is a different day [Data from Metsähovi Observatory, Finland].

The ventilation of the radome of the MIT–Haystack 37–m telescope and the active thermal control of the BUS splice ring (a stiffened BUS support box frame at $\sim 1/2$ radial distance) is explained by Barvainis et al. [1993] and Ingalls et al. [1994]. The ventilation uses outside ambient air, which is heated if necessary to keep the air inside the radome above approximately 10°C . The radome, and by this the telescope, is ventilated in a rather homogeneous way by blowers at the periphery of the radome and at the inside close to the pedestal. The BUS of the telescope is made of aluminium, the yoke is made of steel. In order to have a uniform temperature of the splice ring and the outer panels, the splice ring can be heated with electric heaters and cooled with water coolers (pipe system). The thermal deformations produced in this way on the reflector surface are used together with an active sub-reflector to correct the gravitational deformations of the BUS. Fig. 9.49.a shows the average temperature of the BUS (T_B), the temperature of the air inside the radome ($T_{A,RD}$) and the outside ambient air temperature (T_A). A temperature sensor on a truss at the upper and lower section of the BUS (in tilt direction) allows measurements of the temperature gradient in the direction Up–Down. This gradient is shown in Fig. 9.49.b. During the day the upper part of the BUS is warmer than the lower part, with a reversal during night. The amplitude of the temperature gradient in the direction Up–Down correlates with the daily amplitude of the inside and outside air temperature.

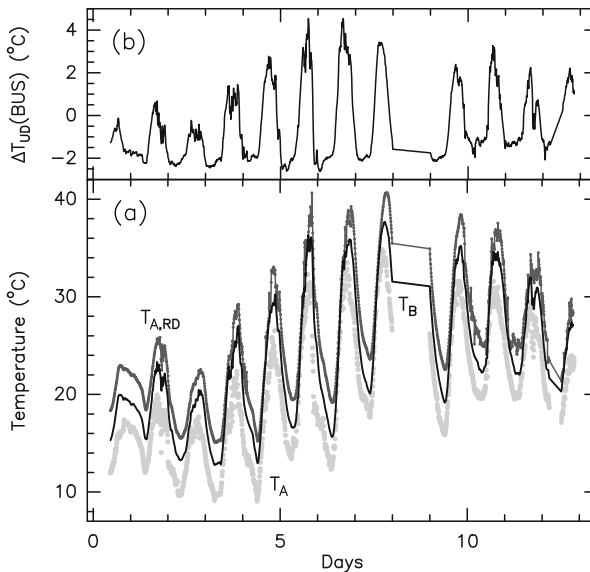


Fig. 9.49 MIT–Haystack 37–m telescope. (a) Average temperature of the BUS: T_B , of the air inside the radome: $T_{A,RD}$ and of the outside ambient air: T_A . (b) Temperature difference between an upper (top) and lower (bottom) BUS member: $\Delta T_{UD}(\text{BUS})$ [Data from MIT–Haystack Observatory, USA].

9.3.7.2 Astrodome enclosed Telescopes with open Slit

The HHT 10-m telescope (Fig. 3.1) and the CSO 9.4-m telescope (Fig. 3.2) use an astrodome with open slit. Temperature measurements (of approximately 3 consecutive days) of the CSO telescope [Chamberlin 2003] reveal that the BUS follows the ambient air temperature inside the astrodome within $\sim 2^\circ\text{C}$ during the night when the slit is opened for observations and within $\sim 5^\circ\text{C}$ during the day when the slit is usually closed. At night, and the telescope pointing below 30° elevation, the upper part of the BUS was cooler than the lower parts by 2 to 3°C . The left-right temperature difference of the BUS was $\sim 2^\circ\text{C}$, during the day and night.

9.3.7.3 Astrodome enclosed Telescopes with Membrane covered Slit

Data of the BUS' thermal behaviour of the JCMT 15-m telescope are published on the web-site <http://www.jach.hawaii.edu/JCMT/telescope/surface>. The layout of the JMCT BUS and its support is shown in Fig. 9.50. The BUS network is supported by a pyramidal cone of centre beams and cone bars with counterweight. The secondary focus cabin is inside the cone structure and some of the centre beams cross the cabin. The air inside the secondary focus cabin is warm (receivers, electronics), the sections of the centre beams inside the focus cabin are insulated and ventilated. Each panel is attached by 3 actuators to the BUS. On the BUS and BUS support structure are 220 temperature sensors. Regular holography measurements and subsequent adjustments of the reflector surface are made to eliminate seasonal temperature effects of the JCMT BUS structure. A real time surface adjustment based on temperature measurements and FEM calculations has been tested for routine application. As documented on the web-site, there is good agreement between the reflector surface map derived from temperature measurements and FEM calculations and the holography map made at the same time (for the IRAM 30-m telescope see Fig. 6.9.)

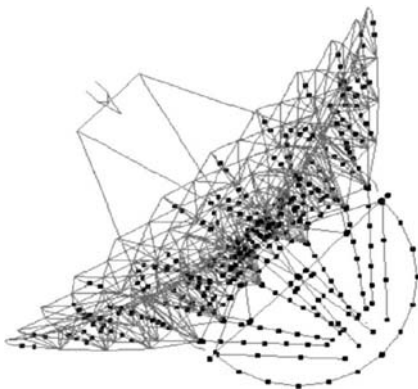


Fig. 9.50 JCMT 15-m telescope. BUS support (centre beams, cone bars) and BUS; the dots indicate the location of temperature sensors [<http://www.jach.hawaii.edu/JCMT/telescope>].

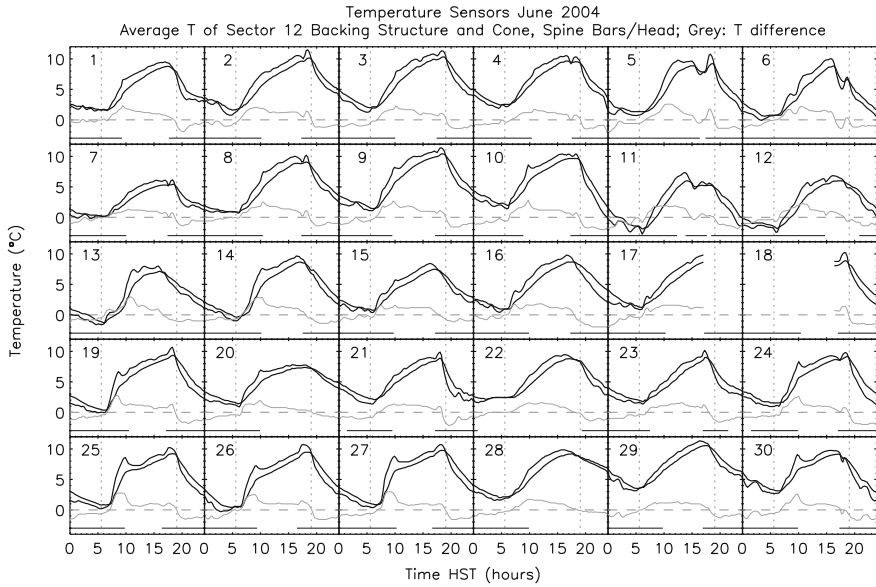


Fig. 9.51.a JCMT 15-m telescope. Temperature measurements (June 2004) of the BUS network and cone and spine bars (BUS support): upper curves in the panels. Lower curves: temperature difference $T(\text{BUS}) - T(\text{BUS support})$. Horizontal lines: time when the roof and doors of the astrodome are open; dashed vertical lines: sunrise and sunset [After J. Wouterloot (2005), Courtesy JCMT].

Figure 9.51.a and 9.51.b show temperature measurements of the JCMT BUS (lower sector 12) and of the BUS support. It is seen in Fig. 9.51.a that the temperature of the BUS and the BUS support increase after sunrise by $\sim 10^\circ\text{C}$ (June 2004) when the roof and doors of the astrodome are closed. When the roof and doors are opened around sunset, the temperature decreases by a similar amount. During the day the heavier BUS support beams are approximately 2 to 3°C cooler than the lighter beams of the BUS, during the night with the roof and doors open the situation is reversed. Fig. 9.51.b shows a similar behaviour of the centre beams and the cone bars with the heavier centre beams showing a smaller amplitude of daily temperature variations. During the night, with the roof and doors open, the temperature difference of the centre beams and the cone bars can reach $\sim 5^\circ\text{C}$. The approximately exponential temperature increase after sunrise and temperature decrease after sunset seen in Fig. 9.51 represents the thermal time constants of this process.

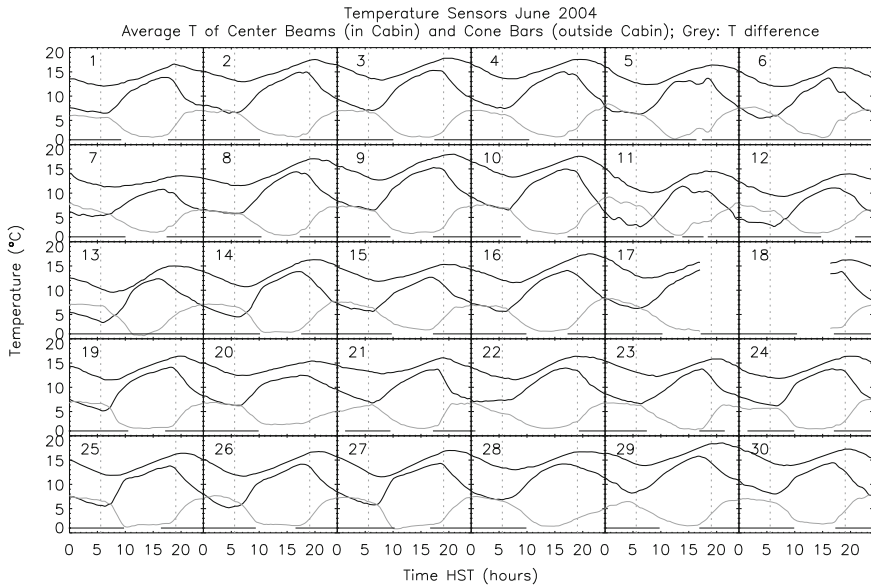


Fig. 9.51.b JCMT 15-m telescope. Temperature measurements (June 2004) of the BUS centre beams, cone bars and spine bars. Horizontal lines: time when the roof and doors of the astrodome are open; dashed vertical lines: sunrise and sunset [After J. Wouterloot (2005), Courtesy JCMT].

9.3.8 Temperature Changes of the BUS and Focus Changes

A change of the BUS temperature may result in a change of the reflector surface contour and this in a change of the focal length. A semi-empirical relation between the BUS temperature and a change in focal length has been used on several telescopes, for instance on the Kitt Peak 11-m telescope [von Hoerner & Herrero 1971, Fig. 6.12], the IRAM 30-m telescope [Baars et al. 1988] and the ALMA VertexRSI 12-m telescope [Baars 2007]. The prediction of focus corrections of the GBT 100-m telescope based on 5 temperature measurements of the BUS and one temperature measurement of the subreflector ('one' feed leg) is published by Prestage et al. [2004]. Real time focus determinations based on 104 temperature measurements of the IRAM 30-m telescope BUS used in the FEM have been successful as explained in Section 6.6.

An interesting explanation of the correlation between the focus change (Δf) and the temperature gradient of the BUS in radial direction (ΔT_r) observed on the FCRAO radome enclosed 14-m telescope ($\Delta f [\text{mm}] \approx \Delta T_r [^\circ \text{C}]$) was proposed by Schloerb [1978] on the basis of different thermal time constants for different parts of the BUS. The inner part of the BUS consists of aluminium beams with 1/4 inch wall thickness, the outer ribs and intercostals consists of plates 1/8 to 1/16 inches thick (Fig. 3.5). The thermal time constant of the inner part, the middle part and the

outer part of the BUS is $\tau_{\text{inner}} \approx 1.5 \text{ h}$, $\tau_{\text{middle}} \approx 0.7 \text{ h}$ and $\tau_{\text{outer}} \approx 0.4 \text{ h}$, the thermal time constant of the quadripod is $\tau_{\text{legs}} \lesssim 0.2 \text{ h}$. A temperature gradient develops between the centre and the rim of the BUS because of the different response times of the BUS sections to a temperature change of the air in the radome. This results in a longer focus if the inner part of the BUS is warmer than the outer part, which occurs when the temperature of the air in the radome decreases. In this situation the reflector (BUS) curls up and the quadripod anchored in the outer parts of the BUS is pushed outside resulting in a longer focal length. A shorter focus occurs if the temperature of the air increases. Regular temperature changes of the air in the radome occur (for instance for the Metsähovi radome see Fig. 10.1) due to solar illumination of the radome and ventilation of the radome with a contribution of ambient air with a regular daily temperature change.

9.4 Panels

On a radio telescope all panels are identical, or at least subgroups of panels of certain panel rings, with identical thermal behaviour. A uniform temperature change and a temperature gradient through a panel may change its form (curvature, buckling), which leads to a reflector surface with repetitive surface deformations. The cumulative effect of these deformations may deform the beam pattern and decrease the gain (sensitivity) though without change of the focus and pointing of the telescope.

There are many types of panels, with different thermal behaviour. The panel front is always in contact with the thermal environment. A panel is in contact with the ambient air through convective heat transfer, which increases with increasing wind speed; it may be exposed to direct solar radiation that can be buffered to some extent by using a low absorption paint; it is radiatively coupled to the cold sky and the warm ground. On an open BUS the rear side of a panel is in similar contact with the thermal environment, on a closed BUS a panel is in thermal contact with the BUS through internal convection and radiation, or it is in thermal contact with the BUS front closure, which can be a layer of insulation. A short thermal time constant of $\sim 1/2 \text{ h}$ is favourable so that a panel can quickly adjust in a uniform way to the variable thermal environment. Large-size mesh wire panels with negligible heat capacity and an immediate thermal response are used on metre and cm-wavelength telescopes (for instance the GMRT telescopes, Picture 1.1, or the perforated panels on the outer part of the Effelsberg reflector, Picture 1.2). There are panels made of single Al-sheets or Al-sheets reinforced by ribs (Fig. 2.13.a) of small size of $\sim 0.8 \text{ m} \times 0.8 \text{ m}$ ('mini-panels' for instance used on the VertexRSI ALMA/APEX telescopes) or of large size of $\sim 1.5 \text{ m} \times 2 \text{ m}$ (for instance used on the Yebes 40-m telescope). There are medium size panels made of an Al-honeycomb core with an aluminium or CFRP or nickel skin for high precision cm-wavelength and mm/sub-mm wavelength telescopes (for instance used on the JCMT, AEC ALMA and IRAM telescopes). The panels may have a special surface finish in order to manipulate the thermal coupling to solar radiation and radiation from the sky and the ground. The

surface finish falls into two categories, i.e. either with significant absorption of solar radiation and high emission in the infrared (like TiO_2 paint, $a_S \approx 0.35$, $e_I \approx 0.7$), or little solar absorption and low emission in the infrared (like anodised aluminium and rhodium coating, $a_S \approx e_I \approx 0.2-0.1$). The panels are attached to the BUS by adjuster screws or actuators allowing real time adjustment (JCMT, GBT, NOTO), or are attached to panel frames that are connected to the BUS (IRAM 30-m telescope, LMT/GTM with actuators on the panel frames). The adjuster connection to the BUS or panel frames can be at 3 points (JCMT), 4 points (IRAM 30-m) or 5 points (IRAM 15-m, VertexRSI ALMA). Some panels can be heated for de-icing.

9.4.1 Experimental Data of Panel Temperatures

The temperature of a panel depends on the absorption coefficient of solar radiation a_S at $\lambda \approx 0.5 \mu\text{m}$ and the emission and absorption coefficient of infrared radiation $e_I \approx a_I$ at $\lambda \approx 2-20 \mu\text{m}$. For many materials are the coefficients available in textbooks and engineering tables. The temperature of a panel depends in addition on the thermal environment at its rear. Many panel tests have been made to determine for instance the surface temperature for different paints and coatings, the temperature gradient through a panel when heated, the change in curvature when heated etc. However, thermal model calculations of panels can be made with good precision for comparative studies of paint characteristics and different insulation and heating, which can hardly be realized in experiments.

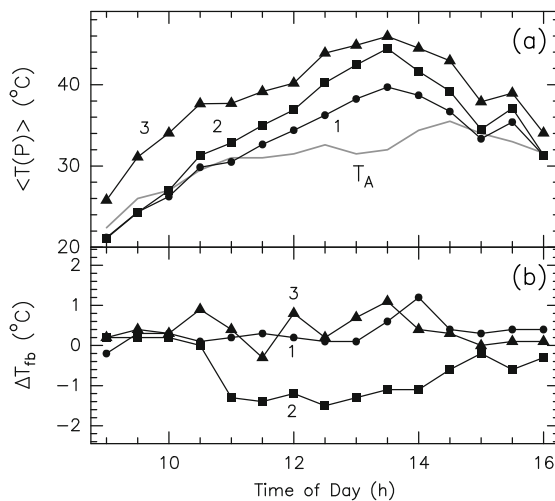


Fig. 9.52 Temperature of Al-honeycomb panels with white front and rear (1), with white front side and 2.5 cm insulation on the rear (2) and with Al-foil cover on front and rear (3). (a) average panel temperature $\langle T(P) \rangle$, ambient air temperature T_A ; (b) temperature gradient $\Delta T_{fb} = T(\text{front}) - T(\text{back})$ through the panels.

Figure 9.52 shows a comparative experimental study of a 5 cm thick Al–honeycomb panel with 2 mm thick CFRP skin on the front and rear, once painted white with TiO_2 paint on both sides (1), once painted white with TiO_2 paint and 2.5 cm insulation glued to the back (2), once covered with Al–foil on both sides (3). The panels were placed next to each other, approximately 40 cm above the ground, the measurements were made at the same time. The temperature gradient ΔT_{fb} through the panels was derived from these measurements. The figure shows that the insulated panel has a larger gradient, i.e. the heat cannot escape at the rear. However, experiments of this type may hardly be representative of the conditions on a telescope at an exposed site. Another example that served to check the thermal model of a panel is shown in Fig. 11.1.

9.4.2 Panel Temperatures measured on Telescopes

Figure 9.53 shows temperature measurements of an Al–plate panel with backing ribs (cassette panel) on the Effelsberg 100–m telescope. This panel is exposed to the thermal environment but shadowing from direct sunshine may have occurred during the measurement. The panel temperature at night is a few degrees below the ambient air temperature because of radiative cooling towards the cool sky, while during the day the panel temperature can be many degrees above the ambient air temperature because of insolation. The rapid temperature increase/decrease during morning and evening indicates a short thermal time constant. A similar situation is observed on the IRAM 30–m telescope, as illustrated in Fig. 9.54. Here the panels consist of a 4 cm thick Al–honeycomb core with a 2 mm thick aluminium front and rear skin, at the outer surface painted white with TiO_2 paint. The panels are separated from the climatized BUS by a 4 cm thick insulation layer. The temperature of the panels falls during the night ~ 5 to 10°C below the ambient air temperature due to radiative cooling towards the cool sky. The excess temperature of 10 to 20°C during the day is due to insolation. The rapid temperature variations illustrate that the panels have a short thermal time constant, of the order of 1/2 hour. The large variation of the panel temperature is not felt by the climatized BUS.

9.4.3 Thermal Panel Buckling

Thermal panel buckling may occur, on the one hand, if the panels and the BUS are built from different materials, for instance steel and aluminium; it may occur, on the other hand, because of a temperature gradient through the panels or the panel frames. On a telescope with a steel BUS and aluminium panels the panel adjusters may be designed as hinges to compensate the higher thermal expansion of the panels. Panel buckling is a transient effect. The buckling produces a repetitive pattern of

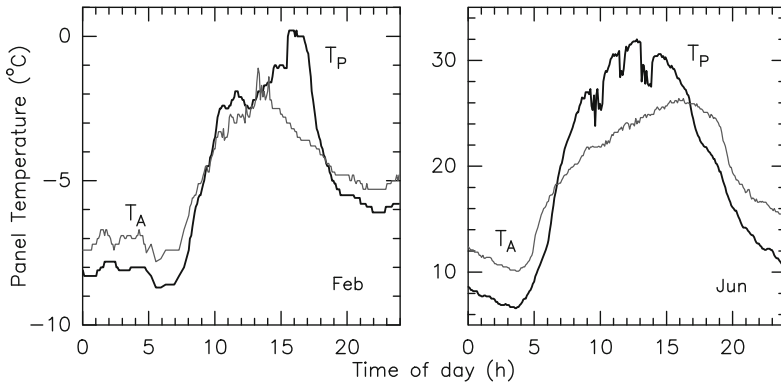


Fig. 9.53 Effelsberg 100-m telescope. Panel temperature T_P and ambient air temperature T_A , during a winter and a summer day [Data MPIfR Effelsberg, Germany].

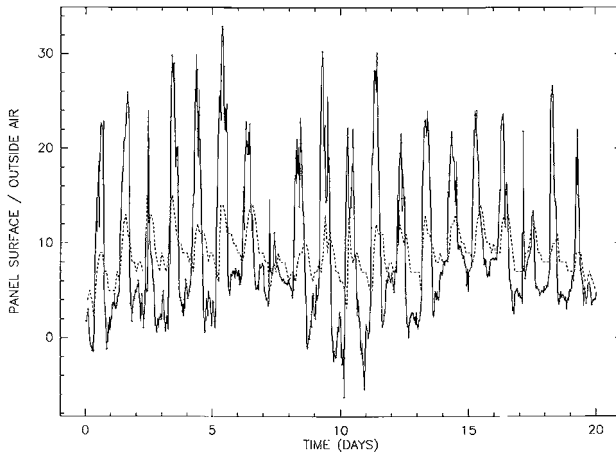


Fig. 9.54 IRAM 30-m telescope. Panel temperature: continuous line, ambient air temperature: dotted line.

reflector surface deformations that appear as a characteristic degradation of the radio beam, as explained in Section 12.4.2. For further details of the associated diffraction patterns see Greve & Morris [2005] and Greve et al. [2009]. The associated problems of adjusting aluminium panels on a steel BUS were already discussed by Schönbach [1968].

Thermal panel buckling has been observed on the Effelsberg 100-m telescope, the IRAM 30-m telescope, probably on the APEX 12-m telescope and on the astrodome enclosed JCMT 15-m telescope. High spatial resolution and high signal to noise radio holography was used for the measurement of panel buckling. Measurements of panel buckling on the Effelsberg telescope and the IRAM 30-m telescope are shown in Fig. 9.55, a difference map revealing panel buckling on the APEX

telescope surface is shown in Fig.9.56 and on the JCMT telescope surface in Fig.9.57. Especially Fig.9.55 illustrates that the panels buckle out of the surface (in the direction of the primary focus) during the day and into the surface during the night. The holography difference map of the JCMT surface (Fig.9.57) is made from a map taken during the morning when the Sun was shining on the reflector and a map made during the evening. It is stated that the buckling seen in the difference map is to the outside, as expected for a warmer reflector illuminated by the Sun.

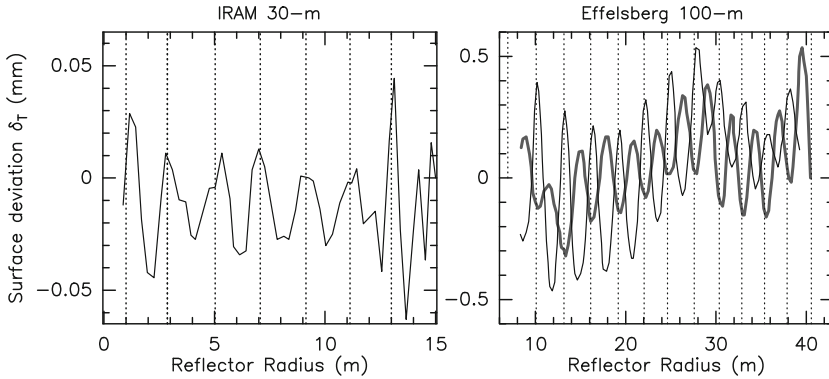


Fig. 9.55 Azimuth-averaged thermal panel buckling of the IRAM 30-m telescope and the Effelsberg 100-m telescope [Morris et al. 2009, Greve & Morris 2005]. The panel rings are indicated by dashed lines. Effelsberg telescope: panel buckling in downward direction during the night: thin line, in upward direction during the day: thick line [from Kesteven et al. 2001]. IRAM 30-m telescope: in order to increase the signal-to-noise of the measurement (precision ~ 0.02 mm) the difference of the day and night buckling is shown. The panels of both telescopes buckle in the same direction [After Greve & Morris (2005), Courtesy IEEE Trans. Ant. Propag.].

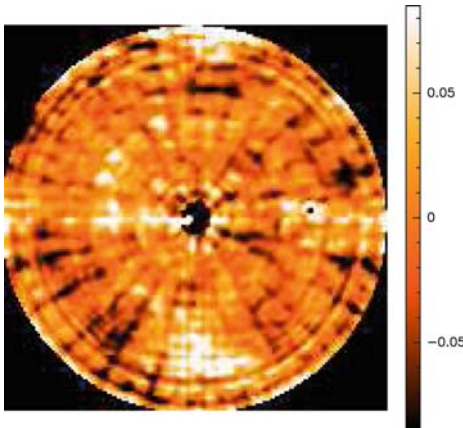


Fig.9.56 Possible thermal panel buckling on the APEX 12-m telescope. The figure shows the difference map between night and day. Scale: 0.05 radians = $12 \mu\text{m}$ [Courtesy R. Güsten, MPIfR, Germany].

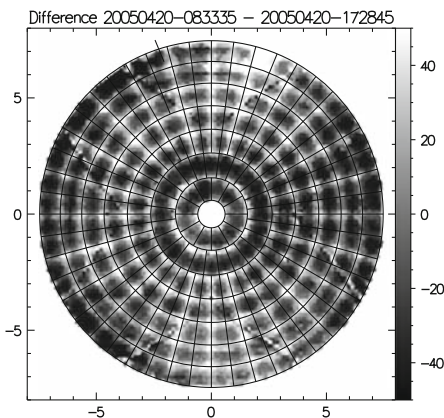


Fig. 9.57 JCMT telescope and thermal panel buckling. The figure shows the difference map between morning (8.5 h) and afternoon (17.5 h). The scale is in μm [After J. Wouterloot (2005), Courtesy JCMT].

Panel buckling can occur in a number of situations:

- (a) the panel ($\text{CTE} = \alpha_P$) and the BUS ($\text{CTE} = \alpha_{\text{BUS}}$) are made of the same material, the buckling occurs because of a temperature difference between the panel and the BUS;
- (b) the panel and the BUS are made of different materials, a uniform temperature change ΔT of the BUS and the panels causes buckling proportional to $\Delta\alpha = \alpha_P - \alpha_{\text{BUS}}$;
- (c) the panel and the BUS are made of different materials, the temperature of the panel and the BUS change in a different way;
- (d) the buckling occurs because of a temperature gradient ΔT_P through the panel;
- (e) the buckling occurs because of a temperature gradient ΔT_{frame} through the panel frame.

For a panel of length ℓ , rigidly attached to the BUS, the situation (a) and (b) can be analysed with the relation of the buckling amplitude Δz_{max} derived by Christiansen & Högbom [1985]

$$\Delta z_{\text{max}} \approx 0.6 \ell (\alpha^* \Delta T)^{1/2} \quad (9.7)$$

with $\alpha^* = \alpha_P$ for case (a) and $\alpha^* = \alpha_P - \alpha_{\text{BUS}}$ for case (b). The situation (c) is a combination of (a) and (b). For situation (d), sketched in Fig. 9.58 of a panel attached rigidly to the BUS, von Hoerner [1977 b] derived that the central amplitude Δz_{max} (sag) of the buckling is in first approximation

$$\Delta z_{\text{max}} = \frac{1}{8} \alpha (\ell^2/d) \Delta T_P \quad (9.8)$$

with ℓ and d the length and depth (thickness) of the panel and α its CTE. The situation (e) of a panel frame can only be analysed from a FEM calculation. Although the amplitude of the buckling Δz_{max} may be large, the rms value of a reflector surface covered with buckled panels is of the order of $\sigma^* \approx \Delta z_{\text{max}}/3$ (see Section 12.4.2).

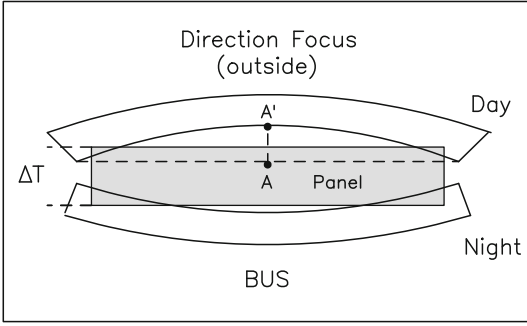


Fig. 9.58 Illustration of a buckled panel with temperature gradient ΔT . The buckling direction is different during daytime (towards the focus) and nighttime (towards the BUS). In Eq.(9.7), Eq.(9.8): $AA' = \Delta z_{\max}$.

The temperature difference between the panels and the BUS measured on the Effelsberg 100–m telescope is shown in Fig. 9.59. The figure indicates that on average the panels are warmer during the day and cooler than the BUS during the night. However, it is not clear from the measurements whether this is the primary source of the panel buckling, or whether a significant temperature gradient through the panels acts as well. The panels of the Effelsberg telescope are made of aluminium plates reinforced with backing ribs, the BUS is made of steel. Taking for the length of the panel $\ell \approx 2$ m, for the thickness (with ribs) $d \approx 5$ cm, for $\Delta T = T(P) - T(BUS) \approx 5^\circ$ C and for the CTE the difference of aluminium and steel $\Delta\alpha \approx 0.01$ m/m/K, then Eq.(9.7) gives $\Delta z_{\max} \approx 0.3$ mm as observed in Fig. 9.55.

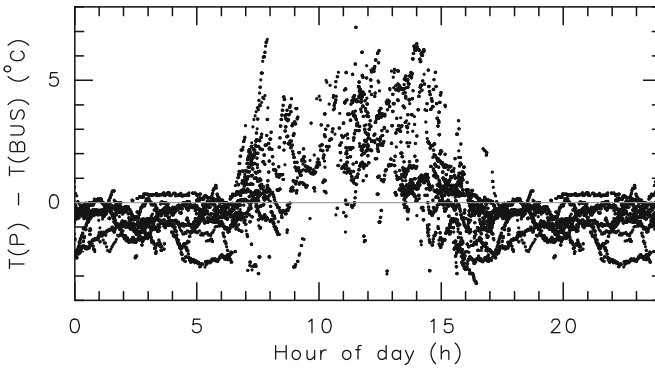


Fig. 9.59 Difference between the panel temperature $T(P)$ (sensor C, Fig. 2.4) and the BUS temperature $T(BUS)$ (sensor D, Fig. 2.4) measured on the Effelsberg 100–m telescope, during 5 consecutive days in summer while the telescope was observing. (The data shown do not correspond to the time of the measurement of Fig. 9.55) [Data MPIfR Effelsberg, Germany].

The buckling of the panels on the IRAM 30–m telescope is caused by thermal buckling of the panel frames (see Fig. 2.14), of 60 cm depth. Holography measurements show that a common buckling occurs always on two panels that are supported on the same frame. Each panel is attached to its frame by 15 screws so that a panel will follow the deformations of the frame. Measurements have shown, as illustrated

in Fig. 9.60, that a temperature gradient through the frame of ~ 1 to 4°C occurs during the day in the direction inwards (from the panel rear side to the BUS) and a gradient of -1 to -2°C outwards during the night. This gradient is due to a temperature increase of the frame at the panel side during the day and a cooling during the night, while the part of the frame deeper inside the BUS is ventilated and of the same temperature as the BUS. The thermal gradient in the frame introduces a buckling of the frame and by this a buckling of the panels. The reversal of the thermal gradient between day and night explains the different direction of buckling during day and night (Fig. 9.55). The reversal of the temperature gradient and of the frame buckling occurs within 1 to 2 hours. FEM calculations have confirmed this effect as the origin of the panel buckling and the magnitude and reversal of the buckling [Plathner 1997].

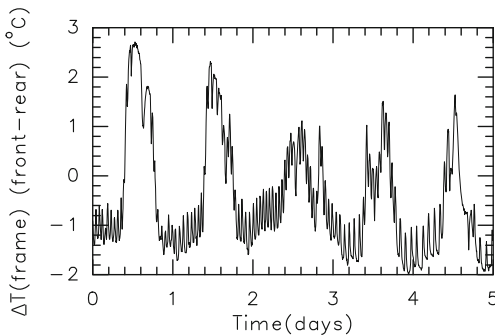


Fig. 9.60 IRAM 30-m telescope. Temperature gradient $\Delta T(\text{frame})$ through a panel frame. At daytime the front side of the frame is warmer, at nighttime cooler.

The Cornell Caltech Atacama 25-m telescope (CCAT) for sub-mm wavelengths is proposed to have an active surface control with edge sensors similar to the Keck 10-m optical telescopes in order to achieve and maintain a surface precision of $\sim 10\ \mu\text{m}$. This proposed metrology system of the CCAT is sensitive to panel buckling due to gravity and temperature gradients through the panels [Woody et al. 2008]. Measurements of temperature gradients through the Al-honeycomb panels on the CSO 10-m telescope [Woody et al. 1994] revealed a value of $\sim 0.3^\circ\text{C}$, with variations of a factor 2 across the surface and with time. Model calculations of thermal gradients through panels have been made in order to explore a number of panel constructions and panel frames for the CCAT [Woody et al. 2008].

9.4.4 Heated Panels, De-icing of Panels

The IRAM 15-m telescopes (Plateau de Bure, 2500 m altitude, France) and the IRAM 30-m telescope (Pico Veleta, 2900 m altitude, Spain) at sites with severe winter conditions have panels that can be heated from the back to prevent snow and ice accumulation. The heating mats are placed between the rear of the panel and an

insulation layer. The average heating power is $\sim 200 \text{ W/m}^2$. If switched on in time, the surfaces remain free of snow and ice.

Tests have been made on Plateau de Bure with panels with back and front heating, manufactured by Media-LarioTM. The panels consist of an Al-honeycomb core (4 cm thickness) and glued-on electroformed Ni-skins (0.6 mm thickness), at the front surface coated with rhodium, at the rear covered with 1 cm thick insulation. The design is shown in Fig. 9.61. When used on the Plateau de Bure 15-m telescope the panels are heated with 600 W/m^2 and a duty cycle of 22 % (4 s on, 18 s off) or 57 % (8 s on, 14 s off). The higher duty cycle can be applied to the lower sector of the reflector; the necessity of this power distribution is evident from Fig. 8.1 that shows in particular icing at the lower surface sections. The heating of a few 100 W/m^2 allows de-icing (panel surface temperature above zero degree) at ambient temperatures above $\sim -15^\circ \text{C}$. Results of these tests are reported by Bremer et al. [2005]⁵ and are summarized here.

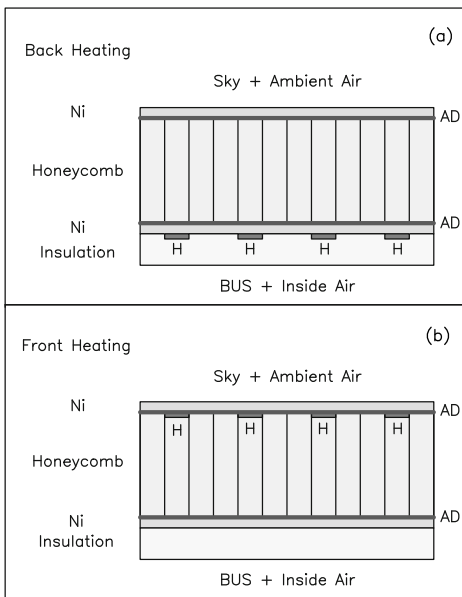


Fig. 9.61 Media-LarioTM panel design of back (a) and front (b) heating. H: heating wires, AD: adhesive.

With the panels installed on one IRAM 15-m telescope on Plateau de Bure, measurements were made to determine the temperature gradient through the panels under a large variety of environmental conditions. Fig. 9.62 shows that the average panel temperature varied during the tests by $\sim 50^\circ \text{C}$, temperature peaks occurred around noon. The temperature gradient through the panels however depends on the wind speed, as illustrated in Fig. 9.63, and thus on the convective cooling of the panel front surface. The measured temperature gradients through the panels are

⁵ The design, construction and tests of the panels were made together with ESA, Noordwijk, The Netherlands, with ESA the principle investigator.

$$\Delta T = T_{\text{front}} - T_{\text{back}} = -1.6 \pm 0.2^\circ \text{C} \quad \text{for back heating}$$

$$\Delta T = T_{\text{front}} - T_{\text{back}} = +0.4 \pm 0.15^\circ \text{C} \quad \text{for front heating}$$

at wind speeds at and above ~ 10 m/s. These gradients were also found from thermal model calculations explained in Section 11.6. Finite element calculations have shown that the gradient $\Delta T = -1.6^\circ \text{C}$ of the back heated panel produces a panel surface error $\sigma = 32 \mu\text{m}$ (rms), the gradient $\Delta T = 0.4^\circ \text{C}$ of the front heated panel produces a panel surface error $\sigma = 6.5 \mu\text{m}$ (rms). The panel surface error contains a large contribution from systematic deformations.

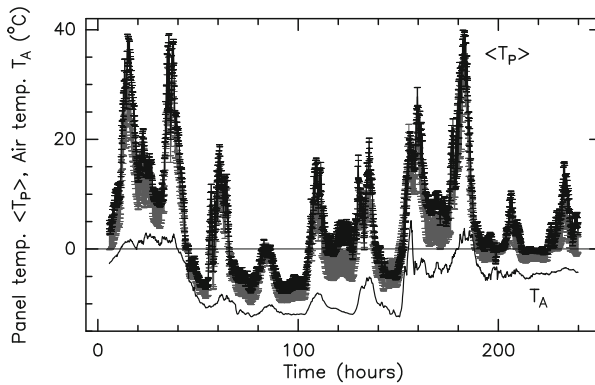


Fig. 9.62 Measured average temperature $\langle T_P \rangle$ of the Media-LarioTM panel with front (black line) and back (grey line) heating. The width of the lines represents the temperature distribution across and through the panels (8 sensors in total). T_A is the temperature of the ambient air.

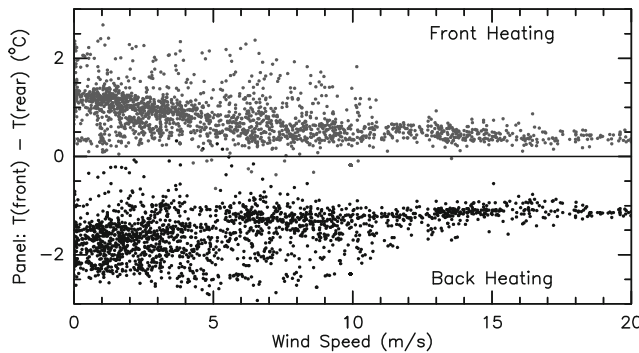


Fig. 9.63 Temperature gradient through the front heated and back heated Media-LarioTM panel as function of the wind speed (convective cooling).

9.5 Quadripod, Subreflector, Focus Cabins

9.5.1 Quadripod

If a telescope is used for primary focus observations the quadripod holds the primary focus cabin and the receiver (Fig. 2.1), if a telescope is used for secondary focus observations the quadripod holds the subreflector that reflects the incident wavefront to the secondary focus (Cassegrain focus or Gregory focus), located near the vertex of the main reflector where a receiver is installed (Figs. 2.2, 2.3). The quadripod is anchored in the BUS, or on a stiffened BUS subframe, or on an independent support frame (for instance the octahedron of the Effelsberg telescope, see Baars [2007], Fig. 2.8). Some characteristics of quadripods and of their thermal control are summarized in Table 9.8.

Table 9.8 Subreflector Support Structures (Quadripods).

Telescope ^{a)}	Reflector Diameter [m]	Quadripod ^{b)} Length [m]	Number of Legs	Material	Thermal Control
Effelsberg	100	30	4	steel/beams	white paint
GBT	100	30	1	steel/beams	white paint
NRO	45	13	3	steel/beams	white paint, internal ventilation
IRAM	30	9	4	steel/tubes	controlled glycol flow , insulation, white paint
IRAM	15	4.5	4	CFRP/tubes	partial cover Al-foil, white paint
ALMA	12	4	4	CFRP/tubes	white paint
BIMA(CARMA)	6	2	3	steel/tubes	insulation, shiny aluminium cover, internal ventilation

^{a)} see list of Acronyms of observatory sites.

^{b)} approximate length of quadripod, calculated from $L \approx f$, $f = nD$, $n = 0.3$.

The quadripod provides the specified alignment between the main reflector and the primary focus receiver (Fig. 2.1) or between the main reflector and the subreflector (Figs. 2.2, 2.3). If a temperature induced deformation of the quadripod results in a constant expansion of the four (three, one) legs, then a focus error and path length error will occur. If a temperature induced deformation results in a differential expansion of the legs, for instance due to asymmetric solar illumination, a lateral shift and tilt may also occur which results in a coma-like beam deformation and an associated pointing error, as explained in Chapter 13 and summarized in Table 9.1. On the off-axis GBT 100-m telescope the displacement of the one-arm supported subreflector also introduces an astigmatic wavefront error [Nikolic et al. 2005].

Since the BUS and the quadripod, with primary focus cabin or subreflector, form the radio-optics system of a telescope, the thermal behaviour of the quadripod

should be considered in relation to the thermal behaviour of the BUS, i.e. from the temperature difference $\langle T_Q \rangle - \langle T_{BUS} \rangle$ that is related to the focus and pointing stability of the telescope. A quadripod is exposed to the environment and its temperature is expected to be correlated to the ambient air temperature and the wind speed since convective heat transfer is involved. Since the mass to surface ratio $\mathcal{M} = M/A$ of a quadripod is small the convective heat transfer is relatively fast and the thermal time constant of the order of $\sim 1/2$ to 2 hours. The quadripod temperature is sensitive to insolation unless thermal protection is applied.

There are several quadripod constructions (Table 9.8). The large cm-wavelength telescopes (for instance Effelsberg and the GBT 100-m telescope) have quadripods made of steel beams or steel tubes of considerable length, diameter and plate thickness. These beams are usually painted white (TiO_2 paint). Since the quadripod is well exposed to the environment, the temperature of the quadripod of the Effelsberg telescope follows the ambient air temperature as illustrated in Fig. 9.32.c. A measurement of the temperature of opposite quadripod legs of the Effelsberg telescope is shown in Fig. 9.64. The telescope was stationary with the reflector pointing towards zenith, the sky was clear. The temperature of the quadripod legs follows the ambient air temperature but may fall below the ambient air temperature during the night because of radiative cooling towards the cool sky. As shown in the figure, temperature differences between the quadripod legs of 2 to 3° did occur, which cause a differential thermal expansion of the ~ 30 m long quadripod legs of $\sim 30 \text{ [m]} 0.012 \text{ [mm/m/K]} 3 \text{ [C]} \approx 1 \text{ mm}$. Reich [1996] reports for the Effelsberg telescope an axial focus shift that is synchronous with the change of ambient air temperature.

The uniformity of the thermal behaviour of the BUS and the quadripod of the Effelsberg 100-m telescope is illustrated in Fig. 9.65 for a summer and winter period. It is seen that the temperature difference $\langle T_Q \rangle - \langle T_{BUS} \rangle$ between the quadripod and the BUS can reach values of 5 to 7° C, especially in summer. The maximum of the temperature difference occurs around noon (at least for the summer period) and therefore is assumed to be caused mainly by solar illumination of the quadripod legs; at noon the quadripod legs are warmer than the BUS. These results must be taken with caution due to the small number of temperature sensors on the Effelsberg telescope.

The mm/sub-mm wavelength telescopes have quadripods made either of single CFRP tubes (IRAM 15-m and ALMA AEC 12-m prototype telescope) or of a network of curved CFRP tubes (ALMA VertexRSI and ALMA-J prototype telescope). The CFRP tubes are painted white. The CFRP quadripod of the IRAM 15-m telescopes is covered at the upper end (approximately 1/3 of the length) with aluminium foil to avoid damaging illumination from a caustic under skew solar illumination. A temperature measurement of the quadripod of the IRAM 15-m telescope is shown in Fig. 9.66.a. The observed daily temperature variation of the quadripod of 10° C introduces a thermal expansion of $\sim 10 \text{ [C]} 0.003 \text{ [mm/m/K]} 4 \text{ [m]} \approx 0.1 \text{ mm}$. It is seen in Fig. 9.66.a that the quadripod temperature is lower than the ambient air temperature, in particular during the night. The temperature difference $T_Q - T_{BUS}$

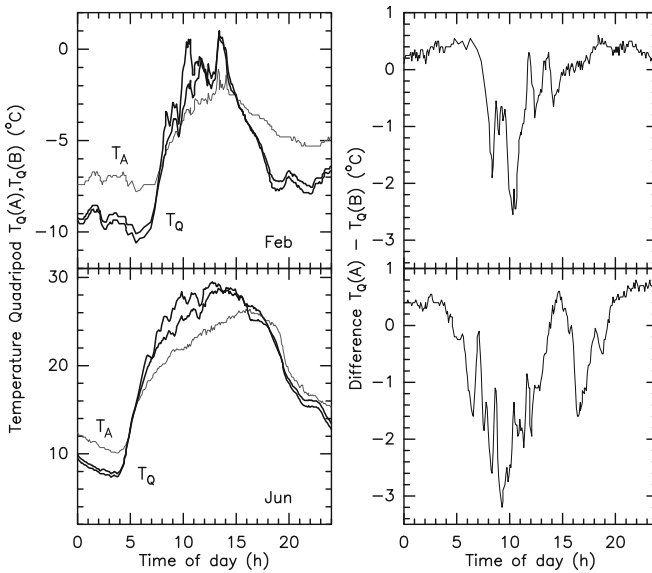


Fig. 9.64 Effelsberg 100-m telescope. Left: Temperature of opposite quadripod legs T_Q (A,B) and ambient air temperature T_A , during a winter and summer day. Right: Temperature difference $T_Q(A) - T_Q(B)$ of opposite quadripod legs [Data MPIfR Effelsberg, Germany].

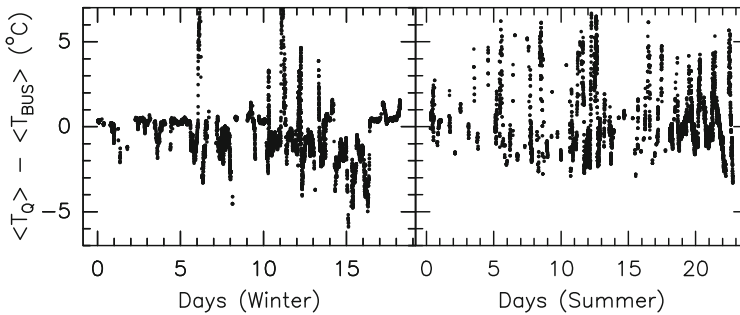


Fig. 9.65 Effelsberg 100-m telescope. Temperature difference $\langle T_Q \rangle - \langle T_{BUS} \rangle$ between the quadripod and the BUS, for a winter and summer period [Data MPIfR Effelsberg, Germany].

between the quadripod and the BUS is shown in Fig. 9.66.b. During the day the quadripod can be $\sim 5^\circ\text{C}$ cooler than the BUS.

A correlation of the quadripod temperature of the IRAM 15-m telescope and the wind speed is illustrated in Fig. 9.67. It is seen that at high wind speeds the convective heat transfer is efficient and the difference $T_Q - T_A$ between the quadripod and ambient air temperature approaches the value of $\sim -3^\circ\text{C}$.

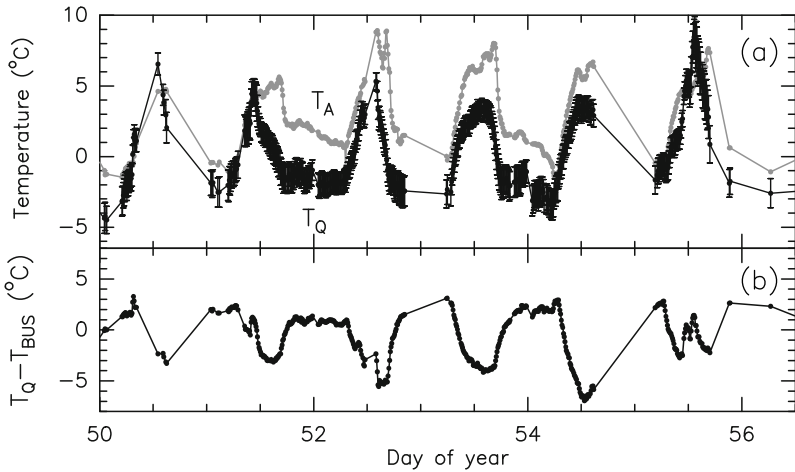


Fig. 9.66 (a) Temperature T_Q of the IRAM 15-m telescope quadripod, T_A is the temperature of the ambient air. (b) Temperature difference between the quadripod and the BUS: $T_Q - T_{BUS}$.

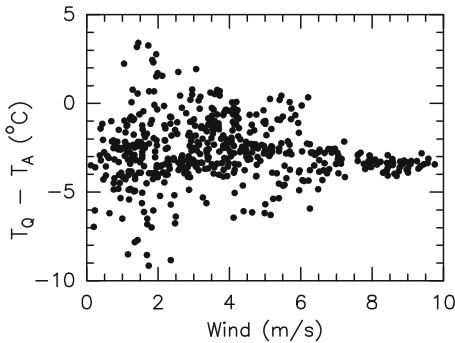


Fig. 9.67 IRAM 15-m telescopes. Correlation of the temperature difference between the quadripod temperature and the ambient air temperature $T_Q - T_A$ with wind speed.

The quadripod of the IRAM 30-m telescope is made of steel tubes covered with insulation that is painted white. Between the steel surface and the insulation is a coiled pipe system through which temperature controlled glycol circulates in order to control the temperature of the quadripod legs to the reference temperature of the yoke. In this way a temperature uniformity between the yoke, the BUS and the quadripod is achieved, as well as a temperature uniformity between the 4 quadripod legs, irrespective of solar illumination. The temperature of the quadripod in the case where the active thermal control is not working is shown in Fig. 9.68.a and Fig. 9.42.a. The quadripod temperature follows the ambient air temperature (although there is also the influence of sunshine) with a time delay of ~ 5 hours (Table 9.6). For the general situation of a working thermal control of the telescope, the temperature measurements shown in Fig. 9.68.b illustrate the close agreement between the quadripod temperature and the BUS temperature (and the yoke temperature), as required in the design specification $|T_Q - T_{yoke}| \approx |T_{BUS} - T_{yoke}| \lesssim 1^\circ\text{C}$, thus also $|T_{BUS} - T_Q| \lesssim 1^\circ\text{C}$.

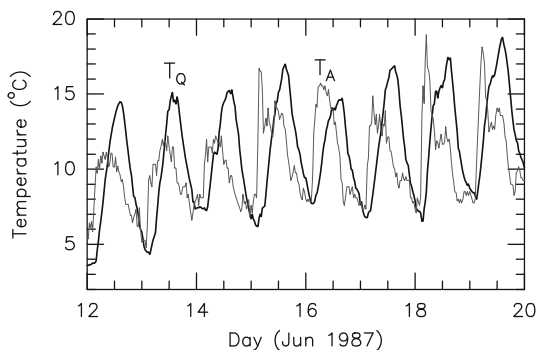


Fig. 9.68.a IRAM 30-m telescope. Temperature of the quadripod legs (T_Q) with NO thermal control (see also Fig. 9.42.a). T_A is the ambient air temperature.

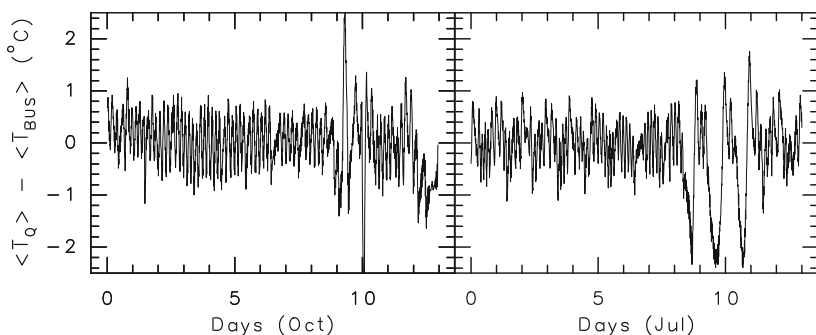


Fig. 9.68.b IRAM 30-m telescope. Temperature difference $\langle T_Q \rangle - \langle T_{BUS} \rangle$ between the quadripod and the BUS, for October and July. The climatisation control of the telescope is working; the oscillations illustrate the control cycle.

9.5.2 Subreflector

A subreflector sees the warm main reflector surface, the cold sky via reflection on the main reflector surface and some part of the warm ground via spill-over. A subreflector is exposed to the ambient air and will follow to a large extent the ambient air temperature because of its small mass to surface ratio $\mathcal{M} = M/A$ and hence short thermal time constant (Eq.(7.83)). A subreflector may receive a considerable heat load when observations are made close to the Sun, or actually of the Sun, as it is possible on a few telescopes. Thermal deformations of a subreflector will introduce large-scale wavefront deformations with associated focus and pointing error. There is very little information in the open literature on subreflector temperatures.

The subreflector of large cm-wavelength telescopes has considerable dimensions (6.5 m diameter on the Effelsberg 100-m telescope); they are usually made from steel panels. The subreflector is painted white with TiO_2 paint and no further thermal precautions are taken, though perhaps avoiding solar observations. The subreflector of mm/sub-mm wavelength telescopes is made of machined aluminium or Al-honeycomb plates covered with aluminium or CFRP surface plates. The IRAM

30-m telescope subreflector is made of Al-honeycomb covered with a CFRP skin. A temperature measurement of the subreflector rear surface made under normal observing conditions (not close to the Sun) is shown in Fig. 9.69. The daily change of the subreflector temperature was $\sim 10^\circ\text{C}$, similar to the change of the ambient air temperature.

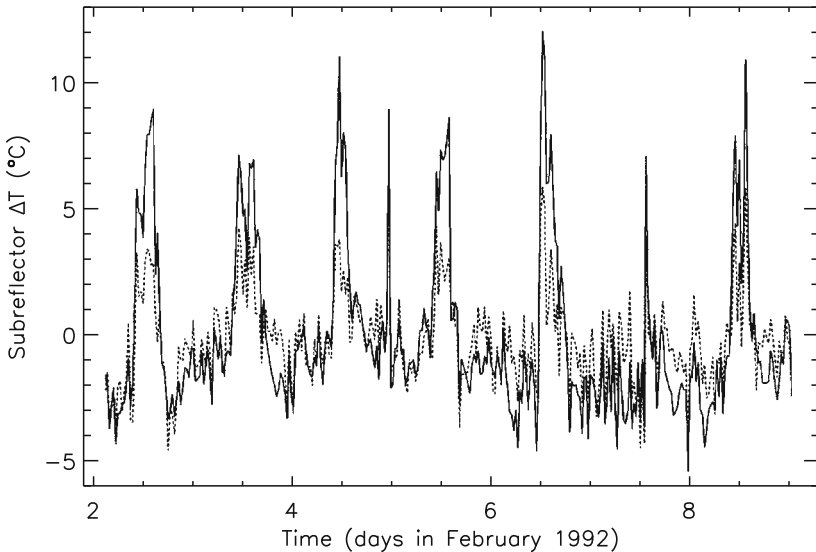


Fig. 9.69 Temperature measurement of the IRAM 30-m telescope subreflector. Solid line: temperature change at the centre of subreflector, dotted line: average temperature change of the subreflector (7 sensors). The days were clear, the telescope was used for observations [Data from J. Peñalver, IRAM, Spain].

9.5.3 Focus Cabins

The primary focus cabin of a large cm-wavelength telescope, like the Effelsberg 100-m telescope, contains receivers and holds the subreflector and its position control. The receivers and the electrical equipment generate heat that is released into the primary focus cabin. The air in the cabin has a high quasi-constant temperature unless it is ventilated. The mm/sub-mm wavelength telescopes are Cassegrain telescopes and seldom used for primary focus observations.

On the Effelsberg 100-m telescope is the lower part of the secondary focus cabin incorporated in the BUS, the upper part of the secondary focus cabin extends above

the reflector surface (see Fig. 2.4). No special thermal protection is applied with the exception of louvres and white paint on the outer surfaces.

The secondary focus cabin of a fork–supported telescope is connected to the elevation bearings in the fork arms and there is negligible heat transfer via the elevation bearings. The secondary focus cabin of the IRAM 15–m telescopes is covered with thermal protection as used on the fork arms, i.e. a layer of 5 cm foam, a 2 cm wide air gap and an outer radiation shield. The vertex opening of the focus cabin is covered with a radio wave transparent membrane. The heat generated by the receivers, the electrical equipment and special heaters produces a stable inside temperature. The central hub is attached to the roof of the secondary focus cabin, the small connection bolts have negligible conductive heat transfer (Fig. 9.26.a).

On the VertexRSI ALMA/APEX 12–m telescope the steel walls of the insulated secondary focus cabin (~ 8 cm foam and metal plate cover) are thermally stabilized by glycol flowing through a pipe system attached to the inside of the walls. This active system creates a stable temperature of the steel walls and of the air inside the focus cabin. The air of the focus cabin is used to ventilate the invar ring that is attached to the upper part of the focus cabin (Fig. 9.26.b, see Güsten et al. [2006]). The thermally stable invar ring supports the BUS, Fig. 9.28 shows representative temperature measurements of the invar ring. The secondary focus cabin of the ALMA AEC 12–m prototype telescope is made of CFRP plates.

9.6 Observations in the Direction of the Sun

Observations of the Sun produce an extreme thermal load on a telescope; on many telescopes this observation is avoided. The main difficulty of solar observations is over–heating of the subreflector, especially those with a CFRP front skin, and excessive loads on the receivers. A white painted or micro–grooved main reflector surface with good scattering properties reduces the heat load on the subreflector. Extremely dangerous are panel surfaces with good specular reflection as used on the original IRAM 15–m telescopes (see cover picture); on these telescopes a large Sun avoidance zone was installed in hardware and software. Calculations of the heat flux incident on the subreflector of the VertexRSI ALMA telescope when observing the Sun are published by Schwab & Cheng [2008] and Lamb [2000], other calculations are presented in Section 5.10. Ezawa et al. [2000] estimate from measured scattering functions of steel–wool scratched, sandpaper scratched and sand blasted panel surfaces that the subreflector of the ASTE 10–m telescope would heat up in solar observations to 300° C, 100° C and 45° C, respectively.

A test observation for the Venus transit in 2004 was made with the IRAM 30–m telescope in order to demonstrate that no over–heating of the subreflector will occur *if a special observing mode is used*. The main reflector surface and the subreflector CFRP surface is painted white with TiO₂ paint, which has a good visible light scattering efficiency. The temperature of the subreflector recorded during the test

observation is shown in Fig. 9.70. From on the 490 min time mark the telescope pointed at the Sun and repeated 8 cycles of 1 min observation on the Sun and 4 min on Mercury at 15° distance from the Sun. At the 550 min time mark the telescope was moved to a safe position far away. A gradual increase in the subreflector temperature of 20 to 25°C occurred, however, this temperature increase depends on the cycle of the observations, i.e. whether the telescope is frequently moved away from the Sun. The decrease of the subreflector temperature after termination of the Sun observation indicates a thermal time constant of the subreflector of $\sim 1/2$ hour.

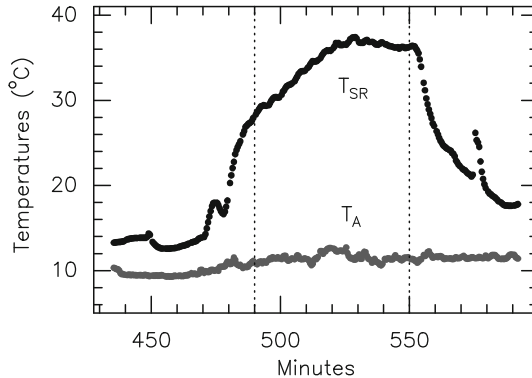


Fig. 9.70 IRAM 30-m subreflector temperature T_{SR} during observations of the Sun. The antenna beam is on the Sun at 490 min and leaves the Sun at 550 min for a far away position. During the solar observation the telescope points in a regular cycle 1 min towards the Sun and 4 min towards Mercury at 15° distance [Data from J. Peñalver, IRAM, Spain].

An observation of the Sun was made with the VertexRSI ALMA 12-m prototype telescope (13 June 2004) tracking the Sun from sunrise to sunset. The average temperature of the BUS and the temperature uniformity (rms value) of the 24 sectors of the BUS are shown in Fig. 9.71 and Fig. 9.40.b. The figure shows for comparison the same parameters measured one day later when the meteorological conditions were similar and the telescope was not pointing at the Sun. The thermal behaviour of the BUS is similar for both conditions. The temperature of the subreflector recorded during the solar observation reached $\sim 100^\circ\text{C}$.

The BIMA (now CARMA) mm-wavelength interferometer can be used for solar observations. The reflector surface consists of machined aluminium panels with grooves that scatter solar radiation. The closed BUS, the three subreflector support legs and the back of the subreflector are ventilated with ambient air. With this protection the temperature of the subreflector remained below 80°C when observing the Sun [Welch et al. 1996].

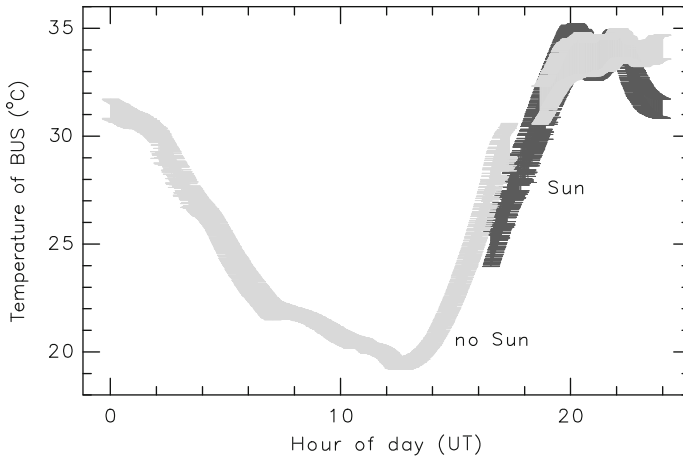


Fig. 9.71 VertexRSI ALMA 12-m prototype telescope at the VLA test site (NM, USA). Temperature measurement of the BUS when tracking the Sun (13 June, 2004) and not observing the Sun one day later, under similar meteorological conditions. The width of the lines is the rms value of the BUS temperature [ALMA Test Data].

9.7 De-icing of a Telescope

The IRAM 30-m telescope is located at 2 900 m altitude in the Sierra Nevada, Spain. During the design study it became known that severe icing can occur when it is raining at temperatures below zero degree. On the cold ground, the rain forms solid ice that sticks to all exposed structures. It was decided to de-ice the telescope rather than to get rid of the ice (and snow) after it had formed on the surfaces. Insulation and heating is installed on the panel rear side, the reflector rear cladding, the yoke surfaces, the quadripod and the subreflector. Electric de-icing of approximately 200 W/m^2 is applied. Ice (icicles) may however still form at cold edges. The applied heating deregulates the thermal control of the telescope, as illustrated in Fig. 9.72, but observations are not possible because of the poor weather condition. After switching off the de-icing the telescope needs 4 to 6 hours to return to a thermally stable state, as seen in Fig. 4.19.

De-icing is also applied to the panels and the quadripod of the IRAM 15-m telescopes, using on average a heat supply of 200 W/m^2 . This power usually keeps the panel surfaces free of ice, except at some panel rims that behave like cold edges (see Fig. 8.3).

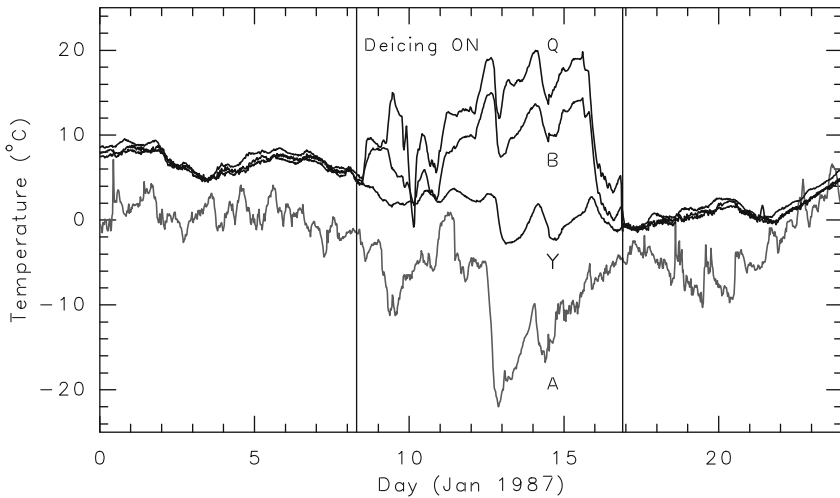


Fig. 9.72 IRAM 30-m telescope and temperature of the yoke: Y, the BUS: B, the quadripod: Q and the ambient air: A. The thermally controlled state of the telescope $T_B(\text{BUS}) = T_Y(\text{Yoke}) = T_Q(\text{Quadripod})$ is deregulated when de-icing is switched on, i.e. $T_B \neq T_Y \neq T_Q$ [From Greve et al. (1992), Courtesy IEEE Trans. Ant. Propag.].

9.8 Measured Temperature Uniformity of Radio Telescopes

The previous Sections reviewed the thermal behaviour of essential telescope components, however, the measurements were presented without paying attention to the thermal state of the entire telescope. Not all telescope components are in direct thermal contact with each other though most of the components are in contact with the thermal environment. The thermal behaviour of telescope components is governed by their thermal time constants. Different thermal time constants may lead to different temperatures in the telescope structure and this to different thermal deformations. The sum of all deformations determines the radio performance of a telescope. This Section explains the temperature uniformity of the Effelsberg 100-m telescope, the IRAM 15-m telescope, the VertexRSI ALMA 12-m prototype telescope and the IRAM 30-m telescope.

The temperature uniformity of the alidade-supported Effelsberg 100-m telescope is illustrated in Fig. 9.73 and Fig. 9.74. The first figure [Schmitz-Görtz 1971] shows two days of temperature measurements at the positions indicated in Fig. 2.4. A good temperature uniformity exists at night, within a few degrees between all parts, while solar illumination introduces a non-uniformity of the order of 5 to 10° C, in particular of the alidade base frame (position H, at the time of measurement still painted blue, see Picture 1.2). There is a good temperature uniformity between the BUS and the panel(s) (position A, B, D, C).

The Effelsberg telescope is well exposed to the environment so that the telescope follows to a large extent the ambient air temperature as illustrated in Fig. 9.32. Solar

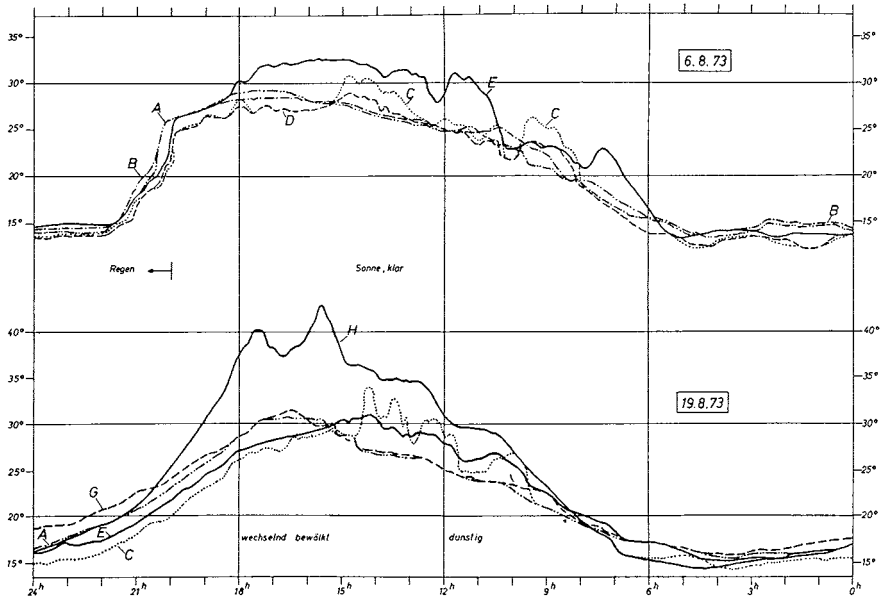


Fig. 9.73 Temperature uniformity of Effelsberg 100-m telescope, measured at the positions shown in Fig. 2.4. Sensors, A,B: BUS, C,D: panel, E: quadripod, G: alidade (upper part), H: alidade (base-frame). Regen: rain, Sonne, klar: sun shine and clear sky, wechselnd bewölkt: occasionally clouds, dunstig: haze [Courtesy Schmitz-Görtz, 1971].

illumination introduces temperature differences in the construction while wind tends to even out temperature differences. Taking the BUS as reference temperature, and realizing that there are only a few temperature sensors on the telescope structure (Table 6.1), Fig. 9.74 reveals that the panel temperature, the quadripod temperature and the alidade temperature (tower A₁ and A₂) may deviate from the BUS temperature by 5 to 10° C, for these days of measurements. There is, however, little thermal interaction between the BUS and the quadripod and the alidade.

Figure 9.75 shows the temperature uniformity of the fork-supported IRAM 15-m telescopes. The BUS (CFRP and steel network) shows large daily temperature variations and during the night a strong cooling towards the cool sky. The insulated fork is rather stable but at an elevated temperature. This is due to heating from electrical equipment inside the pedestal and diffusion of heat into the fork. The BUS and the fork are thermally independent so that this temperature difference does not affect the radio performance. The temperature difference between the BUS and the quadripod can reach ~ 5° C; the temperature uniformity of the BUS and the fork is ~ 2° C (rms).

The thermal uniformity of the VertexRSI ALMA 12-m prototype telescope is illustrated in Fig. 9.76 for May 10, 2004; other days of the same period are similar. The temperature of the pedestal is somewhat higher because of heating from internal

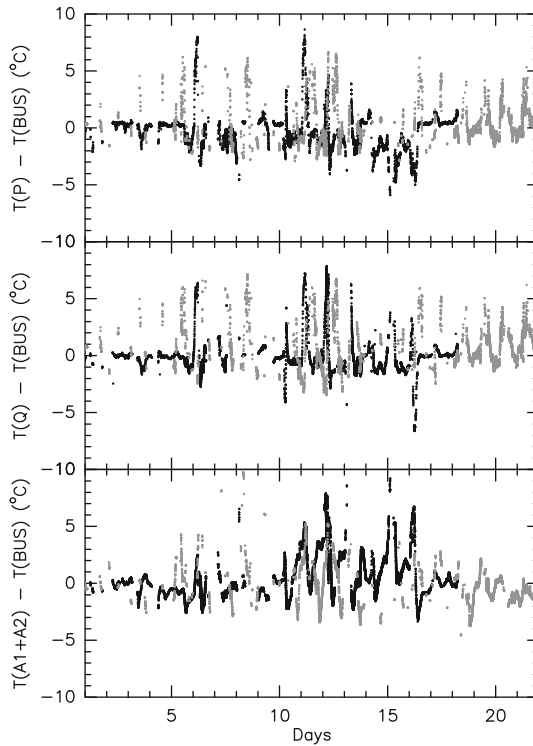


Fig. 9.74 Temperature uniformity of Effelsberg 100-m telescope, expressed as temperature difference between the BUS and the panels $T(P) - T(\text{BUS})$, the BUS and the quadripod $T(Q) - T(\text{BUS})$ and the BUS and the alidade $T(A1+A2) - T(\text{BUS})$. Black dots: winter time, grey dots: summer time [Data MPIfR Effelsberg, Germany].

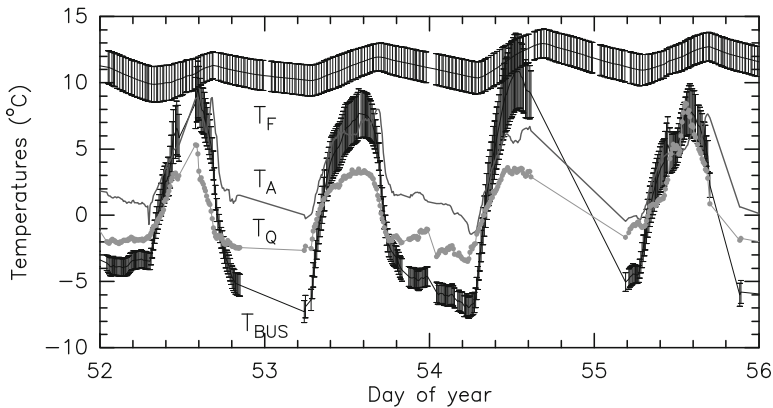


Fig. 9.75 IRAM 15-m telescope. Temperature uniformity between the backup structure (T_{BUS}), the quadripod (T_Q) and the fork (T_F). The width of the lines is the deviation from uniformity (rms value) of the BUS, fork and quadripod. T_A is the temperature of the ambient air.

electrical equipment. The temperatures of the fork traverse and the fork arms are similar and follow the same daily trend, i.e. with reduced amplitude and a delay of ~ 2 hours with respect to the ambient air temperature. The BUS follows the ambient air temperature, the temperature uniformity of the BUS is 2 to 3°C. The BUS is supported on the thermally stabilized and very stable invar ring. The fork support of the telescope decouples the thermal differences and different thermal expansions of the fork and the BUS.

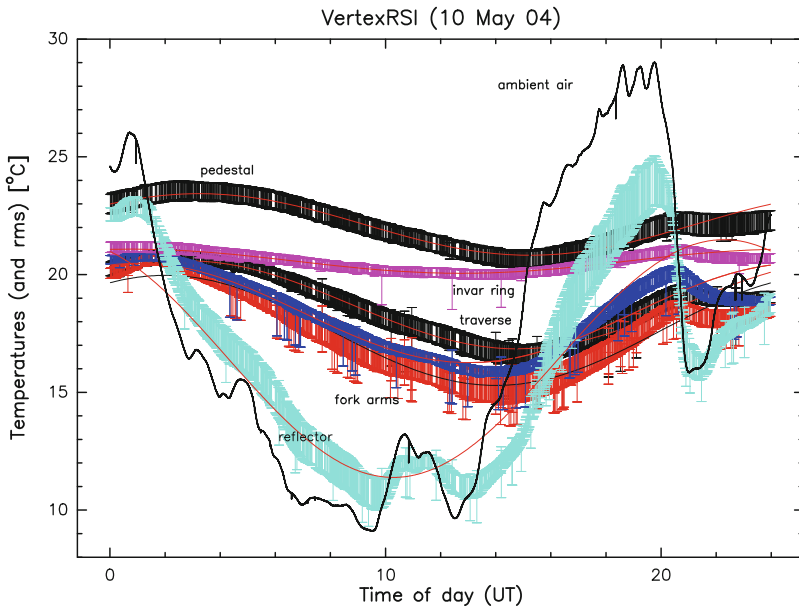


Fig. 9.76 Temperature uniformity of the VertexRSI ALMA 12-m prototype telescope. The structural components are indicated. The CFRP-plated Al-honeycomb BUS follows closely the ambient air temperature [From Greve & Mangum (2008), Courtesy IEEE Ant. Propag. Magazine].

Finally, Fig. 9.77 illustrates the temperature uniformity of the thermally stabilized IRAM 30-m telescope. The temperature of the BUS and the quadripod is controlled against a reference temperature of the yoke. The thermal stabilization of the BUS is by heated or cooled ventilating air, the stabilization of the quadripod is by heated or cooled glycol flowing in pipes around the legs. The yoke is ventilated and heated if the counterweights are 0.15°C cooler than the yoke. Fig. 9.77.a shows that the yoke reference temperature and with this the temperature of the controlled BUS and quadripod do change during the seasons; however, Fig. 9.77.b illustrates that there exists temperature uniformity of the BUS, the yoke and the quadripod with respect to the reference temperature within $\sim \pm 1^\circ\text{C}$.

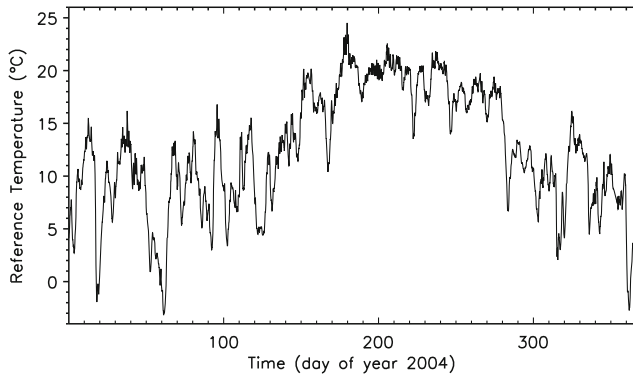


Fig. 9.77.a IRAM 30-m telescope. Variation of the yoke reference temperature throughout the year 2004.

9.9 The measured Thermal Behaviour of Telescopes

The Tables 9.9.a-f summarize the measured temperatures reviewed in the preceding Sections, being aware that the data are inhomogeneous, incomplete and often cover only a very limited period of time.

The temperature differences and temperature gradients listed in Tables 9.9.a-f need an explanation. While temperature differences and gradients involve differential thermal deformations in the structure, they do not necessarily involve heat transfer. The heat transfer depends on the existence and efficiency of conductive connections and the efficiency of natural convection, while radiative heat transfer occurs only as long as there is view contact between the structural sections with different temperatures. The situation is different if ventilation is applied. For illustration consider a fork support. If for instance the left fork arm is warmer than the right fork arm, then an equalizing heat transfer through the fork traverse will not occur because of the long distance and radiative heat transfer between the fork arms will not occur since there is no view contact. Heat transfer by natural convection is ineffective since it works in upward direction but not across the fork structure. Nevertheless, the differential thermal expansion of the fork arms will introduce a pointing error. A temperature difference between the fork arms may disappear through heat exchange with the environment. A similar situation occurs if the left side of a BUS is warmer than the right side. Heat conduction across the diameter of the BUS will hardly occur and natural convection and radiation are poor agents to smooth a horizontal temperature gradient. The left side and the right side of the BUS will experience a different thermal expansion so that a pointing error may occur. The situation is different if active thermal control by forced ventilation is applied. The ventilating air moves through the BUS network and establishes temperature uniformity.

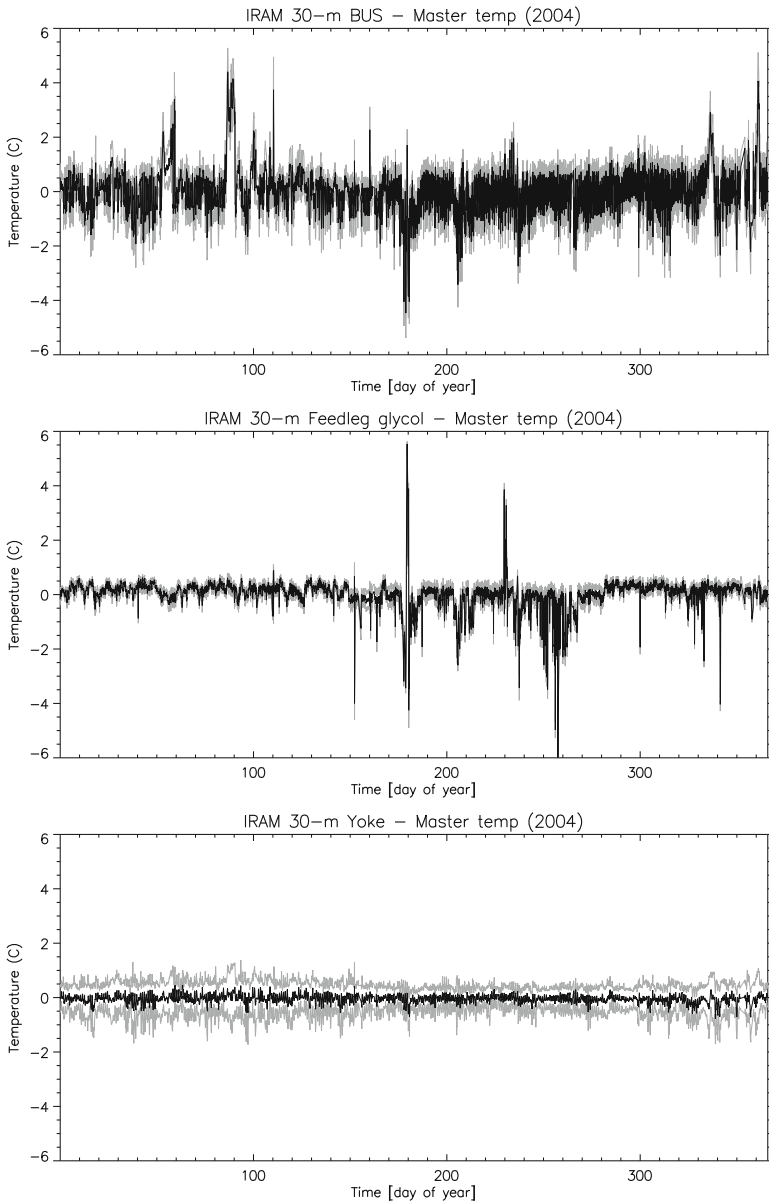


Fig. 9.77.b Temperature uniformity of the thermally controlled IRAM 30-m telescope displayed as the temperature difference of the BUS – reference temperature (upper panel), quadripod – reference temperature (centre panel), yoke – reference temperature (lower panel). The width of the lines is the rms value of the temperature measurements of the BUS (104 sensors), of the yoke (44 sensors) and of the quadripod (4 sensors). The data are for 2004.

Table 9.9.a Pedestal (Temperature T_P).

	Parameter	VertexRSI ALMA 12-m	ASTE 10-m	Ref.
Temperature Uniformity	$rms(T_P)$	0.5 °C		Fig. 9.4
Temperature Change	$\Delta T_P/\Delta t$	< 0.2° C/h		Fig. 9.4
Tilt Change ^{a)}	$\Delta(Tilt_P)/\Delta T_P(S-N)$	1.07±0.04 ″/°C		1
Tilt Change ^{b)}	$\Delta(Tilt_P)/\Delta T_P(E-W)$	1.73±0.23 ″/°C		1
Path Length Stability	$\Delta L_1/\Delta t$	10 μm in 1800 s		Fig. 9.21
	Parameter	Onsala ^{c)}	Wetzell ^{d)}	Ref.
Height Stability	$\Delta H/\Delta T_P$	80 μm/m/K	190 μm/m/K	2,3

Reference 1: Ukita et al. [2007], 2: Wresnik et al. [2006], 3: Nothnagel et al. [1995].

^{a)} direction South–North, ^{b)} direction East–West.

^{c)} concrete, radome–enclosed telescope, H = 12 m (Fig. 9.1);

^{d)} concrete, open–air telescope, H = 8 m (Fig. 9.1).

Table 9.9.b Alidade Towers (Temperature T_{A1} , T_{A2}).

	Parameter	Effelsberg 100-m	JCMT 15-m
Temperature Uniformity	$rms(T(A_1)) \approx rms(T(A_2))$	2–3° C	
Temperature Difference	$T(A_1) - T(A_2)$	± 5° C	
Temperature Difference	$T(\text{front}) - T(\text{rear})$	± 2° C	0–2° C
Illustration		Figs. 9.6, 9.7	Fig. 9.10

Table 9.9.c Fork Support.

	Parameter	IRAM 15-m	VertexRSI ALMA 12-m	ASTE 10-m
Temperature Difference ^{a)}	$\Delta T_{LR} = T(L) - T(R)$	0–2° C	2° C	
Temperature Change	$\Delta(\Delta T_{LR})/\Delta t$	0.4° C/h	0.2° C/h	
Temperature Difference ^{b)}	$\Delta T_{fr} = T(f) - T(r)$	0–1° C	1° C	
Temperature Change	$\Delta(\Delta T_{fr})/\Delta t$	0.2° C/h	0.1° C/h	
Tilt Change ^{c)}	$\Delta Tilt/\Delta t(L-R)$			0.4 ″/° C
Tilt Change ^{d)}	$\Delta Tilt/\Delta t(f-r)$			1.5 ″/° C
Path Length Stability	$\Delta L_2/\Delta t$		8 μm in 1800 s	
Illustration		Figs 9.14, 9.15	Figs. 9.12, 9.13, 9.21	Ref. 1

Reference 1: Ukita et al. [2007].

^{a)} Left and Right fork arm; ^{b)} front and rear of fork arms.

^{c)} in direction of elevation axis; ^{d)} perpendicular to elevation axis.

Table 9.9.d BUS Supports: Yoke, Central Hub, Invar Ring.

Temperature	Uniformity	Difference Left–Right Yoke Arm T(L)–T(R)	Direction Up–Down in Yoke Arms T(Up)–T(Down)	
	$rms(L,R)$			
Yoke (IRAM 30-m)				
With T-Control	0.6° C	0.3° C	0.3° C	Fig. 9.24
Without T-Control	~ 1–2° C	1–3° C	1–3° C	
C-Hub (SEST 15-m)	2–3° C			Fig. 9.27
Invar Ring (VertexRSI 12-m)	0.25° C			Fig. 9.28

Table 9.9.e Backup Structure (BUS, T_B), without and with Ventilation.

BUS		OVRO	IRAM	SEST	VertexRSI
No ventilation		10.4-m	15-m	15-m	ALMA 12-m
Temperature Uniformity	rms(T_B)	1–8° C ^{e)}	2–6° C ^{f)}	1–3° C	1–2° C
Temperature Gradient ^{a)}	ΔT_B (U–D)	0–7° C	2–15° C ^{f)}	0–6° C ^{f)}	0.5–1° C
Temperature Gradient ^{b)}	ΔT_B (L–R)	–2, 2° C	0–3° C ^{f)}	0–5° C ^{f)}	0.5–1° C
Temperature Gradient ^{c)}	ΔT_B (f–r)	0.5° C			
Temperature Gradient ^{d)}	ΔT_B (r)	2° C			
Illustration		Fig. 9.30	Figs. 9.34, 9.35	Fig. 9.38	Fig. 9.40
BUS		Nobeyama	IRAM	Metsähovi	MIT–Haystack
with ventilation		10-m	30-m	14-m	37-m
Temperature Uniformity	rms(T_B)	0.2–0.5° C ^{g)}	0.2–0.6° C	1–3° C	
Temperature Uniformity	rms(T_B)	0.2–0.8° C ^{h)}			
Temperature Gradient ^{a)}	ΔT_B (U–D)		0.5° C	1–2° C	–2–4° C ^{f)}
Temperature Gradient ^{b)}	ΔT_B (L–R)		0.3° C	0–2° C	
Temperature Gradient ^{c)}	ΔT_B (f–r)		0–1° C		
Temperature Gradient ^{d)}	ΔT_B (r)		≈ 1° C		
Illustration		Fig. 9.44	Figs. 9.46, 9.47		Fig. 9.49

^{a)} gradient in direction Up–Down, ^{b)} gradient in direction Left–Right;

^{c)} gradient through BUS, front to rear;

^{d)} radial gradient, centre to rim of BUS;

^{e)} maximum values;

^{f)} low value at nighttime, high value at daytime;

^{g)} circular ventilation, ^{h)} radial ventilation.

Note: for the Nobeyama 45-m telescope ΔT_B (f–r) = 0.5–1° C, ΔT_B (r) = 2–3° C (Fig. 9.41).

Table 9.9.f Temperature Uniformity of Telescopes.

Temperature Difference (° C)	IRAM/SEST 15-m	IRAM 30-m	VertexRSI ALMA 12-m	Effelsberg 100-m
Alidade – BUS				0–10° C
Yoke – BUS		± 1° C		
Fork – BUS	0–15° C		5–10	
BUS – Panel		0–20° C		0–10° C
BUS – Quadripod	0–5° C	± 1° C		0–10° C
BUS – Central Hub	0–1° C			
BUS – Invar Ring			0–20° C	
Illustration	Figs. 9.75, 9.66	Figs. 9.77, 9.68	Figs. 9.28, 9.76	Figs. 9.73, 9.74

9.10 Temperature Monitoring and Trouble–Shooting

The preceding Sections explained the thermal behaviour of telescope components and of several telescopes. A telescope/antenna is usually in a non–steady thermal state with associated transient thermal deformations. As summarized in Table 9.1, temperature variations of the telescope supports (pedestal, alidade, fork) may cause pointing errors, temperature variations of the BUS support, the BUS and the quadripod may cause focus, pointing and reflector surface errors. Temperature variations of interferometer telescopes may in addition cause path length (phase) errors. Regular (thermal) trouble–shooting measurements consist of focus and pointing

measurements and, in addition, path length (phase) measurements of an interferometer array. An example of focus and pointing (and phase, not shown) measurements, at intervals of 2 hours, of the IRAM 15-m telescope array is shown in Fig. 9.16. Temperature and wind induced deformations act together and a separation of the individual influences from a focus and pointing measurement is very difficult. However, temperature monitoring of the telescope components with a relatively small number of sensors may help to trace and estimate in real time the influence of temperature variations on the focus and pointing. Such diagnostic temperature monitoring may lead to the identification of thermal trouble spots, a possible reduction of their influence through, for instance, additional thermal protection and/or consideration of the thermal effect in a correlation relation as, for instance, used in thermal focus control (Fig. 6.12). The influence of a transient temperature induced deformation of a telescope component depends on its thermal time constant and on its contribution to the integrated thermal behaviour of the telescope structure. Telescope components with a short thermal time constant may have an immediately detectable influence. Global estimates of the thermal time constants of the principal telescope components are summarized in Table 9.10.

Table 9.10 Global Thermal Time Constants of Telescope Components.

Telescope Component	Global Estimate of Thermal Time Constant	Error ^{a)}	Illustration
BUS – open	1/2 – 1 h	PE, FE, RSE	Figs. 9.30, 9.31, 9.73
BUS – closed	1 – 3 h	PE, FE, RSE	Figs. 9.34, 9.51, 9.76
BUS – closed + ventilated	2 – 4 h	PE, FE, RSE	Fig. 9.42
BUS–support ^{b)}	1 – 4 h	RSE, PE, FE	Figs. 9.24, 9.27, 9.28
Panel/Panel–frame	1/4 – 1/2 h	–	Figs. 9.53, 9.54, 9.60
Quadripod ^{c)}	1/2 – 1 h	FE, PE	Figs. 9.64, 9.66, 9.68, 9.75
Pedestal (concrete)	2 – 4 h	PE	Fig. 9.3
Alidade ^{d)}	1/2 – 1 h	PE	Figs. 9.6, 9.7, 9.10
Pedestal–Fork ^{e)}	1 – 2 h	PE	Figs. 9.14, 9.15

^{a)} PE: pointing error, FE: focus error, RSE: reflector surface error.

^{b)} consisting of the EL–structure (Fig. 2.8), central hub (Fig. 2.10) or yoke (Fig. 2.9);

^{c)} without or with insulation;

^{d)} usually without insulation;

^{e)} with insulation (thermal protection).

The objectives of diagnostic and trouble-shooting telescope temperature monitoring are summarized as follows:

- (1) *Panels/Panel–Frames*: The panels/panel–frames have the shortest thermal time constant. Temperature influences result in panel buckling that does not affect the focus, pointing and path length. Panel buckling has a negligible or small effect on the telescope gain (sensitivity) since the effective surface rms value is $\sigma^* \approx \Delta z_{\max}/3$ where Δz_{\max} is the buckling amplitude (Sections 9.4.3 and 12.4.2). Once assembled, the panel contours cannot be corrected

and panel buckling not eliminated so that panel temperature monitoring has only an informative character.

- (2) *Open BUS*: The thermal time constant of an open, non-insulated BUS is determined by the thermal time constants of the network members; the average thermal time constant of an open BUS can be relatively short. Temperature influences on an open BUS may cause focus, pointing and reflector surface errors. Temperature measurements are recommended in order to monitor (a) the temperature gradient between the front and rear of the BUS that may cause a focus error, and (b) temperature differences of the BUS in the direction Left-Right and Up-Down that may cause a pointing error in AZ and EL direction. The arrangement of temperature sensors may be that of Fig. 9.33, at the front and rear of the BUS. The minimum number of temperature sensors is 16.
- (3) *Closed BUS*: The same remarks hold for a closed BUS and a closed and ventilated BUS. The thermal time constant is longer than that of an open BUS, however, temperature differences of the closed and closed and ventilated BUS may introduce similar focus, pointing and reflector surface errors, though of smaller amplitude. Temperature monitoring is recommended in the same way as on the open BUS.
- (4) *BUS Support*: The BUS support may consist of an EL-structure (Fig. 2.8), a yoke (Fig. 2.9) or a central hub (Fig. 2.10). Temperature changes, and especially asymmetric temperature changes of the EL-structure may cause pointing errors; temperature changes of the BUS supports may cause reflector surface deformations by print-through to the BUS network. A BUS support, in particular the exposed EL-structure (Fig. 2.8), may need temperature monitoring by 4 to 8 sensors.
- (5) *Quadripod*: The thermal time constant of a quadripod is relatively short. The quadripod provides the correct optical distance, centring and tilt of the primary focus receiver or of the subreflector; temperature changes of the quadripod affect immediately the focus, pointing and path length. Differential thermal expansion of the quadripod legs, for instance due to asymmetric solar illumination, cause a shift and tilt of the subreflector and a coma-like beam deformation with associated pointing error. Temperature monitoring of the quadripod legs is necessary in order to detect (a) a uniform temperature change that may cause a focus and path length error, or to detect (b) temperature differences between the quadripod legs that may cause a pointing error. A temperature difference between the quadripod and the average BUS temperature may indicate the origin of a focus and pointing error. On short quadripod legs of 2 to 3 m length, 1 or 2 temperature sensors per leg are sufficient, on legs of 10 to 20 m length, 2 or 3 sensors per leg are necessary. The minimum number of temperature sensors is ~ 4 to 12.
- (6) *Alidade*: The thermal time constant of an open, non-insulated alidade is determined by the thermal time constant of the alidade beams; the thermal time constant of an alidade can be relatively short. Uniform temperature

changes of an alidade cause path length errors, asymmetric temperature changes cause pointing errors. Temperature monitoring is recommended for investigation of (a) a temperature difference between the Left and Right alidade tower (A-tower) that may cause a pointing error along the EL-axis (Fig. 9.5.a), and (b) of a temperature difference between the front and rear of the alidade towers that may cause a pointing error perpendicular to the EL-axis (Fig. 9.5.b). Per alidade A-tower, 2 sensors at the front and 2 sensors at the rear are sufficient. A minimum of 8 temperature sensors is required.

- (7) *Fork Support*: The thermal time constant of a pedestal-fork support is relatively long since, in general, thermal protection is applied. Temperature monitoring is recommended for investigation of (a) temperature differences between the Left and Right fork arm that may cause a pointing error along the EL-axis, and (b) of temperature differences between the front and rear of the fork arms that may cause a pointing error perpendicular to the EL-axis (Fig. 9.11). A uniform temperature change of the fork arms (and the pedestal) causes a path length error. Each fork arm may have 4 to 6 sensors, distributed between the upper and lower part of the arm and the front and rear. A minimum of 8 to 12 temperature sensors is required.

9.11 Other Thermal Effects

The preceding Sections discussed the thermal behaviour of important structural components of a telescope or of the entire telescope. There are local thermal effects in supports and instrumentation in a telescope that are not part of the global thermal design and behaviour of a telescope, but nevertheless may affect its operation. Examples are the investigation by Ukita [1999] of the thermal effects of the Nobeyama 45-m telescope pointing that were brought back to the thermal behaviour of the master collimator mount; thermal effects of the tower for the master equatorial of the DSS-14 70-m antenna mentioned by Ahlstrom et al. [2000]; the investigation of thermal effects in the coupling of the elevation axis encoder on the IRAM 30-m telescope by Cernicharo & Peñalver [1991].

Chapter 10

Measured Thermal Behaviour of Enclosures

Several radio telescopes for millimetre and sub-mm wavelengths and several communication antennas are protected by a radome or astrodome. The radome is an over-hemispherical enclosure of which the inside climate can be controlled by ventilation or air-conditioned ventilation. The radome is stationary and the Sun illuminates it from a gradually changing direction as explained in Section 5.8. Solar radiation is diffusely transmitted through the radome skin and is next to internal heat sources (receivers, telescope drives) the origin of a vertical temperature gradient of the inside air. The ventilation reduces the vertical temperature gradient and by this also a temperature gradient in the telescope structure. The radome of the Onsala 20-m telescope is shown in Fig. 3.4.

The astrodome is a steel housing with an opening ('slit') in diameter larger than the telescope aperture. The slit is either opened for observation as on the HHT and CSO 10-m telescope (Fig. 3.1, Fig. 3.2) or covered by a radio transparent membrane as on the JCMT 15-m telescope (Fig. 3.3). The astrodome rotates when the telescope tracks an astronomical source. Direct sunshine on the slit/membrane can be avoided by observing in a direction at some distance from the Sun. The solar illumination of an astrodome is explained in Sections 5.6 and 5.7. The astrodome with covered slit allows ventilation of the inside air and natural ventilation through louvres in the steel housing. The telescope in an astrodome with an open slit is exposed to the ambient thermal environment and the cold sky, though there is some wind shielding and reduced convective heating/cooling.

Figure 10.1 shows as an example the temperature of the air inside the radome of the Metsähovi 14-m telescope (Finland). The ventilation of this radome uses a large fraction of outside ambient air so that the temperature of the inside air can fall below zero degree. This is illustrated in Fig. 10.1.a for the cold day of 20 Mar, 2003. Fig. 10.1.b shows that during sunshine the air at the top of the radome is warmer than the air near the floor, the vertical temperature gradient reverses direction during the night. Fig. 10.2 shows the temperature of the air inside the ventilated radome of the MIT-Haystack 37-m telescope (USA). The temperature of the inside air follows the outside ambient air, at least for the time of these measurements. The fans in

this radome are especially arranged so that the airflow also reaches the central air volumes. The ventilating air can be heated so that the temperature of the air inside the radome is several degree above zero [Barvainis et al. 1993].

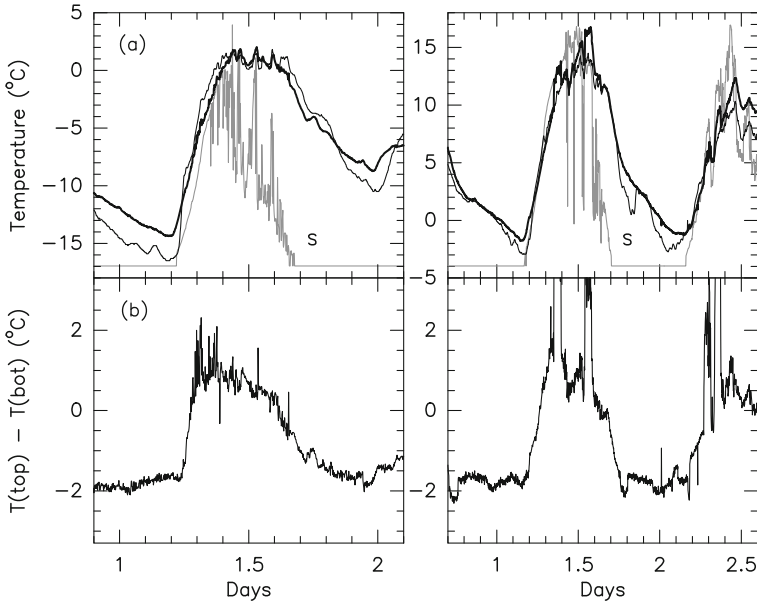


Fig. 10.1 (a) Average temperature $\langle T \rangle = (T_{\text{top}} + T_{\text{bottom}})/2$ of the air inside the radome of Metsähovi 14-m telescope: black line, temperature of the outside ambient air; thin line, temperature of the air inside the radome. S denotes the solar illumination (showing large variations due to clouds). (b) Vertical temperature gradient between the air at the top and the bottom layers of the radome. The left side panels are for 20 Mar, 2003, maximum insolation $S = 500 \text{ W/m}^2$; the right side panels are for 9 Apr, 2001, maximum insolation $S = 660 \text{ W/m}^2$ [Data from Metsähovi Observatory, Finland].

A review of thermal conditions inside radomes/astrodomes was made [Greve & MacLeod 2001] for the design study of the LMT telescope. The facts collected in this review are based on the publication by Schloerb [1978], Barvainis et al. [1993], Baas [1995] and private communications from the Metsähovi observatory, the Onsala observatory, the MIT-Haystack observatory and the JCMT observatory. The measured properties of the air inside a radome or a closed astrodome and the influence of solar illumination were summarized as follows:

- (1) The air inside a radome shows a daily temperature variation of comparable amplitude as the daily temperature variation of the outside ambient air. A large part of the inside temperature variation is due to solar radiation warming the radome skin and entering diffusely the interior of the radome, part of the inside temperature variation is due to ventilation with outside ambient air.

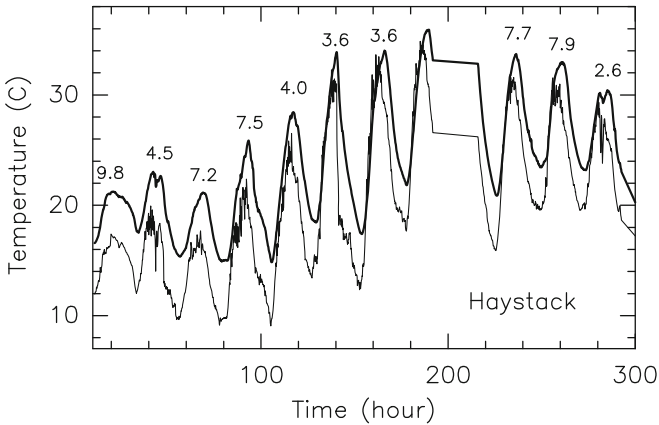


Fig. 10.2 Temperature (24 May to 4 Jun) of the air inside the radome of the MIT-Haystack 37-m telescope: heavy line; temperature of the outside ambient air: thin line. The numbers indicate the sky coverage: 0 = clear, 10 = fully covered [From Greve & MacLeod (2001), Courtesy Radio Science].

- (2) The temperature of the inside air is generally a few degrees above the temperature of the outside ambient air. This is especially the case if the inside air is heated and dried to avoid condensation.
- (3) The largest temperature variation and the largest variation of the vertical temperature gradient occur during morning and evening hours. As a consequence, the largest structural deformations (reflector surface, quadripod) and the largest focus variations are reported during morning and evening hours [Schloerb 1978]. On the FCRAO telescope this is due to a temperature variation of the inside air and an associated radial temperature gradient of the BUS due to different thermal time constants of the inner and outer part of the BUS [Schloerb 1978, see also Section 9.3.8].
- (4) Large temperature differences and a large vertical temperature gradient of the inside air are reported during sunny days, with the air temperature at the top being higher than near the floor of the radome. The massive concrete floor of the radome/astrodome has a slowly varying temperature and acts as a heat sink/heat source. The daily temperature variation and temperature gradient of the inside air is small during overcast days.
- (5) Natural and forced ventilation and exhaust of air through a hatch/opening at the top of the radome/astrodome reduce the temperature variation and the temperature gradient of the inside air. Forced ventilation by fans in a radome is generally made at the periphery of the radome or against the radome walls so that the ventilating air is guided to the top.
- (6) Peripheral ventilation is inefficient for air volumes at the centre of the radome. A more uniform arrangement of fans that allows ventilation of the

central air volume is used for the MIT–Haystack radome [Barvainis et al. 1993].

- (7) During winter conditions the temperature of the inside air may fall below freezing point. In order to reduce/prevent inside icing conditions, the intake air is dried and/or heated above freezing point, i.e. to $\sim 10^{\circ}\text{C}$ for the MIT–Haystack radome [Barvainis et al. 1993].
- (8) In an astrodome/radome with little free space at the walls it is difficult to ventilate the air between the reflector surface and the enclosure and a vertical temperature gradient is reported to occur [Baas 1995].
- (9) In a smaller astrodome, like the astrodome of the JCMT, the temperature variation and temperature gradient can be reduced by ventilation through louvres. The reports indicate that homogenization of the inside air temperature through louvre action is efficient for air volumes close to the walls of the enclosure but less efficient or insufficient for the central air volume. For wind induced natural ventilation through louvres see Karava et al. [2007].
- (10) The air inside a radome is kept at an over–pressure for mechanical stabilization of the radome. This over–pressure can be used to exhaust (warm) air through a hatch/opening at the top of the radome.
- (11) There is no direct sunlight in a radome and a closed astrodome. The solar radiation that enters the radome and astrodome diffusely through the partially transparent skin/membrane is diffusely scattered and partially absorbed inside the enclosure. The radome/astrodome heats up under solar illumination and the warm skin radiates at infrared wavelengths to the interior of the radome/astrodome.
- (12) A cover of white paint, reflective paint or aluminium foil decouples to some extent the telescope from the diffuse radiation background and the illuminated areas of the radome/astrodome. The radome enclosed FCRAO 14–m telescope is covered with aluminium foil (see Fig. 3.5) [Schloerb 1978].
- (13) The mobility of the astrodome can be used to reduce the solar illumination of the slit area.
- (14) The astrodome with an open slit can be moved to avoid direct solar illumination of the telescope. A good adaptation of the telescope to the cool night air can be achieved. The reflector surface will radiatively couple to the cool sky.

Thermal model calculations of the JCMT astrodome and telescope are published by Bregman & Casse [1985]. Thermal model calculations of the air inside the Onsala radome and the MIT–Haystack radome are explained in Section 11.9. The calculations require a good modelling of natural and forced convection of the inside air; the thermal model must contain several air layers in order to obtain a realistic value of the air temperature gradient.

Chapter 11

Thermal Model Calculations

Model calculations are made to obtain for certain load cases information on the thermal behaviour of a telescope, or a telescope and its enclosure or of a specific structural component. The temperatures predicted from model calculations are used for design and/or operational purposes. Design questions addressed in thermal model calculations may concern the type of insulation required to obtain temperature stability, the type and amount of ventilation required to obtain temperature uniformity of a BUS under asymmetric solar illumination, the heat required to counterbalance radiative cooling of a BUS during the night etc. The calculations provide numbers, like 4 cm thick insulation, 10 000 m³/h ventilation, 10 kW heating etc., which are then realized in the construction. Thermal model calculations and associated finite element calculations may investigate for operational purposes the pointing stability of an alidade support, the focus stability of a BUS under the influence of the thermal environment, the development of transient reflector surface deformations due to temperature asymmetry in a yoke structure etc. The thermal load case in the finite element calculation may be of a *static* nature in which the telescope and enclosure experiences one particular temperature change, or of a *dynamic* nature in which the telescope and enclosure experience a time variable temperature change. This temperature change may be of an artificial nature, for instance a sudden temperature drop to determine the thermal time constant of a structure, or it may represent the response of the telescope and enclosure to the change of the thermal environment in which they operate or are expected to operate. The quality of an answer of a thermal problem depends, evidently, on the quality of the thermal model, which is constructed from the basic relations of heat conservation and heat transfer. The confidence of an answer can be judged from thermal calculations of a similar structure of which temperature measurements are available for comparison.

For large telescope structures it can today be assumed that a finite element model (FEM) is available. In the case the temperature distribution throughout the elements of the FEM is known, the thermal deformations can be calculated. The temperature distribution may be taken from actual measurements of the mechanical structure or may be calculated from a thermal model of the telescope, and enclosure, and interaction with the thermal environment. In some cases a mechanical model of a

structure is built and temperature measurements are made to establish the thermal behaviour and to check, in addition, the validity of a corresponding thermal model. A mechanical model is sometimes built to test the mechanical stability under a large number of thermal cycles. This concerns for instance the stability of an adhesive, the stability of CFRP material, and other thermal fatigue questions.

11.1 Mechanical Models of Structural Components

Even though thermal calculations can be made with good accuracy, mechanical models or scaled models have been built of important structural components and these models have been subjected to temperature variations to study their thermal behaviour. Such models involve, for instance, plates with different coatings to study the influence of insolation and radiation towards the sky, to study the thermal behaviour of panel insulation and of panel heating, to study the effect of insulation of a representative section of the IRAM 15-m telescope fork arm, or the thermal behaviour of a section of a BUS (VertexRSI ALMA telescope) etc. The measured thermal behaviour is often reproduced, *a posteriori*, in a thermal calculation. On the other hand, temperature measurements of existing telescopes and enclosures may be used to confirm corresponding thermal models, which are then applied to other similar and scaled structures [see below, and Borovkov et al. 2003, Machuyev & Gimmelman 2006, for the Russian RT 70-m telescope].

In the example of a panel and a section of the IRAM 15-m telescope fork arm the temperature measurements were of first priority, thereafter came a check of the validity of a thermal model, followed by the study of several load cases, then came the final design. The study of a panel and associated model calculations is illustrated in Fig. 11.1. In this experiment and the corresponding model calculations the attention focused on heat transfer through the panel and on the associated temperature gradient. The panel consisted of a 4 cm thick Al-honeycomb core and a 2 mm thick CFRP front and rear skin. The surfaces were painted white with TiO₂ paint. The panel was placed in horizontal position approximately 40 cm above the ground, consisting of gravel. The panel was exposed to the ambient air, solar radiation and the radiative interaction with the sky and the ground. The air was able to circulate freely around the panel, there was a light wind during the measurements. The sky was clear but the solar radiation was reduced by pollution of the air (town). The temperature of the front and rear was measured with sensors protected against direct sunshine (Fig. 6.2). The thermal model of the panel (see Table 11.2, HC-panel) reproduced the measured temperatures for the known environmental condition. This model was then used to study other panels (material and thickness) with other surface finishes.

In the ‘chimney’ experiment of a 2 m high representative section of a fork arm of the IRAM 15-m telescopes the attention focused on the most appropriate type of insulation and whether thermal calculations can simulate with good precision

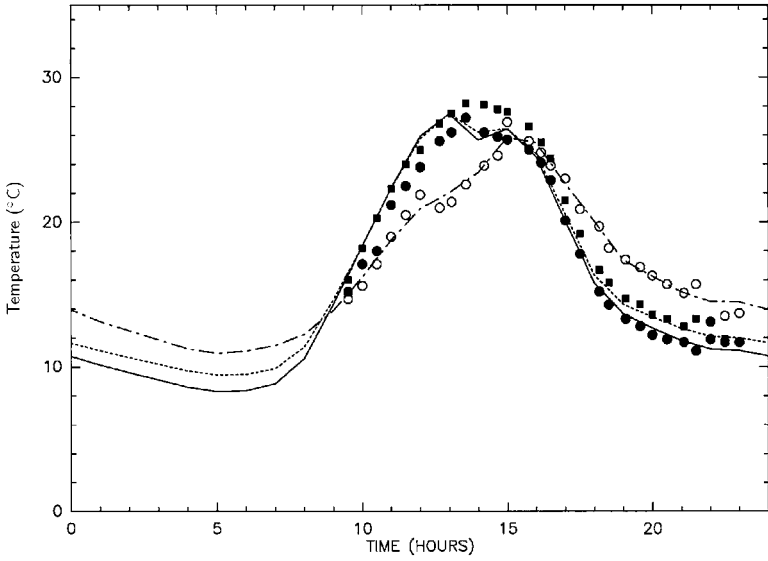


Fig. 11.1 Temperature measurement of an Al-honeycomb panel, painted white. Open circles: ambient air temperature, black dots: temperature of the panel front surface facing the sky, black squares: temperature of the panel rear surface facing the ground. The result of the model calculation is shown by the continuous line (front side) and dashed line (rear side). The ambient air temperature is extrapolated to the time of no measurement.



Fig. 11.2 Model of a fork arm ('chimney' experiment) for the study of different types of insulation. The measurements were made on Plateau de Bure under representative meteorological conditions.

the measured temperatures [Delannoy & Dimper 1985]. As shown in Fig. 11.2, the fork model consisted of a closed box of $0.5\text{ m} \times 0.5\text{ m}$ cross section and 2 m height, made of 12 mm thick steel plates welded together at the intersections. The box was placed 20 cm above the ground. The surfaces of the box were facing East, South, West and North. The temperatures of the northern and southern steel plates were recorded every 5 minutes. Two types of insulation were studied (from inside to outside), i.e. type I: steel plate (S) – 5 cm glued-on hard insulation foam (I) – glued-on aluminium foil (AF) – 2 cm air gap (AG) – MetawellTM radiation shield (RS)¹, i.e. S-I-AF-AG-RS; and type II: steel plate (S) – glued-on aluminium foil (AF) – 7 cm air gap (AG) – MetawellTM radiation shield (RS), i.e. S-AF-AG-RS. The temperatures recorded in this experiment, and reconstructed in model calculations, are shown in Fig. 11.3. From the measurements and thermal model calculations it was decided to use the insulation of type I for the fork and the secondary focus cabin of the IRAM/SEST 15-m telescopes.

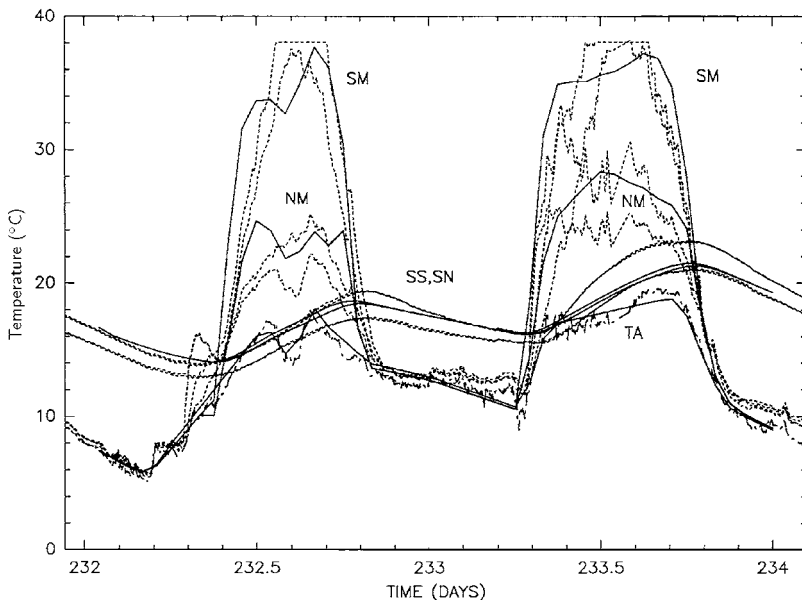


Fig. 11.3 ‘Chimney’ experiment simulating a section of the IRAM 15-m telescope fork arm and its thermal protection by insulation, air gap and radiation shield. Dashed lines: measured temperatures, continuous lines: model calculations. TA: ambient air temperature, SM, NM: temperature of the radiation shield at the southern and northern side, SS, SN: temperature of the fork arm steel plates at the southern and northern side (thermal protection type I).

¹ The MetawellTM radiation shield consisted of two parallel Al-plates, each 1 mm thick, at 5 mm distance, connected by an internal, corrugated Al-profile.

11.2 Static Thermal Calculations (The Use of Known Temperature Distributions)

In a *static* thermal model calculation is the temperature distribution of the telescope or enclosure known and used in the FEM to derive the temperature induced structural deformations. So far, the majority of thermal model calculations of radio telescopes investigated for *static* thermal loads the variation of the reflector surface shape, denoted symbolically as \mathbf{S} , and the pointing and focus, denoted symbolically as \mathbf{P} . For instance, in the case the shape $\mathbf{S}(T_o)$ and the pointing/focus $\mathbf{P}(T_o)$ are known to be perfect for a uniform temperature T_o , the question asked is whether the shape/pointing/focus $\mathbf{S}(T_o+\Delta T)$ and $\mathbf{P}(T_o+\Delta T)$ remain acceptable in the case the temperature is uniformly varied by ΔT , or is varied by a gradient ∇T across the structure, ie. $\mathbf{S}(T_o+\nabla T)$ and $\mathbf{P}(T_o+\nabla T)$, or by a random temperature distribution T_{rms} , ie. $\mathbf{S}(T_o+T_{rms})$ and $\mathbf{P}(T_o+T_{rms})$ etc. The resulting static shape variation $\delta\mathbf{S} = (\partial\mathbf{S}/\partial T)\delta T$, usually expressed as associated change of the reflector surface precision $\delta\sigma = (\partial\sigma/\partial\mathbf{S})\delta\mathbf{S}$ and the pointing/focus variation $\delta\mathbf{P} = (\partial\mathbf{P}/\partial T)\delta T$, are derived from FEM calculations using the selected temperature distribution ΔT , or ∇T or T_{rms} . Such calculations are usually presented in the design studies of the construction firms.

In the context of static thermal model calculations the question arises with which accuracy thermal deformations and by this temperature induced focus, pointing, reflector surface and path length deformations can be predicted when using a known temperature distribution in the FEM. This depends on the precision of the FEM, which usually is very good.

11.3 Dynamic Thermal Model Calculations (The Derivation of Temperature Distributions)

A *dynamic* thermal calculation predicts from a thermal model the temperature distribution of a telescope, or enclosure, or of a structural component when interacting with the ambient thermal environment, as schematically shown in Fig. 11.4. Since the thermal environment changes with time, the calculated temperature distribution of the telescope, enclosure or structural component [i] also changes with time, i.e. $T_i(t)$. The changes of the thermal environment are for instance the daily variation of the ambient air temperature, periodic or interrupted sunshine, the change of convective cooling at different wind speeds etc. The temperature distribution throughout the telescope, enclosure, or structural component calculated in this way is closer to reality and provides information of the thermal behaviour to be expected of the structure. Many thermal model calculations terminate at this point, using the derived temperature distribution for an evaluation of the thermal state of the telescope, enclosure or structural component.

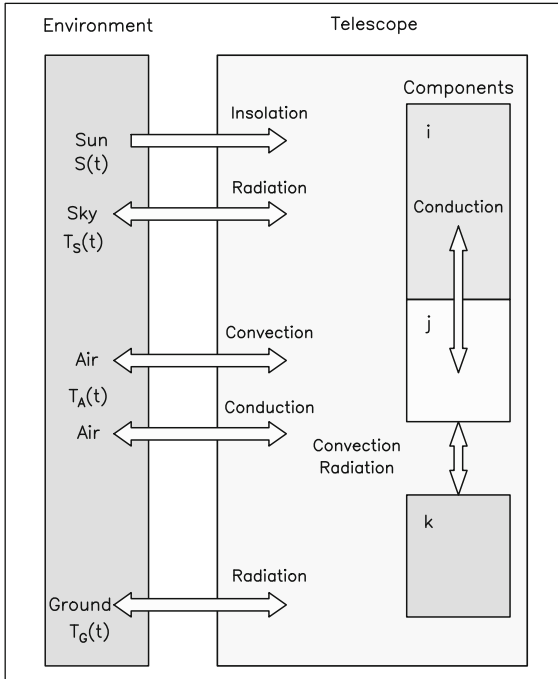


Fig. 11.4 Model of an open air telescope illustrating the thermal interaction of the telescope components (i,j,k) with themselves and the thermal interaction of the telescope with the environment [From Greve & Bremer 2005), Courtesy IEEE Ant. Propagat. Magazine].

However, the calculated temperature distribution [$T_i(t)$, $i = 1, 2, \dots, N$ elements] can be used in the FEM of the telescope to derive the time-dependent reflector surface shape $\mathbf{S}(t) = \mathbf{S}(T_i(t))$ and the time-dependent pointing and focus status $\mathbf{P}(t) = \mathbf{P}(T_i(t))$. The variation of the surface shape is $\delta\mathbf{S} = \Sigma(\partial\mathbf{S}/\partial T_i)(\partial T_i/\partial t)\delta t$, and similarly for the pointing and focus change $\delta\mathbf{P}$. If the associated surface deformations $\delta\mathbf{S}$ and pointing/focus changes $\delta\mathbf{P}$ are too large, then a thermal control is required to reduce $\delta\mathbf{S}$ and/or $\delta\mathbf{P}$ to acceptable values. This can be done through passive thermal protection by paint and insulation and/or through active thermal control by ventilation or climatisation so that $\partial T_i/\partial t$ is small, or through application of materials with low thermal expansion so that $\partial\mathbf{S}/\partial T_i$ and $\partial\mathbf{P}/\partial T_i$ are small. If necessary, the thermal design of the telescope is modified to reduce $\delta\mathbf{S}$ and $\delta\mathbf{P}$ and a further thermal model calculation is made and used in the FEM. In an iterative way a thermal protection is designed.

This Chapter explains dynamic thermal model calculations of telescope components of increasing degree of structural complexity, in contact with a realistic time variable thermal environment.

In general, the result of a thermal model calculation is the temperature $T_i(t)$ of a specific telescope component [i], as a function of time. A thermal model calculation is, however, also a calculation of heat transfer with accountable energy values. Inspection of the involved energy values can be helpful in the understanding of a thermal situation, as explained in Section 11.11 for a simple case. The involved

energy values are important for operational purposes when, for instance, a ventilation system or a ventilation system with heating and cooling is designed.

11.4 Node Structure of Thermal Models

The thermal state of simple structures in contact with the environment can be expressed in analytical form and the textbooks on *Heat Transfer* contain many examples. The analytic approach fails for large and/or complex structures. However, in analogy with simple structures a large and/or complex structure is divided into a large number N of thermal components (thermal nodes), where N may reach values of a few hundred. The thermal nodes are specified by their heat capacities and their thermal connections (conduction, convection, radiation) with other nodes of the structure and the environment. Heat sources (like sunshine) and heat sinks (like the cold sky) are taken into account. The thermal environment (ambient air $T_A(t)$, sky $T_S(t)$, ground $T_G(t)$) consists in the calculations of infinite heat reservoirs. This, for instance, means that a telescope in the immense volume of ambient air may partially follow the temperature of the air while on the other hand the temperature of the ambient air is not affected by the temperature of the telescope (except for the surface layers surrounding the structure). The mathematical description of a complex thermal structure results in a large number of coupled differential equations (easily of the order of $10N$) connecting the heat flow between the individual components (nodes) and between the components and the environment. The differential equations, with time-dependent transient effects included, are solved by iterative numerical methods and by this provide the time-dependent temperature of the structural components. Since the thermal model of a complex structure is analogue to a multi-component electrical circuit [see Chapman 1984], electrical network programmes² can be used for the evaluation of thermal models. The skill and success of constructing a thermal model lies in the selection of significant thermal components and corresponding realistic thermal connections. Evidently, a dynamic thermal model is different from the FEM of a structure although the FEM may be the base for the construction of a thermal model.

The presented thermal models describe structures of increasing complexity, i.e. of increasing mass and increasing surface area of thermal contact with the environment and thus of an increasing number of required thermal components (nodes). The scale of the thermal system is characterized by the amount of energy (heat) ΔQ required to change the temperature of the structure by 1°C . The complexity of the models discussed here is summarized in Table 11.1.

² The calculations of this Chapter were made with the network programme ESACAPTM [Stangerup 1982, 1999].

Table 11.1 Complexity of Thermal Models.

Structure	Surface [m ²]	Material Mass [ton]	Thermal Nodes ^{a)}
Panel			
Plate Panel	1–2	aluminium ~7 kg/m ²	2–10
HC Panel + Insulation	1–2	aluminium 10–15 kg/m ²	20
Alidade			
Beams ^{b)}	10	steel 2	32
Fork Support			
Fork – insulated	40	steel 10	243
Backup Structure			
IRAM 30–m Telescope ^{c)}	2 500	steel 300	310
SRT 64–m Telescope	10 000	steel 450	360
Radome/Astrodome			
Onsala (RD)	2 100	air 10 500 [m ³] ^{d)}	120
MIT–Haystack (RD)	5 000	air 38 000 [m ³] ^{d)}	120
LMT/GMT (AD) ^{e)}	13 500	air 160 000 [m ³] ^{d)}	240 ^{f)}

^{a)} The environment has 3 additional nodes (minimum);

^{b)} size 0.5 × 0.5 × 5 m (hollow);

^{c)} reflector surface and rear side cladding,

the mass and node number include the BUS and the yoke;

^{d)} air enclosed by the radome/astrodome;

^{e)} thermal feasibility study, Greve & MacLeod [2001];

^{f)} including the inside air and the astrodome housing.

11.5 The Thermal Environment as Input Data

A thermal model calculation requires the selection of a thermal environment as input of the model. Evidently, the thermal environment used in the model should have some resemblance to the actual situation, for instance a typical winter condition when studying de-icing or a summer condition when studying cooling of a BUS. The time variable thermal environment in the model calculations has at least 3 nodes, i.e. the ambient air temperature $T_A(t)$, the sky temperature $T_S(t)$, the ground temperature $T_G(t)$ and solar energy as heat source calculated from the relations of Chapter 5. In certain model calculations it is recommended to use also an ambient air temperature for large areas in shadow, i.e. $T_{A,shadow} = T_A - \Delta T_{shadow}$ with ΔT_{shadow} of the order of 5 to 10° C. As evident from Chapter 4, cosine-form approximations of the ambient air temperature, the sky temperature and the ground temperature are for many cases a good representation of the environment. For the model calculations reported here, either actually measured data of the environment were used or a constructed environment was used based on the data and relations explained in Chapter 4. The interaction of the telescope and enclosure with the ambient air is by convection, explained in Section 7.7, with the sky and the ground by radiation, explained in Section 7.8 and Chapter 8.

11.6 Models of Panels

The main interest in numerical thermal studies of a panel is the temperature and the temperature gradient through a panel, in particular under the influence of sunshine and the cool sky. The temperature of a panel relates to the thermal behaviour of panel materials, such as the consistency of CFRP material at elevated temperatures and the bonding performance of glue. The temperature gradient through a panel is related to mechanical deformations and thermal panel buckling. The thermal model of a panel requires only a small number of nodes and is easily constructed. However, it is the proper choice of the ‘rear environment’ of the panel that needs attention, as for instance mentioned in the panel study of the proposed CCAT 25–m telescope [Woody et al. 2008]. A panel on an open BUS experiences the thermal environment at its front and rear, although the rear may not receive sunshine and may not see the cold sky but instead the warm ground. At the rear, or part of the rear, of an open reflector the temperature of the ambient air is realistically that of a shadow area with $T_{A,shadow} \leq T_A$. A panel on a closed BUS is at the front exposed to the thermal environment, on the rear it faces the BUS network and the air in the BUS, or the front cover of the BUS or an insulation layer covering the BUS. For a thermal calculation of a panel a realistic thermal state of the BUS or of the BUS cover must be selected, or even be derived from another thermal model calculation.

Single plate panels, with stiffening ribs, and Al–honeycomb panels are used on open and closed BUS structures. The thermal node structure of a single plate panel and an Al–honeycomb panel is summarized in Table 11.2, the thermal node structure of a Media–LarioTM front heated or back heated Al–honeycomb panel is summarized in Table 11.3. The thermal model of a plate panel either on an open BUS or on a closed BUS is shown in Fig. 11.5.a and Fig. 11.5.b.

Table 11.2 Plate Panel and Aluminium–Honeycomb Panel.

Plate Panel		
Component	Thickness	Thermal Nodes
Plate (Al)	2 mm	2
Honeycomb Panel		
Component	Thickness	Thermal Nodes
Front Skin (CFRP)	2 mm	2
Al-honeycomb	4 cm	2
Rear Skin (CFRP)	2 mm	2
Rear side environment ^{a)}		1
or rear side BUS ^{b)}		2

^{a)} rear side ambient air in shadow, $T_{A,shadow}$.

^{b)} including air inside the BUS and the radiation field in the BUS, or the interaction with the BUS front side closure (insulation).

The environment requires 3 additional nodes.

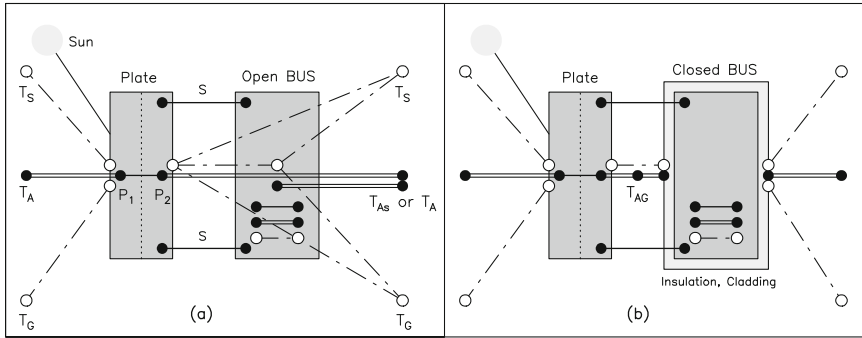


Fig. 11.5 Thermal model of a plate panel either on an open BUS (a) or on a closed BUS (b). Dots: thermal material nodes, open circles: radiative nodes. Single lines: conductive connections, double lines: convective connections, dashed lines: radiative connections. The conductive connection S is the support between the panel and the BUS (screw, adjuster, panel frame etc.). The temperatures are T_A : ambient air, T_{As} : ambient air at shadow side, T_{AG} : air in gap, T_S : sky, T_G : ground. The Sun is a direct heat source. (b) same notation as in (a). Only some thermal connections inside the BUS are indicated. *Although a thermal model can be drawn as an electrical diagram, the presentation used here allows an easier identification of the structural components, their thermal nodes and thermal connections.*

Many panels consist of an Al–honeycomb core, a thin front and rear metal skin or CFRP skin and a surface finish consisting either of paint, anodisation or a coating. In the Al–honeycomb core the heat transfer is primarily through the panel rather than along the panel. The heat transfer is conductive along the hexagonal walls of the honeycomb, radiative between the front and rear skin (and reflections on the honeycomb walls) and conductive (or convective) through the inside air. When considering these modes of heat transfer the thermal model of a honeycomb panel becomes rather complex [see for instance Daryabeigi 2002, Murer & Millan 1998]. However, the manufacturer of honeycomb panels provides data on heat transfer through a panel based on measurements, which combine the effect of all heat transfer modes. Using these data, a honeycomb panel can be described as a plate panel of equivalent thermal properties.

The results of a model calculation of a plate panel (Table 11.2) are shown in Fig. 11.6 to illustrate the influence of the environment on the panel rear side. The selected aluminium panel has a mass of 12 kg/m^2 and a conductivity $k = 100 \text{ W/m/K}$. The panel is mounted either on an open BUS, a BUS closed by the panels and the rear side cladding, or a BUS closed by the panels with attached insulation and the rear side cladding. The thermal BUS model of the SRT 64–m telescope [Greve 2000] was used to simulate the background. The solar illumination of the reflector is asymmetric as explained below (Fig. 11.18), during the day the telescope trails the Sun at a distance of 45° . The circular ventilation of the closed BUS (case a) also reaches the panel rear side and thus reduces the influence of sunshine. This is not the case of the closed BUS with insulation behind the panels (case b) so that

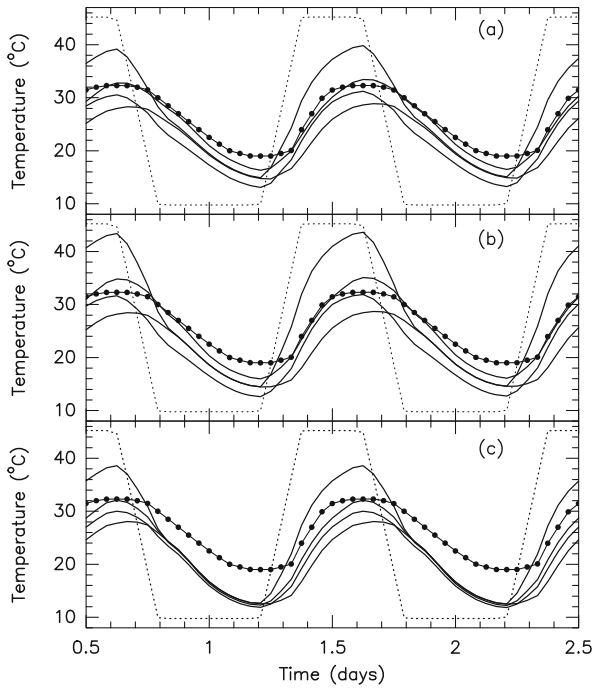


Fig. 11.6 Thermal model calculation of the front side temperature of a plate panel on a closed BUS (a,b) and an open BUS (c). The BUS (a) is closed by the panels and rear side cladding, the BUS (b) is closed by the panels with attached insulation and rear side cladding. The lines are the panel temperature at the top, bottom, right (sunshine) and left side (shadow) of the reflector. The closed BUS structures are ventilated, with 10% intake of ambient air. The dots indicate the ambient air temperature, the dashed lines the time of sunshine.

the panels reach a higher temperature. The panels on the open BUS (case c) can reach a high temperature if in sunshine, however, they cool quickly to the ambient air temperature after sunset. The calculated maximum temperature gradient through the panels in sunshine is 0.6 to 0.8° C, falling to 0.2° C at night.

On a telescope that is frequently exposed to adverse weather conditions the panels may need heating to prevent icing. The front and back heating of an Al-honeycomb panel with Ni-skins and rhodium coating at the front (manufactured by Media-LarioTM) was tested on a 15-m telescope on Plateau de Bure, the measurements are shown in Fig. 9.62 and Fig. 9.63. These tests were combined with calculations based on a thermal model developed by Media-LarioTM & IRAM. The question in this investigation was the temperature gradient through the panel produced by the power from the heating. The accuracy of the calculation had to be of the order of ± 0.1° C. A thermal gradient through the panel of the order of 1° C or larger results in a significant mechanical deformation. The thermal node structure of these panels is summarized in Table 11.3, the node structure of the thermal model of the front

Table 11.3 Media-LarioTM Al-Honeycomb Panel, with front or back heating.

Component	Thickness	Thermal Nodes	Mass ^{b)} [kg]	Heat Capacity ^{b)} [J/K]	Thermal Resistance ^{b)} [m/W]
Front Skin (Ni)	0.6 mm	2	5.4	2 400	5×10^{-6}
Adhesive	0.1 mm	2			0.003
Front Heating					
Al-honeycomb	2 cm	10	5	4 300	0.003
Adhesive	0.1 mm	2			0.003
Rear Skin (Ni)	0.6 mm	2	5.4	2 400	5×10^{-6}
(Back Heating)					
Insulation	1 cm	2	0.35	525	0.25
Rear side BUS ^{a)}		2			

^{a)} including air inside the BUS and radiation field in BUS, $T_{BUS} = T_A + 10^{\circ} C$;

^{b)} for 1 m² panel area.

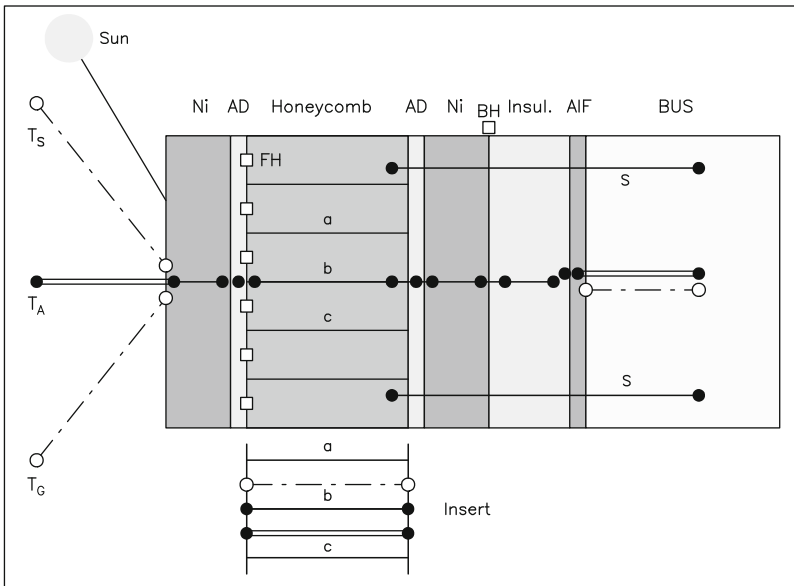


Fig. 11.7 Thermal model of a front/back heated panel (Media-LarioTM). The panel consists of a Ni front and rear skin (Ni) glued to the Al-honeycomb core by a thin layer of adhesive (AD). At the rear side the panel is covered by insulation (Insul.) and an aluminium foil (AIF). FH are the front heating wires, BH is the location where the back heating wires are located. a, b, c, ... are individual walls of the honeycomb core. Dots: thermal material nodes, open circles: radiative nodes. Single lines: conductive connections, double lines: convective connections, dashed lines: radiative connections. The conductive connection S is the support between the panel and the BUS (screw, adjuster, panel frame etc.). The temperatures are T_A : ambient air, T_S : sky, T_G : ground. The insert illustrates the detailed heat transfer through the honeycomb core, conduction along the cell walls, convection and radiation in the volume between the cell walls. The Sun is a direct heat source.

heated panel is shown in Fig. 11.7. A special feature of this calculation is the pulsation of the heating, i.e. a 600 W/m^2 supply with a duty cycle of 22 % with 4 s on and 18 s off. An example of the calculations is shown in Fig. 11.8. The pulsation of the heating is clearly seen in the change of the temperature gradient. The later measured temperature gradients (front heating: $\Delta T_{fb} = 0.4^\circ \text{ C}$, back heating: $\Delta T_{fb} = -1.6^\circ \text{ C}$), shown in Fig. 9.63, were correctly predicted in the calculations.

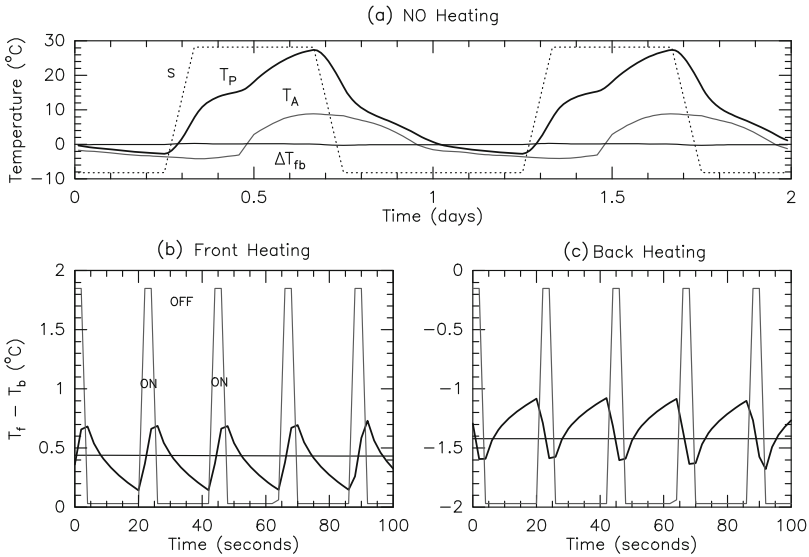


Fig. 11.8 Result of thermal model calculations of panels (Media-LarioTM) with Front Heating (b) and Back Heating (c). Pulsed heating (22 % duty cycle with ON and OFF phases) is applied and the resulting temperature gradient $\Delta T_{fb} = T_f - T_b$ between the front (f) and rear (b) side is shown. The horizontal lines (in (b) and (c)) are the time averaged temperature gradients. Without heating being switched on the panels behave identical (a), panel temperature: T_p , temperature gradient through the panel: $\Delta T_{fb} \leq 0.15^\circ \text{ C}$; ambient air temperature: T_A , time of sunshine: S (dots).

11.7 Model of Telescope Supports

11.7.1 Model of an Alidade

The alidade (and quadripod) consists of beams and tubes. Although the alidade beams are connected, in thermal calculations it is sufficient to consider them individually since the heat transfer at the connections is small. The thermal model of a beam is easily constructed and may have the node structure shown in Fig. 11.9.

A beam can be divided along its length into several segments, with proper thermal connections around its circumference and along its length. As emphasized by Ambrosini et al. [1996], for an understanding of the thermal behaviour of an alidade it is important to know the temperature gradients across the beams. In the thermal model it is therefore necessary to consider radiative heat transfer inside the beam and internal convective heat transfer, especially if inside ventilation is applied. In addition, some alidade/quadripod models need insulation of the beams/tubes.

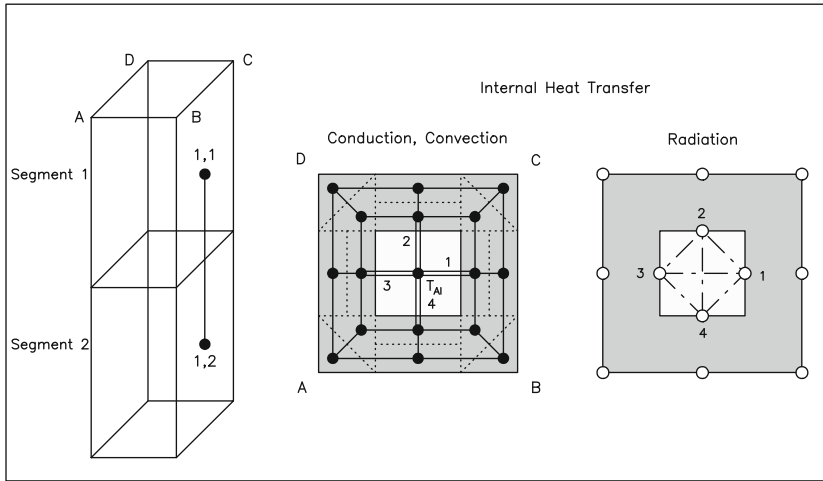


Fig. 11.9 Thermal model of a beam, without insulation. The emphasis of the figure is on thermal connections inside the beam; the external thermal connections are similar to those of Fig. 11.5, 11.7. The length of the beam is divided into segments of which two are shown, the segments are thermally connected of which one conductive connection (1,1) to (1,2) is drawn. The possible conductive, convective and radiative connections in the beam cross section are indicated. Dots: thermal material nodes, open circles: radiative nodes. Single lines: conductive connections, double lines: convective connections, dashed lines: radiative connections. T_{Ai} is the temperature of the inside air.

As reported by Bayley et al. [1994] of the Cambridge MERLIN 32-m telescope, the orientation of an alidade beam with respect to the Sun and the sky determines to a large extent its thermal behaviour and by this the pointing of the telescope. As an example, the thermal model of a $L = 5$ m long beam, of 0.5×0.5 m² cross section, divided into 4 subsections $L/4 = 1.25$ m, made of 20 mm thick welded steel plates, was constructed and exposed in the calculations to the thermal environment. The beam is once in a vertical position, once inclined by 45° against the vertical (see Fig. 9.9.a) and once in a horizontal position. Using Fig. 11.9 for orientation, the beam is inclined in the direction BC and the Sun is shining on the surface AD; the beam follows the Sun in this orientation during the day (summer, geographic latitude = 45°). The beam is not insulated but is painted white with coefficients $a_S = 0.35$ and $e_1 = a_1 = 0.75$. In the model calculation is the sky temperature 25° C below

the ambient air temperature. The convective heat transfer coefficient of the ambient air is $h = 10 \text{ W/m}^2/\text{K}$. Important for the thermal expansion and twist of the beam is the temperature difference between the front (AD) and rear (BC) $\Delta T = T(\text{AD}) - T(\text{BC})$, during the day with sunshine and during the night when exposed to the cold sky. The result of the calculation is shown in Fig. 11.10. The vertical beam is in a symmetrical way radiatively connected to the sky and the ground, hence $\Delta T = 0$ during the night. The inclined and horizontal beam has a stronger or a total connection to the cold sky on the side AD so that $\Delta T < 0$ during night.

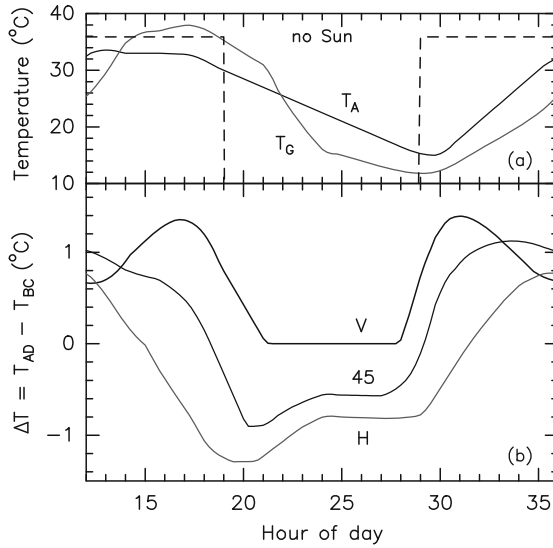


Fig. 11.10 Thermal calculations of an alidade beam with side AD in sunshine and side BC in shadow. (a) Adopted ambient air temperature T_A and ground temperature T_G . The dashed line shows the time of sunshine. (b) Temperature difference ΔT between the front side AD and the rear side BC (see Fig. 11.9) of the vertical beam (V), the beam inclined by 45° (45) and the horizontal beam (H).

11.7.2 Model of a Yoke

A yoke is in essence a combination of beams or box structures with subdivision of the yoke arms and the roof of the yoke (Fig. 2.9, Fig. 9.22). In the case of a box structure, the box has an inner and outer surface and an inside air volume. The boxes may be insulated, the air in the boxes may be ventilated. The thermal model of a box structure is similar to that of a beam (Fig. 11.9) though with different geometrical proportions.

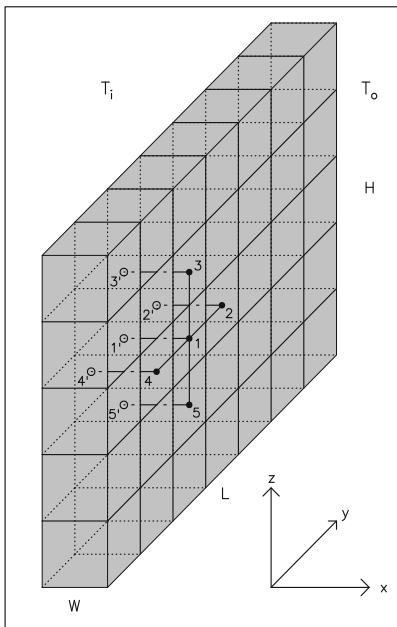


Fig. 11.11 Heat conduction through a plate (x -direction) and in the plane of the plate (y -direction and z -direction). The plate is divided into several smaller sections of which the elements 1,2,3,4,5 ... at the front side and 1',2',3',4',5' ... at the rear side are shown.

The plates of a yoke (and of telescopes and enclosures) can have very large dimensions, for instance $5\text{ m} \times 5\text{ m}$ for the yoke arms of the IRAM 30-m telescope (Fig. 2.9, Picture 1.4). Such large plates cannot be treated as a single plate but should be divided into many elementary sections in order to calculate the temperature distribution in the plane of the plates. The division of a single large plate of dimension L (length), H (height) and W (width) is illustrated in Fig. 11.11. The plate has a front of which the sections 1,2,3,4,5,... are shown, and a rear of which the corresponding sections 1',2',3',4',5', ... are shown. The conductive heat transfer in the plate can be calculated in x -direction (through the plate) and in y -direction along its length and z -direction along its height. This results in many coupled differential equations of the temperatures of the sections. The subdivision of a large plate has the advantage that asymmetric solar illumination (for instance one corner section being in sunshine) and variable convective cooling (wind) can easily be modelled.

11.7.3 Model of a Fork Support

Thermal studies of a fork support are important with respect to temperature induced pointing errors and path length variations as sketched in Fig. 9.11. The calculations assist in the design of a passive thermal protection so that the pointing errors are within the specified tolerances. The basic thermal models are illustrated in Fig. 11.12, which show a fork without thermal protection (a) and with attached protection (b) consisting either of insulation or insulation and a radiation shield.

The outer surface is for instance painted white (TiO_2 paint) or covered with anodised aluminium. The model may include natural convection in the fork arms, or even forced ventilation. In the model calculation the Sun illuminates the fork arms asymmetrically. The thermal protection must produce a tolerable temperature difference between the fork arms (Section 9.1.3: ΔT_{LR} and tilt error $\Delta \epsilon_1$ along the EL-axis) and a tolerable temperature difference between the front and rear side of the fork arms (Section 9.1.3: ΔT_{fr} and cross elevation tilt error $\Delta \epsilon_2$ perpendicular to the EL-axis).

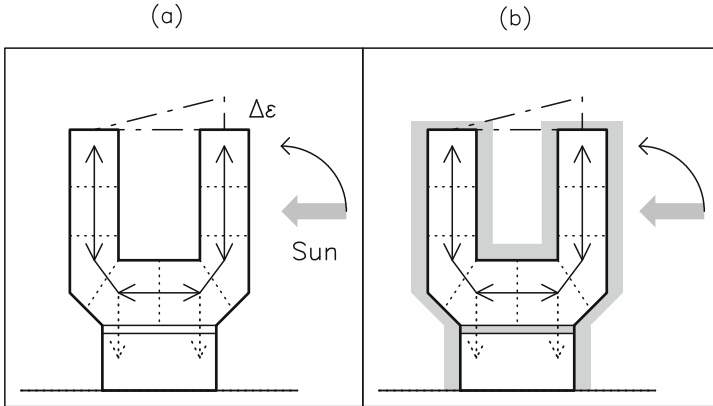


Fig. 11.12 Exploratory fork models investigating temperature differences due to asymmetric and variable solar illumination, indicated by the arrow. (a) NO thermal protection, (b) attached protection (insulation, or insulation + radiation shield, etc.). The outer surface is painted white or covered with anodised aluminium. Internal convection or forced ventilation can be included in the model (indicated by the arrows). The quality of the thermal protection is for instance evaluated from the pointing error $\Delta \epsilon$ along the EL-axis.

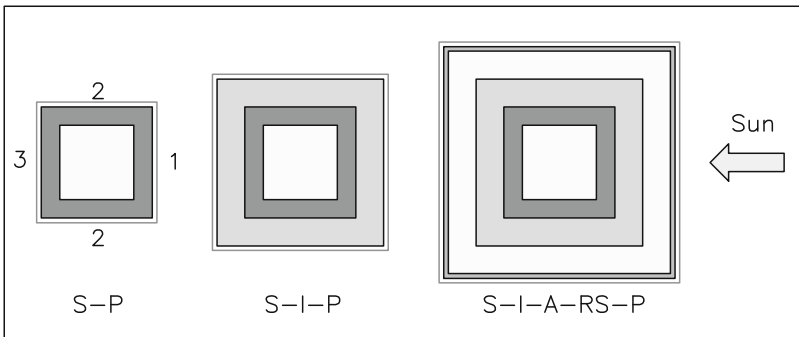


Fig. 11.13 Schematic illustration of a thermal façade around a fork arm (cross section view). S: steel wall of fork arm, P: paint, I: insulation, A: air gap, RS: radiation shield. The Sun is shining from the right side (1), the left side (3) is in shadow.

The efficiency of thermal protection of a fork was studied in experiments (Figs. 11.2, 11.3) and thermal model calculations of façades, since long used in energy-saving buildings (for instance Fohry [1977], Behrndt & Scharpf [1979]). The investigated façades are schematically drawn in Fig. 11.13. The façades consist of a fork arm (steel, S) only covered with paint (P), i.e. S-P, of a fork arm covered with insulation (I) and covered on the outer surface with paint, i.e. S-I-P, and of a fork arm covered with insulation, an air gap (A) and a radiation shield (RS) covered at the outer surface with paint, i.e. S-I-A-RS-P. The thermal node structure of the corresponding thermal models is shown in Fig. 11.14. It is assumed that the Sun is illuminating side 1 while side 3 remains in shadow. The efficiency of the thermal protection is judged from the temperature difference $\Delta T = T(1) - T(3) = T(\text{sunshine}) - T(\text{shadow})$. The results of the calculations are summarized in Table 11.4. An uncertain parameter in the calculation is the thermal resistance R_{CON} of the contact between the insulation and the fork arm, three cases are selected. Table 11.4 indicates that the façade S-I-P may not guarantee the condition of temperature uniformity between the left and right fork arm and the front and rear of a fork arm of $\Delta T_{\text{LR}} \approx \Delta T_{\text{fr}} \lesssim 1^\circ \text{C}$ unless a high contact resistance $2.5 < R_{\text{CON}}$ is realized. It was decided to use on the IRAM/SEST 15-mm telescopes the façade with insulation and radiation shield, i.e. S-I-A-RS-P, of which a section of its construction is shown in Fig. 11.15.

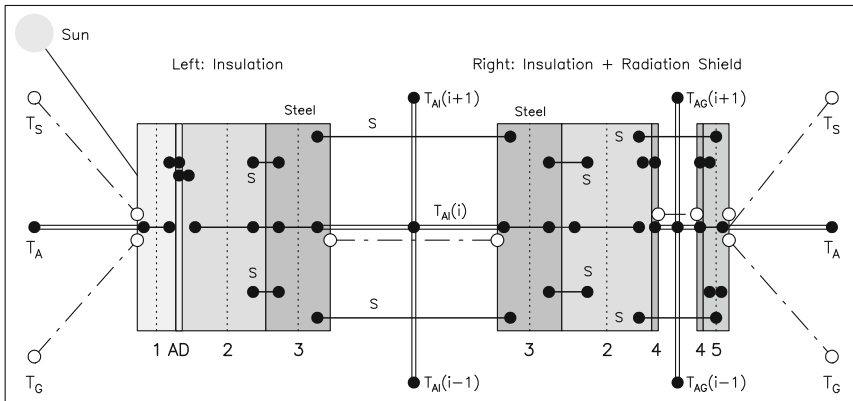


Fig. 11.14 Thermal model of a fork with insulation (Left Side) and a fork with insulation and radiation shield (Right Side). The structural components are 1: Al-skin cover of the insulation, AD: adhesive between Al-skin and insulation, 2: insulation, 3: steel plate of fork arm, 4: Al-foil, 5: radiation shield, T_{Al} : air inside the fork arm, T_{AG} : air inside the air gap between insulation and radiation shield. Dots: thermal material nodes, open circles: radiative nodes. Lines: conductive connections, double lines: convective connections, dashed lines: radiative connections.

Using the results of the façade experiments (Figs. 11.2, 11.3), the façade calculations (Table 11.4) and the construction parameters of Table 11.5, a complete thermal model of the IRAM/SEST 15-m telescope fork was constructed with a subdivision



Fig. 11.15 IRAM 15-m telescopes. The applied thermal protection consists of insulation (5 cm), aluminium foil, an air gap (2 cm) and a radiation shield (Al-plate) that is the outer surface. The supports of the radiation shield are plastic spacers with screws.

into the sections E, D, C, B, A (for both fork arms and the traverse section) as shown

Table 11.4 Thermal Protection with Façades.

Façade ^{a)}	R_{con} ^{b)} [W/m/K]	Material ^{c)}	Paint P: TiO ₂ ^{d)}		Paint P: aluminium ^{d)}	
			T(1) – T(2) – T(3) ^{e)} [° C]	ΔT ^{f)} [° C]	T(1) – T(2) – T(3) [° C]	ΔT [° C]
S–P		S	26.2 – 14.5 – 12.9	13.3	21.8 – 14.4 – 13.4	8.4
S–I–P	0.075	I	23.3 – 10.1 – 9.6		20.6 – 11.1 – 11.0	
		S	9.4 – 7.7 – 7.3	2.1	9.6 – 8.4 – 8.2	1.4
	0.5	I	27.5 – 10.8 – 10.3		24.0 – 12.0 – 11.9	
		S	8.9 – 7.7 – 7.4	1.5	9.3 – 8.5 – 8.3	1.0
		I	33.3 – 11.9 – 11.3		28.6 – 13.2 – 13.1	
2.5	S	9.0 – 8.5 – 8.4	0.60	9.4 – 8.9 – 8.9	0.40	
S–I–A–RS–P	0.075	RS ^{g)}	35.8 – 12.2 – 11.6		30.5 – 13.6 – 13.5	
		I	17.2 – 9.1 – 8.8		15.8 – 10.1 – 9.9	
		S	8.9 – 7.8 – 7.6	1.3	9.3 – 8.6 – 8.4	0.90
	0.5	RS	36.0 – 12.2 – 11.6		30.7 – 13.6 – 13.5	
		I	21.5 – 9.9 – 9.5		19.2 – 10.9 – 10.8	
		S	8.8 – 8.0 – 7.8	1.0	9.2 – 8.6 – 8.5	0.70
	2.5	RS	36.5 – 12.3 – 11.7		31.2 – 13.7 – 13.7	
		I	29.3 – 11.2 – 10.8		25.5 – 12.4 – 12.3	
		S	9.0 – 8.6 – 8.5	0.51	9.3 – 9.0 – 9.0	0.32

^{a)} S–P: steel–paint; S–I–P: steel–insulation–paint,

S–I–A–RS–P: steel–insulation–air gap–radiation shield–paint;

^{b)} thermal contact resistance between insulation and fork;

^{c)} S: 1.2 cm thick steel of fork arm, I: 5 cm insulation, RS: 2 mm thick aluminium radiation shield;

^{d)} TiO₂ with $a_S = 0.35$, $e_1 = 0.75$, aluminium with $a_S = 0.2$, $e_1 = 0.2$;

^{e)} T(1): front side in sunshine, T(2): sides of fork arm, T(3): rear side in shadow, Fig. 11.13;

^{f)} $\Delta T = T(1) - T(3) = T(\text{side in sunshine}) - T(\text{side in shadow})$, Fig. 11.13;

^{g)} inner surfaces of radiation shield with $a_1 = 0.1$, i.e. paint factor $E(1,2) = 0.05$ (Eq.(7.51)).

in Fig. 11.16. A connection of the air inside the pedestal and the fork arms (volume elements E, D, C, B) by natural convection is taken into account. The machinery in the pedestal produces heat; convection transfers this heat from a lower air volume into an upper air volume (for instance from D to C to B in Fig. 11.16). Many thermal calculations were made during the design phase, especially of different solar illumination aspects and shadowing effects from the reflector. After modification of the telescope specific parameters of geometry, materials and masses, this model helped in the design of the thermal protection of the fork of the AEC ALMA 12-m telescope.

Table 11.5 Model of a Fork (IRAM 15-m Telescope).

Component	Material	S ^{a)} [m ²]	V ^{b)} [m ³]	M ^{c)} [kg]	$\mathcal{C} \cdot M$ [kJ/K]	N ^{d)}
EL-Bearing	A steel			1600	720	2
Fork Arms	B steel	9.5	0.15	2400	1080	16
	C steel	10.0	0.15	2600	1170	16
	D steel	6.8	0.11	1800	810	12
	E steel	12.2	0.19	3000	1350	16
Fork Traverse	E steel					
Air in Fork Arms	B air ^{e)}		1.3	1.2	0.9	2
	C air		2.7	2.6	2.0	2
	D air		3.4	3.2	2.5	2
Air in Traverse	E air		7.5	7.1	5.5	2
Insulation Fork Arm	insulation	44.5	2.2	100	220	52
Air Gap	air		0.9	0.8	0.7	52
Radiation Shield	aluminium					52
Compressor Cabin (CB)	steel					5
Air Compressor Cabin (CB')	air		5.1	4.8	3.7	1
Pedestal	steel					4
Reflector (rear)	(Radiation)					4
Total ^{f)}						243

^{a)} S = surface, ^{b)} V = volume, ^{c)} M = mass.

^{d)} N = number of thermal nodes.

^{e)} air at 2 500 m altitude (telescope site), Table 4.1.

^{f)} including the environment (3 nodes).

Figure 11.17.a shows temperature measurements made on the first IRAM 15-m telescope. Using in the thermal model of the fork the recorded parameters of the thermal environment (T_A , wind speed, sunshine), the measured temperatures are reproduced in the calculations as illustrated in Fig. 11.17.b. The agreement between the measurements and the calculations demonstrates, though *a posteriori*, that a reliable model was constructed and that precise predictions were made during the design phase.

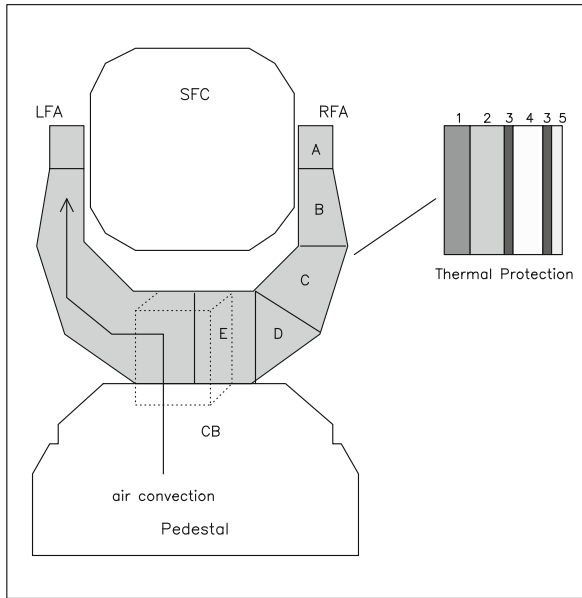


Fig. 11.16 IRAM/SEST 15-m telescope. The fork model consists of the left fork arm (LFA) and the right fork arm (RFA) connected by the traverse. The EL-axis bearings are at A. The fork arms support the secondary focus cabin (SFC) to which the BUS is connected. On one side of the fork is a cabin (CB) that contains the compressor of the receivers. The fork rests on the pedestal. The thermal protection of the fork (insert) consists of 1: steel, 2: hard foam insulation, 3: Al foil, 4: air gap, 5: radiation shield (MetawellTM or aluminium plate).

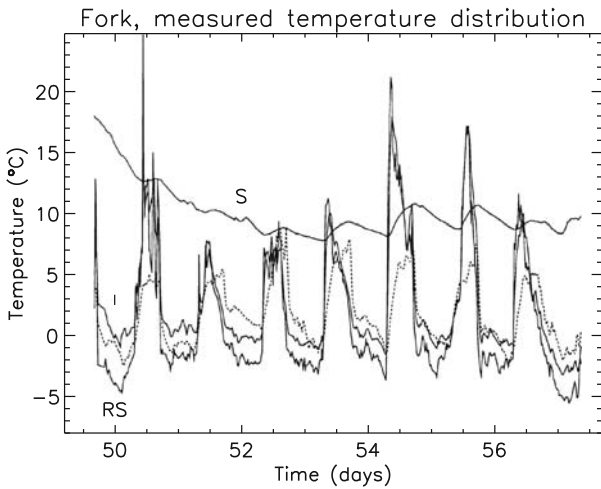


Fig. 11.17.a IRAM 15-m telescope. Measured temperatures of a fork arm: S steel, I: insulation, RS: radiation shield, dashed line: ambient air temperature [From Greve et al. (1992), Courtesy IEEE Trans. Ant. Propag.].

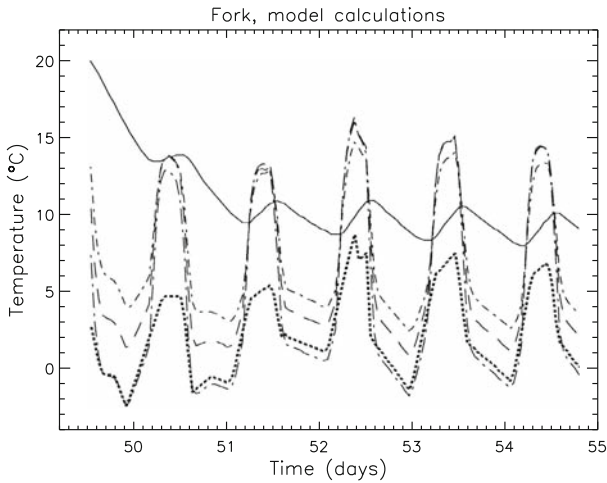


Fig. 11.17.b IRAM 15-m telescope. The thermal model calculation of the fork structure reproduces with good detail and accuracy the measured temperatures shown in Fig. 10.17.a, using the recorded parameters of the environment as input [From Greve et al. (1992), Courtesy IEEE Trans. Ant. Propag.].

11.8 Model of a Backup Structure

The central question of a BUS is its temperature uniformity and the technical means by which temperature uniformity within the specification can be achieved. There exists a large difference between an open BUS and a closed BUS, i.e. the open BUS network interacts directly with the thermal environment, the interaction of a closed BUS network with the thermal environment is buffered by the BUS closure consisting of the panels and the rear side cladding (see Fig. 9.29).

Solar radiation is the main heat source that may disturb the thermal uniformity of a BUS. In order to study an extreme situation, in many calculations an asymmetric solar illumination is selected as illustrated in Fig. 11.18, or any other asymmetric illumination of the front or back. The Sun in Fig. 11.18 is for instance at 45° distance from the telescope axis and the telescope follows the Sun in this orientation during the day. A temperature difference develops in the BUS between the part in sunshine and in shadow unless protective measures are taken. On an open BUS the side of the reflector in shadow has a corresponding BUS rear section in sunshine, and vice versa.

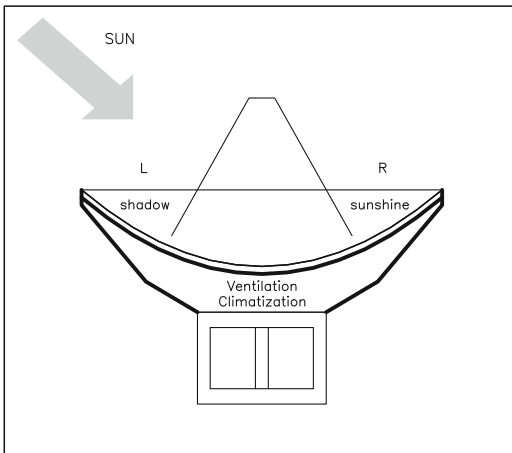


Fig. 11.18 Model of asymmetric solar illumination of a reflector, for investigation of the efficiency of thermal protection to create a uniform temperature between the left (L) and right (R) side of a closed BUS [From Greve & Bremer (2005), Courtesy IEEE Ant. Propag. Magazine].

11.8.1 Model of an Open BUS

On an open BUS all members of the BUS network are exposed to the variable thermal environment. This results in a large thermal model because of the large number of thermal nodes required for the BUS network and the panels. The changing interaction of the BUS members with the environment through changing pointing positions of the telescope requires a considerable amount of programming. The literature does not mention such a thermal model and calculations. For specific thermal questions the open BUS can be reduced to a thermal calculation of representative network members as done by Bregman & Casse [1985] in the study of principle BUS members of the JCMT telescope. Nevertheless, starting from the FEM of an open BUS it should be possible to construct a corresponding complete dynamic thermal model, which probably is a question of effort and patience rather than of method. The static thermal model calculation of the RT 70-m telescope with 378 solid elements, 1360 shell elements and 38 322 rod elements described by Borovkov et al. [2003] and Machuyev & Gimmelman [2006] is a step in this direction.

For exploratory studies a ‘lump-body’ thermal model of an open BUS was constructed consisting of 28 segments of equal reflector surface area as shown in Fig. 11.23 (subdivision). For each segment the mass, heat capacity and surface area of the corresponding network members is used in the thermal model. Each BUS segment is connected by conduction and radiation to adjacent BUS segments and the corresponding rear side panel surfaces and by convection and radiation to the thermal environment. Asymmetric solar illumination as in Fig. 11.18 is assumed. The result of the thermal calculation is shown in Fig. 11.19.

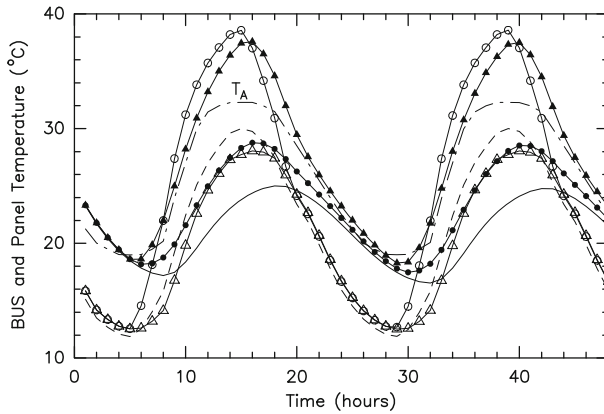


Fig. 11.19 Thermal model calculations of ‘lump-sections’ of an open BUS network under the influence of asymmetric solar illumination as shown in Fig. 11.18. Solid symbols: BUS temperatures, open symbols: panel temperatures. Triangles: left side as in Fig. 11.18 with the BUS rear side partially in sunshine and the panels in shadow; dots: right side as in Fig. 11.18 with the BUS rear side in shadow and the panels in sunshine. The solid line and dashed line is the BUS temperature and panel temperature at the middle section of the BUS. The dashed-dotted line is the ambient air temperature T_A .

11.8.2 Model of a Closed BUS with Natural Ventilation

The simplest configuration, though not the easiest model, is a closed BUS with natural ventilation. In a tilted closed BUS a temperature difference may occur between the upper and lower parts because natural convection moves warmer air to the upper sections. This effect is evident in the measurements of the IRAM 15-m telescope shown in Fig. 9.35.

The formalism of natural convection is explained in Section 7.7.4. To illustrate the action of natural convection, a 10 m high column of air is considered, of 1 m^2 cross section, divided into 10 vertical sections. The total mass of the air is $M = 10 \text{ kg}$. The air has the initial temperature of 10°C . The air of the lowest section is heated with 100 W for 10 minutes so that the air receives the energy $\Delta Q = 10 \times 60 [\text{s}] \times 100 [\text{W}] = 60 \text{ kJ}$. With $\mathcal{C} = 1 \text{ kJ/kg/K}$ the heat capacity of air, the final *average* temperature increase due to the heat supply is $\Delta T = \Delta Q / \mathcal{C} M = 60 [\text{kJ}] / 1 [\text{kJ/kg/K}] 10 [\text{kg}] = 6^\circ \text{C}$. The warmer air moves upward by natural convection, heats the air volumes and establishes a temperature gradient and eventually, or even never, reaches the higher average temperature of 16°C at the end of the process. In the process of natural convection the warm air that moves from a lower air element into a cooler upper air element may mix strongly (coefficient f_{nc} in Eq.(7.40)) with the air of the upper element and thereby loses its identity. In this situation the lower (ℓ) and upper (u) air elements in Eq.(7.40) are adjacent in height. The model calculation of this process is shown in Fig. 11.20.a. If, however, the moving pocket of air retains its identity, or at least partially, the lower (ℓ) and upper (u)

air elements in Eq.(7.40) are not necessarily adjacent in height, since the lower element ℓ may exchange energy only with an air element higher up³. The air at the top becomes warm and a temperature gradient develops. This model calculation is shown in Fig. 11.20.b.

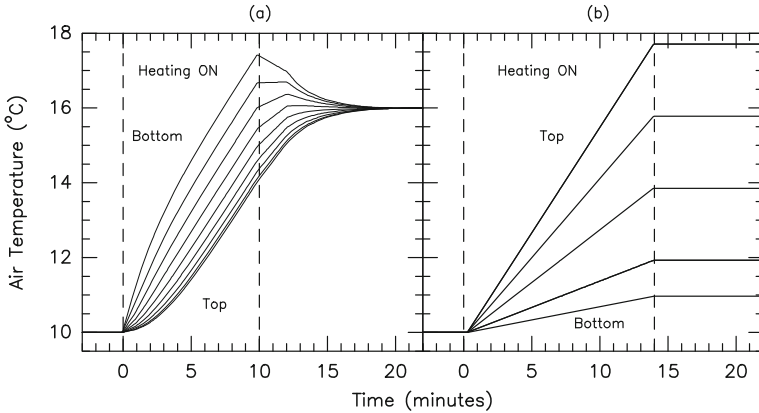


Fig. 11.20 Illustration of natural convection. A 10 m high vertical column of air of 1 m² cross section and 10 vertical elements, at the initial temperature of 10^o C, is heated with 100 W for 10 min at the lowest air element; the warm air moves upwards. (a) Natural convection with strong mixing during upward motion, (b) natural convection with little mixing. The lines in (a) and (b) show the temperature of adjacent air layers between the bottom and the top of the air column.

The result of a model calculation of a closed BUS with natural ventilation is shown in Fig. 11.21. Natural convection is incorporated in the model through Eq.(7.40). This equation is an if–statement that checks whether a lower air volume element is warmer than the next upper one, and if so transfers heat from the lower element to the upper element. Asymmetric solar illumination of the reflector is assumed (Fig. 11.18), the telescope trails the Sun. Fig. 11.21 shows the temperature difference $\Delta T_{UD}(\text{BUS})$ between the upper (U) and the lower (D) part of the BUS, the result has some similarity with the measurements shown in Fig. 9.35. A realistic model of natural convection is difficult because of the unknown detailed airflow and mixing pattern in the BUS network, especially if the network is compact.

11.8.3 Model of a Closed BUS with Forced Ventilation

A study of ventilation of a BUS was published by Greve & Bremer [2005] and Greve et al. [2006]. Models of a BUS with forced ventilation can be constructed using Eq.(7.39) explained in Section 7.7.3. The model may take into account uniform ventilation where each volume element of the BUS is ventilated with the same

³ Bejan [1993] shows pictures of the complicated flow of thermals under natural convection.

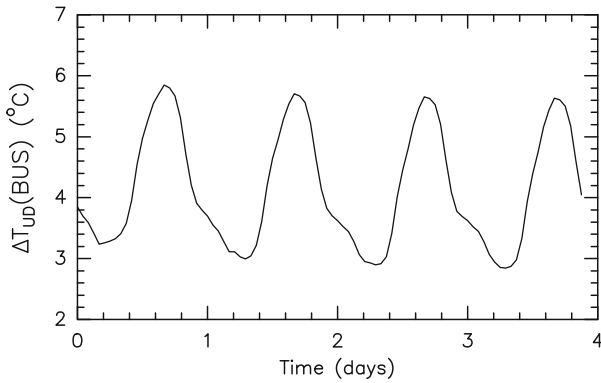


Fig. 11.21 Model calculation of a closed BUS with natural ventilation. The natural convection causes a temperature gradient $\Delta T_{UD}(\text{BUS})$ in the BUS in the direction Up–Down.

amount of air, or may take into account the more realistic cases of radial or circular ventilation where the ventilating air moves through the BUS in radial or circular direction. Radial and circular ventilation can be modelled in the way illustrated in Fig. 11.22. In both cases is the ventilating air assumed to be taken from the centre air volumes A(1,2,3,4), perhaps with a contribution of outside ambient air. Radial ventilation (Fig. 11.22.a) transports air in a duct or through open space from A to B and from B to C and D. The air from A may mix or replace the air at B, the air from B may mix or replace the air at C and D. The degree of mixing/replacement is defined by the coefficient f_{fV} in Eq.(7.39). Circular ventilation (Fig. 11.22.b) transports air in a duct from A to the locations B, C and D where the air is blown in tangential direction into the BUS volume. Dependent on the efficiency f_{fV} of the ventilation, the air from A may mix or replace the air at B, C and D.

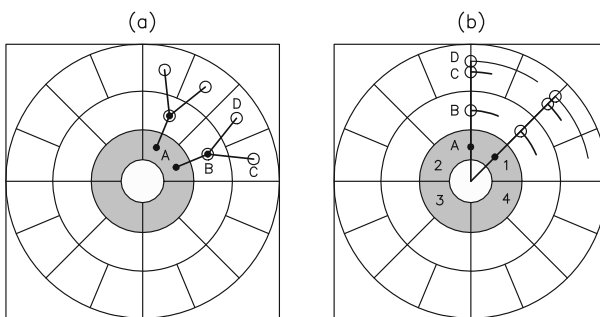


Fig. 11.22 (a) Model of radial ventilation, (b) model of circular ventilation.

The IRAM 30–m telescope serves as an example of a ventilated BUS or a climatised BUS where the ventilating air is heated or cooled to compensate the energy

loss towards the cool sky at night and the energy inflow from insolation during the day. For both cases measurements are available for comparison.

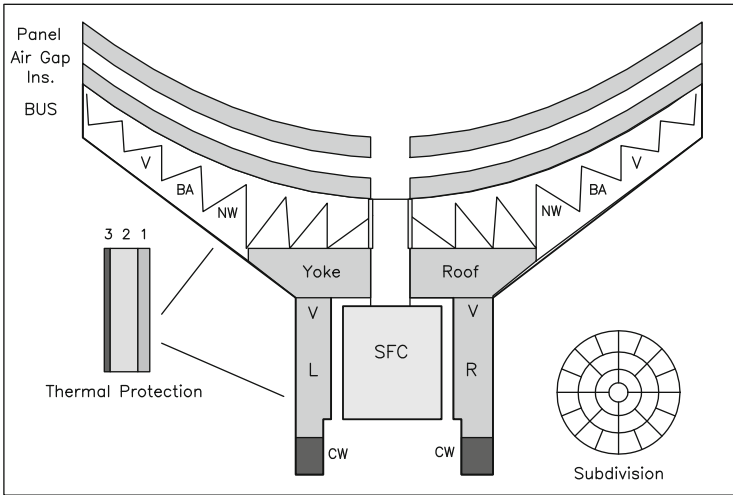


Fig. 11.23 IRAM 30-m telescope: thermal model of the BUS and yoke. The model of the BUS contains the BUS network (NW) with internal air (BA) and ventilation/climatisation (V). At the front side is an insulation layer (Ins), an air gap and the panels. The model of the yoke contains the yoke roof, the left (L) and right (R) yoke arms with ventilation (V) and the counterweights (CW). SFC is the secondary focus cabin. The thermal protection of the BUS rear and of the yoke consists of insulation (2) and Al-plate (3) on the steel structure (1). The subdivision of the Panel-Air Gap-Insulation-BUS structure is illustrated in the insert.

Figure 11.23 sketches the mechanical structure of the IRAM 30-m telescope, Fig. 11.24 shows part of the thermal node structure. The insert in Fig. 11.23 illustrates the division of the BUS into 28 sections⁴. To the 28 sections of equal reflector surface area correspond 28 'panels' (larger in size than the actual panels), 28 air gaps, 28 insulation plates (front closure of the BUS), 28 sections of the BUS network, 28 internal air volumes and finally 28 rear cladding plates. The BUS is connected to the yoke roof. The yoke and the secondary focus cabin are included in the thermal model. A realistic model of the yoke is required to formulate the active climatisation system of this telescope (see below). The secondary focus cabin contains receivers and electrical equipment and is a heat source of $\sim 20^{\circ}\text{C}$ constant temperature. The material and thermal properties of the subsections are summarized in Table 11.6. The model of the telescope uses the knowledge of the earlier Chapters, i.e. for the panels and the insulation of the BUS the radiative heat transfer between plane parallel plates (Section 7.8), for radiative heat transfer between the BUS front cover and rear cover the fact that the BUS enclosure consists to first approximation

⁴ A larger number of subsections can be used, depending on the number of nodes and thermal connections that can be handled by the network programme.

of parallel plates (Section 7.10.3), the coupling of the reflector and rear side to the sky and the ground (Chapter 8) etc.

Table 11.6 Model of a BUS with Yoke and Focus cabin (IRAM 30-m Telescope).

Component	Material	S ^{a)} [m ²]	V ^{b)} [m ³]	M ^{c)} [ton]	$\mathcal{E} \cdot M$ [kJ/K]	N ^{d)}
BUS & Panels						
BUS-network ^{e)}	steel	~200	~50	100	45 000	28
Air in BUS	air ^{f)}	–	2 000	1.8	1 300	28
Membrane ^{g)}	steel	150	3	15	6 750	10
Panels	Al-HC	820	35	15	12 900	2×28 ^{h)}
Insulation of Panels ^{h)}	insulation	820	35	1.1	1 800	2×28
Air Gap P-Ins ^{h)}	air	820	40	0.04	26	2×28
(Panel Frames ⁱ⁾	steel			28	12 600)	
Insulation BUS rear ^{h)}	insulation	1 050	42	1.6	2 400	2×10
Yoke						
Yoke-Roof	steel	220		60	27 000	8
Yoke Arms	steel	2×160		2×60	2×27 000	2×13 ^{j)}
Air in Yoke Arms	air		2×52	2×0.05	2×36	2×4 ^{j)}
Focus Cabin						
SCF-Cabin ^{k)}	Steel			20	9 000	6
Air in SCF-Cabin	Air		240	0.21	150	1
Total ^{l)}						306

^{a)} S = total surface, ^{b)} V = total volume, ^{c)} M = total mass;

^{d)} N = number of thermal nodes;

^{e)} surface of BUS network;

^{f)} air at 2 900 m altitude (telescope site), Table 4.1;

^{g)} connection between BUS network and yoke roof;

^{h)} front and rear side of panel, insulation, air in gap;

ⁱ⁾ included in the BUS network; ^{j)} two yoke arms;

^{k)} SCF: secondary focus cabin at T_{SCF} = 20° C;

^{l)} including the environment (3 nodes);

A large number of BUS sections is required to incorporate forced ventilation and climatisation. On the IRAM 30-m telescope the model of forced ventilation, based on Eq.(7.39), connects the inside air volume elements in a circular way (Fig. 9.43.b), with appropriate coefficients of the air exchange (f_{fv}) and intake of outside ambient air (5 to 10 %). The servo-loop control of the climatisation is considered in the thermal model by if-statements, comparing the temperature of the yoke and the BUS and applying correspondingly heating or cooling to the air volumes of the BUS. The ventilation/climatisation system follows the parameters listed in Table 2.7. When considering forced ventilation of the air inside a BUS or enclosure it is necessary to consider in the model calculations the heat produced by the fans. This heat is often released inside the BUS, or enclosure, and may have to be eliminated

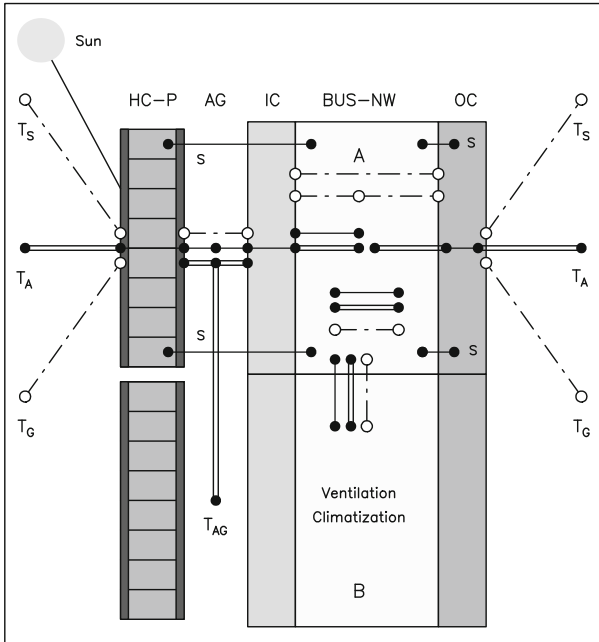


Fig. 11.24 Node structure of a BUS thermal model (IRAM 30-m telescope) of which two adjacent sections (A, B) are shown. The model has honeycomb panels (HC-P), an insulation front cover (IC), the BUS network (BUS-NW) and the rear side cladding (OC). Dots: thermal material nodes, open circles: radiative nodes. Lines: conductive connections, double lines: convective connections, dashed lines: radiative connections.

by additional cooling. For a thermal calculation it is appropriate to assume that 10 to 20 % of the fan power is released as heat.

Temperature measurements shown in Fig. 9.42 and Fig. 11.25 illustrate the thermal behaviour of the *ventilated* but not climatized closed BUS of the IRAM 30-m telescope. In the corresponding model calculations the state of the thermal environment is taken from *in situ* measurements, the solar illumination is calculated from the recorded AZ and EL position of the telescope and the Sun's position at the time of the temperature measurements. Fig. 11.26 shows that the calculations agree well with the measurements. It is seen that in the case of pure ventilation the temperature uniformity between the yoke and the BUS does not fulfil the specification of the IRAM 30-m telescope, i.e. $|T_{BUS} - T_{yoke}| \lesssim 1^\circ\text{C}$. For comparison, a temperature measurement of the IRAM 30-m telescope BUS under climatization control is also shown in Fig. 11.25. The climatization system, and in a similar way the thermal model, applies heating or cooling so that the yoke and BUS temperature agree within $\sim 1^\circ\text{C}$, the corresponding thermal model calculation is shown in Fig. 11.26. The agreement between the measurement and the calculation is again good and illustrates that the complexity of the servo-loop control of the climatization can be handled in a thermal model.

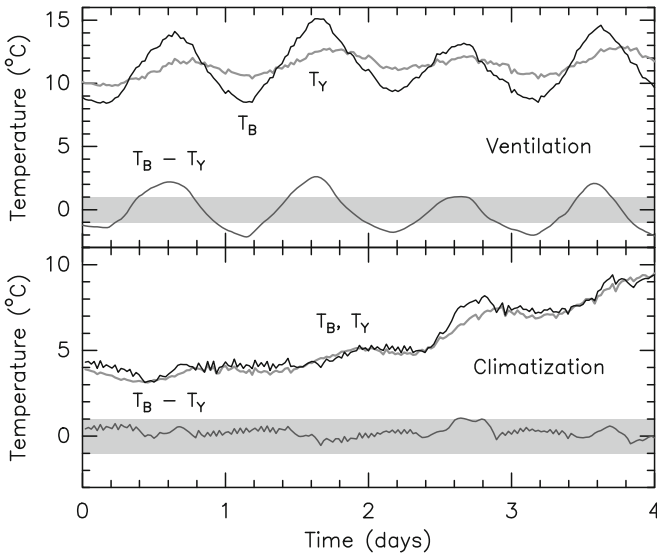


Fig. 11.25 IRAM 30-m telescope. Measurement of the BUS (T_B) and yoke (T_Y) temperature in the case of pure ventilation (no heating/cooling) and in the case of climatization (ventilation + heating/cooling).

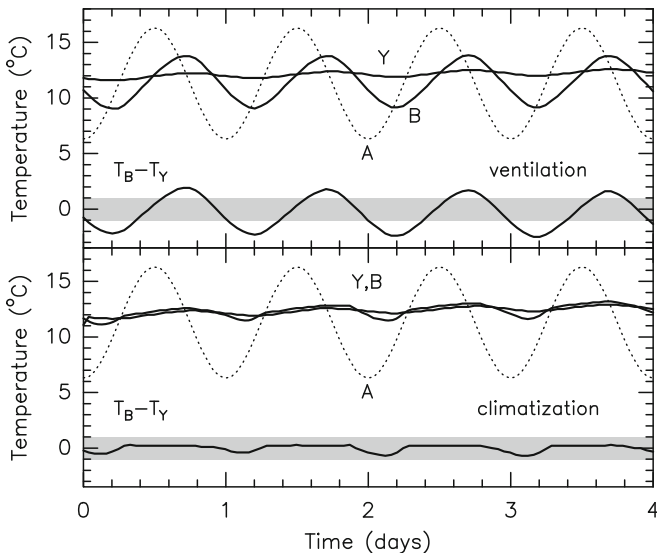


Fig. 11.26 Model calculations of the IRAM 30-m telescope closed BUS with ventilation (upper panel) and with climatization (heating/cooling) (lower panel). Temperature of the BUS: B, of the yoke: Y, adopted ambient air temperature: A. $T_B - T_Y$ is the temperature difference between the BUS and the yoke, the grey band is the tolerated temperature difference [From Greve & Bremer (2005), Courtesy IEEE Ant. Propag. Magazine].

11.9 Model of a Radome and Closed Astrodome

Thermal calculations of a radome or closed astrodome are made to investigate the temperature distribution of the inside air and the possibility of obtaining a uniform air temperature through forced ventilation. The thermal model of a radome/astrodome must include natural convection and forced ventilation. The forced ventilation may use to a large extent outside ambient air. A possible heat input must be considered in the case the ventilating air is conditioned to keep the inside air above a specific lower temperature limit (for instance applied on the MIT–Haystack radome [Barvainis et al., 1993]). The ventilation transports air in a more or less efficient way to the different volume elements of the radome/astrodome. Dependent on the location of the fans the ventilation may reach primarily the air elements close to the periphery or also the central air elements (see Chapter 10). The corresponding formulation in the thermal model is through the degree of heat exchange between adjacent air volume elements defined by the coefficients f_{fv} and f_{nc} in Eq.(7.39) and Eq.(7.40). The components of a thermal model of a radome and astrodome are illustrated in Fig. 11.27 and Fig. 11.28.

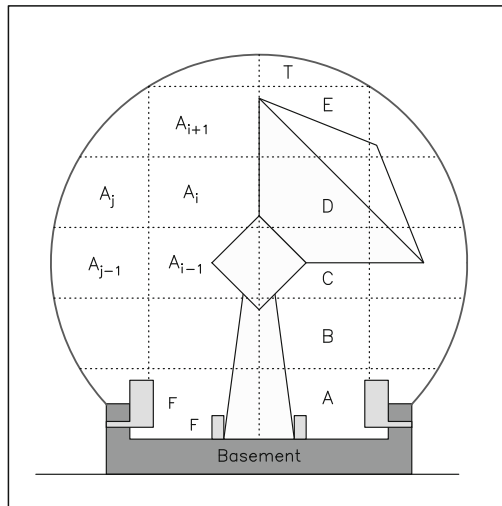


Fig. 11.27 Model of a telescope in a radome with 6 horizontal air layers (A to T) and azimuthal subdivisions A_i , A_j etc. Because of ventilation ($F =$ fans), at the periphery and the centre, exists a forced air exchange between adjacent air volumes A_{i-1} and A_i in vertical direction and, less so, between adjacent air volumes A_i and A_j in horizontal direction. Each radome surface element transmits diffusely some solar radiation and radiates at infrared wavelengths to the inside, i.e. to other surface elements and to the telescope and the floor (basement).

The thermal model of a radome consists of the radome skin, the inside air, the concrete basement, the (air–conditioned) ventilation system and the telescope. The radome, the inside air and the telescope are divided into smaller sections in order

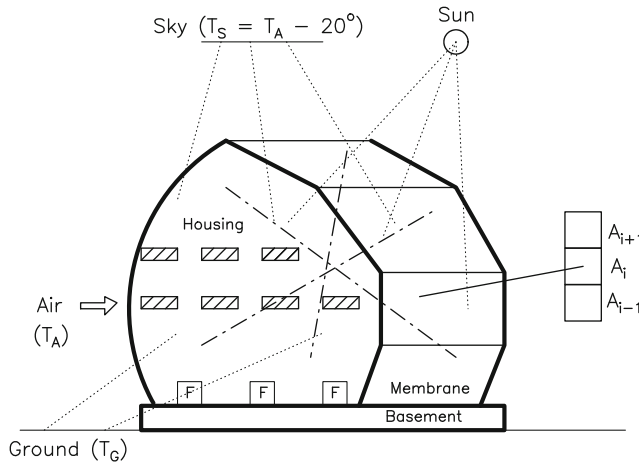


Fig. 11.28 Model of an astrodome with basement (concrete), a steel housing (side walls and rear wall) and a membrane-covered opening. There are ventilation fans (F) and louvres. The astrodome interacts with the ambient air (T_A), the sky ($T_S = T_A - 20^\circ \text{C}$), the ground (T_G) and the Sun. There are several layers of inside air (A_i) connected by ventilation [From Greve & MacLeod (2001), Courtesy Radio Science].

to study vertical temperature gradients. The radome is stationary and the incident, absorbed and transmitted solar radiation is easily calculated as explained in Section 5.8. The thermal model of an astrodome consists of the metal housing (with insulation), the slit with membrane window, the concrete basement, the ventilation system, louvres for natural ventilation and the telescope. The astrodome rotates when tracking the astronomical source so that the solar illumination aspect can be rather variable.

In preparation of thermal model calculations of a possible astrodome for the LMT/GTM 50-m telescope [see for instance Serrano Perez-Gorvas 1996] thermal calculations were made of the radome of the Onsala 20-m telescope and the MIT-Haystack 37-m telescope to check the validity of such models against measured temperatures. The parameters of these radomes are listed in Table 3.2, the thermal model of the Onsala radome is summarized in Table 11.7.

The result of the thermal model calculations is shown in Fig. 11.29. The input of the calculations is the actual thermal state of the environment, i.e. the ambient air temperature and the ground temperature, the convective heat transfer coefficient of the ambient air at the measured low wind speed and the solar illumination at the selected days of measurement (see Fig. 5.18). Fig. 11.29 indicates that the radiative heat transfer from the outside (sunshine, cool sky) to the inside of the radome, the complicated forced motion of the air inside the radome and the convective heat transfer considered in the models reproduce well the measured temperatures. In particular the effect of ventilation is well demonstrated in the case of the Onsala radome where the ventilation was switched off for some time leading to an increase

Table 11.7 Thermal Model of the Onsala Radome.

Component	Material	S ^{a)} [m ²]	M ^{b)} [kg]	$\mathcal{C} \cdot M$ [kJ/K]	N ^{c)}
Radome					
Inside Air A ^{d)}	air		250	250	8
Inside Air B ^{d)}	air		250	250	8
Inside Air C ^{d)}	air		250	250	8
Inside Air D ^{d)}	air		250	250	8
Inside Air E ^{d)}	air		250	250	8
Inside Air Top	air		250	250	1
Radome Skin	Goretex TM	2 100		100	2 × 29 ^{e)}
Floor/Basement ^{f)}	concrete				1
Telescope					
BUS + Panels Ventilation + Air Intake	aluminium	300	50 ton		8
Total ^{g)}					113

- ^{a)} S = surface, ^{b)} M = mass, ^{c)} N = number of thermal nodes;
- ^{d)} values per air volume element, total air volume 10 500 m³;
- ^{e)} outer and inner side of the radome skin;
- ^{f)} the floor has a constant temperature
 $T_F = \langle T_A \rangle - 5^\circ \text{C} = 20^\circ \text{C}$ (Fig. 11.29);
- ^{g)} including the environment (5 nodes),
 with air/ground temperature in sunshine and shadow.

of the vertical temperature gradient (ΔT_{tb}). The results are published in more detail by Greve & MacLeod [2001].

11.10 Servo-loop Controlled Ventilation/Heating/Cooling

The preceding examples illustrate that in dynamic thermal calculations of a BUS or radome etc. a servo-loop controlled air-conditioned ventilation can be considered via if-statements. The servo-loop control may use as control parameter the temperature uniformity of the BUS, the temperature difference between the BUS and the yoke or the vertical temperature gradient in a radome etc. Dependent on the value of the control parameter, the ventilation is switched on or off in the programme. Knowledge of the switching cycle is important for operational purposes, for instance for estimating the power of the fans or the energy required for heating/cooling. If-statements in coupled differential equations may lead to numerical instabilities and spurious oscillations. In some network programmes the degree of non-linearity of the differential equations and the step length of integration can be set to allow a solution.

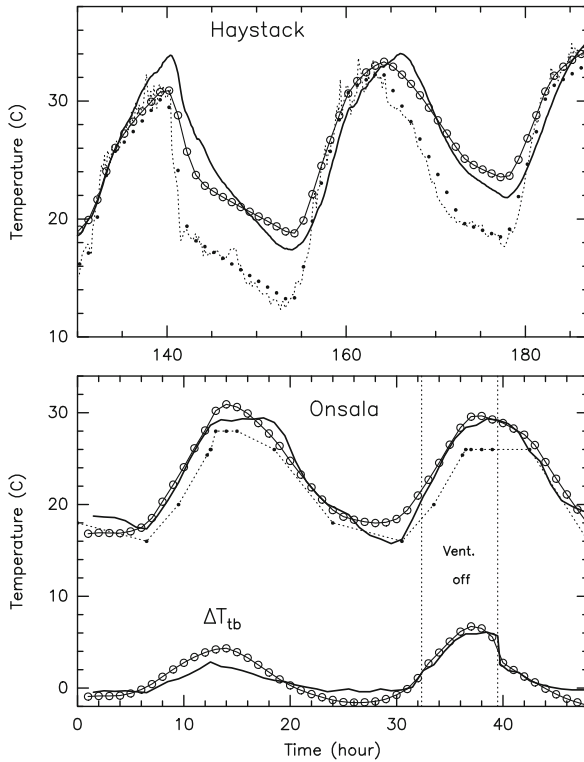


Fig. 11.29 Comparison of measured and calculated temperatures of the air inside the MIT–Haystack and Onsala radome. Thick lines: temperature of the inside air measured at the centre of the MIT–Haystack radome and at the top of the Onsala radome. ΔT_{tb} : temperature gradient of inside air between the top and the bottom of the Onsala radome. Lines with open circles: result of model calculation. Solid dots and dashed lines: measured outside ambient air temperature used in the model calculations. For the Onsala radome the vertical dashed lines indicate the time when the forced ventilation (fans) was switched off. There appears an increase of the temperature gradient, which is reduced when the ventilation is again switched on [From Greve & MacLeod (2001), Courtesy Radio Science].

11.11 Model Calculations and Energy Balance

The result of a thermal model calculation is usually the temperature $T_i(t)$ of a certain telescope component [i], as a function of time. A thermal model calculation is however also a calculation of energy transfer of accountable values. This is explained for the simple, though not unique case of a panel. A panel, fully insulated at the back (no heat transfer), is in convective contact with the ambient air of constant temperature $T_A = 5^\circ\text{C}$ (infinite reservoir) and in radiative contact with the cool sky of constant temperature $T_S = T_A - 20^\circ\text{C}$ (infinite reservoir). The convective heat transfer coefficient is $h = 10\text{ W/m}^2/\text{K}$. The panel faces the sky, the view factor is $\varphi = 1$, the radiative heat transfer is assumed to be between parallel plates (panel and sky)

with corresponding paint factor $E(1,2)$ (Eq.(7.51) and $e_{sky} = 0.85$. The panel surface is painted white with TiO_2 paint with absorption coefficient $a_S = 0.35$ and emission coefficient $e_1 = 0.75$ so that $E(0.85,0.75) = 0.66$, or is a shiny aluminium surface with absorption and emission coefficient $a_S = e_1 = 0.2$ so that $E(0.85,0.2) = 0.19$. The insolation of the panel surface is 1000 W/m^2 (see Fig. 4.27), the Sun is shining from 8 h to 16 h. The calculated panel temperatures T_P are shown in Fig. 11.30, both panels reach approximately the same maximum temperature. Energy conservation requires $\Delta Q_S + \Delta Q_c + \Delta Q_r = 0$ where ΔQ_S is the absorbed solar energy, ΔQ_c the convective heat transfer and ΔQ_r the radiative heat transfer towards the sky. From Fig. 11.30 follows for equilibrium during the night that $\Delta Q_c + \Delta Q_r = 0$, or ΔQ_c (into the panel) = $-\Delta Q_r$ (out of the panel). For equilibrium during sunshine follows ΔQ_S (into the panel) = $-(\Delta Q_c + \Delta Q_r)$ (out of the panel). The temperature increase/decrease of the panel appears as the difference $0 < \Delta Q_S - (\Delta Q_c + \Delta Q_r)$ at the beginning/end of the sunshine. Because of the higher absorption and emission of TiO_2 compared to shiny aluminium the involved energies of the white painted panel are higher.

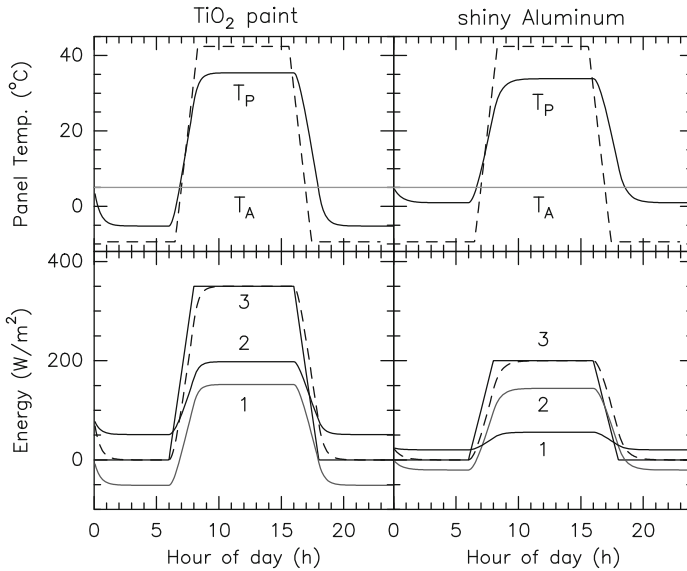


Fig. 11.30 Temperature of a panel T_P with white TiO_2 paint surface finish or shiny aluminium surface finish, in an environment with constant ambient air temperature T_A . The dashed line in the upper panels is the time of sunshine. The lower panels show the energy balance, with 1: loss by radiation towards the cool sky (ΔQ_r), 2: loss/gain towards the ambient air by convection (ΔQ_c), 3: absorbed solar energy (ΔQ_S). The dashed line is the sum $|\Delta Q_r| + |\Delta Q_c| = \Delta Q_S$, illustrating energy balance.

11.12 Model Calculations for Operational Purposes

Thermal model calculations are often made to obtain operational parameters on which to base a telescope design. One example, among many, is the determination of the amount of heating/cooling of a climatized BUS, another example is the determination of the amount and the efficiency of ventilation of a BUS or a radome/astrodome to obtain temperature uniformity. In these cases the thermal calculations concentrate on energy parameters.

Figure 11.31 illustrates the determination of the cooling capacity of the IRAM 30-m telescope climatization system in order to obtain temperature uniformity between the yoke (T_Y) and the BUS (T_B) within $\pm 1^\circ\text{C}$ when the Sun is fully illuminating the reflector surface and warming the BUS. The figure indicates the necessity of a cooling capacity of $\sim 15\text{ kW}$, as is actually installed on the telescope (see Table 2.7). The calculation of Fig. 11.32 was made (around 1975) with a thermal model of the IRAM 30-m telescope that had only 4 sectors but the same structure as the one explained in Fig. 11.23 and Table 11.6.

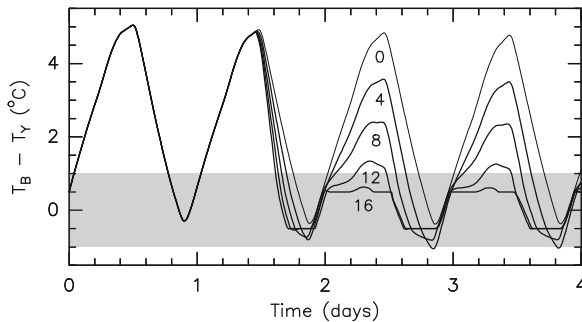


Fig. 11.31 IRAM 30-m telescope. The figure shows the temperature difference between the BUS (T_B) and the yoke (T_Y) when the reflector is exposed to maximum solar illumination and when the ventilation and cooling is switched on at noon of the second day. The capacity of the cooling is indicated by the numbers (in kW). The grey band is the specified tolerable temperature difference between the BUS and the yoke [From Greve & Bremer [2006], Courtesy IEEE Ant. Propag. Magazine].

During the design study of the SRT 64-m telescope the question was asked which type of ventilation⁵ and of which efficiency would be necessary to guarantee a temperature uniformity of the BUS of better than $\sim 3^\circ\text{C}$ under asymmetric solar illumination as sketched in Fig. 11.18. Asymmetric solar illumination will produce a temperature gradient across the BUS and circular ventilation was considered the most appropriate form of ventilation (Fig. 11.22.b). Using the thermal model of the SRT [Greve 2000], the efficiency of the ventilation was deduced from the convective heat transfer coefficient h between the ventilating air and the BUS network that

⁵ The ventilation was omitted in the final design of the SRT; the SRT has an active reflector surface.

would establish the specified temperature uniformity. The result of the calculations is shown in Fig. 11.32, once for a BUS with no insulation behind the panels and once for a BUS with panel insulation. The BUS with no panel insulation needs a higher ventilation efficiency ($h \approx 10$ to $15 \text{ W/m}^2/\text{K}$) compared to the BUS with panel insulation ($h \approx 3$ to $6 \text{ W/m}^2/\text{K}$). Solar heat can penetrate easier into the BUS network without panel insulation. For other details see Greve & Bremer [2005].

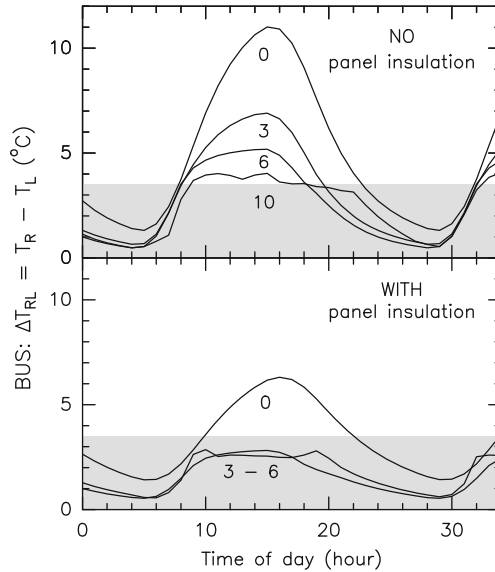


Fig. 11.32 Determination of the efficiency of BUS ventilation (expressed by the convective heat transfer coefficient h) that produces a temperature uniformity of $\Delta T_{RL} \lesssim 3^\circ \text{C}$ of the SRT BUS under asymmetric solar illumination (Fig. 11.18). The parameter on the curves is the value h [$\text{W/m}^2/\text{K}$] [From Greve & Bremer [2006], Courtesy IEEE Ant. Propag. Magazine].

11.13 Precision of Model Calculations

The precision of a thermal model calculation depends on the question to be answered. A high precision of the order of 0.1°C is for instance required for aspects of temperature gradients through a panel (see Fig. 11.8); moderate precision of the order of 0.5 to 1°C for instance is required for aspects of thermal uniformity of a BUS, yoke and quadripod of a mm-wavelength radio telescope (see Figs. 11.25, 11.26); a low precision of the order of 2 to 3°C is sufficient for many thermal aspects of cm-wavelength telescopes (see Figs. 9.73, 9.74). The precision of a thermal model calculation and the confidence in the results depends on the selection of realistic and thermally important structural components, on the precision of thermal

connections between the components and with the thermal environment and on the knowledge of material properties. While the mentioned precisions are more easily achieved in comparative studies that investigate the influence of changes of basic parameters (for instance the absorption and emission coefficients of a surface finish), for large and complex structures the mentioned precisions are (only) obtained from a thermal model that has been cross-checked against measured temperatures of similar structures. Several examples presented in the preceding sections demonstrate the precision achieved in this way. Since thermal calculations provide temperature differences with respect to a starting condition, and since a temperature difference $\Delta T = T_1 - T_2$ is obtained in the calculations from an energy change $\Delta Q = Q_1 - Q_2$, it is important to check the calculations that the basic values Q_1 and Q_2 have understandable values. Unrealistic values Q_1 , Q_2 may give an apparently realistic value ΔQ and hence an apparently realistic value ΔT , even though the energy balance in the calculation may be wrong.

The precision of a thermal model depends on the number of thermal nodes. Today, the restriction is not imposed by computer memory and the network analysis programme but rather by the skill and experience of the engineer in dividing a structure into substructures and in the formulation of the essential conductive, convective and radiative heat transfer connections.

The material properties of heat capacity and conductivity are well known. The value of conductive heat transfer (resistance) between two components that are in contact, bolted, or bonded together is, however, often rather poorly known. Less accurately known is the coefficient (h) of convective heat transfer and the absorption (a) and emission (e) coefficient in radiative heat transfer. With respect to paint, the change in absorption and emission with age may introduce some uncertainty. An insight into the dependence and accuracy of a model calculation on convection and absorption/emission is obtained when performing the calculation for a range of values h and a , e .

11.14 Programmes for Model Calculations

There are several commercial products of electrical circuit network programmes that allow the calculation of network behaviour in the time domain. Since a thermal model can be translated into an electrical circuit, these programmes can usually be applied as well to thermal problems.

Chapter 12

Beam Formation and Beam Degradation

The elaborate technical efforts in the construction of radio telescopes and communication antennas are undertaken in order to obtain a clean beam and the best power sensitivity. This merits an explanation of the beam (image) formation of a telescope/antenna, at first hand expected to be perfect, in the end however always suffering from some degradation because of technical shortcomings and influences from the environment. The knowledge of the origin, the form and the magnitude of beam degradations is the basis on which the tolerance theory of thermal deformations of a telescope is constructed in Chapter 13. An explanation of the diffraction theory of beam formation is found in the textbooks by Born & Wolf [1980], Love [1968], Rush & Potter [1972], Lo & Lee [1988], Christiansen & Högbom [1995], Kraus [1985], Baars [2007], Rohlfs & Wilson [1996], Thompson et al. [2001] and others.

12.1 Wave Propagation and Beam Formation

The properties of wave propagation and beam (image) formation of a telescope are derived from

- (1) the concept that electromagnetic radiation are waves of a certain wavelength (λ), or frequency (ν), amplitude (A) and phase (φ),
- (2) *Huygens'* principle which states that each element of a wavefront is the origin of a secondary spherical wavelet, as illustrated in Fig. 12.1.a,
- (3) the fact that a radio telescope combined with a receiver manipulates the incident wavefront through their phase and amplitude transfer functions (Ω_O, Ω_R) and by this forms a beam (image), as illustrated in Fig. 12.1.b.

Following *Huygens'* principle illustrated in Fig. 12.1.a, the point $a_1(x,y) \equiv a_1(\mathbf{r})$ of the aperture plane $\mathbf{A}^+(\mathbf{r})$ of the incident wavefront is the origin of a spherical wavelet of which the field $\delta E(a')$ at the point $a'(u,v) \equiv a(\mathbf{u})$ of the image plane $\mathbf{I}(\mathbf{u})$ is

$$\delta E(\mathbf{u}) = A(\mathbf{r}) \exp[iks]/s, \quad k = 2\pi/\lambda \tag{12.1}$$

with $s = s(\mathbf{r}, \mathbf{u})$. The same relation holds for another point $a_2(\mathbf{r})$ of the aperture plane $A^+(\mathbf{r})$, thus for any point $a_i(\mathbf{r})$ of the aperture plane.

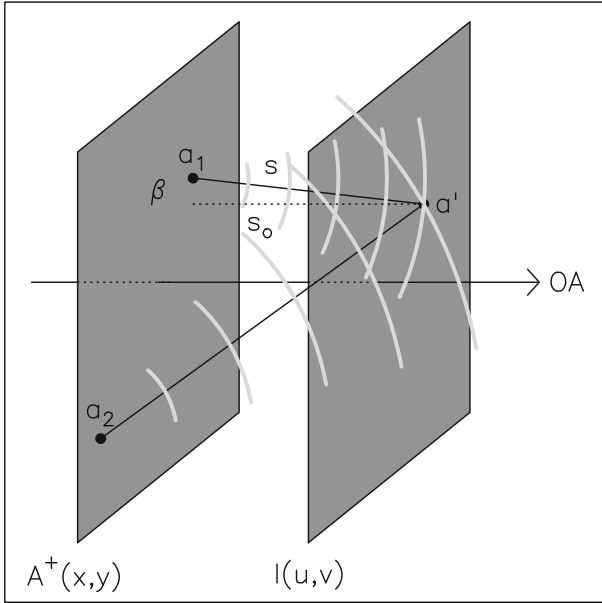


Fig. 12.1.a Illustration of *Huygens Principle*. The individual points (a_1, a_2, \dots) of the aperture plane $A^+(x,y)$ of the incident plane wavefront are the origins of secondary spherical wavelets, which propagate to the right and superpose to form a plane wavefront in the image plane $I(u,v)$. OA is the optical axis and the direction of wave propagation.

Relation (12.1) expresses also the fact that the intensity I of a spherical wave decreases as the inverse square of the distance (s) from the source, i.e. $\delta I \propto \delta E \delta E^* \propto 1/s^2$. The ensemble of spherical wavelets arriving from all points of the aperture plane A^+ at the point $a'(\mathbf{u})$ of the image plane I produce the field

$$E(\mathbf{u}) = \int_{A^+} A(\mathbf{r}) \Lambda(\beta) [\exp(iks)/s] dx dy \tag{12.2}$$

For the paraxial case with the rays not strongly departing or inclined against the direction of wave propagation (i.e. the optical axis OA) the inclination factor Λ can be neglected since $\Lambda(\beta) \approx \cos(\beta) \approx 1$ where β is the angle between s_0 and s (Fig. 12.1.a). Also $|s| \approx |s_0|$ for paraxial rays, while on the other hand $\exp[iks] \neq \exp[iks_0]$ since these are cosine and sine terms of s where a small change in s may

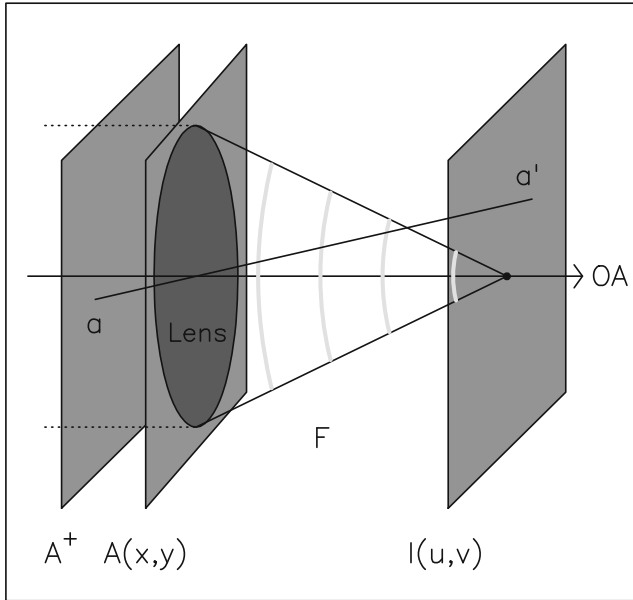


Fig. 12.1.b Illustration of imaging through a lens, which operates in an equivalent way as a complex radio telescope. OA is the optical axis; F the focal length, in this case of the lens. **A** is the aperture plane of the lens, **I** the image plane = focal plane.

produce a large change of the cosine or sine value. For the paraxial approximation it is possible to write for the points $a(x,y,z)$ and $a'(u,v,w) = a'(u,v,0)$

$$s = [(x - u)^2 + (y - v)^2 + z^2]^{1/2} \approx R + g(x, y, R) - (xu + yv)/R \tag{12.3}$$

with

$$R = (x^2 + y^2 + z^2)^{1/2} \text{ and } g(x, y, R) = (x^2 + y^2)/2R \tag{12.4}$$

Using these expressions in Eq.(12.2) gives

$$E(u, v) = [\exp(ikR)/s_0] \int_{A^+} A(\mathbf{r}) \exp[ik(g(x, y, R) - (ux + vy)/R)] dx dy \tag{12.5}$$

Equation (12.5) describes the paraxial propagation of a wavefront, for instance the wavefront emitted by and arriving from a distant (radio) star. In particular, this equation says that without disturbances or manipulations by a radio telescope or optical instrument between **A⁺** and **I** the plane wavefront continues to propagate in straight direction as a plane wavefront.

12.2 The *Perfect* Radio Telescope

A (radio) star is a point source in the sky and a well working telescope should image the star as a ‘point’ in the focal plane. As shown in Fig. 12.1.b, a lens or a radio telescope is placed in the incident beam at the aperture plane **A** with the intention to form an image of the star in the image plane **I**, i.e. the focal plane. A telescope is built in such a way that its transfer function $\Omega_O(\mathbf{r})$ forces the incident plane wavefront of the star to converge in a ‘point’ in the focal plane. The receiver at the focus introduces an additional modulation $\Omega_R(\mathbf{r})$ of the field of the converging wavefront¹. Using this information, the field distribution in the focal plane (**I**) of the telescope of an incident plane wavefront arriving from a far away point-like object is

$$E(\mathbf{u}) = [\exp(ikR)/s_o] \int_{\mathcal{A}} \Omega_O(\mathbf{r}) \Omega_R(\mathbf{r}) A(\mathbf{r}) \exp[ik(g(x, y, R) - (ux + vy)/R)] dx dy \quad (12.6)$$

The integration in Eq.(12.6) extends over the aperture area \mathcal{A} of the telescope, where the aperture area of the telescope is only a small section of the extended plane wavefront arriving from the distant object. The paraxial (on-axis) phase modulation of a telescope with focal length $F (= R)$ is²

$$\Omega_O(x, y) = \exp[-ikg(x, y, F)] \quad (12.7)$$

which inserted into Eq.(12.6) eliminates this term of the exponent so that

$$E(\mathbf{u}) = [\exp(ikF)/F] \int_{\mathcal{A}} \Omega_R(\mathbf{r}) A(\mathbf{r}) \exp[-ik(ux + vy)/F] dx dy \equiv \mathbf{FT}[\Omega_R(\mathbf{r}) A(\mathbf{r})] \quad (12.8)$$

This equation says that for a distant point-like object the field distribution $E(\mathbf{u})$ in the focal plane of the telescope is the *Fourier* transform of the receiver-weighted (tapered) field distribution $A(\mathbf{r})\Omega_R(\mathbf{r})$ of the aperture plane. However, a price is paid for using in a telescope only a limited area of the incident, infinitely extended plane wavefront. For a realistic telescope of diameter D follows $E(\mathbf{u}) \neq \delta(\mathbf{u} - \mathbf{u}_o)$ and $E(\mathbf{u})E^*(\mathbf{u}) \neq \delta(\mathbf{u} - \mathbf{u}_o)$ [$\delta =$ delta function] which expresses the empirical fact that the image of a point-like object is not point-like. In other words, the image of a star is always blurred by the beam pattern (point spread function) of the telescope of width $\theta_{mb} \propto \lambda/D$. Hence, the smaller the diameter of a telescope and thus the smaller the selected section of the incident wavefront, the larger is the blur.

¹ In radio engineering these properties are more easily discussed by reversing the direction of wave propagation and considering a telescope as a transmitting instrument.

² The parameter R in Eq.(12.3) – Eq.(12.6) is not to be confused with the radius of curvature of a lens, a spherical mirror or the paraxial radius of curvature of a parabolic mirror. It is the distance of the aperture plane to the image plane, Eq.(12.4).

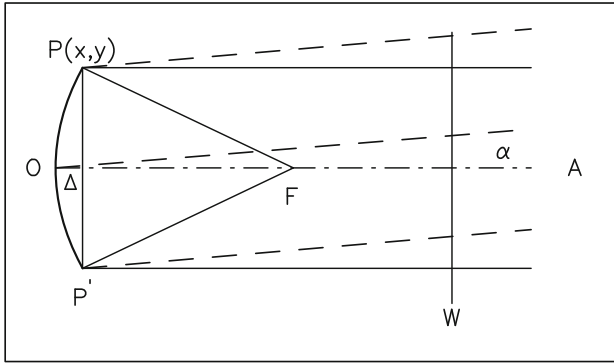


Fig. 12.2 Phase modulation $\Omega_O \equiv \Delta$ of a reflector. The incident plane wavefront (W) propagates to the left and the ray reflected at P(x,y) towards the focus F is shifted in phase by the amount Δ with respect to the on-axis ray. The relation $\Omega \equiv \Delta$ holds for on-axis rays and rays inclined to the optical axis OA (dashed line) at a small angle (α). There are many aperture planes **A**: W is one, and PP' is the one closest to the reflector.

It is easy to show that the telescope manipulates the incident on-axis plane wavefront in the way given by Eq.(12.7). A demonstration of this property is for instance given by Reynolds et al. [1989] and reproduced in Fig. 12.2 for paraxial rays of a reflector of focal length F. The reflector bends a section of the incident plane wavefront into a spherical wavefront that converges to the focal point. From the geometry of the ray paths follows

$$(F - \Delta)^2 + (x^2 + y^2) = F^2 \tag{12.9}$$

which for small Δ becomes

$$\Delta = -(x^2 + y^2)/2F = -g(x, y, F) \rightarrow \Omega_O(\mathbf{r}) \tag{12.10}$$

This is the instrumental phase modulation function Ω_O of Eq.(12.7). Although the proof is given for a reflector, any complex optical instrument, radio telescope, and in particular a combined telescope with main reflector and subreflector, can be treated in a similar way, leading to the same result.

In the construction and operation of a telescope the mathematical form of the phase modulation function Ω_O must be realized and maintained with high precision. Any deviation $\delta(\mathbf{r}) \neq 0$, temporary or permanent, either of the shape (systematic deviation) or the smoothness (random deviations)

$$\Delta'(\mathbf{r}) = \Delta(\mathbf{r}) + \delta(\mathbf{r}) \tag{12.11}$$

produces a beam degradation unless the deviation δ is small compared to the wavelength of observation (λ) and of the order of $\delta \lesssim \lambda/16$. The important value $\sim \lambda/16$ follows from actual diffraction calculations but also from the statistical theory of wavefront deformations and associated beam degradation [for instance Scheffler 1962, Ruze 1966]. Beam degradations introduced by systematic and random deviations $\delta \neq 0$ are discussed below.

The telescope reflector selects a part of the incident plane wavefront and bends this wavefront into a spherical wave that converges to the focus. This spherical wavefront enters the receiver, where it is mixed and down-converted in frequency, amplified and detected. The coupling of the receiver to the converging wavefront is made by a horn or lens-horn combination that guides the focused wave into the receiver. The coupling of the telescope's focal plane field pattern to the field pattern of the lens-horn combination modifies the amplitude (field) of the spherical wavefront in a way expressed by the taper (illumination) function $\Omega_R(\mathbf{r})$. This function weighs the wavefront across the aperture of the reflector, in a radial symmetric way. A Gaussian taper or a parabolic taper is often applied on radio telescopes and for instance expressed by [see Christiansen & Högbom 1985, Baars 2007]

$$\Omega_R(\rho) = \exp(-\gamma\rho^2), \quad \Omega_R(\rho) = p + (1-p)(1-\rho^2) \quad (12.12)$$

with ρ the normalized radius of the circular aperture ($\rho = r/(D/2)$, $0 \leq r \leq D/2$) and with γ and p constants. If $\Omega_R(\rho=1)$ (in dB) is the taper at the edge of the reflector, then $\gamma = \Omega_R(\rho=1) \cdot \ln(10)/20$ and $\log(p) = \Omega_R(\rho=1)/20$.

For $A(\mathbf{r}) = 1$, i.e. an incident plane wavefront arriving without amplitude and phase deformations the diffraction integral Eq.(12.8) is

$$E_T(\mathbf{u}) = \int_{\mathcal{A}} \Omega_R(\mathbf{x}) \exp[-ik\delta(\mathbf{r})] \exp[-ik\mathbf{u}\mathbf{x}] dx dy \quad \text{and} \quad E_T(\mathbf{u})E_T^*(\mathbf{u}) \equiv A_T(\mathbf{u}) \quad (12.13)$$

with E_T the tapered focal plane field distribution and A_T the tapered focal plane beam pattern (power pattern). For a perfect telescope $\delta(\mathbf{r}) = 0$ in Eq.(12.11) and $\exp[-ik\delta(\mathbf{r})] = 1$ in Eq.(12.13). In addition, in the case $\Omega_R(\mathbf{x}) = 1$, i.e. a telescope without taper (as relevant for optical telescopes), then

$$E(\mathbf{u}) = \int \exp[-ik\mathbf{u}\mathbf{x}] dx dy \quad \text{and} \quad E(\mathbf{u})E^*(\mathbf{u}) = [\mathcal{J}_1(u)/u]^2$$

with \mathcal{J}_1 the Bessel function of first order and $[\mathcal{J}_1(u)/u]^2$ the Airy pattern.

The diffraction integral Eq.(12.13) holds for a shallow reflector as used in optical telescopes ($1-2 \leq N = F/D$) but only to some extent for a steep reflector as used in radio telescopes ($F/D = N \leq 0.8$). While the diffraction calculation of a steep radio reflector is more complicated [Minnett & Thomas 1968], the discussion of the shallow reflector based on Eq.(12.13) reveals in a heuristic way the structure of the diffraction pattern and the profile of the main beam. However, the diffraction pattern of the *real* telescope introduces another modification of the diffraction integral that

swamps in the error beam(s) to a large extent the detailed structure of the perfect beam of the steep reflector (Section 12.4.3).

12.3 The Beam Pattern of the *Perfect* Radio Telescope

The circular symmetric collecting and beam bending mirrors of a radio telescope produce a circular symmetric focal plane field distribution $E_T(\mathbf{u})$ and a circular symmetric beam pattern $A_T(\mathbf{u})$. The centre of circular symmetry for an on-axis point-like object is the intersection of the optical axis (OA) with the focal plane. The circular symmetry exists also for the converging and diverging beam inside and outside the focal plane. For many discussions and applications it is sufficient to consider a radial cut through $E_T(\mathbf{u})$ and $A_T(\mathbf{u})$, at least for a perfect telescope. It is convenient to express the field distribution and the beam pattern in polar coordinates θ, ϕ , i.e. $E_T(\mathbf{u}) \equiv E_T(\theta, \phi)$ and $A_T(\mathbf{u}) \equiv A_T(\theta, \phi)$. The linear dimension θ of the one-dimensional cuts $E_T \rightarrow E_T(\theta)$ and $A_T \rightarrow A_T(\theta)$ is frequently expressed in arcseconds as a suitable measure in the focal plane and in the plane of the sky. Fig. 12.3 shows as an example the calculated field distribution $E_T(\theta, \phi)$ and beam pattern $A_T(\theta, \phi)$ of the IRAM 30-m telescope when used at $\lambda = 1.3$ mm (230 GHz) wavelength and a -15 dB edge taper³. In order to illustrate the influence of the taper, Fig. 12.4 shows the beam pattern A_T calculated for a hypothetical receiver without taper $\Omega_R(\rho) = 1$, for a -10 dB edge taper with $\gamma = 1.15$ or $p = 3.16$ and for a -15 dB edge taper with $\gamma = 1.73$ or $p = 5.62$ in Eq.(12.12).

From diffraction calculations and observations with telescopes follows that the field distribution $E_T(\theta, \phi)$ and the beam pattern $A_T(\theta, \phi)$ has a main beam (mb) and sidelobes, separated by concentric rings where $E_T = A_T = 0$. The field/power of the sidelobes decreases with increasing order of the sidelobes, located at increasing distance from the on-axis position. The phase of the field distribution E_T changes by 180° between the main beam and successive sidelobes. The taper does not change the global structure of the field and beam pattern, however, a larger edge taper increases slightly the width of the main beam, while at the same time the level of the sidelobes is reduced. The width θ_{mb} of the main beam of the beam pattern A_T (full width at half maximum = FWHM) is

$$\theta_{mb} = \alpha \lambda / D \quad [\text{rad}] \quad (12.14)$$

with α depending on the applied taper, i.e. $\alpha \approx 1.0 - 1.3$ [Christiansen & Högbom, 1985]. The full width of the main beam θ_{fb} (diameter to first minimum) is

$$\theta_{fb} \approx 2.2 \theta_{mb} \quad [\text{rad}].$$

³ A dB (decibel) is 10 times the logarithm of the power ratio P_2 to P_1 , i.e. $\text{dB} = 10 \times \log_{10}(P_2/P_1)$. If, for instance, $P_2 = 10^{-2} P_1$ then the ratio is -20 dB. For amplitude ratios I the relation is $\text{dB} = 20 \times \log_{10}(I_2/I_1)$.

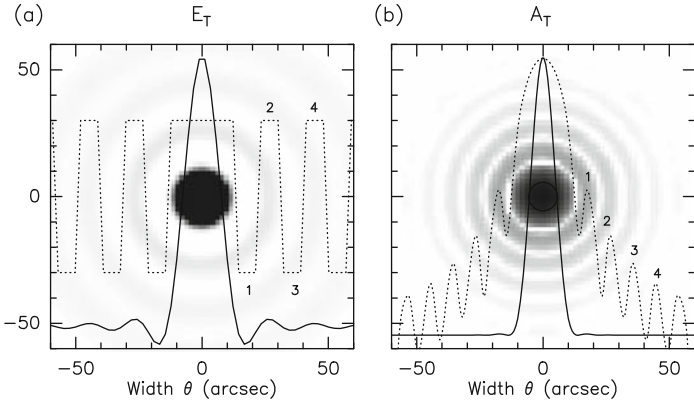


Fig. 12.3 (a) Field distribution E_T and (b) power distribution A_T of a perfect telescope with -15 dB edge taper. Inserted are the on-axis cuts through E_T (amplitude: solid line and periodic phase change of 180° between the main beam and the side lobes: dashed line) and A_T (in linear scale: solid line and dB scale: dashed line). The central part of the beam pattern is the main beam, the 1st, 2nd, 3rd and 4th side lobe is indicated.

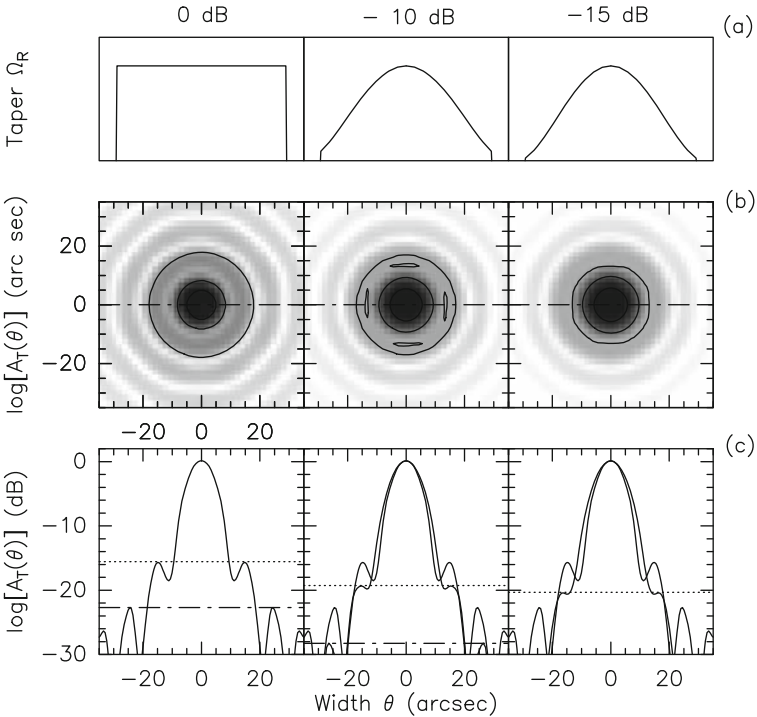


Fig. 12.4 (a) Taper across the aperture of the main reflector Eq.(12.12), the value of the edge taper is indicated. (b) Focal plane beam pattern $A_T(\theta, \phi)$ (in log-scale). (c) Cut through the beam pattern $A_T(\theta, \phi)$. The dashed line shows the level of the 1st side lobe, the dashed-dotted line the level of the 2nd side lobe.

12.4 The *Real* Radio Telescope

A telescope is never perfect because of mechanical, gravity, temperature and wind induced deformations of its structure, because of production imperfections and because of accidental small misalignments of the optics. The resulting degrading effect on the beam pattern is negligible if the corresponding deformation δ of the reflector and the misalignment of the optics (main reflector, subreflector, receiver) is small compared to the wavelength of observation, i.e. smaller than, say, $\sim \lambda/15$. The degradation becomes noticeable and disturbing if the corresponding deformation is larger than, say, $\sim \lambda/10$. The associated wavefront deformation of the imperfections may be of a systematic nature, or a random nature or both. Systematic wavefront deformations usually produce a deformation of the main beam and the profile close to the main beam and a decrease in main beam intensity; random wavefront deformations usually produce an intensity decrease of the main beam and a very extended and more or less intense Gaussian type error beam.

In the general situation the deformation consists of spatially *small*-scale random deformations, which usually do not change the structure of the beam pattern and the focus and pointing, and of *large*-scale deformations, which may do so. The deformation $\delta(\rho, \Theta)$ can be decomposed into large-scale contributions $\delta_Z(\rho, \Theta)$ that can be represented by Zernike polynomials⁴ $Z_{ij}(\rho, \Theta)$ [Born & Wolf 1980] and random deformations $\delta_{rd}(\rho, \Theta)$ so that

$$\begin{aligned} \delta &= \delta_Z + \delta_{rd} = \sum_{i,j} \alpha_{ij} Z_{ij} + \delta_{rd} \\ &= \sum_{i,j} R_i(\rho) [\alpha_{AZ(ij)} \cos(j\Theta) + \alpha_{EL(ij)} \sin(j\Theta)] + \delta_{rd}(\rho, \Theta) \end{aligned} \quad (12.15)$$

with the telescope aperture defined by the normalized radial distance ρ ($0 \leq \rho \leq 1$) and the angle Θ ($0 \leq \Theta \leq 2\pi$) in the aperture plane. The radial terms are $R_i(\rho)$ and the terms $\cos(j\Theta)$ and $\sin(j\Theta)$ are used, for instance, for the azimuth and elevation direction, respectively. The amplitude of the Zernike term (ij) is

$$\alpha_{(ij)} = \sqrt{\alpha_{AZ(ij)}^2 + \alpha_{EL(ij)}^2} \quad (12.16)$$

The known deformation δ can be used in Eq.(12.13) to calculate the degraded beam pattern.

12.4.1 Systematic Wavefront Deformations

Probably most of the temperature induced structural deformations of a telescope and thus of the beam forming wavefront are of systematic nature because they are, for instance, due to large-scale temperature gradients, directional wind and associated

⁴ The Zernike polynomials that may be important for thermal studies are listed in Appendix D.

asymmetric cooling, asymmetric solar illumination and cooling towards the cool sky. Thermal model calculations during the design phase may indicate to which particular systematic deformation a telescope is sensitive (see Chapter 15). Usually the systematic deformations can be decomposed into Zernike polynomials of low order (i,j).

There are three basic systematic wavefront deformations, i.e. defocus ($Z_{2,0}$), coma ($Z_{3,1}$) and astigmatism ($Z_{2,2}$) that are usually due to a traceable temperature induced mechanical defect of the telescope. The beam deformation of these low order systematic wavefront deformations appears close to the main beam. Fig. 12.5 shows the wavefront deformation and the corresponding beam pattern of defocus, coma and astigmatism of geometrical amplitude $\alpha = 0.5 \lambda$ (see below).

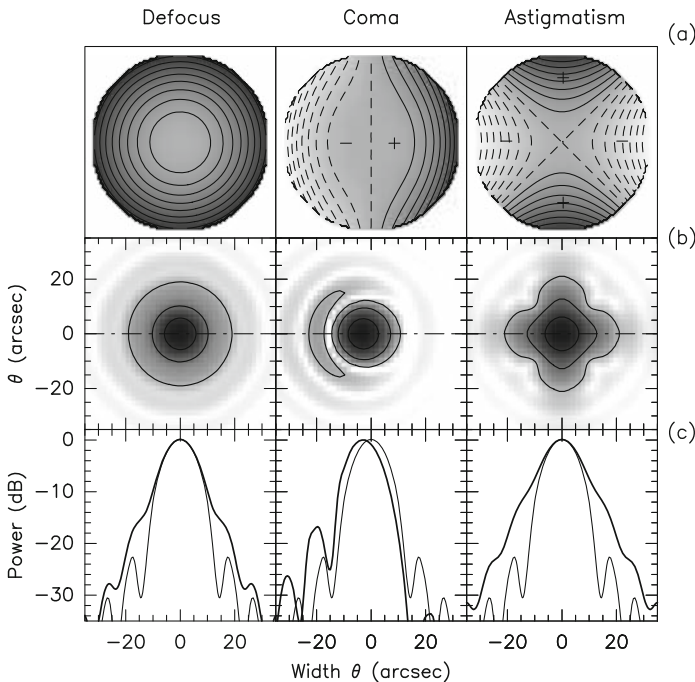


Fig. 12.5 (a) Wavefront deformation of defocus, coma and astigmatism of amplitude $\alpha = 0.5 \lambda$. The contours are shown in steps of $\pm 0.05 \lambda$, dashed lines: negative deformation, solid lines: positive deformation. (b) Beam patterns A_T of defocus, coma and astigmatism. The contours are in steps of -3 dB, the first contour at -3 dB is the beam width (θ_{mb}). (c) Cut through the beam patterns of defocus, coma and astigmatism: heavy lines. The thin line is the perfect beam pattern. The direction of the cuts is shown by the dashed lines in (b).

(1) *Focus*: The most important systematic wavefront deformation is due to a defocused telescope because, for instance, of an axial shift of the subreflector. The corresponding wavefront error is $\varphi_{2,0} = (2\pi/\lambda)\delta_{2,0} = \alpha_{2,0}(2\pi/\lambda)\rho^2$. A focus error is easily detected, measured and corrected from the observation of a radio source at

a number of focus settings. Fig. 12.6 shows, as an example, the beam pattern measured on Jupiter with the IRAM 15-m radio telescope that was gradually defocused by a shift of the subreflector. Evidently, in the defocused telescope the peak power of the main beam decreases and the power in the side lobes increases until finally the beam pattern has completely collapsed. To be on the safe side for observations, the defocus of the telescope should not exceed $\sim \lambda/10$. A defocus does *not* introduce a pointing error.

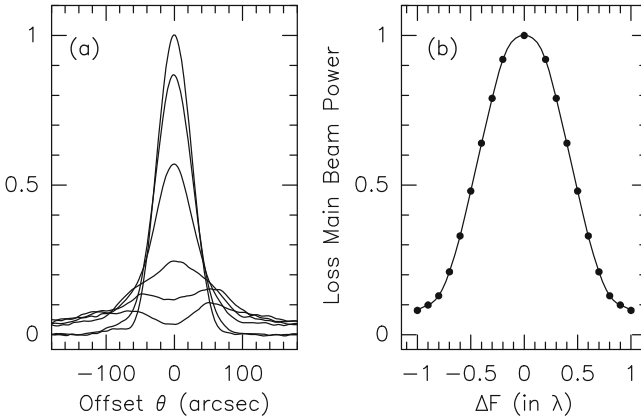


Fig. 12.6 (a) Degradation of the beam pattern (scans across Jupiter) introduced by defocusing the IRAM 15-m telescope (shift of the subreflector in steps of $\lambda/4$, $\lambda = 3$ mm). (b) Calculated loss of main beam intensity of the defocused telescope.

(2) *Coma*: The telescope may have a comatic wavefront deformation for instance due to a misaligned subreflector, either shifted perpendicular to the main reflector axis or tilted against the reflector axis. The corresponding wavefront error is $\varphi_{3,1} = (2\pi/\lambda)\delta_{3,1} = \alpha_{3,1}(2\pi/\lambda)\rho^3\cos(\Theta)$. Fig. 12.7 shows scans through the comatic beam of the IRAM 15-m telescope produced by displacing the subreflector by the indicated amount S perpendicular to the reflector axis. A comatic beam pattern introduces a pointing error and a decrease of the main beam intensity (see also Fig. 13.2). To be on the safe side for observations, the pointing error introduced by coma should not exceed $\sim 1/10$ of the beam width.

(3) *Astigmatism*: The telescope may have an astigmatic wavefront deformation, usually introduced by a mechanical deformation of the main reflector (BUS). The corresponding wavefront error is $\varphi_{2,2} = (2\pi/\lambda)\delta_{2,2} = \alpha_{2,2}(2\pi/\lambda)\rho^2\cos(2\Theta)$. Fig. 12.8 shows the focused beam pattern measured on a telescope with a strong astigmatic main reflector surface (amplitude $\alpha_{2,2} \approx 0.5$ mm, wavelength of observation $\lambda = 1.3$ mm). The astigmatic deformation is easily recognized by the elliptical in-focus and out-focus beam pattern [Greve et al. 1994], as illustrated in Fig. 12.8. An astigmatic beam does *not* introduce a pointing error but a decrease of the main

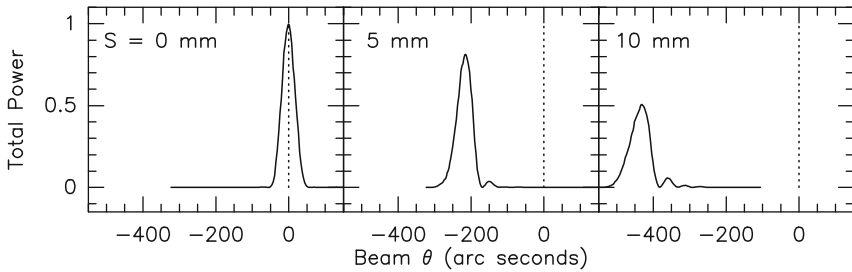


Fig. 12.7 Measurement ($\lambda = 3$ mm) of a comatic beam (scanned in the direction of the coma) produced on the IRAM 15-m telescope by shifting the subreflector by the amount S perpendicular to the main reflector axis. The beam pattern is perfect and centred at $S = 0$. Note the shift of the beam (pointing error) when the subreflector is shifted. The decrease in main beam power appears as increased side lobes.

beam intensity. Temperature induced astigmatic main reflector surface deformations of the IRAM 30-m telescope are explained in Section 9.2.1.

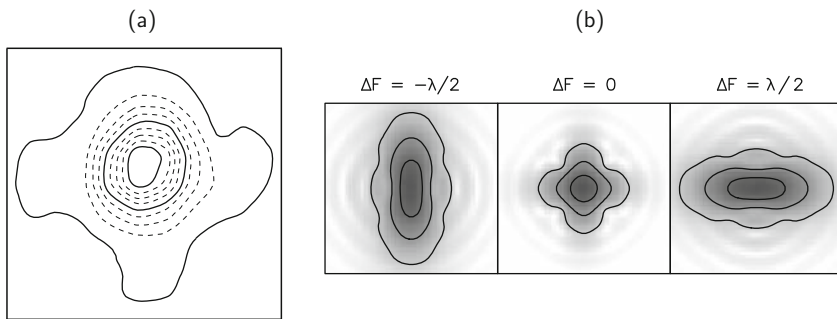


Fig. 12.8 (a) Astigmatic beam pattern measured at 1.3 mm wavelength at best focus; the amplitude of the astigmatic reflector surface deformation is $\alpha_{2,2} \approx \lambda/2$. (b) Calculated beam pattern inside the best focus ($\Delta F = -\lambda/2$), at best focus ($\Delta F = 0$) and outside the best focus ($\Delta F = +\lambda/2$), for $\alpha_{2,2} = \lambda/3$. Note that the direction of the beam ellipticity changes by 90° between the in-focus and the out-focus position. The -3 dB, -6 dB and -9 dB levels are drawn.

12.4.2 Repetitive Wavefront Deformations (Thermal Panel Buckling)

There are systematic deformations that cannot be represented by Zernike polynomials as for instance repetitive deformations resembling to some degree a grating.

A typical example is temperature induced panel buckling. Measured thermal panel buckling is shown in Section 9.4.3.

A mathematical description of a reflector surface with $n \times m$ buckled rectangular panels (n = number of panel rings, m = number of panel sectors) is

$$\delta_p(\rho, \Theta) = \alpha \delta_n(\rho) \delta_m(\Theta) \tag{12.17}$$

with

$$\delta_n(\rho) = |\sin(\pi n \rho)| \tag{12.18}$$

$$\delta_m(\Theta) = |\sin(m\Theta/2)| \tag{12.19}$$

The amplitude of the deformation, i.e. the buckling, is α . The quasi rms value σ^* (see Section 12.5) of a reflector surface covered with buckled panels is $\sigma^* \approx \alpha/3$. It is evident that other sine and cosine approximations than Eqs.(12.18,12.19) can be constructed. The example of $n = 7$ rings and $m = 16$ sectors as appropriate for the IRAM 30–m telescope and the corresponding calculated beam pattern at 230 GHz (1.3 mm) is shown in Fig. 12.9. A measurement of the IRAM 30–m telescope beam pattern at this frequency is shown in Fig. 12.10. The regular panel buckling produces large diameter, incomplete diffraction rings and diffraction plateaus, usually at a low power level, the diffraction rings are visible in Fig. 12.9 and Fig. 12.10. For further details on the diffraction pattern from buckled panels see Greve & Morris [2005] and Greve et al. [2009].

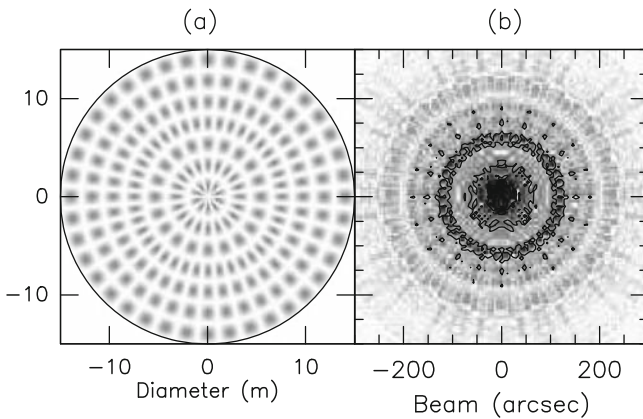


Fig. 12.9 (a) Repetitive panel buckling for $n = 7$ zones (rings) and $m = 16$ sectors of panels. (b) Calculated power pattern of deformation amplitude $\alpha = \lambda/6$ at λ 1.3 mm (230 GHz) wavelength. The grey scale covers -65 dB and -30 dB. The main beam width (FWHP) at this wavelength is 11 arcsec.

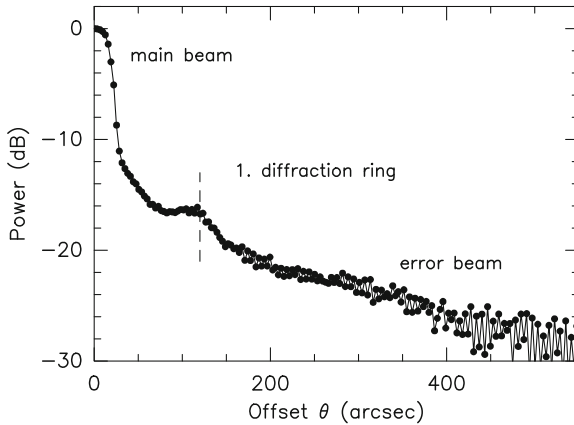


Fig. 12.10 IRAM 30-m telescope. Differentiated Moon limb scan (\approx beam pattern) measured on the IRAM 30-m telescope at 230 GHz (1.3 mm) showing the main beam, the 1st order diffraction ring due to thermal panel buckling (at the dashed line) and the underlying error beam pattern. The main beam width at this wavelength is 11 arcsec.

12.4.3 Random Wavefront Deformations

Random wavefront deformations are primarily due to misaligned reflector panels and/or to deformations of the panels themselves. Random deformations cannot be expressed in analytical form, nevertheless their effect on the beam pattern can be analysed in a statistical way with the *Ruze* theory [Ruze 1966].

There are two parameters that allow a description of random errors, i.e. the rms value σ (root mean square value) of the deformations and their correlation length L . In order to calculate the rms value σ , the reflector aperture is divided into many elements ($i = 1, 2, \dots, N$, $N =$ a few hundred) and for each element $[i]$ the geometrical deformation $\delta(i)$ of the reflector surface is known with respect to a smooth mean surface. For this best-fit surface $\sum_i \delta(i) = 0$. The geometrical rms value of the random surface deformations is

$$\sigma = \sqrt{\sum \delta(i)^2 / N} \quad (12.20)$$

Because of the double path length difference at reflection on the panels, the surface deformations $\delta(i)$ introduce corresponding phase deformations

$$\varphi_p(i) = 2(2\pi/\lambda)\delta(i)\cos\gamma(i) \quad (12.21)$$

with $\tan\gamma(i) = \rho(i)/(4n)$ the steepness of the parabolic reflector of focal ratio n at the normalized radial distance $\rho(i)$. The rms value σ_p of the phase deformations of the reflected wavefront is

$$\sigma_p = \sqrt{\sum_i \varphi_p(i)^2 / N} = 2(2\pi/\lambda) R_p \sigma \quad (12.22)$$

with the factor R_p taking into account the steepness of the reflector. The phase $\varphi_p(i)$ is furthermore weighted by the taper function (Ω_R of Eq.(12.12)) so that the radio effective phase-tapered rms value is

$$\sigma_{pT} \equiv \sigma_\varphi = 2(2\pi/\lambda) R_{pT} \sigma = 2(2\pi/\lambda) \mathbf{R} \sigma \quad (12.23)$$

with the factor \mathbf{R} (≈ 0.8) obtained from numerical calculations for the telescope under consideration [Greve & Hooghoudt 1981]. The rms value σ_φ is important in radio physics since it determines to a large extent the sensitivity of the real telescope. The sensitivity (performance) of a telescope is proportional to the aperture efficiency and the *Ruze* relation [1966] states that the aperture efficiency

$$A_{\text{eff}}/A = \varepsilon_a(\lambda) = \varepsilon_0 \exp[-(\sigma_\varphi)^2] = \varepsilon_0 \exp[-(4\pi \mathbf{R} \sigma / \lambda)^2] \quad (12.24)$$

decreases exponentially at shorter wavelengths (higher frequencies). In Eq.(12.24) is A the aperture area of the telescope, A_{eff} the radio effective aperture area with $A_{\text{eff}}/A < 1$, ε_0 is the aperture efficiency of the telescope at very long wavelengths for which $\varepsilon_a \rightarrow \varepsilon_0 \approx 0.6-0.8$ ($\lambda \rightarrow \infty$).

The statistical description of the wavefront deformation by its rms value σ_φ is, however, incomplete since the value does not contain information on the spatial structure and spatial extent of the deformations, for instance whether they consist of many dents at one part of the aperture, or many scratches at another part. A complete description requires also knowledge of the correlation length L ($L \leq D$) of the deformations, which quantifies the extent over which the randomness of the deformations does not change [Ruze 1966, Scheffler 1962]. For example, the deformations of a reflector constructed from many individual panels, which are to some extent misaligned, has a random error correlation length of the panel size, but also a correlation length of 1/3 to 1/5 of the panel size due to inaccuracies in the fabrication of the panel surfaces. A typical example is the reflector of the IRAM 30-m telescope [Greve et al. 1998].

Important for the validity of the statistical treatment of random errors and the expression of the associated beam pattern explained below is the assumption that the random errors have a Gaussian distribution. The investigation of many radio telescopes has shown that this is generally the case. Fig. 12.11 shows as an example the surface deformations of the Effelsberg 100-m telescope, measured in 1971-1972, and of the IRAM 30-m telescope, measured in 1994.

Knowing the rms value σ_φ and the correlation length L , it is possible to express the resulting beam shape in analytic form that describes well the situation of a real telescope with random surface errors [Ruze 1966, Baars 1973, Greve et al. 1998]. In this description the beam pattern is assumed to be circular symmetric. In the case the surface deformations are reasonably small, i.e. of the order of $\lambda/10$ or smaller, the tapered beam pattern $\mathcal{F}_T(\theta, \phi)$ of a wavefront with random deformations (σ_φ, L)

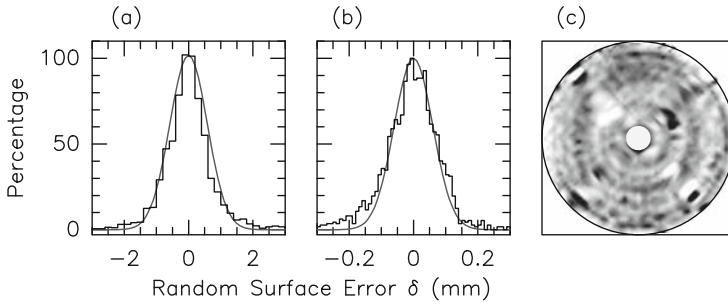


Fig. 12.11 (a) Gaussian distribution of random reflector surface errors of the Effelsberg 100-m telescope (1971–1972), measurements of $\sim 10\,000$ panel corners (2500 panels). The rms value is $\sigma \approx 0.85$ mm. (b) Similar Gaussian distribution of random surface errors on the IRAM 30-m telescope (1994), measurement of ~ 1000 panel corners (250 panels). The rms value is $\sigma \approx 0.08$ mm. (c) Surface deformations on the IRAM 30-m telescope corresponding to the statistics shown in (b).

consists of the degraded coherent diffraction beam $\mathcal{F}_c(\theta, \phi)$ and the incoherent error beam $\mathcal{F}_{eb}(\theta)$, shown in Fig. 12.12, such that

$$\mathcal{F}_T(\theta, \phi) \rightarrow \mathcal{F}_T(\theta) = \mathcal{F}_c(\theta) + \mathcal{F}_{eb}(\theta) \quad (12.25)$$

with

$$\mathcal{F}_c(\theta) = \exp[-(\sigma_\phi)^2] A_T(\theta) \quad (12.26)$$

where $A_T(\theta)$ is the tapered beam pattern (Eq.(12.13)) and

$$\mathcal{F}_{eb}(\theta) = a \exp[-(\pi\theta L/\lambda)^2] \quad (12.27)$$

where

$$a = (L/D)^2 [1 - \exp(-\sigma_\phi^2)] / \varepsilon_o \quad (12.28)$$

In these equations is D the diameter of the reflector, λ the wavelength of observation, θ the angular distance from the beam axis and ε_o the aperture efficiency of the perfect telescope. The error beam $\mathcal{F}_{eb}(\theta)$ has a Gaussian profile of width (FWHP)

$$\theta_{eb} = 0.53 \lambda / L \quad [\text{rad}] \quad (12.29)$$

i.e. the finer the irregular deformations, the smaller is the correlation length L and the broader is the width θ_{eb} of the error beam. If for instance $L \lesssim D/10$, the comparison with Eq.(12.14) shows that the error beam is considerably broader than the main beam, i.e. of the order of $10 \theta_{mb} \lesssim \theta_{eb}$. The Gaussian error beam measured at 230 GHz (1.3 mm) on the IRAM 30-m telescope is seen in Fig. 12.10.

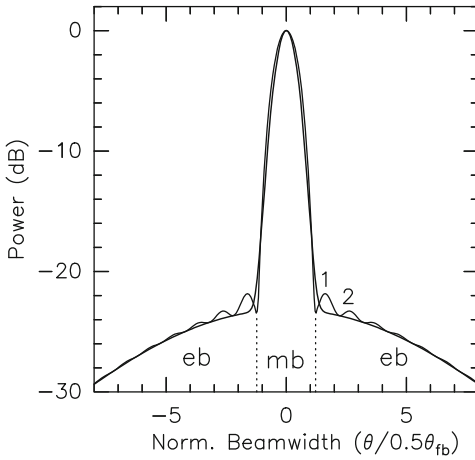


Fig. 12.12 The beam pattern of the real telescope, as described by Eq.(12.25), consists of the main beam (mb) and side lobes (of which 2 are indicated) and of an underlying error beam (eb). The main beam and the error beam can be approximated by Gaussian profiles, as indicated by the heavy line. The beam width is normalized to 1/2 the full beam width $\theta_{fb} \approx 2.2 \theta_{mb}$.

12.5 Superposition of Random and Systematic (Thermal) Deformations

A telescope may have random wavefront deformations, for instance due to random main reflector surface errors from panel misalignment, and systematic wavefront deformations, for instance due to thermal deformations of the telescope structure. Both deformations act together in the formation of the beam. There is no accurate way to evaluate the relative importance of random and systematic deformations without going into lengthy diffraction calculations. However, a first approximation to evaluate the relative importance can use the quasi rms value σ^* of systematic deformations [Greve 1980]. If δ_Z is a systematic deformation, for instance expressed by Zernike polynomials Eq.(12.15) or panel buckling Eq.(12.17), then Eqs.(12.20–12.23) can be used to calculate for the deformation δ_Z a corresponding quasi rms value σ^* and phase-tapered quasi rms value σ_{pT}^* . For a systematic deformation the value σ_{pT}^* gives some information of the decrease of the main beam intensity⁵, but not of the off-axis beam and the concept of an error beam has no meaning. Writing the Zernike polynomial deformation of amplitude α_{nm} as $\delta_{nm} = \alpha_{nm}R_n(\rho)\cos(m\Theta)$, the corresponding quasi rms value is $\sigma^* = \alpha_{nm}/\sqrt{n+1}$ [Born & Wolf 1980]. For primary defocus and primary astigmatism $n = 2$, for primary coma $n = 1$. Thus, when concentrating on the main beam, the relative importance of a random and systematic deformation can be found from the values σ and σ^* . For $\sigma^* < \sigma$ the random deformations and the associated error beam are important, for $\sigma < \sigma^*$ the systematic deformation and the systematic beam degradation are important. The comparison between σ and σ^* becomes important when evaluating the influence and detectability of systematic thermal deformations on a telescope with respect to the achieved reflector precision (see Section 13.3).

⁵ The quasi rms value σ^* used in the *Ruze* relation gives a realistic value of the aperture efficiency, Eq.(12.24), and of the main beam degradation, Eq.(12.26).

An illustration of temperature induced systematic surface deformations and the corresponding beam patterns are given in Fig. 12.13. The situation shown is de-icing of the IRAM 30-m telescope that introduces a large heat load and an associated large, transient reflector deformation. To construct Fig. 12.13, the measurements of the 148 temperature sensors were used in the FEM to calculate the temperature induced reflector surface deviations δ_T and from these the beam pattern at 230 GHz (1.3 mm). The surface deformations δ_T were decomposed with Zernike polynomials into systematic deformations (δ_Z) and random deformations (δ_{rd}), i.e. $\delta_T = \delta_Z + \delta_{rd}$ (Eq.(12.15)). The Zernike decomposition is shown in Fig. 12.14.a, the dominant polynomials in this case are $L = 3, 12,$ and 15 (Appendix D). While the amplitudes of the polynomials are large during the de-icing period, they become small at the end of this period. Fig. 12.14.b shows the corresponding rms values, i.e. $\sigma_T = \sqrt{(\delta_T)^2/N}$ of the thermal surface deformations irrespective of their nature, the quasi rms value $\sigma^* = \sqrt{(\delta_Z)^2/N}$ of the component of systematic deformations and the rms value of the component of random deformations $\sigma = \sqrt{(\delta_{rd})^2/N}$. For comparison, $\sigma_a = 0.05$ mm is the surface rms value achieved from panel frame adjustments [Morris et al. 2009]. From Fig. 12.14.b follows that around 18 hour the rms value σ_T of the temperature induced deformations became smaller than the surface rms value σ_a , so that at later hours the random surface errors of the panel setting determined the beam pattern. The amplitude of the polynomial $L = 3$, which determines the focus change of the surface, decreased from ~ 0.14 mm at 8 h to ~ 0.02 mm at 22–24 h. In Fig. 4.19, which refers to the same situation, it is seen that the focus of the telescope reached a stable position only at 22–24 h.

12.6 Beam Deformations and Thermal Tolerances

The temperature induced structural deformations of a telescope may introduce a shift $\Delta(U, V, W)$, a tilt $\Delta\epsilon$ and a focal change Δf of the main reflector and a shift $\Delta(u, v, w)$ and tilt $\Delta\gamma$ of the subreflector (Fig. 13.4). Ruze [1969] and Zarghamee & Antebi [1985] derived for these shifts and tilts and the focal change the analytic relations of the corresponding deformations $\delta = \Delta(U, V, W, \epsilon, u, v, w, \gamma, f)$. These relations δ can be used in the diffraction integral Eq.(12.13) to derive the corresponding beam pattern and beam degradation. However, the diffraction calculations can be avoided by imposing in tolerance considerations of temperature induced structural deformations the equivalent condition that the associated deformations are smaller than, say, $\delta \leq \lambda/10$. This condition constrains the values of the temperature induced deformations $\Delta(U, V, W, \epsilon, u, v, w, \gamma, f)$ and imposes a tolerance on the temperature uniformity and temperature variation of the telescope. The thermal tolerance conditions derived in this way are explained in Chapter 13.

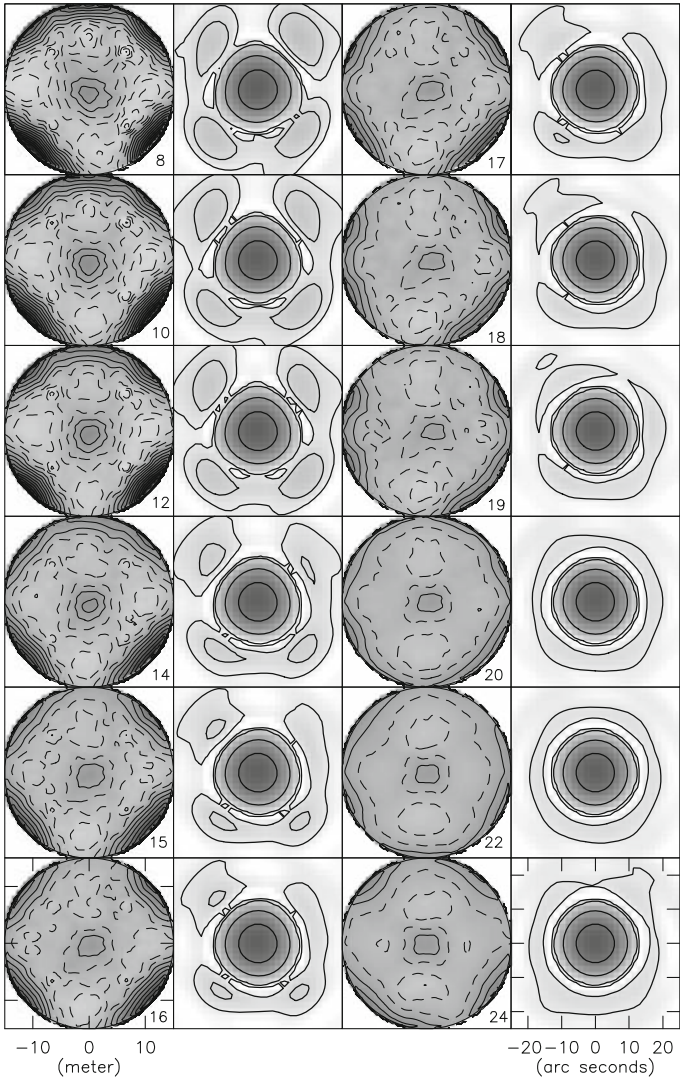


Fig. 12.13 IRAM 30-m telescope. Illustration of systematic reflector surface deformations due to heating for de-icing, and corresponding beam patterns. The plots numbered with the hour of the measurements show the reflector surface deformations calculated from temperature measurements used in the FEM. The contours are in steps of ± 0.04 mm. The corresponding beam patterns are calculated for 230 GHz (1.3 mm). The contours are at -3 dB (beam width), -10 dB, -20 dB and -25 dB.

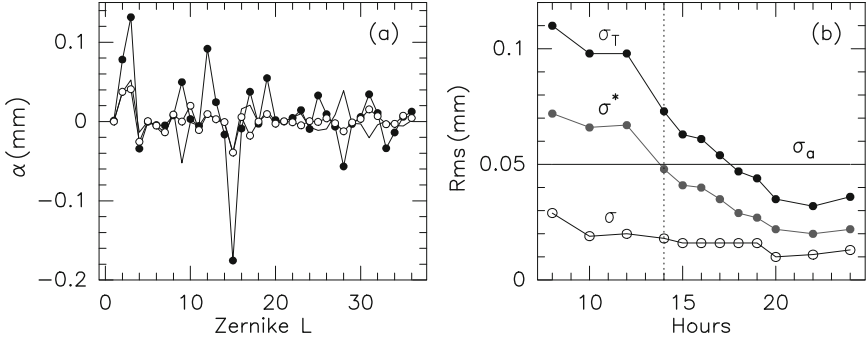


Fig. 12.14 IRAM 30-m telescope with surface deformations due to heating for de-icing. (a) Amplitudes of Zernike polynomials of the associated systematic surface deformations, dots: time 8 h, open circles: time 24 h. The leading Zernike polynomials are L3: $\delta = 6\rho^4 - 6\rho^2 + 1$, L12: $\delta = \rho^3 \cos(3\Theta)$, L15: $\delta = \rho^4 \cos(4\Theta)$. (b) Corresponding rms values as explained in the text. The de-icing was switched off at 14 h.

Chapter 13

Thermal Tolerances

The fundamental information that the designer, construction engineer and telescope operator wants from the preceding Chapters are thermal tolerance criteria on which to build a telescope and that can be used to evaluate the thermal performance of an operating telescope. The thermal tolerance criteria derived in this Chapter are based on beam pattern calculations explained in Chapter 12, which indicate that a good telescope performance is obtained if the deformations of the beam forming wavefront do not exceed $\sim 1/16$ of the wavelength of observation λ , if the focus is stable within $\sim \lambda/10$ and if the pointing is stable within $\sim 1/10$ of the beam width. Interferometer telescopes should have, in addition, a path length stability of $\sim \lambda/10$ or better. These performance criteria should be fulfilled during a considerable length of time before a calibration of the telescope needs to be made. The performance criteria translate into mechanical tolerances and these into thermal tolerances of the telescope structure.

Two examples illustrate the stability of the climatized IRAM 30-m telescope with respect to occasional, transient pointing and focus changes.

A time sequence of pointing and focus corrections made on the IRAM 30-m telescope during a regular observation is shown in Fig. 13.1. It is seen that without pointing correction the telescope would have drifted (in EL) one beam width away from the source within approximately 4 hours, so that in essence the source would have been 'lost'. Likewise, within approximately 6 hours the focus would have drifted by $\sim 0.8 \text{ mm} \approx 0.6 \lambda$ ($\lambda = 1.3 \text{ mm}$) that would have weakened the signal by $\sim 50\%$ (see Fig. 12.6). The illustrated effects are only to some extent due to temperature influences since the behaviour of the entire telescope, the control system and the refraction model appear in the measured pointing and focus corrections.

Temperature induced deformations of the telescope structure usually produce large-scale wavefront deformations, for instance due to asymmetric solar illumination of the quadripod and a corresponding shift/tilt of the subreflector. An example of a transient comatic aberration, perhaps of this origin, observed on the IRAM 30-m telescope is shown in Fig. 13.2. The coma was noticed for several hours and then disappeared.

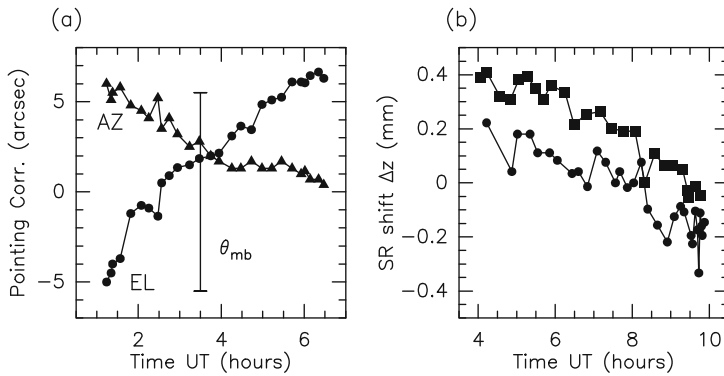


Fig. 13.1 IRAM 30-m telescope. (a) Pointing correction in azimuth (AZ) and elevation (EL) direction. The beam width of $\theta_{mb} = 11$ arcsec (FWHP) at 230 GHz is inserted. (b) Focus correction (= shift of the subreflector) measured at two consecutive days (dots and squares).

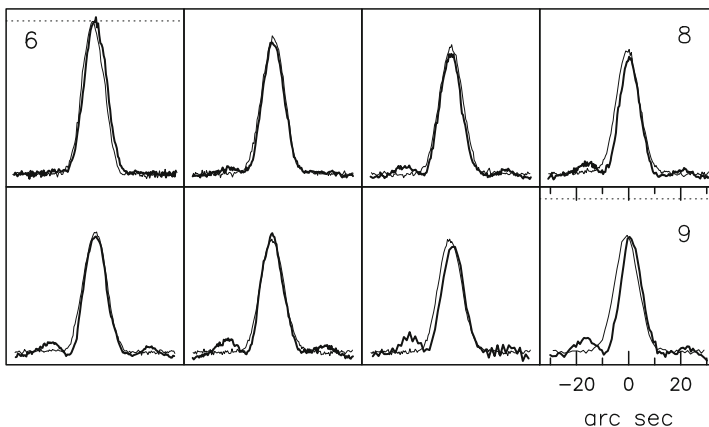


Fig. 13.2 IRAM 30-m telescope. Transient comatic aberration probably due to asymmetric thermal expansion of the quadripod and/or tilt of the subreflector, observed in cross-scans (AZ and EL direction) at 230 GHz at the indicated hour of the day (from left to right). The dashed line indicates the loss in main beam power; see also Fig. 12.7.

13.1 Global Estimates of Temperature Influences

The literature contains several relations that allow an estimate of the influence of temperature changes and temperature gradients on the reflector surface precision, on focus and pointing changes of a BUS, on pointing and path length errors of an alidade or fork support and on panel buckling. These estimates provide an initial orientation of the magnitude of thermal deformations and of the required thermal stability of a BUS, an alidade and fork support and of panels.

13.1.1 Reflector Diameter Estimates

Von Hoerner [1967 a, 1975 a] investigated the largest possible reflector diameter D and the reflector quality D/σ (with σ the reflector surface precision) under the influence of gravity, temperature and wind; a summary of this investigation is shown in the von Hoerner–diagram (see Preface). From the thermal deformation of a reflector built from steel $\Delta z \approx \alpha D\Delta T$ ($\alpha = 12 \mu\text{m/m/K}$) and the condition that the shortest wavelength of observation should be $16 \text{rms}(\Delta z) \lesssim \lambda_{\text{min}}$, von Hoerner derived the relation

$$6 [\text{mm}](D/100[\text{m}])(\Delta T/^{\circ}\text{C}) \lesssim \lambda_{\text{min}} \tag{13.1 a}$$

or

$$\Delta T \lesssim \lambda_{\text{min}}[\text{mm}]/(6D/100[\text{m}]) \text{ (steel)} \tag{13.1 b}$$

For a reflector built from aluminium the CTE ($22 \text{m}\mu\text{/m/K}$) is approximately twice that of steel and λ_{min} is two times longer, for a reflector built from CFRP the CTE ($\sim 3 \text{m}\mu\text{/m/K}$) is approximately 4 times smaller and λ_{min} is 4 times shorter.

Evidently, relation (13.1) can be used to find

- (a) the shortest wavelength of observation for a given reflector diameter and known temperature differences,
- (b) the tolerable temperature differences for a given reflector diameter and wavelength of observation,
- (c) the largest possible reflector diameter for a given shortest wavelength and known and unavoidable temperature differences.

Since an astronomy project defines the wavelength(s) of observation and the required beam width and sensitivity, hence the reflector diameter D , the emphasis of relation (13.1) may lie on the determination of the required temperature uniformity ΔT . For a number of reflector constructions the corresponding values ΔT are listed in Table 13.1.

Table 13.1 Temperature Tolerances of Reflector (BUS) Constructions (Eq.(13.1.b)).

Reflector Diameter D	100 m	30 m	20 m	15 m	12 m	12 m	
Material	steel	steel	aluminium	CFRP–steel	steel	CFRP	
CTE [$\mu\text{m/m/K}$]	12	12	22	5 ^{a)}	12	3	
Example	Effelsberg	IRAM	Onsala	IRAM		ALMA	
$\lambda_{\text{min}} [\text{mm}]/\nu_{\text{min}} [\text{GHz}]$	30/10	1/300	3/100	1/300	0.375/800	0.375/800	
$\Delta T [^{\circ}\text{C}]$	\lesssim	5	0.5	1.25	2.5	0.5	2

^{a)} estimated value for a combination of CFRP and steel.

Von Hoerner and collaborators did measurements to determine representative temperature differences of open telescope structures, for day time with sunshine and night time with radiative cooling towards the sky. The obtained values were $\Delta T = 4^{\circ}\text{C}$ for full sunshine and $\Delta T = 0.8^{\circ}\text{C}$ during the night [von Hoerner 1975 a].

From these temperature measurements they derived estimates of the reflector diameter of telescopes planned to open the millimetre wavelength region for observation [von Hoerner 1975 a, Findlay & von Hoerner 1972]. Compared to these temperature estimates ΔT (night and day) it can be seen from Table 13.1 that the IRAM 30-m telescope and the Onsala 20-m telescope need thermal control, as actually done by application of climatisation on the IRAM 30-m telescope and by protecting the Onsala telescope by a radome. Table 13.1 indicates that the IRAM 15-m telescope (CFRP-steel) and the ALMA 12-m telescopes (CFRP) do not need thermal control while a 12-m telescope built from steel would require ventilation/climatisation to operate at short mm-wavelengths.

13.1.2 Estimated Thermal Behaviour of a BUS

Global thermal deformations of a BUS were discussed by Lamb [1992] in the context of the ALMA project. As illustrated in Fig. 13.3, estimates of the thermal behaviour of a BUS are derived for an axial temperature gradient ΔT_{fr} between the front (panel) and rear of a BUS (case a), for a temperature gradient ΔT_{LR} , ΔT_{UD} along the diameter of a BUS (case b) and for a radial gradient ΔT_r from the centre to the rim of a BUS (case c). There are examples that such gradients occur on operating telescopes, i.e. the IRAM 15-m telescope has a temperature gradient along the BUS, especially during the day, of $\Delta T_{UD} \approx 5$ to 10°C (Fig. 9.35), the Nobeyama 45-m BUS has a radial temperature gradient $\Delta T_r \approx \pm 2^\circ\text{C}$ with a reversal of direction of the temperature gradient between day and night (Fig. 9.41). The axial temperature gradient ΔT_{fr} through the 45-m BUS is approximately 0.5°C during the day and 0.2°C during the night [Akabane 1983].

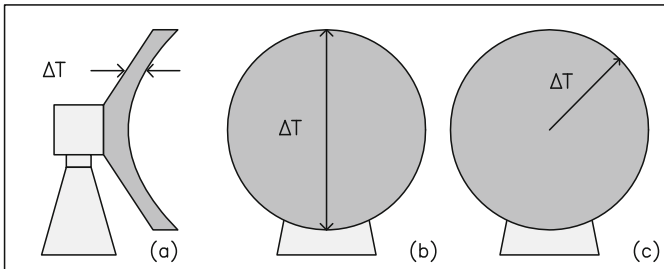


Fig. 13.3 Temperature gradient through a BUS in axial direction (a), along the BUS diameter (b) and in radial direction (c) [Adopted from Lamb [1992]].

Following Lamb [1992], the axial temperature gradient ΔT_{fr} (case a, Fig. 13.3) causes a focus change

$$\Delta f/f = 2f\alpha\Delta T_{fr}/\langle H \rangle \quad (13.2)$$

with f the focal length and $\langle H \rangle$ the average depth of the BUS. Using $f = nD$ with $n = 0.3$, $\langle H \rangle/D = 0.1$ (Table 2.5) and the stability criterion $\Delta f \lesssim \lambda/10$, Eq.(13.2) becomes

$$\Delta T_{fr} \lesssim 0.05 \lambda / (\alpha D) \quad (13.3)$$

If the telescope is not refocused this focal change leads to a surface error of $\sigma \approx 0.02 \Delta f/n^2$. Lamb [1992] reports that relation (13.2) applied to the SMA 6–m telescope BUS design [Raffin 1991] gives for $\alpha = 3 \mu\text{m/m/K}$ (CFRP) the value $\Delta f = 0.054 \text{ mm}/^\circ\text{C}$ that is two times larger than $\Delta f = 0.027 \text{ mm}/^\circ\text{C}$ obtained from a FEM calculation. When applying relation (13.2) to the IRAM 30–m telescope BUS (steel) the value is $\Delta f = 0.65 \text{ mm}$ while the FEM calculation gives $\Delta f = 0.85 \text{ mm}$.

Following Lamb [1992] and using $\langle H \rangle/D = 0.1$, a temperature gradient $\Delta T_{LR} = \Delta T_{UD}$ across the BUS (case b, Fig. 13.3) causes a pointing error (squint)

$$\Delta \theta = \alpha \langle H \rangle \Delta T_{LR} / (2D) = 0.05 \alpha \Delta T_{LR} \quad (13.4)$$

but no associated surface error. Using the stability criterion $\Delta \theta \lesssim \theta/10 = (\lambda/D)/10 \approx 1/10$ beam width, Eq.(13.4) becomes

$$\Delta T_{LR} \lesssim 2 \lambda / (\alpha D) \quad (13.5)$$

Again following Lamb, for the SMA 6–m telescope BUS (steel) as an example, relation (13.4) gives $\Delta \theta = 0.3 \text{ arcsec}$ for $\Delta T_{LR} = 2^\circ\text{C}$ while the FEM calculation gives $\Delta \theta = 0.7 \text{ arcsec}$. For the IRAM 30–m telescope BUS (steel) relation (13.4) gives $\Delta \theta = 0.12 \text{ arcsec}$ while the FEM calculation gives $\Delta \theta = 0.06 \text{ arcsec}$, for $\Delta T_{LR} = 1^\circ\text{C}$.

Finally following Lamb [1992], a radial temperature gradient ΔT_r (case c, Fig. 13.3) causes a focus change

$$\Delta f = n^2 \alpha D \Delta T_r \quad (13.6)$$

and a surface error of $\sigma = 0.02 \alpha \langle H \rangle \Delta T_r$. Using again the stability criterion $\Delta f \lesssim \lambda/10$, $n = 0.3$ and $\langle H \rangle/D = 0.1$, Eq.(13.6) becomes

$$\Delta T_r \lesssim \lambda / (\alpha D) \quad (13.7)$$

For the IRAM 30–m telescope BUS (steel) relation (13.6) gives $\Delta f = 0.032 \text{ mm}$, while the FEM calculation gives $\Delta f = 0.15 \text{ mm}$, for $\Delta T_r = 1^\circ\text{C}$.

Keeping in mind that the relations describe a global thermal behaviour, the temperature tolerances ΔT_{fr} , ΔT_{LR} and ΔT_r are summarized in Table 13.2 for a number of BUS configurations. The values of Table 13.2 indicate that the temperature gradient ΔT_{fr} through the BUS in axial direction (front to rear) is the critical temperature constraint. This temperature gradient determines the focus stability of the reflector (BUS).

Table 13.2 Temperature Tolerances of BUS Constructions (in °C).

Reflector Diameter D	100 m	30 m	20 m	15 m	12 m	Relation
Material	steel	steel	aluminium	CFRP–steel	CFRP	
CTE [$\mu\text{m}/\text{m}/\text{K}$]	12	12	22	5 ^{a)}	3	
Example	Effelsberg	IRAM	Onsala	IRAM	ALMA	
λ [mm]/ ν [GHz]	30/10	1/300	3/100	1/300	0.375/800	
ΔT_{fr}	\lesssim 1.3	0.15	0.35	0.7	0.5	(13.3)
ΔT_{LR}	\gtrsim large	5.5	14	26	20	(13.5)
ΔT_{r}	\gtrsim 25	3	7	13	10	(13.7)

^{a)} estimated value for a combination of CFRP and steel.

13.1.3 Estimated Thermal Behaviour of an Alidade/Fork Support

The thermal deformations of an alidade or fork support cause a pointing error and/or a path length error. The temperature induced pointing error along the EL-axis of an alidade or fork (see Figs. 9.5.a, 9.11) is

$$\Delta\varepsilon \approx \alpha L \Delta T / B = \alpha L (\Delta T / \Delta t) \Delta t / B \quad (13.8)$$

with ΔT the temperature difference between the alidade towers ($\Delta T = T_{A1} - T_{A2}$) or the fork arms ($\Delta T = T_L - T_R$), α the CTE of steel and L and B the height/length and separation of the alidade towers and fork arms. For a tolerable value $\Delta\varepsilon$ is the tolerable temperature difference ΔT derived from Eq.(13.8). As explained in Sections 9.1.2 and 9.1.3, the pointing error perpendicular to the EL-axis cannot reliably be estimated from a simple relation since rotation of the alidade/fork arms seem to play a role. Nevertheless, taking Eq.(13.8) as an estimate of the elevation and cross elevation pointing error, assuming that $B \approx L$ and using the condition $\Delta\varepsilon \lesssim \Delta\theta \approx (\lambda/D)/10 \approx 1/10$ beam width, Eq.(13.8) becomes

$$\Delta T \lesssim 0.1 \lambda / (\alpha D) \quad (13.9)$$

The path length variation is important for interferometer/VLBI operation and can be estimated from

$$\Delta L \approx \alpha L \Delta T = \alpha L (\Delta T / \Delta t) \Delta t \quad (13.10)$$

with L the height/length of the alidade or fork arm and $\Delta T = (\Delta T / \Delta t) \Delta t$ the change of the steel temperature within the time interval Δt . Between regular calibrations of an interferometer array at time intervals Δt the variation ΔL should not exceed the tolerable value $\Delta L \lesssim \lambda/10$ so that $\Delta T \lesssim 0.1 \lambda / \alpha L$. From the condition $\Delta L / \Delta t \lesssim 0.1 \lambda / \Delta t$ follows the tolerable change $\Delta T / \Delta t$ and the time Δt between calibrations. The values ΔT and Δt are related to the rate of change of the ambient air temperature (Fig. 4.9) and the rate of change of insolation.

13.1.4 Estimated Thermal Behaviour of Panels

An estimate of the tolerable thermal behaviour of a panel is not easy since there are different panel constructions (like plates and honeycomb panels) and panel supports (like screws, hinges, actuators) and different panel frames and frame supports. The material of a panel can be different from that of the BUS, leading to differential thermal expansion that may act on the panel or the panel frame. For a plate, attached at the corner points to the BUS, von Hoerner [1977 b] derived the central deformation Δz_{\max} (sag) under the influence of a temperature gradient ΔT_p through the panel

$$\Delta z_{\max} \approx (1/8) \alpha \ell (\ell/d) \Delta T_p \quad (13.11)$$

with ℓ the dimension of the panel and d its thickness (Fig. 9.58). Relation (13.11) describes thermal panel buckling that, if affecting many (all) panels of a reflector, acts with the effective surface rms value $\sigma_T \approx \Delta z_{\max}/3$ [Greve & Morris 2005] that can be used in the *Ruze* relation Eq.(12.24). As will be explained in Section 13.3, the contribution of thermal panel buckling should not exceed $\sim 1/4$ of the total reflector surface rms value, which should not exceed $\lambda_{\min}/16$. Combining these conditions with relation (13.11) gives

$$\Delta z_{\max}/3 \approx 0.04 \alpha \ell (\ell/d) \Delta T_p \approx \sigma_T \lesssim \lambda/64 \quad (13.12)$$

or

$$\Delta T_p \lesssim 0.4 \lambda / \alpha \ell (\ell/d) \quad (13.13)$$

For an Al-honeycomb panel with aspect ratio $\ell/d = 1 \text{ m}/2 \text{ cm} = 50$, to be used at $\lambda = 1 \text{ mm}$, relation (13.13) gives $\Delta T_p \lesssim 0.4^\circ \text{C}$. From relation (13.13) follows quantitatively that a small panel (small ℓ) and a panel with a small aspect ratio (small ℓ/d) allows a larger temperature gradient ΔT_p . A rather simple thermal model calculation can give the value ΔT_p for instance under the extreme condition of sunshine or cooling towards the cold sky (Section 11.6).

13.2 System Alignment Tolerances

13.2.1 Displacements and Tilts of Main Reflector and Subreflector

The main reflector, the subreflector and other mirrors of a radio telescope must have and keep the correct contour and correct alignment, i.e. the distance, centring and tilt (Figs. 2.1, 2.2, 2.3), under the influence of gravity, temperature and wind. The possible system misalignments of a Cassegrain (Gregory) system are illustrated in Fig. 13.4, the misalignment parameters are summarized in Table 13.3. From a system misalignment δ follows a characteristic wavefront (phase) deformation $\Delta \varphi = (2\pi/\lambda)\delta$ in which, according to diffraction theory, δ should not exceed the tolerable

value of $\sim \lambda/16$ (rms) or $\sim \lambda/10$ as maximum amplitude. From these conditions follow the tolerable structural deformation that limits the tolerable thermal inhomogeneity or thermal instability. Dependent on the alignment error, the corresponding wavefront deformation causes a focus error (FE), a pointing error (PE), a path length error (PLE) or combinations of these (Table 13.3).

The orthogonal displacements $\Delta U'$ and $\Delta V'$ of the main reflector and $\Delta u'$, $\Delta v'$ of the subreflector (Fig. 13.4) can be combined to the effective lateral displacements $\Delta U = \sqrt{(\Delta U')^2 + (\Delta V')^2}$ and $\Delta u = \sqrt{(\Delta u')^2 + (\Delta v')^2}$.

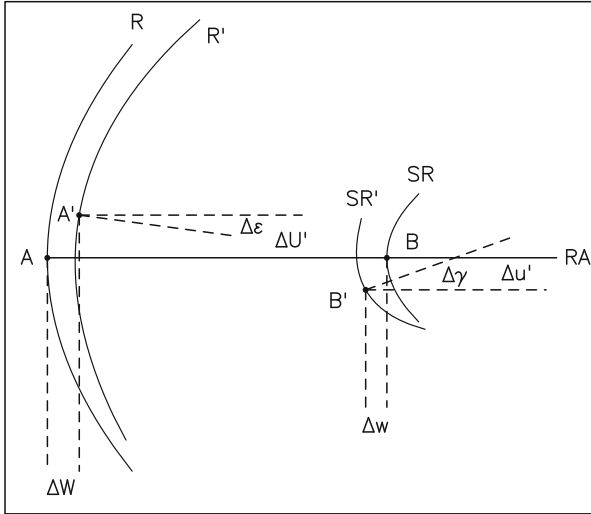


Fig. 13.4 Illustration of misalignments of a Cassegrain system. The reflector moves from R to R' and tilts ($\Delta\epsilon$), the subreflector moves from SR to SR' and tilts ($\Delta\gamma$). The displacements ΔW , Δw are along the reflector axis (RA), the displacements $\Delta U'$ (and $\Delta V'$) and $\Delta u'$ (and $\Delta v'$) are perpendicular to the reflector axis. Further details in Table 13.3.

Approximate values of the temperature induced shifts $\Delta U(\Delta T)$, $\Delta W(\Delta T)$, $\Delta u(\Delta T)$, $\Delta w(\Delta T)$, tilts $\Delta\epsilon(\Delta T)$, $\Delta\gamma(\Delta T)$ and focus change $\Delta f(\Delta T)$ are derived for a general geometry of a radio telescope and temperature differences ΔT in the BUS and quadripod. It is assumed that a shift and tilt of the subreflector is due to a thermal expansion of the quadripod. Using the fact that the BUS depth $\langle H \rangle$ to diameter D ratio is $\langle H \rangle/D \approx 0.1$ (Table 2.5), that the subreflector diameter d to main reflector diameter D is $d/D \approx 1/10$ to $1/15$, that the quadripod length is $L \approx 1.3 f = 1.3 n D = 0.4 D$, that the subreflector position is $|c - a|/f \approx 1/10$ to $1/15$ (Figs. 2.2, 2.3; $|c - a| = f\sqrt{5}$) and denoting by

- ΔT a uniform temperature change of the BUS,
- ΔT_{fr} a temperature gradient through the BUS from front to rear (Fig. 13.3.a),
- ΔT_{LR} a temperature gradient across the BUS (in the direction Left-Right or

Table 13.3 Alignment Errors.

Notation	Type of Misalignment ^{b)}	Telescope Component	FE, PE ^{c)} PLE
Main Reflector			
ΔU (ΔV)	lateral displacement	BUS/BUS support	PE
ΔW	axial displacement	BUS/BUS support	FE, PLE
$\Delta \varepsilon$	tilt	BUS/BUS support	PE
Δf	change in focal length	BUS	FE, PLE
Receiver(PF) ^{a) d)}			
ΔR_{PF}	axial displacement	QP, RE support	FE, PLE
ΔL_{PF}	lateral displacement	QP, RE support	PE
Subreflector			
Δu (Δv)	lateral displacement	QP	PE
Δw	axial displacement	QP	FE, PLE
$\Delta \gamma$	tilt	QP, SR support	PE
Receiver(CF, GF) ^{a) d)}			
ΔR_{CF}	axial displacement	QP, RE support	FE, PLE
ΔL_{CF}	lateral displacement	QP, RE support	PE

^{a)} PF: prime focus, CF: Cassegrain focus, GF: Gregory focus;

^{b)} BUS: backup structure, QP: quadripod, RE: receiver, SR: subreflector;

^{c)} FE: focus error, PE: pointing error, PE: path length error.

^{d)} the receiver misalignments are not discussed, they are not directly dependent on the telescope structure.

Up–Down etc.) (Fig. 13.3.b),

– ΔT_r a temperature gradient in radial direction of the BUS (Fig. 13.3.c),

– ΔT_Q a temperature difference between quadripod legs,

then the shifts and tilts of the main reflector (mr) and subreflector (sr) and the change of the main reflector focal length are approximately

$$\Delta U(\text{mr}) \approx \alpha (D/2) \Delta T_{LR} \quad (13.14)$$

$$\Delta W(\text{mr}) \approx \alpha \langle H \rangle \Delta T = 0.1 \alpha D \Delta T \quad (13.15)$$

$$\Delta \varepsilon(\text{mr}) \approx \alpha \langle H \rangle \Delta T_{LR}/D = 0.1 \alpha \Delta T_{LR} \quad (13.16)$$

$$\Delta f_1(\text{mr}) \approx 20 n^2 \alpha D \Delta T_{fr} = 1.8 \alpha D \Delta T_{fr} \quad (13.17.a)$$

$$\Delta f_2(\text{mr}) \approx 1.6 n^2 \alpha D \Delta T_r = 0.15 \alpha D \Delta T_r \quad (13.17.b)$$

$$\Delta u(\text{sr}) \approx 0.5 \alpha L \Delta T_Q = 0.2 \alpha D \Delta T_Q \quad (13.18)$$

$$\Delta w(\text{sr}) \approx 0.5 \alpha L \Delta T_Q = 0.2 \alpha D \Delta T_Q \quad (13.19)$$

$$\Delta \gamma(\text{sr}) \approx 0.5 \alpha L \Delta T_Q/d = 2 \alpha \Delta T_Q \quad (13.20)$$

In the derivation of Eq.(13.17) the equation of the parabolic reflector is used with $(D/2)^2 = 4 f \bar{z}$ and $\bar{z} \Delta f + f \Delta \bar{z} = 0$ or $\Delta f = 16 n^2 \Delta \bar{z}$. For the radial temperature gradient ΔT_r the relation $\Delta \bar{z} = \alpha \langle H \rangle \Delta T_r$ is used, for the axial temperature gradient ΔT_{fr} the relation $\Delta \bar{z} = (1/8) \alpha D (D/\langle H \rangle) \approx \alpha D$. The relations (13.2), (13.4), (13.6) derived by Lamb [1992] and (13.17.a), (13.16), (13.17.b) agree within a factor of 2.

The wavefront deformations associated with the alignment errors were derived by Ruze [1969] and Zarghamee & Antebi [1985]. The relations connect the structural deformations ΔU , ΔW , $\Delta \varepsilon$, Δf and Δu , Δw , $\Delta \gamma$ with geometrical deformations δ_U , δ_W , δ_ε , δ_f and δ_u , δ_w , δ_γ in the corresponding wavefront deformations $\Delta \varphi = (2\pi/\lambda)\delta$. Following Ruze and Zarghamee & Antebi and using normalized polar coordinates of the aperture plane (ρ, Θ ; $0 \leq \rho \leq 1$, $0 \leq \Theta \leq 2\pi$) and the relations of the primary focus system (p) and the Cassegrain/Gregory system (s)

$$\sin \alpha_p(\rho) = (\rho D/2f)/[1 + (rD/4f)^2] = (\rho/2n)/[1 + (\rho/4n)^2] \quad (13.21)$$

$$\sin \alpha_s(\rho) = (\rho D/2F)/[1 + (rD/4F)^2] = (\rho/2Mn)/[1 + (\rho/4Mn)^2] \quad (13.22)$$

(D = reflector diameter, n = focal ratio main reflector = f/D , M = magnification of the Cassegrain/Gregory system, $F = Mf$), the corresponding geometrical deformations $\delta = \delta(\rho, \Theta)$ are given by Eqs.(13.23–13.33).

Primary Focus System :

$$\Delta U: \quad \delta_U = \sin(\alpha_p) \sin\Theta \times \Delta U \quad (13.23)$$

$$\Delta W: \quad \delta_W = [1 - \cos(\alpha_p)] \times \Delta W \quad (13.24)$$

$$\Delta \varepsilon: \quad \delta_\varepsilon = D [(\rho/2) + n \sin(\alpha_p)] \sin\Theta \times \Delta \varepsilon \quad (13.25)$$

$$\Delta f: \quad \delta_f = 16 n^2 \times \Delta z(\rho) \quad (13.26)$$

Cassegrain/Gregory System :

$$\Delta U: \quad \delta_U = \sin(\alpha_s) \sin\Theta \times \Delta U \quad (13.27)$$

$$\Delta W: \quad \delta_W = [1 - \cos(\alpha_s)] \times \Delta W \quad (13.28)$$

$$\Delta \varepsilon: \quad \delta_\varepsilon = D [(\rho/2) + n \sin(\alpha_p)] \sin\Theta \times \Delta \varepsilon \quad (13.29)$$

$$\Delta f: \quad \delta_f = 16 n^2 \times \Delta z(\rho) \quad (13.30)$$

$$\Delta u: \quad \delta_u = [\sin(\alpha_p) \mp \sin(\alpha_s)] \sin\Theta \times \Delta u \quad (13.31)$$

$$\Delta w: \quad \delta_w = [(1 - \cos(\alpha_p)) + (1 - \cos(\alpha_s))] \times \Delta w \quad (13.32)$$

$$\Delta \gamma: \quad \delta_\gamma = |c-a| [\sin(\alpha_p) + M \sin(\alpha_s)] \sin\Theta \times \Delta \gamma \quad (13.33)$$

The $-$ sign in Eq.(13.31) holds for the Cassegrain system, the $+$ sign for the Gregory system. The relations δ can be used in Eq.(12.13) to calculate the actual diffraction pattern caused by a misalignment. It is seen that the lateral displacements and tilts produce coma-like wavefront deformations, the other wavefront deformations are radial symmetric. Fig. 13.5 illustrates these wavefront deformations and the corresponding beam patterns (see also Fig. 12.5).

The maxima of the deformations $\bar{\delta}$ occur at the edge of the aperture ($\rho = 1$). For the primary focus system and the Cassegrain/Gregory system they are $\bar{\delta}_U \approx \Delta U$, $\bar{\delta}_u \approx \Delta u$, $\bar{\delta}_W \approx 0.8 \Delta W$, $\bar{\delta}_w \approx 0.8 \Delta w$, $\bar{\delta}_\varepsilon \approx 2.65 f \Delta \varepsilon$, $\bar{\delta}_f = 16 n^2 \Delta z$ and $\bar{\delta}_\gamma \approx 2.65 |c-a| \Delta \gamma$. The combination of the relations $\bar{\delta}$ with the temperature dependent shifts $\Delta U(\Delta T)$, $\Delta W(\Delta T)$, $\Delta u(\Delta T)$, $\Delta w(\Delta T)$, tilts $\Delta \varepsilon(\Delta T)$, $\Delta \gamma(\Delta T)$ and focal

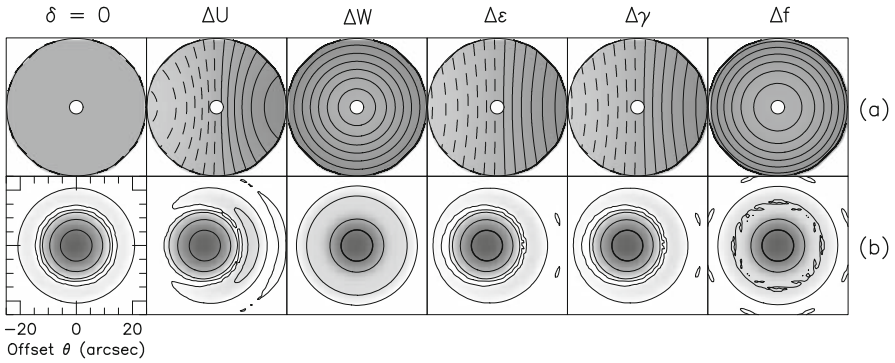


Fig. 13.5 (a) System alignment errors and corresponding wavefront deformations, contours in steps of 0.040 mm, (b) corresponding beam patterns in arcseconds (IRAM 30-m telescope at 230 GHz), contours - 3 dB, - 10 dB, - 20 dB, - 30 dB.

change $\Delta f(\Delta T)$, Eqs.(13.14) – (13.20), and the condition that the wavefront deformation at the edge of the aperture should not exceed $\lambda/10$, i.e. $\bar{\delta}_1 \lesssim \lambda/10$, gives the tolerances of the **BUS** temperature

$$\Delta U: \quad \Delta T_{LR} \lesssim 0.2 \lambda / (\alpha D) \quad (13.34)$$

$$\Delta W: \quad \Delta T \lesssim \lambda / (\alpha D) \quad (13.35)$$

$$\Delta \epsilon: \quad \Delta T_{LR} \lesssim 1.25 \lambda / (\alpha D) \quad (13.36)$$

$$\Delta f_1: \quad \Delta T_{fr} \lesssim 0.05 \lambda / (\alpha D) \quad (13.37.a)$$

$$\Delta f_2: \quad \Delta T_r \lesssim 0.7 \lambda / (\alpha D) \quad (13.37.b)$$

and in a similar way the tolerances of the **quadripod** temperature

$$\Delta u, \Delta w: \quad \Delta T_Q \lesssim 0.2 \lambda / (\alpha L) \approx 0.5 \lambda / (\alpha D) \quad (13.38)$$

$$\Delta \gamma: \quad \Delta T_Q \lesssim 0.25 \lambda / (\alpha L) \approx 0.6 \lambda / (\alpha D) \quad (13.39)$$

13.2.2 Temperature induced Pointing Errors

The temperature induced lateral shifts $\Delta U(\Delta T)$, $\Delta u(\Delta T)$ and tilts $\Delta \epsilon(\Delta T)$, $\Delta \gamma(\Delta T)$ of the main reflector and the subreflector (Table 13.3) introduce coma-like wavefront deformations and by this a pointing error. The pointing errors are calculated from the relations published by Ruze [1969] and Zarghamee & Antebi [1985] taking into account the beam deviation factor (see Baars [2007]) of the main reflector (Bdf) and the Cassegrain (Gregory) system (BDF). The values are $Bdf \approx 0.75$ and $BDF \approx 1$ for radio telescopes with main reflector focal ratio $n \approx 0.3$, magnification $M \approx 20$ of the Cassegrain/Gregory system and an edge taper between - 10 dB and

– 15 dB. Concentrating on the commonly used Cassegrain system with $F = Mf$, the corresponding pointing errors $\Delta\theta(\Delta T)$ [rad] are

$$\Delta U(\text{mr}): \quad \Delta\theta = \quad (\text{BDF}/F) \times \Delta U \quad (13.40)$$

$$\Delta \varepsilon(\text{mr}): \quad \Delta\theta = \quad (1 + \text{BDF}) \times \Delta \varepsilon \quad (13.41)$$

$$\Delta u(\text{sr}): \quad \Delta\theta = \quad (\text{BDF}/f) \times \Delta u - (\text{BDF}/F) \times \Delta u \quad (13.42)$$

$$\Delta \gamma(\text{sr}): \quad \Delta\theta = \quad |c - a| (\text{BDF} + \text{BDF}) \Delta \gamma / f \quad (13.43)$$

Using the relations (13.14), (13.16), (13.18) and (13.20), $n = 0.3$, $M = 20$, $|c - a|/f = 0.1$ and $d/D = 0.1$, for a pointing stability of $\Delta\theta \lesssim \theta/10 \approx 1/10$ beam width the required thermal stability of the BUS and quadripod is

$$\Delta U: \quad \Delta T_{\text{LR}} \lesssim 1.2 \lambda / (\alpha D) \quad (13.44)$$

$$\Delta \varepsilon: \quad \Delta T_{\text{LR}} \lesssim 0.6 \lambda / (\alpha D) \quad (13.45)$$

$$\Delta u: \quad \Delta T_{\text{Q}} \lesssim 0.8 \lambda / (\alpha L) \approx 0.2 \lambda / (\alpha D) \quad (13.46)$$

$$\Delta \gamma: \quad \Delta T_{\text{Q}} \lesssim 0.1 \lambda / (\alpha L) \approx 0.4 \lambda / (\alpha D) \quad (13.47)$$

13.2.3 Alignment Errors: Temperature Tolerance Estimates

Using the results of the preceding Sections, Table 13.4 lists the temperature tolerances of a large cm-wavelength telescope and several mm-wavelength telescopes built from steel, or aluminium, or CFRP or a combination of CFRP and steel. The values are calculated for those temperature tolerance relations that give the tightest constraint, the corresponding relations are indicated in the table. The table indicates that the BUS is most sensitive to temperature gradients ΔT_{LR} and ΔT_{fr} . The temperature tolerances are tight for the quadripod, for all telescope constructions.

From Table 13.4 it is seen that a large cm-wavelength telescope operating at $\lambda = 3$ cm or longer wavelengths allows temperature differences in the BUS and quadripod (feed leg) of 5 to 10° C; such temperature differences are for instance observed on the Effelsberg 100-m telescope. However, if operating at $\lambda = 3$ mm as used for instance for VLBI at Effelsberg, the temperature tolerances become tight and a factor 5 to 10 smaller. The values in Table 13.4 obtained for a 30-m mm-wavelength telescope built from steel indicate the necessity of passive and active thermal control, as actually installed on the IRAM 30-m telescope. A 20-m mm-wavelength telescope built from aluminium has small temperature tolerances, especially with respect to a focal change of the main reflector and the thermal stability (pointing) of the quadripod. Such telescopes, like the Onsala 20-m telescope, operate in a ventilated radome. Table 13.4 indicates that the thermal stability is very relaxed for a mm-wavelength telescope built exclusively from CFRP; on such telescopes the thermal stability of the fork support (made of steel with insulation) may ultimately determine the pointing stability. Table 13.4 indicates that a high thermal stability of the alidade and fork support is required to guarantee a good pointing stability.

Table 13.4 Temperature Tolerances of the BUS, Quadripod and Telescope Support (in °C).

Reflector Diameter D	100 m	30 m	20 m	15 m	12 m	Relation
Material	steel	steel	aluminium	CFRP–steel	CFRP	
CTE [$\mu\text{m}/\text{m}/\text{K}$]	12	12	22	5 ^{a)}	3	
Example	Effelsberg	IRAM	Onsala	IRAM	ALMA	
λ [mm]/ ν [GHz]	30/10	1/300	3/100	1/300	0.375/800	
Main Reflector						
Shift ΔU :	$\Delta T_{LR} \lesssim$	5	0.5 ($\lesssim 0.5$) ^{b)}	1.5	0.7 (2–15) ^{d)}	2 ($\lesssim 1$) ^{e)} (13.34)
Shift ΔW :	$\Delta T \lesssim$	25	3	7	13	10 (13.35)
Tilt $\Delta \varepsilon$:	$\Delta T_{LR} \lesssim$	15	2	4	8	6 (13.45)
Focus Δf_1 :	$\Delta T_{fr} \lesssim$	1.3	0.15 (0–1) ^{b)}	0.35	0.7	0.5 (13.37.a)
Focus Δf_2 :	$\Delta T_r \lesssim$	17.5	2 ($\lesssim 1 $) ^{c)}	5	9	7 ($\lesssim 7 $) ^{e)} (13.37.b)
Quadripod (Subreflector)						
Shift $\Delta u, \Delta w$:	$\Delta T_Q \lesssim$	5	0.5	1.5	0.7	2 (13.46)
Tilt $\Delta \gamma$:	$\Delta T_Q \lesssim$	7.5	1	2	5	3 (13.47)
Alidade, Fork Support						
Beam Width ^{f)} (arc sec) θ		70	8	35	16	7 (12.14)
	$\Delta T \lesssim$	2.5 ^{g)}	0.3 ^{g)}	1.2 ^{g)}	0.5 ^{h)}	0.2 ^{h)} (13.9)

^{a)} estimated value for a combination of CFRP and steel;

^{b)} measured value, Fig. 9.47 and Table 9.9.e;

^{c)} measured value, Table 9.9.e;

^{d)} measured value, Fig. 9.35 and Table 9.9.e;

^{e)} measured value, ALMA VertexRSI prototype telescope, Table 9.9.e.

^{f)} for the diameter D and wavelength λ , Eq.(12.14).

^{g)} assuming an alidade support, ^{h)} assuming a fork support.

The derivation of the temperature tolerances uses the condition that the maximum of the deformation δ is smaller than $\sim \lambda/10$ and that a pointing error is smaller than $\sim 1/10$ of the beam width. However, a telescope operates also under the influence of gravity and wind. Allowing for equal influences on the telescope performance, the temperature tolerances of Tables 13.2 and 13.4 may need to be reduced by a factor of $\sim 1/\sqrt{3}$ or $\sim 40\%$.

13.3 Random Reflector Errors

The discussion of a radio telescope's performance often concentrates on the reflector surface accuracy (σ) that is affected by gravity, temperature and wind induced deformations of the BUS. The BUS deformations appear as panel misalignments. The gravity induced deformations are elevation dependent (E). To simplify the discussion one may assume that the gravity (g), temperature (T) and wind (w) forces produce random surface deformations that are characterized by corresponding rms values $\sigma_g(E)$, σ_T , σ_w . The random panel surface error and adjustment error is σ_p . Independent random deformations, related to the best-fit surface, can be added

quadratically so that the total reflector surface accuracy $\sigma(E)$ is

$$\sigma(E) = \sqrt{\sigma_g(E)^2 + \sigma_T^2 + \sigma_w^2 + \sigma_p^2} \quad (13.48)$$

The rms value $\sigma(E)$ can be used in the *Ruze* relation Eq.(12.24) to calculate the reduction of the aperture efficiency $\eta(E)$. At the shortest wavelength of observation λ_{\min} a tolerable reduction of the aperture efficiency not exceeding, say, $\sim 30\%$ requires that

$$\sigma(E) \lesssim \lambda_{\min}/16 \quad (13.49)$$

A realistic distribution of the error contributions, in particular for design considerations, is $\sigma_g(E) \approx \sigma_T \approx \sigma_w \approx \sigma_p = \sigma(E)/4$. With this assumption the tolerance condition of temperature induced random surface deformations is

$$\sigma_T \lesssim \lambda_{\min}/64 \quad (13.50)$$

The situation with respect to the IRAM 30-m telescope is illustrated in Fig. 13.6. From temperature measurements of the BUS and yoke and FEM calculations it is found that $\sigma_T \approx 0.02$ mm. At the shortest wavelength of observation $\lambda_{\min} = 1.3$ mm (230 GHz) this value σ_T agrees with Eq.(13.50). For $\sigma_p \approx 0.05$ mm (derived from holography measurements) and $\sigma_g \approx 0.03$ mm for intermediate high and low elevations (derived from FEM calculations) the values σ_T , $\sigma(T,p) = \sqrt{(\sigma_T)^2 + (\sigma_p)^2}$ and $\sigma(T,p,g) = \sqrt{(\sigma_T)^2 + (\sigma_p)^2 + (\sigma_g)^2}$ are shown in Fig. 13.6.

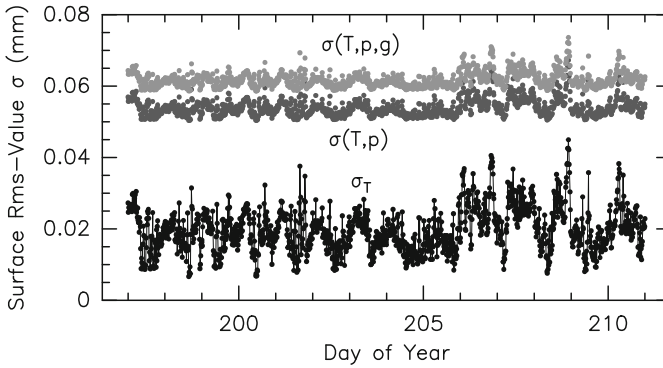


Fig. 13.6 IRAM 30-m telescope. Thermal rms value σ_T derived from temperature measurements of the BUS and yoke and FEM calculations. $\sigma(T,p)$ is the rms value of the reflector taking a panel and adjustment error of $\sigma_a = 0.05$ mm into account (measured by holography). $\sigma(T,p,g)$ is the rms value taking in addition a gravity deformation of $\sigma_g = 0.03$ mm into account.

There remains the question whether a BUS can have random temperature distributions that cause random temperature induced surface deformations. Obviously, in

order to investigate this question a BUS must have many temperature sensors as it is the case for the IRAM 30-m telescope and the ALMA VertexRSI 12-m prototype telescope. The distribution of the 104 temperatures measured on the climatized BUS of the IRAM 30-m telescope (Fig. 9.45) is shown in Fig. 13.7, once for a particular day of measurement and once for 10 days of measurements. The distribution of the temperatures with respect to the average value is Gaussian with $\sim 0.2^\circ\text{C}$ dispersion. Fig. 13.7 shows also the temperature distribution of the BUS of the ALMA VertexRSI 12-m prototype telescope (24 sensors). The distribution is approximately Gaussian with $\sim 2^\circ\text{C}$ dispersion.

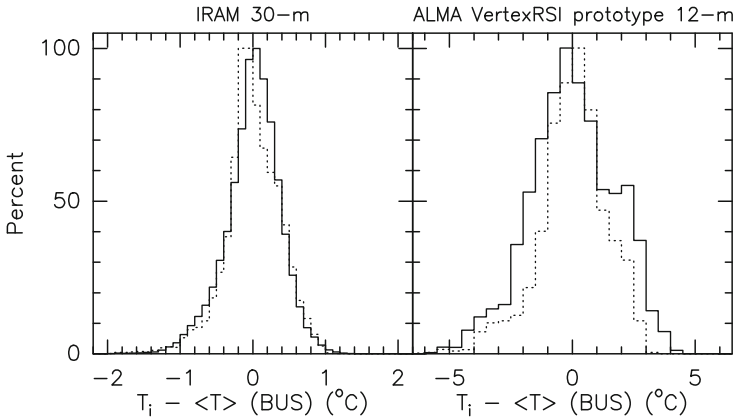


Fig. 13.7 Temperature distribution of the BUS of the IRAM 30-m telescope (104 temperature sensors) and the BUS of the ALMA VertexRSI 12-m prototype telescope (24 temperature sensors). Dashed line: data of a particular day, solid line: data of 10 days.

A measurement of temperature induced reflector surface deformations is difficult and especially so at the spatial resolution of the panels. Using the measured temperatures of the IRAM 30-m telescope BUS, the FEM calculation provides temperature induced surface deformations δ_T at the 260 support points of the panels frames (see Chapter 6). As shown in Fig. 13.8, the distribution of the deviations δ_T is Gaussian with $\sim 0.02\text{ mm}$ dispersion. However, the Zernike polynomial analysis (Fig. 15.2) indicates that the temperature induced surface deformations contain a systematic component of higher order defocus ($L = 3$) and astigmatism ($L = 12, 15$). Nevertheless, for many cases the rms value σ_T can be based on a Gaussian distribution of surface deformations δ_T and Eq.(13.48) can be applied.

The tolerance criteria for temperature induced random deformations σ_T of a centimetre, millimetre and sub-mm wavelength telescope are summarized in Table 13.5. The table gives the material of which the BUS is built and a typical length L of a tube/plate member of the BUS. From the given value $\sigma(E) \lesssim \lambda_{\min}/16$ are derived the tolerable thermal surface deformations σ_T and the thermal stability $\Delta L_T/\sigma_T = \alpha L/\sigma_T$, for $\Delta T = 1^\circ\text{C}$.

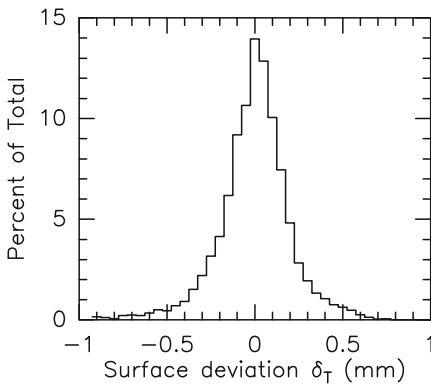


Fig. 13.8 Thermal deformations δ_T of the IRAM 30-m telescope reflector surface derived from temperature measurements and FEM calculations. Data for one day, temperature measurements every 1/2 hour.

Table 13.5 Thermal Tolerance Criteria for Random BUS/Reflector Surface Deformations.

Telescope for	Reflector Diameter [m]	Material	$\lambda_{\min} / \nu_{\min}$ [mm / GHz]	$\sigma(E)$ [mm]	$\sigma_T = \sigma(E)/4$ [mm]	L [m]	$\alpha L / \sigma_T$
centimetre	50–100	steel	20 / 15	1.25	0.312	10	2.5
millimetre	20–50	steel/Al	1 / 300	0.06	0.015	3	0.8/0.4
sub-millimetre	10–15	CFRP	0.35 / 850	0.02	0.005	1	5

13.4 Design Specifications and Error Budget

A telescope is built to observe in a specified wavelength region with a beam width $\theta \approx \lambda/D$ and sensitivity $S \propto D^2 \exp[-(4\pi R \sigma/\lambda)^2]$. For evaluation of the quality of a design, the expected telescope performance derived from a finite element and flexible body analysis [Kärcher 2006] is summarized in the error budget tables of the reflector surface precision and the pointing precision. These tables define the relative importance of gravity, temperature and wind and their individual contributions to the total error budget are separately listed. Table 13.6 is an example of the parameters of the error budget. The entries of the table give representative values for a 30 to 50-m diameter mm-wavelength telescope. With modern control technology, actuator panel supports and temperature sensors, some of the errors can be reduced using FEM generated look-up-tables (LUT) for correction. Some possibilities are entered in the table (see also Greve & Kärcher [2009]).

Table 13.6 Example of an Error Budget Table ^{a)}.

Surface Precision	rms-Deformations [μm]	Correction Method	Corrected [μm]
a) Gravity Influence			
BUS	< 65 ^{b)}	LUT-actuators	20
Panels	10		
b) Wind Influence (at 15 m/s)			
BUS	35		
Panels	15		
c) Temperature Influence			
BUS	35	T-sensors-FEM-actuators	20
Panels	15		
d) Manufacturing			
Panels	25		
Panel Alignment	50		
Total (RSS) ^{c)}	102		80

Pointing Precision	rms-Pointing ^{d)} [arcsec]	Correction Method	Corrected [arcsec]
a) Gravity Influence			
Alidade/Fork	1	(Inclinometer), FEM-LUT	0.5
BUS	10 ^{b)}	FEM-LUT	1.5
b1) Wind Influence (at 15 m/s)			
Alidade/Fork	2		
BUS	2		
Quadripod	1.5		
b2) Gust Influence (< 20 m/s)			
c) Temperature Influence			
Alidade/Fork	1-2	T-sensors-FEM-LUT	0.5
BUS	1.5	T-sensors-FEM-LUT	1
Quadripod	1.5	T-sensors-FEM-LUT	0.5
d) Encoders			
e) Servo Controller			
Total (RSS) ^{c)}	11		3.8 ^{e)}

^{a)} this table is based on error budget tables of the IRAM 30-m telescope [Baars et al. 1987] and the LMT/GMT [Kärcher 2006];

^{b)} homology deformations and correction of homology deformations;

^{c)} RSS: root-sum-square added;

^{d)} beam width $\theta = 24$ arcsec for $D = 30$ m and $\lambda = 3$ mm; $\theta/10 = 2.4$ arcsec.

^{e)} the value is lower during calm weather ($v < 10$ m/s).

Chapter 14

Optical Telescopes and Enclosures

Although the specific thermal aspects under discussion may be different for a radio telescope and an optical telescope, for instance concerning on the one hand the thermal stability of the reflector backup structure and on the other hand temperature induced man-made dome seeing, the physics and the treatment of thermal problems is nevertheless in many ways similar. The similarity of thermal issues is high for (sub)mm-wavelength radio telescopes and optical/IR telescopes, although an optical telescope is always covered by a dome. The structural similarities between mm-wavelength radio telescopes and optical telescopes are summarized in Table 14.1.

Table 14.1 Similarity of Radio Telescopes and Optical Telescopes.

Radio Telescope	Optical Telescope
Backup Structure and Panels	Mirror Cell and Mirror(s)
Yoke, Quadripod	Yoke, Telescope Tube, Spider, Cage
Pedestal, Alidade, Fork	Support Tower
Radome, Astrodome	Dome or Enclosure

Optical telescopes exist as ground-based telescopes and space telescopes, for visible, infrared and ultraviolet wavelengths. Evidently, the specification of the thermal behaviour and thus of the telescope structure is different for ground-based telescopes and space telescopes. While aspects of the thermal behaviour of ground-based telescopes include heat convection through the ambient air, the thermal interaction of telescopes in space is by radiation.

An optical telescope is affected by the global thermal environment *and* by the thermal environment inside the enclosure. Conventional optical telescopes are protected by a dome as shown in Fig. 14.1. The dome usually consists of a hemispherical steel structure with white painted or aluminium surfaces and insulation on the inside. During the night the slit of the dome is opened for observations, unless day time observations are also made. During the day the closed dome buffers the influence

of the thermal environment, and in particular solar radiation, so that the air and the telescope inside the dome remain at a temperature close to stable nighttime conditions. The air in the dome and the dome floor itself may be ventilated and cooled. This holds, in particular, also for a thick and heavy conventional optical mirror with a long thermal time constant. Ventilation may be applied on the heavy mirror rear side and on the mirror surface (flushing) to reduce mirror seeing. Additional care is taken to reduce, or avoid, heat sources in the dome or enclosure, for instance heat generated by the drives and the detector equipment, in order to reduce man-made dome seeing. The warm air generated in the telescope building may be exhausted at a place far away from the enclosure.



Fig. 14.1 Conventional dome with slit of the ESO 3.6-m telescope (La Silla, Chile) [Courtesy ESO, Germany].

Modern optical telescopes, as for instance the Multi-Mirror-Telescope (MMT), the ESO New-Technology-Telescope (NTT) and Very-Large-Telescope (VLT), the Large-Binocular-Telescope (LBT), the Gemini telescopes and other telescopes use more open box-type enclosures (VLT, Fig. 14.2) with passive and active thermal control, in particular through louvres and ventilation systems. The large modern telescopes may have a thin mirror (for instance the NTT, VLT) or a segmented thin mirror (Keck telescopes) of relatively short thermal time constant. The thin mirrors have active control of the contour. The design of several modern optical telescopes

and their enclosures is based on airflow studies and dynamic thermal model calculations.

A special optical telescope is the Infrared–Wavelength telescope where the investigated radiation of astronomical objects is at the same wavelength as the thermal radiation from the telescope and enclosure surfaces itself. Likewise, Solar Telescopes always point towards the Sun and receive the full thermal load of solar radiation. Special care of thermal influences is taken in the construction of these telescopes.



Fig. 14.2 Very–Large–Telescope VLT (Paranal, Chile) with box–type enclosure and louvers for ventilation with ambient air [Courtesy ESO, Germany].

There is one significant difference between a radio telescope and an optical telescope. The optical telescope provides a visible image of a star that can be used for pointing and guiding, and may be analysed for degradations of the telescope structure and the mirror. An active optic system can eliminate a significant part of the wavefront deformations and by this also the thermal deformations of the telescope structure and the mirror. A radio telescope does not provide a signal for guiding, which explains the significant operational efforts in the construction of a reliable pointing model.

In summary, with respect to thermal aspects the main engineering efforts in optical telescope constructions concern

- the telescope structure,
- the mirror and its cell and mirror seeing,
- the enclosure and its inside and outside seeing.

These aspects are treated in the textbooks *Reflecting Telescope Optics, I & II* by Wilson [1999], *Design and Construction of Large Optical Telescopes* by Bely (ed.) [2002] and many publications in Applied Optics, Optical Engineering etc. and publications by the International Society for Optical Engineering (SPIE) and SPIE Conference Proceedings.

Chapter 15

A Summary and Further Studies

15.1 A Summary of the Present State

Radio telescopes are built for observations from metre to sub-millimetre wavelengths (Table 1.1). The steerable telescopes have a parabolic reflector of 10 to 100-m diameter and the optics can be designed for observations in primary focus, Cassegrain focus or Gregory focus (Section 2.1). The telescopes have a support, i.e. a pedestal, an alidade or a fork, a reflector backup structure and panels and a quadripod with subreflector (Fig. 1.1, Chapter 2). The construction material is steel, aluminium, low thermal expansion reinforced carbon fibre plastic (CFRP) and invar, and concrete for the pedestal and foundation (Section 2.4). The design of a telescope is based on a finite element analysis, a flexible body analysis (which considers the telescope, the drives and the control system as one dynamical unit [Kärcher 2006, Gawronski 2007]) and static and/or dynamic thermal model calculations (Section 11.2 and 11.3). The backup structure can be a homologous design (Section 2.4.2). The technical efforts applied in the control of temperature (and wind) induced deformations must be seen in the context of the envisaged sensitivity and directivity, but also in the context of the time spent in focus and pointing measurements.

A telescope operates under the influence of gravity, temperature and wind. The gravity induced deformations of a telescope are derived from a finite element model that contains several 10 000 elements. The repeatable gravity induced deformations are considered in the pointing model of the telescope and the gain-elevation curve. If available, the gravity induced reflector surface deformations can be corrected with an active main reflector or active subreflector. As evident from the entries of Table 13.4, the cm-wavelength telescopes need a temperature uniformity of ~ 2 to 5°C that can be achieved with passive thermal protection; the mm/submm-wavelength telescopes need passive or passive and active thermal protection to obtain the required temperature uniformity of ~ 0.5 to 2°C , or must be built from low thermal expansion materials. The passive thermal protection may consist of paint, anodised and shiny aluminium covers, insulation, radiation shields, and a radome or astrodome. The active thermal protection may consist of ventilation or climatization

(air-conditioned ventilation) (Section 2.4). The temperature distribution throughout the telescope can be monitored with temperature sensors (Chapter 6). Such temperature monitoring with a small number of sensors is used with success to control temperature induced focus errors. The temperature distribution of the BUS, yoke, quadrupod and alidade or fork measured with ~ 100 to 200 sensors can be used in a finite element analysis to predict the temperature induced reflector surface deformations and focus, pointing and path length errors. The predicted thermal reflector surface deformations can be corrected with an active mirror. Table 13.4 indicates that a high thermal uniformity of the alidade or fork support is required so that the temperature induced pointing errors are small. On cm-wavelength telescopes the thermal protection of alidade and fork structures is TiO_2 paint, on open mm-wavelength telescopes the thermal protection of the fork support is insulation, TiO_2 paint and anodised aluminium covers.

A new generation radio telescope is perhaps designed every 15 to 20 years. It is difficult to image on these time scales the developments in engineering and the novelties that may be incorporated in future designs. The present state of thermal engineering of radio telescopes and communication antennas however indicates several issues that want further attention.

15.2 Temperature Measurements and Dynamic Thermal Models

A number of temperature measurements of long wavelength radio telescopes (Russia) are collected in the textbook on *Climatic Influences on Antenna Systems* published by Bairamov et al. [1988]. Ten years later, in 1996, the situation of thermal engineering of communication antennas was summarized by Levy [1996], pointing out that

Unfortunately, there are almost no successful measurement data available to establish the temperature distribution for an antenna structure. In the absence of substantial data, it has been practice to make a few rudimentary temperature estimates and extrapolate them into arbitrary distributions for computer analysis. As an alternative, an accurate and also practical analytical procedure that can incorporate thermal conductivity, convection, radiation, and reradiation appears to be beyond current technology because of overwhelming complexity, uncertainty in physical parameters, and requirements for computer resources.

The situation is not desperate with respect to empirical data and model calculations. Although the collection of temperature measurements of Chapter 9 is incomplete and provides only a limited view of the thermal behaviour of radio telescopes, it nevertheless may form the starting point of a more systematic database. For future thermal design of radio telescopes and communication antennas it will be useful to have a set of representative and complete temperature measurements of the three basic telescope constructions (Fig. 1.1) with precise documentation of the dimensions, materials, masses, surface finishes and of the environmental conditions (ambient air temperature, wind speed and direction, sky coverage, sunshine) under which the data were obtained. The data will provide information on the thermal behaviour of

telescopes and on the efficiency of thermal protection, if applied. The data can be used for tests of thermal model calculations with the intention to scale thermal models for use on other similar structures. Chapter 11 gives several examples where this approach has been successful, providing at the same time confidence in the calculations. There are several telescopes with a sufficient number of temperature sensors from which a data base can be built (Table 6.1), i.e. the radome enclosed JCMT telescope, the climatized IRAM 30-m telescope, the VertexRSI ALMA 12-m prototype telescope (archive data), the ASTE 10-m telescope, and in future the LMT/GMT 50-m telescope and the SRT 64-m telescope.

The design, and operation, of a radio telescope/communication antenna is based on a finite element analysis (FEA) or/and a flexible body analysis (FBA). As used since long, in the most compressed form of the thermal part of a FEA and FBA a uniform temperature change, a temperature gradient and a random temperature distribution throughout the telescope/antenna structure are considered. However, a more realistic input can be used in the FEA and FBA if information from a dynamic thermal model calculation is considered. The finite element model of the telescope/antenna design can serve as starting point from which to build a dynamic thermal model in which a large number of structural components is connected by conduction, convection and radiation. This thermal model is connected to the time-dependent thermal environment in which the telescope/antenna is intended to operate. The output of the thermal model is a realistic temperature distribution of the telescope/antenna components, as a function of time. The use of these temperature distributions in the FEA and FBA provides a realistic prediction of a telescope's thermal and mechanical behaviour.

In this context it is worthwhile to develop a 'telescope thermal element software', similar to available finite element software, which models the dynamic thermal structures of the basic telescope constructions. The basic models can be a pedestal, alidade and fork supported telescope with open, closed and ventilated backup structures. A particular telescope/antenna under discussion is specified in this software by its geometry, the materials, heat capacities, thermal resistances, surface finishes and ventilation, if necessary. The environment can be specified in the software by cosine-form functions of the ambient air temperature, sky temperature and the ground temperature (Sections 4.3.2, 4.5.2, 4.7.2). Wind is considered through selected directions of interaction and appropriate convective heat transfer coefficients.

15.3 Further Studies

There are several thermal issues that may want further study and guidelines for application.

(a) *View Factors of Backup Structures.* Radiative heat transfer is proportional to the 4th power of the temperature and proportional to the view factor of interacting

surfaces (Eqs.(7.48,7.49)). The view factors of regular structures like plates and box-type configurations is easily calculated or taken from tables. The determination of view factors of a backup structure (BUS) is considerably more complicated. Section 7.10.3 explains the radiative heat transfer in an open and a closed BUS, in radial (centre to rim) and axial (front to rear) direction, and gives estimates of view factors between BUS network sections and between BUS network sections and panels and rear side cladding. However, a rigorous derivation of BUS network view factors is required for more confidence in thermal calculations. The derivation may concentrate in a first step on a compact BUS network, as for instance shown in Fig. 2.14. This study may provide a compilation of BUS network view factors in the form of tables or graphs.

(b) *View Factors of a Parabolic Reflector.* Section 8.3 explains the radiative coupling of a parabolic reflector to the sky and the ground. It may be worthwhile to perform a more rigorous calculation of the sky and ground view factors taking also into account the radiative coupling in azimuth direction, a shiny reflector surface with a high contribution of specular reflection and a sky with elevation-dependent temperature.

(c) *Natural Ventilation.* Natural ventilation occurs through temperature differences in air and temperature differences between air and walls. Natural convection in confined volumes leads to temperature gradients in the confined air and temperature gradients in the confining walls. Sections 7.7.2 and 7.7.4 explain natural convection and a formalism (if-statements) by which natural convection can be incorporated in a thermal model. The explained formalism has been used in a few calculations, with some success, however this issue needs further studies and guidelines for applications. The convective heat transfer coefficient of air moving in a natural way or under forced condition through a BUS network needs a closer investigation.

(d) *Paint Aging.* A telescope and enclosure interacts with solar radiation and with the cold sky. The interaction with solar radiation is governed by the absorption coefficient a_S of the surface finish at visible wavelengths, the interaction with the cold sky is governed by the emission and absorption coefficient e_I and a_I at infrared wavelengths. The manufacturer provides the absorption and emission coefficients of new paint. It is known that old paint darkens, especially if exposed to enhanced UV radiation at high altitude observatory sites. However, there is little quantitative information by which amount the optical properties of paint change. Important is not only the change of the absorption and emission coefficient *per se*, i.e. $a_S(\text{new}) \rightarrow a_S(\text{old})$, $a_I(\text{new}) \rightarrow a_I(\text{old})$ and $e_I(\text{new}) \rightarrow e_I(\text{old})$, but also the relative change $a_S(\text{new})/e_I(\text{new}) \rightarrow a_S(\text{old})/e_I(\text{old})$ that determines the energy balance of a telescope component with respect to heating by solar radiation and cooling towards the sky. Since a telescope may operate for 20 to 30 years, information of the change of paint properties is important for time scales of, say, at least 10 years, under high altitude conditions.

A model calculation of a fork arm illustrates the effect of paint aging. Fig. 15.1.a shows the temperature difference ΔT of fork arms with one arm in sunshine and the other in shadow, similar to the situation of Fig. 11.13. In the calculation the new

paint has the absorption coefficient $a_S = 0.35$, which is assumed to change in time by 25 % to $a_S = 0.44$. The infrared emission/absorption coefficients are assumed to change by 15 %. Correspondingly, the temperature difference changes from $\Delta T = 1.5^\circ\text{C}$ to $\Delta T = 1.75^\circ\text{C}$, i.e. by 17%.

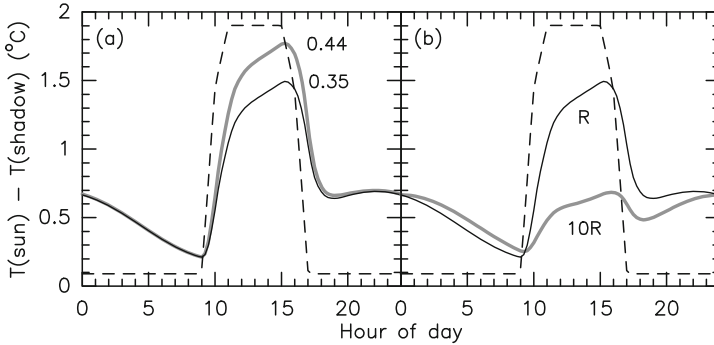


Fig. 15.1 Temperature difference between one fork arm in sunshine and the other one in shadow. (a) Influence of the aging of white paint with $a_S = 0.35$, $e_1 = 0.7$ for new paint and $a_S = 0.44$, $e_1 = 0.80$ for old paint. (b) Influence of the contact resistance (R and 10R) between the insulation and the steel walls of the fork. The dashed lines indicate the time of sunshine. The calculations use the fork model shown in Fig. 11.14.

(e) *Contact Resistance.* An important quantity in thermal calculations is the thermal resistance between bodies in contact, and especially between insulation and a metal surface. Since the contact resistance depends on the contact geometry, the surface finish (roughness, contact under pressure etc.) and the properties of a possible bonding material, it is evident that a large spectrum of actual situations does exist. A summary of thermal contact resistances of realistic engineering cases will be a valuable help for thermal model calculations.

The model calculation of the fork arm (Fig. 15.1) illustrates also the effect of the contact resistance between insulation and the steel wall of the fork. In the standard situation the contact resistance is assumed to be $R = 1\text{ m}^2/\text{K}/\text{W}$. Fig. 15.1.b shows that the temperature difference $\Delta T = 1.5^\circ\text{C}$ of the standard situation changes to $\Delta T = 0.70^\circ\text{C}$ for a ten times higher resistance 10R. However, the confidence of the prediction ΔT should be $\sim 0.2^\circ\text{C}$ when using these calculations to estimate the thermal pointing stability of a fork (Section 9.1.3).

(f) *Temperature Monitoring and Pointing Corrections.* Experience and the entries of Table 13.4 indicate that temperature differences and temperature variations of an alidade or fork support can be the limiting factor of a telescope’s pointing stability. Encouraging results of alidade temperature measurements and pointing corrections are reported for the JCMT 15–m telescope and the Cambridge MERLIN 32–m telescope (Section 9.1.2). However, today there is no proven metrology based on inclinometers, laser devices and accelerometers for real time measurement

of temperature induced alidade and fork structure deformations that result in pointing errors (see Greve & Kärcher [2009]). This issue is of particular importance for alidade structures of large telescopes (Effelsberg, GBT, LMT/GMT, SRT) where metrology could measure the integral effect of temperature (and wind) induced deformations causing pointing errors, instead of relying on temperature measurements and finite element calculations. Although the temperature influence on an alidade can be reduced with insulation, an efficient thermal protection with insulation becomes impractical for the ~ 60 to 100 -m telescopes because of the additional mass. Experimental research on existing large telescopes supported by flexible body calculations is needed to arrive at a proven metrology system for real time pointing control.

15.4 A Dynamic Thermal Error Budget for Design

Gravity and wind induced deformations of a telescope/antenna structure are evaluated in a finite element analysis (FEA) and flexible body analysis (FBA) [Kärcher 2006, Gawronski 2007] where the FBA takes into account the entire telescope consisting of the mechanical structure, the drives and the control system. The dynamic influence of wind is considered in the FBA through the wind power spectrum and the wind attack directions and corresponding tables of pressure distributions [Levy 1996]. The results of the FBA are, on the one hand, the telescope's eigenfrequencies and the response of the drives and control system and, on the other hand, the pointing, focus and reflector surface errors.

Since the thermal environment is slowly changing with time, the thermal part of the FEA and FBA is usually based on assumed static temperature distributions throughout a telescope/antenna structure. This analysis, together with estimates of the telescope/antenna's thermal time constants, provides the classic entries of the error budget tables. However, the time-dependent temperature distribution throughout a telescope/antenna [$T_i(t)$, $i = 1, 2, \dots, N$ components] can today be derived from a dynamic thermal model and a realistic time-dependent thermal environment. The FEA and FBA applied to the distribution [$T_i(t)$] provides the focus $F(t)$, pointing $P(t)$ and reflector surface precision $\sigma(t)$ and their derivatives $\Delta F/\Delta t$, $\Delta P/\Delta t$ and $\Delta \sigma/\Delta t$ as a function of time. In particular the time derivatives $\Delta F/\Delta t$, $\Delta P/\Delta t$ and $\Delta \sigma/\Delta t$ provide insight in the temperature sensitivity of the focus, pointing and surface precision and the frequency of focus and pointing determinations and corrections. The value $\Delta \sigma/\Delta t$ gives insight in the gain stability of the telescope (see Eq.(12.24)) and the necessity of a reflector surface upgrade in the case an active surface is available. This dynamic thermal behaviour quantifies in essence the operational ease of a telescope/antenna, and should be added to the commonly used error budget tables (see Table 13.6).

15.5 A Fundamental Investigation of Radio Telescope/Antenna Constructions

The reflector is the crucial part of a telescope and much effort is spent in the optimization of its precision, for instance using the homology principle (Section 2.3.2). The gravity induced reflector surface (BUS) deformations are derived from a FEA. The calculated reflector surface deformations can be decomposed into systematic and random deformations (Section 12.4). The analysis of the Effelsberg 100–m reflector and the IRAM 30–m and 15–m reflectors has shown that ~ 50 % of the surface errors are systematic and can be represented by low order Zernike polynomials (Appendix D) while the other part are random errors. The Zernike decomposition of the IRAM 30–m reflector deformations is shown in Fig. 15.2.b, the leading Zernike terms of the gravity induced deformations are summarized in Table 15.1.

In future designs of radio telescopes/communication antennas it will be worthwhile to derive from a FEA the gravity induced reflector surface deformations, determine in a subsequent analysis the leading Zernike terms and try to understand their structural origin. A subsequent optimization of the structure (BUS) may try to reduce the leading Zernike polynomial(s) in a similar way as homology optimizes the parabolic term.

Table 15.1 IRAM 30–m telescope. Zernike polynomial decomposition of Reflector Surface Deformations.

Reflector Surface Deformations	Zernike Polynomials (L)						
	3	7	9	12	13	15	17
Gravity	3	7			13	15	17
Temperature	3		9	12		15	
De-icing	2	3	9	12		15	

The Zernike decomposition of temperature induced reflector surface deformations of the IRAM 30–m telescope is shown in Fig. 15.2.a, the leading Zernike terms are summarized in Table 15.1. The leading Zernike terms under regular thermal control of the telescope are $L = 3$ (higher order defocus), $L = 9$ (astigmatism) and $L = 15$; the corresponding geometry of these deformations is illustrated in Fig. 15.3. It is obvious that astigmatism is a dominant term and its origin is most probably residual thermal bending of the yoke even though ventilation and heating is applied (Section 9.2.1).

In future designs of radio telescopes/communication antennas it will be worthwhile to derive from a dynamic thermal model and a realistic thermal environment the temperature distribution throughout the telescope/antenna, derive from a FEA the corresponding temperature induced reflector surface deformations, derive in a subsequent analysis the leading Zernike terms and try to understand their structural origin. A design may then be optimized that reduces the leading Zernike term(s).

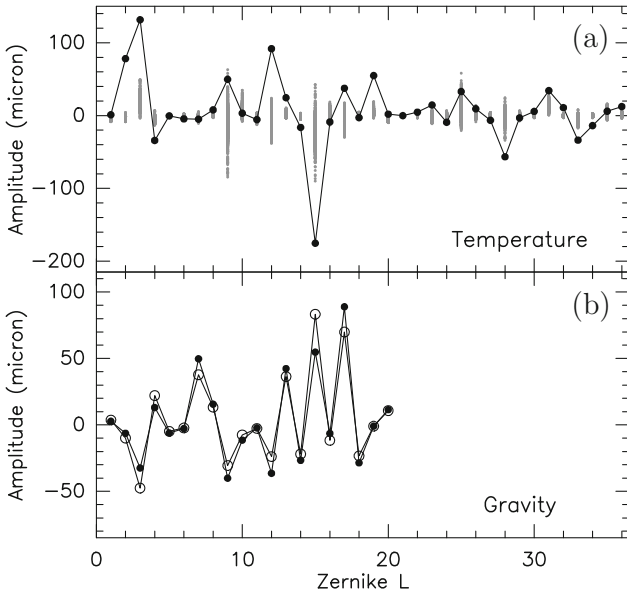


Fig. 15.2 IRAM 30-m telescope. Zernike decomposition of temperature induced and gravity induced reflector surface deformations. The Zernike polynomials corresponding to the parameter L are listed in Appendix D. (a) Temperature induced deformations: the grey dots represent the amplitudes of the Zernike polynomials under climatized operation of the telescope; the dots is the decomposition of the reflector surface under de-icing conditions (see also Figs. 12.13, 12.14). (b) Gravity induced deformations: dots for deformations at horizon position, open circles at zenith position (amplitudes multiplied by -1), for surface adjustment at 45° elevation. The deformation is symmetric with respect to the tilt plane so that only cosine-term polynomials are necessary.

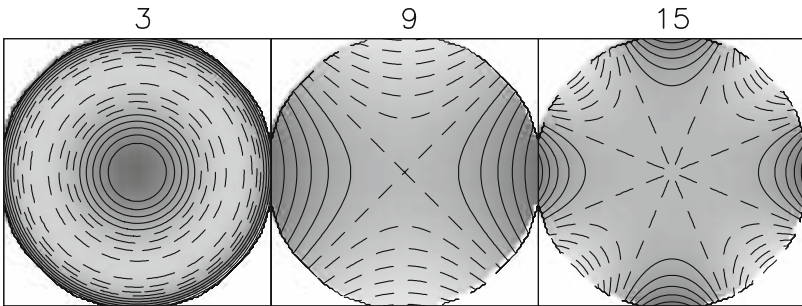


Fig. 15.3 IRAM 30-m telescope. Thermal surface deformations represented by the Zernike polynomials $L = 3, 9$ and 15 .

15.6 Future Design

The future of radio astronomy, and space research, depends on the continued interest in science and astronomy and the willingness of governments and the public to fund large instrumental projects. From today's situation one can safely extrapolate that future projects of radio astronomy will involve large and/or many telescopes and, in view of the high costs, the need of technical and engineering success in their construction. Future technical developments in telescope/antenna constructions may involve new, stiff, thermally stable and inexpensive plastic and composite materials, active surface coatings that adjust to the thermal environment, reliable real time telescope metrology, robotics and control, and other unforeseeable novelties. The fundamentals of radio physics, thermo physics and aerodynamics on which a telescope/antenna is built however remain unchanged.

Appendix A

Units and Fundamental Constants

Two systems of units are used for thermal calculations. The English–American system is based on the British Thermal Unit (BTU), the foot and inch, the pound, the second of time and the Fahrenheit temperature (F). A summary of the British units can be found in Chapman, *Heat Transfer* [1974]. The other system is the SI system based on the meter [m], the kilogram [kg], the second of time [s], the energy unit of Joule [J], the Watt as unit of power [$W = J/s$] and the Kelvin temperature [K].

The central parameter in heat transfer is the temperature. The absolute temperature is measured in degree Kelvin [K]; a more common temperature scale uses degree Celsius [C] with

$$T[C] = T[K] - 273.15.$$

One degree [K] equals one degree [C] while the zero–point of the scales is different. Celsius degrees are generally be used in the text, with freezing water at 0°C and boiling water at 100°C (at sea level). The scale of degree Fahrenheit is

$$T[F] = 9/5 T[C] + 32.$$

One degree [C] equals $9/5 = 1.8$ degree [F].

The range of temperatures of telescope and enclosure structures under discussion is, say, between $\sim -40^{\circ}\text{C}$ and $\sim 60^{\circ}\text{C}$, with the exception of very high mountain and polar regions. In this temperature range the material constants of solid materials are considered to be independent of temperature; this is not the case for gases.

Table A.1 summarizes parameters and units used in heat transfer relations. Table A.2 gives the correspondence between British Thermal Units (BTU) and the SI system (see Chapman [1974], *Heat Transfer*, for a more extended conversion table). Table A.3 summarizes fundamental constants. A few complex parameters used in convective heat transfer are summarized in Table A.4.

Table A.1 Parameters and Units.

Parameter	Symbol	Unit (SI)
Length	L, ℓ	meter [m]
Surface/Area	S, A, F	square-meter [m ²]
Volume	V	cubic-meter [m ³]
Angle	$\alpha, \beta, \gamma \dots$	degree (radian) [rad]
Solid Angle	ω	steradian [ster]
Mass	m, M	kilogram [kg]
Density	$\rho = M/V$	[kg/m ³]
Time	t	second [s]
Frequency	ν	Hertz [Hz = 1/s]
Velocity	v, υ	[m/s]
Pressure	p	Pascal [Pa]
Temperature	C or K	degree Celsius [C]; degree Kelvin [K]
Energy (heat)	E or Q	Joule [J]
Power	$q = \partial Q/\partial t$	Watt [W]
Heat Capacity	\mathcal{C}	[J/kg/K]
Thermal Conductivity	k	[W/m/K]
Kinetic Viscosity	ν	[m ² /s]
Absolute Viscosity	μ	[kg/s/m]

Related Units.

Parameter	Unit (SI)	Related Units
Length	meter [m]	1 m = 100 cm = 1000 mm = 10 ⁶ μ m, 1 km = 1000 m
Surface	square-m [m ²]	1 m ² = 10 ⁴ cm ²
Volume	cubic-m [m ³]	1 m ³ = 10 ⁶ cm ³
Angle	degree [°]	1° = 60 arcmin = 3 600 arcsec
Mass	kilogram [kg]	1 kg = 1000 gr; 1 ton = 1000 kg
Density	[kg/m ³]	1 kg/m ³ = 10 ³ gr/cm ³
Time	second [s]	1 hour = 3 600 s, 1 min = 60 s
Velocity	[m/s]	1 km/h = 0.28 m/s, 1 m/s = 3.6 km/h
Pressure	Pascal (Pa)	1 Pa = 10 ⁻⁵ bar
Energy (heat)	Joule [J]	1 kWh = 3.6 \times 10 ⁶ J
Power	Watt [W]	1 W = J/s

Table A.2 BTU and SI Units.

Parameter	Symbol	BTU	SI
Energy	E, Q	1 BTU	= 1.0551 \times 10 ³ J
Specific Heat	\mathcal{C}	1 BTU/lb _m -F	= 4.1868 \times 10 ³ J/kg/K
Thermal Conductivity	k	1 BTU/hr-ft ² -F	= 1.7307 W/m/K

Other fundamental constants are found in Allen, *Astrophysical Quantities* [2000]. See also the table of fundamental constants, and conversions, published by the National Institute of Standards and Technology, U.S. Department of Commerce; NIST Special Publication 811, 2008 Edition.

Table A.3 Fundamental Constants.

Parameter	Symbol	Unit
Speed of Light	c	2.998×10^8 [m/s]
Gravitational Acceleration	g	9.807 [m/s ²]
Boltzmann constant	k	1.381 [J/K]
Stefan–Boltzmann constant	σ	5.670×10^{-8} [W/m ² /K ⁴]
Planck constant	h	6.626×10^{-34} [Js]
Ideal Gas constant	R	8.314 [J/mol/K]

Table A.4 Parameters used in Convective Heat Transfer.

Parameter	Symbol	Parameter	Use
Thermal Diffusivity	α [m ² /s]	$\alpha = k/(\rho c)$	
Prandtl number	PR	ν/α	
Reynolds number	RE	$\nu L/\nu$	forced convection
Nusselt number	NU	$\nu L/k$	forced convection
Grashof number	GR	$gL^3\beta\Delta T/\nu^2$	free convection

The parameters PR, RE, NU, GR have no dimension.

Appendix B

Average Value, Root–Mean–Square Value (rms)

The average value $\langle a \rangle$ of a set of N individual values a_i is

$$\langle a \rangle = \sum_{i=0, N} a_i / N \quad (B.1)$$

The root–mean–square value $\text{rms}(a)$ of the set of N individual values is

$$\text{rms}(a) = \sqrt{\sum_{i=0, N} (a_i - \langle a \rangle)^2 / N} \quad (B.2)$$

The rms value has a statistical meaning in case N is a large number.

Appendix C

Pointing Model

The classical papers on pointing models are published by Meeks et al. [1968] and Stumpff [1972]. An investigation of the pointing model used on the IRAM 30-m telescope was published by Greve et al. [1996 b].

The IRAM 30-m telescope uses a pointing model with 8 (9) parameters P_i , $i = 1, 2, \dots, 9$. If δA and δE is the difference between the commanded and the measured position of a radio source in azimuth (A) and elevation (E) direction, then the horizontal (δh) and vertical (δv) components (true angles) of this mispointing are

$$\delta h = \delta A \cos E \quad \text{and} \quad \delta v = \delta E \quad (C.1)$$

with E the elevation angle of the measured source. For a large number of observations, covering a large part of the visible sky, the pointing model is the least squares solution of the P_i 's in the relations

$$\delta h = \sum P_i H_i(A, E) \quad \text{and} \quad \delta v = \sum P_i V_i(A, E) \quad (C.2)$$

with the functions $H_i(A, E)$ and $V_i(A, E)$ given in Table C.1.

The variation of the P_i 's in pointing model determinations throughout 1991 – 1992 is shown in Fig. C.1. Here the tilt of the AZ-axis is related to P_4 and P_5 by

$$P_4 = -\Delta \cos A_0 \quad \text{and} \quad P_5 = -\Delta \sin A_0 \quad (C.3)$$

with Δ the amount of tilt and A_0 the tilt direction.

The parameters P_1, P_2, P_3, P_6, P_7 , and P_9 show random variations and do not provide information of the source of the variations. The parameters of the AZ-axis tilt $P_4, P_5 \equiv \Delta, A_0$ show a systematic variation of Δ throughout a year, while A_0 remains in the range of $\sim 50^\circ$ to 100° . This is interpreted as an effect of a seasonal variation of the insclination of the pedestal (AZ bearing), probably introduced by the seasonal variation of the solar illumination and variation of the ambient temperature.

Table C.1 Pointing Model Parameters.

Type of error		$H_i(A,E)$	$V_i(A,E)$
Zero-offset AZ encoder	P_1	$\cos E$	0
Collimation error ^{a)}	P_2	1	0
Inclination EL-axis ^{b)}	P_3	$\sin E$	0
Inclination AZ-axis ^{c)} N-S	P_4	$\cos A \sin E$	$-\sin A$
Inclination AZ-axis ^{c)} E-W	P_5	$\sin A \sin E$	$\cos A$
Zero-offset EL encoder	P_7	0	1
Gravitational bending ^{d)}	P_8	0	$\cos E$
Gravitational bending ^{d)}	P_9	0	$\sin E$
Declination error of source ^{e)}	P_6	$\sin A$	$\cos A \sin E$

^{a)} non-orthogonality of radio beam axis and EL-axis.

^{b)} non-orthogonality of AZ-axis and EL-axis.

^{c)} the values $\delta h_A = \delta h_4 + \delta h_5$ and $\delta v_A = \delta v_4 + \delta v_5$ determine the inclination of the AZ-axis.

^{d)} the values $\delta h_B = \delta h_8 + \delta h_9$ and $\delta v_B = \delta v_8 + \delta v_9$ determine the gravitational bending of the telescope.

^{e)} catalogue declination error of source; no longer used.

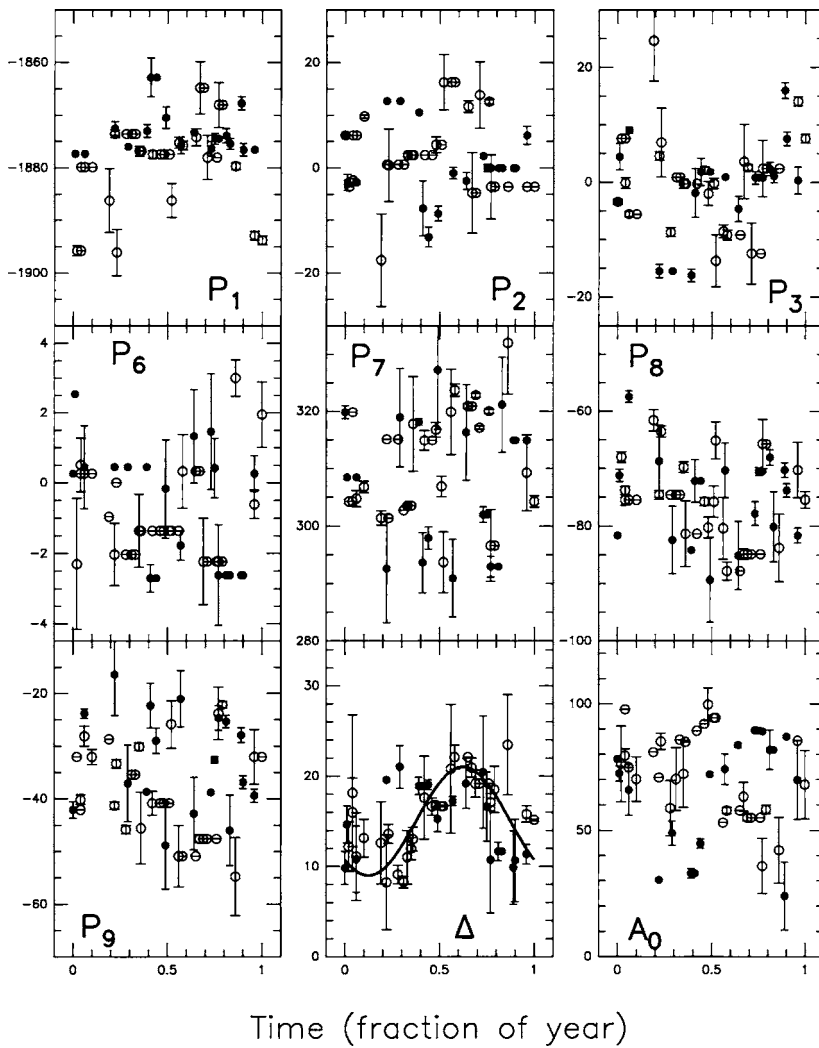


Fig. C.1 IRAM 30-m telescope. Variation of the pointing model parameters P_i throughout the years 1991 – 1992. For the AZ-axis inclination Δ and A_0 see Eq.(C.3).

Appendix D

Zernike Polynomials

The Zernike polynomials (see Born & Wolf [1980]) have the form

$$Z(\rho, \Theta) = R(\rho) \cos(m\Theta), \quad Z(\rho, \Theta) = R(\rho) \sin(m\Theta)$$

or a linear combination of both. In these the normalised polar coordinates of the aperture plane are: ρ ($0 \leq \rho \leq 1$), Θ ($0 \leq \Theta \leq 2\pi$). Relevant Zernike polynomials are:

L = 1 : $\delta(1) = 1$	L = 11 : $\delta(11) = (15\rho^6 - 20\rho^4 + 6\rho^2) \cos(2\Theta)$
L = 2 : $\delta(2) = 2\rho^2 - 1$	L = 12 : $\delta(12) = \rho^3 \cos(3\Theta)$
L = 3 : $\delta(3) = 6\rho^4 - 6\rho^2 + 1$	L = 13 : $\delta(13) = (5\rho^5 - 4\rho^3) \cos(3\Theta)$
L = 4 : $\delta(4) = 20\rho^6 - 30\rho^4 + 12\rho^2 - 1$	L = 14 : $\delta(14) = (21\rho^7 - 30\rho^5 + 10\rho^3) \cos(3\Theta)$
L = 5 : $\delta(5) = \rho \cos(\Theta)$	L = 15 : $\delta(15) = \rho^4 \cos(4\Theta)$
L = 6 : $\delta(6) = (3\rho^3 - 2\rho) \cos(\Theta)$	L = 16 : $\delta(16) = (6\rho^6 - 5\rho^4) \cos(4\Theta)$
L = 7 : $\delta(7) = (10\rho^5 - 12\rho^3 + 3\rho) \cos(\Theta)$	L = 17 : $\delta(17) = \rho^5 \cos(5\Theta)$
L = 8 : $\delta(8) = (35\rho^7 - 60\rho^5 + 30\rho^3 - 4\rho) \cos(\Theta)$	L = 18 : $\delta(18) = (7\rho^7 - 6\rho^5) \cos(5\Theta)$
L = 9 : $\delta(9) = \rho^2 \cos(2\Theta)$	L = 19 : $\delta(19) = \rho^6 \cos(6\Theta)$
L = 10 : $\delta(10) = (4\rho^4 - 3\rho^2) \cos(2\Theta)$	L = 20 : $\delta(20) = \rho^7 \cos(7\Theta)$

The polynomial L = 21, ... is the polynomial L = 5, ... but with $\sin(\Theta)$ term, etc. By combining polynomials of $\cos(\Theta)$ and $\sin(\Theta)$ terms the systematic deformations can have an orientation skew to the x,y-axes.

Picture and Graphic Credits

Some of the material presented in this text was published in refereed journals or has been kindly provided by third parties. Several copyrights were granted under the condition that full credits and detailed references are included, as provided in the listing. The quality of several scanned or internet-provided graphics was improved as indicated.

ALMA Test Data: Data obtained by the Antenna Evaluation Group during the VertexRSI and AEC ALMA 12-m prototype antenna tests (VLA site, NM, USA). Some of the data are contained in NRAO/ESO reports and the data archive. For a description see Mangum et al. [2006].

Data MPIfR Effelsberg, Germany: Data of the Effelsberg 100-m telescope, made available by A. Kraus and H. Koch, Effelsberg.

- 2.5 Copyright A&A. Fig. 1 in Baars et al. 1988, A&A **195**, 364
- 2.7 Courtesy SPIE. Fig. 1 in A. Greve, D.R. Smith, M. Bremer, A multi-layered thermal model of backup structures for mm-wavelength radio telescopes, SPIE **6271**, 20 (2006)
- 2.9 Courtesy SPIE. Fig. 1 in M. Bremer & J. Peñalver, FE model based interpretation of telescope temperature variations, SPIE **4757**, 186 (2002)
- 2.11 Courtesy SPIE. Fig. 6 in A. Greve, D.R. Smith, M. Bremer, A multi-layered thermal model of backup structures for mm-wavelength radio telescopes, SPIE **6271**, 20 (2006)
- 3.2 Image courtesy Sub-mm Observatory (CSO), California Institute of Technology, USA. Picture taken by R. Howard, CSO Site Manager
- 4.3.b Web-site: Andalucia, Spain, Tourist Information
- 4.19 Courtesy SPIE. Fig. 6 in A. Greve, Radio Telescopes in Practice: Halfway Towards End-to-End?, SPIE **4757**, 174 (2002)
- 4.22 Reprinted from Infrared Physics **25**, Ch. Zürcher, IR in building physics, p. 497, Copyright (1985), with permission from Elsevier
- 6.4 Courtesy N. Emerson and NRAO/AUI/NSF, also Courtesy IEEE Ant. Propag. Magazine **50**, No 2, 66 (2008), Fig. 20 in A. Greve & J.G. Mangum (2008)

- 6.6 Courtesy IEEE. Fig. 2 in A. Greve et al., IEEE Trans. Ant. Propag. **AP- 53**, 851 (2005)
- 6.7 Courtesy IEEE. Fig. 21 in A. Greve & J.G. Mangum, IEEE Ant. Propag. Magazine **50**, No 2, 66 (2008)
- 6.8 Courtesy SPIE. Fig. 2 in M. Bremer & J. Peñalver, FE model based interpretation of telescope temperature variations, Proc. SPIE **4757**, 186 (2002)
- 6.9 Holography map: courtesy D. Morris, IRAM, France
- 6.10 Courtesy IEEE. Fig. 3 in A. Greve et al., IEEE Trans. Ant. Propag. **AP-53**, 851 (2005)
- 6.11 Courtesy IEEE. Fig. 4 in A. Greve et al., IEEE Trans. Ant. Propag. **AP-53**, 851 (2005)
- 9.3.a Courtesy A&A. Fig. 6 b in A. Greve et al., A&AS, **115**, 379 (1996)
- 9.3.b Courtesy A&A. Fig. 6 c in A. Greve et al., A&AS, **115**, 379 (1996)
- 9.8 Courtesy Springer Science + Business Media, with kind permission from R. Ambrosini. Fig. 6 in Analysis of the alidade temperature behaviour of the Medicina VLBI radiotelescope, R. Ambrosini et al., Astrophysics and Space Sciences **239**, 247 (1996)
- 9.9.a Courtesy A&A. Fig. 4 in A.M. Bayley et al., A&A **283**, 1051 (1994)
- 9.9.b Courtesy A&A. Fig. 5d in A.M. Bayley et al., A&A **283**, 1051 (1994)
- 9.10 Courtesy JCMT. Based on <http://www.jach.hawaii.edu/telescope/-surface>, pages by J. Wouterloot (2005). Reproduction by MB
- 9.17 Courtesy IEEE. After Fig. 2 in A. Greve & J.G. Mangum, IEEE Ant. Propag. Magazine **50**, No 2, 66 (2008)
- 9.18 Courtesy IEEE. Part of Fig. 19 (day 22/8 and 23/8) in A. Greve & J.G. Mangum, IEEE Ant. Propag. Magazine **50**, No 2, 66 (2008)
- 9.21 Courtesy IEEE. After Fig. 5 in A. Greve & J.G. Mangum, IEEE Ant. Propag. Magazine **50**, No 2, 66 (2008)
- 9.23 Courtesy SPIE. Part of Fig. 3 in M. Bremer & J. Peñalver, FE model based interpretation of telescope temperature variations, SPIE Vol. **4757**, 186 (2002)
- 9.25 Courtesy IEEE. Fig. 8 in A. Greve et al., IEEE Trans. Ant. Propag. **AP-53**, 851 (2005)
- 9.30 Courtesy J. Lamb, from J. Lamb & D. Woody, 1998
- 9.31 Courtesy SPIE. Fig. 3 in A. Greve et al., A multi-layered thermal model of backup structures for mm-wavelength radio telescopes, SPIE **6271**, 20 (2006)
- 9.40.a Courtesy IEEE. Fig. 24 in A. Greve & J.G. Mangum, IEEE Ant. Propag. Magazine **50**, No 2, 66 (2008)
- 9.41 Courtesy Springer, with kind permission from K. Akabane. After Fig. 7 in K. Akabane, A Large Millimeter Antenna, Internat. J. Infrared and Millimeter Waves, Vol. **4**, No. 3, 793 (1983)

- 9.42.a Courtesy IEEE. Fig. 10 in A. Greve et al., IEEE Trans. Ant. Propag. **AP-40**, 1375 (1992)
- 9.43.b Courtesy A&A. Fig. 2 in Baars et al., A&A **195**, 364 (1988)
- 9.44 based on data from N. Satou (1998)
- 9.45 Courtesy SPIE. Part of Fig. 3 in M. Bremer & J. Peñalver, FE model based interpretation of telescope temperature variations, SPIE Vol. **4757**, 186 (2002)
- 9.46 Left picture: Courtesy SPIE. Part of Fig. 4 in M. Bremer & A. Peñalver, FE model based interpretation of telescope temperature variations, SPIE Vol. **4757**, 186 (2002). Right picture: Courtesy IEEE, Fig. 7 in A. Greve & J.G. Mangum, IEEE Ant. Propag. Magazine **50**, No 2, 66 (2008)
- 9.48 Data from Metsähovi Observatory, Finland, priv. comm.
- 9.49 Data from MIT-Haystack Observatory, USA, priv. comm.
- 9.50 Courtesy JCMT, J. Wouterloot (2005)
- 9.51.a, 9.51.b Courtesy JCMT. Based on <http://www.jach.hawaii.edu/telescope/-surface>, pages by J. Wouterloot (2005). Reproduction by MB
- 9.55 after A. Greve & D. Morris. Courtesy IEEE Trans. Ant. Propag. **AP-53**, 2123, (2005)
- 9.57 Courtesy JCMT. Based on <http://www.jach.hawaii.edu/telescope/-surface>, pages by J. Wouterloot (2005). reproduction by MB
- 9.72 Courtesy IEEE. Fig. 12 in A. Greve et al., IEEE Trans. Ant. Propag. **AP-40**, 1375 (1992)
- 9.73 Courtesy H.T. Schmitz-Görtz, 1971 (MPIfR, Germany)
- 9.76 Courtesy IEEE. Fig. 22 in A. Greve & J.G. Mangum, IEEE Ant. Propag. Magazine **50**, No 2, 66 (2008)
- 10.2 Courtesy Radio Science. Fig. 2 in A. Greve & G. MacLeod, Radio Science **36**, 1111 (2001)
- 11.4 Courtesy IEEE. Fig. 2 in A. Greve & M. Bremer, IEEE Ant. Propag. Magazine **48**, No 3, 9 (2005)
- 11.17 Courtesy IEEE. Figs. 6a and 6b in A. Greve et al., IEEE Trans. Ant. Propag. **AP-40**, 1375 (1992)
- 11.18 Courtesy IEEE. Fig. 3 in A. Greve & M. Bremer, IEEE Ant. Propag. Magazine **48**, No 3, 9 (2005)
- 11.26 Courtesy IEEE. Fig. 6 in A. Greve & M. Bremer, IEEE Ant. Propag. Magazine **48**, No 3, 9 (2005)
- 11.28, 11.29 Courtesy Radio Science. Figs. 3 and 6 in A. Greve & G. MacLeod, Radio Science **36**, 1111 (2001)
- 11.31, 11.32 Courtesy IEEE. Figs. 11 and 4 in A. Greve & M. Bremer, IEEE Ant. Propag. Magazine **48**, No 3, 9 (2005)
- 13.3 After Fig. 2 in J.W. Lamb, Thermal considerations for MMA antennas, MMA Memo **83**, (1992)

References

There are several Textbooks, either on the fundamental physics of heat transfer or its engineering applications. These books contain also tables of material properties. There are a number of Journals and Conference Reports. A biased selection is: Journal of Heat Transfer, Journal of Thermophysics and Heat Transfer, Solar Energy, Infrared Physics, IEEE Transactions Antennas and Propagation, Radio Science, Applied Optics, Optical Engineering, and the Proceedings of the International Society for Optical Engineering (SPIE).

A large amount of information is available as Observatory Reports, often advertized on the observatory/institute web-sites. Special information is contained in Reports of Construction Firms and Telescope Design Studies; these publications are not easily available. *Abbreviations:*

ANY-1964: Cohen, E. (editor): Large Steerable Radio Antennas – Climatological and Aerodynamic Considerations, Annals of the New York Academy of Sciences, Volume 116 (1964)

ML-1969: Mar, J.W., Liebowitz, H.: Structural Technology for Large Radio and Radar Telescope Systems, Cambridge MA, MIT Press (1969)

Ahlstrom, H.G., Gawronski, W., Girdner, D., Noskoff, E., Sommerville, J.N.: Tilts of the master equatorial tower, TMO Progress Report, 42-143 (2000)

Akabane, K.: A large millimeter wave antenna, Intern. J. of Infrared and mm Waves **4**, 793 (1983)

Allen, C.W.: Astrophysical Quantities, 4th edition, Springer, Heidelberg (2000)

Ambrosini, R., Grueff, G., Morsiani, M., Maccaferri, G., Zacchirolì, P., Orfei A.: Analysis of the alidade temperature behaviour of the Medicina VLBI radiotelescope, Astrophys. Space Sci. **239**, 247 (1996)

Ando, H., Barr, L., Miyashita, A., Sakato, K., Shindo, S.: Some airflow properties of telescope enclosures estimated from water-tunnel tests, PASP **103**, 597 (1991)

Ardeberg, A., Woltjer, L.: Testing for Future Large Telescopes, ESO Workshop, La Silla (1983)

Arny, T., Valeriani, G.: The Five College Radio Astronomy Observatory, Sky & Telescope **56**, 431 (1977)

Baas, F.: Temperature analysis of the JCMT telescope: comparison with early model calculations”, JCMT Techn. Report **3** (1995)

- Baas, F., Wouterloot, J.: The active surface control system, <http://www.jach.hawaii.edu/JCMT/telescope/surface> (2002)
- Baars, J.W.M.: The measurement of large antennas with cosmic radio sources, *IEEE Trans. Antennas Propagat.* **AP-21**, 461 (1973)
- Baars, J.W.M., Hooghoudt, B.G.: The synthesis radio telescope at Westerbork. General layout and mechanical aspects, *Astron. Astrophys.* **31**, 323 (1974)
- Baars, J.W.M.: Technology of Large Radio Telescopes for Millimeter and Submillimeter Wavelengths, in *Infrared and Millimeter Waves* **9**, 241, ed. K. Button, Academic Press, New York (1983)
- Baars, J.W.M., Hooghoudt, B.G., Mezger, P.G., de Jonge, M.J.: The IRAM 30-m millimeter radio telescope on Pico Veleta, Spain, *Astron. Astrophys.* **175**, 319 (1987)
- Baars, J.W.M., Greve, A., Hooghoudt, B.G., Peñalver, J.: Thermal control of the IRAM 30-m millimeter radio telescope, *Astron. Astrophys.* **195**, 364 (1988)
- Baars, J.W.M., Greve, A., Hein, H., Morris, D., Peñalver, J., Thum, C.: Design parameters and measured performance of the IRAM 30-m millimeter radio telescope, *Proc. IEEE* **82**, 687 (1994)
- Baars, J.W.M., Martin, R.N., Mangum, J.G., McMullin, J.P., Peters, W.L.: The Heinrich Hertz Telescope and the Submillimetre Telescope Observatory, *PASP* **111**, 627 (1999)
- Baars, J.W.M., Buzzoni, B., Gemünd, H-P., Polsak, A.: Reflectivity, scattering and emissivity measurements on samples of prospective ALMA reflector panels, *ALMA Memo* **566**, NRAO, USA (2006)
- Baars, J.W.M.: The Paraboloidal Reflector in Radio Astronomy and Communication, *Astrophysics and Space Science Library* **348**, Springer (2007)
- Bairamov, R.B., Baum, I.V., Vorobev, A.M., Gurbanyazov, M.A., Knyazev, I.N., Machuyev, Yu.I., Fokin, V.G.: Climatic Influences on Antenna Systems, Ashkhabad, USSR (1988) (in Russian)
- Barvainis, R., Ball, J.A., Ingalls, R.P., Salah, J.E.: The Haystack Observatory λ 3 mm upgrade, *PASP* **105**, 1334 (1993)
- Bayley, A.M., Davis, R.J., Haggis, J.S., Kärcher, H.: Thermal effects on the pointing of the 32-m MERLIN radio telescope at Cambridge, *Astron. Astrophys.* **283**, 1051 (1994)
- Beaupuits, J.P.P., Otarola, A., Rantakyro, F.T., Rivera, R.C., Radford, S.J.E., Nyman, L.-A.: Analysis of wind data gathered at Chajnantor, *ALMA Memo* **497**, NRAO, USA (2004)
- Behrndt, Ch., Scharpf, B.: Energiesparen mit hinterlüfteten Fassaden, *Schweiz. Aluminium Rundschau* **5**, 192 (1979)
- Bejan, A.: *Heat Transfer*, John Wiley & Sons Inc., New York (1993)
- Bely, P.Y. (ed.): *The Design and Construction of Large Optical Telescopes*, *Astronomy & Astrophysics Library*, Springer, New York – Berlin (2002)
- Berdahl, P.: Pigments to reflect the infrared radiation from fire, *J. Heat Transfer* **117**, 355 (1995)
- Berdahl, P., Fromberg, R.: The thermal radiance of clear skies, *Solar Energy* **29**, 299 (1982)
- Berger, X., Buriot, D., Garnier, F.: About the equivalent radiative temperature of clear skies, *Solar Energy* **32**, 725 (1984)
- Birkebak, R.C., Eckert, E.R.G.: Effects of roughness of metal surfaces on angular distribution of monochromatic reflected radiation, *J. Heat Transfer* **87**, 85 (1965)
- Blackadar, A.F.: Wind velocity profiles, in *ANY-1964*, 116 (1964)
- Bliss, R.W.: Atmospheric radiation near the surface of the ground: a summary for engineers, *Solar Energy* **5**, 103 (1961)
- Booth, R.S., Delgado, G., Hagström, M., Johansson, L.E.B., Murphy, D., Olberg, M., Whyborn, N.D., Greve, A., Hansson, B., Lindström, C.O., Rydberg, A.: The Swedish-ESO submillimeter telescope (SEST), *Astron. Astrophys.* **216**, 315 (1989)
- Born, M., Wolf, E.: *Principles of Optics*, Pergamon Press, UK (1980)
- Borovkov, A.I., Shevchenko, D.V., Gimmelman, V.G., Machuev, Yu.I., Gaev, A.V.: Finite element modeling and thermal analysis of the RT-70 radio telescope main reflector, *Int. Conf. on Antenna Theory and Techniques*, Vol. 2, 651, Sevastopol, Ukraine, (2003)

- Bregman, J.D., Casse, J.L.: A simulation of the thermal behaviour of the UK–NL mm wave telescope, *Intern. J. of Infrared and MM Waves* **6**, 25 (1985)
- Bremer, M., Peñalver, J.: FE model based interpretation of telescope temperature variations, *SPIE* **4757**, 186 (2002)
- Bremer, M., Greve, A., van't Klooster, K., Grewing, M., Eder, J., Valsecchi, G: Front and rear side heated prototype panels for the IRAM 15–m telescopes, in 28th ESA Antenna Workshop on Space Antenna Systems and Technologies, ESTEC – Noordwijk, The Netherlands, 943 (2005)
- Bridgeland, M.T., Jenkins, C.R.: Measurement of mirror seeing in the laboratory and at the telescope, *MNRAS* **287**, 87 (1997)
- Buck, A.L.: New equations for computing vapor pressure and enhancement factor, *J. Appl. Meteorol.* **20**, 1527 (1981)
- Carlsson T.R.: Site dependent error sources in geodetic Very-Long-Baseline Interferometry”, Techn. Report **224**, Chalmers University of Technology, Göteborg, Sweden (1996)
- Casse, J.L., Bregman, J.D.: Analysis of time constants in the thermal model for the UK–NL millimeter wave telescope, *URSI Int. Symp. on Millimeter and Submillimeter Wave Astronomy*, Granada, 11 (1984)
- Castets, A., Lucas, R., Lazareff, B. et al.: The 2.5–m millimeter telescope on Plateau de Bure, *Astron. Astrophys.* **194**, 340 (1988)
- Chamberlin, R.A.: Temperature measurements on the Leighton telescope: Surface Memo **2**, <http://www.caltech.edu/CSO> (2003)
- Chapman, A.J.: *Heat Transfer*, MacMillan Publ. Co., New York (1974); 4th edition (1984)
- Cheng, J.: Forced air cooling at high altitude, *MMA Memo* **203**, NRAO, USA (1998)
- Cheng, J.: *Principles of Astronomical Telescope Design*, Springer, Heidelberg – New York (2009)
- Cernicharo, J., Peñalver, J.: Can we improve the 30–m telescope pointing accuracy ? Thermal effects on the azimuth and elevation encoders, *IRAM Internal Report* **232**, IRAM, Grenoble (1991)
- Christiansen, W.N., Högbom, J.A.: *Radiotelescopes*, University Press, Cambridge, 2nd edition (1985)
- Chu, T.S., Wilson, R.W., England, R.W., Gray, D.A., Legg, W.E.: The Crawford Hill 7–m millimeter wave antenna, *Bell Syst. Tech. J.* **57**, 1257 (1978)
- Cogdell, J.R. et al.: High resolution mm reflector antennas, *IEEE Trans Ant. Propagat.* **AP–18**, 515 (1967)
- Cohen, E., Vellozzi, J., Suh, S.S.: Calculation of wind forces and pressures on antennas, in *ANY-1964*, 161 (1964)
- Coulson, I.M., Sandell, G.: Pointing at JCMT, in *Workshop on Pointing and Pointing Models*, ed. W.J. Altenhoff, *MPIfR Techn. Report* **78**, 59 (1996)
- Cowley, D.J., Sovka, J.A., Salmon, D., McLaren, R.A.: Control of dome seeing, in *ESO Conf. on Very Large Telescopes and their Instrumentation*, ed. M.–H. Ulrich, ESO, Garching, 897 (1988)
- Crane, R.K.: Refraction of the neutral atmosphere, in *Methods of Experimental Physics*, Vol. **12**, Part B (Radio Telescopes), Academic Press, New York – San Francisco – London, 186 (1976)
- Daryabeigi, K.: Heat transfer in adhesively bonded honeycomb core panels, *J. Thermophysics Heat Transfer* **16**, 217 (2002)
- Davenport, A.G.: The buffeting of large superficial structures by atmospheric turbulence, in *ANY-1964*, 135 (1969)
- Dawson, J.W.: A 28–ft liquid spun radio reflector for mm–wavelengths, *Proc. IRE* **50**, 1541 (1962)
- Deacon, E.L.: Gust variation with height up to 150 m, *Quart. J. Roy. Meteorol. Soc.* **81**, 562 (1952)
- Delannoy J.: Status of the IRAM 15–m antennas and the SEST telescope in 1985, *Proc. ESO – IRAM – ONSALA Workshop on (Sub)–Millimetre Astronomy*, ESO Conf. and Workshop

- Proc. **22**, eds. P.A. Shaver and K. Kj ar, 25 (1985)
- Delannoy, J., Dimper, R.: Thermal insulation tests with a steel chimney on the Plateau de Bure, IRAM Working Report **167**, Grenoble, France (1985)
- De Young, D.S.: Numerical simulations of air flow in telescope enclosures, *Astron. J.* **112**, 2896 (1996)
- Doyle, D., Pilbratt, G., Tauber, J.: The Herschel and Planck Space Telescopes, *Proc. IEEE* **97** (8), 1403 (2009)
- Drolen, B.L.: Bidirectional reflectance and specularity of twelve spacecraft thermal control materials, *J. Thermophysics and Heat Transfer* **6**, 672, (1992)
- Emery, A.F., Johansson, O., Lobo, M., Abrous, A.: A comparative study of methods for computing the diffuse radiation view factors for complex structures, *J. Heat Transfer* **113**, 413 (1991)
- Eriksson, T.S., Granqvist, C.G.: Radiative cooling computed for model atmospheres, *Appl. Optics* **21**, 4381 (1982)
- Eschenauer, H., Gatzlaff, H., Kiedrowski, H.W.: Entwicklung und Optimierung hochgenauer Paneeltragstrukturen, *Techn. Mitt. Krupp Forschg.–Ber.*, Band **38**, 43 (1980)
- Ezawa, H., Ishiguro, M., Matsuo, H., Miyawaki, K., Satou, N., Ukita, N.: Development of the reflector panel for the new 10–m mm/submm telescope, *SPIE* **4015**, 515 (2000)
- Feynman, R.: *Lectures on Physics*, Vol. II, Addison–Wesley Publishing Comp. (1966)
- Findlay, J.W.: Radio Telescopes, *IEEE Trans. Ant. Propagat.* **AP–12**, 853 (1964)
- Findlay, J.W., von Hoerner, S.: A 65–m Telescope for Millimeter Wavelengths, NRAO, USA (1972)
- Fohry, R.: Berechnung des Transmissionsw armestroms durch hinterl uftete Fassaden, *Luft u. K lletechnik* **4**, 205 (1977)
- Gawronski, W., Baher, F., Quintero, O.: Azimuth–track level compensation to reduce blind–pointing errors of the Deep Space Network Antennas, *IEEE Ant. Propagat. Magazine* **42**, No 2, 28 (2000)
- Gawronski, W.: Control and pointing challenges of large antennas and telescopes, *IEEE Trans. Control Syst. Techn.* **15**, 276 (2007)
- Geiger, R.: *Climate near the Ground*, Harvard University Press, Cambridge, Mass. (1973)
- Geldmacher, E.: Radioteleskop f ur das Max–Planck–Institut f ur Radioastronomie, *Tech. Mitteilungen Krupp* **28**, 187 (1970)
- Goldsmith, P.F.: Quasi–Optical Techniques at Millimeter and Submillimeter Wavelength, in *Infrared and Millimeter Waves*, Vol. **6**, ed. K.J. Button, Academic Press, New York–London (1982)
- Goldsmith, P.F. (ed.): *Instrumentation and Techniques for Radio Astronomy*, IEEE Press, New York (1988)
- Granqvist, C.G.: Radiative heating and cooling with spectrally selective surfaces, *Appl. Optics* **20**, 2606 (1981)
- Greve, A.: Strehl number degradation of large–scale systematic surface deformations, *Appl. Optics* **19**, 2948 (1980)
- Greve, A., Hooghoudt, B.G.: Quality evaluation of radio reflector surfaces, *Astron. Astrophys.* **93**, 76 (1981)
- Greve, A.: Thermal design and thermal behaviour of millimeter wavelength radio telescopes, IRAM Int. Report **253**, Grenoble (1992)
- Greve, A.: 64–m SRT Thermal Design Study, VertexRSI, Santa Clara, USA (2000)
- Greve, A., Dan, M., Pe alver, J.: Thermal behavior of millimeter wavelength radio telescopes, *IEEE Trans. Ant. Propagat.* **AP–40**, 1375 (1992)
- Greve, A., Hein, H., LeFloch, B., Morris, D., Navarro, S.: Astigmatism in reflector antennas: measurements and correction, *IEEE Trans. Ant. Propagat.* **AP–42**, 1345 (1994)
- Greve, A., Baars, J.W.M., Pe alver, J., LeFloch, B.: Near–focus active optics: An inexpensive method to improve mm–wavelength radio telescopes, *Radio Science* **31**, 1053 (1996 a)
- Greve, A., Panis, J.–F., Thum, C.: The pointing of the IRAM 30–m telescope, *Astron. Astrophys. Suppl.* **115**, 379 (1996 b)

- Greve, A., Kramer, C., Wild, W.: The beam pattern of the IRAM 30-m telescope, *Astron. Astrophys. Suppl.* **133**, 271 (1998)
- Greve, A., Neri, R., Sievers, A.: The gain-elevation dependence of the IRAM 30-m telescope, *Astron. Astrophys. Suppl.* **132**, 413 (1998)
- Greve, A., MacLeod, G.: Thermal model calculations of enclosures for millimeter wavelength radio telescopes, *Radio Science* **36**, 1111 (2001)
- Greve, A., Bremer, M., Peñalver, J., Raffin, P., Morris, D.: Improvement of the IRAM 30-m telescope from temperature measurements and finite element calculations, *IEEE Trans. Ant. Propagat.* **AP-53**, 851 (2005)
- Greve, A., Morris, D.: Repetitive radio reflector surface deformations, *IEEE Trans. Ant. Propagat.* **AP-53**, 2123 (2005)
- Greve, A., Bremer, M.: Calculated thermal behavior of ventilated high precision radio telescopes, *IEEE Ant. Propagat. Magazine* **48**, No 3, 9 (2005)
- Greve, A., Smith, D.R., Bremer, M.: A multi-layered thermal model of backup structures for mm-wavelength radio telescopes, *SPIE* **6271**, 20 (2006)
- Greve, A., Mangum, J.G.: Mechanical measurements of the ALMA prototype antennas, *IEEE Ant. Propagat. Magazine* **50**, No 2, 66 (2008)
- Greve, A., Kärcher, H.J.: Performance improvement of a flexible telescope through metrology and active control, *Proceedings IEEE* **97** (8), 1412 (2009)
- Greve, A., Morris, D., Peñalver, J., Thum, C., Bremer, M.: The beam pattern of reflector antennas with buckeled panels, *IEEE Trans. Ant. Propagat.*, in print (2009)
- Gruett, G., Alvito, G., Ambrosini, R. et al.: Sardinia Radio Telescope: the new Italian project, *SPIE* **5489**, 773 (2004)
- Güsten, R., Booth, R.S., Cesarsky, C., Menten, K.M. et al.: APEX – The Atacama Pathfinder Experiment, *SPIE* **6267**, 37 (2006)
- Guilloteau S., Delannoy, J., Downes, D. et al.: The IRAM interferometer on Plateau de Bure, *Astron. Astrophys.* **262**, 624 (1992)
- Hachenberg, O.: The new Bonn 100-meter Radio Telescope, *Sky & Telescope* **40**, 2 (1970)
- Hachenberg, O., Grahl, B.H., Wielebinski, R.: The 100-m radio telescope at Effelsberg, *Proc. IEEE* **61**, 1288 (1973)
- Hamberg, I., Svenson, J.S.E.M., Eriksson, T.S., Granqvist, C.G., Arrenius, P., Norin, F.: Radiative cooling and frost formation on surfaces with different thermal emittance: theoretical analysis and experience, *Appl. Optics* **26**, 2131 (1987)
- Heat Transfer Data Book, General Electric Company, New York (1970) (ISBN 0-931690-02-1)
- Ho, P.T.P., Moran, J.M., Lo, K.Y.: The Submillimeter Array, *ApJ* **616**, L 1 (2004)
- Inagaki, T., Okamoto, Y.: Surface temperature measurement using infrared radiometer by applying pseudo-gray-body approximation: estimation of radiative property for metal surface, *J. Heat Transfer* **118**, 73 (1996)
- Ingalls, R.P., Antebi, J., Ball, J.A. et al.: Upgrading the Haystack Radio telescope for Operation at 115 GHz, *Proc. IEEE* **82**, 742 (1994)
- Janes, C.: VLA and VLBA antenna temperature measurements, *VLA Test Memo* **160**, NRAO, USA (1991)
- Jeffery, M.H.: Construction and operation of the 210-ft radio telescope at Parkes, Australia, in *ANY-1964*, 62 (1964)
- Jeffery, M.H.: Construction and performance of the 150-ft NRC antenna at Algonquin Radio Observatory, Ontario, Canada, in *ML-1969*, 219 (1969)
- Jewell, P.R., Prestage, R.M.: The Green Bank Telescope, *SPIE* **5489**, 312 (2004)
- Johansson, L.A., Stodne, F., Wolf, S.: The Pisa project, Variations in the height of the foundation of the 20m radio telescope, *Research Report* **178**, Onsala Space Observatory, Chalmers University of Technology, Göteborg (1996)
- Kadanoff, L.P.: Turbulent heat flow: Structures and scaling, *Physics Today* **54**, 34, (2001)
- Karava, P., Stathopoulos T., Athinities, A.K.: Wind induced natural ventilation analysis, *Solar Energy* **81**, 20 (2007)
- Kärcher, H.J.: Telescopes as mechatronic systems, *IEEE Ant. Propagat. Magazine* **48**, 17 (2006)

- Kärcher, H.J., Baars, J.W.M.: The design of the Large Millimeter Telescope/Gran Telescopio Millimetrico, *SPIE* **4015**, 155 (2000)
- Kaufmann, P., D'Amato, R.: A Brazilian radio telescope for millimeter wavelengths, *Sky & Telescope* **45**, 144 (1973)
- Kesteveen, M., Graham, D.A., Fürst, E., Lochner, O., Neidhöfer, J.: The Effelsberg holography campaign – 2001, *Technischer Bericht* **80**, Max Planck Institut für Radioastronomie, Bonn, Germany (2001)
- King, H.C.: 1955, *The History of the Telescope*, Dover Publ. Inc., New York (1955)
- King, J.C., Turner, J.: *Antarctic Meteorology and Climatology*, Atmospheric and Space Science Series, Cambridge (1997)
- Kraus, J.D.: *Radio Astronomy*, Cygnus–Quasar Books, Powell, Ohio, 2nd edition (1986)
- Krishnaprakas, C.K.: View factor between inclined rectangles, *J. Thermophysics Heat Transfer* **11**, 480 (1997)
- Lamb, J.W.: Thermal considerations for mm–array antennas, *Millimeter Array Memo* **83**, OVRO, USA (1992)
- Lamb, J.W.: Scattering of solar flux by panel grooves: update, *ALMA Memo* **329**, Owens Valley Radio Observatory, USA (2000)
- Lamb, J.W., Forster, J.R.: Temperature measurements on the BIMA 6–m antennas, Part I: Backing Structure, OVRO, USA (1993)
- Lamb, J.W., Woody, D.P.: Thermal Behavior of the Leighton 10–m Antenna Backing Structure, *MMA Memo* **234**, NRAO, USA (1998)
- Levy, R.: *Structural Engineering of Microwaves Antennas*, IEEE Press, New York (1996)
- Lo, Y.T., Lee, S.W. (ed.): *Antenna Handbook, Theory, Application, and Design*, van Nostrand Reinhold Company, New York (1988)
- Love, A.W. (ed.): *Reflector Antennas*, IEEE Press, The Institute of Electrical and Electronics Engineers, Inc. New York (1978)
- Machuyev, Yu.I., Gimmelman, V.G.: Temperature state of radio antennas under climatic influences, 7th Intern. Symp. on Antennas and EM Theory (2006)
- Mangum, J.G., Baars, J.W.M., Greve, A., Lucas, R., Snel, R., Wallace, P., Holdaway, M.: Evaluation of the ALMA Prototype Antennas, *PASP* **118**, 1257 (2006)
- Mar, J.W., Liebowitz, H.: *Structural Technology for Large Radio and Radar Telescope Systems*, Cambridge MA, MIT Press (1969)
- Martin, M., Berdahl, P.: Emissivity of clear skies, *Solar Energy* **32**, 663 (1984 a)
- Martin, M., Berdahl, P.: Characteristics of infrared sky radiation in the United States, *Solar Energy* **33**, 321 (1984 b)
- Mecherikunnel, A.T., Gatlin, J.A., Richmond, J.C.: Data on total and spectral solar irradiance, *Applied Optics* **22**, 1354 (1983)
- Meeks, M.L., Ball, J.A., Hull, A.B.: The pointing calibration of the Haystack antenna, *IEEE Trans. Ant. Propagat.* **AP–16**, 746 (1968)
- Menzel, D.H.: A new radio telescope for Sweden, *Sky & Telescope* **52**, 241 (1976)
- Minnet, H.C., Thomas, B.M.: Fields in the image space of symmetrical focusing reflectors, *Proc. IEE* **115**, 1419 (1968)
- Morris, D., Bremer, M., Butin, G., Carter, M., Greve, A., Lamb, J.W., Lazareff, B., Lopez–Perez, J., Mattiocco, F., Peñalver, J., Thum, C.: Surface measurement of the IRAM 30 m radio telescope, *IET Microwaves, Antennas & Propagation* Vol. **3**, Issue **1**, 99 (2009)
- Murer, Y., Millan, P.: Two–dimensional modeling of heat transfer through sandwich plates with inhomogeneous boundary conditions on the faces, *J. Heat Transfer* **120**, 606 (1998)
- Nikolic, B., Balsler, D.S., Prestage, R.M.: Astigmatism and thermal effects on the GBT, *PTCS Project Note* **50.1**, NRAO, USA (2005)
- Nikolic, B., Prestage, R.M., Balsler, D.S., Chandler, C.J., Hills, R.E.: Out–of–focus holography at the Green Bank Telescope, *Astron. Astrophys.* **465**, 685 (2007)
- Norrod, R.D.: Test Report on solar diffusion of painted reflectors, *GBT Memo* **128**, NRAO, USA (1995)

- Nothnagel, A., Pilhatsch, M., Haas, R.: Investigation of thermal height changes of geodetic VLBI telescopes, Proc. 10th Meeting on European VLBI for Geodesy and Astrometry, eds. Lanotte R, Bianco G., Matera, Italy, 121 (1995)
- Nowak, H.: Radiative heat transfer between the outside of a flat roof and the thermal environment, CIRP 3, ETH Zürich, Switzerland, 23-27 July, 347 (1984)
- Nowak, H.: The sky temperature in net radiant heat loss calculations from low-sloped roofs, *Infrared Phys.* **29**, 231 (1989)
- Peñalver, J., Lisenfeld, U., Mauersberger, R.: Pointing with the IRAM 30-m telescope, *SPIE* **4015**, 632 (2001)
- Peñalver, J., Greve, A., Bremer, M.: First results of the IRAM 30-m telescope improved thermal control system, *IRAM Newsletter* **54**, 8 (2002)
- Perry, R.H., Chilton, C.H.: *Chemical Engineer's Handbook*, McGraw-Hill Book Company, New York (1973)
- Plathner, D.: Studies on 30-m panel frames under thermal gradient, Working Report **244**, IRAM, Grenoble (1997)
- Polyak, V.S., Bervalds, E.Ya.: Precision Construction of Reflector Radiotelescopes, Riga Zinatne (1990) (in Russian)
- Prestage, R.M., Constantikis, K.T., Balsler, D.S., Condon, J.J.: The GBT precision telescope control system, *SPIE* **5489**, 1029 (2004)
- Prestage, R.M., Constantikis, K.T., Hunter, T.R., King, L.J., Lacasse, R.J., Lockman, F.J., Norod, R.D.: The Greenbank Telescope, Proc. IEEE **97** (8) 1382 (2009)
- Raffin, P.: The Onsala 66-ft Telescope. Structural Analysis of the Reflector, IRAM Report, Grenoble (1989)
- Raffin, P.: Analysis of the reflector backup structure, Submm Array Tech. Memo, SAO **51**, USA (1991)
- Ray, J.: Antenna Temperature Sensor Installation Plan, PTCS Project Note **7.1**, GBT Archive PR 015, NRAO, USA (2003)
- Reich, W.: Pointing related activities at the Effelsberg 100-m telescope, in Workshop on Pointing and Pointing Models, ed. W.J. Altenhoff, MPIfR Techn. Report **78**, 35 (1996)
- Reynolds, G.O., DeVries, J.B., Parrent, G.B., Thompson, B.J.: *The New Optics Notebook: Tutorials in Fourier Optics*, SPIE Optical Engineering Press, Washington (1989)
- Rohlfs, K., Wilson T.L.: *Tools of Radio Astronomy*, Springer A&A Library, Berlin, Heidelberg, New York (1996)
- Ruhl, J.E. et al.: The South Pole Telescope, *SPIE* **5498**, 11 (2004)
- Rush, W.V.T.: The current state of the reflector art, *IEEE Trans. Ant. Propagat.* **AP-32**, 313 (1984)
- Rush, W.V.T., Potter, P.D.: *Analysis of Reflector Antennas*, Academic Press, New York – London (1970)
- Ruze, J.: Antenna tolerance theory – A review, Proc. IEEE **54**, 633 (1966)
- Ruze J.: Small displacements in parabolic reflectors, MIT, Lincoln Laboratory, Lexington, Massachusetts, USA (unpublished) (1969)
- Satou, N.: Temperature uniformity of the NMA 10-m antenna structures, NRO Techn. Rep. **59**, NRO, Japan (1998)
- Scheffler, H.: Über die Genauigkeitsforderungen bei der Herstellung optischer Flächen für astronomische Teleskope, *Z. Astrophys.* **55**, p. 1 (1962)
- Schloerb, F.P.: Effect of thermal instabilities on the performance of the FCRAO 14-m antenna, Internal Report, Five College Radio Astronomy Obs., Univ. Mass., USA (1978)
- Schmitz-Görtz, H.T.: Temperaturmessungen am 100 m Teleskop, MPIfR, Bonn, Int. Report, No. **1** (1973)
- Schönbach, W. 1968: Einige Temperaturprobleme bei Entwurf und Bau von Grossantennen, *Der Stahlbau*, Heft **12**, 1 (1968)
- Schroeder, D.J.: *Astronomical Optics*, Academic Press Inc., San Diego (1987)
- Schwab, F., Cheng, J.: Flux concentration during solar observation for ALMA antennas, ALMA Memo **575**, NRAO, USA (2008)

- Serrano Perez-Grovas, A.: The Large Millimeter Telescope (LMT), *Rev. Mex. Astron. Astrophys.*, Ser. Conf. **4**, 67 (1996)
- Sherlock, R.H.: Variation of wind velocity and gusts with height, *Proc. ASCE* **78**, Separate 126 (1955)
- Siegel, R., Howell, J.R.: *Thermal Radiation Heat Transfer*, Hemisphere Publishing Corporation, Washington and McGraw-Hill Book Company, New York (1982)
- Silver, S. (ed): *Microwave Antenna, Theory and Design*, Peter Peregrinus Ltd., London (1984)
- Simpson, H.: Large Steerable Antennas – Climatological and Aerodynamic Considerations, *Monograph Publ. New York Acad. Science* **116**, 58 (1964)
- Smart W.M.: *Textbook on Spherical Astronomy*, Cambridge University Press (1977)
- Smith, I.A.: JCMT active surface control system: implementation, *SPIE* **3511**, 190 (1998)
- Snyder, L.A., Radford, J.E., Holdaway, M.A.: Underground temperature fluctuations and water drainage at Chajnantor, *ALMA Memo* **314**, NRAO, USA (2000)
- Stangerup P.: A minicomputer-oriented network analysis program, *ESA Journal* **6**, 301 (1982)
- Stangerup P.: Simulation de la convection naturelle au moyen d'un programme d'analyse électrique, *Revue Generale de Thermique Francaise* **280**, 409 (1985)
- Stangerup P.: Implementation of sensitivity calculation in a general-purpose simulation program, *Computer Physics Comm.* **117**, 130 (1999)
- Stanghellini S.: Status of the ALMA antenna production, *ESO Messenger* **130**, 15 (2007)
- Stumpff, P.: *Astronomische Pointingtheorie für Radioteleskope*, Kleinheubacher Berichte **15**, 431 (1972)
- Swinbank, W.C.: Long-wave radiation from clear skies, *Quart. J. Roy. Meteorolog. Soc.* **89**, 339 (1963)
- Synnefa, A., Santamouris, M., Livada, I.: A study of the thermal performance of reflective coatings for the urban environment, *Solar Energy* **80**, 968 (2006)
- Thompson, A.R., Moran, J.M., Svenson, G.W.: *Interferometry and Synthesis in Radio Astronomy*, Wiley, New York (2001)
- Tofani, G. et al.: Status of the Sardinia Telescope project, *SPIE* **7012**, 70120F–12 (2008)
- Tournair, A.: Contrôle thermique du télescope et du bâtiment Themis, *INSU/TECH/AT/CT/No 86/8*, France (1986)
- Ukita N.: Thermal effects in the pointing of the Nobeyama 45-m telescope, *Publ. Natl. Astron. Obs Japan* **5**, 139 (1999)
- Ukita, N., Saito, M., Ezawa, H., Ikenoue, B., Ishizaki, H., Iwasita, H., Yamaguchi, N., Hayakawa, T., and ATF-J Team: Design and performance of the ALMA-J prototype antenna, *SPIE* **5489**, 1085 (2004)
- Ukita, N., Ezawa, H., Ikenoue, B., Saito, M.: Thermal and wind effects on the azimuth axis tilt of the ASTE 10-m antenna, *Publ. Nat. Astron. Obs. Japan* **10**, 25 (2007)
- Unsöld, A., Baschek, B.: *The New Cosmos*, Springer, Heidelberg (2001)
- Usuda, T., Takato, N., Kanzawa, T. et al.: Subaru Telescope: Current performances and future upgrade plans, *SPIE* **5489**, 278 (2004)
- VDI-Wärmeatlas, VDI-Verlag Düsseldorf, Germany (1984), ISBN 978-3-540-29650-8
- Velds, C.A.: *Zonnestraling in Nederland*, KNMI/Thieme, De Bilt/Baarn, The Netherlands (1992) (in Dutch)
- Vernin J., Benkhaldoun Z., C. Muñoz-Tuñon C. (editors): *Astronomical Site Evaluation in the Visible and Radio Range*, *ASP Conf. Proc. Vol. 266*, ASP, San Francisco (2002)
- Vogiatzis, K., Hiriart, D.: Numerical wind modeling for the San Pedro Martir Sierra in Baja California, *Rev. Mex. de Astron. Astrophys.* **40**, 81 (2004)
- von Hoerner, S.: Design of large steerable telescopes, *Astron. J.* **72**, 35 (1967 a)
- von Hoerner, S.: Homologous deformation of tiltable telescopes, *Journal of the Structural Division, Proc. of the Americ. Soc. of Civil. Eng., ASCE* **93**, 461 (1967 b)
- von Hoerner, S.: Thermal deformations of telescopes, *NRAO Memo* **17**, NRAO Archive, USA (1967 c)
- von Hoerner, S., Herrero, V.: Thermal deformations of the 65-m telescope, *NRAO Report* **37**, NRAO, USA (1971)

- von Hoerner, S.: Radio Telescopes for Millimeter Wavelengths, *Astron. Astrophys.* **41**, 301 (1975 a)
- von Hoerner, S.: 140-ft Pointing errors and possible corrections, NRAO Electr. Div. Int. Report **164**, USA (1975 b)
- von Hoerner S.: The design and improvement of tiltable radio telescopes, *Vistas in Astronomy* **20**, Pergamon Press, 411 (1977 a)
- von Hoerner, S.: Accuracy and thermal deformation of ESSCO panel, 25-m Telescope Memo **81**, NRAO, USA (1977 b)
- Weiss, H.G., Fanning, W.R., Folino, F.A., Muldoon, R.A.: Design of the Haystack antenna and radome, in *ML-1969*, 151 (1969)
- Welch, W.J. et al.: The Berkeley–Illinois–Maryland–Association millimeter array, *PASP* **108**, 93 (1996)
- Williams, J.T., Beckers, J.M., Salmon, D., Kern, P.: IR thermography and observatory thermal pollution, *SPIE* **628**, 30 (1986)
- Wilson, R.N.: *Reflecting Telescope Optics I, II*, Astronomy Astrophysics Library, Springer, Berlin, Heidelberg, New York (1999)
- Woody, D., Vail, D., Schaal, W.: Design, construction, and performance of the Leighton 10.4-m diameter radio telescope, *Proc. IEEE* **82**, 673 (1994)
- Woody, D., MacDonald, D., Bradford, M., Chamberlin, R., Dragovan, M., Goldsmith, P., Lamb, J., Radford, S., Zmuidzinas, J.: Panel options for large precision radio telescopes, *SPIE* **7018**, 70180T (2008)
- Wooten, A., Thompson A.R.: The Atacama Large Millimeter/Submillimeter Array, *Proc. IEEE* **97** (8), 1463 (2009)
- Wouterloot, J.: <http://www.jach.hawaii.edu/JCMT/telescope/surface> (2005)
- Wresnik, J., Haas, R., Boehm, J., Schuh, H.: Modeling thermal deformation of VLBI antennas with a new temperature model, *J. Geodesy* **81**, 423 (2006)
- Zarghamee, M.S., Antebi, J.: Surface accuracy of Cassegrain antennas, *IEEE Trans. Ant. Propagat.* **AP-33**, 828 (1985)
- Zernecke, R.: Seasonal variations in height demonstrated at the radio telescope reference point, *Proc. 13th Working Meeting on European VLBI for Geodesy and Astronomy*, Viechtach, 15 (1999)
- Zienkiewicz, O.C., Taylor, R.L.: *Finite Element Method*, Volume I and II, McGraw–Hill Book Company, London (1994)
- Zürcher, Ch.: IR in building physics, *Infrared Phys.* **25**, 497 (1985)
- Zürcher, Ch., Finger, G., Kneubühl, F.K., Thiebaud, F., Vetsch, H., Frank, Th., Sagelsdorff, R.: The influence of thermal and solar radiation on the energy consumption of buildings, *Infrared Phys.* **22**, 277 (1982)

Indices

Historical Names Index

A

Airy, G.B. 310

B

Bessel, F.W. 310

C

Cassegrain, L. 15

Celsius, A. 107, 357

F

Fahrenheit, G. 107, 357

Fourier, J. 8, 127, 308

Fresnel, A.-J. 8

G

Gauss, J.C.F. 104, 320

Grashof, F. 138, 359

Gregory, J. 15

H

Huygens, Ch. 8, 305

K

Kelvin, Lord; alias Thomson, W.
107, 357

L

Laplace, P.-S. 153

M

Maxwell, J.C. 8

N

Navier, C.L. & Stokes, G.G. 134

Newton, I. 131

Nusselt, W. 138, 139, 359

P

Planck, M. 141, 359

Poisson, S. 153

Prandtl, L. 134, 139, 359

R

Reynolds, O. 68, 134, 139, 359

S

Stefan, J. & Boltzmann, L. 142, 359

W

Wien, W. 141

Z

Zernike, F. 313, 321, 353, 367

Author Index

A

- Ahlstrom, H.G. et al. 261
 Akabane, K. 110, 204, 216
 Ambrosini, R. et al. 180, 182, 191, 280
 Ando, H. et al. 67

B

- Baars, J.W.M. et al. 22, 24, 37, 103,
 104, 120, 174, 222, 231
 Baars, J.W.M. 38, 319, 335
 Baas, F. & Wouterloot, J. 117
 Baas, F. 109, 117, 204, 226, 264, 266
 Bairamov, R.B. et al. 110
 Barvainis, R. et al. 52, 204, 226, 228,
 264, 266, 297
 Bayley, A.M. et al. 108, 120, 183, 280
 Beaupuits, J.P.P. et al. 65
 Behrndt, Ch. & Scharpf, B. 284
 Berdahl, P. & Fromberg, R. 76
 Berdahl, P. 103
 Berger, X. et al. 76
 Birkebak, R.C. & Eckert, E.R.G. 103
 Blackadar, A.F. 68
 Bliss, R.W. 75
 Booth, R.S. et al. 25, 26, 174, 204
 Borovkov, A.I. et al. 36, 268, 289
 Bregman, J.D. & Casse, J.L. 53, 101,
 185, 266, 289
 Bremer, M. & Peñalver, J. 113, 115
 Bremer, M. et al. 28, 240
 Bridgeland, M.T. & Jenkins, C.R. 67
 Buck, A.L. 73

C

- Carlsson, T.R. 196
 Casse, J.L. & Bregman, J.D. 159
 Castets, A. et al. 38
 Cernicharo, J. & Peñalver, J. 261
 Chamberlin, R.A. 109, 204, 226, 229
 Cheng, J. 135, 138

- Chu, T.S. et al. 18
 Cogdell, J.R. et al. 9
 Coulson, I.M. & Sandell, G. 185
 Cowley, D.J. et al. 110
 Crane, R.K. 73

D

- Daryabeigi, K. 276
 Dawson, J.W. 38
 De Young, D.S. 67
 Deacon, E.L. 68
 Delannoy, J. & Dimper, R. 270
 Delannoy, J. 26
 Delgado G. 110
 Doyle D. et al. 10
 Drolen, B.L. 105

E

- Emery, A.F. et al. 148
 Eriksson, T.S. & Granqvist, C.G. 75
 Eschenauer, H. et al. 31
 Ezawa, H. et al. 103, 248

F

- Findlay, J.W. & von Hoerner, S. 328
 Findlay, J.W. 9
 Fohry, R. 284

G

- Güsten, R. et al. 26, 44, 201, 248
 Güsten, R. 109
 Gawronski, W. et al. 185
 Gawronski, W. 347, 352
 Geldmacher, E. 21
 Granqvist, C.G. 75, 79
 Greve, A. & Bremer, M. 96, 139,
 140, 291, 303
 Greve, A. & Hooghoudt, B.G. 319
 Greve, A. & Kärcher, H.J. 121, 340,
 352

Greve, A. & Mangum, J.G. 109, 191, 194, 204
 Greve, A. & McLeod, G. 101, 139, 140, 264, 299
 Greve, A. & Morris, D. 235, 317, 331
 Greve, A. et al. 22, 24, 42, 43, 110, 115, 139, 140, 197–199, 204, 222, 223, 226, 235, 315, 317, 319, 363
 Greve, A. 110, 204, 216, 218, 276, 291, 302, 321
 Grueff, G. et al. 21
 Guilloteau, S. et al. 26

H

Hachenberg, O. et al. 21, 204
 Hachenberg, O. 21, 204
 Hamberg, I. et al. 79

I

Inagaki, T. & Okamoto, Y. 110
 Ingalls, R.P. 226, 228

J

Janes, C. 187
 Jeffery, M.H. 22, 110, 174, 204, 206
 Jewell, P.R. & Prestage, R.M. 18
 Johansson, L.A. et al. 196

K

Kärcher, H.J. & Baars, J.W.M. 40
 Kärcher, H.J. 31, 226, 340, 347, 352
 Kadanoff, L.P. 134
 Karava, P. et al. 266
 Kraus, A. 110
 Krishnaprakas, C.K. 149

L

Lamb, J.W. & Forster, J.R. 109, 204, 216
 Lamb, J.W. & Woody, D.P. 109, 204, 208
 Lamb, J.W. 103, 159, 248, 328, 329, 333

M

Machuyev, Yu.I. & Gimmelman, V.G. 37, 110, 268, 289
 Mangum, J.G. et al. 9, 26, 44, 177, 194, 204, 214
 Martin, M. & Berdahl, P. 76
 Mecherikunnel, A.T. et al. 80
 Meeks, M.L. et al. 363
 Menzel, D.H. 174
 Minnet, H.C. & Thomas, B.M. 310
 Morris, D. et al. 322
 Murer, Y. & Millan, P. 276

N

Nikolic, B. et al. 43, 185, 226, 242
 Norrod, R.D. 103
 Nothnagel, A. et al. 181, 196
 Nowak, H. 76

P

Peñalver, J. et al. 22, 24, 176, 198
 Plathner, D. 239
 Prestage, R.M. et al. 18, 43, 120, 121, 185, 231

R

Raffin, P. 28, 115, 199, 329
 Ray, J. 110
 Reich, W. 243
 Rogers, A.E.E. 226
 Ruhl, J.E. et al. 18
 Rush, W.V.T. 9
 Ruze, J. 310, 319, 322, 334, 335

S

Satou, N. 109, 204, 216, 221
 Schönbach, W. 40, 235
 Scheffler, H. 310, 319
 Schloerb, F.P. 102, 109, 217, 226, 231, 264–266
 Schmitz-Görtz, H.T. 180, 251
 Schwab, F. & Cheng, J. 105, 248

Serrano Perez-Gorvas, A. 298
Sherlock, R.H. 68
Smith, I.A. 117
Snyder, L.A. et al. 70
Stangerup, P. 133, 140
Stanghellini, S. 67
Stumpff, P. 363
Swinbank, W.C. 76
Synnefa, A. et al. 105

T

Tofani, G. et al. 21
Tournaire, A. 76

U

Ukita, N. et al. 26, 109, 177, 188, 201,
214
Ukita, N. 110, 261
Usuda, T. et al. 69

V

Vogiatzis, K. & Hiriart, D. 67
von Hoerner, S. & Herrero, V. 120, 231
von Hoerner, S. x, 9, 21, 29, 30, 34,
159, 180, 237, 327, 328, 331

W

Welch, J. et al. 249
Williams, J.T. et al. 110
Woody, D. et al. 40, 204, 206, 239, 275
Wootten A. & Thompson, A.R. 9
Wouterloot, J. 110, 117, 204, 226
Wresnik, J. et al. 196

Z

Zürcher, Ch. 75
Zarghamee, M.S. & Antebi, J. 322,
334, 335
Zernecke, R. 196

Book Index

A

- Allen, C.W. 80, 358
 Ardeberg, A. & Woltjer, L. 56

B

- Baars, J.W.M. 7, 9, 14, 19, 180, 231,
 242, 305, 310, 335
 Bairamov, R.B. et al. xiii, 110, 348
 Bejan, A. 124, 126, 134, 148, 151–
 154, 291
 Bely, P.Y. (edt.) 10, 56, 67, 75, 83, 346
 Born, M. & Wolf, E. 7, 305, 313,
 321, 367

C

- Chapman, A.J. 103, 124, 126, 135, 136,
 138, 143, 147, 148, 151, 154,
 156, 273
 Cheng, J. 14
 Christiansen, W.N. & Högbom, J.A.
 6, 237, 305, 310, 311
 Cohen, E. (edt.) 68

F

- Feynman, R. 134

G

- Geiger, R. 57
 Goldsmith, P.F. 7, 14

K

- King, H.C. 6
 King, J.C. & Turner, J. 57
 Kraus, J.D. 7, 9, 14, 305

L

- Levy, R. 9, 14, 31, 348, 352
 Lo, Y.T. & Lee, S.W. (editors) 7, 305

- Love, A.W. (edt.) 6, 7, 14, 305

M

- Mar, J.W. & Liebowitz, H. (edts.) 14,
 31, 38

P

- Perry, R.H. & Chilton, C.H. 135
 Polyak, V.S. & Bervalds, E.Ya. 14, 38

R

- Reynolds, G.O et al. 309
 Rohlf K. & Wilson T.L. 9, 305
 Rush, W.V.T. & Potter, P.D. 7, 15, 305

S

- Schroeder, D.J. 6, 7, 14
 Siegel, R. & Howell, J.R. 145
 Silver, S. (edt.) 7, 8
 Smart, W.M. 86

T

- Thompson A.R. et al. 9, 305

U

- Unsöld, A. & Baschek, B. 80

V

- Velds, C.A. 80
 Vernin, J. (edt.) 56

W

- Wilson, R.N. xiii, 6, 7, 14, 346

Z

- Zienkiewicz, O.C. & Taylor, R.L. 31

Subject Index

A

Active reflector 42, 225, 347

Airflow

laminar 133, 135

turbulent 133, 135

Alidade mount 20

height changes of 181

pointing errors 179

telescope with 11

temp. measurements of 178, 257

thermal construction 47

thermal tolerance 330

Alignment, optics

distance, centring, tilt 18

tolerances of 331

Aluminium backup structure xi, 33, 47

Aluminium honeycomb

panel 40, 48, 232, 275

thermal model 276

Aluminium panels 40, 48

Ambient air

gas equation of 57

temperature 59

approximation 62

daily 63

measurements 59

rate of change 64

seasonal 62

vertical profiles of 58

Ambient air temperature at

Chajnantor 61

Effelsberg 61

Pico Veleta 61

Anemometer 59

Antenna

communication xiii, 9

in space 10

Aperture efficiency 319

Aperture plane 306

Approximation, of temperature

air 62

ground 70

seasonal 59

sky 76, 77

Array *see* interferometer

Astigmatism

beam pattern 315

equation 315

measurement 315

Astrodome

basic structure 49

solar illumination 98

solar radiation captured 101

telescopes with 49, 51

with membrane 51, 52

with ventilation 54

Atmosphere

infrared window 75, 80

isothermal 57

ozone absorption 80

polytrope 57

scale height, dry and wet 58

solar absorption in 80

turbidity 80

B

Backup structure (BUS)

climatisation 24

closed 30, 37, 205, 206

construction

mechanical 29, 31

thermal protection 47

dimensions 34

geometry 31, 33, 34

homologous 30, 34, 36

mass 33

models of *see* thermal model

network 30–32

open 35, 205, 206

support

central hub 19, 26, 30, 32

elevation structure 19, 21

- invar ring 26
 - pyramidal 30, 31
 - yoke 19, 30, 32
- ventilation
 - circular 220
 - climatisation 24
 - radial 220
- view factors in 150
- Beam pattern
 - astigmatism 315
 - coma 315
 - defocus 314
 - error beam 313, 318, 320
 - formation 305
 - main beam 311
 - side lobes 311
 - taper 312
 - telescope
 - perfect 308
 - real 313
 - width 311
- Beam pattern degradation
 - de-icing 323
 - error beam 313, 318, 320
 - random deformation 318
 - repetitive deformation 316
 - systematic 313
 - tolerance 309, 318
- Black-body radiation 141
- BUS temperature measurement
 - climatised BUS 217
 - closed BUS 210
 - in astrodome 229
 - in radome 226
 - open BUS 208
 - summary 258
 - ventilated BUS 216, 217
- C**
- Cassegrain telescope
 - example 18
 - optics 15
 - system parameters 16
- Central hub
 - construction 32, 199, 202
 - temperature measurement 202
- Climate zone 56
- Climatisation 24, 222
 - thermal model of 292
- Cloud
 - coverage 79
 - temperature 75
- Coefficient of
 - absorption, radiation [a] 141, 142
 - emission, radiation [e] 142
 - heat capacity [\mathcal{C}] 126
 - heat conduction [k] 127
 - heat convection [h] 131, 133
 - reflection, radiation [ρ] 141
 - thermal expansion [α] 44
 - transmission, radiation [τ] 141
- Coma
 - beam pattern 315
 - equation 315
 - measurement 316
 - thermal tolerance 335
- Communication antennas xiii, 9
- Condensation 41, 71
- Conductance
 - convective 131
 - radiative 144
 - thermal 129, 133
- Conservation, energy, heat 123, 152
- Constants
 - fundamental 359
 - thermal 359
- Contact resistance *see* thermal resistance
- Convection
 - forced 134, 139
 - natural 138, 140
- Convective conductance 131
- Coordinate system
 - horizon 85, 86
 - thermal 153
- Culmination *see* Sun

D

De-icing

- beam pattern
 - degradation 72, 323
 - Zernike polynomials 353
- measurement 239, 240, 250
- necessity of 71
- power 72, 250

Declination *see* Sun

Defocus

- beam pattern 314
- equation 314
- measurement 315
- thermal tolerance 329, 333

Deformations

- reflector, wave front 313

Dew point temperature 73

Diameter

- electromagnetic 7, 8
- reflector 31, 33, 34
- relation to mass 31, 33

E

Elevation structure 19

Enclosure

- astrodome 49
- optical telescope 343
- radio telescope 49, 226
- radome 49

Energy balance calculation 300

Environment

- ambient thermal 55
- space 83

Error budget

- classic 341
- thermal 352

F

Façade

- chimney experiment 270
- thermal model 284
- thermal model calculation 286
- thermal protection with 284

Finite element

- analysis 31, 352
- model 271
- temperature interpolation 111

Flexible body analysis 352

Focus

- change, measurement 73, 225, 326
- error 13
- primary observing mode 15
- Primary, secondary
 - Cassegrain 16
 - Gregory 17
- ratio 14, 16
- stability 13
- thermal tolerance 329, 332, 336

Focus cabin 43

Fork mount

- path length 186, 192
- pointing error 186, 187
- telescope with 12
- temp. measurement 187, 257, 288
- temperature gradient 187
- thermal
 - construction 47, 282
 - model 282
 - protection 187, 284
 - tolerance 330

Fourier transform, optics 8, 308

Fourier's law (heat conduction) 127, 152

Frost 71

Future Design 355

GGain, of a telescope *see* aperture efficiencyGoretexTM material 52

Grashof number 138

Gregory telescope

- example 18
- off-axis system 18
- optics 15, 17
- system parameters 18

- Ground
 temperature
 approximation 70
 general 69
 measurement 69
 thermal properties 69
- H**
- Heat content 126
 Heat transfer
 combination of 132, 145
 conduction 127
 convection 130
 forced 134
 natural 138
 parameters 359
 modes of 123
 radiation 141
 Homology, reflector 34
 Honeycomb, panel core 28, 40, 48, 275
 Horizon coordinate system 85, 86
 Humidity
 measurements 71, 73, 74
 related formulas 73
 Huygen's principle 305
- I**
- Ice
 de-icing 71
 on telescope 71, 163
 possible damage by 72
 Image (focal) plane 306
 Infinite thermal reservoirs 55
 Influence matrix (thermal) 111
 Infrared radiation, thermal 142
 Infrared windows *see* atmosphere
 Insolation
 incident 81, 89
 manipulation of 79, 102
 measurement
 Chajnantor 81
 Metsähovi 264
 Plateau de Bure 81
 parabolic reflector 92
- Interferometer array
 connected 9
 path length change 186,
 194, 258
 VLBI 9, 181, 196
 reference height 192, 196
 Invar ring (BUS support)
 construction 201
 temp. measurement 203
 Irradiation *see* insolation
- L**
- Lambert scatterer 105
 Laminar flow
 characteristics 133, 135
 heat transfer of 136
 Laser metrology 191, 194
 Louvre 52, 54, 298
- M**
- Meteorology
 design specifications 82
 measurement of 58
 site tests 56
 Misalignment
 Cassegrain, Gregory system 331
 telescope optics 18, 333
 thermal tolerances 334
- N**
- Newton's law *see* heat convection
 Node structure, thermal 273
 Nusselt number 135
- O**
- Observatory sites
 climate zone 56
 pictures of 60
 testing of 56
 Off-axis telescope 2, 18, 242
 Optical configurations 14
 Ozone absorption *see* atmosphere

P**Paint**

- aging 144, 350
- infrared emission 145
- radiation scattering 103
- solar absorption 81

Paint factor 143**Panel**

- actuators *see* reflector surface
- buckling 234, 317
- construction 38, 48, 232
- deformation 234, 317
- frame 40
- heating 28, 239
- mass 40
- size 38
- support 40
- thermal
 - buckling, sag 239
 - calculation 277
 - construction 48
 - gradient 237
 - model 275
 - tolerances 331
- type
 - alum. honeycomb 28, 40, 232, 275
 - machined 40, 232
 - mesh wire 38, 232
 - perforated plate 38
 - spin cast 38

Panel temperature measurements

- buckled panels 238, 239
- frame 239
- gradient 240
- on telescope 234, 235, 238, 241
- test panel 234

Parabolic reflector

- radiative coupling to
 - ground 166, 167
 - sky 166, 167
- shadow line in 92
- solar illumination (power) 94
- telescope 14

Path length 192**Path length measurement** 194, 196**Pedestal**

- examples 174
- height (VLBI) 196
- inclination 175
- mount, with fork 12, 25
- mount, with yoke 11, 22
- telescopes with (schematics) 11, 12, 23, 27
- temperature measurement 176, 257
- thermal construction 47

Performance criteria *see* stability criteria**Planck's radiation law** *see* black body radiation**Pointing error**

- alidade 178
- fork 186, 191
- measurement and correction
 - IRAM 30-m 326
 - IRAM PdB 192
- pedestal 175
- quadripod 242
- thermal tolerance 335

Pointing model 175, 363**Prandtl number** 134**Q****Quadripod**

- climatisation 245, 246
- general 43, 242
- temp. measurements 243–245
- thermal construction 48, 242
- thermal tolerance 335, 336
- ventilation 242

R**Radiative conductance** 144**Radio emission processes** 2**Radio spectrum** 1, 2**Radio telescopes**

- construction 10, 18, 19, 21, 22, 26
- description

- Effelsberg 20
- IRAM 15-m, SEST 26
- IRAM 30-m 22
- stability criteria 13
- thermal aspects 14
- Radio window 1
- Radiosity 147
- Radome
 - dimension 51
 - internal climate 263, 264
 - radiative coupling
 - to ground 165
 - to sky 165
 - skin material 52
 - solar illumination 99
 - solar radiation
 - entering 54, 99
 - reflected 54, 99
 - transmitted 54, 99
 - temperature measurement
 - Metsähovi 264
 - MIT-Haystack 265, 300
 - Onsala 300
 - thermal model
 - MIT-Haystack 298
 - Onsala 298
 - thermal parameters 54
 - ventilation 54
 - view factor of 165
- Random surface errors *see* wavefront deformation
- Reflection, from panel
 - diffuse 103
 - scattered Gaussian 105
 - scattered Lambert 105
 - specular 103
- Reflector surface
 - active 42, 225, 347
 - deformation *see* wavefront deformation
 - error
 - random 318, 337
 - systematic 313
 - homology 34
 - view factor 166
- Reynolds number 134
- Root-mean-square value (rms) 361
- Ruze relation 319
- S**
- Scale height *see* atmosphere
- Site tests 56
- Sky
 - effective temperature 71, 164
 - calculation of 75, 77, 79, 164
 - measurements of 75, 76
 - emission coefficient 78
- Snow
 - de-icing 71
 - thermal properties 69
- Solar constant 80
- Solar illumination
 - backup structure
 - closed 96
 - open 96
 - box-type enclosure 97
 - cylindrical enclosure 98
 - of a tube 91
 - of astrodome 98
 - of Onsala radome 101
 - of radome 99
 - parabolic reflector 92, 288
 - plane surface, horizontal 89
 - plane surface, vertical 89
 - power
 - at ground level 80
 - in space 80
 - on curved reflector 94
 - subreflector 104
- Solar observation
 - illumination subreflector 104
 - panel scatter function 104
- Solar radiation, incident *see* insolation
- Space
 - environment 83
- Specifications
 - error budget 341, 352
 - meteorological design 82

Stability criteria, of telescope 13

Stefan Boltzmann law 142

Subreflector

construction 43, 246

misalignment 315, 331, 335

solar observation

CARMA 249

IRAM 30-m 248

VertexRSI 12-m 249

solar power load 104

temperature measurement 247–
249

Sun

apparent motion 85

culmination 86

declination 86, 87

effective temperature 80

elevation 86

hour angle 85

radiation spectrum 80

shine, duration 87

sunrise, sunset 86

Surface deformation *see* wavefront
deformation

Surface finish

grooves 103

paint 103

sand blasted 103

scattering 104

specular reflection 104

Swinbank–Nowak relation 76

Systematic surface errors *see* wave-
front deformation

T

Taper

Gaussian 310

influence on beam pattern 311

parabolic 310

receiver weighted 308

Telescope

Cassegrain 15

Gregory 15

off-axis 2, 18, 242

parabolic reflector 14

Telescope components

alidade 19, 20

central hub 26, 28

counterweight(s) 19

focus cabin 19, 43

fork 19, 25

pedestal–fork 25

pedestal–yoke 22

quadripod 19, 43

reflector 14

active 42, 225, 347

backup structure 19, 29, 34, 35

panels 38

subreflector 19, 43

yoke 22

Telescope mount

alidade 19

pedestal–fork 25

pedestal–yoke 22

Telescope pictures 2–7

Temperature

Celsius 107, 357

Fahrenheit 107, 357

Kelvin 107, 357

Temperature data collection 348

Temperature induced deformations

empirical relations 120

prediction of

focus variation 119

pointing variation 119

reflector surface error 118

Temperature measurement

(telescopes)

alidade 180

BUS

climatised 214, 222

closed 209, 211, 212, 214

de-icing 250

open 206, 209

ventilated 216

central hub 202

fork 188, 286, 287

fork path length 194

invar ring (BUS support) 202

monitoring 258, 259

panels 234

- quadripod 243, 244
- subreflector 247, 249
- yoke 199
- Temperature sensing
 - infrared sensor 110
 - on telescopes 109
 - precision 118
 - related measurements 120
 - resistance sensor 108
 - sampling rate 110
- Temperature sensor
 - location 111
 - on telescopes 109
- Temperature uniformity
 - telescope components 257, 258
 - telescopes, integral 251, 258
 - Effelsberg 100-m 251
 - IRAM 15-m 252
 - IRAM 30-m 254
 - VertexRSI ALMA-12m 252
- Thermal conductance 129, 133
- Thermal design
 - operating telescopes
 - BUS 47
 - mount 47
 - panel 48
 - quadripod 48
- Thermal environment xii, 55, 274
- Thermal expansion coefficient *see* coefficient
- Thermal facade *see* facade
- Thermal model
 - alidade beam 279, 280
 - dynamic 271
 - environmental input data 274
 - fork 282, 284, 287
 - mechanical 268
 - node structure 273
 - panel
 - honeycomb core 276, 278
 - plate 275
 - precision 303
 - programmes 273, 304
 - purpose 267
 - servo-loop control 299
 - specific
 - IRAM 15-m fork 284, 286
 - IRAM 30-m BUS, yoke 293
 - MIT Haystack radome 297
 - Onsala radome 299
 - static 271
 - summary 274
 - yoke 281
- Thermal model calculation
 - alidade beam 281
 - BUS
 - climatisation 295
 - closed 291
 - natural ventilation 291
 - open 289
 - ventilation 295
 - energy balance 301
 - operational purposes
 - BUS heating, cooling 302
 - BUS ventilation 303
 - panel
 - heated 279
 - honeycomb 279
 - plate 276, 277
 - radome, astrodome 300
- Thermal protection
 - climatisation 24
 - insulation 283
 - means of 45
 - paint 103
 - summary 46
 - surface finish 102
 - ventilation 38, 39
- Thermal resistance
 - combination
 - in sequence 128
 - parallel 129
 - conduction 128
 - contact 284, 351
 - convection 131
 - radiation 144
 - through pipe 130, 133
 - through plate 128, 132
- Thermal state
 - non-steady 155

- steady 155
 - Thermal time constant
 - examples 158
 - external 155, 157, 158
 - FCRAO telescope 231
 - for convection 155
 - for convection and radiation 158
 - for radiation 157
 - in trouble shooting 259
 - internal (conduction) 159
 - IRAM 15-m fork arm 156
 - Thermal tolerances
 - alignments, optical system 331, 336
 - beam deformations 322
 - BUS 328, 335
 - panel 331
 - pointing errors 335
 - quadripod 335
 - reflector diameter 327
 - reflector surface error 337
 - stability *see* stability criteria
 - telescope support
 - alidade 330
 - fork 330
 - path length 330
 - Thermal trouble-shooting 258
 - Thermodynamic law 123
 - Turbulent flow
 - characteristics 135
 - heat transfer of 136
- U**
- Units
 - conversion 357
 - definitions 357
- V**
- Ventilation
 - BUS 216
 - circular 220
 - climatisation 222
 - radial 220
 - convection
 - forced 139
 - natural 140, 350
 - installed 38, 39
 - power 39
 - quadripod 48
 - subreflector 249
 - yoke 198
 - View factor
 - BUS network 151, 349
 - definition 142
 - external 161
 - internal 149
 - paint factor 143
 - parabolic reflector 350
 - parallel disks 151
 - plate
 - parallel 143, 149, 150
 - right-angle 149, 150
 - to ground 163
 - to sky 164
 - radiative heat transfer 125
 - radome 165
 - reflector
 - to ground 169
 - to sky 169
 - theorem
 - additive 148
 - enclosure 149
 - reciprocal 148
 - VLBI *see* interferometer
 - von Hoerner-diagram x, 29, 327
- W**
- Water vapour
 - altitude dependence 58
 - sky radiation 73
 - Wave propagation 305
 - Wavefront deformation
 - random 318, 321
 - repetitive 316
 - systematic 313, 321
 - tolerance 309
 - Wiens's law 141
 - Wind

- daily profiles 65, 68
- direction, prevailing 59, 66
- measurement 59, 65
 - Chajnantor 67, 68
 - Effelsberg 67, 68
 - PdB 66
 - Pico Veleta 67, 68
 - VLA 66
- seasonal profiles 67, 68
- speed and direction 65
- studies 67
- thermal influence 65, 68
- vertical profile 57, 59

Y

Yoke

- construction 32, 47
- temperature measurement 198, 199
- thermal deformation
 - induced astigmatism 197
 - print-through 197, 199
- thermal model 281

Z

Zernike polynomial

- mathematical relation 367
- reflector surface
 - design optimization 353
- reflector surface deformation
 - de-icing 324
 - gravity 353
 - thermal 353